Luminescent Cyclometalated Ruthenium Complexes

A thesis submitted in partial fulfillment of
the requirements for the degree of
Doctor of Philosophy in Chemistry at the
University of Canterbury.

Robert Bruce Currie

University of Canterbury
Christchurch
New Zealand
2014

Dedicated to my mother, Jennifer Ann Binns,

for always putting Dave and me first, no matter the obstacle.

Perseverance produces character; and character gives hope.

Romans 5:4

Acknowledgements

This work would not have been possible without the help of a large number of people, both here at Canterbury University and throughout the world. I loved my time working on this thesis and I could not have imagined a project that would have suited me any better.

My supervisor, Dr. Chris Fitchett, inspired me through all the challenging moments of this work, always coming up with alternative methods or ideas. He really is an amazing supervisor and a credit to Canterbury University. Dr. Sarah Masters had a large part in introducing me to the world of computational chemistry. Dr. Masters also had access to the NSCCS supercomputer at Imperial college London which was crucial to the computational calculations we completed in this work. She helped to show me the benefit of using calculations in parallel with experimental work. Prof. Peter Steel always shared his extensive knowledge in all areas of chemistry and was very helpful during the course of my PhD. Dr. Matt Polson is another extremely helpful and knowledgeable person and I was very grateful for his help over the last few years. Dr. Paula Brooksby taught me how to use the cyclic voltammetry equipment and extending my knowledge of electrochemistry. Prof. Bryce Williamson offered his expertise in running our luminescence measurements and provided the necessary equipment for measurements at 77 K. Dr. Marie Squire ran all mass spectrometry sample analysis and maintained the NMR instruments. I would also like to thank Dr. Richard Garland for giving me financial assistance to complete this work.

All of the work in this thesis would not have been possible without all of the technical staff, especially Wayne Mackay, Nick Oliver, Rob McGregor, Gill Ellis and Laurie Anderson. We needed a large amount of specialist equipment for this work and Wayne and Nick always came up with new designs that were required for our work. We also needed a large amount of specialist glass equipment, for which Rob was especially helpful. Gill and Laurie were both very good to me during my time at Canterbury University and I thank them for the work they do in the chemical store room.

I was very lucky to have the help and friendship of a large number of students here at Canterbury University and I really valuable their support over the last few years. I would like to particularly thank Jayne, Paul, Will, Nic and Samantha from the Fitchett group and Siji, Rakesh, Solomon, Chris, Marky and Dave from the Steel and Kruger groups.

During my time away from the lab, I was lucky to have some amazing friends who kept me going and who were always there for me when needed. I would like to acknowledge the Scott family; Donald, Janice, Jonathon, Shannon, David, Caleb, Harriet and Joseph who have been a massive part of my life in Christchurch. I also had the pleasure of being part of the Christchurch Cavaliers football team, and together we won every tournament, league or cup we played in at some point over the last five seasons. I'm especially grateful to our manager and my very good friend, Sofi Crosley, who I will miss very much once I leave Christchurch. I would also like to thank my good friend Pavithra Vigneswaran for inspiring me to study chemistry nearly a decade ago.

I'm also very lucky to part of several loving families who have inspired and looked after me during my time in Christchurch. I'm especially grateful for my grandparents; Helen and David Binns, who have always been a major part of my life. Grandma offers every single person she meets unconditional love, and has been very generous to me during my lifetime and Granddad inspired my inquisitive nature and love for science and technology, and always took a special interest in my life.

The biggest thank you of all needs to go to my close family; my mother Jennifer Binns, my father Bruce Currie, my brother David Currie and his wife Inga Nemirovskaia, and my wife Kylie Currie, who have given me never-ending support throughout my life, but especially during my time here at Canterbury. Mum constantly went the extra mile to help, any possible way she could. Dave was always there inspiring me as we were growing up, and despite living a whole world away, is still very important to me. Both him and Inga keep me going. Kylie was the one there on the front line helping me every day, coming to work when I needed a safety buddy or just moral support. We definitely got through this together as we're very much a team, in everything we do. All these people were the ones who kept me going through earthquakes, floods, snow storms, equipment failure and general fatigue on the quest to complete this work.

I really hope you enjoy reading my thesis. I have thoroughly enjoyed my time doing this work, learning a broad range of new synthetic and analytical techniques. It means a lot to me, so thank you for spending time to read my work.

Table of contents

Abstract:

This thesis describes the synthesis and structural characterisation of cyclometalated heteroleptic bis(tridentate)ruthenium(II) complexes based on [Ru(terpyridine)(1,3-dipyridylbenzene)]PF_6, a cyclometalated analogue of [Ru(terpyridine)$_2$]$(PF_6)_2$. These complexes are investigated photophysically, photochemically and electrochemically, and also studied by computational methods.

Electron donating, electron withdrawing and large aryl groups have been incorporated at three different positions, and pyrazol-1-yl or 1,2,3-triazol-4-yl used as the N-heterocycle instead of 2-pyridyl groups, as in the parent complex, [Ru(terpyridine)(1,3-dipyridylbenzene)]PF_6. The ligands are substituted at the 4 position of the central benzene or pyridine ring, or attached to the N-heterocycle.

The positions of these modifications have been specifically chosen to direct electronic effects into the Ru-C bond, the opposite Ru-N bond or directly into the N-heterocycle to analyze their effect. This has provided an understanding as to which stereoelectronict features are most important with regards to changing the electronic nature of the complex, and thus tuning the properties of these complexes. This proves particularly effective in analysing the energy of the visible absorptions resulting from metal-to-ligand charge transfer and emission energy and its related quantum yield.

Abbreviations

bpy	2,2'-bipyridine
CD_3Cl	Chloroform-D3
CD_3CN	Acetonitrile-D3
CH_3CN	Acetonitrile
CIS	coordination induced shift
COSY	correlation spectroscopy
DFT	Density Functional Theory
DMF	Dimethylformamide
DMSO	Dimethyl sulfoxide
dpybH	1,3-dipyridylbenzene
ESI–MS	electron spray ionisation mass spectrometry
eV	electron volts
HMBC	heteronuclear multiple–bond correlation spectroscopy
HOMO	highest occupied molecular orbital
HSQC	heteronuclear single–quantum correlation spectroscopy
ISC	intersystem crossing
LUMO	lowest unoccupied molecular orbital
^{3}MC	metal-centred triplet state
MLCT	metal–to–ligand charge transfer
mV	millivolts
NMR	nuclear magnetic resonance
OLED	organic light-emitting diode
SOC	spin-orbit coupling
TD-DFT	Time Dependent-Density Functional Theory
TOCSY	total correlation spectroscopy
tpy	2,2':6',2''–terpyridine

.

CHAPTER 1

INTRODUCTION

1. Introduction.

Ruthenium(II) polypyridine complexes have been the subject of a large amount of research, especially in areas of photochemistry, owing to their long excited state lifetimes and relatively high quantum yields at room temperature.[1-5] Longer lifetimes are often (but not exclusively) considered to be beneficial, as this means the excited state is available for longer and thus can be used in a range of applications, such as photosensitizers, which are used in solar energy conversion,[6] photoluminescent (bio)sensors[7] or electroluminescent dyes in organic light-emitting devices.[8-9] Increasing the excited state lifetime and quantum yields further will increase the efficiency of these applications.

Ruthenium has a high spin-orbit coupling (SOC) constant, which dramatically increases the rate of intersystem crossing (ISC) between the ^{1}MLCT and ^{3}MLCT, meaning that, upon excitation, the lowest energy triplet state is populated almost instantaneously.[10] Fast ISC and high yields of triplet formation are also possible in organic compounds,[11] but the extent to which the high SOC in ruthenium complexes can violate the spin selection rule ($\Delta S = 0$) is much greater. This significantly increases the rate of radiative decay from the triplet state and allows phosphorescence to compete with non-radiative decay pathways that would normally predominate at room temperature.[12] Since $T_1 \rightarrow S_0$ transitions are still only partially allowed, the lifetime of phosphorescence is typically significantly longer than fluorescence lifetimes, often being of the order of a microsecond rather than a subnanosecond.[13]

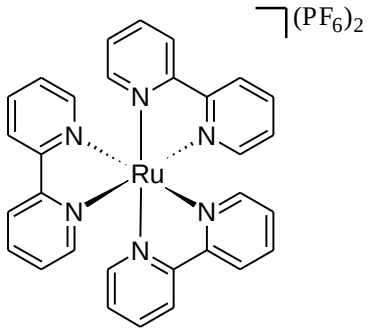

Figure 1.1: Structure of $[Ru(bpy)_3](PF_6)_2$.

The interest in these systems initially resulted from the desirable photochemical properties of $[Ru(bpy)_3](PF_6)_2$ (Figure 1.1), which was first isolated by Burstal in 1930.[14] It was found that

the complex is photostable, with an emission lifetime at room temperature of 640 ns in acetonitrile and has a quantum yield of 6.2% at room temperature. At 77 K its emission lifetime is significantly increased to 5 μs and its quantum yield is increased to 0.38.[15] Ruthenium(II) polypyridine complexes are also diamagnetic which enables a range of spectroscopy studies, such as ^{1}H and ^{13}C NMR spectroscopy, to analyze their solution state structures.

Since the original discovery of $[Ru(bpy)_3](PF_6)_2$, research has focused on synthesizing new complexes which utilize ligands similar to 2,2'-bipyridine (bpy), with the goal of modifying the electronic properties of the system, and thus the energy of the visible absorption and emission profiles and also increasing the lifetime and quantum yield of emission at room temperature.

The ruthenium atom at the center of the complex is a key reason for the observed photophysical and electrochemical properties of these complexes. Ruthenium (II) is a d_6 metal which has the propensity to form octahedral or pseudo-octahedral complexes. Polypyridyl ligands, such as 2,2'-bipyridine, chelate the ruthenium through σ-donating nitrogen atoms and π* accepting orbitals from the aromatic framework of the ligand (Figure 1.2)

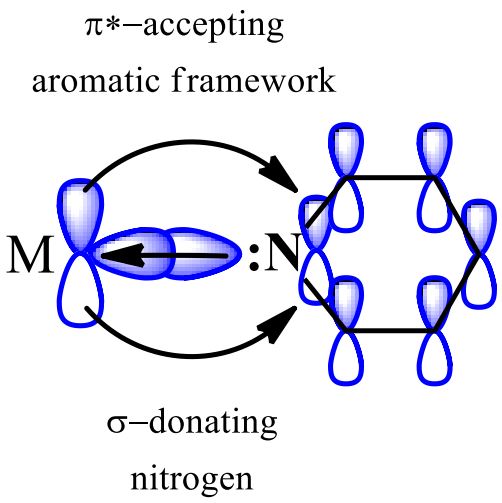

Figure 1.2: Molecular orbital diagram showing σ-donating nitrogen atom and π* accepting orbitals of the aromatic framework of the ligand.

Analysis of the molecular orbitals of $[Ru(bpy)_3](PF_6)_2$ reveals the key components are the π-bonding and π*-antibonding orbitals centered on the bipyridine ligands and the 4d orbitals on the metal center and a general molecular orbital diagram for $[Ru(bpy)_3](PF_6)_2$ is shown in Figure 1.3.

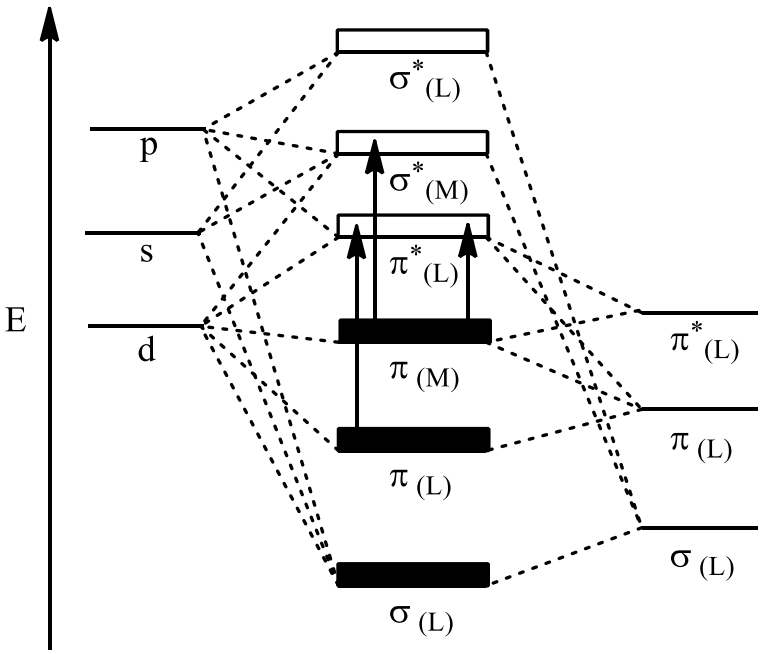

Figure 1.3: Block molecular orbital diagram for a general ruthenium complex, with arrows indicating the ligand centered transition (left), metal centered transition (middle) and metal-to-ligand charge transfer transition (right).

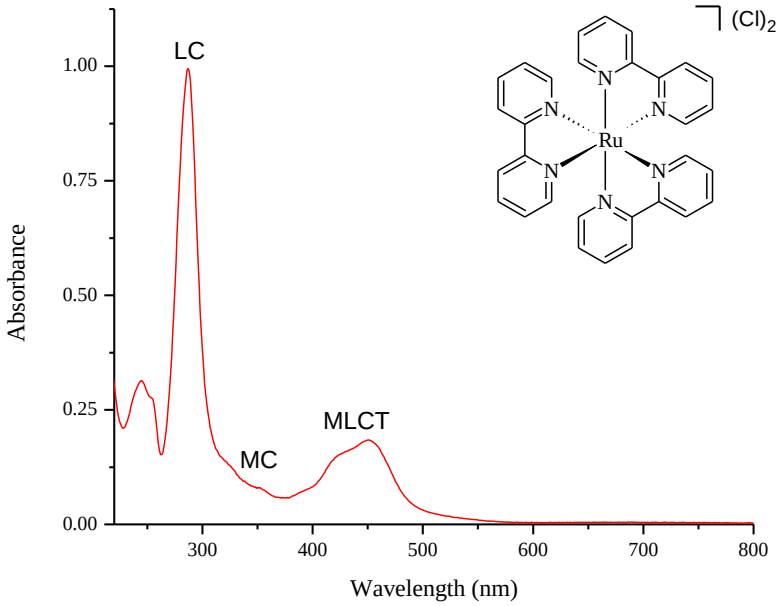

Figure 1.4: UV-Vis spectrum of $[Ru(bpy)_3](Cl)_2$ in acetonitrile.

The important electronic transitions for $[Ru(bpy)_3]^{2+}$ are indicated in Figure 1.4. The most important is the metal-to-ligand charge transfer (MLCT) transition in the visible region of the UV-vis. The other being the strong $\pi \rightarrow \pi^*$ (LC) transition in the UV region. The metal centered (MC) transition is weak, as it is symmetry forbidden by the Laporte selection rule ($t \rightarrow e$).

1.1 Ruthenium bis-2,2':6,2"-terpyridine complexes.

Among the large number of ligand modifications used to form ruthenium (II) polypyridine complexes is 2,2':6,2"-terpyridine (tpy), which forms the complex $[Ru(tpy)_2](PF_6)_2$ (Figure 1.5).

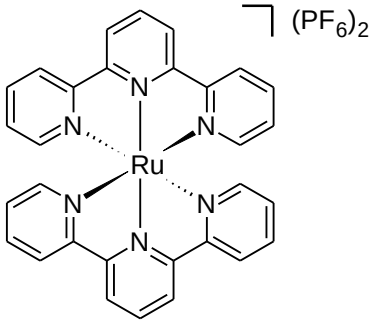

Figure 1.5: Ruthenium complex $[Ru(2,2':6,2"\text{-terpyridine})_2](PF_6)_2$

$[Ru(tpy)_2]^{2+}$ type structures have a distorted octahedral geometry, with each ligand coordinated in a tridentate, meridional fashion to the ruthenium(II) ion. The geometric distortion results from the need to fit both terpyridine ligands around the metal center. A search on the Cambridge structural database[16-17] shows that the mean bond angle (N-Ru-N) for nitrogen atoms on adjacent pyridine rings in $[Ru(tpy)_2]^{2+}$ and $[Ru(bpy)_3]^{2+}$ based complexes are similar at 78.9° and 78.8°, respectively. The chelate bite angle is defined in this work as the angle between the two terminal, coordinated nitrogen atoms on the same ligand and the ruthenium metal center (N1-Ru1-N3, Figure 1.6).

The mean chelate bite angle $[Ru(tpy)_2]^{2+}$ type complexes is 157.8° and the mean angle between trans nitrogen atoms and ruthenium for $[Ru(bpy)_3]^{2+}$ type complexes is 172.9°.[16-17] This shows the geometric constraints of the $[Ru(tpy)_2]^{2+}$ system, which results in lower ligand field splitting. This means that the metal centered (^{3}MC) states are thermally accessible to the ^{3}MLCT, which quench the emission via non-radiative decay processes,[1] resulting in shorter excited-state

lifetimes and lower room temperature emission quantum yields compared to $[Ru(bpy)_3]^{2+}$ type complexes.

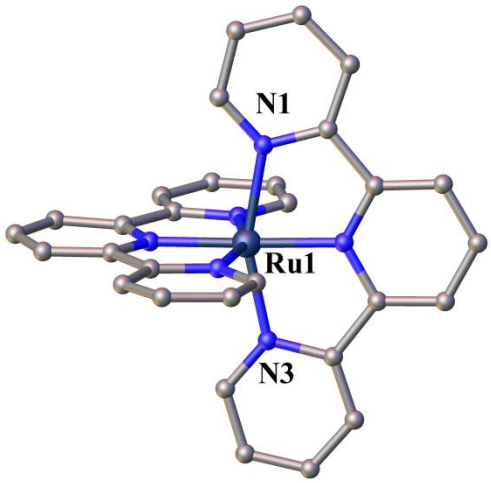

Figure 1.6: Structure of $[Ru(tpy)_2](PF_6)_2$, showing the chelate bite angle formed between N1-Ru1-N3.

Despite this, bis-tridentate ruthenium complexes offer a range of advantages, primarily that they offer the possibility of controlling the stereochemistry. By using two symmetrical tridentate ligands about the octahedral metal center only a single stereoisomer is formed with D_{2d} symmetry, in contrast to $[Ru(bpy)_3]^{2+}$. Substitution at the 4' position of the central pyridine ring can be achieved without necessarily altering the symmetry of the overall complex, thus it provides a route to generating a diverse range of complexes, without the added difficulty of diasteriomers and enantiomers being formed. Another benefit of using tridentate ligands, such as terpyridine is that they have a stronger chelate effect, due to additional coordination compared to bipyridine systems. In photovoltaic applications, the excited state of the complex occurs when an electron is promoted into the LUMO, which is generally a π*-antibonding orbital and thus dissociation of the ligand can occur. In tridentate systems the tridentate ligand is less likely to fully dissociate which can lead to longer emissive lifetimes.

In order for tridentate systems to compete with $[Ru(bpy)_3]^{2+}$ and to gain access to the benefits of tridentate systems, changes to the structure of the complex need to be made to increase the emission quantum yield and excited state lifetime. A common method of achieving this is to increase the energy gap between the radiative ^{3}MLCT and quenching ^{3}MC states. This can be achieved by substitution of the terpyridine ligands with electron withdrawing functionalities,[18]

or introduction of coplanar aromatic groups[19] which can produce enhanced emission lifetimes as it establishes a population equilibrium between ^{3}MLCT and the chromophore ^{3}LC states. Despite its effectiveness, the problem with this strategy is that it uses the same substitution positions that would be used to build larger systems.

Another approach to increase the ligand field splitting is to more clearly match a octahedral coordination geometry around the ruthenium metal center by using ligands with larger bite angles (Increase chelate bite angle of N1-Ru1-N3, Figure 1.6).[20-22] Recent work has investigated the effect of using ligands which allow bite angles closer to 180° when co-ordinated to ruthenium.[23] The resulting bistridentate ruthenium complexes exhibited up to microsecond excited state lifetimes at room temperature, and while it was demonstrated that extended bite angles did not necessarily ensure long life times by themselves, it was shown to be a contributing factor.

1.2 N^C^N cyclometalated complexes.

An alternate strategy that has recently shown very promising results uses cyclometalated complexes to tune the frontier orbital energies. In cyclometalated ligands the nitrogen atom is replaced with an anionic carbon, which dramatically changes the electronic properties of the complex.[24-26] Because only a nitrogen donor atom is replaced by a carbon donor atom, the overall geometry of the complex remains the same, but the charge of the complex is decreased. Using complexes of this type has been shown to enable room-temperature luminescence, with both N^C^N or C^N^N binding motifs (Figure 1.7).[27-29]

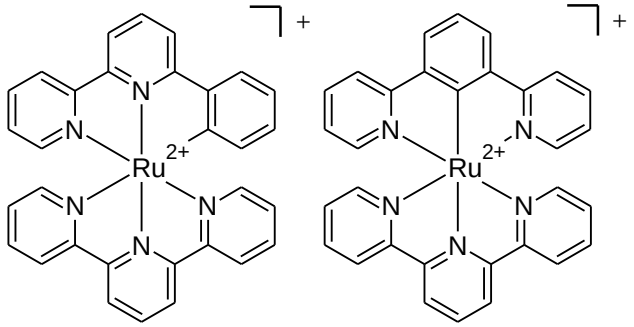

Figure 1.7: Two types of cyclometalating binding motifs, N^N^C (left) and N^C^N (right), which are bound to a typical ruthenium/terpyridine system.

Cyclometalation processes use an activated C-R bond (R = -H, -OMe, -halogen) to generate a metal-carbon bond and a metallacycle.[30-31] This procedure was discovered in the early 1960s and has since been widely used for forming organometallic bonds. Due to the stability of C-H bonds, cyclometalation generally occurs as an intramolecular metalation with formation of a chelate ring containing a metal-carbon σ-bond. In the case of cyclometalated ruthenium complexes, cyclometalation is promoted by the specific ligand shape (N^C^N), in which the ruthenium can coordinate to the available nitrogen atoms, which can hold the ruthenium atom in position and promote cyclometalation. Once the Ru-C bond forms, it is locked in position as the Ru-C bond is very strong,[32] generating the target complex. There are four different general mechanisms by which C-H activation can occur; oxidative addition, electrophilic metalation, concurrent metalation-deprotonation and an agostic pathway; all of which are shown in Figure 1.8.

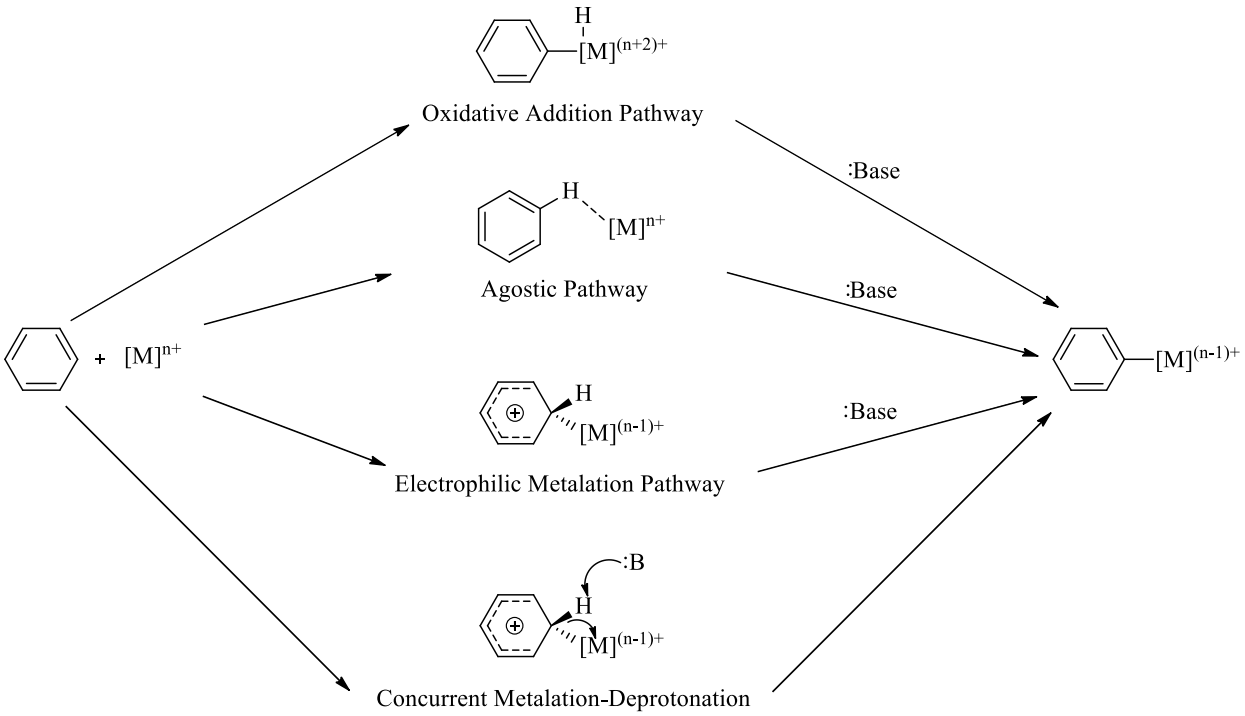

Figure 1.8: Four different potential pathways for C-H activation.

The most likely metalation pathway for the ruthenium complexes formed during this work is electrophilic metalation because the water/ethanol mixtures used have been found to be effective at stabilizing the loss of H^+. The concurrent metalation-deprotonation pathway is also possible as

several of the cyclometalation reactions occur faster with a small quantity of triethylamine.[33] The oxidative addition pathway requires two vacant sites on the ruthenium for the formation of both M-C and M-H bonds and this is unlikely to occur with $[Ru(tpy)Cl]_3$, a typical precursor in these types of reactions, as it is improbable for the terpyridine ligand to dissociate due to the chelate effect[34] and while the chlorides will dissociate in the ethanol/water reaction solution, they will be replaced by solvent and the ruthenium will not have vacant coordination positions. The oxidative addition pathway also requires the ligand to orientate the C-H bond with respect to the accepting ruthenium orbital and this is unlikely to occur due to steric hindrance. It is also unlikely that an agostic cyclometalation pathway occurs for these cyclometalated ruthenium complexes, in which the ruthenium is σ-bonded to the hydrogen.[35]

While both binding motifs (N^C^N vs. N^N^C) are potentially interesting, N^C^N binding types are favorable due to their symmetry. Cyclometalating ligands which have intraligand π-π interactions have been shown to be more likely to produce efficient luminescence, although complexes do not always produce luminescence at room temperature due to non radiative decay pathways that can occur. Methods of preventing these pathways are being investigated.[36] Since the original work by van Koten and co-workers regarding cyclometalated ruthenium complexes as promising dyes for DSSCs,[37-38] there has been a range of research in this area, namely studies by Berlinguette,[39-40] Nazeeruddin[9] and Zhong.[27, 29, 41-42] Most modifications to the cyclometalated ligand, compared to 1,3-di(2-pyridyl)benzene (dpybH), have investigated extending the central benzene ring with electron withdrawing/donating groups. Other approaches have swapped the 2-pyridyl rings on the cyclometalated ligand with an alternative N-heterocycle. This has been briefly explored using benzimidazole as the N-heterocycle and also by using 1,2,3-triazole substituted ligands synthesized by using CuAAC "click" chemistry reaction conditions (see section 1.7.5 Triazole synthesis, via "click" chemistry for further details).

Pyrazole, an electron rich 5-membered N-heterocycle, has been used previously in cyclometalated complexes, however not with ruthenium. Williams and co-workers have used pyrazole in a range of their platinum cyclometalated complexes[43] to give interesting results and while the platinum cyclometalated system is inherently different to the ruthenium system, it shows various effects that can occur by changing 2-pyridine for pyrazole. While ruthenium is the focus of this work, there are other metals which can be used with polypyridyl ligands to produce

complexes which absorb in the visible spectrum, such as iridium,[44-46] rhodium,[47-48] and platinum.[43, 49-51]

1.3 Large aromatic systems.

Large aromatic systems can also be incorporated onto a ruthenium(II) complex to impact the energy of an electronic system, by acting as an additional chromophore. While electron withdrawing/electron donating groups are known to have an important effect on the wavelength of transitions that are measured,[52] the properties of large aromatic systems can also be introduced to show similarly interesting effects.

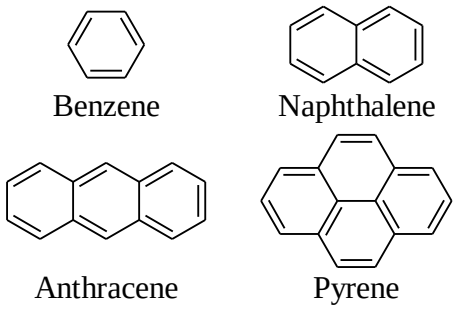

Figure 1.9: Benzene and Three polyaromatic hydrocarbons (PAHs) important to this work.

Polycyclic aromatic hydrocarbons, PAHs, contain only hydrogen and carbon and are composed of multiple aromatic rings, in which the electrons are delocalized. Common examples included throughout this work are naphthalene, anthracene and pyrene and their structures are shown in Figure 1.9. These conjugated systems can have a large impact on wavelengths and intensities of absorption peaks.[53] The UV-vis spectra for selected PAHs are shown in Figure 1.10, along with the UV-vis spectrum for benzene for comparison. As shown, the peak wavelengths are shifted towards the red. The extinction coefficients for these peaks are also dramatically increased as the size of the PAH is increased, with values of 6,000 $M^{-1}cm^{-1}$ for naphthalene, 9,549 $M^{-1}cm^{-1}$ for anthracene and 83,200 $M^{-1}cm^{-1}$ for pyrene compared to the value of 255 $M^{-1}cm^{-1}$ for benzene.

The effect of conjugation on the molecular orbitals is shown in Figure 1.11, showing the decreased energy gap between the HOMO and LUMO as a result of conjugation. While the energy of the orbitals involved in electronic transitions have fixed values, and as energy is quantized, it may be expected that absorption peaks should be sharp, however in practice this is

rarely observed. Instead, broad absorption peaks are observed, especially for large PAHs. This is because there are a number of vibrational energy levels available at each electronic energy level, and transitions can occur to and from the different vibrational levels. This results in $\pi \rightarrow \pi^*$ transitions getting increasingly broad as the size of the conjugated system increases.

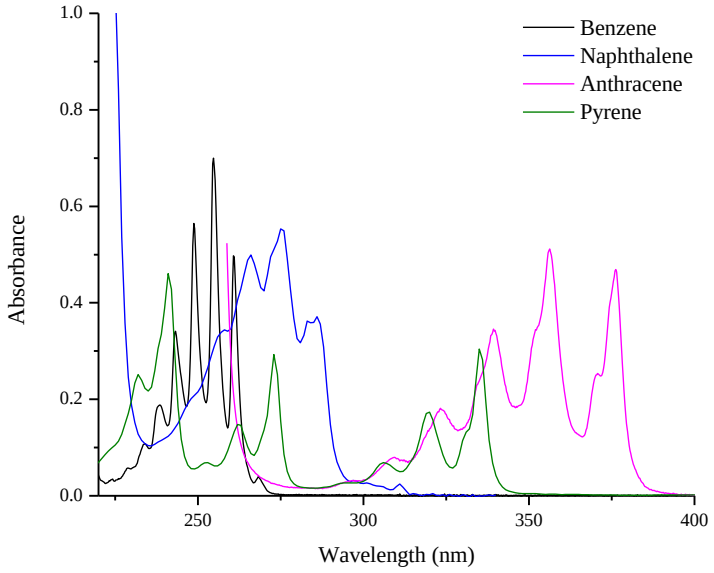

Figure 1.10: UV-vis for selected polycyclic aromatic hydrocarbons. Spectra were measured in cyclohexane with concentrations adjusted to produce peaks with similar absorbance.

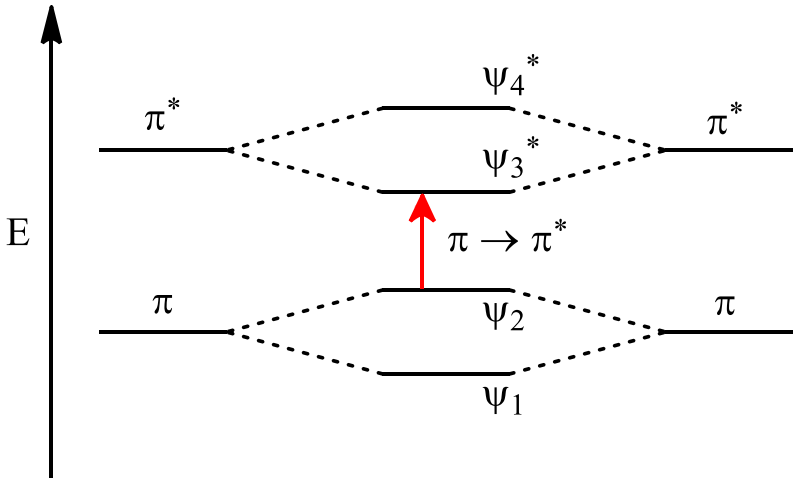

Figure 1.11: Effect of conjugation on orbitals' energy and resulting $\pi \rightarrow \pi^*$ transition for a simple system.

As the electrons in larger conjugated systems have more available space to move, the electrons will have less energy, as shown by the zero-point energy equation (Equation 1.1)[54] which is based on the particle in a box model from quantum mechanics. The particle in a box model describes how a particle is free to move anywhere within its defined space, but cannot leave the system. In the case of PAHs, the electron is free to move anywhere throughout the conjugated system. This shows that the energy is inversely proportional to the square of the distance ($E_1 \propto \frac{1}{L^2}$), and thus the energy is significantly reduced as the distance the particle has to move in (size of the PAH) increases, as shown in the UV-vis spectra for the PAHs (Figure 1.10).

$$E_1 = \frac{\hbar^2 \pi^2}{2mL^2}$$

Equation 1.1: Zero point energy formula, where E is energy, ħ is the reduced Planck constant, m is the mass of the particle and L is the length of the space available that the particle is free to move in.

The nature of the substituents on the cyclometalated ligand is especially important in cyclometalated ruthenium complexes because it will significantly influence the properties of the complex due to the HOMO being delocalised over the metal and cyclometalated ligand. This means that introduction of PAHs will potentially have an interesting effect when combined with cyclometalated ruthenium complexes by means of a red shift or a large increase in the intensity of the peaks.

1.4 UV-vis spectroscopy.

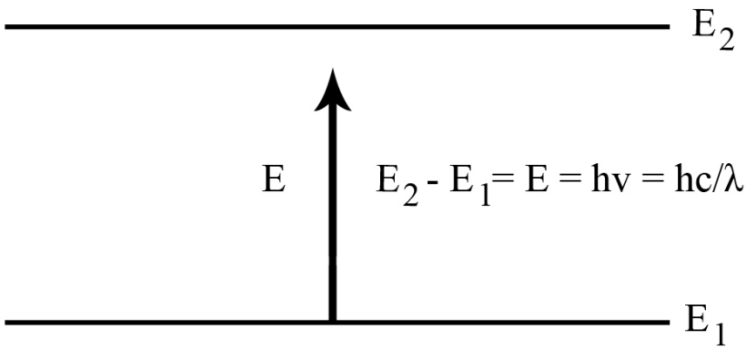

Figure 1.12: General energy transition for the absorption of electromagnetic radiation.

Absorption spectroscopy examines the process of absorption of a discrete amount of energy in a molecule. This is especially important for ruthenium(II) polypyridyl complexes because it shows the wavelength at which the complex absorbs light, which is especially important applications utilizing their photochemical properties, such as solar cells The amount of energy required for the transition from a state of lower energy (E_1) to a state of higher energy (E_2) is exactly equivalent to the energy of electromagnetic radiation that causes the transition (Figure 1.12). Electrons can absorb energy in the form of ultraviolet or visible light, which excites the electron to higher energy molecule orbitals. The lower the energy gap between the HOMO and the LUMO, the easier it is to excite the electron, which results in absorption of longer wavelengths of radiation.[55]

There are four important terms used when comparing absorption shifts. Hyperchromic shifts are when there is a shift to greater absorbance and hypochromic shifts are a decrease in the intensity of the absorbance, which are comparable between compounds once values are converted to extinction coefficients. Bathochromic shifts, also called red shifts, are a shift to longer wavelengths/lower energy and hypsochromic shifts, or blue shifts, are a shift to shorter wavelengths/higher energy.[56]

As discussed polypyridine ruthenium(II) complexes are generally characterized by their medium intensity absorptions in the visible region, which are traditionally assigned as being MLCT transitions[2]. The transitions are in fact a collection of mixed metal/ligand to ligand charge transfer arising from the HOMO being largely metal based but also mixing with part of one or both ligands. Despite this, transitions are described as being MLCT as it offers the most concise description. The MLCT in $[Ru(bpy)_3](Cl)_2$, (Figure 1.4, pg. 4) is at 450 nm and this is red shifted in $[Ru(tpy)_2](PF_6)$ to 476 nm.[39] There is a further red shift in $[Ru(ttpy)_2](PF_6)$, which has an MLCT at 490 nm[37] and this is due to the extended aryl groups lowering the energy of the transition. Of two well-studied cyclometalated complexes, [Ru(N^C^N)(tpy)](PF_6) has an MLCT at 500 nm[37] and [Ru(N^N^C)(tpy)](PF_6) has an MLCT at 511 nm[37]. These results show the red shift that occurs upon cyclometalation or introduction of conjugated aryl systems.

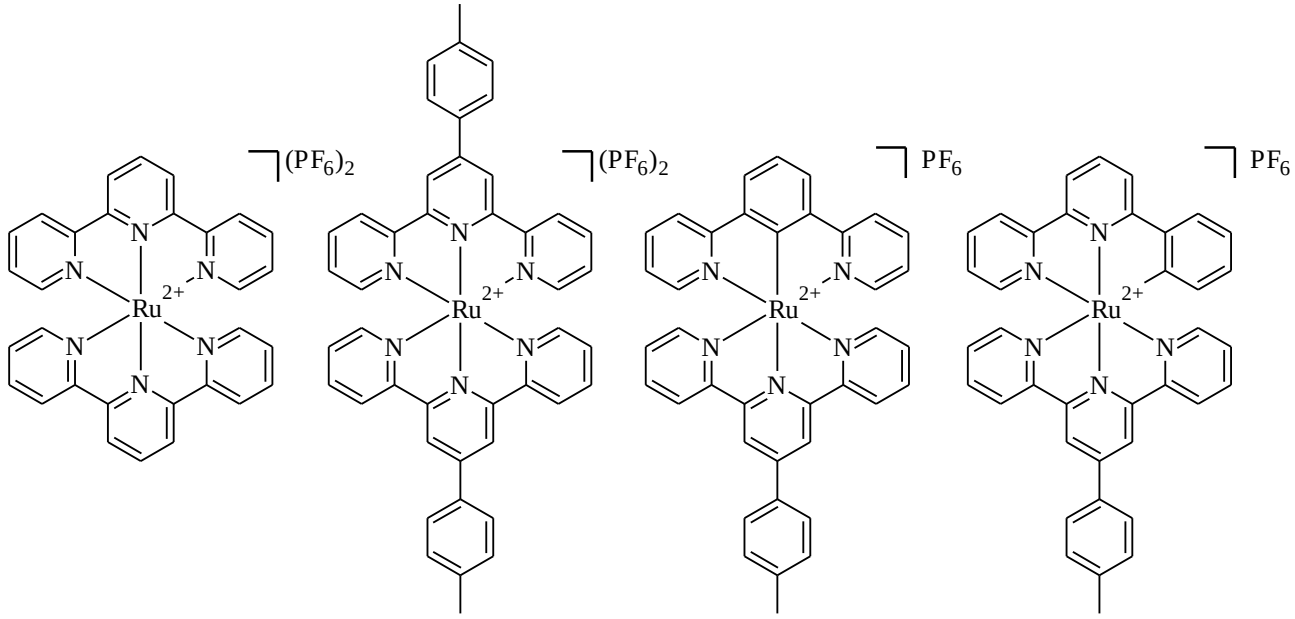

$[Ru(tpy)_2](PF_6)_2$ $[Ru(ttpy)_2](PF_6)_2$ $[Ru(N\hat{}C\hat{}N)(ttpy)]PF_6$ $[Ru(N\hat{}N\hat{}C)(ttpy)]PF_6$

Figure 1.13: Various well-studied ruthenium complexes.

1.5 Luminescence.

Luminescence is a process in which a compound in an excited electronic state returns to its ground state by emission of light. Luminescence can be divided into several different categories depending on how the excited state is formed. An important process is photoluminescence, in which the excited state is formed by absorption of light. A modified Jabłonski diagram which illustrates the photophysical processes in the ground and excited states of a molecule is shown in Figure 1.14.[57] The excited state can also be formed from electroluminescence, in which the excited state is generated by passage of an electric current. Applications which use photoluminescence are photovoltaic in solar cells and applications utilizing electroluminescence are organic light emitting diodes (OLEDs).

The bold vertical arrows in Figure 1.14 represent various possible radiative transitions, whereas the wavy arrows show the non-radiative transitions between electronic or vibrational states. The singlet ground state is labelled as S_0, and the first, second and higher electronic excited singlet states are represented by S_1, S_2 and S_n, respectively, with n = 3, 4, 5 etc. A molecule exhibits a singlet state when there is no net electronic spin associated with the state due to all the spins being paired. The triplet states are labelled as T_1 and T_2, whereas 'T' indicates that there are

three possibilities of spin orientation of two unpaired electrons (Figure 1.15). The spin multiplicity formula $2S + 1$ gives the number of states which can arise, where the 'S' is the total spin quantum number. In the case where all electrons of a molecule are spin-paired, $S = 0$, and the spin multiplicity = 1, which represents the singlet state. In contrast, when the molecule has two unpaired spins, $S = 1$, it has a spin multiplicity of 3, which represents the triplet state.

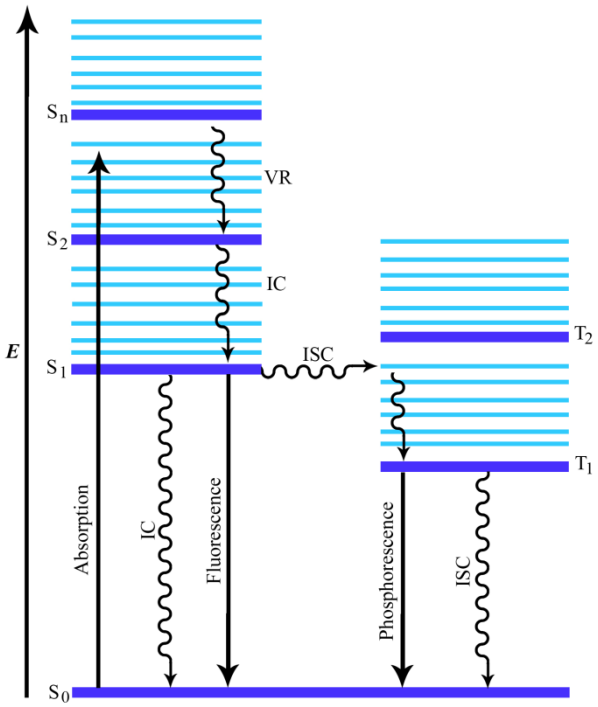

Figure 1.14: Jablonski diagram showing photophysical transitions between electronic states within a single molecule.

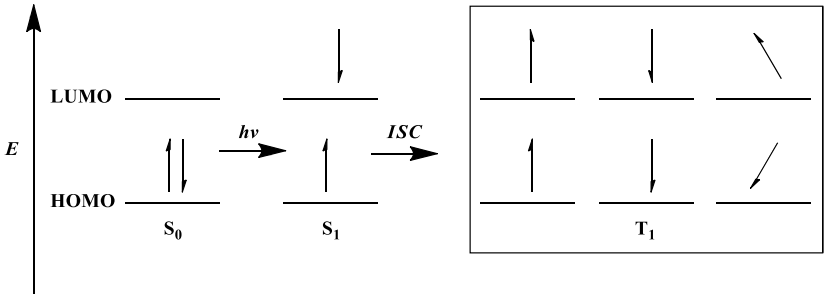

Figure 1.15: General diagram of the electron orientation in the ground (S_0), singlet (S_1) and triplet (T_1) excited states of a molecule for HOMO-LUMO transition.

When a photon is absorbed, the molecule can be excited from the ground state to an energetically higher lying singlet excited state with two spin-paired electrons (Figure 1.15), following the spin selection rule ($\Delta S = 0$).[58] If the molecule is excited to the second singlet excited state ($S_0 \rightarrow S_2$), it rapidly relaxes to the lowest vibrational level of S_2 via vibrational relaxation (VR). Internal conversion (IC) occurs when the molecule releases excess energy from the second singlet excited state to the first singlet excited state ($S_2 \rightarrow S_1$). These processes occur very quickly (less than 10^{-12} s) and are generally complete before the emission occurs. Fluorescence results if the molecule returns back to the ground state from the lowest singlet excited state ($S_1 \rightarrow S_0$) by emission of a photon. Fluorescence lifetimes are typically about 10^{-9} to 10^{-7} s. Kasha's rule states that the emission generally occurs from the lowest excited state to the ground state.[59] Phosphorescence lifetimes on the other hand are significantly longer, with values in the order of a microsecond rather than a nanosecond as a result of $T_1 \rightarrow S_0$ transitions still being formally forbidden ($\Delta S = 0$) despite the spin-orbit coupling from the heavy ruthenium atom.[13]

The efficiency of an emission process is measured by the quantum yield, Φ, which for any given sample is defined as the ratio of photons emitted to photons absorbed. Under certain conditions, the molecule in the singlet excited state may undergo a non-radiative process, known as intersystem crossing (ISC) to a triplet state ($S_1 \rightarrow T_1$), in which the molecule has two electrons with parallel spin (Figure 1.15). However, in some cases, ISC from higher lying singlet states to higher lying triplet states ($S_n \rightarrow T_n$, where, n = 2, 3, 4 and higher) can also be possible. Similarly, the molecule at the higher vibrational energy levels of T_1 state can release the excess energy via VR to the lowest vibrational energy level of T_1 state. Phosphorescence results if the molecule returns back to the ground state from the lowest T_1 state ($T_1 \rightarrow S_0$). The rate constants for phosphorescence are several orders of magnitude smaller ($10^6 - 10^0$ s^{-1}) than those for fluorescence due to the transition from T_1 to S_0 being spin-forbidden. As T_1 is often lower in energy than S_1, phosphorescence generally occurs at lower energy relative to fluorescence.

Non-radiative decay processes such as ISC and IC, from an excited state to the ground state can significantly reduce the quantum yield of a luminescence process. Typically, non-radiative decay processes depend on several factors such as the nature of the molecular structure, in particular its molecular rigidity, and the energy gap (ΔE) between the excited states (S_1 or T_1) and S_0. In general, the more rigid a molecule, the higher is its luminescence efficiency.[60] Another decay

pathway is self-quenching of the excited state, which occurs when the concentration of the complex in solution is increased and results in a decrease in excited state lifetime and intensity which is undesirable as it is a waste of energy.[61] At higher concentrations excited states have an increased chance of interacting with another excited species in solution resulting in energy transfer and thus less intensity of the desired emission.

The emission spectrum for $[Ru(bpy)_3](PF_6)_2$ shows a very broad profile, centered around 600 nm, with a lifetime of 640 ns and a quantum yield of 0.062.[15] At 77 K its emission lifetime is significantly increased to 5 μs and its quantum yield is increased to 0.38.[15] While $[Ru(tpy)_2](PF_6)_2$ has limited room temperature emission at 629 nm, it is generally considered as being non-emissive as its lifetime is 0.25 ns. The emission spectrum for $[Ru(tpy)(dpyb)]PF_6$ shows a broad emission profile at 781 nm, with a quantum yield of 9.4×10^{-6}.[37] Generally the lifetimes of cyclometalated complexes are short compared to non-cyclometalated complexes due to the energy gap law.[62-64] The energy gap law shows that as the energy gap is decreased and emission is red shifted, non-radiative decay processes increase which results in shorter emission lifetimes. This does not prevent them from being successfully incorporated into photovoltaic devices however, as they have been successfully used in dye-sensitized solar cells.[6] This is because the complex is immobilized and there is fast electron injection into the semiconductor. This means that tuning properties other than the lifetime of the complex are of more importance.

1.6 Computational chemistry.

Computational chemistry allows chemical structures to be simulated, which can be used in combination with fundamental laws of physics to calculate their corresponding properties. With the shift to using powerful computers to complete complicated calculations using programs such as Gaussian,[65] along with the huge increase in computing power,[66] it is now common to see computational results alongside experimental data in scientific publications.

Computed models are an important tool to gain understanding of a system, and provide much more than aesthetics. Entry level students use models to gain an understanding of 3D structure using plastic systems and this progresses to using drawing software to create digital models. These models are produced using a predefined set of rules, which are generalised for types of

atoms, bonding etc. As students progress and use more complicated systems, more sophisticated models are required.

In the field of computational chemistry there are two broad areas which can be used to analyze the structure and properties of molecules. The first area is molecular mechanics, which uses the laws of classical physics to predict structure and properties. The second area is electronic structure theory, which uses the laws of quantum mechanics as the basis of the calculations. The Schrödinger equation[67] (general time-independent is shown in Equation 1.2) can be solved to obtain specific energy and related properties for a molecule.

$$\hat{\mathrm{H}}\Psi = E\Psi$$

Equation 1.2: General time-independent Schrödinger equation, where $\hat{\mathrm{H}}$ is the Hamiltonian operator, Ψ is the wave function and E is the energy.

The challenge is that the Schrödinger equation can only be solved for 1 e^- systems and thus achieving a solution for anything but the smallest of systems is not computationally practical. This requires approximations to be made. One potential solution is to use semi-empirical methods, which solve an approximate form of the Schrödinger equation using parameters derived from experimental data. This presents its own problem of needing to be experimentally prepared beforehand. An alternate method is to use *ab Initio* methods, which use no experimental parameters, but instead reduce the complexity of the calculation by using values from a number of physical constants, such as the speed of light, the masses and charges of electrons and nuclei and Planck's constant, along with a series of rigorous mathematical approximations.[68]

An alternate electronic structure method is density functional theory, DFT, which is similar to the previously mentioned *ab Initio* methods. DFT calculations require a similar amount of time compared to the most basic *ab Initio* methods and are generally viewed as being more accurate. The increased accuracy comes from DFT methods incorporating electron correlation, which models the electrons in a molecular system reacting to one another's motion and attempts to keep them out of each other's way.[68]

Using different levels of theory, with different approximations, can make analyzing results from different-sized systems difficult. Calculations for smaller systems generally require less

approximation than for larger systems leading to potential discrepancies and thus it is important to have a theoretical model that holds true for all sizes and types of systems, where the limiting factor should only be the availability of computational resources. While this is the goal, not every model can completely achieve these results, and thus after rigorous testing against known experimental results they are put into categories, based on which type of system they are best suited for. Of the range of different methods, the Becke-style 3-parameter Density Function Theory, using the Lee-Yang-Parr correlation function, B3LYP,[69] has been shown to work well for transition metal complexes with organic ligands, with the predicted structures and their related properties being in better agreement with experimental results compared to other methods. It is important to note that the B3LYP method is not a pure DFT method, but rather a hybrid. It has a Hartree-Fock (HF) factor included which removes the bias that pure DFT methods have towards delocalized structures. This is especially important in cyclometalated ruthenium complexes in which the orbitals have mixing between the metal and the organic ligands.[70] There are a range of alternate methods, with (potentially) increased accuracy, however these are generally more computationally demanding and thus B3LYP is the method of choice for a range of different research groups currently working on cyclometalated ruthenium complexes.[29, 39, 71]

The next important decision to be made is which basis set is going to be best for the specific molecule that is being calculated. A basis set is a mathematical representation of the molecular orbitals that make up a molecule and it generally has the role of limiting the region of space that is available to each electron. The choice of the basis set is of fundamental importance to the calculation because it determines the accuracy of the calculation. With the increasing use of computational chemistry to assist non-specialist users it is especially important that good decisions are made about which basis sets to use. An important tool for selecting basis sets is available at the EMSL basis set exchange,[72] whilst a reasonable method of choosing a basis set is simply using what has been previous employed for calculations on similar complexes.[68]

During the process of choosing a basis set, calculations were performed based on previous work by Wadman *et al*.[37] The initial goal was to replicate their results using the coordinates and calculation setup from their supplementary information. Successful replication of results meant that the (with B3LYP functional) DZ Dunning basis set[20-21] was chosen for all atoms except

ruthenium, which used the Stuttgart RSC 1997 ECP relativistic core potential[22] and bromine, which used LAND2DZ ECP.[23-25] An additional benefit of using previously determined methods/procedure is that results are directly comparable. This is more beneficial than trying to (potentially) increase accuracy by a small amount.

Large systems, such as the cyclometalated ruthenium complexes studied in this work, require a significant amount of computational time. Simple computer systems were not suitable, thus the Columbus and Slater supercomputers were used. These are administered by the EPSRC UK National Service for Computational Chemistry Software (NSCCS) at Imperial College London, UK.

DFT calculations have been used in this work to fully optimize the geometries of all complexes studied and TD-DFT calculations have been performed on optimized geometries at the same level of theory. These calculations have provided important structural information, and also important UV-vis transitions, molecular orbital energies and electron density maps for these molecular orbitals, displayed as isodensity plots (Kohn–Sham orbitals). These results will be used in parallel to experimental results to gain a deeper understanding of these complexes' properties.

1.7 Reaction pathways.

1.7.1 Synthesis of terpyridines

Pyridine rings can be synthesised *via* ring-closing methodologies, using classical Hantzsch synthesis conditions, which date back over a century.[73] This methodology was modified by Case and Kasper in the 1950s, for the preparation of aryl substituted bipyridine and terpyridine derivatives.[74] The multi-step synthesis pathway (Scheme 1.1) involves the condensation of two ketones, along with an aldehyde in the presence of ammonia, from which becomes the nitrogen atom for the central pyridyl ring, followed by aromatisation.

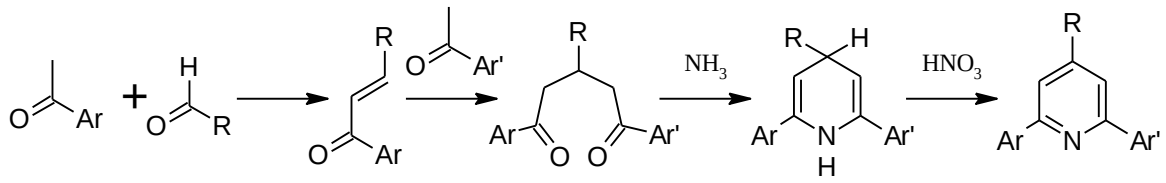

Scheme 1.1: The Hantzsch synthesis of 4'-aryl pyridines.

The Kröhnke synthesis (Scheme 1.2) is an adaptation of the Hantzsch method, which was developed in 1962.[75] The method is advantageous because it is convenient, but also economically and environmentally friendly. Another advantage of this method over the Hantzsch synthesis is the exclusion of the dehydrogenation step, which means carboxylate appended ketones can be used in place of aryl ketones, allowing 2,4-disubstituted pyridine rings to be formed due to the fact that thermal decarboxylation can be carried out following ring closure. This also enables a reliable method of forming 4-aryl bipyridines.[76]

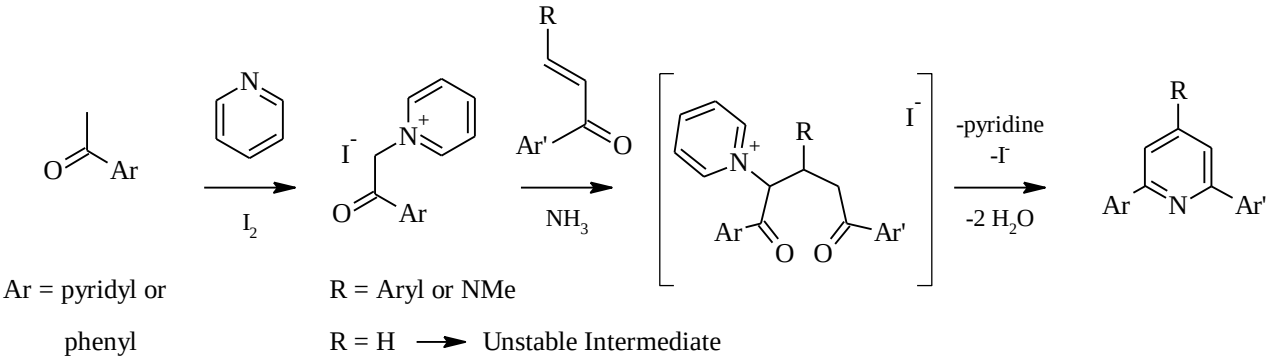

Scheme 1.2: General Kröhnke synthesis.

1.7.2 Ullmann coupling

The Ullmann coupling is a reaction between aryl halides with copper, which uses harsh conditions to achieve the product, in unreliable yields.[77] Typically the Ullmann coupling was used for the synthesis of symmetrical biaryls, using a copper catalyzed homocoupling as shown in Scheme 1.3.

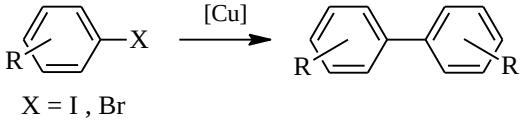

Scheme 1.3: General Ullmann coupling.

A modified Ullmann coupling was later devised, which reacts nucleophiles with aryl halides *via* copper catalyzed nucleophilic aromatic substitution. This modified method typically uses L-proline and K_2CO_3 with CuI in solvent with a high boiling point (e.g. DMSO) over long time periods (2-72 hours) to achieve the desired product. Aryl iodides generally require shorter reaction times compared to aryl bromides, whereas aryl chlorides need to be specifically activated in order to be reactive enough.[78] With the large number of options that are available for this reaction type, it requires that the system is optimized for the specific aryl halide and nucleophile being used. Catalyst, coligand, choice of base, solvent and temperature can all be modified to suit the system and maximize the yield achieved. Also, because the CuI is added in its active form, it generally requires purification immediately prior to use.[79] A modified Ullmann coupling was used to introduce pyrazole during the synthesis of all cyclometalated ligands from chapters two and three and also the three pyrazole containing ligands in chapter four.

A potential mechanism for the modified Ullmann coupling is shown as a catalytic cycle (Figure 1.16). The Cu(I) associates with the already deprotonated nucleophile and then it undergoes oxidative addition with an aryl halide. This is followed by reductive elimination giving the product and regenerating the catalyst for the cycle to continue.

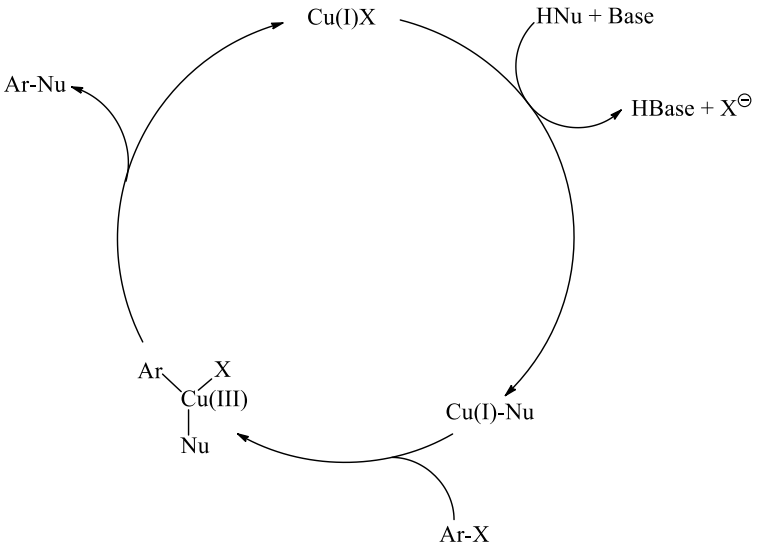

Figure 1.16: Catalytic cycle for copper catalyzed modified Ullmann coupling.

1.7.3 Sonogashira coupling

The Sonogashira coupling is used to form C-C bonds *via* a cross coupling reaction which is commonly used in organic synthesis. It uses both palladium and copper catalysts together, to react a terminal alkyne with an aryl or vinyl halide, as shown in Scheme 1.4.[80] The reaction can be carried out using mild conditions as opposed to the Ullmann coupling and can also be carried out in aqueous conditions. It only requires a mild base, for which triethylamine is commonly added in excess. It has been utilized for formation of two ligands in chapter three and has also been utilized en route to all the triazole substituted ligands in chapter four.

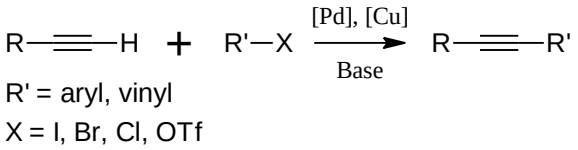

Scheme 1.4: General Sonogashira coupling.

The complete mechanism for the Sonogashira coupling is not entirely understood despite it being a widely used method. This is due to the difficulty of isolating and analyzing the organometallic compounds which are present as reactive intermediates, during the reaction.[81] Despite not having a full understanding, the generally accepted mechanism is shown in Figure 1.17. There are two cycles working together to form the target product. The palladium cycle starts when the inactive Pd(II) compound added is reduced to form the active Pd(0) catalyst. It then undergoes oxidative addition with the aryl (or vinyl) halide to form the Pd(II) intermediate, which is considered to be the rate determining step of the cycle. The next step is a transmetallation with the copper acetylide, formed during the copper cycle, which produces the copper halide, thus continuing the copper cycle and also forms the next Pd(II) intermediate in the cycle. The next step involves an isomerization, in which the alkyne and the aryl group from a more trans to cis orientation before the final reductive elimination step, which produces the target alkyne and regenerates the catalyst to enable the cycle to continue.

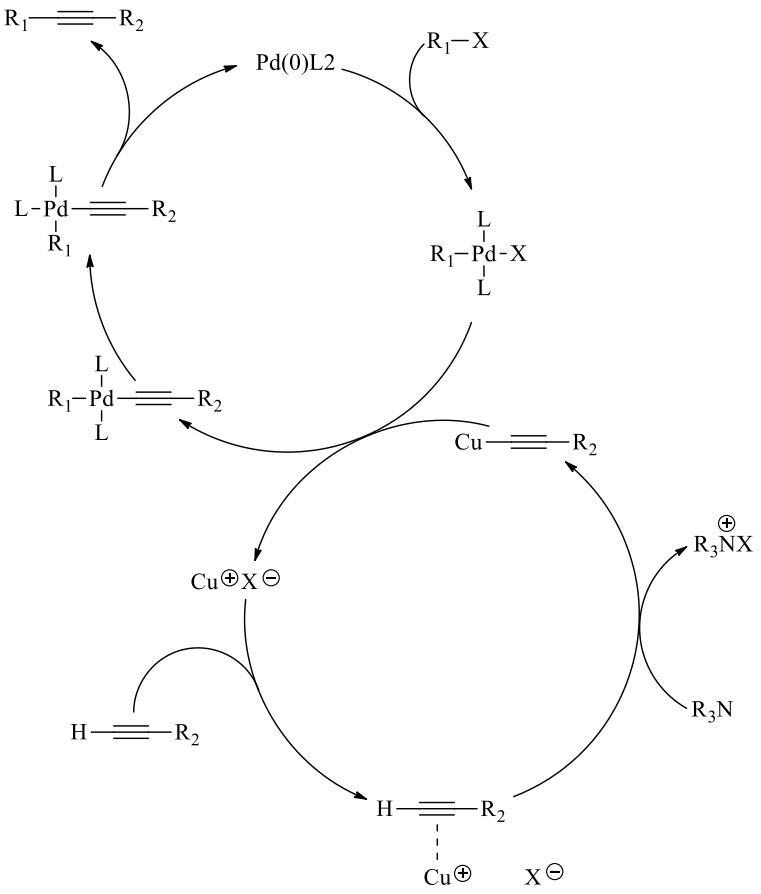

Figure 1.17: Catalytic cycles involved in the Sonogashira coupling.

The proposed mechanism for the copper cycle starts with the CuX associating with the pi system of the alkyne, which with the assistance of the base, leads to the formation of the copper acetylide by making the terminal proton more acidic. This copper acetylide then reacts with palladium, giving back the copper halide to continue through the copper cycle. Common catalyst systems usually use CuI and $[Pd(PPh_3)_2(Cl)_2]$ with PPh_3, although a large variety of catalyst systems have been successfully developed, including copper free systems.[82]

1.7.4 Suzuki coupling

The Suzuki reaction is another organic reaction which forms C-C bonds by coupling together a boronic acid and an aryl halide, catalyzed by a Pd(0) complex.[83] Suzuki, together with Heck and Negishi were awarded the Nobel Prize in chemistry in 2010 for their work developing palladium catalyzed cross couplings.[84-85] The reaction is very useful because it can be carried out reliably,

in both organic solvents and aqueous media, both in high yields. Catalyst loading can be as low as 0.01 mol% and the source of palladium is normally Pd(II), which is reduced to Pd(0) *in situ*.

The Suzuki coupling is favorable compared to other similar coupling reactions such as the Stille coupling and the Negeshi coupling because of the ease of preparation and low toxicity of the boronic acids needed for the reaction. This reaction was used to extend the aryl system of the cyclometalating ligand, from which several new ligands were formed, these have been used to make the ruthenium complexes in chapter two.

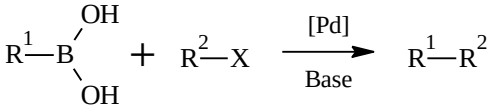

Scheme 1.5: General Suzuki coupling.

The catalysis cycle for the Suzuki coupling is shown in Scheme 1.5. The cycle begins upon the activation of the Pd(II) to form the active catalyst, Pd(0), which then undergoes oxidation addition with the aryl halide to form the organopalladium complex. This then reacts with the base to give the next intermediate which then undergoes transmetallation with the boronate complex to form a new organopalladium complex.

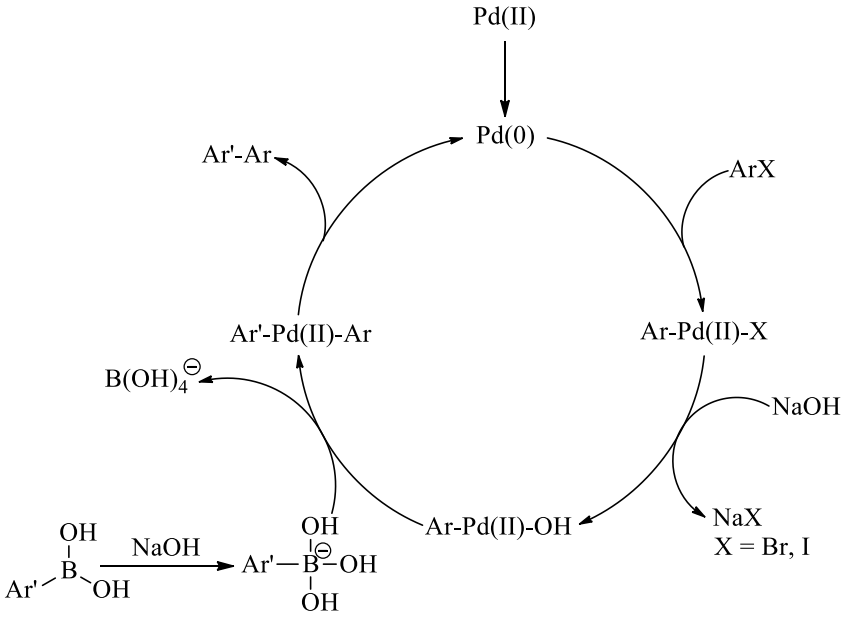

Figure 1.18: Catalytic cycle for the Suzuki coupling.

An important step occurs before entering the catalytic cycle, in which the boronic acid is activated. This is typically achieved by addition of a base, such as K_2CO_3, KO^tBu, K_3PO_4 or by using excess Et_3N as part of the solvent mixture. Activation of the boronic acid enhances the polarization of the organic ligand, which promotes transmetallation. The final step is the reductive elimination of the target product, which also restores the active palladium catalyst to enable the cycle to continue.

1.7.5 Triazole synthesis, via "click" chemistry

The term 'click chemistry' was coined by K. B. Sharpless in 1988 and is used to describe reactions used in chemical synthesis in which small units are quickly and reliably joined together in high yield. 'Click chemistry' is not a single reaction, but instead a reaction classification which follows guidelines set out by nature. The conditions are that the reaction should be modular, wide in scope, of high yield, generate inoffensive byproducts, be stereospecific and regiospecific, physiologically stable, exhibit a large thermodynamic driving force and have high atom economy.[86]

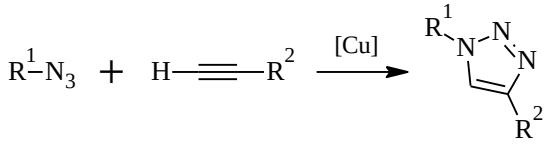

Scheme 1.6: General copper catalyzed azide-alkyne cycloaddition (CuAAC).

One example of a reaction that occurs within the criteria of 'click chemistry' is the azide-alkyne Huisgen cycloaddition, which was described by Sharpless in his 2001 paper as "the cream of the crop".[86] Due to its huge success since, it is often misinterpreted as the only 'click chemistry' reaction. The cycloaddition reacts an azide with an alkyne to give a 1,2,3-triazole. It was later found that the addition of copper(I) catalyzed the reaction, producing exclusively 1,4-disubstituted-1,2,3-triazoles. It should be noted that because of the addition of the copper, the reaction is formally no longer a 1,3-dipolar cycloaddition and thus is referred to as a copper(I)-catalyzed azide-alkyne cycloaddition (CuAAC) instead of a Huisgen cycloaddition. Cyclometalated ligands featuring triazoles synthesised using this reaction type, are used in a number of complexes that are analysed in chapter four.

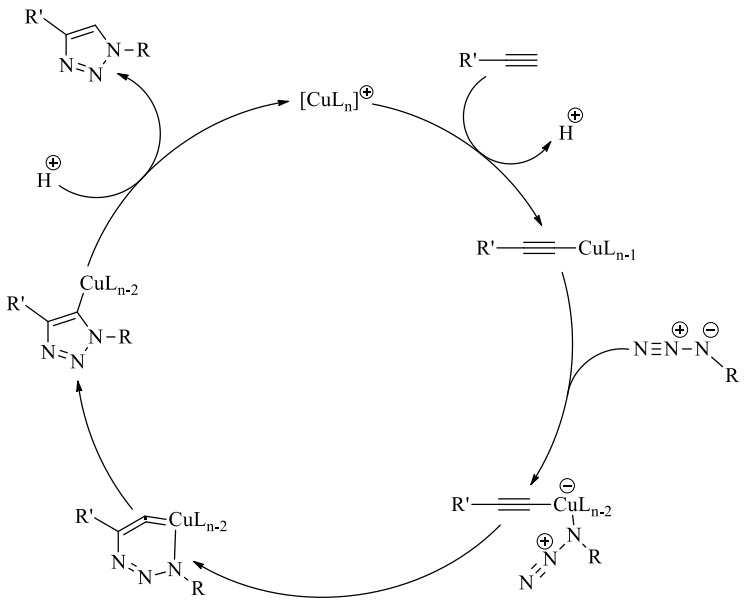

Figure 1.19: Potential catalytic cycle for CuAAC "click" reaction.

A potential mechanism for the CuAAC "click" reaction is shown in Figure 1.19. As with most catalytic cycles, the cycle begins when the catalyst is activated *in situ*, which in this case uses Cu(I) or Cu(II) salts, which can be reduced with sodium ascorbate to produce the active catalyst. A slight excess of sodium ascorbate is typically used as it has also been found to prevent the formation of oxidative homocoupled byproducts.[87] Once the catalyst is activated, the first step is coordination of the copper to the acetylene, which is followed by the displacement of another ligand by the organic azide on the copper. The next step involves the formation of an interesting six-membered Cu(III) metallacycle; the energy barrier for which is lowered, compared to the uncatalysed equivalent, due to the copper.[87] The final step involves ring contraction to a five membered triazole with the copper ejected from the ring and bound to the carbon, followed by protonolysis to give the 1,4-disubstituted-1,2,3-triazole which also regenerates the active copper to continue the catalytic cycle.

1.8 Applications.

1.8.1 Organic light-emitting devices

The first observations of electroluminescence in organic materials were reported in the early 1950s by André Bernanose and co-workers at the Nancy-Université in France.[88] Based on this research, the first organic diode device was reported at Eastman Kodak by Ching W. Tang and

Steven Van Slyke in 1987.[89] Organic light emiting devices (OLEDs) have received considerable attention since this original design, with development aimed at using the devices in flat panel displays instead of liquid crystal displays (LCDs), which are currently in use in a range of devices. OLEDs have many advantages when compared to other available products because they require lower initiator voltages to other devices, which means they use less power. They also require less sophisticated, cheaper fabrication methods, which enable thinner more flexible displays.[90] One downside is that their lifetimes are inferior compared to other inorganic light emitting devices (LEDs), which are an alternative technology. Modifications to the organic molecules involved in the OLEDs can tune the emission intensity, colour and lifetime produced by the device, which enable better devices to be made.[91]

OLEDs are made up of an organic emissive semiconductor, which is sandwiched between two electrodes. When an electric potential is applied, the organic layer is oxidised at the anode, which injects holes into the HOMO, and the cathode is simultaneously reduced, which injects electrons into the LUMO. These electron and hole carriers travel, *via* a hopping mechanism, towards the opposite electrode under the applied field. While the two types of carriers travel across the applied field they have the potential to recombine, forming an excited state which is called an exciton. From this exciton, the emission of light is produced; a process called electroluminescence. This process differs from photoluminescence as it allows both singlet and triplet excitons to be produced, in a 1:3 ratio. This results in a large amount of undesirable heat in electroluminescent devices because phosphorescence from triplet states is spin-forbidden, and as a result, it is very rarely observed in organic molecules at room temperature. This gives the devices which utilise electroluminescence a maximum efficiency of 25%.[92-93]

OLEDs can have a very thin design, which is made up of several layers of material, deposited upon a substrate made of either glass or a polymer (Figure 1.20). Directly on top of the substrate is the anode, which needs to be transparent, for which indium tin oxide is typically used. The next layer is made up of the emissive organic substrate, which is sandwiched in place by the cathode. The cathode layer is made up of either a metal, for example, aluminium, magnesium, indium or an alloy such as Mg:Ag, which requires protection from the atmosphere to prevent oxidation.[93-94]

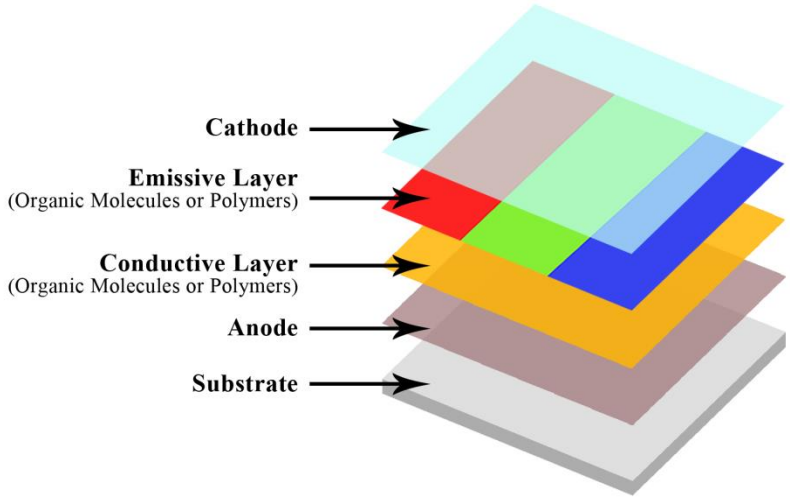

Figure 1.20: General organic light emitting diode (OLED) diagram.

As outlined earlier, the device efficiency of purely fluorescent OLEDs is limited to 25%, based on the statistical amount of formation of singlet excitons. This limitation can be improved upon by incorporating phosphorescent compounds into the emissive organic layer by introducing heavy metal complexes which allows emission from both singlet and triplet excitons, which enables theoretical internal efficiency of 100%.[92, 95-96] In systems of this type, the excited state generated upon electron-hole recombination is trapped in the complex and undergoes triplet state harvesting. Spin-orbital coupling occurs; a process which results in singlet-triplet mixing and from which phosphorescent emission is observed at room temperature. For this to occur the metal complexes require high electron mobility, phosphorescent quantum yields as well as relatively short lifetimes. When these properties occur in combination with one another, they result in high device efficency and brightness. To be used in commercial products, true blue, red and green emitters are required, which enable a full colour range to be available to the device. Typically blue emitters are more difficult to produce, owing to the excited state being higher in energy, which makes them more susceptible to degradation.[97-98]

The first OLEDs utilised platinum complexes as the triplet state harvesters which gave long triplet lifetimes of more than 10 μs. The problem of long lifetimes however, is that prolonged exposure to high currents can lead to triplet-triplet destruction, which limits the potential effiency of the device.[95, 99-100] Phosphorescent systems which use iridium(III) complexes have also been

investigated, because they are known to have shorter luminescence lifetimes of around 1 μs, which makes them more favourable systems. One example of which is *fac*-[Ir(ppy)$_3$] (Figure 1.21a), which was first reported in 2000 by Thompson *et al.* The device was found to have an external efficiency of 15%, with an internal efficiency of 80%.[101]

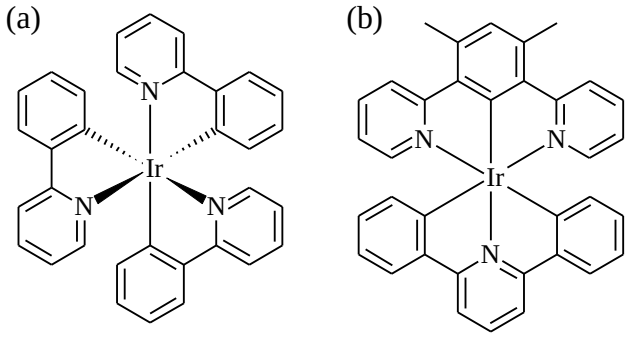

Figure 1.21: Structures of two phosphorescent iridium(III) complexes. (a) *fac*-[Ir(ppy)$_3$]. (b) [Ir(dpydmb)(dppy)]

Another alternative is to use polymeric hosts as the organic substrate. The complex and the polymer can be covalently linked in specific systems to prevent the aggregation and self quenching of the complex. This was first ultilized in 2000, when a single layer device incorporated a poly(vinylcarbazole) (PVK) and the emitting layer was doped with *fac*-[Ir(ppy)$_3$] to produce a device with an external efficently of 1.9%.[102] While this efficiency was very low compared to the original *fac*-[Ir(ppy)$_3$], it has since been improved upon by using a different multilayered structure to the device, increasing the external efficency to 8.5%.[103] A range of different modifications to the ligand structure in *fac*-[Ir(ppy)$_3$] have also been carried out with mixed results. The most successful substitutions used bulky groups which allow the use of higher concentrations of dopant in the system without causing self-quenching.[96] Also fluorinated substituted complexes were found to result in blue shifted emission, cause a reduction in radiationless decay and self-quenching and also result in enhanced electron mobility. All of these features combined together to produce higher device efficiencies.[104-106]

Another Iridium based complex [Ir(dpydmb)(dppy)] (Figure 1.21b) was developed in 2004 by Williams *et al*.[107] This complex is a charge neutral bis-terpyridine complex which was found to produce intense room temperature emission. The neutral charge of the complex also made it a

suitable candidate for use in solid state OLEDs. While neutral organic molecules and complexes have been heavily researched, charged transition metal complexes also offer a viable alternative for use in OLEDs. The first examples studied were complexes based on $[Ru(bpy)_3]^{2+}$,[108-109] which lead onto the research based on $[Ru(tpy)_2]^{2+}$ and similar cyclometalated derivatives.

1.8.2 Dye-sensitised solar cells

An application which has had a lot of promising results incorporating ruthenium (II) polypyridyl complexes is dye-sensitised solar cells (DSSCs). These have the ability to directly convert sunlight into electrical energy and offer a promising alternative to current energy sources at a time when there is a large amount of interest in finding sources of renewable energy. They are made up of a sensitiser, which is the luminescent metal complex, that is bound to the surface of a semiconductor using anchoring ligands. The most common semiconductor used is TiO_2 because it is low cost, non toxic and readily available. DSSCs work by using light to cause excitation, which oxidizes the sensitizer and injects electrons into the conduction band of the semiconductor. The surrounding electrolyte subsequently donates electrons back to the sensitizer, which returns it back to its original form. As the electron migrates to the counter electrode through the external circuit, the system is regenerated. This process is catalysed by the deposition of a small amount of catalyst on the anode.[110-113]

Ruthenium (II) polypyridyl complexes make good sensitizers because of their intense MLCT bands in the visible region of the electromagnetic spectrum and also their ability to inject charge into the conduction band of devices in which they are incorporated. Ruthenium (II) polypyridyl complexes have been shown to be better sensitizers compared to alternate d^6 polypyridyl metal complexes. This is due to their redox, spectroscopic and excited state properties, as well as having a similar energy compared to the TiO_2 semiconductor.[112] Two of the most successful DSSCs are 'black dye'[114] (Figure 1.22a) and the N3 dye[115] (Figure 1.22b). The carboxylic acid functional groups enable facile attachment to the surface of a semiconductor. The 'black dye' has an efficency of 10.4%[114] for the conversion of light to chemical energy, compared to the 8.6% efficiency of the N3 dye.[115-116] They both have MLCT character, by which an electron is transfered from the metal to the bpy ligand, which is attached to the TiO_2 surface.

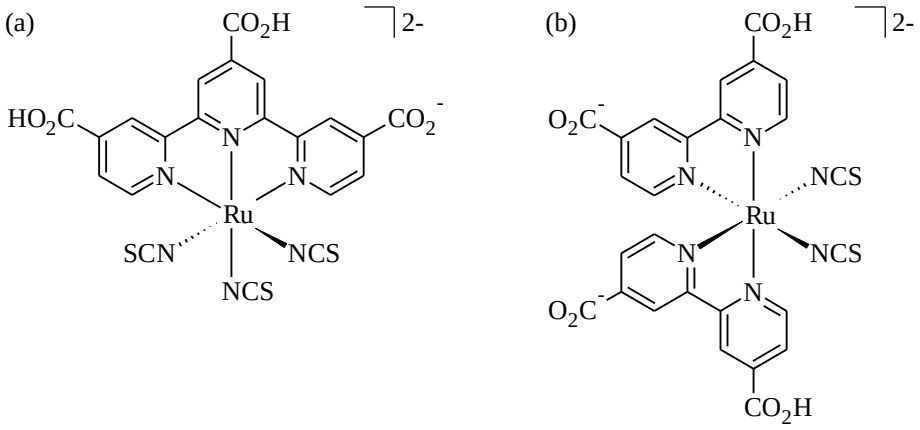

Figure 1.22: Successful ruthenium (II) sensitisers used in DSSCs. (a) 'black dye'. (b) N3 dye.

More recent research into potential DSSCs made from ruthenium (II) polypyridine complexes has utilized substituted bis(tridentate) and tris(bidentate) polypyridyl ruthenium complexes. Of the two, the bis(tridentate) derivatives are more stable and can be more easily synthesised, without different isomers forming, however they tend to have short excited state lifetimes.[1] Due to their favourable nature, a lot of optimization strategies have been developed to try and prolong the excited state lifetime.[117] The use of very strong, anionic donors have been able to slightly prolong the lifetimes and tune the wavelength of absorption for the broadened MLCT transition. One of the benefits of using these complexes in DSSCs is that the shortened lifetimes are not as important because the complex is immobilized and there is fast electron injection into the semiconductor, which makes tuning other properties rather than the lifetime more important.

One of the main problems with the N3 and 'black dye' is the monodentate thiocynate ligands which limit the stability and options for further functionalization being added to the complex. This is where cyclometalated ligands with aromatic carbanion donors in place of the thiocyanate ligand have been used with great success.[28-29, 37, 39] Cyclometalation overcomes the previous problems by increasing stability and enabling a wide range of functionalization options, and thus cyclometalated complexes offer an alternate method of optimizing the photophysical and electrochemical properties of ruthenium complexes.

1.9 Thesis coverage.

This work focuses on making modifications to [Ru(tpy)(dpyb)]PF_6 to gain an understanding as to which structural features are most important in tuning the photochemical and photophysical properties and to compare these results with similar, previously synthesized complexes.

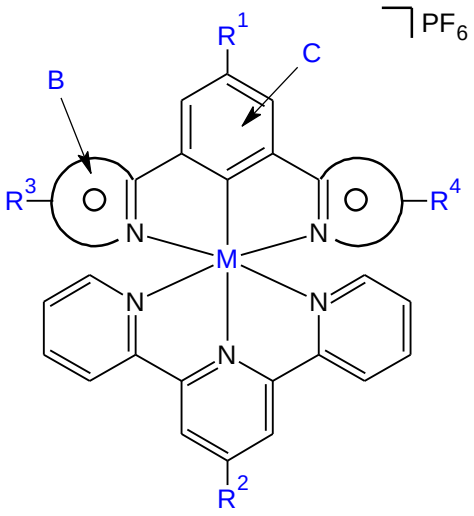

Figure 1.23: Possible structural modifications to general cyclometalated complex.

Chapter two focuses on modifying the central benzene ring of the cyclometalated ligand (C and R^1, Figure 1.23). Modification to R^1 can be achieved by synthesizing 1,3-di(pyrazol-1-yl)-5-bromobenzene and then using the bromine to substitute aryl groups onto the cyclometalated ligand, using Suzuki[83] and Sonogashira[80] coupling conditions. Aryl systems will be introduced using these methods including large aromatic groups, such as substituted phenyl, naphthalene and pyrene groups. Modification to C is also achieved by using 1,3-disubstituted pyrene.

Chapter three examines the effect of substituting at the opposite end of the complex in comparison to the first research chapter, with the 4' position of the central pyridine ring on the terpyridine ligand being extended (R^2, Figure 1.23). Electron withdrawing, electron donating and large aryl groups will be introduced at this position on the terpyridine to analyse the impact it has on the electrochemical and photophysical properties of the complex. To achieve this, the substituted aryl group needs to be introduced during the synthesis pathway itself. This requires the appropriate aryl aldehyde to be used to synthesise the substituted terpyridines using reliable

synthesis conditions. Complexes synthesised using these substituted terpyridine ligands make up the second chapter of research.

Chapter four focuses on changing the N-heterocycle (B, Figure 1.23) and adding large aryl groups onto the side of the N-heterocycle (R^3 and R^4, Figure 1.23), for which substituted triazoles or substituted pyrazoles are used. The substituted triazoles are formed using 'click' chemistry conditions, which react 1,3-di(ethynyl)-5-bromobenzene with either a substituted benzyl bromide to form non conjugated substituted triazoles or a boronic acid to form a conjugated substituted triazole. A triazole with two different substituted aryl groups (R^3 and R^4, Figure 1.23) is also analysed to examine the impact of having two different substituted triazoles. Three cyclometalating ligands with pyrazole as the N-heterocycle, and also incorporating aryl groups bound to the pyrazole (R^3 and R^4, Figure 1.23) are also investigated to compare their properties with the analogous substituted triazole cyclometalating ligands.

Characterization of the free ligands and cyclometalated ruthenium(II) complexes was achieved by ^{1}H and ^{13}C NMR spectroscopy and mass spectrometry. Ruthenium(II) complexes were also characterized by UV-visible spectroscopy, fluorometry, electrochemistry and X–ray crystallography where possible.

CHAPTER 2

MODIFICATION AT THE 4' POSITION ON THE CYCLOMETALATING LIGAND

2. Modification at the 4' position on the cyclometalating ligand.

2.1 Introduction.

There are a range of different changes that can be made to modify the general structure of N^C^N cyclometalated ruthenium complexes. Initial modifications were made to the N-heterocycle by using pyrazole in place of pyridine on each side of the cyclometalating ligand. Due to the nature of pyrazole, a π-excessive five-membered heterocyclic ring,[118] the properties of the resulting ruthenium complex should be modified. This is due to the significantly different π-acceptor properties of π-excessive pyrazole compared to π-deficient pyridine.[118] Pyrazole is also a better σ-donor than pyridine.[118]

While pyrazole has not been utilized in cyclometalated ruthenium complexes, it has been used in 2,6-di(pyrazol-1-yl)pyridine as a mimic for terpyridine with ruthenium to form the non-cyclometalated structures. An example of this is $[Ru(bpp)_2](PF_6)_2$ (Figure 2.1), which has a significantly shifted MLCT at 377 nm compared to $[Ru(tpy)_2](PF_6)_2$.[119]

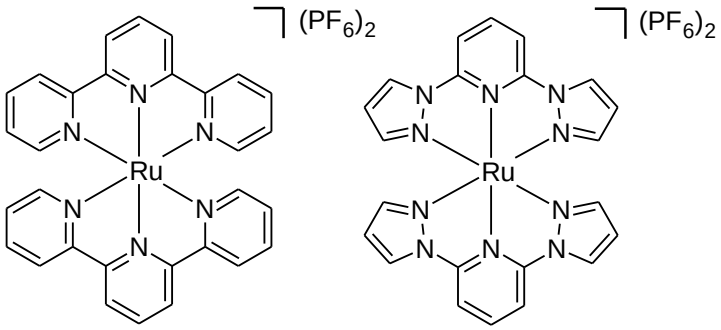

Figure 2.1: Two ruthenium complexes, $[Ru(tpy)_2](PF_6)_2$ and $[Ru(bpp)_2](PF_6)_2$.

Pyrazole has also been used to form cyclometalated complexes in 1,3-di(pyrazol-1-yl)benzene, although not with ruthenium. The ligand has been used with platinum to form cyclometalated platinum complexes (Figure 2.2)[43]. The poorer π-acceptor nature of the pyrazole compared to pyridine increases the energy of the LUMO, which results in blue shifted emission. The development of new blue phosphorescent emitters is important, as currently utilized phosphors at these wavelengths have poor emission efficiency and stability, which is undesirable for use in OLEDs and various other applications.[120] Similar tridentate pyrazolyl ligands have been used to form cyclometalated iridium complexes which also show blue shifted emission.[121] In other

areas of chemistry, 1,3-di(pyrazol-1-yl)benzene has been used in supramolecular assemblies with silver[122] and to form metallacyclophanes with copper.[123]

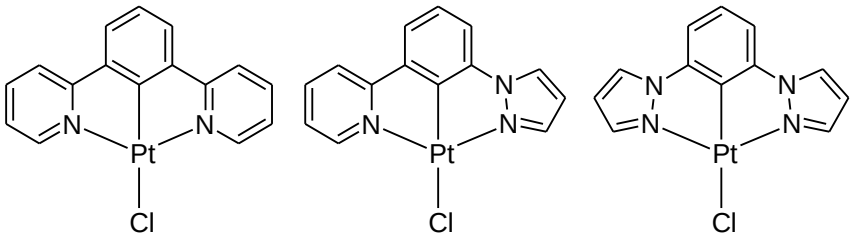

Figure 2.2: Three cyclometalated platinum structures which compare pyridine and pyrazole as N-heterocycles in platinum complexes.

The effect of using pyrazole in cyclometalated ruthenium complexes compared to pyridine is explored in this work. While all of these complexes incorporate pyrazole, a large focus of this work examines the effect of modifying the 4'-position of the central benzene ring on the cyclometalating ligand. There are only a few examples of modifications to the central benzene ring or the 4' position of the cyclometalating ligand. One example is [Ru(dpyb-4'-OMe)(tpy)]PF_6, which incorporates an electron donating methoxy group at the 4'-position of the cyclometalating ligand to donate electron density onto the metal (Figure 2.3) and shows the impact changes in this position can have to the properties of the complex.

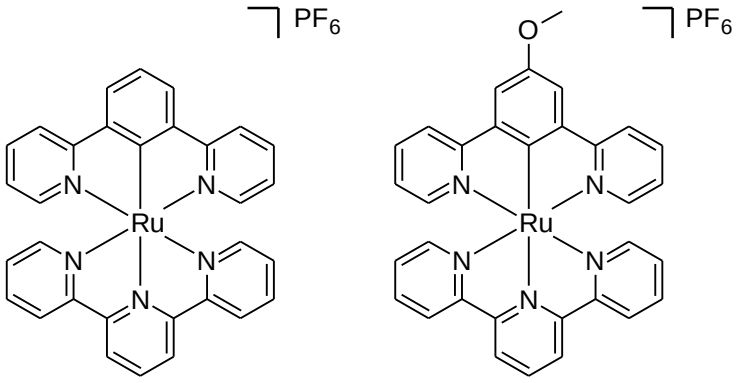

Figure 2.3: Two cyclometalated ruthenium complexes, [Ru(dpyb-4'-OMe)(tpy)]PF_6 and [Ru(dpyb)(tpy)]PF_6.

This results in the HOMO being raised in energy and the MLCT to be red shifted as a result of a decreased energy gap. The MLCT has a peak in the visible region of the UV-vis at 535 nm (ε =

15,900) compared to the comparable peak in the parent complex, [Ru(dpyb)(tpy)]PF_6 (500 nm, ε = 11,700).[39]

2.2 Research outline.

The work in this chapter examines the effect of making modifications to the core benzene unit of the cyclometalated ligand. This is achieved by modifying the 4' position of the central benzene ring, or by replacing the central benzene ring with pyrene. A series of nine new ligands and eleven new complexes have been synthesized (Figure 2.4) and the effects of these modifications are examined by analyzing their structural, spectroscopic and electrochemical properties. In parallel to these experimental results, DFT calculations have been used to calculate structural information *in vacuo* and TD-DFT calculations were carried out on optimized structures to support experimental results.

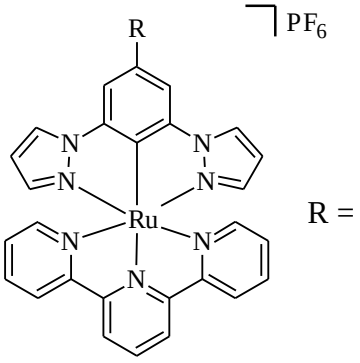

R =

H	**2.1**
Br	**2.2**
4-Tertbutylphenyl	**2.3**
Mesityl	**2.4**
4-Methoxyphenyl	**2.5**
1-Naphthyl	**2.6**
2-Naphthyl	**2.7**
1-Pyrenyl	**2.8**
3,3-Dimethylbutanoyl	**2.9**
Phenylacetyl	**2.10**

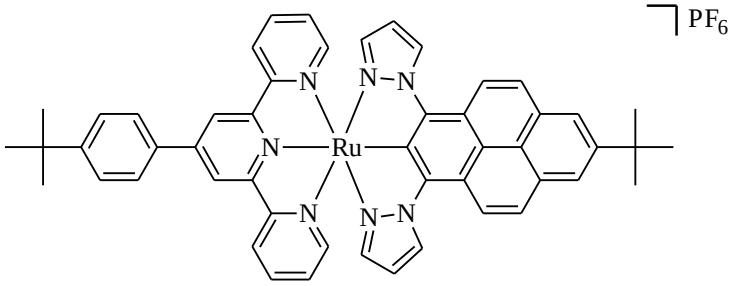

2.11

Figure 2.4: Complexes described in this chapter.

2.3 Ligand synthesis.

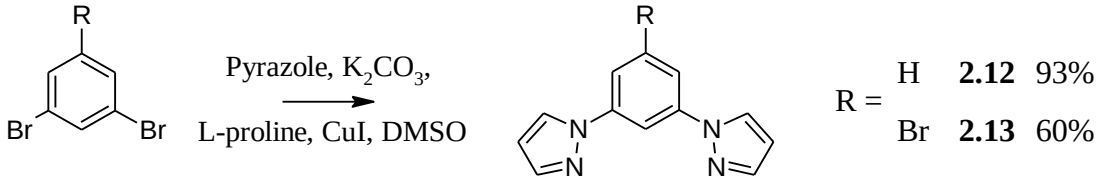

Scheme 2.1: Synthesis of potential ligands **2.12** and **2.13** using a modified Ullmann coupling.

Potential ligands **2.12** and **2.13** were synthesised from 1,3-dibromobenzene and 1,3,5-tribromobenzene respectively using a modified Ullmann coupling (Scheme 2.1).[124] The yield for **2.12** was significantly higher (93%) because excess pyrazole was able to be used to form the disubstituted product, as opposed to **2.13** which had to use stoichiometric amounts of reagents to target the disubstituted product over the mono and tri substituted alternatives. This was most effectively achieved using 2.2 equivalents of pyrazole and gave the target product in moderate yield (60%).

The ligands required to form complexes **2.3**-**2.8** required aryl boronic acids to be synthesized from aryl bromides. All of the aryl bromides required were able to be purchased from commercial sources except for 1-bromopyrene, which was synthesised in 85% yield using a method by Hu *et al.*[125] (Scheme 2.2). The boronic acids (**2.14**-**2.19**) were synthesized from these aryl bromides using literature procedures (Scheme 2.3).[126-131] Once synthesized, the boronic acids (**2.14**-**2.19**) were reacted with **2.13** using typical Suzuki coupling conditions[126] to form **2.20**-**2.25**, as shown in Scheme 2.4. All of these potential ligands (**2.20**-**2.25**) had not been previously synthesised and were characterized by ^{1}H and ^{13}C spectroscopy and mass spectrometry.

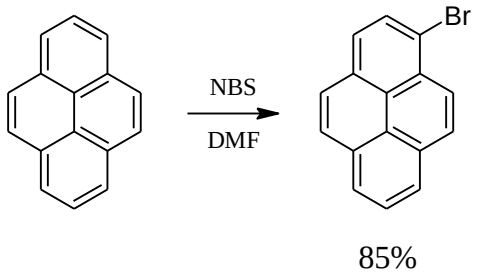

Scheme 2.2: Synthesis of 1-bromopyrene.

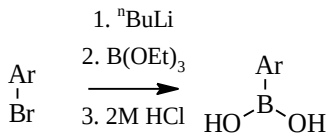

R =

4-Tertbutylphenyl	**2.14**	73%
Mesityl	**2.15**	81%
4-Methoxyphenyl	**2.16**	78%
1-Naphthyl	**2.17**	68%
2-Naphthyl	**2.18**	63%
1-Pyrenyl	**2.19**	68%

Scheme 2.3: Synthesis of boronic acids (**2.14**-**2.19**) from aryl bromides.

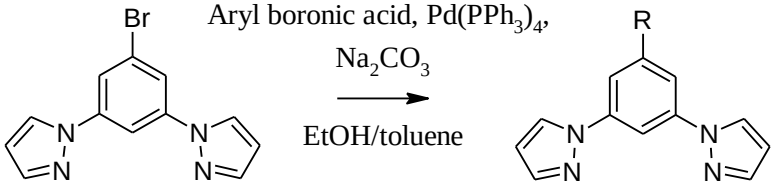

R =

4-Tertbutylphenyl	**2.20**	78%
Mesityl	**2.21**	73%
4-Methoxyphenyl	**2.22**	82%
1-Naphthyl	**2.23**	83%
2-Naphthyl	**2.24**	63%
1-Pyrenyl	**2.25**	59%

Scheme 2.4: Synthesis of potential ligands **2.20**-**2.25** from **2.13**, using Suzuki coupling reactions.

Potential ligands **2.26** and **2.27** were synthesised using typical Sonogashira coupling conditions[80] with tertbutylacetylene (**2.26**, 76%) and phenylacetylene (**2.27**, 83%) as shown in Scheme 2.5. All of the compounds made using these Suzuki and Sonogashira couplings are novel and have been characterized. Both **2.26** and **2.27** have not been previously synthesised and were characterized by ^{1}H and ^{13}C spectroscopy and mass spectrometry.

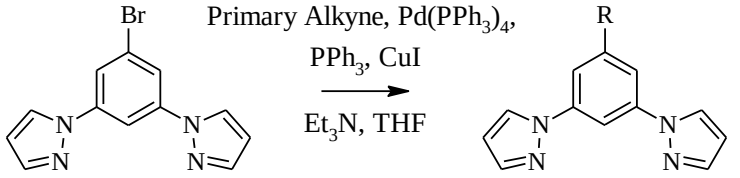

R =

Tertbutylacetylene	**2.26**	76%
Phenylacetylene	**2.27**	83%

Scheme 2.5: Synthesis of potential ligands **2.26** and **2.27** from **2.13**, using Sonogashira coupling reactions.

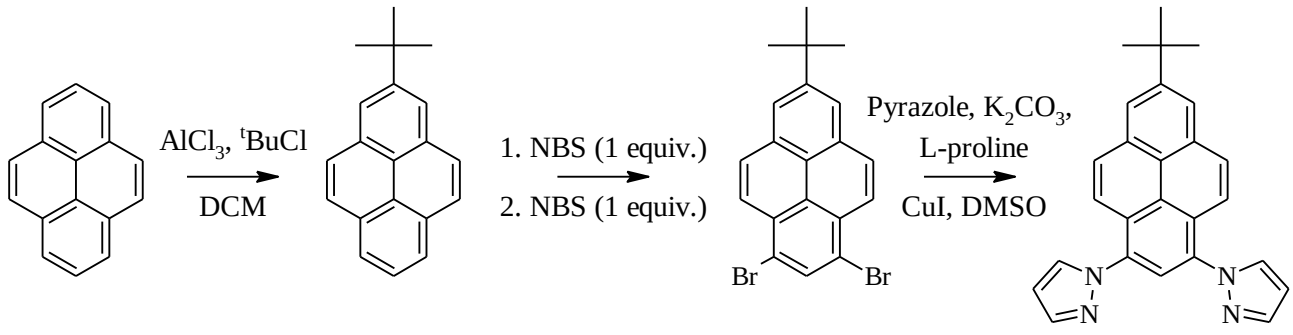

2.28 45% **2.29** 58% (2 steps) **2.30** 60%

Scheme 2.6: Synthesis of potential ligand **2.30**.

Synthesis of 1,3-di(pyrazol-1-yl)-7-tertbutylpyrene (**2.30**) was achieved using a multistep synthesis in an overall yield of 16% (Scheme 2.6). The initial step required pyrene to be selectively mono-tertbutylated to afford 2-tertbutylpyrene (**2.28**) which was achieved in 45% yield. Separation of the target product from a mixture which also included 2,7-ditertbutylpyrene and pyrene was achieved using column chromatography (SiO_2), eluting with hexane, although very similar R_f values resulted in poor separation, and thus a low yield. The next step involved reaction of **2.28** with NBS, which was completed in two individual steps to first produce 1-bromo-7-tertbutylpyrene (75%) and then 1,3-dibromo-7-tertbutylpyrene (**2.29**, 81%), in a combined yield of 58% over two steps. This was necessary as addition of two equivalents of NBS to **2.28** only gave a very small amount of the target product (<10% yield), with a large amount of insoluble byproduct. This was also observed when bromine was added to **2.28**, and thus it is likely that tribromo and tetrabromo derivatives were forming despite the steric hindrance from the tertbutyl group and compounds similar to these are known to be insoluble.[132] Compound **2.29** was then reacted, using previously optimized modified Ullmann coupling conditions,[78] to give 1,3-di(pyrazol-1-yl)-7-tertbutylpyrene, **2.30** in 60% yield.

2.4 Synthesis of complexes.

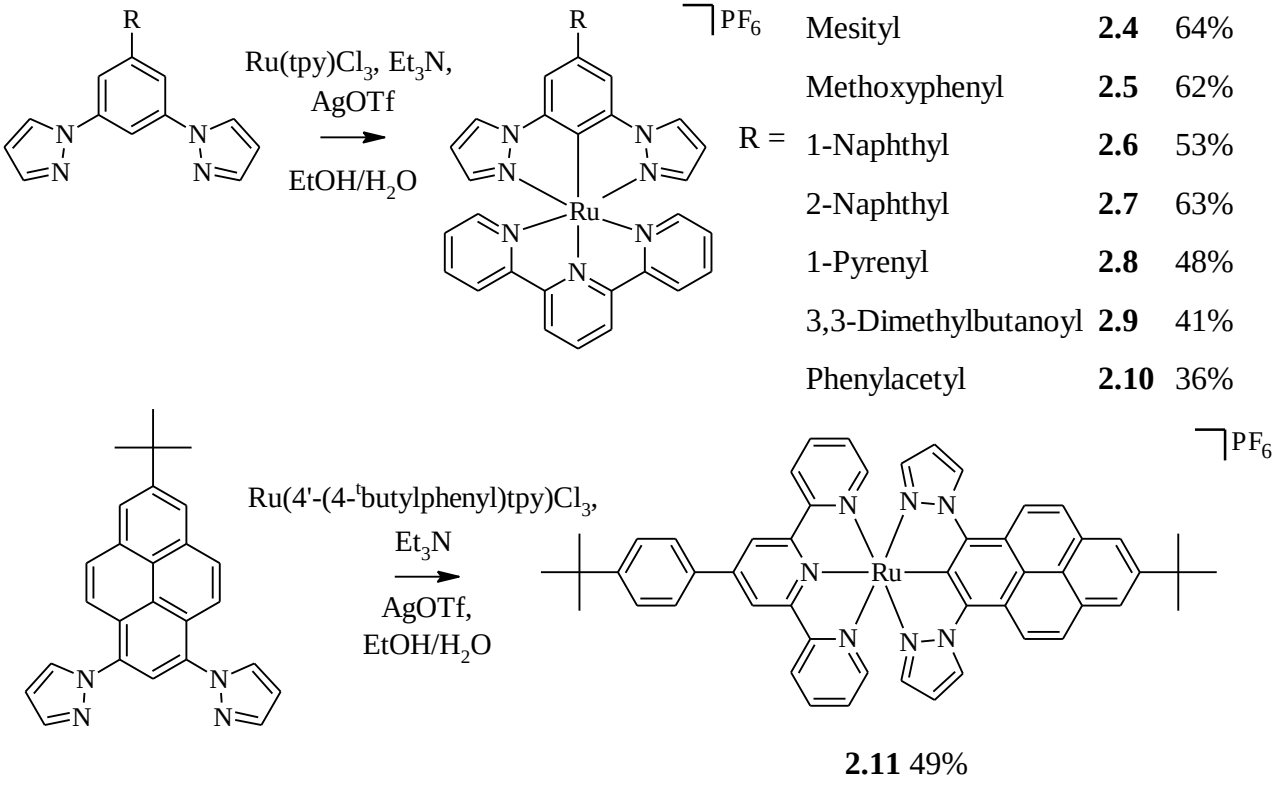

Scheme 2.7: Synthesis of ruthenium cyclometalated complexes **2.1**-**2.11.**

Synthesis of N^C^N cyclometalated ruthenium complexes using these ligands and terpyridine is typically achieved by first forming $Ru(tpy)Cl_3$ by reacting $RuCl_3.xH_2O$ with terpyridine in ethanol.[133] The most common method is to then react the $Ru(tpy)Cl_3$ with the N^C^N cyclometalating ligand and a silver salt ($AgBF_4$, AgOTf etc.) in an alcohol/water mixture.[39, 71] This only gave trace amounts of the target product however, and so alternative methods were necessary. Thummel et al.[33] devised an alternate method, in which they use the addition of a small amount of base instead of the silver salt, to increase the reaction yield. This method was followed successfully but required long reaction times (2-5 days) and also generated several byproducts. The majority of these byproducts were unable to be identified or isolated, however

2.5a (Figure 2.5) was able to be crystallized from a crude reaction mixture and shows one potential byproduct that can be generated using these conditions**.** Full analysis of the solid state structure of **2.5a** is in section 2.6.3. Forming a range of products can be a problem in cyclometalated reactions, especially in N^C^N pincer ligands.[134-136] as the target cyclometalated Ru-C bond usually forms the thermodynamic product, but there are a range of possible cyclometalated Ru-C bonds, which are less sterically hindered and thus form various kinetic products. This is exemplified by the formation of **2.5a** in addition to the target complex, **2.5**. Once **2.5a** forms, it is unlikely to form the target product **2.5**, which is one reason low yields are observed when using non-optimized reaction conditions.

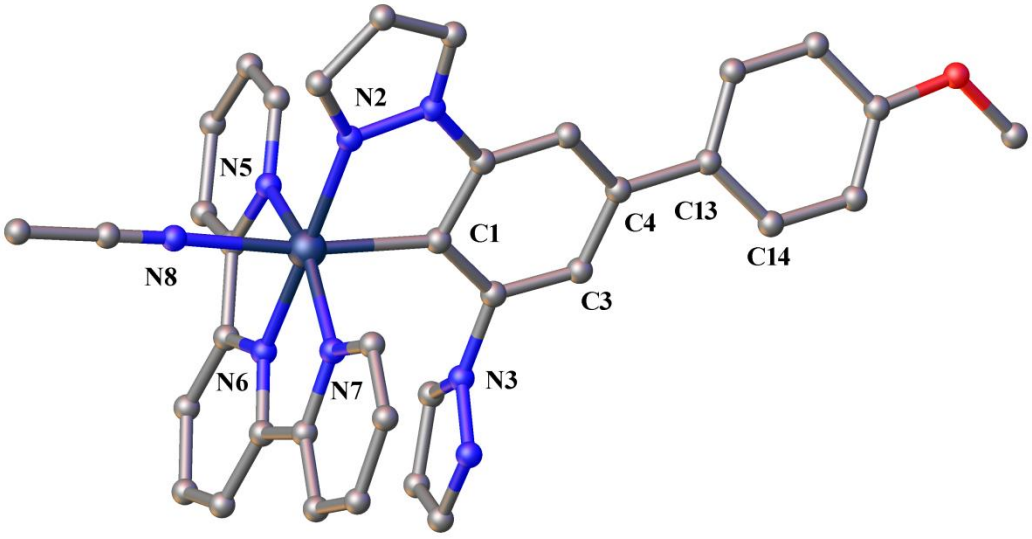

Figure 2.5: Crystal structure of complex **2.5a**. Full discussion of this crystal structure is provided in chapter 2.6.3 Crystal Structure of **2.5a**.

Using AgOTf and Et_3N together in an ethanol/water mixture with $Ru(tpy)Cl_3$ and the cyclometalating ligand gave only the target complex in moderate yield and minimized for formation of the various byproducts. These conditions thus enabled high yields (Scheme 2.7) and significantly shorter reaction times (ca. 8-12 hours).

The products were separated from the crude mixture by column chromatography (SiO_2). The other components in the mixture were a small amount of unreacted ligand, which was removed with 10% EtOAc/DCM and a small amount of the unreacted $Ru(tpy)^{3+}$ starting material, with the chlorides from the $Ru(tpy)Cl_3$ exchanged for various other ligands and these required a

KNO_3/MeCN mixture to remove them from the column. The target complex was separated on the column using 10% MeCN/EtOAc, which was characterized by ^{1}H and ^{13}C spectroscopy and mass spectrometry.

All eleven complexes had not been previously synthesised and were confirmed as the target complexes in all cases, except for complexes **2.9** and **2.10**. Analysis of **2.9** by mass spectrometry showed a complex with an additional 18 atomic mass units. A possible reason for this was that the alkyne bond was being hydrated, either during analysis by mass spectrometry or during the reaction/work up process. NMR spectroscopy showed no ^{13}C peaks in the typical range for acetylene carbons (70-100 ppm)[137] but instead peaks at 200.0 ppm and 50.88 ppm. 2D NMR studies (HMBC, COSY, HSQC) suggested the structure shown in Scheme 2.8, which was later confirmed by X-ray crystallography. Based on similar mass spectrometry and ^{1}H and ^{13}C NMR spectroscopy results it is likely that this also occurred for **2.10**, although crystals suitable for X-ray diffraction could not be grown. The hydration of these disubstituted acetylenes to form the substituted ketones likely occurs through a similar pathway as for oxymercuration, which uses Hg^{2+} and H_2O to result in electrophilic addition of an alkyne to form an enol, which tautomerizes into a ketone.[138] In the reaction mixture which was used to form **2.9** and **2.10**, the Ru^{3+}, a borderline Lewis acid[139-140], can coordinate to the alkyne in a similar fashion to how the Hg^{2+}, a soft Lewis acid[139-140], coordinates.[138] This is supported by another reported reaction pathway, in which ruthenium complexes are used in the hydration of alkynes into a ketones.[141]

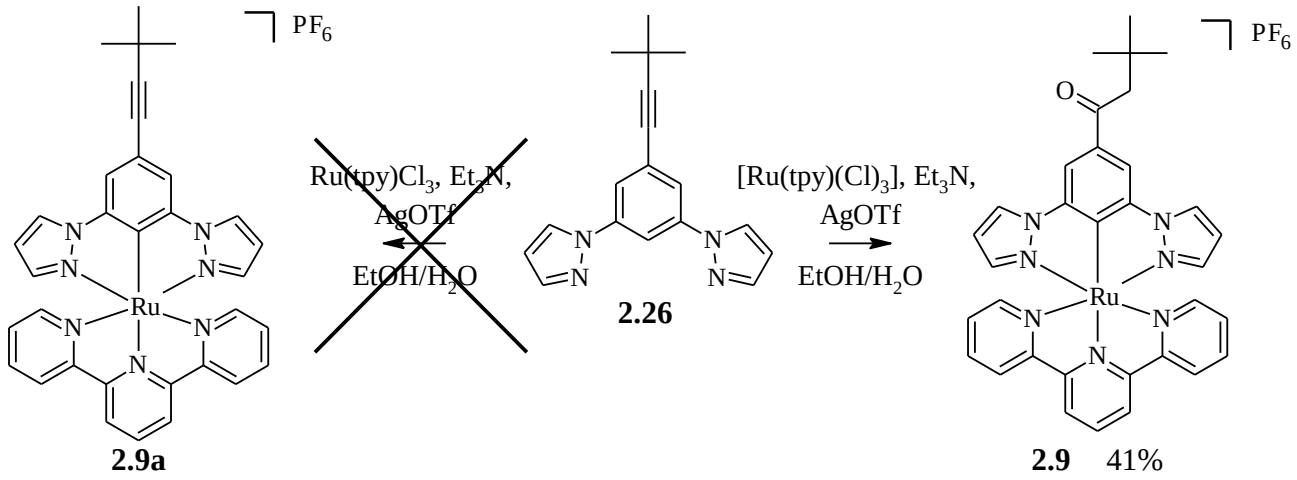

2.9a **2.26** **2.9** 41%

Scheme 2.8: Reaction of 2.26 with Ru(tpy)Cl3 to produce 2.9, but not 2.9a.

2.5 Structural analysis.

2.5.1 NMR spectroscopy

The NMR spectra of these ligands and complexes show significant changes upon cyclometalation of the free ligand to ruthenium and these changes can be examined by analysis of coordination induced shifts (CIS = $\delta_{complex} - \delta_{ligand}$). The sign and magnitude of the CIS in ruthenium(II) complexes results from a range of effects, such as through–space ring–current anisotropy effects, conformational changes due to chelation, ligand–to–metal σ donation and metal–to–ligand π back-donation.[142-145] Positive values indicate downfield shifts and negative values indicate upfield shifts. To achieve meaningful results it is important that NMR spectra for the free ligand and the complex are carried out in the same solvent. Complexes **2.1**-**2.8** and their corresponding unbound N^C^N ligand were both able to be dissolved in acetone-D6 and analysis of their CIS were carried out.

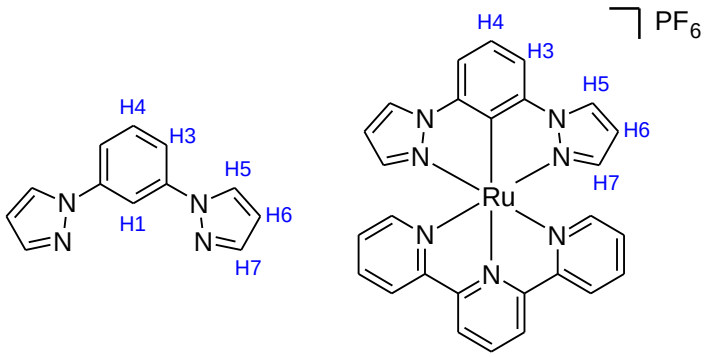

Figure 2.6: Labeling Scheme for ^{1}H CIS analysis for complex 2.1 and its corresponding free ligand.

	H1	H3	H4	H5	H6	H7
2.12	8.36	7.77	7.59	8.43	6.54	7.74
2.1	-	7.90	7.44	8.72	6.24	6.69
CIS	-	+0.13	-0.15	+0.29	-0.30	-1.05

Table 2.1: ^{1}H CIS analysis for complex **2.1**.

Analysis of the ^{1}H NMR spectra for complex **2.1** and the corresponding free ligand shows a large negative CIS of -1.05 for H7 (Figure 2.6, Table 2.1) due to interligand through-space ring-current anisotropy effects in which the H7 proton lies over the shielding plane of the central pyridine ring of the terpyridine ligand as a result of the distorted octahedral geometry (Figure 2.7). This is also the case for H6, which shows a negative CIS, albeit much smaller because it is

further away. The proton adjacent to the nitrogen on the pendant 2-pyridine rings has previously been shown to have a similar effect due to the central ring on the opposite ligand, but the CIS involving the terpyridine ligands were not able to be analyzed due to solubility constraints.

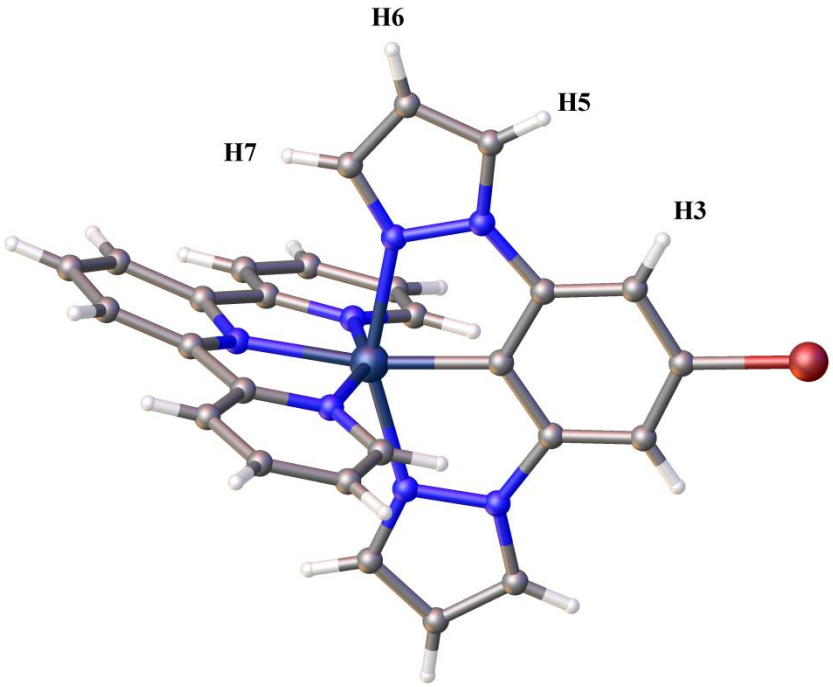

Figure 2.7: Crystal structure of **2.2**, showing H7 proton lying over the shielding plane of the central pyridine ring of the terpyridine ligand.

Conformational effects typically occur in 2,6-disubstituted pyridyl ligands and cause significant CIS[146] due to the free ligand preferring a transoid conformation to minimize steric interactions, whereas the ligand in the complex is locked in the cisoid conformation. This leads to neighboring protons (to the central nitrogen) experiencing different shielding effects in the free and complexed environments. In 1,3-disubstituted benzene ligands, the N-heterocycle rings are also able to freely rotate, however there is less preference for the transoid conformation because there is less interaction between the C-H compared to the N (and its lone pair of electrons) and thus the CIS resulting from chelation-imposed conformational changes are not as large in these complexes compared to similar 2,6-disubstituted pyridine based ligands/complexes, which have CIS values up to -1.46 ppm for neighboring hydrogens.[145] The CIS value for H5 in **2.1** is small (-0.29 ppm), which results from the transoid/cisoid conformers being of similar energy in the free ligand before the ligand is locked in the cisoid conformation in the complex.

Conformation effects have less impact on H3 with pyrazole compared to pyridine because the ring is smaller and the H5 proton (Figure 2.6) is positioned further away from H3. Once again, there is less of a preference for a transoid conformer with the benzene core compared to the alternate pyridine core. This is shown by H3 in **2.1** having a small CIS value of +0.13 ppm compared to the CIS value of +0.46 ppm for the corresponding proton in $[Ru(tpy)_2]PF_6$.[147]

The CIS value of H4 in **2.1** (Figure 2.6) is -0.15 ppm and while this is only a small shift, it shows that there is more electron density on the H4 position of the ligand in the complex compared to the free ligand. Generally there is less electron density on the overall ligand due to σ-donation upon coordination as shown by a similar 2,6-disubstituted pyridine ligands, which have CIS values ranging from ca. +0.3 ppm to +0.6 ppm for the comparable H4 proton.[145] With cyclometalated complexes however, there is a well-documented *para*-directing effect resulting from the σ-bond between the metal and the carbon from the aryl system, which facilitates electrophilic aromatic substitution under mild conditions.[148] This is because the polarity of the M-C bond results in a partial negative charge and this can be delocalized throughout the aryl ring to influence electrophilic substitution pathways. This effect has been explored by Gagliardo *et al.*, in which they were able to achieve regioselective substitution at the *para*-position across from the Ru-C bond, using reaction conditions which do not occur on non-activated aryl systems.[148]

The CIS for the cyclometalated ligands in complexes **2.2**-**2.5** compared to the respective free ligand are very similar for H3, H5, H6 and H7 as these protons are in similar environments and their CIS values reflect those for **2.1**. The only significant differences are H3 and H5 in **2.2**, which show a negligible difference in their chemical shift. The protons on the attached aryl groups all show small positive CIS which are due to ligand to metal σ-donation, which decreases electron density for these protons on the attached aryl ring, which results in their small positive CIS.

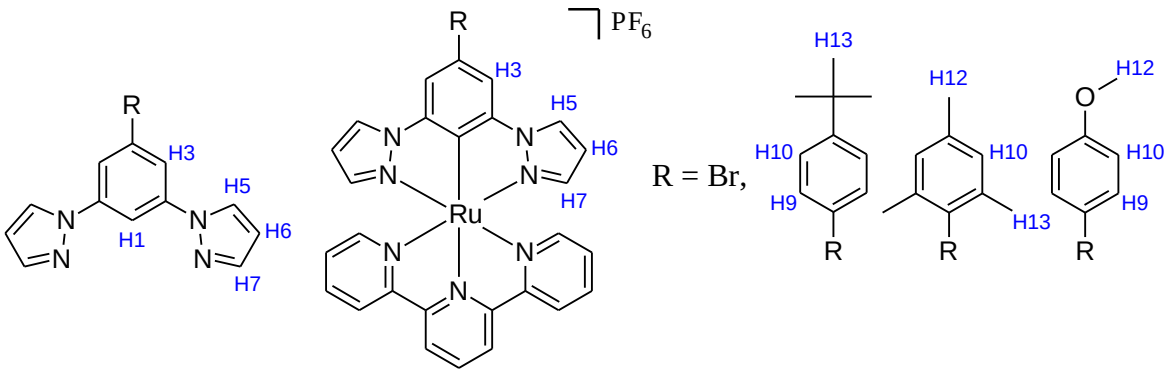

Figure 2.8: Labeling Scheme for ^{1}H CIS analysis for complexes **2.2**-**2.5** and their corresponding free ligand.

	H1	H3	H5	H6	H7	H9	H10	H12	H13
2.13	8.33	7.97	8.51	6.57	7.77				
2.2	-	7.97	8.46	6.21	6.57				
CIS	-	0.00	-0.05	-0.36	-1.20				
2.20	8.35	8.04	8.58	6.58	7.77	7.76	7.58		1.38
2.3	-	8.28	8.90	6.29	6.73	7.95	7.64		1.44
CIS	-	+0.24	+0.32	-0.29	-1.04	+0.19	+0.06		+0.06
2.21	8.41	7.56	8.52	6.55	7.75		6.98	2.07	2.32
2.4	-	7.69	8.75	6.26	6.74		7.08	2.31	2.38
CIS	-	+0.13	+0.23	-0.29	-1.01		+0.10	+0.24	+0.06
2.22	8.31	8.02	8.57	6.57	7.77	7.09	7.79	3.88	
2.5	-	8.26	8.90	6.27	6.73	7.17	7.96	3.92	
CIS	-	+0.24	+0.33	-0.30	-1.04	+0.08	+0.17	+0.04	

Table 2.2: ^{1}H CIS analysis for complexes **2.2**-**2.5**.

The CIS for the cyclometalated ligands in complexes **2.6**-**2.8** compared to their respective free ligand are very similar for H3 and H5-H7 as these protons are in similar environments and their CIS values reflect previous complexes studied. The CIS for the larger aryl groups (naphthalene and pyrene) are less obvious because the protons in the free ligands (**2.23**, **2.24** and **2.25**) are mostly overlapping. In all three complexes (**2.6**-**2.8**) the CIS result in a wider range of ^{1}H peaks, which allows for a more thorough assignment. The general trend for all three of these complexes is a small positive CIS, with the majority of the peaks shifting further downfield in the complexes which results from ligand-to-metal σ donation.

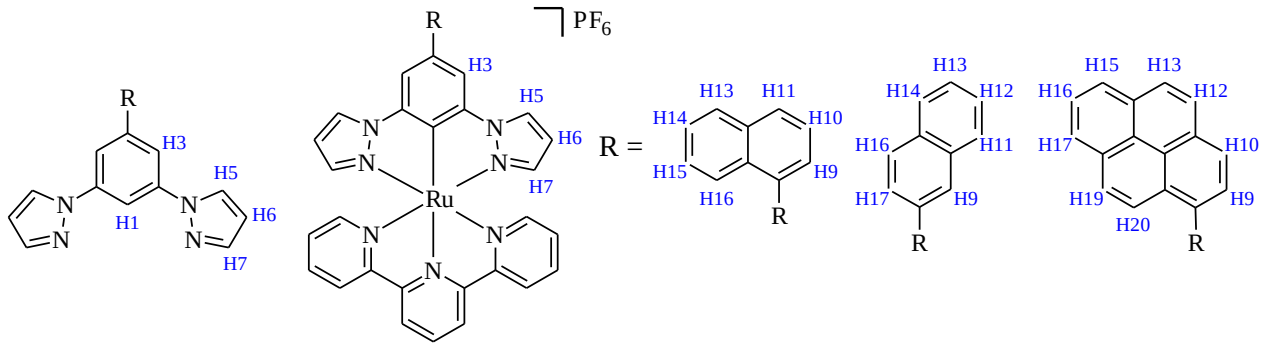

Figure 2.9: Labeling Scheme for ^{1}H CIS analysis for complexes **2.6**-**2.8** and their corresponding free ligand.

	H1	H3	H5	H6	H7	Aryl System
2.23	8.50	7.90	8.57	6.58	7.77	8.07 - 7.96 (3H, H10, H14, H15), 7.67 - 7.49 (4H, H9, H11, H13, H16).
2.6	-	8.05	8.86	6.29	6.76	8.38 (H9), 8.09 (H11), 8.05 (H13), 7.80 (H16), 7.72 (H14), 7.67-7.54 (H10, H15).
CIS	-	+0.15	+0.29	-0.29	-1.01	
2.24	8.40	8.21	8.61	6.60	7.80	8.40 (H9), 8.09-7.95 (H11, H14, H16, H17), 7.57 (H12, H13).
2.7	-	8.46	8.94	6.30	6.75	8.53 (H9), 8.23 (H16), 8.13 (H17), 8.06 (H11), 8.02 (H14), 7.61 (H13), 7.56 (H12).
CIS	-	+0.25	+0.33	-0.30	-1.05	
2.25	8.56	8.07	8.63	6.60	7.80	8.44-8.09 (H9, H10, H12, H13, H15, H16, H17, H19, H20).
2.8	-	8.22	8.90	6.31	6.79	8.70 (H20), 8.51 (H9), 8.43 (H10), 8.36 (H17, H15), 8.30 (H12), 8.29 (H13), 8.26 (H19), 8.14 (H16).
CIS	-	+0.15	+0.27	-0.29	-1.01	

Table 2.3: ^{1}H CIS analysis for complexes **2.6**-1.**8**.

Complex	**2.1**	**2.2**	**2.3**	**2.4**	**2.5**	**2.6**	**2.7**	**2.8**	**2.9**	**2.10**
^{13}C	181.3	180.8	181.1	179.3	180.4	181.1	182.0	182.0	196.0	196.2

Table 2.4: Chemical shift of cyclometalated carbon atom in complexes **2.1**-**2.10**, measured in acetone-D6, except for **2.10**, which was measured in acetonitrile-D6. Shifts are given in ppm and are referenced to the appropriate solvent signals.

The most interesting ^{13}C NMR shift in each complex is the cyclometalated carbon. The peaks are dramatically shifted downfield upon cyclometalated and occur between 179.3 ppm and 196.0 ppm for complexes **2.1**-**2.10** due to electron withdrawal, thus observation of this peak is a strong indication of cyclometalation.

2.5.2 Computational structural analysis

DFT calculations were carried out *in vacuo* for all new complexes in this chapter, including the target complexes **2.9a** and **2.10a** and with the interest of comparing structural implications of these cyclometalation ruthenium structures with directly comparable non-cyclometalated structures, DFT calculations were also carried out *in vacuo* for [Ru(2,6-di(pyrazol-1-yl)pyridine)(terpyridine)] (**2.31**, Figure 2.10) and [Ru(1,3-di(pyridyl-2-yl)(terpyridine)] (**2.32**, Figure 2.10) The bonds lengths for the five Ru-N bonds and the Ru-C bond are shown in Table 2.5 and selected bond angles and dihedral angles are shown in Table 2.6.

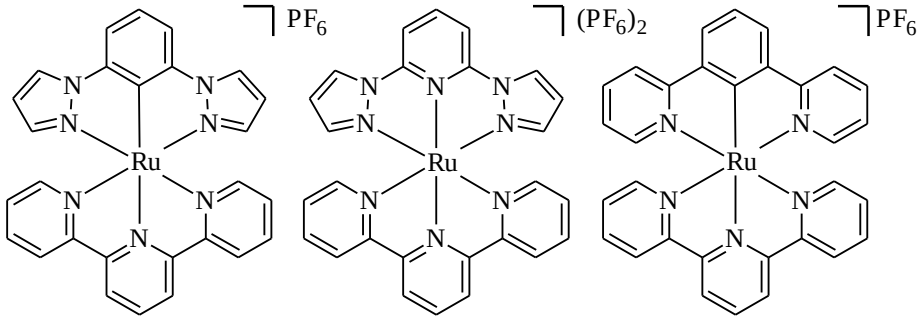

2.1 **2.31** **2.32**

Figure 2.10: Structures of **2.1**, [Ru(2,6-di(pyrazol-1-yl)pyridine)(terpyridine)]PF_6 (**2.31**) and [Ru(1,3-di(pyrid-2-yl)benzene)(terpyridine)]PF_6 (**2.32**).

There are two very important bond lengths to analyze in cyclometalated ruthenium complexes. They are the C-Ru bond between the ruthenium and the central unit on the cyclometalated ligand and the opposite Ru-N6 bond between the ruthenium and the central 2-pyridyl ring on the terpyridine ligand. The reason for these being important is that the replacement of the dative Ru-N bond with the Ru-C bond results in significant shortening of the bond length because of the strong σ-donating, π-donating and electrostatic properties from the anionic, aromatic carbon donor.

Complex	Cyclometalated Ligand			Terpyridine Ligand		
	N2-Ru	C-Ru	N4-Ru	N5-Ru	N6-Ru	N7-Ru
2.1	2.10590	1.99121	2.10580	2.09150	2.03081	2.09136
2.2	2.10680	1.98857	2.10678	2.09269	2.03190	2.09272
2.3	2.10626	1.92723	2.10631	2.10665	2.09874	2.10776
2.4	2.11602	1.93666	2.11048	2.10720	2.10167	2.09810
2.5	2.10668	1.99055	2.10697	2.09083	2.03039	2.09084
2.6	2.10577	1.99022	2.10741	2.09090	2.03105	2.09125
2.7	2.10607	1.98996	2.10659	2.09106	2.03153	2.09122
2.8	2.10200	1.92881	2.10163	2.10695	2.08907	2.10793
2.9	2.10652	1.98121	2.10526	2.09304	2.03585	2.09301
2.9a	2.10670	1.98891	2.10671	2.09098	2.03093	2.09107
2.10	2.10593	1.98087	2.10595	2.09287	2.03616	2.09312
2.10a	2.10661	1.98754	2.10660	2.09145	2.03165	2.09146
2.11	2.07813	1.99780	2.07816	2.09170	2.02992	2.09166
2.31	2.08769	2.02218[a]	2.08750	2.10565	2.00294	2.10573
2.32	2.12215	1.93099	2.12216	2.10472	2.11273	2.10471

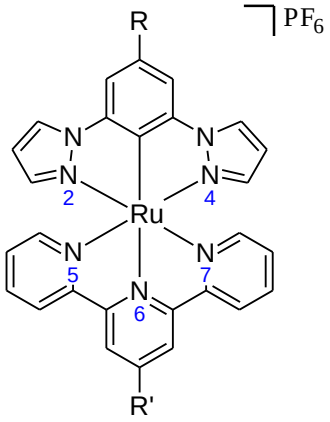

Table 2.5: Calculated bond lengths for **2.1**-**2.11** from DFT calculations *in vacuo*, along with a general figure showing the labeling scheme used. (a) Denotes N atom instead of labeled C atom.

The Ru-C bond length in complexes **2.1**-**2.11** varies from 1.93 Å and 2.00 Å, which are all shorter than the comparable bond length in **2.31**, which has a calculated value of 2.02218 Å. While most complexes have a value around 1.99 Å, complexes **2.3**, **2.4** and **2.8** have values of 1.92723 Å, 1.93666 Å and 1.92881 Å respectively. Complexes **2.3** and **2.4** have an electron rich phenyl groups donating into the cyclometalated carbon, which results in more electron density in the Ru-C bond, hence a stronger, shorter bond. A similar effect is likely occurring in **2.8**, in which the pyrene is donating electron density into the Ru-C bond. The aryl substitutions in the remaining complexes do not have a significant influence on the Ru-C bond length as their values are all very similar to the value in **2.1**.

Due to the increased electron donation ability of the carbanion, the opposite Ru-N6 bond becomes elongated as a result of the trans effect.[149-150] The opposite Ru-N6 bond length in complexes **2.1**-**2.11** varies between 2.02 Å and 2.11 Å and these are all longer than the bond length for **2.31**, which has a calculated value of 2.00294 Å. This shows that there is an inverse relationship occurring because of the trans effect in these complexes. Results from searching the Cambridge structural database shows that the mean bond length between the central nitrogen in a substituted terpyridine ligand and the ruthenium atom in $[Ru(tpy)_2]^{2+}$ based complexes is

1.984,[16-17] which shows the shortening for the Ru-C bond length and the elongation of the opposite Ru-N bond length in these cyclometalated structures.

The Ru-N5 and Ru-N7 bonds, which incorporate the peripheral pyridines on the terpyridine ligand are also shortened as a result of increased π-back donation from the more electron rich ruthenium in the cyclometalated complex.

The bond lengths for the Ru-N2 and Ru-N4 bonds, from the pyrazole to the ruthenium are all of a similar value, ranging from 2.10 Å to 2.12 Å for all complexes except **2.11** which has a calculated value of 2.07816 Å. Complex **2.11** incorporates pyrene as the core instead of benzene, which results in steric hindrance between the H16 and H19 protons on the pyrene and the H12 and H13 protons on each pyrazole (Figure 2.11). This results in the Ru-N2 and Ru-N4 bond lengths being shorter because the pyrazole rings are moved closer to the ruthenium (Figure 2.11). To minimize the steric hindrance the pyrazole rings are also twisted out of the plane by 1.84°, with one ring being pushed down and the other up, along with a slight twist in the pyrene.

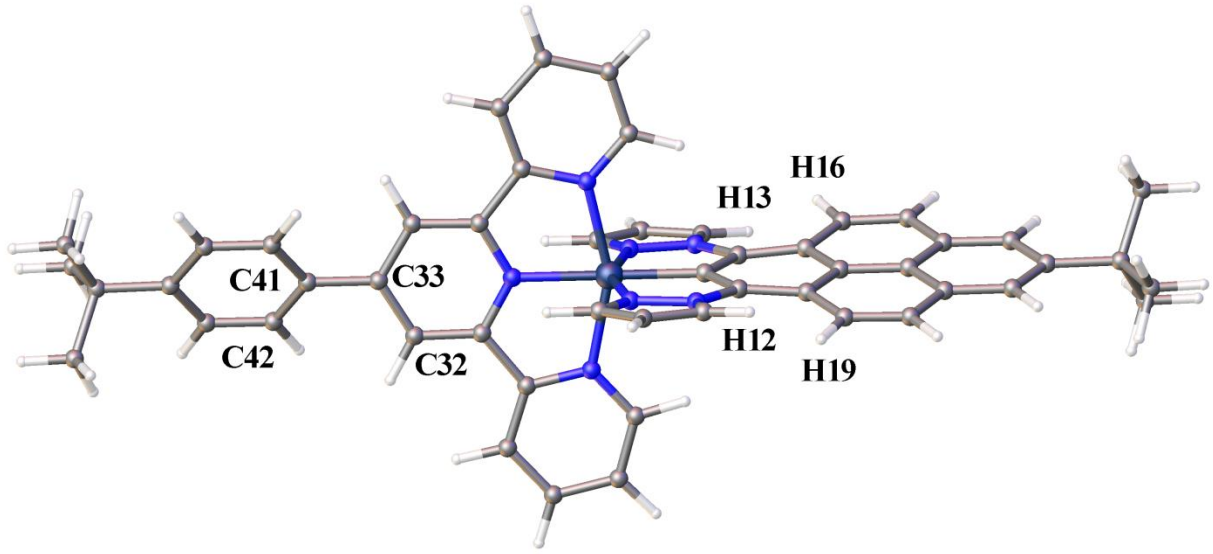

Figure 2.11: Calculated structure of **2.11** using DFT *in vacuo* showing the steric hindrance between H12, H13, H16 and H19, as well as the dihedral angle (C32-C33-C41-C42).

The Ru-N5 and Ru-N7 bond lengths are also of a similar value, which ranges from around 2.09 Å to 2.11 Å. This shows that there is minimal effect on the Ru-N bond lengths for the peripheral pyridines from the aryl substitutions on the cyclometalated ligand.

The bite angle of the cyclometalated ligand (N2-Ru-N4) to the ruthenium in complexes **2.1**-**2.11** ranges from 154.6° to 158.1°. These measurements show that there is also a relationship between the Ru-C bond length and the bite angle. Complexes **2.3**, **2.4** and **2.8** have shortened Ru-C bond lengths, which brings the rest of the cyclometalated ligand closer to the metal, which results in their corresponding bite angle (N2-Ru-N4) being increased. The effect of using pyrazole as the N-heterocycle instead of pyridine is a smaller angle, as the value for **2.32** is 160.0°.

Complex	C-Ru-N5	C-Ru-N6	C-Ru-N7	N2-Ru-N4	N5-Ru-N7	Dihedral A	Dihedral B
2.1	101.529	179.995	101.517	154.942	156.954	N/A	N/A
2.2	101.545	179.997	101.538	154.896	156.917	N/A	N/A
2.3	103.252	179.997	103.604	158.120	153.144	28.220	N/A
2.4	105.761	177.519	101.274	158.027	152.912	76.613	N/A
2.5	101.535	179.817	101.480	154.633	156.985	35.784	N/A
2.6	101.650	179.648	101.381	154.720	156.969	53.461	N/A
2.7	101.513	179.911	101.549	154.680	156.938	36.791	N/A
2.8	103.003	179.538	103.023	157.901	153.974	43.407	N/A
2.9	101.602	179.972	101.644	155.182	156.754	N/A	N/A
2.9a	101.543	179.974	101.497	154.810	156.960	N/A	N/A
2.10	101.578	179.756	101.670	155.224	156.752	N/A	N/A
2.10a	101.534	179.995	101.533	154.878	156.933	N/A	N/A
2.11	101.655	179.952	101.729	156.100	156.616	N/A	32.604
2.31	100.953[a]	179.999[a]	100.951[a]	156.485	158.096	N/A	N/A
2.32	103.869	179.999	103.871	160.012	152.261	N/A	N/A

Table 2.6: Calculated bond angles for complexes **2.1**-**2.11** from DFT calculations *in vacuo*. Dihedral A is the dihedral angle between the substituted aryl group (a) and the central benzene ring (b) on the cyclometalated ligand. Dihedral B is the dihedral angle between the central pyridine ring and the substituted aryl group on the terpyridine ligand. Bond lengths are measured in angstroms, Å. (a) Denotes N atom instead of labeled C atom.

The bond angles between C1-Ru-N5 and C1-Ru-N7 are between 101° and 106° for **2.1**-**2.11** and there is no significant difference between their value and the 101.0° value for **2.31**. All these angles are greater than the 90° required for a standard octahedral geometry and this is due to the geometric constraints of the two ligands and thus they are described as being distorted octahedral. The calculated C1-Ru-N6 bond angle varies between 180.0° and 179.5°, showing the Ru-C bond and the Ru-N bond are almost directly opposite for all complexes.

The calculated dihedral angles are shown in Table 2.6. The angle between the benzene ring on the cyclometalated ligand and the substituted aryl group is listed as dihedral A (Figure 2.12) and the angle between the central pyridine ring and the aryl ring on the substituted terpyridine ligand is listed as dihedral B (Figure 2.12).

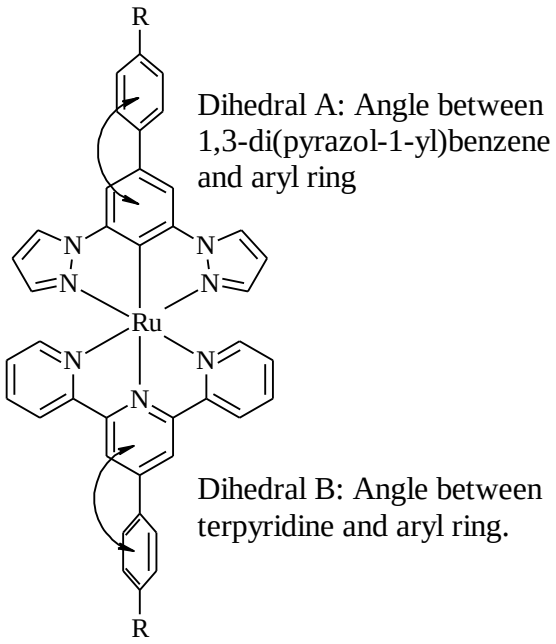

Figure 2.12: Showing the twisting between the core of each ligand and the substituted aryl group, labeled dihedral angle A and dihedral angle B.

The 4-substituted phenyl groups are calculated to be twisted by 28.220° and 35.784° for **2.3** and **2.5**, respectively. This slight twist is due to the small amount of steric hindrance that occurs between between the protons on the central benzene ring and the adjacent protons on the aryl ring. The mesityl group in **2.4** is calculated to twist by 76.613° and be nearly perpendicular as a result of a larger amount of steric hindrance from the protons on the central benzene ring and the adjacent methyl groups on the aryl group. For the 1-naphthyl and 2-naphthyl groups in **2.6** and **2.7** there is a calculated dihedral angle of 53.461° and 36.791° respectively between the planar naphthyl groups and the central benzene ring, with a slightly larger twist in **2.6** due to the 1-naphthyl group being bent with respect to the 1,3-di(pyrazol-1-yl)benzene unit and thus a larger amount of steric hindrance. In complex **2.8**, the pyrenyl group is planar and has a dihedral angle of 43.407 with the central benzene ring, showing that the pyrenyl group is calculated to be half way between being planar and perpendicular. Also, complex **2.10a** is calculated to have the

phenylacetylene in the same plane as the cyclometalated ligand as a result of the acetylene separating the two parts of the structure, reducing the steric hindrance. This could thus lead to potentially interesting properties if it was able to be synthesized.

2.6 Crystal structure determination.

*2.6.1 Crystal structure of **2.1***

Dark red crystals suitable for X-ray analysis of **2.1** (Figure 2.13) were grown by slow evaporation of a solution containing **2.1** dissolved in an acetone/toluene mixture and these crystals were successfully characterized by X-ray diffraction. The structure solved in the monoclinic space group $P2_1/c$ and contained two molecules of complex **2.1**, two hexafluorophosphate anions and two acetone solvate molecules in the asymmetric unit. There is a large amount of disorder resulting from the similarities between the terpyridine ligand and the cyclometalated ligand and thus it is difficult to eliminate the disorder due to a lack of distinguishing features on each ligand relative to each another.

Both molecules of complex **2.1** are independent of each other and the central ruthenium atom has a distorted octahedral geometry. The two independent terpyridine ligands have chelate bite angles of 156.2(4)° (N5-Ru1-N7) and 155.3(3)° (N9-Ru2-N11) and the two independent cyclometalated ligands have angles of 155.1(3)° (N2-Ru1-N4) and 155.5(3)° (N13-Ru2-N15). Typically the cyclometalated ligand has a smaller chelate bite angle compared to the corresponding angle in the terpyridine ligand due the size of the pyrazole compared to the pyridine. As a result of this the similarities between the chelate bite angles in the 2nd molecule of **2.1** are a result of a more disordered structure. The calculated structure has values of 154.942° and 156.954° for the cyclometalated ligand chelate bite angle and the terpyridine chelate bite angle, respectively. These calculated angles are similar to the corresponding angle in the other similar structures in this series and also similar to the corresponding angle in the crystal structures of other complexes in this series, which have a better refinement. The cyclometalated bond lengths are 1.984(9)° (Ru1-C1) and 1.997(9)° (Ru2-C28) which do not show the expected shortening of the Ru-C bond length compared to the Cambridge structural database mean bond length of 1.984° for the comparable Ru-N bond length in similar non-cyclometalated complexes. [16-17] This is a result of disorder in the solved crystal structure due to similarities between both ligands. There is also a smaller than expected increase in the Ru-N bond length opposite the

cyclometalated Ru-C bond, with the expected increase due to the trans effect.[149-150] The bond length of these Ru1-N6 and Ru1-N14 bonds are 2.000(9) Å and 2.005(8) Å respectively.

The crystal packing also exhibits extensive short F···H–C contacts between the hexafluorophosphate anions and the ligand molecules in the range of 2.5-3.3 Å, which further stabilizes the solid–state structure.

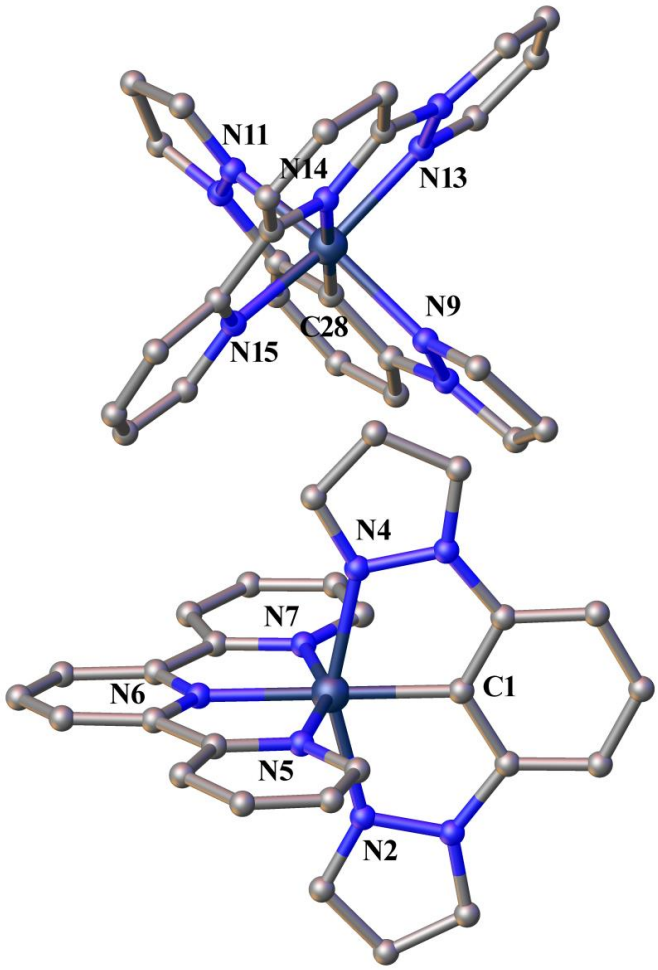

Figure 2.13: Crystal structure of complex **2.1**. Hydrogen atoms, counterions and the solvate molecules are omitted for clarity. Selected bond distances (Å): Ru1-N2 2.095(8), Ru1-C1 1.984(9), Ru1-N4 2.094(9), Ru1-N5 2.066(9), Ru1-N6 2.000(9), Ru1-N7 2.069(9), Ru2-N9 2.068(9), Ru2-C28 1.997(9), Ru2-N11 2.083(9), Ru2-N13 2.047(9), Ru2-N14 2.005(8), Ru2-N15 2.074(8). Selected bond angles (°):C1-Ru1-N5 102.2(4), C1-Ru1-N6 179.9(5), C1-Ru1-N7 101.7(4), N2-Ru1-N4 155.1(3), N5-Ru1-N7 156.2(4), C28-Ru2-N13 102.1(4), C28-Ru2-N14 178.6(4), C28-Ru2-N15 102.4(3), N13-Ru2-N15 155.5(3), N9-Ru2-N11 155.3(3).

*2.6.2 Crystal structure of **2.2***

Dark red crystals suitable for X-ray analysis of **2.2** (Figure 2.14) were grown by slow evaporation of a solution containing **2.2** dissolved in an acetonitrile/toluene mixture and these crystals were successfully characterized by X-ray diffraction. The structure solved in the triclinic space group *P*-1 and contained one molecule of complex **2.2**, one trifluoromethanesulfonate anion and one disordered toluene solvate molecule in the asymmetric unit.

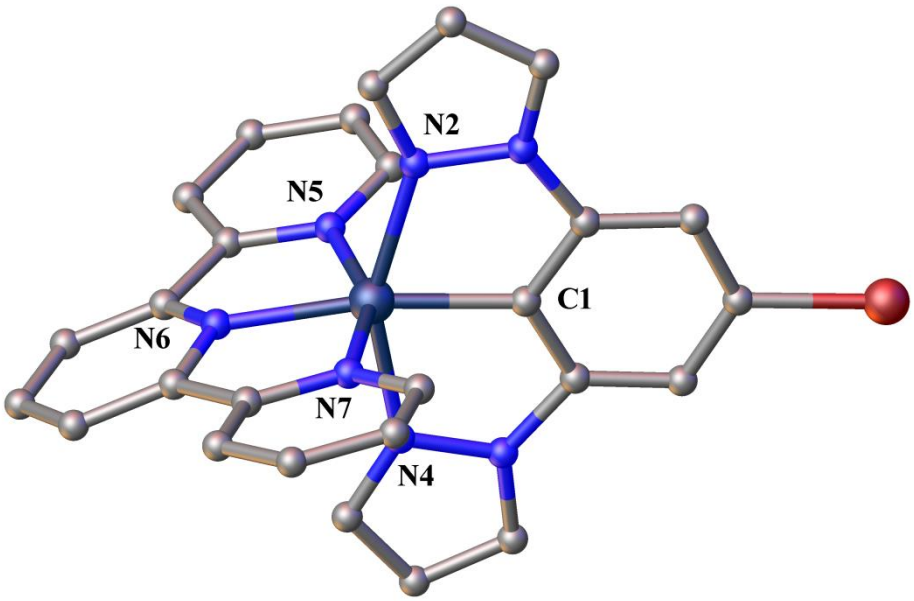

Figure 2.14: Crystal structure of complex **2.2**. Hydrogen atoms, counterions and the solvate molecules are omitted for clarity. Selected bond distances (Å): Ru1-N5 2.062(3), Ru1-N6 2.013(3), Ru1-N7 2.062(3), Ru1-N2 2.094(3), Ru1-C1 1.978(3), Ru1-N4 2.072(3). Selected bond angles (°):C1-Ru1-N5 100.6(1), C1-Ru1-N6 169.5(1), C1-Ru1-N7 102.7(1), N2-Ru1-N4 154.6(1), N5-Ru1-N7 156.7(1).

The ruthenium atom possesses a distorted octahedral geometry, with the substituted terpyridine ligand and cyclometalated ligand having chelate bite angles of 156.7(1)° (N5-Ru1-N7) and 154.6(1)° (N2-Ru1-N4), respectively. These angles reflect the corresponding calculated value for each angle (156.917° and 154.896°), with only a small difference between the calculated and experimental measurements. The Ru-C bond length is 1.978(3) Å, which is slightly shorter than the two independent Ru-C bond lengths in the X-ray structure of **2.1** as a result of a better refinement for **2.2**. This shortening of the Ru-C bond length is reflected in the elongated bond length of Ru-N6, which has a value of 2.013(3) Å. The calculated bond lengths of Ru-C and Ru-

N6 are 1.98857 Å and 2.03190 Å respectively, which are both slightly longer than the experimental X-ray structures as a result of DFT calculations tending to slightly overestimate bond lengths. The observation of these overestimated bond lengths has been tentatively explained by Hiberty and co-workers as a result of from electron self-interaction in the DFT calculation process, which leads to slightly high energies for the bonds and thus they are expressed as being slightly elongated. In similar structures these factors are observed as a systematic error in the bond lengths and related properties.[151]

The other bond lengths and angles are similar to the corresponding values in complex **2.1**, except the C1-Ru-N6 bond angle is 169.5(1)° compared to the two corresponding values of 179.5(5)° and 178.6(4)° in the X-ray structure of **2.1**. This angle is smaller than the calculated value of 179.997° and results from the entire terpyridine ligand being bent, most likely a result of the crystallization process.

The crystal packing also exhibits extensive short F···H–C contacts between the trifluoromethanesulfonate anions and the ligand molecules in the range of 2.5-3.3 Å. There is also hydrogen bonding between the oxygen atoms on the cyclometalating ligand and trifluoromethanesulfonate anions and the ligand molecules. Both these interactions further stabilize the solid–state structure.

*2.6.3 Crystal structure of **2.5a***

Red crystals suitable for X-ray analysis of **2.5a** were grown by slow evaporation of an acetonitrile/toluene solution containing a crude mixture of various byproducts from the reaction which produced **2.5**. These crystals were successfully characterized by X-ray diffraction and the structure was solved in the monoclinic space group $P2_1/c$. The asymmetric unit contains one molecule of **2.5a** and one hexafluorophosphate anion.

The ruthenium atom has a distorted octahedral geometry, with the cyclometalated ligand only co-ordinated to the ruthenium *via* one nitrogen atom in addition to the cyclometalated bond. The nitrogen on the other pyrazole (N4) which typically binds to the ruthenium to is not co-ordinated and there is instead an acetonitrile opposite the Ru-C bond. This shows one of the possible alternate structures that can form during the complexation reaction and shows why the reaction conditions required optimization in order to generate the target complex in higher yield. The

dihedral angle between the main part of the cyclometalated ligand and the substituted aryl ring (C3-C4-C13-C14) is 23.8(4)° and shows that there is a slight twist to minimize the steric strain from the neighboring hydrogen atoms.

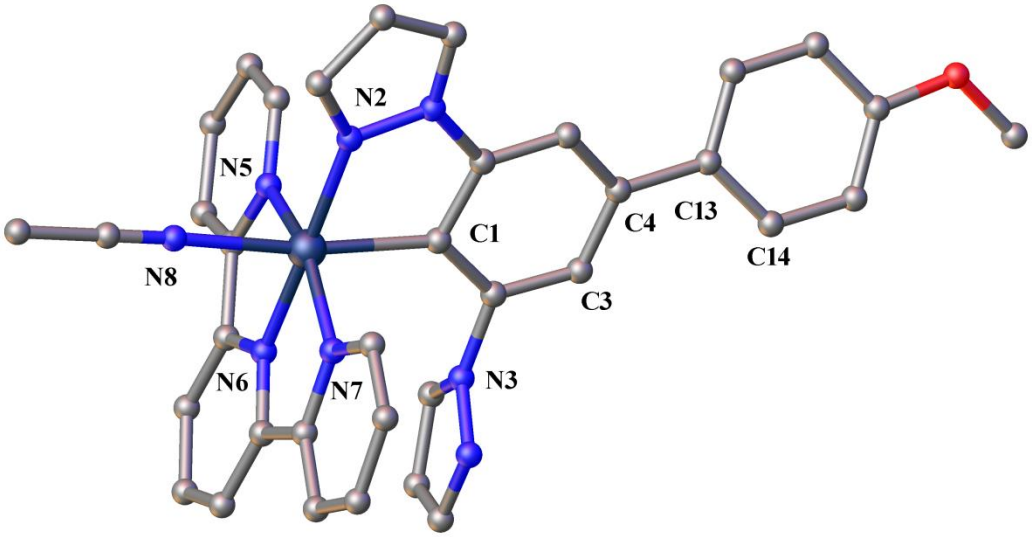

Figure 2.15: Crystal structure of complex **2.5a**. Hydrogen atoms, counterions and the solvate molecules are omitted for clarity. Selected bond distances (Å): Ru1-N2 2.073(2), Ru1-C1 2.057(2), Ru1-N5 2.074(2), Ru1-N6 1.958(2), Ru1-N7 2.055(2), Ru1-N8 2.162(2). Selected bond angles (°): N5-Ru1-N7 159.28(9), C1-Ru1-N2 78.85(9), C1-Ru1-N5 89.49(9), C1-Ru1-N8 170.16(9). Selected dihedral angle (°): C3-C4-C13-C14 23.8(4).

The crystal packing also exhibits extensive short F···H–C contacts between the hexafluorophosphate anions and the ligand molecules in the range of 2.5-3.3 Å, which further stabilizes the solid–state structure.

*2.6.4 Crystal structure of **2.7***

Dark red crystals of complex **2.7** (Figure 2.16) were obtained by slow evaporation of a toluene/acetonitrile/acetone solution containing the complex and these were suitable for X–ray analysis. The structure solved in the orthorhombic space group $P2_12_12_1$ and contained one molecule of complex **2.7** and one hexafluorophosphate anion in the asymmetric unit.

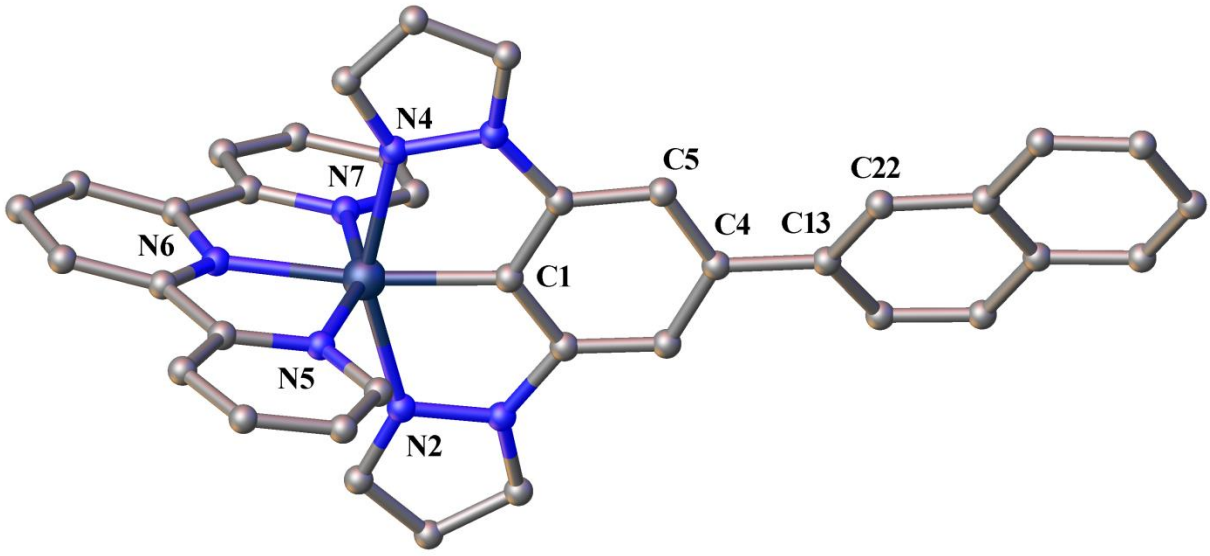

Figure 2.16: Crystal structure of complex **2.7**. Hydrogen atoms, counterions and the solvate molecules are omitted for clarity. Selected bond distances (Å): Ru1-N2 2.091(3), Ru1-C1 1.961(4), Ru1-N4 2.083(4), Ru1-N5 2.071(3), Ru1-N6 2.016(3), Ru1-N7 2.066(4). Selected bond angles (°): C1-Ru1-N5 105.0(2), C1-Ru1-N6 173.3(2), C1-Ru1-N7 98.6(2), N2-Ru1-N4 154.9(1), N5-Ru1-N7 156.4(1). Selected dihedral angle (°): C5-C4-C13-C22 18.4(6).

The ruthenium atom possesses a distorted octahedral geometry, with the substituted terpyridine ligand and cyclometalated ligand having chelate bite angles of 156.4(1)° (N5-Ru1-N7) and 154.8(1)° (N2-Ru1-N4), respectively. These angles reflect the corresponding calculated value for each angle (156.938 and 154.680), with only a small difference between the calculated and experimental measurements. The C-Ru bond length is 1.961(4) Å, which is shorter compared to the X-ray structure of **2.1** showing that the Ru-C bond has more electron density and is thus stronger. A consequence of the shorter bond length is that the chelate bite angle is slightly increased, albeit a very small increase, with the value of 154.9(1)° for N2-Ru-N4 compared to the corresponding angle in **2.2** of 154.6(1)°. The other bond lengths and angles are similar to the corresponding values in complex **2.1**, except the C1-Ru-N6 bond angle which is 173.3(2)° compared to the two corresponding values of 179.5(5)° and 178.6(4)° in the X-ray structure of **2.1**. This angle is smaller than the calculated value of 179.911° and results from the entire terpyridine ligand being bent, but to a lesser extent than in **2.2**, which had a value of 169.5(1). The dihedral angle between the main part of the cyclometalated ligand and the naphthalene ring

introduced (C5-C4-C13-C22) is 18.4(6)° and shows that there is a slight twist to reduce the steric strain from the neighboring hydrogen atoms.

The crystal packing also exhibits extensive short F···H–C contacts between the hexafluorophosphate anions and the ligand molecules in the range of 2.5-3.3 Å, which further stabilizes the solid–state structure.

*2.6.5 Crystal structure of **2.9***

Slow diffusion of petroleum ether into an acetone solution of the complex gave dark red crystals of **2.9** suitable for X-ray crystallography. Complex **2.9** (Figure 2.17) crystallized in the monoclinic space group $P2_1/c$. The asymmetric unit contains one molecule of **2.9** and one trifluoromethanesulfonate anion.

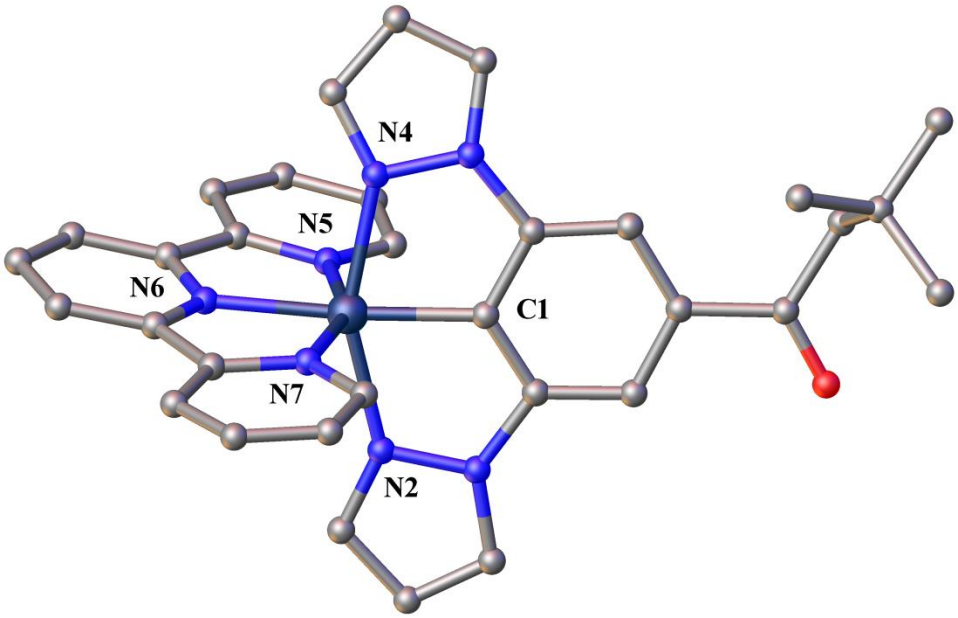

Figure 2.17: Crystal structure of complex **2.9**. Hydrogen atoms, counterions and the solvate molecules are omitted for clarity. Selected bond distances (Å): Ru1-N2 2.084(7), Ru1-C1 1.970(8), Ru1-N4 2.073(7), Ru1-N5 2.090(7), Ru1-N6 2.047(7), Ru1-N7 2.076(7). Selected bond angles (°): C1-Ru1-N5 102.9(3), C1-Ru1-N6 175.6(3), C1-Ru1-N7 101.0(3), N4-Ru1-N2 155.4(3), N5-Ru1-N7 156.1(3).

The ruthenium atom in complex **2.9** possesses a distorted octahedral geometry, with the substituted terpyridine ligand and cyclometalated ligand having chelate bite angles of 156.1(3)° (N5-Ru1-N7) and 155.4(3)° (N2-Ru1-N4), respectively. These angles reflect the corresponding

calculated value for each angle (156.754 and 155.182), with only small difference between the calculated and experimental measurements. The C-Ru bond length is 1.970(8) Å, which is of a similar bond length compared to the two independent C-Ru bond lengths in the X-ray structure of **2.2.** The other bond lengths and angles are similar to the corresponding bond lengths and angles in complex **2.1**.

The crystal packing also exhibits extensive short F···H–C contacts between the trifluoromethanesulfonate anions and the ligand molecules in the range of 2.5-3.3 Å. There is also hydrogen bonding between the oxygen atoms on the cyclometalating ligand and trifluoromethanesulfonate anions and the ligand molecules. Both these interactions further stabilize the solid–state structure.

2.7 Photophysical properties of ruthenium complexes.

2.7.1 Photophysical properties of ruthenium complexes

UV-vis spectra have been recorded in acetonitrile for all complexes in this series (**2.1**-**2.11**) and to assist in the assignment of observed transitions computational studies have been completed. Density functional theory (DFT) calculations have been used to calculate optimized structures for each of the complexes in this study, and time dependent density functional theory (TD-DFT) calculations have been performed to provide further insight into the UV-vis characteristics of these complexes. TD-DFT calculations were performed based on previous work by Wadman et al.[37] using the B3LYP functional with the DZ Dunning basis set[152-153] for all atoms except ruthenium, which used the Stuttgart RSC 1997 ECP relativistic core potential[154] and bromine, which used LAND2DZ ECP, as explained in the introduction section.[155]

Computational studies of large complex systems require considerable computational time, and thus it is important to balance precise data against the time required to achieve it. There are several methods which can be used to reduce overall calculation time, for example, using an effective core potential (ECP), which replaces the chemically inert inner core electrons which are not involved in bonding. This results in a dramatic reduction in the time required with only a very small loss in the accuracy of the overall system. Another consideration that is very important is the number of transitions calculated when running the TD-DFT. During early

experiments, twenty to thirty transitions were calculated as this provided enough data to examine the lower energy MLCT transitions.

In the interest of a more complete understanding, a smaller number of calculations were run up to n=75 states, which gave enough transitions to examine the higher energy transitions which fall between 200-350 nm, whereas the earlier studies only provide transitions to around 300 nm. The transitions in the UV are more difficult to assign, as there are often several transitions within a small energy range and thus they are generally not assigned. The next important consideration is whether to run the calculations *in vacuo*, or whether to model solvent in the calculation, in this case acetonitrile. Studies performed in solution using acetonitrile as solvent with the polarization continuum model[156-157] took around fifty times as long to complete and thus were very computationally demanding. To examine the difference between the studies *in vacuo* and in acetonitrile the parent complex, **2.1** was calculated in both conditions and both sets of results were analysed alongside the experimental UV-vis results.

2.7.2 Comparing calculations in vacuo and in acetonitrile

The UV-vis spectrum for the parent complex, **2.1**, is shown in Figure 2.18 along with the calculated TD-DFT data. The measured UV-vis spectrum shows that the lowest energy MLCT has a peak at 487 nm (ε = 4,700), although it is very broad with two distinct shoulders at lower energy. The two calculated UV-vis spectra both show three transitions which make up the broad MLCT envelope. The calculations in acetonitrile and *in vacuo* show the MLCT peak at 474 nm and 467 nm respectively, both providing a reasonable fit to the experimental data. Both calculations show the same transitions in the visible region for **2.1** despite the small difference in wavelength. The three transitions are S_2, S_5 and S_6, which represent the transitions HOMO-1 → LUMO, HOMO-2 → LUMO+1 and HOMO-2 → LUMO respectively. The calculations also provide information about the nature of transitions and which molecular orbitals are involved which can be analysed using isodensity plots.

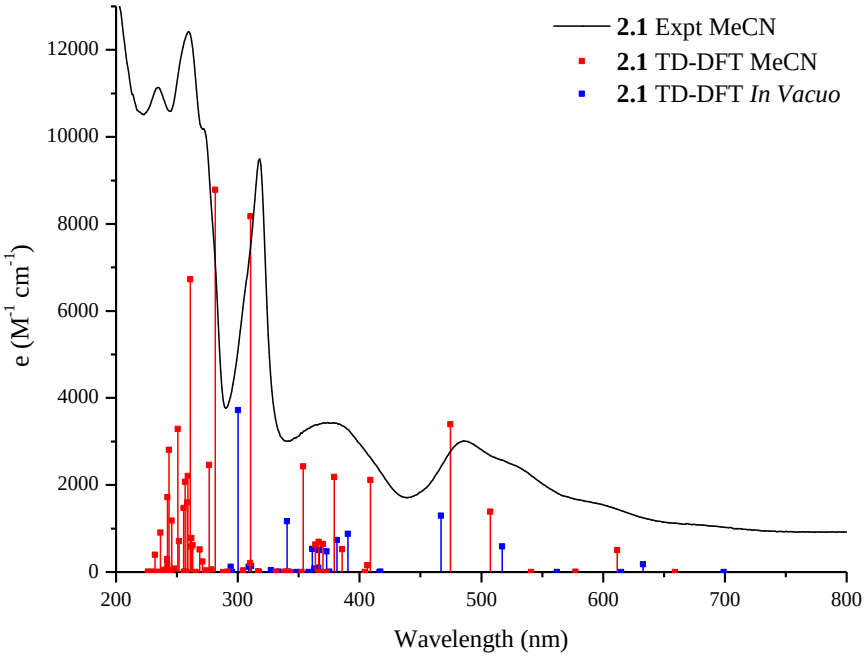

Figure 2.18: Electronic absorption spectra of ruthenium complex **2.1** along with TD-DFT calculated data for **2.1** in MeCN and *in vacuo*. Calculated intensities from TD-DFT measured in oscillator strength and are arbitrary units.

The isodensity plots for these orbitals (Figure 2.19) show that the HOMO-1 and HOMO-2 are predominately metal based while the HOMO-1 has a significant contribution from each pyrazole ring on the cyclometalating ligand. The HOMO-2 has a minor contribution from the central pyridine on the terpyridine ligand. The LUMO and LUMO+1 on the other hand are both very similar and the isodensity plots predominately show a large contribution from the terpyridine ligand, although there is still some metal based electron density. This description fits into the mixed metal/ligand to ligand charge transfer description and is thus described as being MLCT.

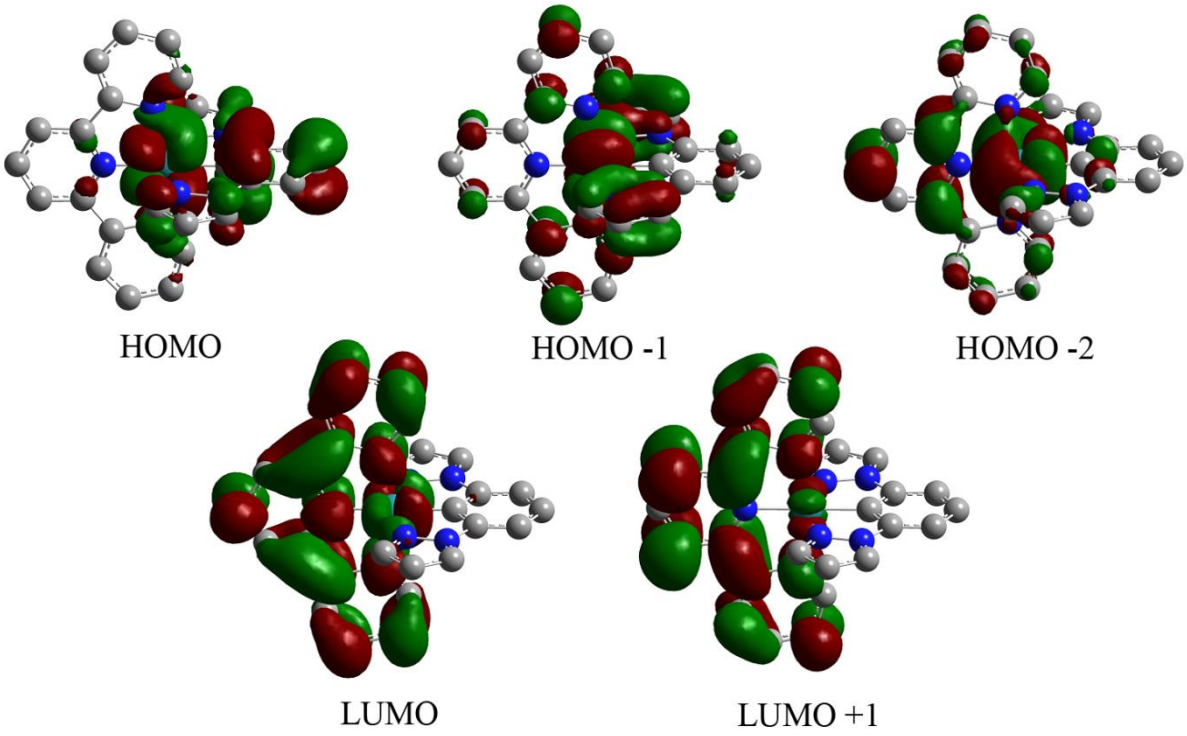

Figure 2.19: Isodensity plots (isovalue 0.02) of selected frontier orbitals that are involved in the lowest energy MLCT for **2.1** from DFT calculation in acetonitrile.

S_n	E/nm	f	Dominant Transition			Percentage Contribution
2.1 (*In Vacuo*)						
S1	699.0	0.000	HOMO	→	LUMO	98
S2	632.8	0.010	HOMO -1	→	LUMO	96
S5	517.2	0.050	HOMO -2	→	LUMO +1	96
S6	467.0	0.100	HOMO -2	→	LUMO	62
2.1 (MeCN)						
S1	659.2	0.000	HOMO	→	LUMO	99
S2	611.7	0.040	HOMO -1	→	LUMO	98
S5	507.5	0.110	HOMO -2	→	LUMO +1	98
S6	474.5	0.260	HOMO -2	→	LUMO	59

Table 2.7: Selected calculated UV-vis transitions from TD-DFT calculations for **2.1** *in vacuo* and in acetonitrile over the range of 450-700 nm (1st MLCT).

The next lowest energy peak appears at 375 nm (ε = 5,400) and the TD-DFT results in which acetonitrile is included in the study suggest three transitions contribute to this peak. Transitions S_7, S_{11} and S_{17} result from the transitions HOMO → LUMO+2 (409.0 nm), HOMO-1 → LUMO+3 (379.2 nm) and HOMO-1 → LUMO+5 (353.8 nm), respectively. The TD-DFT calculations *in vacuo* are not as straight forward for this 2nd low energy peak showing at least five different potentially important transitions.

S_n	E/nm	f	Dominant Transition			Percentage Contribution
2.1 (*In Vacuo*)						
S9	390.4	0.070	HOMO	→	LUMO +4	85
S10	381.4	0.060	HOMO -1	→	LUMO +2	89
S12	372.9	0.040	HOMO -1	→	LUMO +3	60
S14	367.0	0.040	HOMO -2	→	LUMO +3	78
S15	366.2	0.010	HOMO -2	→	LUMO +2	92
S17	361.1	0.040	HOMO	→	LUMO +5	31
S21	340.5	0.090	HOMO -1	→	LUMO +5	82
S28	300.2	0.290	HOMO -5	→	LUMO	91
2.1 (MeCN)						
S7	409.0	0.160	HOMO	→	LUMO +2	91
S11	379.2	0.170	HOMO -1	→	LUMO +3	98
S17	353.8	0.190	HOMO -1	→	LUMO +5	90
S26	310.5	0.630	HOMO -5	→	LUMO	93
S31	281.6	0.680	HOMO -5	→	LUMO +1	58
S42	261.0	0.520	HOMO	→	LUMO +9	56
S52	250.8	0.250	HOMO -9	→	LUMO +1	90

Table 2.8: Selected calculated UV-vis transitions from TD-DFT calculations for **2.1** *in vacuo* in acetonitrile over the range of 350-410 nm (2nd MLCT).

The isodensity plots from the acetonitrile TD-DFT study of the HOMO orbital show a significant contribution on both the metal and over the entire cyclometalating ligand. The HOMO-1, as described previously, has contribution predominately on the metal but also spread over the pyrazole on each side of the cyclometalating ligand. The electron density of the LUMO+2 is entirely on the terpyridine ligand, with slightly less contribution on the central pyridine. The

LUMO+3 is similar to the LUMO+2, but in this case there is no electron density on the central pyridine, and only a small amount on the cyclometalating ligand and metal. The LUMO+5 has a significant contribution from the pyrazoles on the cyclometalating ligand but shows electron density around the cyclometalated carbon atom. There is also a small amount of electron density on the metal center. This explains the reason for the broad nature of the experimental peak, as it results from three quite different transitions. All three can be described as being MLCT, S_7 and S_{11} show charge transfer onto the terpyridine ligand, while S_{17} shows charge transfer onto the cyclometalated ligand.

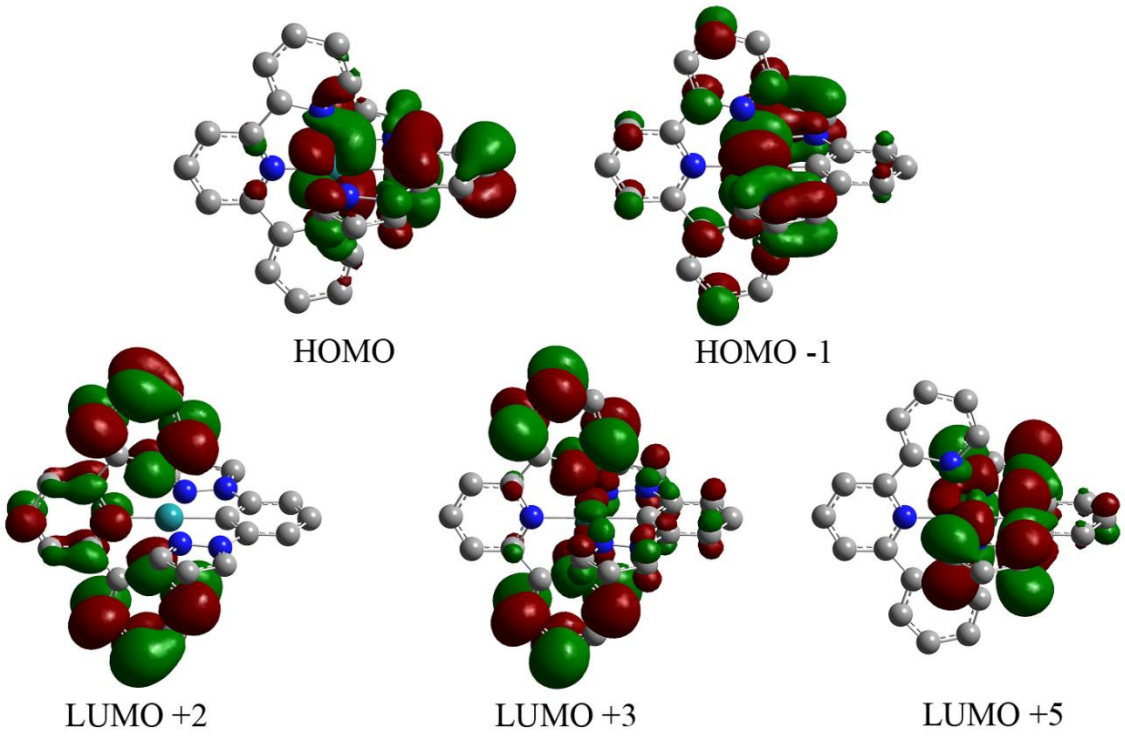

Figure 2.20: Isodensity plots (isovalue 0.02) of selected frontier orbitals that are involved in the 2nd lowest energy MLCT for **2.1** from DFT calculation in acetonitrile.

The next peak of interest occurs at 318 nm nm (ε = 15,200) for **2.1**, for which the TD-DFT calculates transitions occurring at 300.2 nm *in vacuo* and 310.5 nm in acetonitrile. This is calculated as resulting from the same transition, HOMO-5 → LUMO in both. The isodensity plot for the HOMO-5 orbital not only has contribution from the terpyridine ligand and the LUMO electron density on the terpyridine ligand, but also shows a small amount on the metal. Despite this small metal contribution the transition appears to be LC (π→π*).

The remaining part of the UV-vis spectrum (200-300 nm) is typically not very well modeled by TD-DFT calculations, mainly because of the large number of transitions in this range and the difficulty matching them to experimental results. The measured UV-vis for **2.1** shows two main peaks in this range, 259 nm (19.9) and 234 nm (17.6). These are presumed to be high energy ligand-ligand based transitions.

2.7.3 Comparing pyrazole versus 2-pyridine

Complex	Absorption 298 K, MeCN, λ_{max} (nm) ($\varepsilon(10^3\ M^{-1}\ cm^{-1})$)
2.32[37]	499 (14.4), 424 (9.6), 368 (8.2), 315 (37.0), 277 (47.0), 243 (49.8).
2.1	536 (2.7), 487 (4.7), 375 (5.4), 318 (15.2), 259 (19.9), 234 (17.6).

Table 2.9: Electronic absorption data for prepared ruthenium complexes **2.32** and **2.1**.

The UV-vis spectra for **2.32** and **2.1** are shown in Figure 2.22 along with the results from their respective TD-DFT calculations. The experimental UV-vis spectrum for **2.32** shows that the lowest energy peak envelope has a single λ_{max} at 499 nm. Complex **2.1** has a peak envelope that expands over the same energy range as **2.32** but instead has a λ_{max} at 487 nm (ε = 4,700) and a distinct shoulder at 536 nm (ε = 2,700). The λ_{max} for **2.1** is blue shifted by 12 nm compared to **2.31** and the intensity of the λ_{max} in **2.1** is significantly less than in **2.32**.

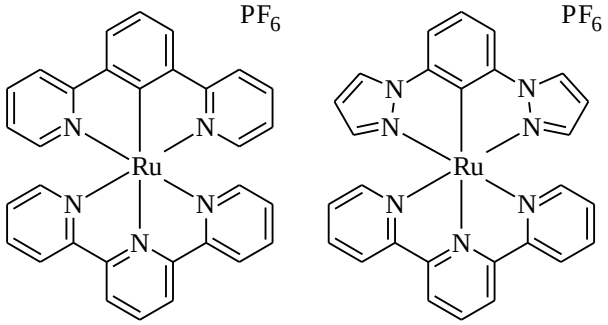

2.32 **2.1**

Figure 2.21: Structures of **2.32** and **2.1**

The TD-DFT calculations for **2.32** show four transitions over the range of the lowest energy peak envelope. The largest of these is the HOMO-1 → LUMO transition, which has a calculated energy of 475.2 nm. The isodensity plot for the HOMO-1 of **2.32** (Figure 2.23) shows that the HOMO-1 has electron density predominantly on the metal, but also spread over both ligands. The isodensity plot for the LUMO of **2.32** shows electron density predominantly on the

terpyridine ligand, with a small amount on the metal. The isodensity plot for the HOMO shows that the electron density is spread over both the cyclometalated ligand and the metal. While it is not involved in the dominant transition in **2.32** it shows the mixing between the cyclometalated ligand and the metal in complexes of this type. This shows that the main transition for **2.32** is MLCT and that modifying the cyclometalated ligand should change the energy of the relevant occupied orbital and modifying the terpyridine ligand has a large impact on the LUMO.

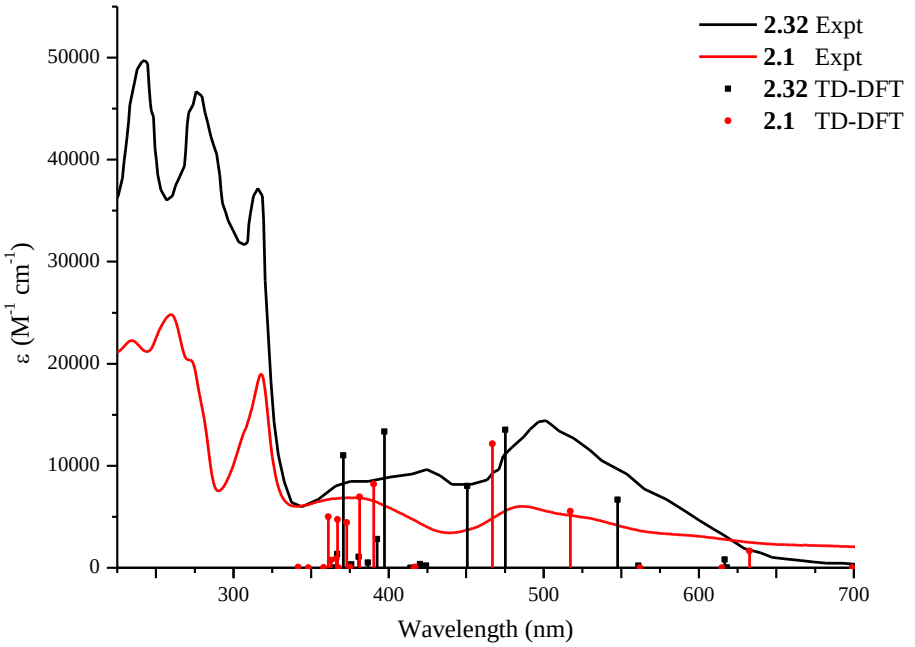

Figure 2.22: Electronic absorption spectra of ruthenium complex **2.32** and **2.1** along with calculated TD-DFT data *in vacuo* for comparison. UV-vis spectral data for **2.32** was obtained from Wadman et al.[37] Calculated intensities from TD-DFT measured in oscillator strength and are arbitrary units.

The TD-DFT calculations for **2.1** show three transitions over the range of the lowest energy peak envelope. The largest of these three transitions is at 467.0 nm, giving a calculated blue shift of 8.2 nm and reflecting the experimentally observed results. This dominant transition corresponds to a HOMO-2 to LUMO transition. The isodensity plot for the HOMO-2 (Figure 2.23) shows that electron density is predominantly on the metal and the central pyridine of the terpyridine ligand. There is also a small amount on the remaining parts of the terpyridine ligand and the pyrazole rings of the cyclometalated ligand. The isodensity plot for the LUMO (Figure 2.23)

shows that electron density is predominantly on the terpyridine ligand, with a small amount also on the metal. The overall energies of both the HOMO-2 and LUMO are increased in **2.1** compared to **2.32**, as shown by the orbital energy diagram (Chapter 7.4, Figure 7.4.1) with a larger increase in the energy of the LUMO than for the HOMO-2, which results in the blue shift. Pyrazole is an electron rich N-heterocycle and its introduction in **2.1** leads to more electron density on the metal through σ donation and more electron density on the terpyridine through π back donation, which results in the observed blue shift.

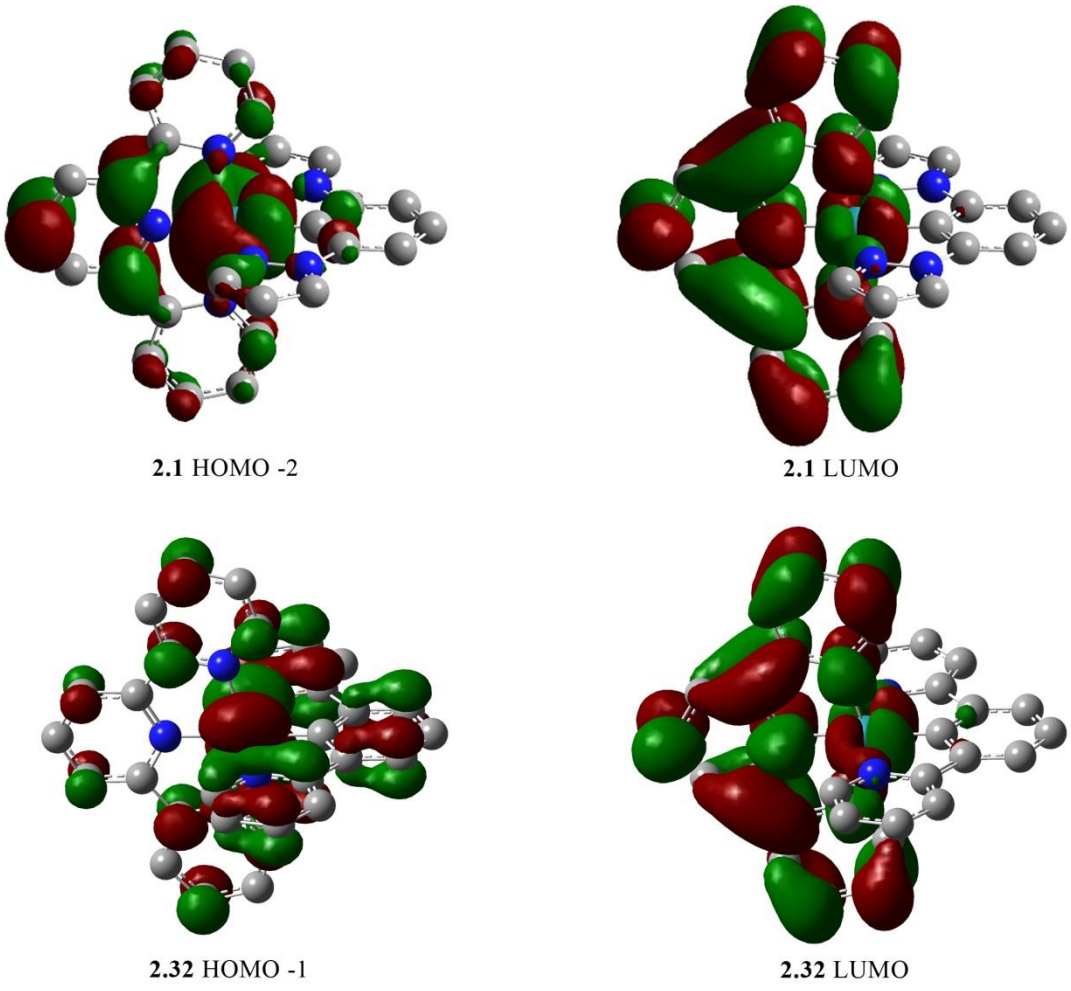

Figure 2.23: Isodensity plots involved in lowest energy peak envelope for **2.1** and **2.32**.

S_n	E/nm	f	Dominant Transition			Percentage Contribution
2.32						
S1	699.0	0.000	HOMO	→	LUMO	98
S3	616.8	0.009	HOMO -2	→	LUMO	90
S5	547.6	0.048	HOMO -1	→	LUMO +1	91
S6	475.2	0.109	HOMO -1	→	LUMO	47
S7	450.8	0.072	HOMO	→	LUMO +2	86
S13	397.4	0.111	HOMO -2	→	LUMO +3	86
S14	392.5	0.024	HOMO -2	→	LUMO +2	68
S16	380.8	0.013	HOMO -1	→	LUMO +5	96
S18	370.8	0.092	HOMO -2	→	LUMO +5	84
S19	366.8	0.014	HOMO -2	→	LUMO +4	49
2.1						
S1	699.0	0.000	HOMO	→	LUMO	98
S2	632.8	0.014	HOMO -1	→	LUMO	96
S5	517.2	0.051	HOMO -2	→	LUMO +1	96
S6	467.0	0.101	HOMO -2	→	LUMO	62
S9	390.4	0.072	HOMO	→	LUMO +4	85
S10	381.4	0.061	HOMO -1	→	LUMO +2	89
S12	372.9	0.039	HOMO -1	→	LUMO +3	60
S14	367.0	0.039	HOMO -2	→	LUMO +3	78
S15	366.2	0.014	HOMO -2	→	LUMO +2	92
S17	361.1	0.041	HOMO	→	LUMO +5	31
S21	340.5	0.092	HOMO -1	→	LUMO +5	82
S28	300.2	0.293	HOMO -5	→	LUMO	91

Table 2.10: Selected calculated UV-vis transitions from TD-DFT calculations for reference complex, **2.32** and **2.1** *in vacuo*.

The UV-vis spectra for **2.32** and **2.1** show a 2nd broad peak envelope between 340 nm and 440 nm, with **2.32** having two λ_{max} in this range at 424 nm (ε = 9,600) and 368 nm (ε = 8,200) and **2.1** having a single λ_{max} in this range at 375 nm (ε = 5,400). The TD-DFT calculations for **2.32** and **2.1** show a large number of transitions occurring over the range of this peak envelope and the isodensity plots for these orbitals show that they are all different types of MLCT transitions. The remaining higher energy transitions between 200 nm and 340 nm are all most likely LC ($\pi \rightarrow \pi^*$) transitions although only limited information from the TD-DFT calculations can be obtained due to the large number of transitions in this range and the limits of the computational processes at this energy.

*2.7.4 Complexes **2.2-2.5***

Complex	Absorption 298 K, MeCN, λ_{max} (nm) ($\varepsilon(10^3\ M^{-1}\ cm^{-1})$)
2.2	590 (sh), 530 (sh), 482 (9.4), 361 (9.8), 317 (31.5), 263 (40.2), 233 (35.0).
2.3	600 (sh), 534 (sh), 488 (6.0), 373 (6.9), 317 (24.5), 270 (sh), 263 (33.9), 232 (32.6).
2.4	606 (sh), 530 (sh), 487 (7.1), 363 (10.7), 317 (29.7), 272 (37.3), 262 (37.0), 235 (31.7).
2.5	603 (sh), 532 (sh), 487 (6.7), 362 (9.4), 318 (29.2), 271 (38.4), 263 (sh), 234 (26.6).

Table 2.11: Electronic absorption spectra for ruthenium complexes **2.2-2.5**.

The UV-vis spectra for complexes **2.2**, **2.3**, **2.4** and **2.5** are shown in Figure 2.24 and the calculated TD-DFT data is shown in Figure 2.25. The measured UV-vis spectrum for **2.2** shows that the lowest energy peak envelope has a λ_{max} at 482 nm (ε = 9,400), with a distinct shoulder between 515 nm and 545 nm and a significantly lower intensity shoulder between 570 nm and 625 nm. This peak envelope has shifted 5 nm towards the blue, compared to **2.1** (487 nm) and the absorption has approximately doubled for **2.2** compared to **2.1**. The lowest energy peak envelopes for complexes **2.3**, **2.4** and **2.5** are very similar to each other, and also to **2.1**, with a λ_{max} at 488 nm for **2.3** (ε = 6,000) and 487 nm for both **2.4** (ε = 7,100) and **2.5** (ε = 6,700). All of these complexes have two shoulders over a similar range to **2.2** and the intensity of the absorption is decreased for **2.3**-**2.5** compared to **2.2**, but still significantly larger than **2.1**.

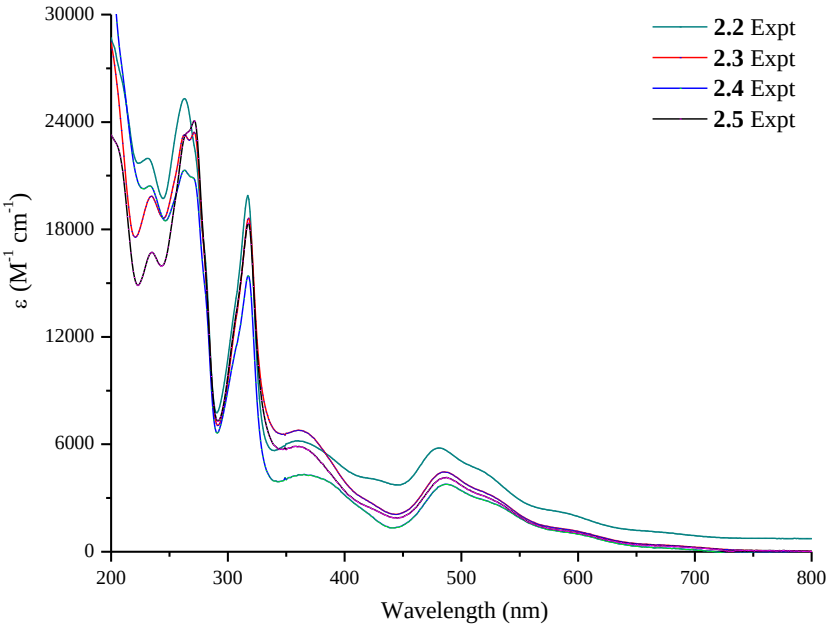

Figure 2.24: Electronic absorption spectra of ruthenium complexes **2.2-2.5**.

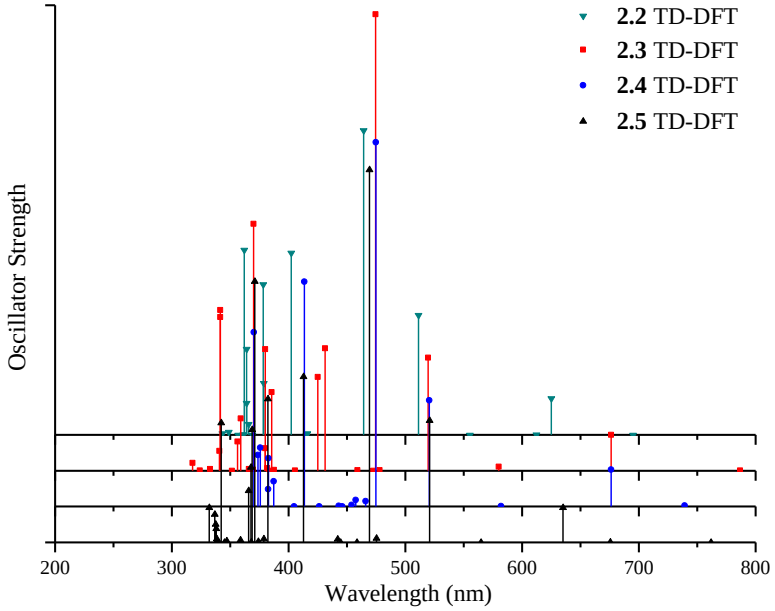

Figure 2.25: Calculated TD-DFT data for **2.2-2.5** *in vacuo*.

The TD-DFT calculations *in vacuo* for each of these four complexes show three significant transitions, over the range of 400 nm – 700 nm, with the HOMO → LUMO transition having no oscillator strength in any of these complexes, meaning that it has no effect on the experimental UV-vis spectrum, this is a common result for all complexes through this work. The three transitions for each complex relate to the λ_{max} and the two shoulders, with the oscillator strengths reflecting the intensity of the measured peak/shoulders in each.

The lowest energy, and highest oscillator strength transition for **2.2** within this range is the HOMO-2 → LUMO transition, which has a calculated energy of 464.3 nm and has a small blue shift compared to the TD-DFT calculations for the comparable transition in **2.1** (467.0 nm). This corresponds with the blue shift in the measured UV-vis spectra for **2.2** (482 nm) compared to **2.1** (487 nm). Analysis of the isodensity plots for the corresponding HOMO-2 orbitals shows that electron density is predominantly on the metal for both **2.1** and **2.2**, with a small amount on the central pyridine of the terpyridine ligand. The LUMO in both complexes has a large amount of electron density on the terpyridine ligand, with a small amount on the metal. The energies of these orbitals shows that the HOMO-2 in **2.2** is lower in energy compared to the HOMO-2 in **2.1** and the same is true for the LUMO in **2.2** compared to **2.1**, but to a lesser extent. This results in an increase in energy, which leads to the observed blue shift. The bromine atom in **2.2** has an electron withdrawing effect, which results in less electron density on the metal and the terpyridine ligand, but the effect is greater on the metal than the terpyridine ligand and so the HOMO-2 is lowered in energy more than the LUMO. This is because the metal receives more σ donation from the cyclometalated ligand compared to the amount of π back donation the terpyridine ligand receives from the metal.

The TD-DFT calculations for complexes **2.3**, **2.4** and **2.5** *in vacuo* show similar results as for **2.2**, in which there are three dominant transitions involved in the lowest energy peak envelope in the experimental UV-vis. The main transition in each complex is HOMO-3 → LUMO for **2.4** and HOMO-2 → LUMO for **2.3** and **2.5**, for which the energy of the transition is comparable for **2.3** and **2.4**, with the transition in **2.5** transition having a small blue shift compared to the others.

The isodensity plots (Figure 2.26) for the relevant occupied orbitals for each of these four complexes show electron density predominantly on the metal, with a small amount on the central pyridine of the terpyridine ligand, with no electron density of the cyclometalated ligand in each.

The LUMO has electron density predominantly on the terpyridine ligand, with a small amount on the metal. These are very similar to the isodensity plots for **2.1** and **2.2** and thus they are very similar transitions, for which the 4' substituted aryl ring has little impact as there is no electron density on the cyclometalated ligand.

The energy of the HOMO is significantly raised due to the introduced 4' aryl group, however the HOMO is not involved in any of the transitions in this range and therefore no significant change in energy is observed. The energy of the relevant HOMO-2/HOMO-3 orbitals is not significantly changed in any of the complexes and neither is the energy of the LUMO in any of the complexes, which results in no change in energy of the transition for these complexes, as shown in the experimental UV-vis results. The isodensity plots for all these complexes show that the transition is made up of a mixed terpyridine ligand and metal occupied orbital and a terpyridine unoccupied orbital, which means that the transition is in fact MLCT.

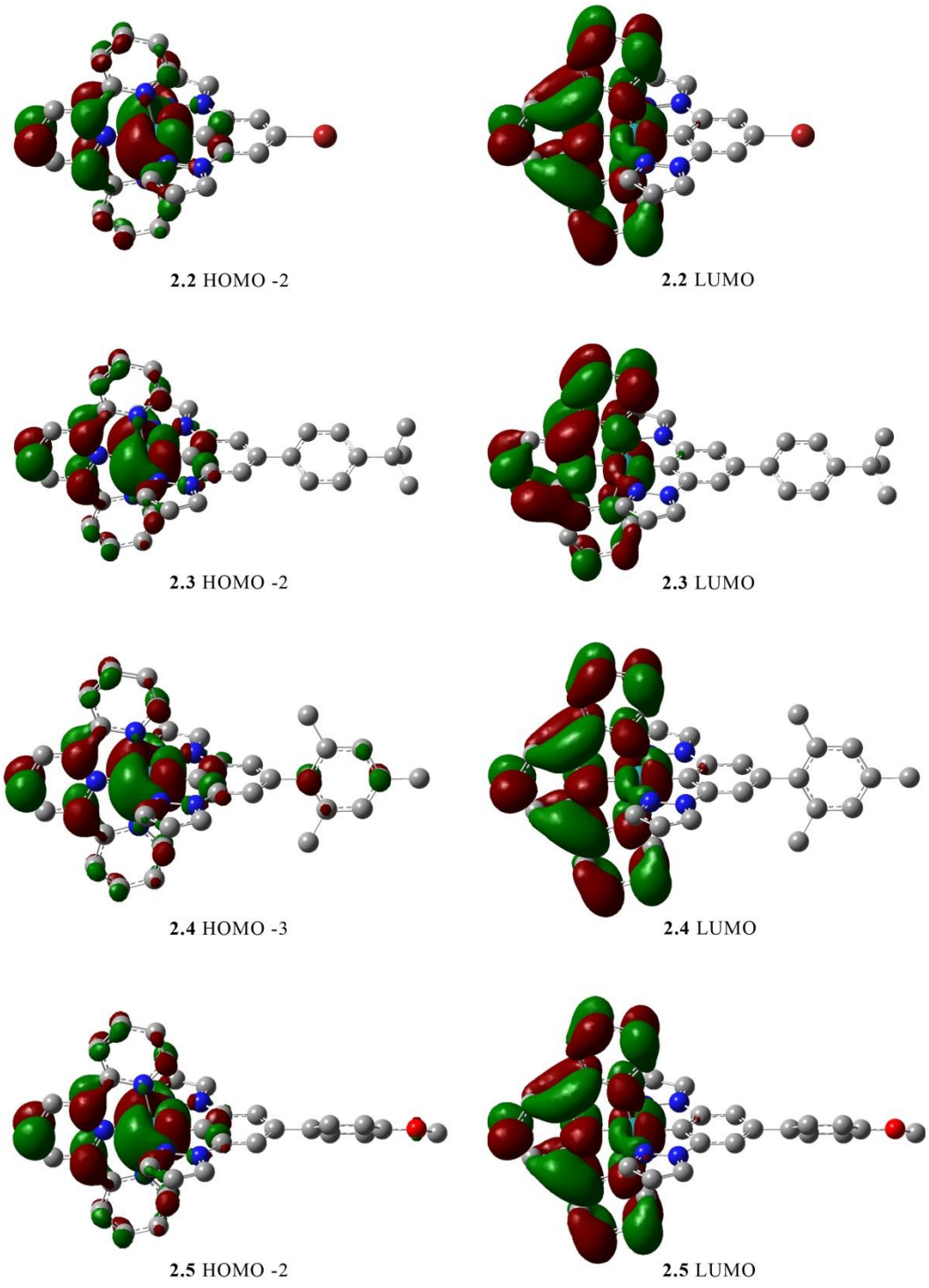

Figure 2.26: Isodensity plots (isovalue 0.02) of selected frontier orbitals that are involved in the dominant transition for the lowest energy MLCT for **2.2**-**2.5** from DFT calculation *in vacuo*.

S_n	E/nm	f	Dominant Transition			Percentage Contribution
2.2						
S1	695.1	0.000	HOMO	→	LUMO	98
S2	625.1	0.014	HOMO -1	→	LUMO	96
S5	511.3	0.045	HOMO -2	→	LUMO +1	96
S6	464.3	0.113	HOMO -2	→	LUMO	62
2.3						
S1	945.8	0.000	HOMO	→	LUMO	93
S3	676.3	0.013	HOMO -1	→	LUMO	93
S5	519.6	0.042	HOMO -2	→	LUMO +1	81
S7	474.6	0.170	HOMO -2	→	LUMO	49
2.4						
S1	883.5	0.000	HOMO	→	LUMO	98
S3	676.2	0.014	HOMO -1	→	LUMO	97
S5	520.4	0.040	HOMO -3	→	LUMO +1	92
S6	474.8	0.136	HOMO -3	→	LUMO	53
2.5						
S1	761.7	0.000	HOMO	→	LUMO	88
S3	635.0	0.013	HOMO -1	→	LUMO	96
S5	520.6	0.045	HOMO -2	→	LUMO +1	94
S7	469.2	0.139	HOMO -2	→	LUMO	59

Table 2.12: Selected calculated UV-vis transitions from TD-DFT calculations for **2.2**-**2.5** *in vacuo* over the range of 450-800 nm (1^{st} MLCT).

The 2^{nd} lowest energy peak for **2.2** is at 361 nm (ε = 9,800), a blue shift of 14 nm compared to **2.1** (375 nm) and the intensity of the absorbance is approximately doubled for **2.2** compared to **2.1**. The 2^{nd} lowest energy peak for **2.3** and **2.5** are also blue shifted compared to **2.1**, but to a slightly lesser extent, with the peak for **2.3** at 363 nm (ε = 10,700) and the peak for **2.5** at 362 nm (ε = 9,400). The value for **2.4** is similar to **2.1**, but has a small blue shift, with a value of 373 nm (ε = 6,900). The intensities of all these peaks are approximately the same, with **2.4** being slightly reduced compared to the other three in this series. The TD-DFT calculations for these complexes do not provide much additional information about this 2^{nd} lowest energy peak, because there are a large number of transitions in this range, the largest of which are shown in Table 2.13. However, all the transitions are MLCT transitions, in which the occupied orbitals show electron density predominantly on the metal in all cases, with a mixing into either of the ligands, and in some cases, both ligands. The relevant unoccupied orbitals are predominantly based on the terpyridine.

The remaining lower energy peaks for **2.2**-**2.5** have peaks at approximately 317 nm, 271 nm, 262 nm and 234 nm in each complex. These are all most likely LC ($\pi \rightarrow \pi^*$) transitions, and are relatively unchanged by the modifications to the cyclometalated ligands in this series. Due to the large number of transitions in this range, the transitions in this range were not able to be assigned based on the TD-DFT calculations.

S_n	E/nm	f	Dominant Transition			Percentage Contribution
2.2						
S9	402.3	0.068	HOMO	→	LUMO +4	63
S11	378.2	0.056	HOMO -1	→	LUMO +2	90
S14	364.0	0.032	HOMO -2	→	LUMO +3	86
S16	361.9	0.069	HOMO -2	→	LUMO +2	51
2.3						
S13	413.5	0.084	HOMO	→	LUMO +4	92
S20	370.2	0.065	HOMO -1	→	LUMO +3	66
2.4						
S10	431.3	0.046	HOMO	→	LUMO +4	53
S11	424.9	0.035	HOMO -3	→	LUMO +1	55
S14	385.6	0.029	HOMO	→	LUMO +5	78
S17	380.1	0.045	HOMO -1	→	LUMO +2	59
S19	370.0	0.092	HOMO -1	→	LUMO +3	60
2.5						
S11	412.7	0.062	HOMO	→	LUMO +4	89
S12	382.4	0.053	HOMO -1	→	LUMO +2	87
S15	371.0	0.097	HOMO -1	→	LUMO +3	67
S16	368.9	0.042	HOMO -2	→	LUMO +3	70
S18	367.6	0.028	HOMO -2	→	LUMO +2	77

Table 2.13: Selected calculated UV-vis transitions from TD-DFT calculations for **2.2**-**2.5** *in vacuo* over the range of 350-435 nm (2nd MLCT).

*2.7.5 Complexes **2.6**-**2.8***

Complex	Absorption 298 K, MeCN, λ_{max} (nm) ($\varepsilon(10^3\ M^{-1}\ cm^{-1})$)
2.6	601 (sh), 531 (sh), 486 (8.5), 366 (12.9), 318 (31.7), 271 (43.3), 266 (43.3), 221 (78.1).
2.7	602 (sh), 527 (sh), 484 (7.6), 372 (13.4), 318 (28.1), 271 (43.7), 263 (42.4), 254 (42.2), 234 (41.5), 211 (37.5).
2.8	598 (sh), 528 (sh), 482 (11.2), 377 (18.1), 339 (26.1), 318 (40.2), 276 (59.4), 266 (sh), 237 (62.5).

Table 2.14: Electronic absorption spectra for ruthenium complexes **2.6**-**2.8**.

The UV-vis spectra for complexes **2.6**, **2.7** and **2.8** are shown in Figure 2.27 and the calculated TD-DFT data is shown in Figure 2.28. The measured UV-vis spectrum for **2.6** shows a similar lowest energy peak envelope to previous complexes, in which there is a λ_{max} at 486 nm (ε = 8,500) and two small shoulders between 520 nm and 560 nm and between 580 nm and 640 nm.

The measured UV-vis spectrum for **2.7** has a similar lowest energy peak envelope to **2.6**, although the blue shift of the λ_{max} is slightly more prominent in this case at 484 nm (ε = 7,600). The two typical shoulders are observed between 530 nm and 550 nm and between 580 nm and 620 nm, although they are slightly reduced in intensity compared to **2.6**. The UV-vis spectrum for **2.8** shows that the lowest energy peak envelope is even further blue shifted compared to the others in this series, with a λ_{max} at 482 nm (ε = 11,200). The two typical shoulders are obscured for **2.8**, with the peak envelope appearing almost as a single peak. The intensity is also significantly increased compared to the corresponding peak envelope in all other complexes in this series.

The TD-DFT calculations, completed *in vacuo*, for complexes **2.6** and **2.7** both show three transitions, and complex **2.8** has six transitions over the 400 nm – 700 nm range. The three main transitions in **2.6** and **2.7** are also apparent in **2.8**, with the three additional transitions being smaller, with two around 460 nm and one at 576 nm. The dominant transition incorporates the HOMO-3 and the LUMO in **2.6** and **2.7** and the HOMO-4 and the LUMO+1 in **2.8**.

The isodensity plots for these three complexes are very similar to those from previous complexes in this chapter, in which the corresponding occupied orbital in each complex has electron density predominantly on the metal, with a small amount on the central pyridine of the terpyridine ligand. The LUMO for each complex has electron density on the terpyridine ligand, with no significant electron density on the cyclometalated ligand in any of these three complexes. This is because the orbitals involved in this transition have the majority of electron density on areas that are largely unchanged. As the modifications in this chapter are mostly on the cyclometalated ligand only, it follows that the energy of the LUMO does not change by a large amount.

The energy of the HOMO-2 and LUMO is the same for **2.6** and **2.7** and thus the energy of the transition is equivalent with values of 468.7 nm and 468.8 nm respectively. Interestingly the energies of the HOMO, HOMO-1 and HOMO-2 in **2.7** are higher than for the corresponding orbitals in **2.6**, which shows the effect of the 1-naphthyl vs. 2-naphthyl substitution. While the observed small blue shift is not directly portrayed in these TD-DFT results, the results show that the LUMO does not change in energy throughout the series, so the blue shift likely results from either a subtle change in energy of the HOMO-3 or a difference between *in vacuo* TD-DFT experiments and the experimental solution studies. This is supported by the blue shift observed

for **2.8**, in which the TD-DFT calculations show two additional transitions, at lower energy compared to the large transition at 474.3 nm.

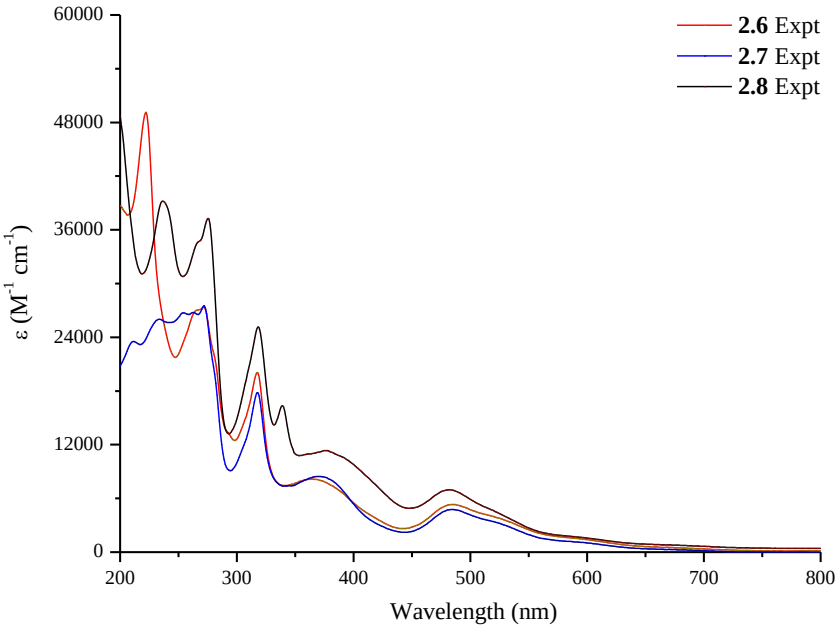

Figure 2.27: Electronic absorption spectra of complexes **2.6**-**2.8**.

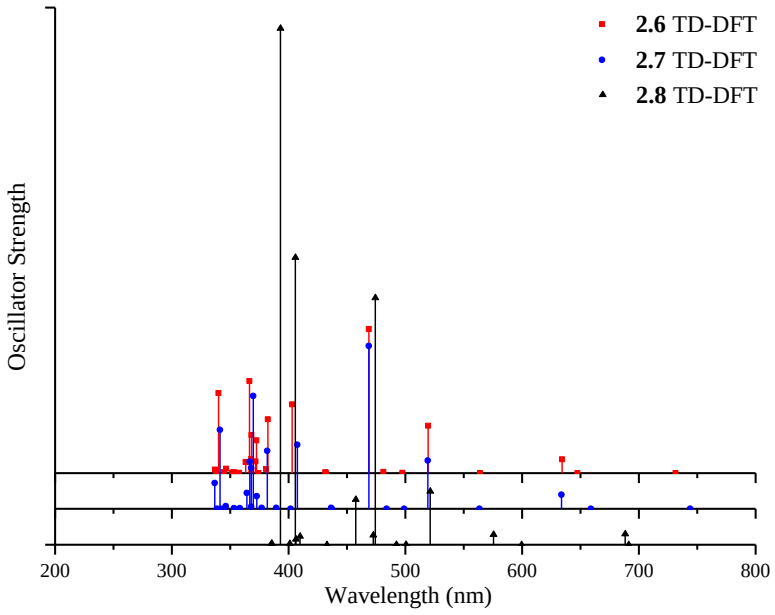

Figure 2.28: Calculated TD-DFT data for **2.6**-**2.8** *in vacuo*.

The isodensity plots for the HOMO-4 and LUMO+1 (Figure 2.29) are very similar to the orbitals involved previously, in which the HOMO-4 is predominantly metal based, with a small amount of electron density on the central pyridine on the terpyridine ligand and the LUMO+1 has the majority of electron density on the terpyridine ligand, with a small amount on the metal. This shows that the two additional peaks are important to the observed blue shift, and the isodensity plots for the HOMO-3 and HOMO (Figure 2.29) show electron density on the metal and also on the pyrene on the cyclometalated ligand. The LUMO has electron density on the terpyridine ligand and the LUMO+4 has electron density on the 1,3-di(pyrazol-1-yl)benzene unit, which shows that both these additional transitions in **2.8** are different types of MLCTs and likely effect the observed λ_{max} for the lowest energy peak envelope.

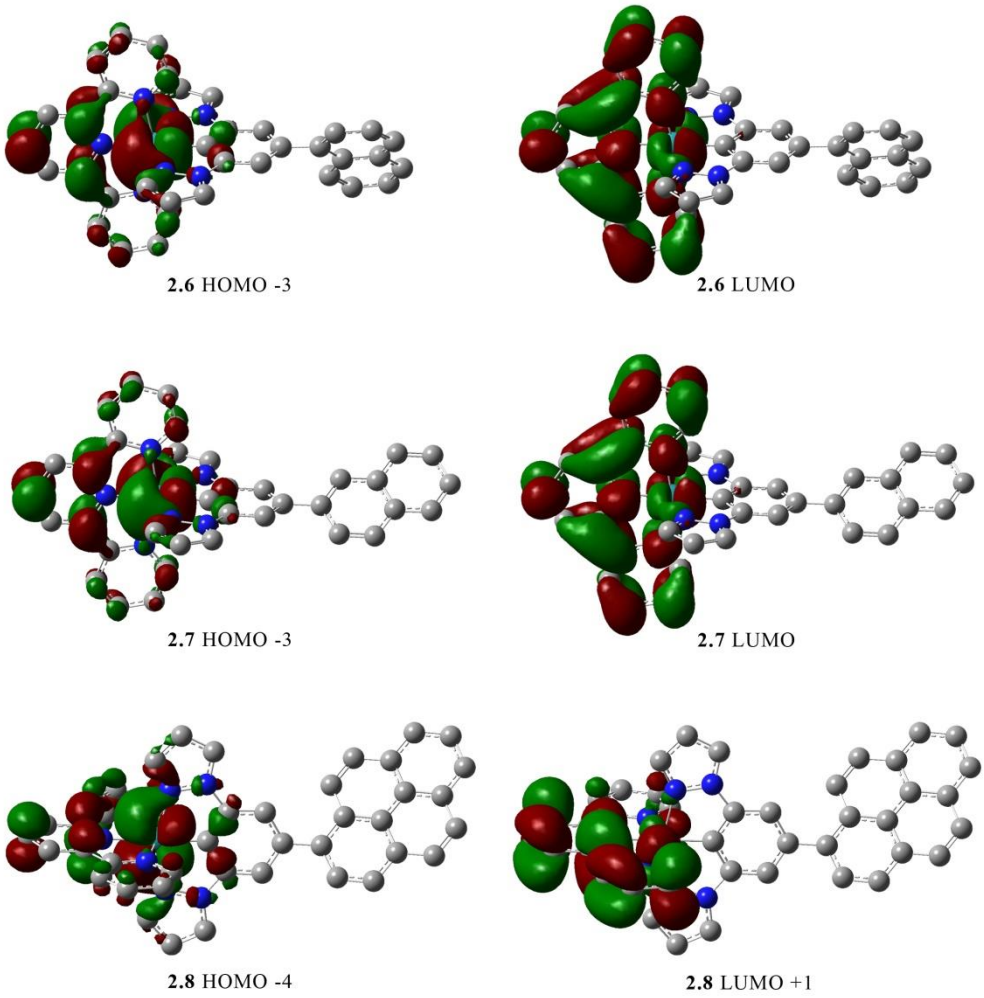

Figure 2.29: Isodensity plots (isovalue 0.02) of selected frontier orbitals that are involved in the dominant transition for the lowest energy MLCT for **2.6-2.8** from DFT calculation *in vacuo*.

S_n	E/nm	f	Dominant Transition			Percentage Contribution
2.6						
S1	731.6	0.000	HOMO	→	LUMO	82
S3	634.3	0.013	HOMO -1	→	LUMO	94
S5	519.5	0.044	HOMO -3	→	LUMO +1	95
S8	468.7	0.134	HOMO -3	→	LUMO	62
2.7						
S1	743.9	0.000	HOMO	→	LUMO	84
S3	633.7	0.013	HOMO -2	→	LUMO	96
S5	519.3	0.045	HOMO -3	→	LUMO +1	96
S8	468.8	0.151	HOMO -3	→	LUMO	62
2.8						
S1	728.4	0.000	HOMO	→	LUMO	80
S4	688.2	0.010	HOMO -2	→	LUMO	89
S6	575.6	0.009	HOMO -2	→	LUMO +1	65
S7	521.3	0.050	HOMO -4	→	LUMO +1	54
S10	474.3	0.230	HOMO -4	→	LUMO +1	36
S11	472.4	0.009	HOMO -3	→	LUMO	92
S12	457.5	0.042	HOMO	→	LUMO +4	92

Table 2.15: Selected calculated UV-vis transitions from TD-DFT calculations for **2.6**-**2.8** *in vacuo* over the range of 450-800 nm (1st MLCT).

The 2nd lowest energy peak for **2.6** is at 366 nm (ε = 12,900), a blue shift of 9 nm compared to **2.1** (375 nm), and the intensity of the peak is over double the intensity of **2.1**. The 2nd lowest energy peak for **2.7** is blue shifted by 3 nm compared to the corresponding peak in **2.1** with a value of 366 nm (ε = 12,900) and the 2nd lowest energy peak in **2.8** is slightly red shifted compared to **2.1**, with a value of 377 nm (ε = 18,100). Complex **2.8** has an additional peak at 339 nm (ε = 26,100) which is indicative of a LC (π→π*) transition on the pyrene. The intensities of the peaks in **2.7** and **2.8** are significantly higher than **2.1**, showing the impact of the large aromatic groups, naphthalene and pyrene. Due to the large number of transitions in this range additional information about these transitions is unable to be obtained, but once again all the transitions within this range are MLCT, with all the occupied orbitals involved showing electron density which is predominantly on the metal, but also on cyclometalated ligand. The unoccupied orbitals involved show electron density is predominantly based on the terpyridine ligand.

The remaining lower energy peaks for **2.6**, **2.7** and **2.8** are all very similar, with peaks at approximately 317 nm, 271-276 nm, 263-266 nm and 234-237 nm in each. The pyrene containing complex, **2.8** has an additional peak at 339 nm (ε = 26,100) and **2.7** has two additional peaks at 254 nm (ε = 42,400) and 211 nm (ε = 37,500), while **2.6** has the same

transitions except it is missing the transition between 234-237 nm. These are all most likely LC ($\pi \rightarrow \pi^*$) transitions, and they show the effect of expanding the aryl system.

S_n	E/nm	f	Dominant Transition			Percentage Contribution
2.6						
S11	403.1	0.064	HOMO	→	LUMO +4	86
S12	382.3	0.050	HOMO -1	→	LUMO +2	81
S15	372.5	0.030	HOMO -1	→	LUMO +3	39
S17	368.3	0.035	HOMO -3	→	LUMO +3	69
S20	366.5	0.086	HOMO -3	→	LUMO +2	48
2.7						
S11	407.4	0.060	HOMO	→	LUMO +4	85
S14	381.8	0.054	HOMO -2	→	LUMO +2	88
S17	369.6	0.105	HOMO -2	→	LUMO +3	43
S18	368.1	0.038	HOMO -3	→	LUMO +3	72
S20	366.8	0.044	HOMO -3	→	LUMO +2	85
2.8						
S14	409.7	0.008	HOMO -6	→	LUMO	77
S15	406.3	0.005	HOMO -1	→	LUMO +2	82
S16	405.8	0.267	HOMO	→	LUMO +5	47
S18	393.0	0.481	HOMO		LUMO +6	54

Table 2.16: Selected calculated UV-vis transitions from TD-DFT calculations for **2.6**-**2.8** *in vacuo* over the range of 350-410 nm (2nd MLCT).

*2.7.6 Complexes **2.9**-**2.10***

Complex	Absorption 298 K, MeCN, λ_{max} (nm) ($\varepsilon(10^3\ M^{-1}\ cm^{-1})$)
2.9	596 (0.9), 517 (2.8), 479 (4.3), 388 (5.5), 316 (12.1), 272 (14.9), 262 (15.7), 234 (12.8).
2.10	595 (0.9), 481 (4.9), 361 (4.1), 316 (9.2), 271 (12.5), 264 (12.5), 226 (13.3).

Table 2.17: Electronic absorption spectra for ruthenium complexes **2.9** and **2.10**.

The UV-vis spectra for complexes **2.9** and **2.10** are shown in Figure 2.30 and the calculated TD-DFT data is shown in Figure 2.31. For each complex there are results from two sets of TD-DFT calculations; firstly the data for each complex produced, and secondly, the data for the target acetylene substituted complexes which are included for comparison. The measured spectrum for **2.9** shows that the lowest energy peak envelope has a λ_{max} at 479 nm (ε = 4,300), which is significantly blue shifted compared to all the other complexes in this series, especially **2.1** (487 nm) and it also has two small shoulders at 517 nm (ε = 2,800) and 596 nm (ε = 900). The measured UV-vis spectrum for **2.10** shows that the lowest energy peak is also significantly blue shifted compared to **2.1**, with a λ_{max} of 481 nm (ε = 4,900). This value is similar compared to **2.9**, with a small red shift of 2 nm. In this case there is only a single small shoulder, which is

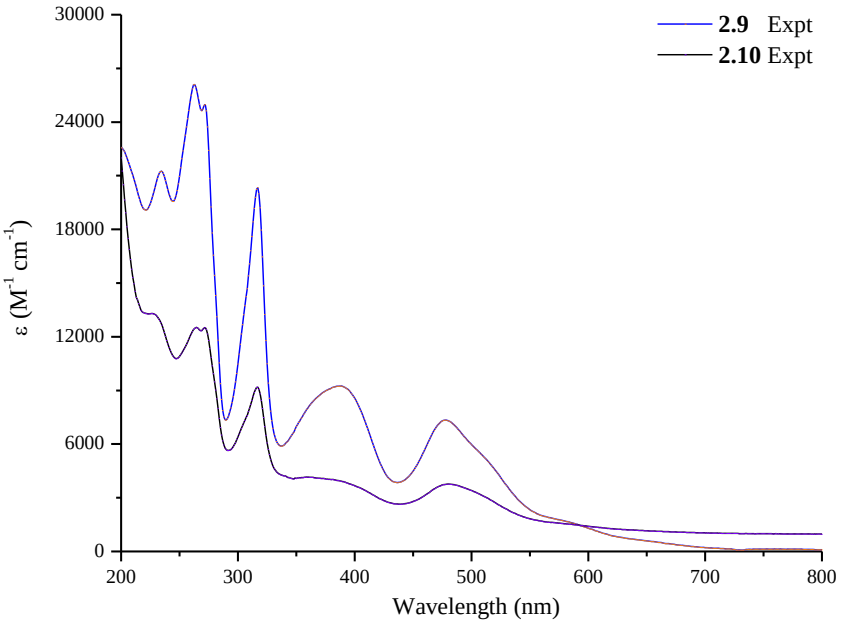

Figure 2.30: Electronic absorption spectra of complexes **2.9**-**2.10**.

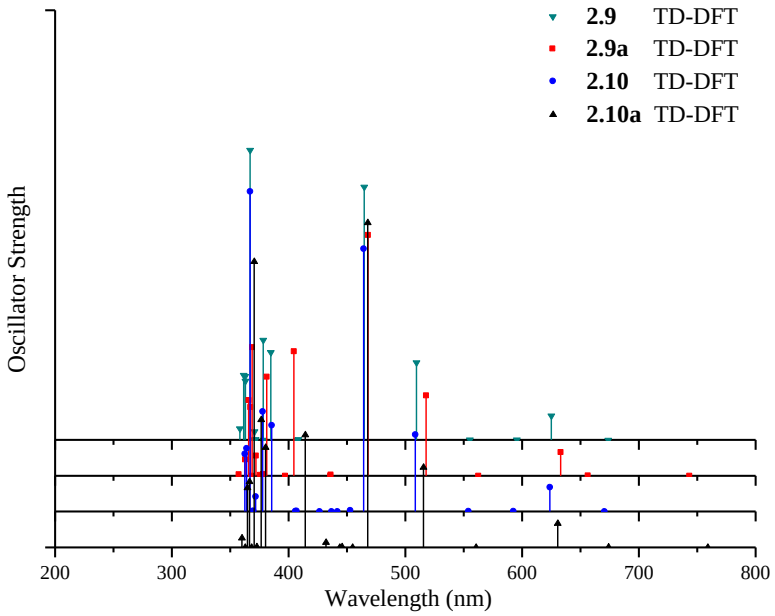

Figure 2.31: Calculated TD-DFT data *in vacuo* for **2.9** and **2.10**, and the initial target structure for complex **2.9** and **2.10**.

observed at 595 nm (ε = 900) instead of the typical two shoulders. The intensities of the lowest energy peak envelopes in **2.9** and **2.10** are both similar to the intensity of the corresponding peak envelope in **2.1**

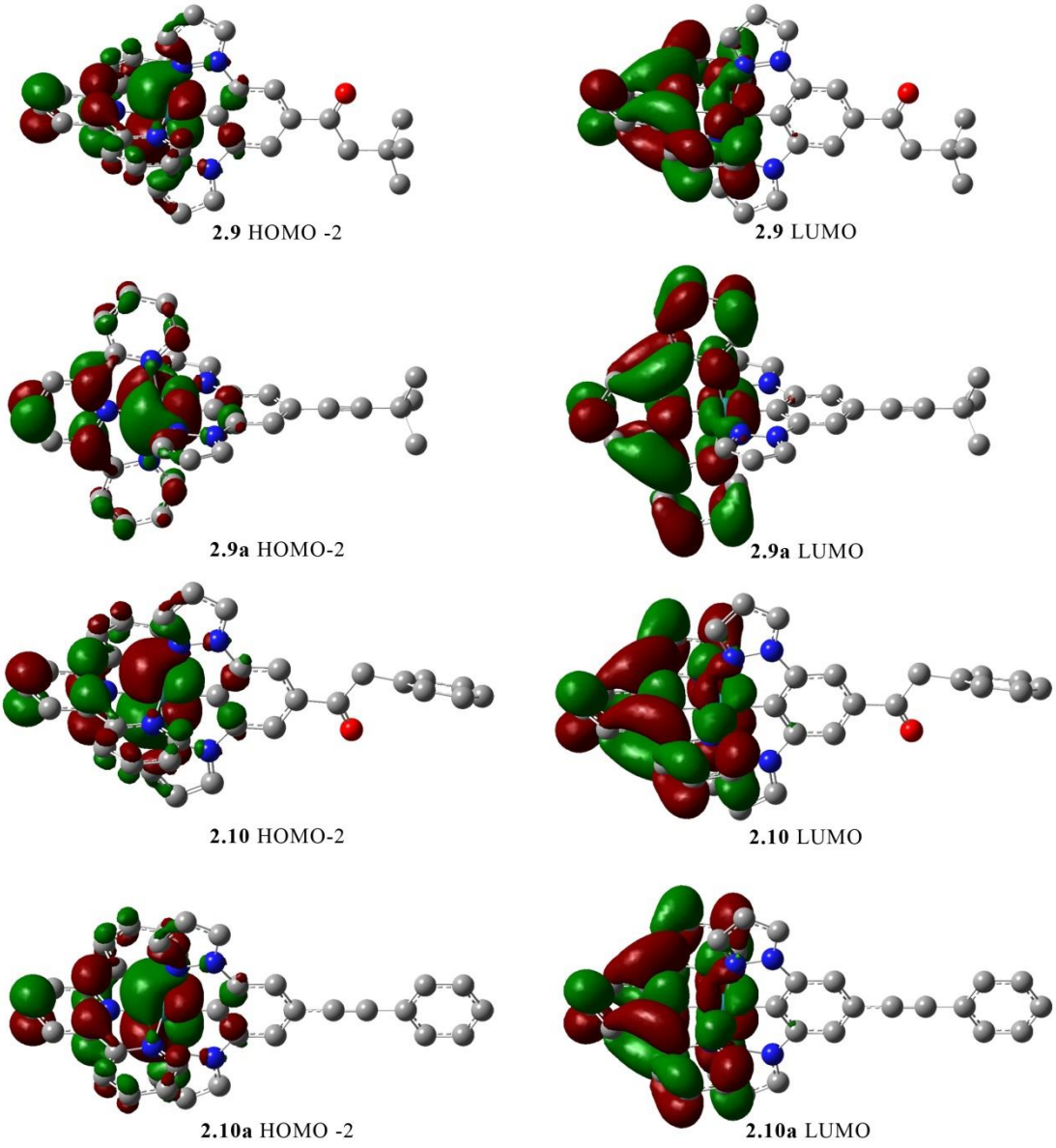

Figure 2.32: Isodensity plots (isovalue 0.02) of selected frontier orbitals that are involved in the dominant transition for the lowest energy MLCT for **2.9**, **2.9a**, **2.10** and **2.10a** from DFT calculation *in vacuo*.

TD-DFT calculations were completed *in vacuo* for **2.9** and **2.10**, and calculations based on the target complex for each (**2.9a** and **2.10a**) were also completed for comparison. As with previous results, all four calculations show three transitions within the range of the lowest energy peak

S_n	E/nm	f	Dominant Transition			Percentage Contribution
2.9						
S1	743.14	0.0000	HOMO	→	LUMO	96
S3	632.88	0.0133	HOMO -1	→	LUMO	96
S5	517.64	0.0449	HOMO -2	→	LUMO +1	96
S6	467.92	0.1345	HOMO -2	→	LUMO	62
2.9a						
S1	673.8	0.0000	HOMO	→	LUMO	98
S2	624.99	0.0136	HOMO -1	→	LUMO	97
S5	509.52	0.0433	HOMO -2	→	LUMO +1	96
S6	464.73	0.1413	HOMO -2	→	LUMO	63
2.10						
S1	670.40	0.0000	HOMO	→	LUMO	98
S2	623.76	0.0136	HOMO -1	→	LUMO	96
S5	508.39	0.0430	HOMO -2	→	LUMO +1	95
S6	464.37	0.1467	HOMO -2	→	LUMO	61
2.10a						
S1	758.92	0.0000	HOMO	→	LUMO	91
S3	630.60	0.0134	HOMO -1	→	LUMO	96
S5	515.59	0.0448	HOMO -2	→	LUMO +1	96
S6	467.80	0.1813	HOMO -2	→	LUMO	62

Table 2.18: Selected calculated UV-vis transitions from TD-DFT calculations for **2.9** and **2.10** and the corresponding target complex **2.9a** and **2.10a** *in vacuo* over the range of 450-800 nm (1^{st} MLCT).

envelope, which suggests there are in fact two shoulders coming off the lowest energy λ_{max} for **2.10**. The transition with the largest oscillator strength for **2.9** and **2.10** is at 467.92 nm and 467.80 nm respectively, corresponding to a HOMO-2 → LUMO transition in both **2.9** and **2.10**, which is assigned as corresponding to the λ_{max} of the lowest energy peak envelope. The matching transition is also the HOMO-2 → LUMO in **2.9a** and **2.10a** with the transition occurring at 464.73 nm (**2.9a**) and 467.80 nm (**2.10a**).

The isodensity plots for the HOMO-2 in all four complexes (Figure 2.32) show electron density predominately on the metal, but also on the central pyridine of the terpyridine ligand. The isodensity plots for the LUMO in all four complexes (Figure 2.32) show electron density only on the terpyridine ligand. The HOMO for each complex shows electron density on the cyclometalated ligand and the metal, however this orbital is not involved in any of the transitions

that produce this peak envelope and thus the cyclometalated ligand has minimal effect the energy of the transition (Chapter 7.3, Figures 7.3.8-7.3.11). The calculations for the alkyne substituted complexes, **2.9a** and **2.10a**, suggest a blue shift compared to their hydrated counterparts and the result is the same for either alkyne versus either hydrated derivative. The orbital energies for the HOMO-2 and LUMO in all four complexes are all very similar, and equivalent in energy compared to the corresponding orbitals in **2.1** (Chapter 7.4, Figure 7.4.1).

The 2nd lowest energy peak envelope occurs between 336 nm and 437 nm in **2.9** and **2.10**, with a λ_{max} at 388 nm (ε = 5,500) for **2.9** and a λ_{max} at 361 nm (ε = 5,500) in **2.10**, although both peak envelopes are very broad. There is a red shift of 12 nm for **2.09** compared to **2.1** and a blue shift of 15 nm for **2.10** compared to **2.1**. and both are red shifted compared to **2.1**, with a small shift of 2 nm for **2.9** and a larger shift of 13 nm for **2.10**.

The TD-DFT calculations for **2.9** and **2.10** and their corresponding hydrated complexes **2.9a** and **2.10a** show a large number of transitions for the 2nd lowest energy peak envelope (350 nm – 435 nm). There are six transitions calculated to occur over this range for **2.9** and **2.9a** and six and seven calculated transitions for **2.10** and **2.10a** respectively over the same range. The observed peaks at 388 nm (**2.9**) and 361 nm (**2.10**) likely result from a combination of these calculated transitions, with none of the transitions significantly larger than the others.

The occupied orbitals involved in the transitions in this range are the HOMO, HOMO-1 and HOMO-2 for these four complexes, with **2.10** also having the HOMO-3 involved and **2.10a** also having the HOMO-4 involved but not the HOMO-2. The unoccupied orbitals involved are the LUMO+2, LUMO+3, LUMO+4 and LUMO+5, with **2.9** and **2.10** also having the LUMO+1 involved. The isodensity plots for these relevant orbitals (Chapter 7.3, Figures 7.3.8-7.3.11**)** follow the trend for previous complexes in which all the occupied orbitals involved have electron density that is predominantly metal based.

The isodensity plots also show that the unoccupied orbitals have electron density that is on one of the two ligands, or a small amount on both and that there is almost no electron density on the metal. This shows that of the large number of calculated transitions over this energy range, they are all only MLCT transitions as opposed to other types of transitions, which can also potentially occur in this wavelength range.[158]

S_n	E/nm	f	Dominant Transition			Percentage Contribution
2.9						
S9	404.53	0.0696	HOMO	→	LUMO +1	73
S11	381.33	0.0554	HOMO -1	→	LUMO +4	88
S14	371.90	0.0112	HOMO -1	→	LUMO +2	89
S15	368.71	0.0718	HOMO -1	→	LUMO +5	58
S17	367.32	0.0384	HOMO -2	→	LUMO +3	80
S18	365.85	0.0423	HOMO -2	→	LUMO +3	71
2.9a						
S9	384.8	0.0490	HOMO	→	LUMO +4	73
S11	378.22	0.0559	HOMO -1	→	LUMO +2	91
S16	366.99	0.1619	HOMO -1	→	LUMO +3	66
S17	363.09	0.0329	HOMO -2	→	LUMO +3	81
S18	362.73	0.0356	HOMO -1	→	LUMO +5	76
S19	361.62	0.0362	HOMO -2	→	LUMO +2	93
2.10						
S10	432.01	0.0027	HOMO -3	→	LUMO +1	73
S11	414.26	0.0629	HOMO	→	LUMO +4	88
S12	380.34	0.0558	HOMO -1	→	LUMO +2	89
S13	376.51	0.0713	HOMO	→	LUMO +5	58
S15	370.61	0.1596	HOMO -1	→	LUMO +3	80
S17	366.43	0.0368	HOMO -2	→	LUMO +3	71
S18	364.86	0.0333	HOMO -2	→	LUMO +2	95
2.10a						
S13	385.42	0.0481	HOMO	→	LUMO +4	70
S14	377.71	0.0559	HOMO -1	→	LUMO +2	91
S18	366.93	0.1787	HOMO -1	→	LUMO +3	68
S19	363.98	0.0352	HOMO -1	→	LUMO +5	75
S20	362.53	0.0322	HOMO -4	→	LUMO +3	78

Table 2.19: Selected calculated UV-vis transitions from TD-DFT calculations for **2.9** and **2.10** and the corresponding target complex **2.9a** and **2.10a** *in vacuo* over the range of 350-400 nm (2nd MLCT).

*2.7.7 Complex **2.11***

Complex	Absorption 298 K, MeCN, λ_{max} (nm) ($\varepsilon(10^3\ M^{-1}\ cm^{-1})$)
2.1	604 (sh), 536 (sh), 487 (4.7), 375 (5.4), 318 (15.2), 259 (19.9), 234 (17.6).
2.8	598 (sh), 528 (sh), 482 (11.2), 377 (18.1), 339 (26.1), 318 (40.2), 276 (59.4), 266 (sh), 237 (62.5).
2.11	505 (12.6), 375 (40.5), 358 (46.5), 315 (65.4), 285 (92.7), 239 (83.7).

Table 2.20: Electronic absorption spectra for ruthenium complexes **2.1**, **2.8** and **2.11**.

The UV-vis and TD-DFT data for complex **2.11** are shown in Figure 2.33. The lowest energy peak envelope is at 505 nm (ε = 4,200) and unlike the majority of complexes in this work does not have any visible shoulders. This shows a large red shift compared to the other complexes in this series and the intensity of the lowest energy peak envelope is of a similar value to **2.8.**

TD-DFT calculations run *in vacuo* for **2.11** show that there is a single dominant transition, HOMO-3 → LUMO, and also several other much smaller transitions. The HOMO-3 → LUMO transition is calculated to occur at 482.1 nm, a calculated red shift of 15.1 nm compared to the dominant transition in **2.1** which is calculated to occur at 467.0 nm and this reflects the experimental results. The small oscillator strength of these other transitions helps to explain why there are no observable shoulders.

The isodensity plot of the HOMO-3 (Figure 2.34) shows that the electron density is predominantly on the metal and also spread onto parts of both ligands. On the terpyridine ligand, electron density is on the central pyridine and the attached phenyl ring. On the cyclometalated ligand there is electron density on both pyrazoles and closest benzene ring to the metal on the pyrene. The isodensity plot of the LUMO shows that the electron density is on the terpyridine and the attached phenyl ring.

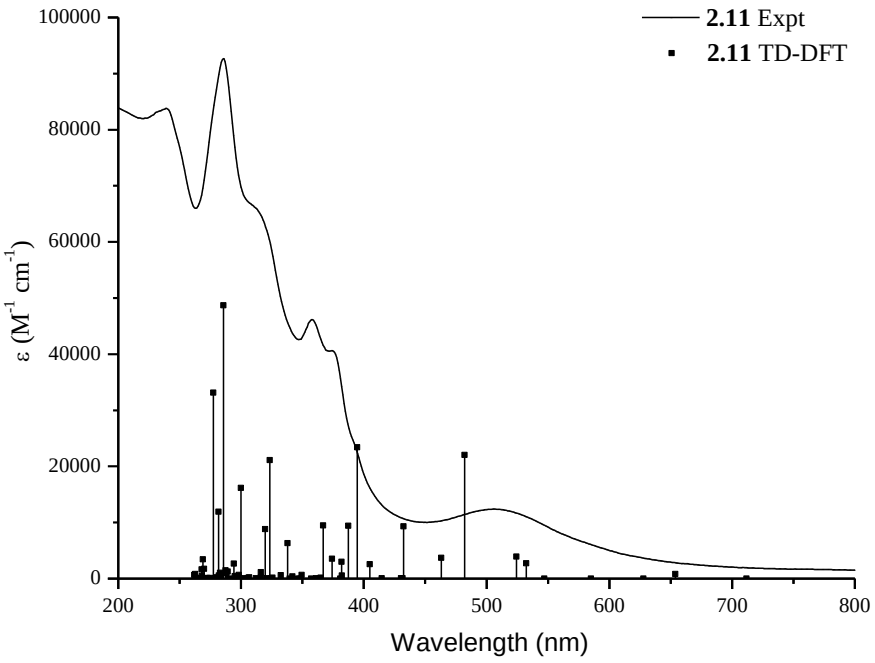

Figure 2.33: Electronic absorption spectra of ruthenium complex **2.11** along with TD-DFT calculated data for **2.1** *in vacuo*.

The calculated energies for these orbitals show that both contributing orbitals in **2.11** have been raised in energy compared to their corresponding orbitals in **2.1**, except that the energy of the occupied orbital is raised by a larger amount than the unoccupied orbital which results in the observed red shift for **2.11**. The energy is increased for both contributing orbitals in **2.11**, with the HOMO-3 increased in energy due to the pyrene and the LUMO increased in energy additional aryl group compared to the parent complex, **2.1**.

At higher energy there are two peaks, the first is observed at 375 nm (ε = 13,500) and corresponds to the same peak of equivalent energy in **2.1** and a peak of similar energy to the LC (π→π*) transition in **2.8** at 358 nm (ε = 15,500). Although red shifted compared to the corresponding peak in **2.8**, it has a similar intensity to the transition in **2.8.**

S_n	E/nm	f	Dominant Transition			Percentage Contribution
2.11						
S1	711.9	0.0002	HOMO	→	LUMO	54
S2	653.9	0.0120	HOMO-2	→	LUMO	48
S6	532.4	0.0404	HOMO-3	→	LUMO+1	87
S7	524.5	0.0585	HOMO-2	→	LUMO+1	29
S8	482.1	0.3305	HOMO-3	→	LUMO	44
S9	463.0	0.0554	HOMO	→	LUMO+2	53
S10	432.4	0.1394	HOMO-2	→	LUMO+2	37
S14	404.9	0.0384	HOMO-1	→	LUMO+3	47
S15	394.6	0.3511	HOMO-2	→	LUMO+2	37
S16	387.4	0.1409	HOMO-1	→	LUMO+4	25
S17	382.2	0.0085	HOMO-3	→	LUMO+4	84
S18	381.8	0.0445	HOMO-3	→	LUMO+3	91
S20	374.2	0.0531	HOMO-2	→	LUMO+3	76
S21	367.0	0.1419	HOMO-2	→	LUMO+4	65
S22	364.9	0.0025	HOMO-4	→	LUMO+1	51

Table 2.21: Selected calculated UV-vis transitions from TD-DFT calculations for **2.11** *in vacuo* over the range of 350-800 nm (1st MLCT and 2nd MLCT).

The TD-DFT calculation for **2.11** shows nine transitions between 360 nm and 440 nm, and any combination of these could result in the observed peaks at 375 nm and 358 nm. The main difficulty in assigning these calculated transitions is the large number of transitions which are spread over a small energy range, and in addition to this, the percentage contribution of several of these transitions is low (Table 2.21), which means there are several different transitions involved. The isodensity plots for the various occupied orbitals involved (Figure 2.34) show that

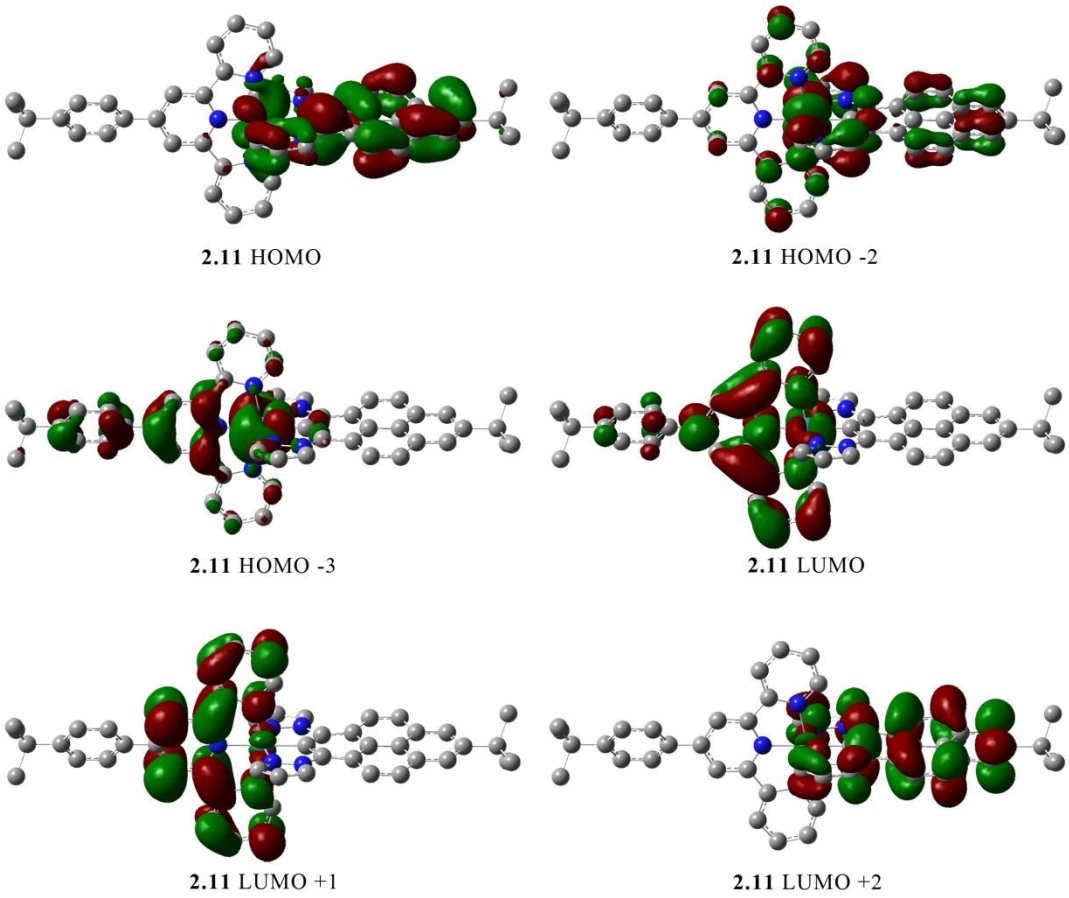

Figure 2.34: Isodensity plots (isovalue 0.02) of selected frontier orbitals that are involved in the dominant transition for the lowest energy MLCT for **2.11** from DFT calculation *in vacuo*.

there is electron density on the cyclometalated ligand, in addition to a large contribution on the metal in the HOMO, HOMO-1, HOMO-2 and HOMO-4. The HOMO-3 shows electron density predominantly on the metal, but also spread largely over the terpyridine ligand, with a small amount on the cyclometalated ligand. The HOMO-5 has electron density spread over central pyridine and the phenyl ring of the substituted terpyridine ligand, in addition to the electron density on the metal. The isodensity plots for the unoccupied orbitals show electron density on one of the two ligands, with almost no electron density on the metal in any of the relevant orbitals. The isodensity plots for the LUMO+1, LUMO+3 and LUMO+4 all show electron density on parts of the terpyridine ligand, and the LUMO+2 shows electron density spread over all of the cyclometalated ligand. This shows that despite the large number of calculated

transitions, they are all different types of MLCT, and not LMCT or MC transitions, which can also potentially occur in this wavelength range.[158]

2.8 Emission Studies.

Emission studies were carried out in degassed acetonitrile at ambient temperature and in butyronitrile at 77 K using a continuous flow cryostat from oxford instruments limited. At room temperature none of these complexes (**2.1**-**2.11**) showed distinct emission spectra using the spectrofluorimeter at hand and thus 77 K emission studies were carried out. Emission spectroscopy at low temperature provides greater emission intensity in cases where the dominant non-radiative channels are thermally activated.[159]

All of the complexes in this series (**2.1**-**2.11**) are emissive at 77 K and show emission profiles with a single peak that have a similar shape to previously reported spectra for cyclometalated ruthenium complexes.[28] As the measurements are recorded at low temperature the transition is assigned as being an intense 0-0 transition.[160] The luminescence spectra recorded for complexes **2.1**-**2.6** are shown in Figure 2.35 and luminescence spectra recorded for complexes **2.7**-**2.11** and **2.1** are shown in Figure 2.36 and spectral data is shown in Table 2.22. There is a distinct λ_{max} for each complex, ranging from 666 nm to 729 nm, which gives a Stokes shift between 5,600 cm^{-1} and 6,710 cm^{-1} for each complex.

Complex	77K Emission λ_{max} (nm) ($\tilde{\nu}$, cm^{-1})	Stokes Shift ($\tilde{\nu}$, cm^{-1})	Quantum Yield
2.1	712 (14,040)	6,490	0.16
2.2	700 (14,290)	6,380	0.68
2.3	718 (13,930)	6,560	0.16
2.4	715 (13,990)	6,460	0.08
2.5	729 (13,720)	6,490	0.02
2.6	705 (14,180)	6,480	0.27
2.7	714 (14,010)	6,530	0.19
2.8	670 (14,930)	5,820	0.18
2.9	674 (14,840)	6,000	0.95
2.10	666 (15,020)	5,600	0.93
2.11	702 (14,250)	5,640	0.27

Table 2.22: Luminescence data for complexes **2.1**-**2.11**. Measurements were carried out in ca. 10^{-6} M butyronitrile and quantum yields were calculated using $[Ru(bpy)_3](Cl)_2$ in MeOH/EtOH (1:4, Φ_{PL} = 0.38).[15]

The emission profiles for **2.1**-**2.11** are significantly red shifted compared to $[Ru(tpy)_2]PF_6$, which shows an emission band at 602 nm at 77 K upon excitation at 475 nm and shows a Stokes shift of 4,400 cm^{-1}.[37] The emission profiles are also red shifted compared to $[Ru(bpy)_3](Cl)_2$, which has an emission band peak at 580 nm and a shoulder at around 630 nm when measured at 77 K and excited at 450 nm. This shows that there is a Stokes shift of 5,000 cm^{-1} for $[Ru(bpy)_3](Cl)_2$. The large Stokes shift for these complexes is a result of the strong HOMO destabilization due to the cyclometalation. The functionalization of the 4' position of the central benzene ring of the cyclometalated ligand has a similar effect on the wavelength of the emission as it did for the absorption, with the Stokes shift remaining relatively unchanged for complex **2.2**-**2.8**, with a value of 6,380 cm^{-1} to 6,560 cm^{-1}. The Stokes shift for **2.1** is the largest in this series, with a value of 6,710 cm^{-1}. The Stokes shift for **2.9** is reduced to 6,000 and the Stokes shift for **2.10** and **2.11** is even smaller, with a value of 5,640 cm^{-1}. The reduced Stokes shift in **2.9**-**2.11** is a result of the ^{1}MLCT and ^{3}MLCT being closer in energy, as the emission wavelength is blue shifted in comparison to the emission in other complexes. The emission for complex **2.5** is the most red shifted in this series at 729 nm and the emission for **2.10** is the most blue shifted in this series at 666 nm. As the Stokes shifts are very similar in **2.1**-**2.8**, they likely have similar processes occurring.

Generally room temperature emission is red shifted compared to low temperature emission studies, because the rigid solvent matrix at low temperatures prevents solvent reorganization and thus avoids the stabilization of the more polar charge-separated excited state.[161] It is thus possible that these complexes are slightly luminescent at room temperature but at levels below the detection limit of our experimental setup. As these complexes, if emissive, would be expected to produce emission at energy lower than ca. 720 nm it would be difficult to observe. An important reason is that the spectral resolution decreases at higher wavelengths due to decreasing spectrometer sensitivity resulting in lower than expected emission intensity. Another reason for no room temperature emission is that the peak occurs above the detection limit of the machine at approximately 800 nm. The most likely situation however is that the complexes are virtually non-emissive, shown by their very low quantum yields, resulting in only a small amount of emission to detect. This would ideally be corrected by using more concentrated samples however luminescent samples need to be less than ca. 0.1 Abs due to problematic concentration effects. To gain insight about the nature of the relevant excited states and whether they should be

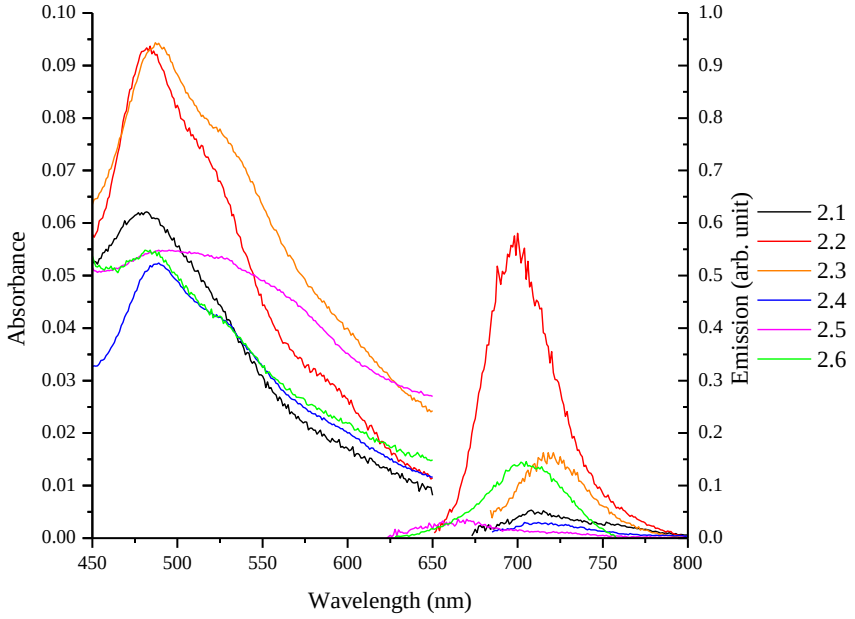

Figure 2.35: UV-vis spectra for **2.1-2.6** in butyronitrile at ca.10^{-6} M at ambient temperature and corresponding emission spectra in butyronitrile at ca. 10^{-6} M at 77 K.

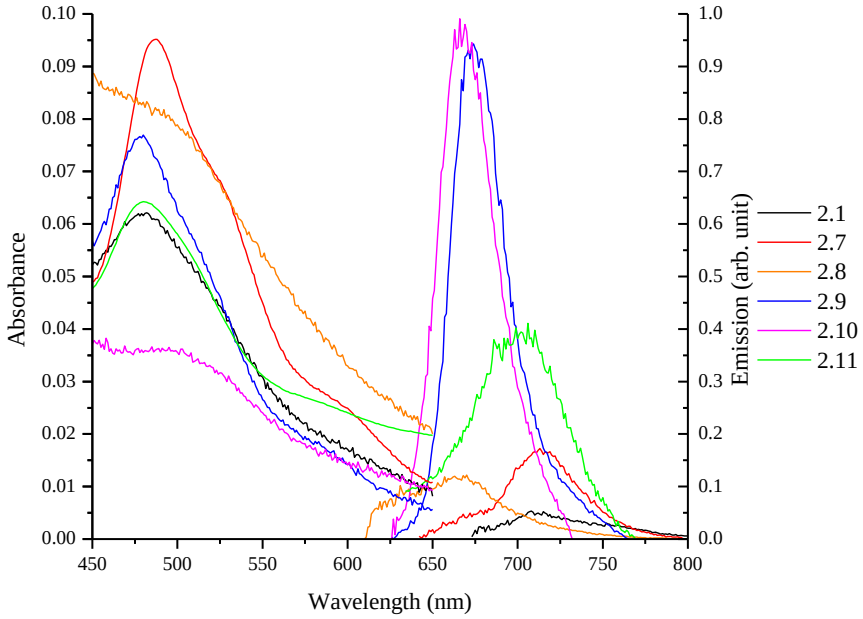

Figure 2.36: UV-vis spectra for **2.7-2.11** and **2.1** in butyronitrile at ca.10^{-6} M at ambient temperature and corresponding emission spectra in butyronitrile at ca.10^{-6} M at 77 K.

expected to be emissive at room temperature ΔSCF-DFT calculations can be performed, however they are not included in this work. These calculations have been previous used by Schulze et al. to calculate emission energies by calculating the energy difference between the first triplet excited states and the closed-shell ground state, using previously optimized geometries.[28]

The key argument against room temperature emission is that the ^{3}MC state is both thermally assessable to the ^{3}MLCT and has strong coupling to the ground state, which results in rapid relaxation of the ^{3}MC state once populated. While there is no direct spectroscopic evidence to support this, it is widely considered to be the cause of reduced emission. This is supported however by theoretical calculations, which have shown that the ^{3}MC and ^{3}MLCT states are similar in energy, and low temperature luminescence studies which show that there are longer lifetimes and higher quantum yields at 77 K as the ^{3}MC state is no longer thermally accessible. The reason the ^{3}MC state is deactivating is that in the ^{3}MC state antibonding orbitals are occupied and this matches the ground state geometry when there are high energy vibrations.

The quantum yields for complexes **2.1**-**2.11** were found to be between 8% and 95%, using $[Ru(bpy)_3](Cl)_2$ in MeOH/EtOH (1:4, Φ_{PL} = 0.38) at 77 K as a standard.[15] The quantum yield for $[Ru(bpy)_3](Cl)_2$ is relatively high, at 38%, at 77 K,[15] but it drops to ca. 4% at room temperature[162] showing the effect of the ^{3}MC state being thermally accessible. The quantum yields were calculated using Equation 2.1, which calculates the quantum yield of a sample compound by balancing its properties against a well-established compound with similar properties, in this case $[Ru(bpy)_3](Cl)_2$.[162-163]

$$QY = QY_{REF} \cdot \frac{\eta^2}{\eta_{REF}^2} \cdot \frac{I}{I_{REF}} \cdot \frac{A_{REF}}{A}$$

Equation 2.1: Relative quantum yield equation, where QY is the quantum yield, η is the refractive index of the solution, I is the integrated fluorescence intensity and A is the absorbance at the excitation wavelength. The reference used is $[Ru(bpy)_3](Cl)_2$ in MeOH/EtOH (1:4) and has a quantum yield of 0.38 at 77 K.[15]

The quantum yield for the parent complex **2.1** is less than half of the value for standard $[Ru(bpy)_3](Cl)_2$ complex, with a value of 16% at 77 K. There is a general trend for the complexes with emission that is red shifted to **2.1**, with the quantum yield decreasing as the

emission energy decreases, which includes complexes **2.3**, **2.4**, **2.5** and **2.7**, for which the quantum yields at 77 K are 16%, 8%, 2% and 19% respectively. The trend continues for complexes **2.6** and **2.11**, which both have quantum yields of 27% at 77 K for their emission at 705 nm and 702 nm respectively. At higher energy the trend no longer fits, with the quantum yield for complex **2.2** being 68% at 77 K for its 700 nm emission and the quantum yield for complex **2.8** being 18% at 77 K. Complexes **2.9** and **2.10**, which are significantly different from other complexes in this series as they have substituted ketones bound to the central benzene ring of the cyclometalated ligand both have very high quantum yields of 95% and 93% respectively. While the error associated with these values is very high, it is still a very promising result. The very high quantum yields for these two complexes, as well as complex **2.11**, reflect their Stokes shifts, which are significantly smaller than for the other complexes in this series. The high quantum yields and small Stokes shifts for these three complexes show that the ^{1}MLCT and ^{3}MLCT are closer in energy than in the other complexes in this series and that there are less non-radiative deactivation pathways available to the excited state in these complexes at 77 K. This does not mean that the intersystem crossing process is more efficient in **2.9**-**2.11** however, as Demas and co-workers have shown that intersystem crossing to various MLCT excited states occurs with a quantum yield near unity in fluid solution for ruthenium(II) photosensitizers.[164]

The relative quantum yield calculation method provides insight into the quantum yield for new compounds, however there are large errors associated with the method, mostly as a result of poor integration and/or a poor baseline, with typical errors believed to be up to 30%.[165] Errors can be minimized by running multiple measurements at different concentrations, however this was not practical at 77 K using the experimental setup at hand due to the large amount of time required to run a single sample. While the relative error associated with each quantum yield is potentially very high, it is largely a systematic error and the observed trends within a particular series of results are reproducible.[165]

Another important excited state parameter is the lifetime which reflects the stability of the excited state. While emission lifetimes were not able to be measured in this work, it is understood that as the emission energy decreases, the lifetime will also decrease in accordance with the energy gap law.[62-64] The energy gap law shows that as the energy gap is decreased and emission is red shifted, non-radiative decay processes increase which results in shorter emission

lifetimes. This has large implications for cyclometalated ruthenium complexes, which show shorter lifetimes compared to their corresponding non-cyclometalated analogues because they have a small band gap.[37, 39] This observation also applies to smaller changes in energy, resulting from modifications to the cyclometalated ligand, such as in complexes **2.1**-**2.11**. While it has not been measured, it is likely that the lifetime of **2.5** will be the smallest as its emission is the most red shifted, which follows its very small quantum yield. While measuring the lifetime of an excited state is important to gaining further understanding about what factors influence the emission lifetime and thus how to modify the complex so they are luminescent at room temperature, it is less important for these complexes as they are not luminescent at room temperature. An example of luminescence lifetimes not being largely important is their use in dye-sensitized solar cells. Their short lifetimes are less important because the complex is immobilized and there is fast electron injection into the semiconductor, meaning other properties are more important for cyclometalated ruthenium complexes.

2.9 Electrochemical Studies.

Complex	$E_{1/2}$ anodic[a]	$E_{1/2}$ cathodic[a]	ΔE[c]
$[Ru(tpy)_2](PF_6)_2$[37]	0.89 (64)	-1.66 (63), -1.90 (63)	2.55
2.32[37]	0.12 (62), 1.36[b]	-1.95 (63)	2.07
2.1	0.11 (116), 1.05[b]	-1.96 (121)	2.07
2.2	0.14 (61), 1.16[b]	-1.97 (80)	2.11
2.3	0.09 (69), 0.92[b]	-1.97 (103)	2.06
2.4	0.09 (65) 0.86[b]	-1.97 (95)	2.06
2.5	0.13 (191), 0.81[b]	-1.94 (185)	2.07
2.6	0.12 (84), 0.81[b]	-1.95 (118)	2.07
2.7	0.12 (48), 0.89[b]	-1.96 (113)	2.08
2.8	0.09 (66), 0.90[b]	-2.07 (155)	2.16
2.9	0.24 (76), 0.92[b]	-1.92 (85)	2.16
2.11	0.13 (93), 0.94[b]	-1.91 (91)	2.04

Table 2.23: Electrochemical data for complexes **2.1**-**2.9**, **2.11** and relevant literature complexes $[Ru(tpy)_2](PF_6)_2$ and **2.32**. (a) The potential is reported as the $E_{1/2}$ value vs Fc/Fc^+. (b) Ep, irreversible. (c) Energy difference between first reversible oxidation and reduction. Complex **2.10** had irreproducible results and thus does not appear in this analysis.

The electrochemical properties of **2.1**-**2.11** were examined by cyclic voltammetry, using degassed acetonitrile solutions containing 0.1 M Bu_4NPF_6. Measured redox couples for the modified terpyridine series of ruthenium complexes are reported in Table 2.23. All complexes

exhibit a chemically reversible redox couple for both oxidation and reduction. Ruthenium(II) polypyridine complexes have a predominately metal based HOMO and a ligand based LUMO which leads to oxidation being associated with the metal center, while reduction occurs on the ligand, which is supported by the previously discussed TD-DFT calculations for these complexes.

The first oxidation process for each of the complexes **2.1-2.11** is quasi-reversible under cyclic voltammetry conditions and is assigned as being a $Ru^{2+/3+}$ redox couple. For complex **2.1**, the $E_{1/2}$ is at 0.11 V (versus Fc) for the $Ru^{2+/3+}$ couple, which is comparable to **2.32,** which has an $E_{1/2}$ of 0.12 V.[37] Complex **2.1** shows a cathodic shift of 780 mV compared to $[Ru(tpy)_2](PF_6)_2$ for the metal-based oxidation showing the effect of cyclometalation, in which the ruthenium atom becomes more electron rich due to the anionic carbon donating electron density onto the metal. It is also typical for these cyclometalated complexes to show an irreversible oxidation at a higher positive potential along the anodic scan. Complex **2.1** shows this peak at 1.05 V (versus Fc), a relatively large anodic shift compared to **2.32** (1.36 V) and this potential is reported to be due to a $Ru^{III/IV}$ process or ligand based decomposition.[29]

On the cathodic scan for **2.1** there is a single quasi-reversible redox process at -1.96 V under cyclic voltammetry conditions, which is assigned as being reduction of the terpyridine ligand. The value of this process in **2.1** is comparable to **2.32** (-1.95 V), as this reduction process only occurs on the unmodified terpyridine ligand. Another consequence of cyclometalation, is that there is increased π back donation onto the ligand from the electron rich metal, resulting in the terpyridine based reduction occurring at a more negative potential compared to the non-cyclometalated $[Ru(tpy)_2]PF_6$ (-1.66 V).

Modifications to the cyclometalated ligand typically lead to changes in the HOMO and changes to the terpyridine ligand generally lead to changes in the LUMO. This is shown by the TD-DFT isodensity plots of **2.1** (Chapter 2.7.2, Figure 2.19), in which the HOMO and HOMO-1 are both largely metal based with contribution from the cyclometalated ligand, whereas the LUMO is almost entirely terpyridine based. This means that the oxidation potentials should be affected by the changes to the cyclometalated ligand directly, and a smaller effect should occur on the LUMO because of π back donation from the metal onto the terpyridine ligand.

Analysis of the complexes in this series, **2.2**-**2.11** shows only a small variation in the potential for the quasi-reversible $Ru^{2+/3+}$ process in each complex. The oxidation potential for most of these complexes varies by around 60 mV and they generally fall into one of two categories. The first group of results has a small cathodic shift compared to **2.1**, with values between 0.08 V and 0.09 V (**2.3**, **2.4** and **2.8**). The other group shows a small anodic shift compared to **2.1** with values between 0.12 V and 0.14 V (**2.2**, **2.5**, **2.6**, **2.7** and **2.11**). Complex **2.9** is the only exception to this with a value of 0.24 V, which is a large anodic shift compared to **2.1**. The electron withdrawing ketone group removes a significant amount of electron density from the metal, making it harder to oxidize and thus the large anodic shift. Complex **2.2** also shows a large anodic shift because of the electron withdrawing effect of the bromine atom, which results in a less electron rich metal but not to the same extent as **2.9**. The overall effect on the potential $Ru^{2+/3+}$ process that results from these modifications is very small, as the range of potentials for these ten complexes is only 60 mV.

The anodic scan to a more positive potential led to the appearance of a single irreversible oxidation between 0.81 V and 1.16 V for all the complexes in this series. The irreversible oxidation peak is once again most likely attributable to a $Ru^{3+/4+}$ process, or ligand based decomposition.[29]

All of these complexes have at least one quasi-reversible reduction process, which occurs over a small range for the majority of the complexes in this series. The $E_{1/2}$ for the reduction process in **2.2** – **2.7** occurs between -1.97 V and -1.94 V and occurs at -2.07 V for **2.8**, at -1.92 V for **2.9** and at -1.91 V for **2.11**. The reduction potential of the complexes in this series is relatively unchanged for the majority of complexes because the reduction potential is based on the LUMO, which incorporates the unmodified terpyridine ligand. In addition to this, changes to the oxidation process can impact the reduction potential, although for the complexes in this series, the oxidation process is also relatively unchanged.

The reduction potential in **2.8** has a large cathodic shift compared to the others in this series and this is explained by the TD-DFT calculation for **2.8** which shows that the LUMO only incorporates two of the pyridine rings on the terpyridine ring. Previous work by Thummel *et al*. has shown that the greater the degree of delocalization in the terpyridine ligand, the easier it is for the terpyridine ligand to be reduced.[166] Thus it is likely that the cathodic shift results from

limited delocalization in the terpyridine ligand in **2.8**, as shown by the isodensity plot for the LUMO (Chapter 7.3, Figure 7.3.7). The reduction potential in **2.9** has a small anodic shift compared to **2.1**, with the large anodic shift of the $Ru^{2+/3+}$ process (compared to **2.1**) resulting in a moderate amount of π back donation onto the terpyridine ligand, which results in the anodic shift of the reduction process.

The reduction potential in **2.11** has a large anodic shift compared to **2.1** and this occurs because of enhanced delocalization that occurs as a result of the additional phenyl group on the terpyridine ligand, as opposed to reduced delocalization, as was the case in **2.8**.

All these small changes in the oxidation and reduction potentials result in changes to the overall energy gap between the HOMO and LUMO, in which the small changes either cancel out if both processes change by the same amount, or result in a change if the effect of one change is greater than the other. The E_{gap} is larger for **2.2** (2.11 V) compared to **2.1** (2.07 V) because of an anodic shift to the oxidation potential and a small cathodic shift to the reduction potential. The E_{gap} in **2.3** and **2.4** is slightly reduced compared to **2.1** with a value of 2.06 V which results from a small cathodic shift in both the oxidation and reduction potentials, with a slightly larger shift in the oxidation potential. The E_{gap} for **2.5** and **2.6** is 2.07 V, the same as for **2.1**. Both the oxidation and reduction processes for **2.6** have an anodic shift of 10 mV compared to **2.1**, but since the change is equivalent there is no change in the E_{gap}. The same is true for **2.5**, but with an equivalent change of 20 mV in each process compared to **2.1**. The E_{gap} for **2.8** is the largest in this series, with a value of 2.16 V, which results from a small cathodic shift in the oxidation potential compared to **2.1** and a much larger cathodic shift in the reduction potential compared to **2.1**. The TD-DFT calculation for **2.8** shows that the E_{gap} between the HOMO and the LUMO is very small compared to the others in this series, but as the calculations show the lowest energy MLCT transition results does not result from a HOMO → LUMO transition, but instead a HOMO-4 → LUMO+1 transition and thus the E_{gap} is much larger. The E_{gap} for **2.9** is slightly smaller than for **2.8**, with a value of 2.14 V. This results from the large anodic shift in the oxidation potential, and the small cathodic shift in the reduction potential for **2.9** compared to **2.1**. Complex **2.11** has the smallest E_{gap} for any of the complexes in this series with a value of 2.04 V. There is an anodic shift in both the oxidation potential and the reduction potential,

however the shift in the reduction potential is approximately doubled, which results in a smaller E_{gap} for **2.11** compared to **2.1**.

2.10 Summary.

The synthesis of eleven new cyclometalated ruthenium complexes, which incorporate 5' substituted 1,3-di(pyrazol-1-yl)benzene and terpyridine (**2.1**-**2.10**) or 1,3-di(pyrazol-1-yl)pyrene and 4-(4-^{t}butylphenyl)terpyridine (**2.11**) have been investigated and their electrochemical and spectroscopic properties have been studied. These results have been compared with $[Ru(tpy)_2](PF_6)_2$, [Ru(2,6-di(pyrazol-1-yl)pyridine)(terpyridine)]PF_6, (**2.31**) and [Ru(1,3-di(pyridyl-2-yl)(terpyridine)]PF_6 (**2.32**) to analyze the effect of introducing electron withdrawing groups, electron donating groups or large aromatic rings onto the 4' position of the central ring of the cyclometalated ligand. To gain further understanding about the structure of these complexes DFT calculations were used to calculate optimized structures. From these preliminary calculations, TD-DFT calculations were used to gain a more thorough understanding of the photophysical and electrochemical properties to provide further insight into the structure-property relations of these complexes.

All of the complexes were analyzed using NMR spectroscopy and their ^{1}H and ^{13}C spectra were fully assigned. Analysis of the coordination induced shifts for complexes **2.1**-**2.8** showed significant changes occurred upon coordination of the cyclometalated ligand. Large shifts occurred for the proton on the pyrazole ring that was pointing directly into the ring current of the terpyridine ring was a distinct indication that the target cyclometalated complex had formed. This proton had a CIS between -1.01 ppm and -1.20 ppm and occurred due to interligand through-space ring-current anisotropy effects. The protons on the aryl rings substituted at the 4' position of the central benzene ring had less electron density due to ligand-to-metal σ donation.

DFT calculations, which were completed for **2.1**-**2.11** and showed that the key bond length indicative of cyclometalation was the Ru-C bond length, which was calculated to vary from 1.93 Å to 2.00 Å in complexes **2.1**-**2.11**, which was shorter than the calculated bond length for [Ru(2,6-di(pyrazol-1-yl)pyridine)(terpyridine)]PF_6, (**2.31**). Complexes **2.3**, **2.4** and **2.8** had bond lengths similar to [Ru(1,3-di(pyrid-2-yl)benzene)(terpyridine)]PF_6 (**2.32**), with values of ca. 1.93 Å, while the remaining complexes had longer bond lengths of ca. 1.99 Å. The strongly electron donating groups resulted in the shorter, stronger Ru-C bond lengths, with the other modifications

have little effect on the Ru-C bond length as it was relatively unchanged compared to **2.1**, with a calculated value of 1.99121 Å. The Ru-N bond opposite the Ru-C bond was elongated due to the trans effect for all complexes compared to **2.31**, with the especially short Ru-C bond lengths for **2.3**, **2.4** and **2.8** resulting in slightly longer Ru-N bond lengths.

The bite angle of the cyclometalated ligand (N2-Ru-N4) to the ruthenium in complexes **2.1**-**2.11** ranges from 154.6° to 158.1°. These measurements show that there is also a relationship between the Ru-C bond length and the bite angle. Complexes **2.3**, **2.4** and **2.8** have shortened Ru-C bond lengths, which brings the rest of the cyclometalated ligand closer to the metal, which results in their corresponding bite angle (N2-Ru-N4) being increased. The effect of using pyrazole as the N-heterocycle instead of pyridine is a smaller angle, as the calculated value for **2.32** is 160.0°.

The crystal structures of target complexes **2.1**, **2.2**, **2.7** and **2.9** and a reaction byproduct, **2.5a** were obtained from X-ray crystallography. The structure of **2.9** confirmed that the alkyne had been hydrated during the reaction from the aqueous conditions and provided insight into the structure of **2.10**. The experimental structures reflected the calculated structures for **2.1**, **2.2**, **2.7** and **2.9**, with **2.1** being the most different of the four as it had a large amount of disorder due to the similarity between the terpyridine and 1,3-(dipyrazol-1-yl)benzene ligands. The crystal structures confirmed the disordered octahedral structures of these complexes and the experimental chelate bite angles of both ligands reflected the calculated results with values of between 154° and 157°, which is smaller than for **2.32**, which has a chelate bite angle of 160.012° for the binding of the 1,3-di(pyridyl)benzene to the ruthenium and152.261° for the binding of the terpyridine to the ruthenium.

The dihedral angle was calculated *in vacuo* at ca. 30° for **2.3**, **2.5**, **2.7** due to a small amount of steric hindrance between ring systems. More sterically hindered systems such as for complexes **2.6** and **2.8** had calculated dihedral angles of 53.461° and 43.407° respectively due to the larger amount of steric hindrance resulting from the naphthyl and pyrenyl groups. Complex **2.4** had a calculated dihedral angle of 76.613° due to the large amount of steric hindrance from the attached mesityl group. The X-ray structures for **2.5a** and **2.7** showed dihedral angles of 23.8(4)° and 18.4(6)°, respectively.

The UV-vis absorption spectra for **2.1**-**2.11** were measured and all showed a broad MLCT in the visible spectrum. The λ_{max} of this broad peak envelope is at 487 nm for **2.1** and is blue shifted by 12 nm compared to **2.32**, showing the effect of changing the electron deficient pyridyl to the electron rich pyrazole. TD-DFT calculations for **2.1** showed three transitions occurred over the range of the lowest energy peak envelope, and the largest of these was at 467.0 nm. This showed a calculated blue shift of 8.2 nm, which reflected the experimentally observed blue shift. The TD-DFT calculations also showed that the dominant transition was from the HOMO-2 to the LUMO. Isodensity plots of these orbitals showed that electron density for the HOMO-2 was predominantly metal based, with electron density also spread onto the terpyridine ligand and the LUMO showed electron density on the terpyridine ligand.

The UV-vis absorption spectra for **2.2**-**2.11** showed the energy of the frontier orbitals could be modified by various substitutions on the cyclometalated ligand, as the lowest energy MLCT was shifted between 479 nm and 505 nm. The lowest energy MLCT in complex **2.2**-**2.5** is relatively unaffected by the modifications to the cyclometalated ligand. Of particular interest however were the changes in energy of the MLCT in **2.6**-**2.8**. They showed a small blue shift of 40 cm^{-1} for **2.6**, a blue shift of 130 cm^{-1} for **2.7** and a further blue shift of 210 cm^{-1} for **2.8** compared to **2.1** upon introduction of 1-naphthyl, 2-naphthyl and 1-pyrenyl groups respectively. Typically, introduction of large aryl groups results in a red shift however in these complexes the orbitals are unable to overlap, due to twisting of the respective aryl group and a blue shift is observed. The ketone group substituted at the 4' position of central benzene ring of the cyclometalated ligand in **2.9** and **2.10** results in the energy of the MLCT being 479 nm and 481 nm respectively, a blue shift compared to all other complexes in this series.

Complex **2.11** was the furthest red shifted in this series at 505 nm, as the central pyrene group on the cyclometalated ligand and the aryl substituted terpyridine ligand lowered the energy gap between the relevant occupied and unoccupied orbitals. As the benzene rings in pyrene were fused to the benzene ring containing the cyclometalated carbon atom the orbitals were forced to be aligned, which enabled the electron density to extend through the rings, resulting in a larger shift than cannot be solely accounted for by the aryl substituted terpyridine ligand. This was in contrast to the substitutions on the cyclometalated ligand in complexes **2.3**-**2.10** which could freely rotate and potentially favor a twisted or perpendicular orientation of the substituted aryl

group. The complexes incorporating pyrene (**2.8** and **2.11**) also have significantly increased extinction coefficients compared to the parent complex **2.1**.

The potential emission of all of these complexes was measured at room temperature in degassed acetonitrile but did not show distinct peaks. At 77 K all complexes were emissive with excitation of the lowest energy MLCT producing broad emission profiles between 666 nm and 729 nm. Following the absorption properties for **2.1**-**2.11**, namely the energy of the MLCT, complex **2.5** (729 nm) was the most red shifted compared to **2.1** (712 nm). The majority of the complexes in this series had similar Stokes shifts between 6,500 cm^{-1} and 6,600 cm^{-1}, with a reduced Stokes shift of 6,000 cm^{-1} for **2.9** and 5,600 cm^{-1} for **2.10** and **2.11**. These Stokes shifts are all larger than for $[Ru(tpy)_2](PF_6)_2$ and $[Ru(bpy)_3](PF_6)_2$, which have values of 4,400 cm^{-1} and 5,000 cm^{-1} respectively.

The quantum yields of complexes **2.1**-**2.11** were measured at 77 K and varied between 4% and 95%, with 2.2, 2.9 and 2.10 having very high quantum yields of 68%, 95% and 93% respectively. These results cannot be directly related to $[Ru(dpyb)(tpy)]PF_6$,[37] as its emission spectrum has not been measured at 77 K and none of these complexes had detectable luminescence at room temperature using the experimental setup at hand. At room temperature $[Ru(dpyb)(tpy)]PF_6$,[37] has been shown to produce emission at 781 nm (12,800 cm^{-1}) with a very low quantum yield of 9.4×10^{-6}.

The electrochemical properties of **2.1**-**2.11** were also examined by cyclic voltammetry. All complexes exhibit a chemically quasi-reversible redox couple for both oxidation and reduction, with the oxidation occurring on the metal center and reduction occurring on the terpyridine ligand. This was supported by the TD-DFT calculations which showed that the HOMO was associated with the metal center and the LUMO was associated with the terpyridine ligand and not the cyclometalated ligand.

The potential of the quasi-reversible oxidation process was modified between 0.09 V and 0.24 V and the potential of the quasi-reversible reduction process was modified between -1.91 V and -2.07 V for complexes **2.1**-**2.11**. These potentials are slightly modified compared to the values for $[Ru(dpyb)(tpy)]PF_6$[37] which has quasi-reversible oxidation and reduction processes at 0.12 V and -1.95 V respectively. These potentials also show the large shift that occurs upon

cyclometalation, as $[Ru(tpy)_2](PF_6)_2$[37] has quasi-reversible oxidation and reduction processes at 0.89 V and -1.66 V respectively. These potentials for complexes **2.1**-**2.11** show a ΔE between 2.04 V and 2.16 V, compared to the ΔE for $[Ru(dpyb)(tpy)]PF_6$[37] and $[Ru(tpy)_2](PF_6)_2$[37] of 2.07 V and 2.55 V respectively. This showed that the electrochemical properties could be modified by changes to the 4'-position of the central benzene ring on the cyclometalated ligand, with changes to both the quasi-reversible oxidation and reduction processes, as well as the energy gap between them (ΔE).

CHAPTER 3

MODIFICATION AT THE 4' POSITION ON THE TERPYRIDINE LIGAND.

3. Modification at the 4’ position on the terpyridine ligand.

3.1 Introduction.

A large number of substituted terpyridine ligands that have been synthesized, which have been successful at fine tuning the HOMO-LUMO energy gap and thus the energy of the MLCT. Electron withdrawing groups, such as R-CO_2Et, have been attached at the 4’-position of terpyridine and incorporated into ruthenium(II) complexes to produce room temperature phosphorescence (Figure 3.1). $[Ru(tpy)(4\text{-}(CO_2Et)tpy)](PF_6)_2$ has a broad MLCT transition in the visible spectrum at 492 nm (ε = 13,800), showing a large red shift compared to $[Ru(tpy)_2](PF_6)_2$, which has a MLCT transition at 475 nm (ε = 10,400). Excitation at this wavelength leads to emission from the ^{3}MLCT at 667 nm, which has a lifetime of 32 ns and a quantum yield of 2.7 x 10^{-4}. This is a significant improvement compared to $[Ru(tpy)_2](PF_6)_2$, which is not emissive at room temperature and shows that changes at the 4’-position of terpyridine can result in significant changes to the photochemical properties.

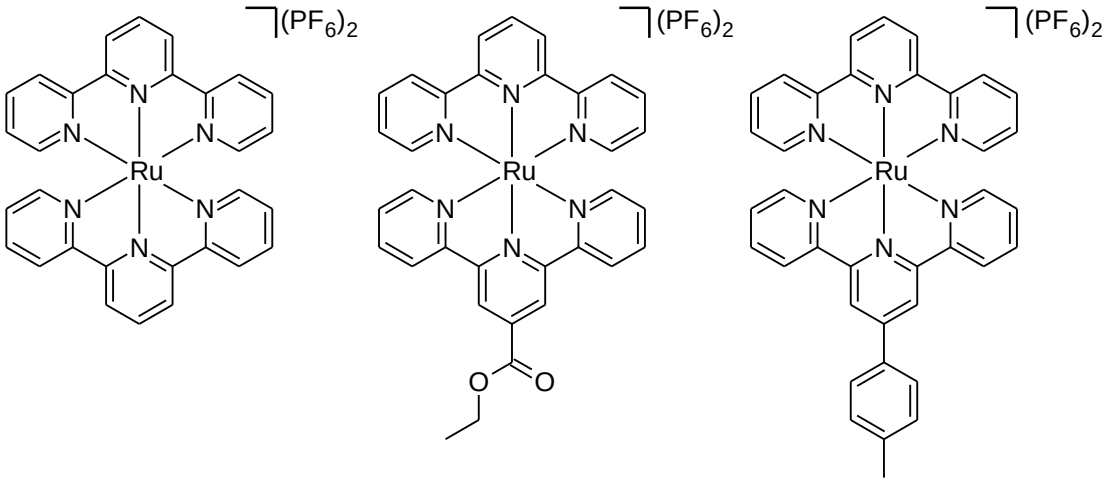

Figure 3.1: Three ruthenium(II) complexes, $[Ru(tpy)_2](PF_6)_2$, $[Ru(tpy)(4\text{-}(CO_2Et)tpy)](PF_6)_2$ and $[Ru(tpy)(ttpy)](PF_6)_2$

Large aryl groups have also been attached to the 4’-position of terpyridine to cause changes in the absorption and emission properties of these complexes. Using 4-(p-tolyl)terpyridine (ttpy) to form a heteroleptic ruthenium complex with terpyridine also results in a red shift, with a broad MLCT transition at 482 nm (ε = 15,600).[167] The extended conjugated system due to the additional aryl group leads to a significant increase in the extinction coefficient compared to

$[Ru(tpy)_2](PF_6)_2$. A similar structure incorporating anthracen-9-yl at the 4'-position on the terpyridine results in an equivalent red shift as for $[Ru(ttpy)(tpy)](PF_6)_2$, but only a small increase in the extinction coefficient compared to $[Ru(tpy)_2](PF_6)_2$. There is no change in the wavelength of absorption in these two complexes, despite the significantly different sizes of their π-conjugation systems, as a result of the anthracene twisting out of the plane of the terpyridine. By using increasingly large aryl groups, substituted at the 4'-position of the terpyridine, a balance will be targeted between increased size of the π-conjugation systems and a planar geometry between the aryl group and terpyridine which will allow a greater amount of orbital overlap. More recent research has examined this by synthesizing a series of ligands which incorporate phenyl, 2-naphthyl, 1-pyrenyl and 9-anthracenyl groups at the 4'-position of terpyridine (Figure 3.2).[168]

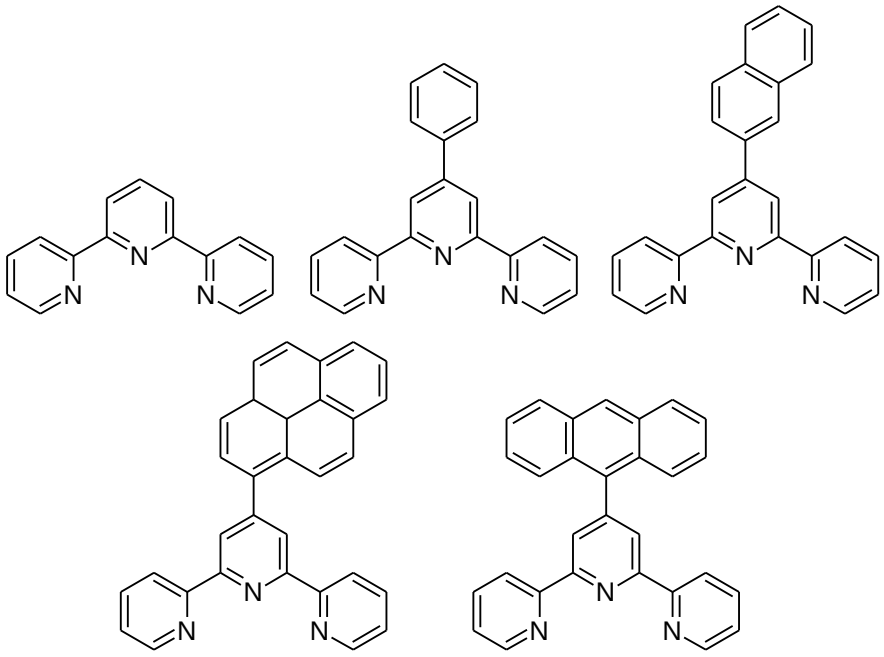

Figure 3.2: Terpyridine and four 4'-substituted terpyridines incorporating phenyl, 2-naphthyl, 1-pyrenyl and 9-anthracenyl groups.

All of these complexes exhibited strong and relatively broad absorption peak envelopes in the visible range, with values ranging between 484 nm and 503 nm (ε = 12200−15750). These MLCT transitions are red shifted compared to $[Ru(tpy)_2](PF_6)_2$ (475 nm) and the extinction coefficients are increased by ca. 50%.

Not all 4'-substituted terpyridines result in complexes that have red shifted MLCT envelopes compared to their respective parent complex however. [Ru(dpyb)(4-(CO_2Me)tpy)](PF_6) has a broad MLCT transition with a peak at 492 nm which is blue shifted compared to [Ru(dpyb)(tpy)](PF_6), which has a broad MLCT transition with a peak at 499 nm. [Ru(dpyb)(4-(CO_2Me)tpy)](PF_6) is also luminescent at room temperature, with an emission profile peak at 743 nm and a quantum yield of 1.5×10^{-5}.

These complexes show that emission at room temperature can be achieved through substitution at the 4'-postion of terpyridine, but improvements need to be made to increase the lifetime and quantum yield. There are several methods available to increase the photochemical properties of these complexes, namely increasing the room temperature lifetimes and quantum yields and understanding which areas of these complexes result in the largest changes to these photophysical properties is important.

3.2 Research outline.

In this chapter a series of N^C^N cyclometalated ruthenium complexes are described which incorporate a range of 4' substituted 2,2′:6′,2″-terpyridines. There are eleven new N^C^N cyclometalated ruthenium complexes included with three different cyclometalating ligands and nine different terpyridine ligands.

Complexes have been synthesized based on the parent complex, **2.1**, with the goal of extending the aryl system on the terpyridine ligand, in a similar fashion to chapter two except at the 4' position on the central pyridine of the terpyridine ligand. By extending the ring system in this position with large aryl groups or electron withdrawing/donating groups, the properties of the system can be modified. By modifying the ring system in this position the symmetry of the overall structure of the ruthenium complex is retained, which will enable direct comparison of which structural modifications are important in changing the electrochemical and photophysical properties of the complex. As shown in chapter two, the electron density on the LUMO generally extends over the terpyridine ligand and thus by modifying this ligand in this position, the energy of transitions incorporating the LUMO/terpyridine would be expected to be altered.

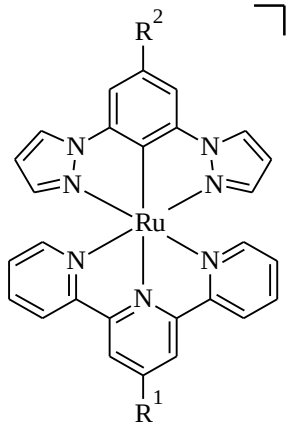

R^1 = H	R^2 = H	**2.1**
R^1 = 4-Tertbutylphenyl	R^2 = H	**3.1**
R^1 = 3,4,5-Trimethylphenyl	R^2 = H	**3.2**
R^1 = 4-Methoxyphenyl	R^2 = H	**3.3**
R^1 = 4-Nitrophenyl	R^2 = H	**3.4**
R^1 = Cl	R^2 = H	**3.5**
R^1 = 4-Bromophenyl	R^2 = H	**3.6**
R^1 = 4-Bromophenyl	R^2 = Br	**3.7**
R^1 = 2-Naphthyl	R^2 = H	**3.8**
R^1 = 9-Anthracenyl	R^2 = H	**3.9**
R^1 = 9-Anthracenyl	R^2 = 1-Pyrenyl	**3.10**

Figure 3.3: Ruthenium(II) complexes described in this chapter.

Complexes **3.1** and **3.2** will examine the impact of adding a conjugated benzene ring onto the terpyridine ligand. Building on these results, complexes **3.3** and **3.4** have been synthesised to introduce an electron donating group (EDG) and an electron withdrawing group (EWG) by substituting in 4-methoxyphenyl and 4-nitrophenyl into the ring. Complexes **3.5**, **3.6** and **3.7** were synthesised as they are useful intermediates, as aryl halogens leave them open to future modifications. From this research, conclusions will be able to be made about what impact substitutions at the 4' position of the central terpyridine will have and how that may affect potential applications utilizing substitution in this position. To probe the effect of increasing the size of the aryl system further by introducing further expansion, **3.8** was synthesized with 2-naphthalene incorporated and **3.9** with 9-anthracene. Complex **3.10** also used anthracene but also incorporated 1-pyrenyl onto the 4' position of the central benzene on the cyclometalating ligand.

3.3 Ligand and complexes synthesis.

The ligands for this section of work were prepared as outlined in **Scheme 3.15**. Ligand **3.11** was synthesized using the method of Constable *et al.*[169] in high yield over the three steps. Ligands **3.12-3.17** were synthesized in a single step from the corresponding substituted benzaldehyde

with 2-acetylpyridine, sodium hydroxide and ammonia in methanol. All of these ligands had previously been prepared[169-176] except for **3.13** which was characterized by ^{1}H and ^{13}C NMR spectroscopy and mass spectrometry. Synthesis of dpyzbH is discussed in chapter two.

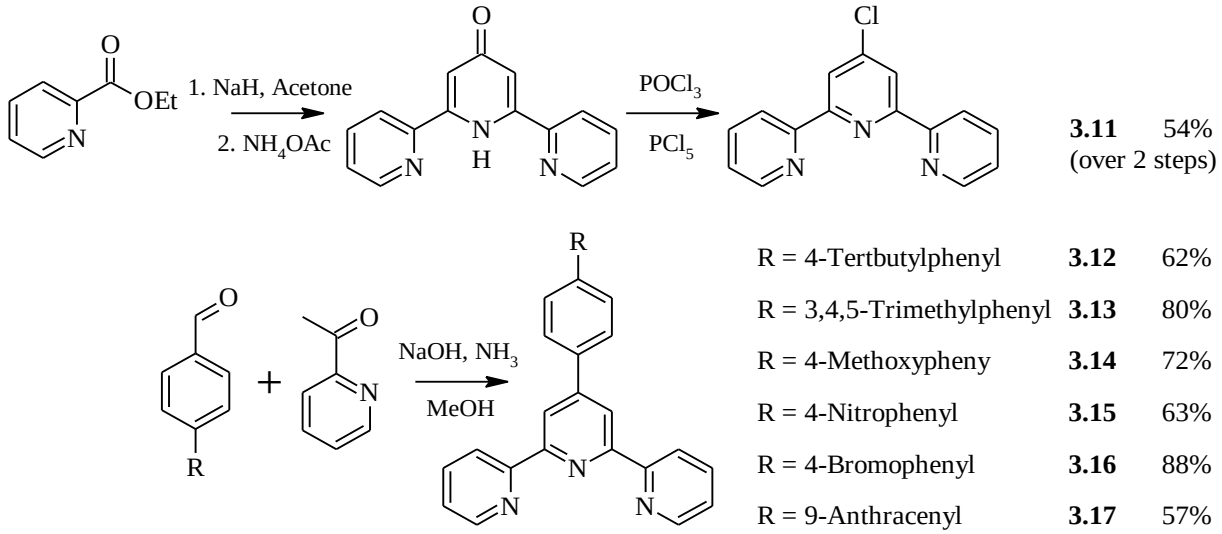

	3.11	54% (over 2 steps)
R = 4-Tertbutylphenyl	**3.12**	62%
R = 3,4,5-Trimethylphenyl	**3.13**	80%
R = 4-Methoxypheny	**3.14**	72%
R = 4-Nitrophenyl	**3.15**	63%
R = 4-Bromophenyl	**3.16**	88%
R = 9-Anthracenyl	**3.17**	57%

Scheme 3.15: Synthesis of terpyridine ligands, **3.11**-**3.17**.

The substituted terpyridines were then reacted with $RuCl_3.xH_2O$ in ethanol to precipitate the ruthenium precursor complex, Ru(tpy-R)Cl_3, which was identified using mass spectrometry and used without further purification with 1,3-di(pyrazol-1-yl)-5-bromobenzene (**2.12**) to form the cyclometalated ruthenium complex using previously optimized conditions from chapter two.

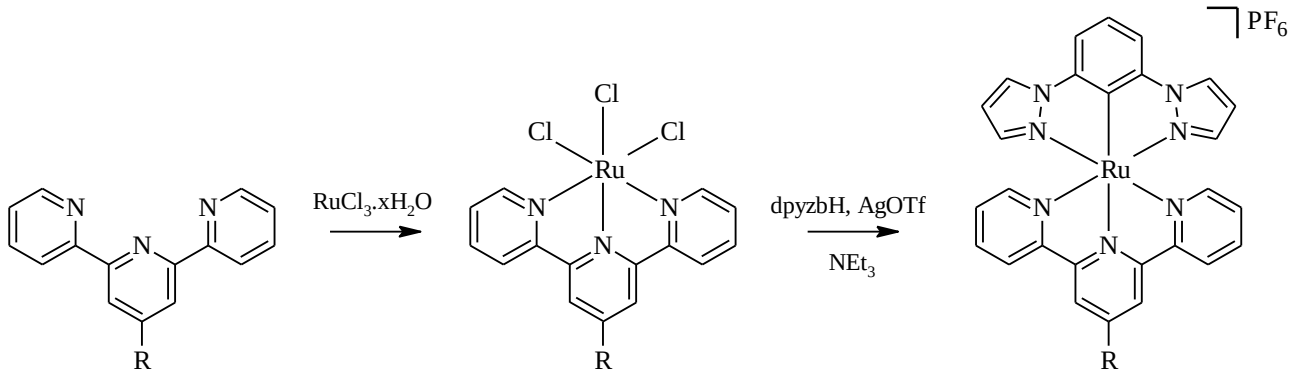

Scheme 3.2: Synthesis of precursor, Ru(tpy-R)Cl_3, followed by cyclometalated ruthenium complex, [Ru(tpy-R)(dpyzb)]PF_6.

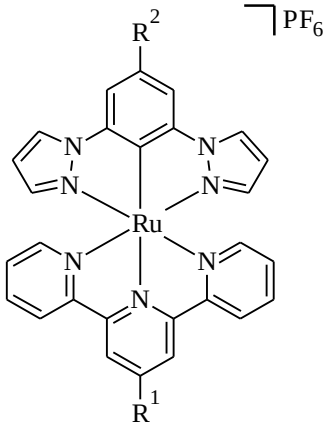

R^1 = H	R^2 = H	**2.1**
R^1 = 4-Tertbutylphenyl	R^2 = H	**3.1**
R^1 = 3,4,5-Trimethylphenyl	R^2 = H	**3.2**
R^1 = 4-Methoxyphenyl	R^2 = H	**3.3**
R^1 = 4-Nitrophenyl	R^2 = H	**3.4**
R^1 = Cl	R^2 = H	**3.5**
R^1 = 4-Bromophenyl	R^2 = H	**3.6**
R^1 = 4-Bromophenyl	R^2 = Br	**3.7**
R^1 = 2-Naphthyl	R^2 = H	**3.8**
R^1 = 9-Anthracenyl	R^2 = H	**3.9**
R^1 = 9-Anthracenyl	R^2 = 1-Pyrenyl	**3.10**

Figure 3.4: Successfully synthesized ruthenium(II) complexes.

3.4 NMR spectroscopy.

One of the principle methods of characterization used in this work is NMR spectroscopy. Most of the ligands and their complexes synthesised had signals for different protons which were well separated, making assignment straightforward and unambiguous, however ligands and corresponding complexes with naphthalene (**3.8**), anthracene (**3.9**, **3.10**) and pyrene (**3.10**) become more difficult to assign based solely on ^{1}H and ^{13}C NMR spectra. This difficulty can be reduced by using a range of two-dimensional techniques, such as COSY, HSQC and HMBC in partnership with similar compounds' analysis.

The NMR spectra of these ligands significantly changes upon cyclometalation to ruthenium and these changes can be examined by analysis of coordination induced shifts (Refer Chapter 2.5.1 NMR Spectroscopy. Complexes **3.1-3.10** and their corresponding free N^C^N ligand were both able to be dissolved in acetone-D6 and analysis of their CIS were carried out. The CIS results for complexes **3.1-3.10** (Tables 3.1-3.3**)** are very similar to each other and the parent complex **2.1** due to the modifications in this series being made to the terpyridine ligand and thus only provide a limited amount of new information. The large negative shift for H7 of between -1.05 ppm and -0.75 ppm supports the assigned distorted octahedral geometry due to interligand through-space ring-current anisotropy effects in which the H7 proton lies over the shielding plane of the central

pyridine ring of the terpyridine ligand as a result of the distorted octahedral geometry. The other CIS follow similar trends as for **2.1**-**2.8** and their results are discussed in more detail in chapter two.

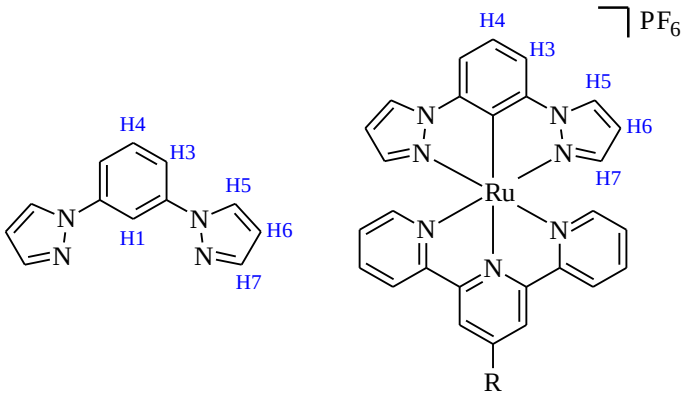

Figure 3.5: General structure of complexes **3.1**-**3.10**, with labeling system for CIS discussion.

	H1	**H3**	**H4**	**H5**	**H6**	**H7**
2.12	8.36	7.77	7.59	8.43	6.54	7.74
2.1	-	7.90	7.44	8.72	6.24	6.69
CIS	-	+0.13	-0.15	+0.29	-0.30	-1.05
2.12	8.36	7.77	7.59	8.43	6.54	7.74
3.1	-	7.94	7.43	8.73	6.26	6.75
CIS	-	+0.17	-0.16	+0.30	-0.28	-0.99
2.12	8.36	7.77	7.59	8.43	6.54	7.74
3.2	-	7.92	7.46	8.75	6.27	6.75
CIS	-	+0.15	-0.13	+0.32	-0.27	-0.99
2.12	8.36	7.77	7.59	8.43	6.54	7.74
3.3	-	7.92	7.45	8.74	6.26	6.78
CIS	-	+0.15	-0.14	+0.31	-0.28	-0.96
2.12	8.36	7.77	7.59	8.43	6.54	7.74
3.4	-	7.94	7.49	8.76	6.27	6.78
CIS	-	+0.17	-0.10	+0.33	-0.27	-0.96

Table 3.1: CIS for complexes **3.1**-**3.4** and **2.1** for comparision.

	H1	H3	H4	H5	H6	H7
2.12	8.36	7.77	7.59	8.43	6.54	7.74
3.5	-	7.92	7.46	8.73	6.25	6.80
CIS	-	+0.15	-0.13	+0.30	-0.29	-0.94
2.12	8.36	7.77	7.59	8.43	6.54	7.74
3.6	-	7.93	7.44	8.73	6.25	6.76
CIS	-	+0.16	-0.15	+0.30	-0.29	-0.98
2.13	8.33	7.97	-	8.51	6.57	7.77
3.7	-	8.13	-	8.82	6.31	6.83
CIS	-	+0.16	-	+0.31	-0.26	-0.94
2.12	8.36	7.77	7.59	8.43	6.54	7.74
3.8	-	7.94	7.48	8.75	6.28	6.81
CIS	-	+0.17	-0.11	+0.32	-0.26	-0.93
2.12	8.36	7.77	7.59	8.43	6.54	7.74
3.9	-	7.96	7.50	8.79	6.34	6.96
CIS	-	+0.19	-0.09	+0.36	-0.20	-0.78

Table 3.2: CIS for complexes **3.5**-**3.9**.

	H1	H3	H4	H5	H6	H7	Pyrene Ring Protons (H9-H20)
2.25	8.56	8.07	-	8.63	6.6	7.8	8.09-8.44 (10H, m)
3.11	-	8.28	-	8.97	6.4	7.05	8.75 (H10), 8.52 (H12), 8.44 (H13), 8.41-8.35 (H15), 8.41-8.35 (H17), 8.33 (H19), 8.28 (H9), 8.28 (H20), 8.15 (H16).
CIS	-	+0.21	-	+0.34	-0.20	-0.75	

Table 3.3: CIS for complex **3.10**.

Compound	**2.1**	**3.1**	**3.2**	**3.3**	**3.4**	**3.5**
^{13}C	181.3	180.5	181.4	181.6	181.0	180.8
Compound	**3.6**	**3.7**	**3.8**	**3.9**	**3.10**	**2.12**
^{13}C	180.9	180.7	181.4	181.4	181.3	109.9

Table 3.4: Chemical shift of cyclometalated carbon atom (C1) in complexes **3.1**-**3.10** and **2.1** and the corresponding carbon in free ligand **2.12**.

A large CIS also occurs in the ^{13}C for the cyclometalated carbon in each complex (Table 3.4). The free ligand, 1,3-di(pyrazole-1-yl)benzene has a peak at 109.9 ppm in the ^{13}C NMR spectrum corresponding to the C1 carbon and upon cyclometalated it shifts largely downfield to around

181 ppm in complexes **3.1**-**3.10** (acetone-d6). There is also an observable broadening of all the carbon peaks for the ruthenium complexes, compared to the free ligand.

3.5 Computational structural analysis.

Complex	Cyclometalated Ligand			Terpyridine Ligand		
	N2-Ru	C-Ru	N4-Ru	N5-Ru	N6-Ru	N7-Ru
2.1	2.10590	1.99121	2.10580	2.09150	2.03081	2.09136
3.1	2.10505	1.98966	2.10501	2.09261	2.03186	2.09278
3.2	2.10430	1.99015	2.10433	2.09330	2.03330	2.09327
3.3	2.10519	1.98982	2.10517	2.09266	2.03160	2.09240
3.4	2.10586	1.99324	2.10582	2.09226	2.02548	2.09231
3.5	2.10637	1.99192	2.10638	2.09195	2.02864	2.09197
3.6	2.10551	1.99103	2.10550	2.09241	2.02938	2.09240
3.7	2.10636	1.9883	2.10636	2.09368	2.03058	2.09367
3.8	2.10509	1.99024	2.10367	2.09316	2.03180	2.09211
3.9	2.10510	1.99106	2.10514	2.09230	2.03230	2.09226
3.10	2.10566	1.98945	2.10629	2.09244	2.03173	2.09273

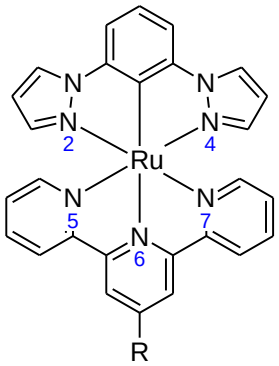

Table 3.5: Calculated bond lengths for **3.1**-**3.10** and **2.1** from DFT calculations in vacuo, along with a general figure showing the labeling scheme used. The cyclometalated carbon is labeled C.

As discussed in chapter two, the Ru-C bond in the cyclometalated complex is shortened compared to the corresponding Ru-N bond in the non-cyclometalated complex. In addition to this, the Ru-N6 bond opposite the Ru-C bond is elongated due to the trans effect.[149-150] The calculated bonds lengths for the five Ru-N bonds and the Ru-C bond are shown in Table 3.5 and selected bond angles are shown in Table 3.6. Complexes which have an aryl group substituted onto the cyclometalated ligand (dihedral A) or terpyridine ligand (dihedral B) also have their dihedral angles shown in Table 3.6.

The substitutions to the terpyridine ligand in complexes **3.1**-**3.10** do not result in a change to the Ru-C bond length. The Ru-N bond length of the parent complex, **2.1** is 1.99121 Å and the Ru-N bond lengths in complexes **3.1**-**3.10** are all within 0.15% of this value showing their bond lengths are equivalent. This is also true for the Ru-N6 bond opposite the Ru-C bond, which has a value of 2.0308 Å for **2.1** and complexes **3.1**-**3.10** are all within 0.26%, showing the Ru-N6 bond lengths in **3.1**-**3.10** are equivalent to in **2.1**. The other Ru-N bond lengths for **3.1**-**3.10** are also very similar compared to **2.1**, with the bond lengths for N2-Ru and N4-Ru all between 2.1064 Å

and 2.1037 Å. The bond lengths for N5-Ru and N6-Ru range from 2.0915 Å to 2.0937 Å for **3.1**-**3.10**, also showing no significant change in bond length compared to **2.1**.

Complex	C-Ru-N5	C-Ru-N6	C-Ru-N7	N2-Ru-N4	N5-Ru-N7	Dihedral A	Dihedral B
2.1	101.529	179.995	101.517	154.942	156.954	N/A	N/A
3.1	101.714	179.940	101.719	155.068	156.567	N/A	32.948
3.2	101.776	179.982	101.755	155.052	156.469	N/A	32.727
3.3	101.705	179.920	101.734	155.059	156.562	N/A	31.714
3.4	101.589	179.993	101.588	154.856	156.823	N/A	34.122
3.5	101.585	179.999	101.587	154.914	156.828	N/A	N/A
3.6	101.656	179.974	101.676	154.987	156.667	N/A	33.874
3.7	101.680	179.982	101.697	154.949	156.623	N/A	33.802
3.8	101.931	179.532	101.497	155.071	156.572	N/A	33.317
3.9	101.681	179.995	101.676	155.012	156.643	N/A	67.880
3.10	101.626	179.644	101.719	154.766	156.655	52.677	70.349

Table 3.6: Calculated bond angles for complexes **3.1**-**3.10** and **2.1** from DFT calculations *in vacuo*. Dihedral A is the dihedral angle between the central benzene ring and the 4' substituted aryl ring on the cyclometalated ligand. Dihedral B is the dihedral angle between the central pyridine ring and the 4' substituted aryl ring on the terpyridine ligand.

The bond angles between C-Ru-N5 and C-Ru-N7 for **2.1** are 101.529° and 101.517° respectively, and the corresponding bond angles in **3.1**-**3.10** are all within 0.4%, showing they are equivalent. The bond angle between C-Ru-N6 for **2.1** is 179.995° and the corresponding bond angles for **3.1**-**3.10** are all within 0.26%, showing the bond angles are calculated to be equivalent. The bite angle of the cyclometalated ligand with the metal (N2-Ru-N4) in **2.1** is 154.942°, with the corresponding angles in **3.1**-**3.10** all within 0.11%, showing the N2-Ru-N4 calculated bond angles in **3.1**-**3.10** are equivalent to **2.1**. The bite angle of the terpyridine ligand with the metal (N5-Ru-N7) in **2.1** is calculated to be 156.954°, with the corresponding angles in **3.1**-**3.10** all within 0.31% showing they are equivalent to **2.1**.

The dihedral angle between the central pyridine ring and the substituted aryl group on the substituted terpyridine ligand is between 30° and 35° for complexes **3.1**-**3.4** and **3.6**-**3.8**, which offsets the steric hindrance from the hydrogens on the aryl ring and the two hydrogens on the central pyridine ring of the substituted terpyridine ligand. The anthracene in **3.9** and **3.10** is offset by 67.880° and 70.349° respectively, showing that the anthracene is offset from being

perpendicular to the terpyridine ring, which minimizes the steric hindrance between the anthracene and the central pyridine ring.

The interesting result for this series is that modifications to the 4' position of the central pyridine ring on the terpyridine ligand do not result in changes to any of key bond lengths, and thus the majority of bond angles are also unchanged. In chapter two changes to the 4' position of the central benzene ring of the cyclometalating ligand were able to vary the Ru-C bond length between 1.92 Å and 2.01 Å. This lead to changes in the Ru-N6 bond length opposite the Ru-C bond, with values varied between 2.02 Å to 2.11 Å due to the trans effect.[149-150] This shows changes to the terpyridine ligand do not affect the overall structure of the complex as much as changes to the cyclometalated ligand.

3.6 Crystal Structure Determination.

*3.6.1 Crystal structure of **3.5***

Single crystals suitable for X-ray analysis for **3.5** were grown by slow evaporation of an acetonitrile/toluene solution and were successfully characterized by X-ray diffraction. The structure solved in the orthorhombic space group *P*nna and contained half of complex **3.5**, half a hexafluorophosphate anion and half of a disordered toluene solvate molecule in the asymmetric unit.

The ruthenium atom possesses a distorted octahedral geometry, with the substituted terpyridine ligand and cyclometalated ligand having chelate bite angles of 156.6(1)° and 154.5(1)° respectively. These angles reflect the corresponding calculated value for each angle (156.828 and 154.914), with only a small difference between the calculated and experimental measurements. The C-Ru bond length is 1.963(2) Å and reflects previous results from chapter two which have shown that this bond is shortened as a result of cyclometalation compared to similar non-cyclometalated complexes. The N4-Ru bond is 2.060(2) Å and is slightly elongated due to the trans effect.[149-150] The calculated C-Ru and N4-Ru bond lengths are both shorter than the calculated structures as bond lengths from DFT calculations tend to be elongated compared to comparable experimental x-ray structures.[28] The crystal structure shows where the internal proton on each pyrazole would be located as a result of the distorted octahedral geometry, in

which it is in the shielding plane of the central pyridine ring of the terpyridine ligand. This causes the interligand through-space ring-current anisotropy effects and the large negative CIS.

The crystal packing also exhibits extensive short F···H–C contacts between the hexafluorophosphate anions and the ligand molecules in the range of 2.5-3.3 Å, which further stabilizes the solid–state structure.

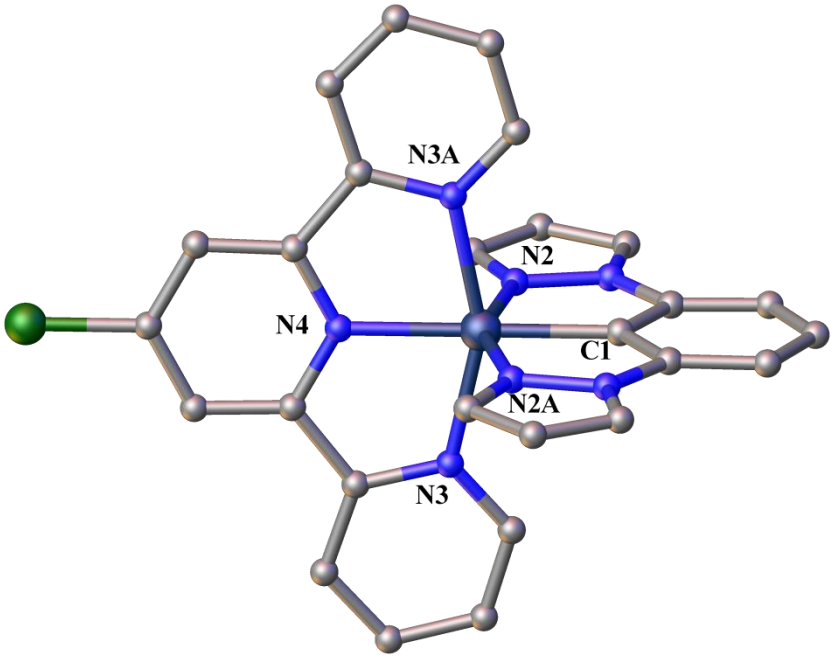

Figure 3.6: Crystal Structure of complex **3.5**. Hydrogen atoms, counterions and the solvate molecules are omitted for clarity. Selected bond distances (Å): N2-Ru 2.074(2), C1-Ru 1.963(2), N3-Ru 2.010(2), N4-Ru 2.060(2). Selected bond angles (°): C1-Ru-N3 101.72(5), C1-Ru-N4 179.99(1), N2-Ru-N2A 154.5(1), N3-Ru-N3A 156.6(1).

*3.6.2 Crystal structure of **3.6***

Dark red crystals of complex **3.6** (Figure 3.6) were obtained by slow evaporation of a toluene/acetonitrile/acetone solution containing the complex and these were suitable for X–ray analysis. The structure solved in the orthorhombic space group $P2_12_12_1$ and contained one molecule of complex **3.6**, one hexafluorophosphate anion, one toluene molecule and one disordered acetone molecule in the asymmetric unit.

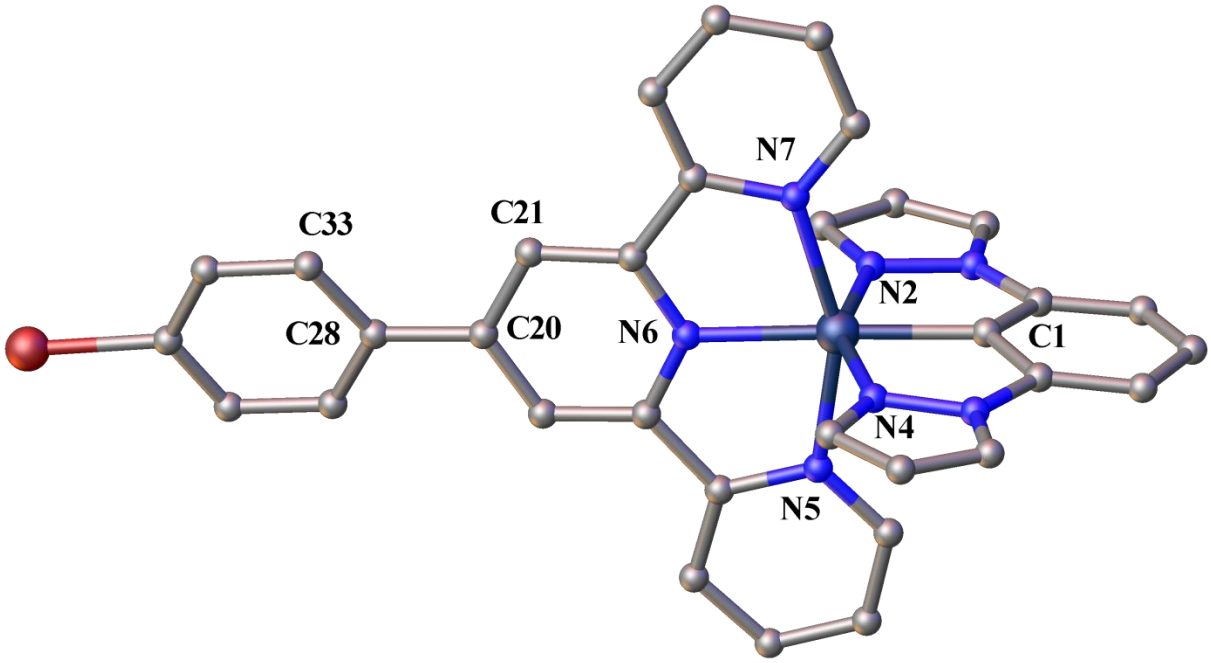

Figure 3.7: Crystal Structure of complex **3.6**. Hydrogen atoms, counterions and the solvate molecules are omitted for clarity. Selected bond distances (Å): N2-Ru 2.067(7), C1-Ru 1.979(9) N4-Ru 2.101(6), N5-Ru 2.064(5), N6-Ru 2.020(5), N7-Ru 2.075(6). Selected bond angles (°):C1-Ru-N5 97.1(3), C1-Ru-N6 76.9(4), C1-Ru-N7 106.3(3), N2-Ru-N4 154.7(3), N5-Ru-N7 156.5(2). Selected dihedral angle (°): C21-C20-C28B-C37B 9.5(12).

For **3.6**, the ruthenium atom possesses the same distorted octahedral geometry as for the crystal structure of **3.5**, with the substituted terpyridine ligand and cyclometalated ligand having chelate bite angles of 156.5(2)° and 154.7(3)° respectively. The Ru-C bond length is 1.979(9) Å and the opposite Ru-N4 bond length is 2.020(5) Å, which is slightly longer for the Ru-C bond in **3.6** and slightly longer than the Ru-N4 bond length in **3.5**. The remaining Ru-N bond lengths are also very similar to the corresponding bond lengths in **3.5**. The dihedral angle between the terpyridine and the 4' substituted phenyl ring (C19-C20-C28-C29) is measured at 9.5(12)°, showing only a small amount of twisting between the rings, which is induced to reduce the steric interactions between H19 and H29. The calculated value *in vacuo* is shows a much larger twist, with a value of 33.874°. The calculated structure does not take into account packing effects in the crystal, or effects resulting from counteranions or solvate molecules and it is calculated *in vacuo* and thus the calculated dihedral angle is not consistent with the experimental dihedral angle from the

crystal structure. The remaining bond lengths and angles in the crystal structure are consistent with the calculated structure.

The crystal packing also exhibits extensive short F···H–C contacts between the hexafluorophosphate anions and the ligand molecules in the range of 2.5-3.3 Å, which further stabilizes the solid–state structure.

*3.6.3 Crystal structure of **3.8***

Slow diffusion of petroleum ether into an acetone solution of the complex gave dark red crystals of **3.8** suitable for X-ray crystallography. Complex **3.8** (Figure 3.8) crystallized in the monoclinic space group *C*2/c. The asymmetric unit contains one molecule of **3.8**, one disordered hexafluorophosphate anion and one acetone molecule.

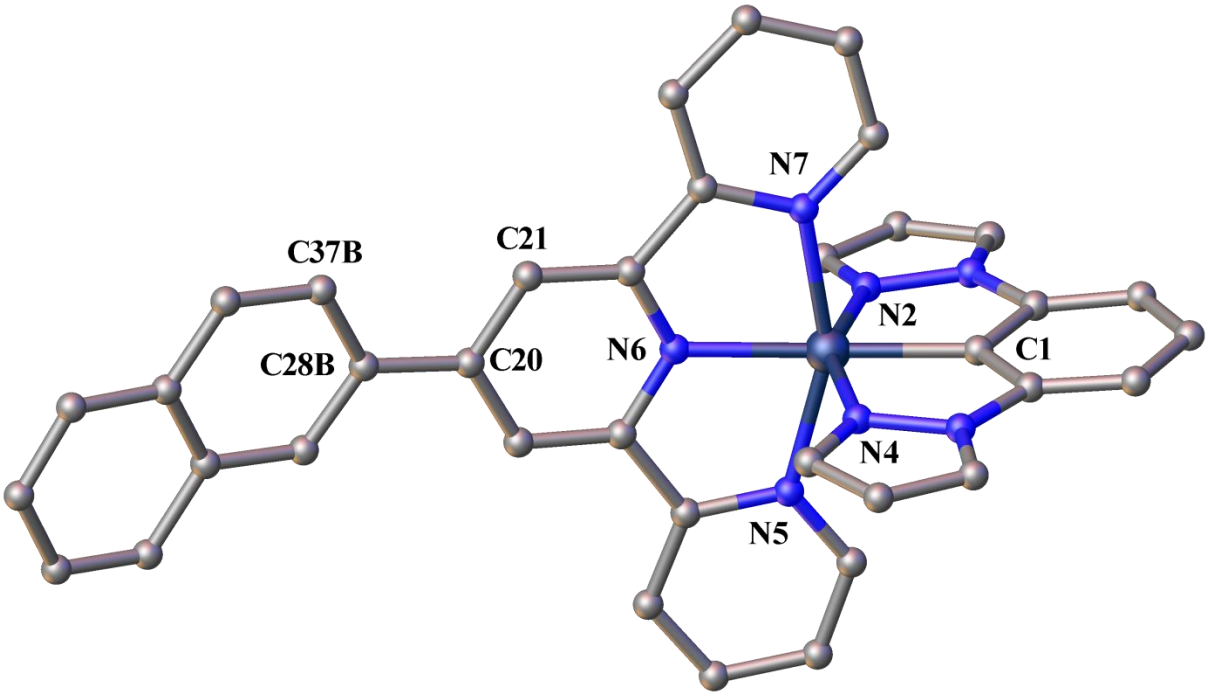

Figure 3.8: Crystal structure of complex **3.8**. Hydrogen atoms, counterions and the solvate molecules are omitted for clarity. Selected bond distances (Å): N2-Ru 2.083 (2), C-Ru 1.965 (2), N4-Ru 2.083(2), N5-Ru 2.081(2), N6-Ru 2.008(2), N7-Ru 2.062 (2). Selected bond angles (°): C-Ru-N5 104.9 (1), C-Ru-N6 173.5(1), C-Ru-N7 98.2(1), N2-Ru-N4 155.0(1), N5-Ru-N7 156.9(1). Selected dihedral angle (°): C21-C20-C28B-C37B 8.4(7).

The naphthalene ring was found to be disordered over two positions through rotation of the C20-C28 bond with part one having 2/3 occupancy and part two having 1/3 occupancy, with only part two shown for clarity in Figure 3.8. The ruthenium atom possesses the same distorted octahedral geometry as for the two previous crystal structures for **3.5** and **3.6**, with the substituted terpyridine ligand and cyclometalated ligand having chelate bite angles of 156.9(1)° and 155.0(1)°, respectively. The Ru-C bond length is 1.965(2) Å, which is equivalent to the comparable bond length in **3.5** and the opposite Ru-N6 bond length is 2.008(2) Å, which is shorter than in both **3.5** and **3.6**. The calculated structure of **3.8** does not show a large amount of variation compared to the other calculated structures and thus show the small difference between the solid state crystal and the *in vacuo* calculations.

The crystal packing also exhibits extensive short F···H–C contacts between the hexafluorophosphate anions and the ligand molecules in the range of 2.5-3.3 Å, which further stabilizes the solid–state structure.

3.7 Photophysical properties of ruthenium complexes.

*3.7.1 Complexes **3.1**-**3.4**.*

Complex	absorption 298 K, MeCN, λ_{max} (nm) ($\varepsilon(10^3\ M^{-1}\ cm^{-1})$)
2.1	536 (2.7), 487 (4.7), 375 (5.4), 318 (15.2), 259 (19.9), 234 (17.6)
3.1	530 (9.0), 493 (11.9), 361 (14.5), 317 (29.5), 285 (40.1), 260 (40.5)
3.2	530 (7.6), 494 (9.7), 356 (sh, 11.0), 316 (27.7), 279 (27.1), 259 (33.1), 211 (51.9)
3.3	531 (9.6), 493 (12.6), 357 (sh, 15.6), 315 (36.8), 282 (35.0), 260 (42.5), 234 (41.0)
3.4	537 (13.3), 502 (14.8), 393 (13.8), 321 (29.0), 279 (44.4), 260 (44.9), 241 (37.5)

Table 3.7: Electronic absorption data for group two complexes (**3.1**-**3.4**) and parent complex (**2.1**).

The UV-Vis spectra for complexes **3.1**-**3.4** are shown in Figure 3.9 and the corresponding calculated TD-DFT data is shown in Figure 3.10. The measured UV-vis spectrum for 3.1 shows that the lowest energy peak is at 493 nm (ε = 11,900), with a distinct shoulder around 530 nm and a very small shoulder around 607 nm. The UV-vis for complex **3.2** has a comparable profile, with its lowest energy peak at 494 nm (ε = 9,700) and a distinct shoulder around 530 nm and a minor shoulder around 608 nm. These two complexes are very similar, as expected, as the terpyridine ligands on each only differ very slightly (3,4,5-trimethylbenzene vs 4-^{t}butylbenzene). There is a significant difference however between these two complexes and **2.1**. Complexes **3.1**

and **3.2** have had their lowest energy peaks shifted towards longer wavelengths (bathochromic shift) and their extinction coefficients have been approximately doubled. Extending an aromatic system typically results in a bathochromic shift and greater absorbance (hyperchromic shift),[53] which is reflected in these results. Complex **3.3**, where 4-methoxyphenyl has been introduced into the central ring of the terpyridine ligand, shows a peak at 493 nm (ε = 12,600). The electron donating methoxy phenyl group causes no significant difference compared to the ^{t}Butyl phenyl group (**3.1**) or the trimethylphenyl group (**3.2**). On the other hand, introduction of an electron withdrawing group (EWG), such as 4-nitrobenzene (**3.4**) at the 4-position of the central pyridine on the terpyridine ligand results in a very significant shift. The lowest energy peak is at 502 nm (ε = 14,800). Both these peaks in **3.3** and **3.4** have the distinct shape previously described in which there is a distinct shoulder around 531 nm in **3.3** and around 545 nm in **3.4**.

The TD-DFT calculations *in vacuo* for each of these four complexes show four significant transitions (peaks) within the range of 400 nm to 700 nm except for **3.4** which has six. In each case, only one of these transitions has a large oscillator strength at 474.4 nm (**3.1**), 476.2 (**3.2**), 482.2 nm (**3.3**) and 480.9 nm (**3.4**) with the other transitions increasing the broadness of the profile and accounting for the shoulders. While the calculated peaks for **3.1** and **3.2** are very similar, the calculated peak in **3.3** in which the EDG has been incorporated has a bathochromic shift, while **3.4**, with the EWG, has a hypsochromic shift. The calculated shift in **3.4** reflects the experimental measurements however there is a negligible shift in **3.3**.

The predominant transition is calculated as being HOMO-2 → LUMO in the case of all four of these complexes. The isodensity plots (Figure 3.11) show that the HOMO-2 is very similar in all four complexes, in which the electron density is primarily located on the metal center with a small amount of electron density located on the central pyridine and the 4' substituted aryl ring. In complexes **3.1** and **3.2**, the electron density is spread over the aryl groups, but there is no contribution from either the ^{t}butyl group on **3.1** or the methyl group in **3.2** as they offer no π electrons to the system, thus they are very similar in energy. In **3.3** there is significant electron density on the methoxy group but there is no electron density on the nitro group in complex **3.4**. Isodensity plots (Figure 3.11) of the LUMO for the four complexes show that the electron density is now primarily on the terpyridine ligand, with a small amount remaining on the ruthenium atom. There is only a moderate contribution from the aryl ring on the terpyridine

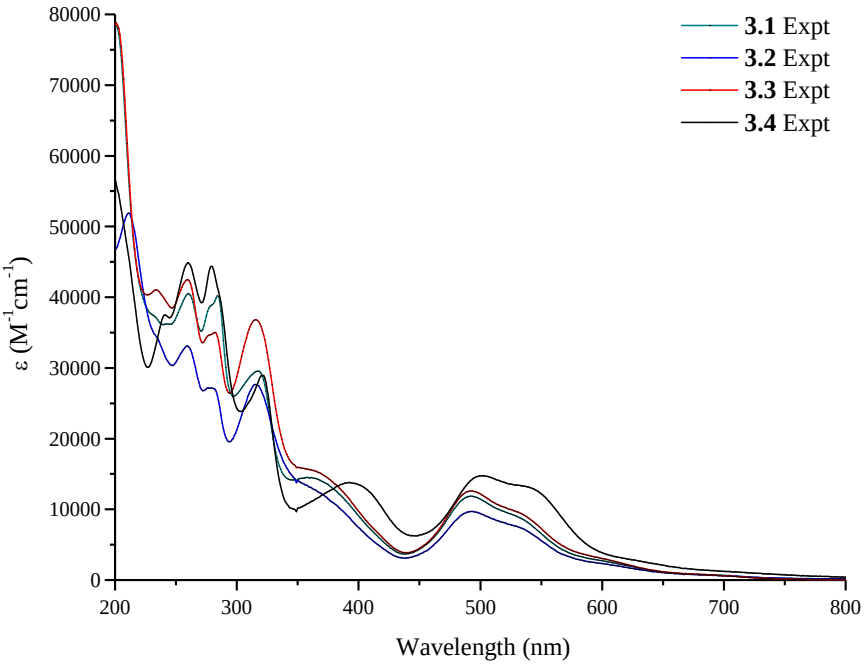

Figure 3.9: Electronic absorption spectra of complexes **3.1**-**3.4**.

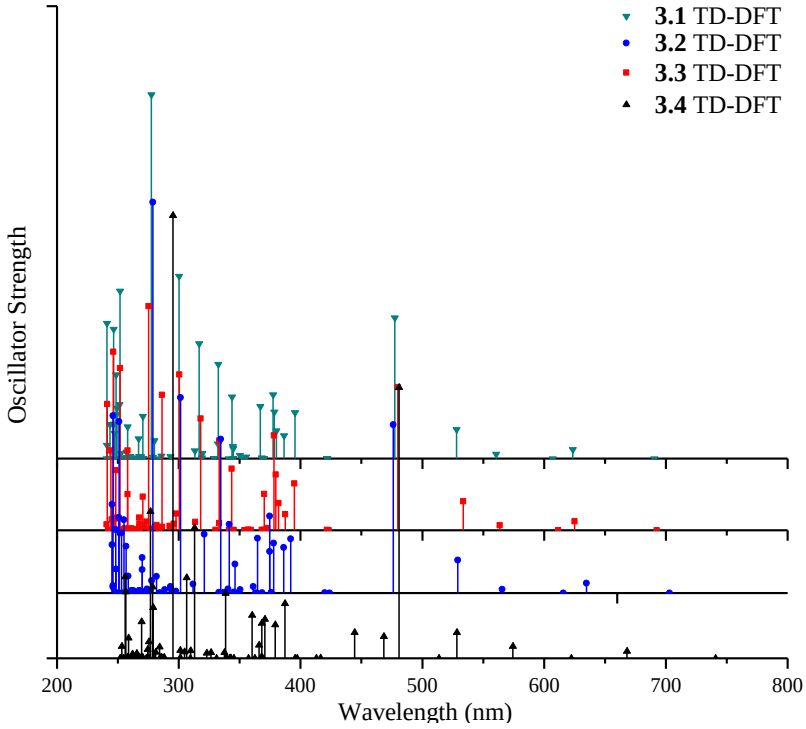

Figure 3.10: Calculated TD-DFT data for **3.1**-**3.4** *in vacuo*.

ligand in the case of **3.1**, **3.2** and **3.3**, while **3.4** shows significant electron density over the phenyl ring and nitro group due to inductive/resonance properties from the nitro group. There is no contribution from the ^{t}butyl groups on **3.1** or methyl groups on **3.2** once again. In the case of **3.3** there is a small amount of electron density on the methoxy group as well as the adjacent benzene ring.

Together this shows that **3.1** and **3.2** are not significantly different from one another as there is no contribution from the extra substituents on the benzene ring. In the case of **3.4**, there is a significant difference in the observed lowest energy peak due to the large contribution from the nitro group to the LUMO. The plot of orbital energies (Chapter 7.4, Figure 7.4.2) shows that the HOMO-2 is very similar in energy in complexes **3.1** and **3.4** however the energy of the LUMO is lower for **3.4** than in **3.1** resulting in a smaller energy gap overall and thus the observed red shift. In the case of **3.3** there appears to be an equal contribution from the methoxy in both the HOMO-2 and the LUMO resulting in an increase in the energy of both of these orbitals. However as there appears to be an approximately equal contribution in both, the result of this is that they effectively cancel the others change out, resulting in no change in the lowest energy peak in the observed UV-vis spectrum (compared to **3.1** and **3.2**). While all of these lowest energy peaks are defined as MLCT, they are different to **2.1** as the metal contribution mixes over the terpyridine ligand instead of the cyclometalating ligand.

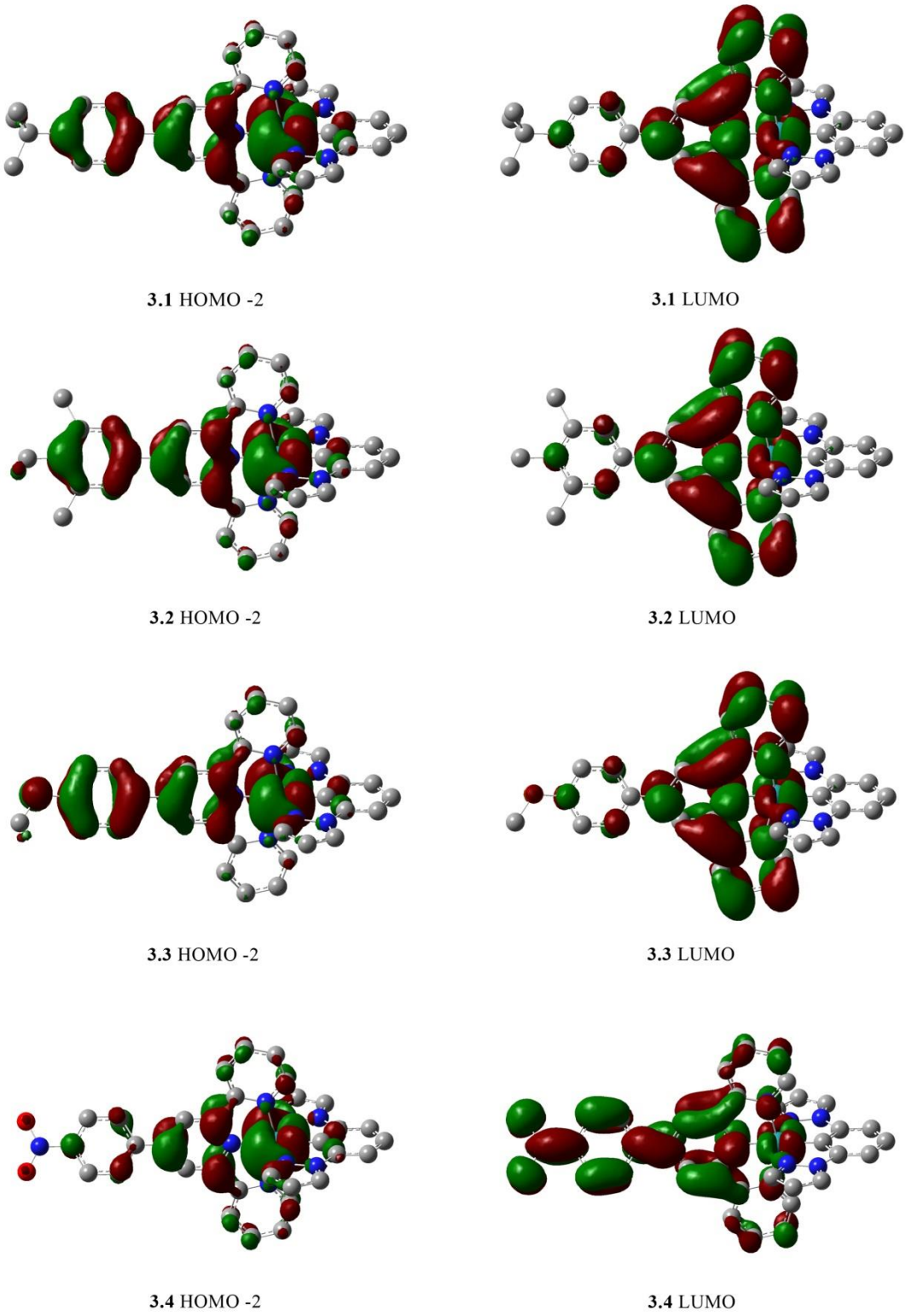

Figure 3.11: Isodensity plots (isovalue 0.02) of selected frontier orbitals that are involved in the dominant transition for the lowest energy MLCT for **3.1**-**3.4** from DFT calculation in vacuo.

S_n	E/nm	f	Dominant Transition			Percentage Contribution
3.1						
S1	690.5	0.000	HOMO	→	LUMO	98
S2	623.6	0.013	HOMO-1	→	LUMO	96
S4	560.5	0.007	HOMO-1	→	LUMO+1	64
S5	528.0	0.042	HOMO-2	→	LUMO+1	95
S6	477.4	0.200	HOMO-2	→	LUMO	54
3.2						
S1	703.2	0.000	HOMO	→	LUMO	98
S2	634.8	0.012	HOMO-1	→	LUMO	96
S4	565.7	0.005	HOMO-1	→	LUMO+1	68
S5	529.2	0.041	HOMO-2	→	LUMO+1	95
S6	476.2	0.207	HOMO-2	→	LUMO	58
3.3						
S1	689.3	0.000	HOMO	→	LUMO	98
S2	622.2	0.013	HOMO-1	→	LUMO	94
S4	563.0	0.011	HOMO-1	→	LUMO+1	61
S5	535.6	0.040	HOMO-2	→	LUMO+1	92
S6	482.2	0.222	HOMO-2	→	LUMO	53
3.4						
S1	740.7	0.000	HOMO	→	LUMO	78
S2	668.2	0.009	HOMO-1	→	LUMO	79
S4	574.3	0.015	HOMO-1	→	LUMO+1	66
S5	528.4	0.032	HOMO-2	→	LUMO+1	95
S7	480.9	0.332	HOMO-2	→	LUMO	59

Table 3.8: Selected calculated UV-vis transitions from TD-DFT calculations for **3.1**-**3.4** *in vacuo* over the range of 450nm to 800 nm (1st MLCT).

The 2nd lowest energy peak for complexes **3.1**-**3.4** occurs between 340 nm and 400 nm. In complex **3.1** there is a distinct single peak at 361 nm (ε = 14,500) whereas in **3.2** and **3.3** it appears as a broad shoulder, also around 361 nm. All three of these are blue shifted compared to **2.1** (375 nm). Complex **3.4** has a distinct peak at 393 nm (ε = 13,800), a considerable red shift compared to **2.1**. TD-DFT calculations run for each of these complexes *in vacuo* show six

similar transitions of similar energy, except **3.4** which has an additional two transitions at lower energy, as shown in Table 3.9. It is important to note that the energy of these main six transitions do not change very much relative to each other between complexes, however the calculated oscillator strength (intensity) of certain transitions is more dominant in some complexes leading to their blue/red shifts.

In **3.1** and **3.2** the dominant calculated transition is at 377.4 nm and 374.6 nm respectively, corresponding to HOMO-1 → LUMO+3. This same transition occurs in the TD-DFT for **2.1** at 372.9 nm, but the oscillator strength is significantly reduced. The same can be said about the majority of the transitions, where an increased aryl ring causes the expected red shift in the corresponding transitions, however it is the change in the dominant transition which causes the λ_{max} in the UV-vis and thus there is a shift in energy of this peak in these complexes. In **3.4**, the TD-DFT results show that the dominant transition is the lowest energy of the 6, at 387.2 nm, but there are also two smaller transitions at lower energy, 468.5 nm and 444.5 nm which affects the overall energy of the λ_{max} in the measured UV-vis, resulting in the observed red shift.

The transitions in **3.1**-**3.3** are present in **3.4** but once again the oscillator strength of these transitions is reduced. Due to the large number of transitions involved analysis of specific details of the isodensity plots (Chapter 7.3, Figures 7.3.13-7.3.16) is difficult, although they do show that all of the transitions in this range are different types of MLCT transitions. All of the occupied orbitals are predominately metal based, but also incorporate some terpyridine ligand, some cyclometalated ligand or have a mixture of both ligands. The unoccupied orbitals all show a majority of character from one ligand or the other only, without any contribution from the metal. This shows that despite the large number of calculated transitions, they are all different types of MLCT, and not LMCT or MC transitions, which can also occur in this wavelength range.[158]

S_n	E/nm	f	Dominant Transition			Percentage Contribution
3.1						
S9	395.4	0.066	HOMO	→	LUMO+4	84
S10	386.4	0.033	HOMO-1	→	LUMO+2	71
S11	380.3	0.039	HOMO-2	→	LUMO+2	94
S12	378.5	0.066	HOMO-2	→	LUMO+3	66
S13	377.4	0.091	HOMO-1	→	LUMO+3	63
S17	366.9	0.074	HOMO	→	LUMO+6	38
3.2						
S9	391.9	0.067	HOMO	→	LUMO+4	86
S10	386.2	0.056	HOMO-1	→	LUMO+2	83
S11	377.9	0.061	HOMO-2	→	LUMO+2	94
S13	374.7	0.051	HOMO-2	→	LUMO+3	73
S14	374.6	0.094	HOMO-1	→	LUMO+3	63
S16	364.6	0.067	HOMO	→	LUMO+6	38
3.3						
S9	395.8	0.066	HOMO	→	LUMO+4	85
S11	387.1	0.121	HOMO-3	→	LUMO	66
S12	385.8	0.024	HOMO-1	→	LUMO+2	39
S13	384.1	0.085	HOMO-2	→	LUMO+2	88
S14	381.0	0.077	HOMO-2	→	LUMO+3	51
S19	363.6	0.018	HOMO	→	LUMO+6	39
3.4						
S8	468.5	0.027	HOMO-1	→	LUMO+2	79
S9	444.5	0.0319	HOMO-2	→	LUMO+2	86
S14	387.2	0.067	HOMO	→	LUMO+5	87
S15	379.3	0.041	HOMO-1	→	LUMO+3	85
S16	370.6	0.048	HOMO-1	→	LUMO+4	61
S18	368.1	0.043	HOMO-2	→	LUMO+4	78
S20	366.0	0.016	HOMO-2	→	LUMO+3	85
S22	360.2	0.053	HOMO	→	LUMO+7	44

Table 3.9: Selected calculated UV-vis transitions from TD-DFT calculations for **3.1**-**3.4** *in vacuo* over the range of 350 nm to 470 nm (2nd MLCT).

*3.7.2 Complexes **3.5-3.7***

The UV-vis of these three complexes (Figure 3.13), **3.5**-**3.7** all follow the general trends of the previous results in which the lowest energy λ_{max} is at 494 nm (ε = 8,000) for **3.5**, 494 nm (ε = 13,000) for **3.6** and 490 nm (ε = 12,300) for **3.7**. The λ_{max} at 494 nm in both **3.5** and **3.6** is red shifted compared to **2.1** (487 nm, ε = 4,700). Despite **3.5** and **3.6** having a comparable λ_{max} there is a significant increase in the intensity of the absorbance for **3.6** due to the additional aryl group, which reflects the results of **3.1**-**3.4** earlier. In Complex **3.7** the lowest energy peak is red shifted compared to **2.2** (481 nm, ε = 5,800), but blue shifted compared to **3.6**. More information about what causes these effects can be obtained by examining TD-DFT calculations (Figure 3.14, Table 3.11). Calculations were run *in vacuo* and show that the lowest energy peak in each complex results primarily from a predicted large transition at 472.0 nm in **3.5**, 476.2 nm in **3.6** and 473.7 nm in **3.7**. These result from the dominant transition HOMO-2 → LUMO+1 in **3.5** and the dominant transition HOMO-2 → LUMO in **3.6** and **3.7**. In addition to these, there are three other predicted transitions in the range of the measured UV-vis peak which explains the broad nature of the profile.

Complex	absorption 298 K, MeCN, λ_{max} (nm) (ε(10^3 M^{-1} cm^{-1}))
2.1	536 (2.7), 487 (4.7), 375 (5.4), 318 (15.2), 259 (19.9), 234 (17.6)
3.5	545 (4.7), 494 (8.0), 371 (8.8) 317 (24.7), 275 (28.2), 258 (36.4), 239 (40.0)
3.6	530 (9.9), 494 (13.0), 364 (16.3), 319 (29.7), 285 (44.8), 278 (43.7), 260 (44.2), 233 (39.8)
3.7	525 (9.5), 490 (12.3), 359 (15.2), 317 (27.8), 285 (41.7), 277 (40.1), 266 (41.2), 226 (36.0)

Table 3.10: Electronic absorption data for group three complexes (**3.5**-**3.7**) and parent complex (**2.1**).

The HOMO-2 is involved in all of the main transitions for each complex and they are very similar in nature to each other. The electron density sits on the metal predominately in each, but also is spread over the terpyridine ligand, especially the central pyridine ring. Complex **3.5** also has electron density sitting on the chlorine atom and **3.6** and **3.7** have electron density spread over the attached benzene ring and bromine atom. All of them have a small amount of electron density on the peripheral pyrazole rings of the cyclometalating ligand but show no electron density over the rest of the cyclometalated ligand. Analysis of the isodensity plots for the LUMO+1 for **3.5** and the LUMO in **3.6** and **3.7** (Figure 3.12) show that the electron density is predominantly on the entire terpyridine ligand, with a small amount also on the ruthenium atom. Complex **3.5** also has electron density on the chlorine atom and **3.6** and **3.7** have electron density

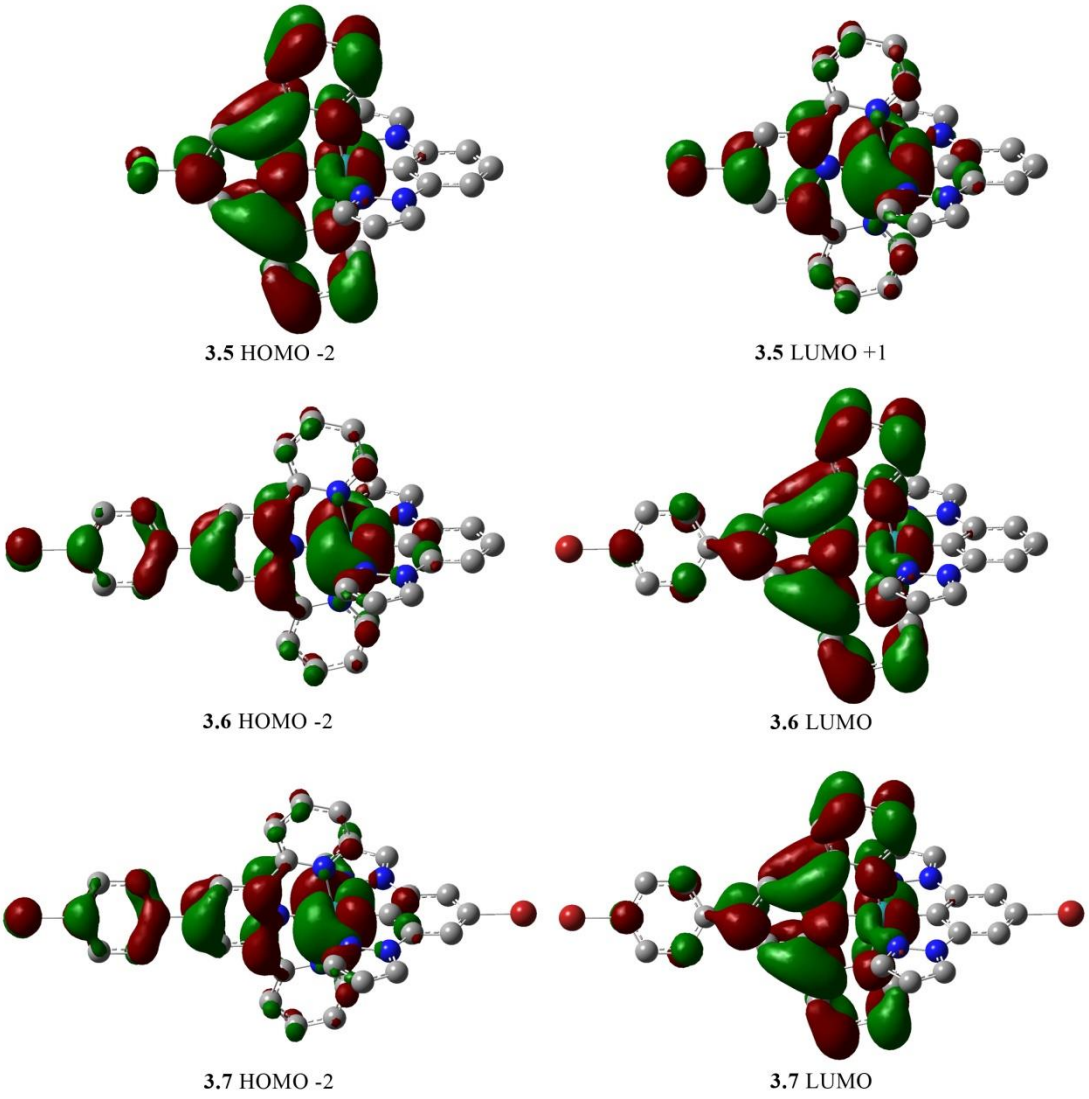

Figure 3.12: Calculated molecular orbitals involved in the transition leading to the MLCT for **3.5**, **3.6** and **3.7**.

on the aryl ring attached to the central pyridine ring on the terpyridine ligand, but no electron density on the bromine atom. The plot of orbital energies (Chapter 7.4, Figure 7.4.2) shows that the HOMO-2 in **3.5**, **3.6** and **3.7** all have quite different energies, however as the LUMO+1 (**3.5**) and LUMO (**3.6**/**3.7**) also have electron density in similar positions compared to the HOMO-2, the energy it offset by a similar amount leading to a comparable difference in energy in all three complexes. The results show the transition is MLCT, as was the case for complexes **3.5** and **3.6**

earlier, where the metal had mixed over the terpyridine ligand instead of the cyclometalating ligand in the HOMO-2.

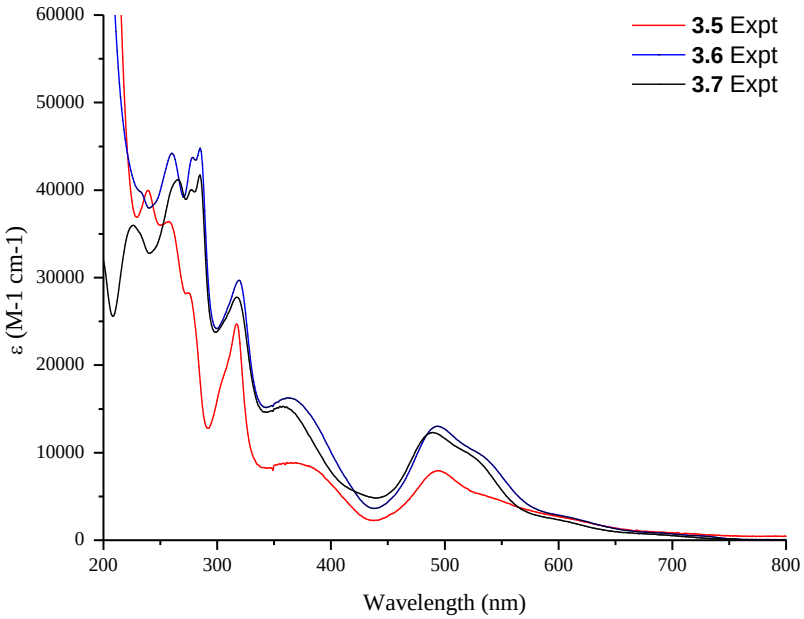

Figure 3.13: Electronic absorption spectra of complexes **3.5-3.7**.

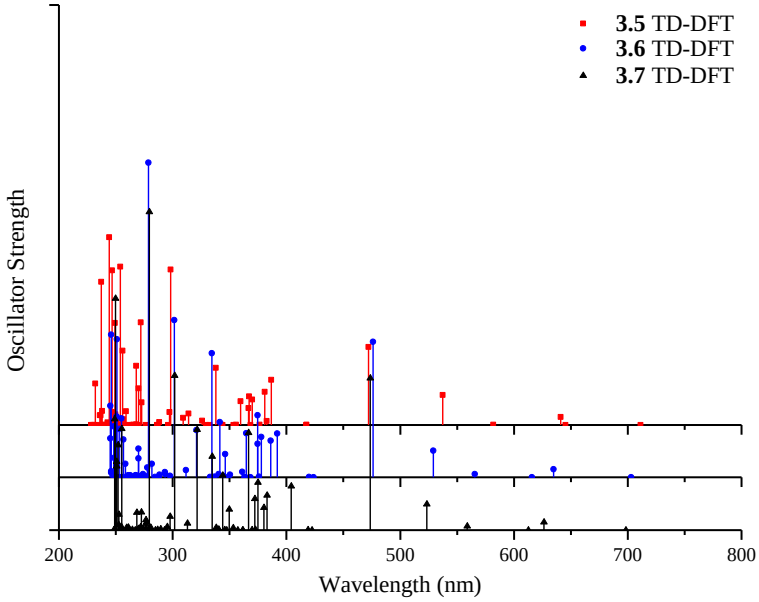

Figure 3.14: Calculated TD-DFT data for **3.5-3.7** *in vacuo*.

S_n	E/nm	f	Dominant Transition			Percentage Contribution
3.5						
S1	711.3	0.000	HOMO	→	LUMO+1	98
S2	645.3	0.000	HOMO	→	LUMO	98
S3	641.0	0.012	HOMO-1	→	LUMO+1	95
S5	537.4	0.046	HOMO-2	→	LUMO	95
S6	472.0	0.119	HOMO-2	→	LUMO+1	67
3.6						
S1	703.2	0.000	HOMO	→	LUMO	98
S2	634.8	0.012	HOMO-1	→	LUMO	96
S4	565.7	0.005	HOMO-1	→	LUMO+1	68
S5	529.2	0.041	HOMO-2	→	LUMO+1	95
S6	476.2	0.207	HOMO-2	→	LUMO	58
3.7						
S1	698.4	0.000	HOMO	→	LUMO	98
S2	626.3	0.012	HOMO-1	→	LUMO	96
S4	558.8	0.006	HOMO-1	→	LUMO+1	67
S5	523.3	0.040	HOMO-2	→	LUMO+1	95
S6	473.7	0.232	HOMO-2	→	LUMO	57

Table 3.11: Selected calculated UV-vis transitions from TD-DFT calculations for **3.5**-**3.7** *in vacuo* over the range of 450nm to 800 nm (1st MLCT).

The 2nd lowest energy peak for complexes **3.5**, **3.6** and **3.7** occurs at 371 nm (ε = 8,800), 364 nm (ε = 16,300) and 359 nm (ε = 15,200) respectively. Each modification results in a small blue shift compared to the parent complex (**2.1**, 375 nm) and also an increase in intensity for **2.7** and **2.8** with the additional aryl ring introduced. This series has similar aspects to the series presented earlier, in which there are six similar transitions involved and the TD-DFT calculations show that there is an evident red shift between comparable individual transitions, however once again the dominant transition changes throughout the series, resulting in the observed blue shift when comparing **3.5** to **3.6** and then **3.6** to **3.7**. Isodensity plots (Chapter 7.3, Figures 7.3.17-7.3.19) for all of these complexes show that the six transitions are all different types of MLCT transitions once again.

S_n	E/nm	f	Dominant Transition			Percentage Contribution
3.5						
S9	386.8	0.069	HOMO	→	LUMO+4	87
S11	380.8	0.050	HOMO-1	→	LUMO+2	78
S13	370.0	0.039	HOMO-1	→	LUMO+3	62
S15	367.3	0.044	HOMO-2	→	LUMO+3	79
S16	366.6	0.026	HOMO-2	→	LUMO+2	91
S17	359.8	0.036	HOMO	→	LUMO+5	44
3.6						
S9	391.9	0.067	HOMO	→	LUMO+4	86
S10	386.2	0.056	HOMO-1	→	LUMO+2	83
S11	377.9	0.061	HOMO-2	→	LUMO+2	94
S13	374.7	0.051	HOMO-2	→	LUMO+3	73
S14	374.6	0.094	HOMO-1	→	LUMO+3	63
S16	364.6	0.067	HOMO	→	LUMO+6	38
3.7						
S9	404.1	0.067	HOMO	→	LUMO+4	66
S10	382.9	0.053	HOMO-1	→	LUMO+2	83
S11	380.2	0.034	HOMO-1	→	LUMO+3	66
S12	374.8	0.073	HOMO-2	→	LUMO+2	95
S14	372.2	0.048	HOMO-2	→	LUMO+3	69
S16	366.6	0.149	HOMO	→	LUMO+6	32

Table 3.12: Selected calculated UV-vis transitions from TD-DFT calculations for **3.5**-**3.7** *in vacuo* over the range of 320 nm to 410 nm (2nd MLCT).

*3.7.3 Complexes **3.9**-**3.10***

Complex	absorption 298 K, MeCN, λ_{max} (nm) ($\varepsilon(10^3\ M^{-1}\ cm^{-1})$)
2.1	536 (2.7), 487 (4.7), 375 (5.4), 318 (15.2), 259 (19.9), 234 (17.6)
3.8	531 (10.1), 495 (13.0), 372 (sh, 16.0), 319 (31.7), 278 (45.9), 261 (48.1), 226 (63.2), 204 (67.6)
3.9	533 (6.7), 491 (10.4), 385 (16.9), 366 (16.2), 348 (12.4), 318 (28.7), 276 (33.3), 252 (110)
3.10	529 (10.1), 490 (16.2), 385 (28.9), 368 (26.7), 339 (36.7), 320 (45.7), 277 (76.7), 266 (64.8), 251 (114)

Table 3.13: Electronic absorption data for group four complexes (**3.8**-**3.10**) and parent complex (**2.1**).

The UV-vis spectra for complexes **3.8**-**3.10** and **2.1** are shown in Figure 3.15 and the calculated TD-DFT data is shown in Figure 3.16. The measured UV-vis spectrum for **3.8** shows that the lowest energy λ_{max} is at 495 nm (ε = 13,000) and it has distinct shoulder at around 531 nm. Complex **3.9** has a UV-vis with a similar profile where the lowest energy λ_{max} is at 491 nm (ε = 10,400) and also a distinct shoulder at around 533 nm. The lowest energy λ_{max} for **3.10** is at 490 nm (ε = 16,200) and has a shoulder at 529 nm. The λ_{max} in all three is similar, with a small blue shift upon introduction of an anthracene group instead of naphthalene, and another small shift upon introduction of the pyrene onto the cyclometalating ligand. Typically introduction of aryl rings of increasing size has the opposite effect (red shift) due to the increased size reducing the energy of the system, so it is likely that this shift, albeit small, occurs due to alternate factors.

The TD-DFT calculations *in vacuo* for these three complexes provide insight into which transitions are involved in forming the lowest energy λ_{max}, measured for these complexes and their broad profile. The results show that for **3.8** there are four predicted transitions with the range of the 450 nm to 700 nm, but for **3.9** and **3.10** there are six. In each case, only one of these transitions is of a large oscillator strength at 480.3 nm (**3.8**), 466.5 (**3.9**) and 469.3 (**3.10**) with the other transitions leading to the broadness of the peak envelope in each complex. These calculated transitions also predict a blue shift when going from the 2-naphthalene (**3.8**) to the 9-anthracene (**3.9**) as seen in the measured UV-vis spectra. The predominant transition is calculated as being HOMO-2 → LUMO for **3.8**, HOMO-3 → LUMO for **3.9** and HOMO-4 → LUMO for **3.10**.

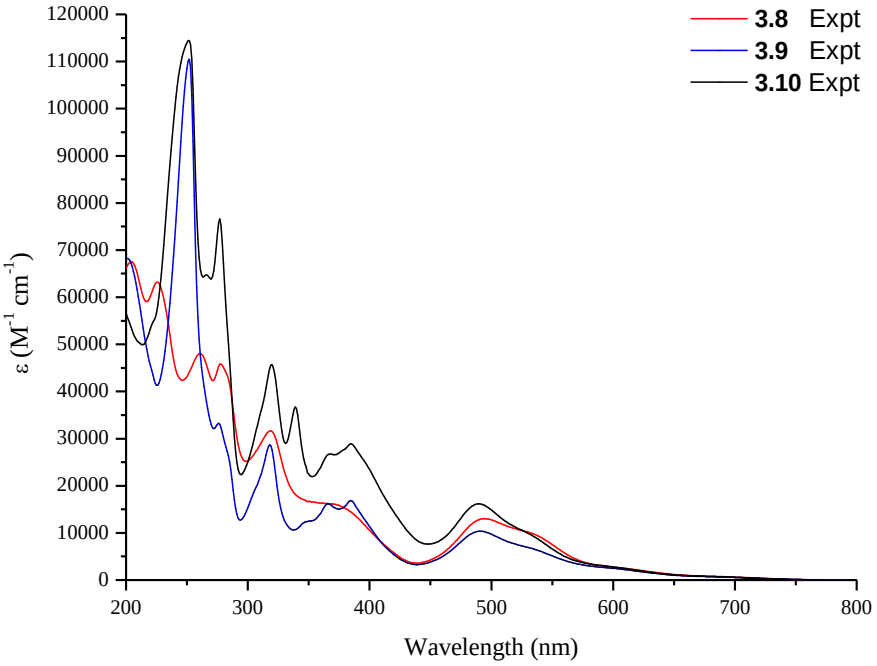

Figure 3.15: Electronic absorption spectra of complexes **3.8**-**3.10**.

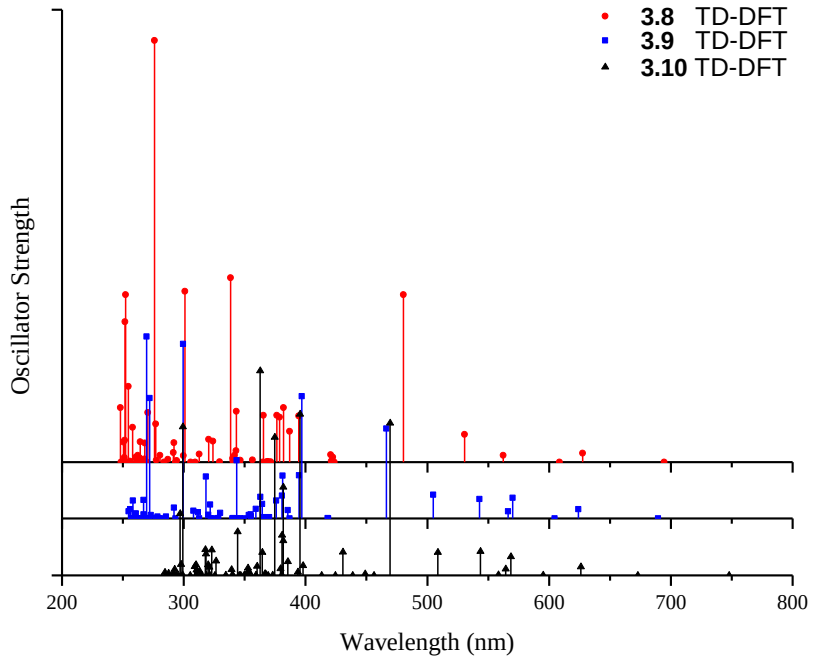

Figure 3.16: Calculated TD-DFT data for **3.8**-**3.10** *in vacuo*.

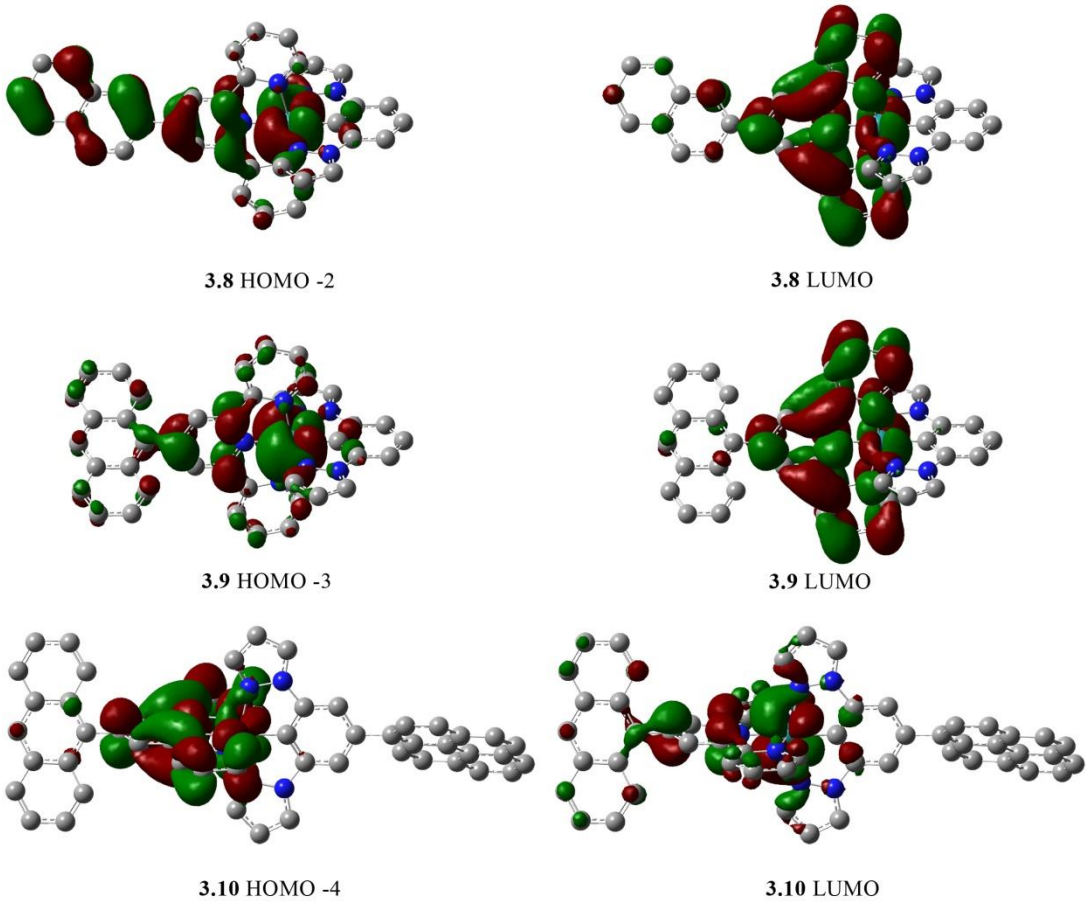

Figure 3.17: Isodensity plots of **3.8**, **3.9** and **3.10** for molecular orbitals involved in lowest energy MLCT peak.

The isodensity plots (Figure 3.17) for these complexes show that the relevant molecular orbitals involved in causing the lowest energy peak in the UV-vis are reasonably different. The HOMO-2 in **3.8** is primarily located on the ruthenium atom, but also extends over the central pyridine and 2-naphthalene. There is only a small amount of electron density on the peripheral pyridines and none on the cyclometalating ligand. The HOMO-3 in **3.9** is similar in that it is also largely metal based and extends in a similar fashion onto the central pyridine of the terpyridine ligand, however there is a very small amount on the anthracene and peripheral pyridine rings and a small amount on the cyclometalating ligand. The HOMO-4 on **3.10** also has the majority of electron density on the metal center, but also has a large amount on the peripheral pyrazole rings of the

cyclometalating ligand. Interestingly there is no electron density on the anthracene and only a small amount on the terpyridine ring. This is a consequence of the anthracene favoring a perpendicular conformation with respect to the terpyridine unit to minimize steric interactions, and thus there is only limited orbital overlap between the anthracene and terpyridine. The LUMO on **3.8**, **3.9** and **3.10** is very similar in all three complexes with electron density predominantly on the terpyridine ligand, with a small amount on the metal. In all three complexes there is a small amount of electron density on the naphthalene/anthracene.

The plots of orbital energies (Chapter 7.4, Figure 7.4.2) show that for the corresponding occupied orbitals for these three complexes (**3.8**, **3.9** and **3.10**) the energy of the HOMO-4 in **3.10** is the highest and at a comparable energy to **2.1**. The energy of the HOMO-3 is slightly lower than for **3.10** and the HOMO-2 for **3.8** is lower again. The electron density in the HOMO-2 of **3.8** is spread onto the naphthalene whereas the electron density in the corresponding occupied orbitals in **3.9** and **3.10** is not spread onto the anthracene, but instead the electron density is confined to a smaller area. The area to which electrons are confined is proportional to the energy that they have,[54] and thus the energy is lower in **3.8** compared to **3.9** and **3.10**.

This also follows for the HOMO-4 in **3.10** in which the electron density is spread only over the metal center and pyrazoles, resulting it in being higher in energy. The LUMO in **3.9** and **3.10** is essentially the same, and as a result they have very similar energies. The LUMO in **3.8** extends over the naphthalene once again resulting in it being lower in energy. This results in the energy gap of the HOMO-2 → LUMO transition being the smallest of the three and a small blue shift for the HOMO-3 → LUMO transition in **3.9** and another very small blue shift for the HOMO-4 → LUMO transition in **3.10** which is reflected in the experimental results with λ_{max} values of 495 nm, 491 nm and 490 nm values for **3.8**, **3.9** and **3.10** respectively.

S_n	E/nm	f	Dominant Transition			Percentage Contribution
3.8						
S1	694.6	0.000	HOMO	→	LUMO	98
S2	627.6	0.013	HOMO-1	→	LUMO	95
S4	562.4	0.010	HOMO-1	→	LUMO+1	62
S5	530.6	0.039	HOMO-2	→	LUMO+1	91
S6	480.3	0.237	HOMO-2	→	LUMO	55
3.9						
S1	689.6	0.000	HOMO-1	→	LUMO	97
S2	624.2	0.013	HOMO-2	→	LUMO	96
S4	570.0	0.029	HOMO	→	LUMO	64
S5	566.4	0.010	HOMO	→	LUMO+1	94
S6	542.8	0.027	HOMO-2	→	LUMO+1	47
S7	504.9	0.033	HOMO-3	→	LUMO+1	93
S8	466.5	0.127	HOMO-3	→	LUMO	62
3.10						
S1	747.9	0.000	HOMO	→	LUMO	61
S3	626.0	0.012	HOMO-3	→	LUMO	95
S5	568.6	0.027	HOMO-1	→	LUMO	53
S6	564.4	0.009	HOMO-1	→	LUMO+1	93
S8	543.7	0.034	HOMO-1	→	LUMO	44
S9	508.5	0.033	HOMO-4	→	LUMO+1	93
S10	469.3	0.216	HOMO-4	→	LUMO	62

Table 3.14: Selected calculated UV-vis transitions from TD-DFT calculations for **3.8**-**3.10** *in vacuo* over the range of 450 nm to 800 nm (1st MLCT).

The 2nd lowest energy transition for **3.8** is obscured by a neighboring intense peak at higher energy and thus occurs as a broad shoulder at around 372 nm (ε = 8,800). The TD-DFT calculations explain the broad nature as several of the six transitions occur at similar intensity. Of all the complexes in this chapter **3.8** is the closest to **2.1**, which results from **3.8** having large red shifts between comparable individual transitions (compared to **2.1**) as a result of the introduced aryl system, and so the measured UV-vis is not largely shifted when comparing the different dominant transitions in each (390.4 nm in **2.1** and 381.9 nm in **3.8**). Both complexes **3.9** and **3.10**

follow the same trends as previous complexes, but there is increased complexity owing to anthracene and its corresponding $\pi \rightarrow \pi^*$ transitions being at a wavelength that overlaps with the MLCT transitions. Experimental UV-vis measurements show peaks at 385 nm (ε = 16,900), 366 nm (ε = 16,200) and 348 nm (ε = 12,400) for **3.9** and 385 nm (ε = 28,900), 368 nm (ε = 26,700) and 339 nm (ε = 36,700) for **3.10**.

S_n	E/nm	f	Dominant Transition			Percentage Contribution
3.8						
S11	394.5	0.065	HOMO	→	LUMO+4	85
S12	387.0	0.044	HOMO-1	→	LUMO+2	74
S13	381.9	0.077	HOMO-2	→	LUMO+2	87
S14	378.6	0.063	HOMO-2	→	LUMO+3	65
S15	376.5	0.066	HOMO-1	→	LUMO+3	59
S19	365.5	0.066	HOMO	→	LUMO+6	40
3.9						
S11	397.0	0.173	HOMO	→	LUMO+2	84
S12	394.6	0.061	HOMO-1	→	LUMO+5	82
S15	381.2	0.061	HOMO	→	LUMO+3	37
S16	380.7	0.032	HOMO	→	LUMO+4	73
S17	375.8	0.025	HOMO-2	→	LUMO+3	55
S23	362.8	0.030	HOMO-3	→	LUMO+2	34
3.10						
S18	395.3	0.228	HOMO-1	→	LUMO+2	77
S21	381.7	0.125	HOMO	→	LUMO+7	22
S26	374.7	0.195	HOMO-3	→	LUMO+4	64
S32	362.8	0.290	HOMO	→	LUMO+7	42

Table 3.15: Selected calculated UV-vis transitions from TD-DFT calculations for **3.8**-**3.10** *in vacuo* over the range of 300 nm to 435 nm (2nd MLCT).

These complexes when compared to **2.1** show the impact of increased aromatic systems being introduced into the complex, as was the case when comparing their lowest energy peak. TD-DFT calculations for **3.9** show six relevant transitions, although these are not comparable with the typical six transitions that were observed for previous complexes, as four of these are largely

associated with just the anthracene unit. The TD-DFT calculations also show that for **3.10** there are only four transitions within the range of the experimental peaks, of which two are anthracene based transitions. This shows that the peaks at 385 nm and 366/368 nm can be assigned as being $\pi \rightarrow \pi^*$ anthracene based transitions. Analysis of the isodensity plots (Chapter 7.3, Figures 7.3.20-7.3.22) for the remaining transitions shows that they are MLCT based, although the intensity of the anthracene masks them in the experimental UV-vis. Complex **3.10** has an additional peak at 339 nm (ε = 36,700) most likely resulting from a $\pi \rightarrow \pi^*$ transition on the pyrene.

3.8 Emission Studies.

Emission studies were carried out in degassed acetonitrile at ambient temperature and in butyronitrile at 77 K using a continuous flow cryostat from oxford instruments limited. At room temperature none of these complexes (**3.1**-**3.10**) showed distinct emission spectra using the spectrofluorimeter at hand, and thus 77 K emission studies were carried out. Emission spectroscopy at low temperature provides greater emission intensity in cases where the dominant non-radiative channels are thermally activated.[159]

Complex	77K Emission λ_{max} (nm) ($\tilde{\nu}$, cm^{-1})	Stokes Shift ($\tilde{\nu}$, cm^{-1})	Quantum Yield
2.1	712 (14,040)	6,490	0.16
3.1	718 (13,930)	6,400	0.09
3.2	717 (13,950)	6,420	0.31
3.3	715 (13,990)	6,210	0.20
3.4	753 (13,280)	6,600	0.13
3.5	728 (13,740)	6,380	0.15
3.6	727 (13,760)	6,400	0.04
3.7	712 (14,050)	6,320	0.22
3.8	724 (13,810)	6,390	0.19
3.9	715 (13,990)	6,420	0.10
3.10	720 (13,890)	6,520	0.16

Table 3.16: Luminescence data for complexes **3.1**-**3.10** and parent complex **2.1**. Measurements were carried out in ca. 10^{-6} M butyronitrile and quantum yields were calculated using $[Ru(bpy)_3](Cl)_2$ in MeOH/EtOH (1:4, Φ_{PL} = 0.38).[15]

All of the complexes in this series (**3.1**-**3.10**) are emissive at 77 K and show emission profiles with a single peak that are of a similar shape to previously reported spectra for cyclometalated

ruthenium complexes.[28] As the measurements are recorded at low temperature the transition is assigned as being an intense 0-0 transition.[160] The luminescence spectra recorded for complexes **3.1**-**3.10** is shown in Figure 3.18 and Figure 3.19 and spectral data is shown in Table 3.16. There is a distinct λ_{max} for each complex, ranging from 712 nm to 753 nm, which gives a Stokes shift between 6,200 cm^{-1} and 6,600 cm^{-1} for each complex.

The emission profiles are significantly red shifted compared to $[Ru(tpy)_2]PF_6$, which shows an emission band at 602 nm at 77 K upon excitation at 475 nm and shows a Stokes shift of 4,400 cm^{-1}.[37] The emission profiles are also red shifted compared to $[Ru(bpy)_3](Cl)_2$, which has an emission band peak at 580 nm and a shoulder at around 630 nm when measured at 77 K and excited at 450 nm. This shows that there is a Stokes shift of 5,000 cm^{-1} for $[Ru(bpy)_3](Cl)_2$. The large Stokes shift for these complexes is a result of the strong HOMO destabilization due to the cyclometalation. The functionalization of the 4' position of the terpyridine has a similar effect on the wavelength of the emission as it did for the absorption, with the Stokes shift remaining relatively unchanged for each complex. The emission for complex **3.4** is the most red shifted in this series at 753 nm and all of the emission profiles are red shifted compared to **2.1** except **3.7** which has an equivalent value. These shifts generally reflect the shifts observed for the lowest energy MLCT for the corresponding absorbance spectra.

Generally room temperature emission is red shifted compared to low temperature emission studies, because the rigid solvent matrix at low temperatures prevents solvent reorganization and thus avoids the stabilization of the more polar charge-separated excited state.[161] It is thus possible that these complexes are slightly luminescent at room temperature but at levels below the detection limit of our experimental setup. As these complexes, if emissive, would be expected to produce emission at energy lower than ca. 720 nm it would be difficult to observe. An important reason is that the spectral resolution decreases at higher wavelengths due to decreasing spectrometer sensitivity resulting in lower than expected emission intensity. Another reason for no room temperature emission is that the peak occurs above the detection limit of the machine at approximately 800 nm. The most likely situation however is that the complexes are virtually non-emissive, shown by their very low quantum yields, resulting in only a small amount of emission to detect. This would ideally be corrected by using more concentrated samples

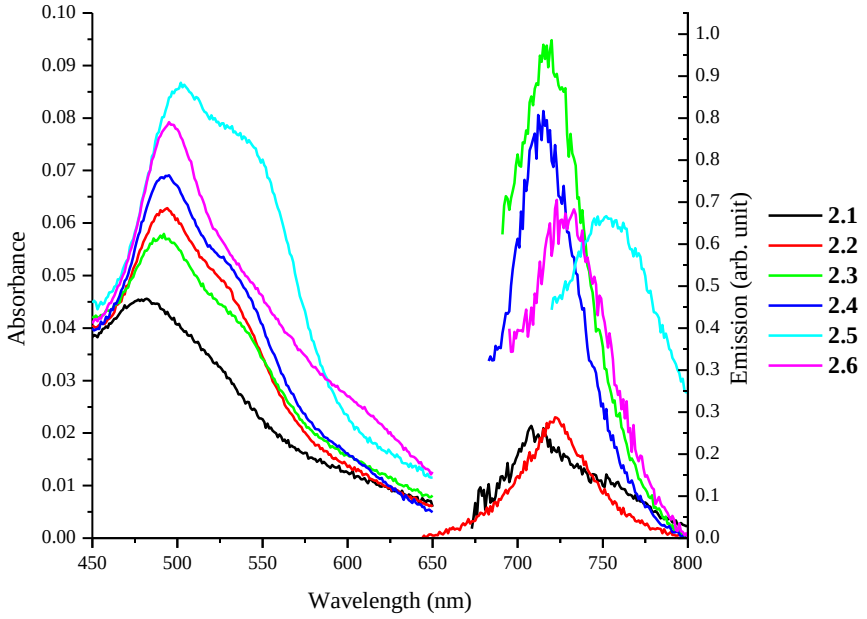

Figure 3.18: UV-vis spectra for **3.1-3.5** and **2.1** in butyronitrile at ca.10^{-6} M at ambient temperature and corresponding emission spectra in butyronitrile at ca.10^{-6} M at 77 K.

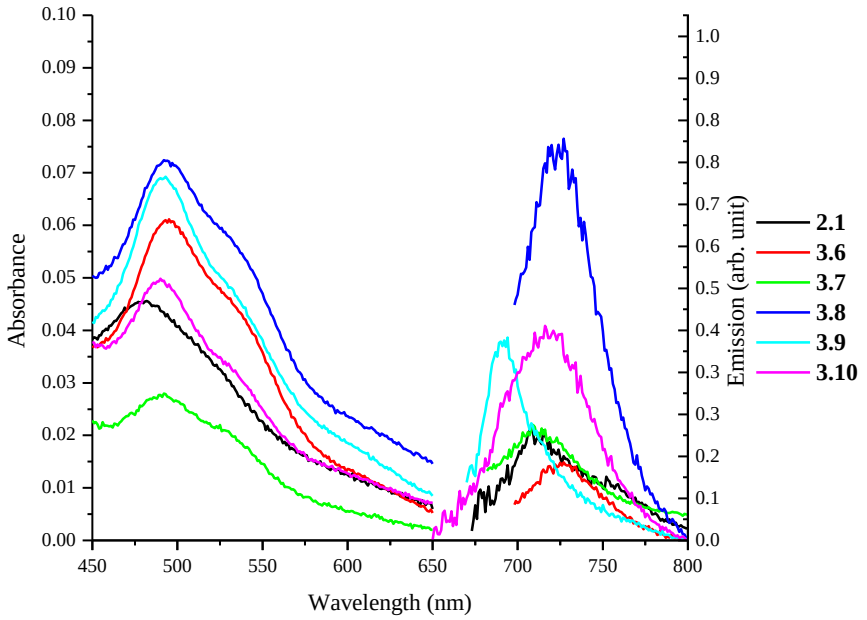

Figure 3.19: UV-vis spectra for **2.1** and **3.6**-**3.10** in butyronitrile at ca.10^{-6} M at ambient temperature and corresponding emission spectra in butyronitrile at ca.10^{-6} M at 77 K.

however luminescent samples need to be less than ca. 0.1 Abs due to problematic concentration effects. To gain insight about the nature of the relevant excited states and whether they should be expected to be emissive at room temperature ΔSCF-DFT calculations can be performed, however they are not included in this work. These calculations have been previous used by Schulze et al. to calculate emission energies by calculating the energy difference between the first triplet excited states and the closed-shell ground state, using previously optimized geometries.[28]

The key argument against room temperature emission is that the ^{3}MC state is both thermally assessable to the ^{3}MLCT and has strong coupling to the ground state, which results in rapid relaxation of the ^{3}MC state once populated. While there is no direct spectroscopic evidence to support this, it is widely considered to be the cause of reduced emission. This is supported however by theoretical calculations, which have shown that the ^{3}MC and ^{3}MLCT states are similar in energy, and low temperature luminescence studies which show that there are longer lifetimes and higher quantum yields at 77 K as the ^{3}MC state is no longer thermally accessible. The reason the ^{3}MC state is deactivating is that in the ^{3}MC state antibonding orbitals are occupied and this matches the ground state geometry when there are high energy vibrations.

The quantum yields for complexes **3.1**-**3.10** were found to be between 4% and 31%, using $[Ru(bpy)_3](Cl)_2$ in MeOH/EtOH (1:4, Φ_{PL} = 0.38) at 77 K as a standard.[15] The quantum yield for $[Ru(bpy)_3](Cl)_2$ is relatively high, at 38%, at 77 K[15], but it drops to ca. 4% at room temperature[162] showing the effect of the ^{3}MC state being thermally accessible. The quantum yields were calculated using Equation 2.1 (Section 2.8) and are relative to $[Ru(bpy)_3](Cl)_2$.[162-163]

The relative quantum yield calculation method provides insight into the quantum yield for new compounds, however there are large errors associated with the method, mostly as a result of poor integration and/or a poor baseline, with typical errors believed to be up to 30%.[165] Errors can be minimized by running multiple measurements at different concentrations, however this was not practical at 77 K using the experimental setup at hand due to large amount of time required to run a single sample. While the relative error associated with each quantum yield is potentially very high, it is largely a systematic error and the observed trends within a particular series of results are reproducible.[165]

Another important excited state parameter is the lifetime which reflects the stability of the excited state. While emission lifetimes were not able to be measured in this work, it is understood that as the emission energy decreases, the lifetime will also decrease in accordance with the energy gap law.[62-64] The energy gap law shows that as the energy gap is decreased and emission is red shifted, non-radiative decay processes increase which results in shorter emission lifetimes. This has large implications for cyclometalated ruthenium complexes, which show shorter lifetimes compared to their corresponding non-cyclometalated analogues because they have a small band gap.[37, 39] This observation also applies to smaller changes in energy, resulting from modifications to the terpyridine ligand, such as in complexes **3.1**-**3.10**. While it has not been measured, it is likely that the lifetime of **3.4** will be the smallest as its emission is the most red shifted. While measuring the lifetime of an excited state is important to gaining further understanding about what factors influence the emission lifetime and thus how to modify the complex so they are luminescent at room temperature, it is less important for these complexes as they are not luminescent at room temperature. An example of luminescence lifetimes not being largely important is their use in dye-sensitized solar cells. Their short lifetimes are less important because the complex is immobilized and there is fast electron injection into the semiconductor, meaning other properties of using cyclometalated ruthenium complexes can be utilized without the short lifetimes being a problem.

3.9 Electrochemical Studies.

The electrochemical properties of **3.1**-**3.10** were examined by cyclic voltammetry, using degassed acetonitrile solutions containing 0.1 M Bu_4NPF_6 and were compared with the values for **2.1**. Measured redox couples for the modified terpyridine series of ruthenium complexes are reported in Table 20. All complexes exhibit a chemically reversible redox couple for both oxidation and reduction. Ruthenium(II) polypyridine complexes have a predominately metal based HOMO and a ligand based LUMO which leads to oxidation being associated with the metal center, while reduction occurs on the ligand, which is supported by the previously discussed TD-DFT calculations for these complexes.

Complex	$E_{1/2}$ anodic[a]	$E_{1/2}$ cathodic[a]	ΔE[c]
$[Ru(tpy)_2](PF_6)$[37]	0.89 (64)	-1.66 (63), -1.90 (63)	2.55
$[Ru(dpyb)(tpy)]PF_6$[37]	0.12 (62), 1.36[b]	-1.95 (63)	2.07
2.1	0.11 (116), 1.05[b]	-1.96 (121)	2.07
3.1	0.10 (73), 1.23 [b]	-1.97 (100)	2.07
3.2	0.11 (76), 1.05 [b], 1.20 [b]	-1.96 (117)	2.07
3.3	0.10 (77), 1.24 [b]	-1.98 (98), 2.33[b]	2.08
3.4	0.14 (62)1.26 [b]	-1.38 (80), -2.11[b]	1.52
3.6	0.12 (67), 1.07 [b]	-1.95 (98), -2.15 (113)	2.07
3.7	0.18 (79), 1.26 (131)	-1.89 (140), -2.13 (122)	2.07
3.8	0.10 (68), 1.26 [b]	-1.96 (85), -2.29[b]	2.06
3.9	0.14 (68), 1.12 [b]	-1.92 (72), -2.12 (145)	2.06
3.10	0.11 (68), 0.83 (76), 0.99 (84), 1.40 (104)	-1.93 (76), -2.11 (127)	2.04

Table 20: Electrochemical data for complexes **3.1-3.10** and **2.1** and relevant literature complexes. (a) The potential is reported as the $E_{1/2}$ value vs Fc/Fc^+. (b) Ep, irreversible. (c) Energy difference between first reversible oxidation and reduction. Complex **3.5** had irreproducible results and thus does not appear in this analysis.

The first oxidation process for each of the complexes **3.1-3.10** is quasi-reversible under cyclic voltammetry conditions and is assigned as being a $Ru^{2+/3+}$ redox couple. For complex **2.1**, the $E_{1/2}$ is at 0.11 V (versus Fc) for the $Ru^{2+/3+}$ couple, which is comparable to $[Ru(dpyb)(tpy)]PF_6$ which has an $E_{1/2}$ of 0.12 V[37]. Complex **2.1** shows a cathodic shift of 780 mV compared to $[Ru(tpy)_2](PF_6)_2$ for the metal-based oxidation showing the effect of cyclometalation, in which the ruthenium atom becomes more electron rich due to the anionic carbon donating electron density onto the metal. It is also typical for these cyclometalated complexes to show an irreversible oxidation at a higher positive potential along the anodic scan. Complex **2.1** shows this peak at 1.05 V (versus to Fc), a relatively large anodic shift compared to $[Ru(dpyb)(tpy)]PF_6$ (1.36 V) and this potential is reported to be due to a $Ru^{III/IV}$ process or ligand based decomposition.[29]

On the cathodic scan for **2.1** there is a single quasi-reversible redox process at -1.96 V under cyclic voltammetry conditions, which is assigned as being reduction of the terpyridine ligand. The value of this process in **2.1** is comparable to $[Ru(dpyb)(tpy)](PF_6)_2$ (-0.95 V), as this reduction process only occurs on the unmodified terpyridine ligand. Another consequence of cyclometalation however, is that there is greater back donation onto the ligand from the electron

rich metal, resulting in the terpyridine based reduction occurring at a more negative potential compared to the non-cyclometalated $[Ru(tpy)_2](PF_6)_2$ (-1.66 V).

Modifications to the cyclometalated ligand typically lead to changes in the HOMO and changes to the terpyridine ligand generally lead to changes in the LUMO. This is shown by the TD-DFT isodensity plots of **2.1** in which the HOMO and HOMO-1 are both largely metal based with contribution from the cyclometalated ligand, whereas the LUMO is almost entirely terpyridine based. This meant that while the oxidation potentials were not expected to very greatly for this series, the reduction potentials for the complexes would be likely to show greater variability. This has been shown to be partially true, although not for the predicted reasons. In this series of complexes introducing the aryl group on the terpyridine ligand appears to cause the contribution in the occupied orbitals to result from the substituted terpyridine ligand rather than the substituted cyclometalated ligand. This causes the relevant occupied orbital and the LUMO to have similar characteristics, resulting in a change in one also occurring in the other and thus a comparable ΔE.

Analysis of the complexes in this series, **3.1**-**3.10**, shows only subtle changes to the quasi-reversible oxidation potential, which ranges from 0.10 V-0.12 V for all complexes except for **3.4** (0.14 V), **3.9** (0.14 V) and **3.7** (0.18 V). The p-nitrophenyl substituted terpyridine in **3.4** has an impact on the oxidation potential as the electron withdrawing nitro group results in the ruthenium atom being less electron rich (compared to **2.1**) and thus a slightly higher potential is observed. The large aromatic ring of anthracene, which is substituted onto the terpyridine in **3.9** results in an increase in the oxidation potential compared to **2.1** (0.11 V). Complex **3.7** has a value of 0.18 V, due to the introduction of two electron withdrawing bromine atoms onto both ends of the structure. The value for **3.6** (0.12 V) in which only the terpyridine ligand is substituted with a bromine atom shows that the cyclometalated ligand substitution has a greater effect on the anodic potential rather than the terpyridine ligand due to the σ-donating anionic carbon on the cyclometalated ligand. Complex **3.5**, in which the terpyridine was substituted with a 4-Cl in place of the hydrogen did not give reproducible results using cyclic voltammetry methods and is therefore not included in this discussion.

Analysis of the cathodic potential shows similar results, in which the potential is observed to shift to a similar extend to the anodic potential, resulting in the ΔE for the majority of these

complexes to be very similar. The quasi-reversible reduction for **3.4** shows a considerable shift however with a value of -1.38 V. The electron withdrawing nature of the nitro group on the substituted terpyridine causes its potential to be more positive (compared to **2.1**) because the nitro group makes the terpyridine ligand easier to reduce. The ΔE value for this complex is thus 1.52 V, a significantly smaller energy gap than the other complexes in this series, reflecting the UV-vis results in which the lowest energy MLCT for **3.4** was red shifted compared to the other complexes in this series. Complexes **3.1**-**3.10** (excluding **3.4**) all have a cathodic potential with an approximately equivalent change in voltage to the anodic potential, although once again there are only subtle differences in these values compared to **2.1**.

3.10 Summary.

The synthesis of ten new cyclometalated ruthenium complexes, which incorporate 4' substituted terpyridine ligands and 1,3-di(pyrazol-1-yl)benzene have been investigated. Their electrochemical and spectroscopic properties have been studied to analyze the effect of introducing electron withdrawing groups, electron donating groups or large aromatic rings onto the 4' position of terpyridine. To gain further understanding about the structure of these complexes DFT calculations were used to calculate optimized structures. From these preliminary calculations, TD-DFT calculations were used to gain a more thorough understanding of the photophysical and electrochemical properties to provide further insight into the structure-property relations of these complexes.

All of the complexes were analyzed using NMR spectroscopy and their ^{1}H and ^{13}C spectra were fully assigned. Analysis of their coordination induced shifts showed significant changes occurred upon coordination, however the changes for **3.1**-**3.10** were all very similar compared to the changes in **2.1**. This showed that substitution at the 4' position on the terpyridine ligand had minimal impact on the structure of the inner sphere surrounding the ruthenium atom in these complexes. The results from the DFT calculations supported this observation as the key bond lengths and angles did not change significantly throughout complexes **3.1**-**3.10**. This was also supported by the crystal structures of **3.5**, **3.6** and **3.8** which showed similar bond lengths and angles compared to their corresponding calculated structures.

Analysis of the photophysical properties of complexes **3.1**-**3.10** showed that substitution at the 4' position on the terpyridine ligand had an effect on the energy of the lowest energy MLCT. All

complexes were red shifted compared to **2.1** as the increased size of the conjugated system resulted in a lower energy transition. TD-DFT calculations showed that the LUMO was always involved in the lowest energy MLCT and generally incorporated just the terpyridine ligand. The relevant occupied orbital involved in the lowest energy MLCT varied depending on the specific electronic nature of the complex (HOMO-1, HOMO-2, HOMO-3 or HOMO-4), but in most cases the electron density was predominantly on the metal, with a small amount on the central pyridine on the terpyridine ligand.

In complexes with an additional aryl group, the relevant occupied orbital also showed electron density on the aryl ring if the dihedral angle between the rings allowed orbital overlap. The phenyl groups in **3.1**-**3.4**, **3.6** and **3.7** were calculated to have a twist of ca. 30° *in vacuo* and the crystal structure of **3.6** showed a small dihedral angle of 9.5(12)°, which supports the observation of electron density spreading onto the phenyl ring due to favorable overlap of the orbitals. This resulted in the small red shift for these complexes (493 nm to 495 nm) compared to **2.1** (487 nm), with **3.4** (502 nm) having an especially large red shift due to the electron withdrawing nitro group.

The larger aromatic groups, 2-naphthyl and 9-anthracenyl, which were substituted at the 4' position of the terpyridine ligand inherently had more steric hindrance than the phenyl rings and so they had the potential to twist further to minimize these interactions. The dihedral angle between the terpyridine and the naphthalene was calculated at 33.3° *in vacuo* for **3.8** and the comparable angle in the crystal structure was 8.4(7)°. This enabled orbital overlap in the HOMO-2 onto the naphthalene and thus the energy of the lowest energy MLCT was red shifted compared to **2.1**. The anthracene substituted at the 4' position of the central pyridine on the terpyridine ligand in **3.9** and **3.10** had a dihedral angle of ca. 70°, which only allowed a limited amount of orbital overlap between the anthracene and the terpyridine ligand and thus the electron density in the relevant occupied orbital was not spread the large ring system. This resulted in a blue shift for **3.9** (491 nm) compared to **3.8** (495 nm) and a further blue shift in **3.10** (490 nm).

The potential emission of all of these complexes was measured at room temperature in degassed acetonitrile but did not show distinct peaks. At 77 K all complexes were emissive with excitation of the lowest energy MLCT producing broad emission profiles between 712 nm and 753 nm. Following the absorption properties for **3.1**-**3.10**, complex **3.4** (753 nm) was the most red shifted

compared to **2.1** (712 nm), with of the complexes having similar Stokes shifts between 6,200 cm^{-1} and 6,600 cm^{-1}. These Stokes shifts are all larger than for $[Ru(tpy)_2](PF_6)_2$ and $[Ru(bpy)_3](PF_6)_2$, which have values of 4,400 cm^{-1} and 5,000 cm^{-1} respectively. The quantum yields of complexes **3.1**-**3.10** were measured at 77 K and varied between 0.09 and 0.31. These results cannot be directly related to $[Ru(dpyb)(tpy)]PF_6$,[37] as its emission spectrum has not been measured at 77 K, however at room temperature it has been shown to produce emission at 781 nm (12,800 cm^{-1}) with a very low quantum yield of 9.4×10^{-6}.

The electrochemical properties of **3.1**-**3.10** were also examined by cyclic voltammetry. All complexes exhibit a chemically reversible redox couple for both oxidation and reduction, with the oxidation occurring on the metal center and reduction occurring on the terpyridine ligand. This was supported by the TD-DFT calculations which showed that the HOMO was associated with the metal center and the LUMO was associated with the terpyridine ligand and not the cyclometalated ligand. The electrochemical results showed that while the energy of the HOMO and LUMO did change throughout the measurements, the difference in energy between the two molecular orbitals (ΔE) did not change for most complexes. The first oxidation process varied between 0.10 V and 0.18 V for **3.1**-**3.10** and the first reversible reduction process varied between -1.98 V and -1.89 V for all complexes except **3.4**, which had a value of -1.38 V due to the electron withdrawing nature of the nitrophenyl group making it more difficult for the LUMO to be reduced. This resulted in the energy between the first reversible oxidation and reduction being similar for most complexes with values between 2.04 V and 2.07 V except for **3.4** which had a value of 1.52 V. This showed that the electrochemical properties were affected by the modifications to the 4' position of the terpyridine ligand, however this resulted in a change to both the HOMO and LUMO, effectively canceling out the change in energy of each orbital. These results were very similar to $[Ru(dpyb)(tpy)]PF_6$,[37] which shows a reversible oxidation at 0.12 V, a reversible reduction at -1.95 V and a ΔE of 2.07 V.

CHAPTER 4

MODIFICATION TO THE N-HETEROCYCLE ON THE CYCLOMETALATING LIGAND

4. Modification to the N-heterocycle on the cyclometalating ligand.

4.1 Introduction.

Since the original synthesis of [Ru(tpy)(dpyb)](PF_6), as a cyclometalated analogue of [Ru(tpy)$_2$](PF_6)$_2$, found that the electronic properties of the complex were dramatically modified there has been a range of different approaches to tuning their electronic properties further. One method is to change the N-heterocycle on each side of the cyclometalating ligand. One approach to achieving this is to use triazole instead of pyridine rings as the N-heterocycle. These are prepared in high yield by utilizing CuAAC "click" reactions to synthesize substituted 1,3-bis(1,2,3-triazol-4-yl)benzene ligands. Triazole is a π-excessive five membered heterocyclic ring[177] that can be used as an alternative to pyridine as the N-heterocycle on the cyclometalating ligand. Using triazole instead of pyridine changes the N-heterocycle from being π-deficient to π-excessive and thus the ability of the N-heterocycle as a π-acceptor is changed. Triazole was originally incorporated into cyclometalated ruthenium complexes by Zhong and co-workers[29, 178-179] and has since been used by Schulze et al.[28]

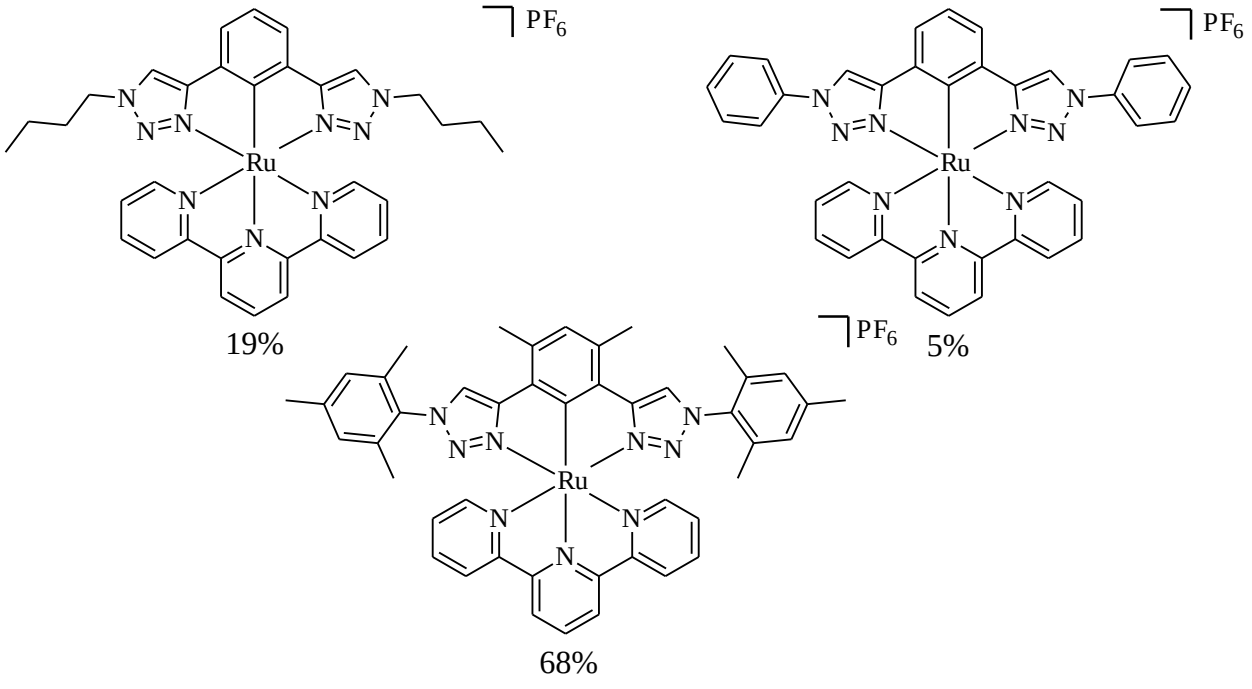

Figure 4.1: Three cyclometalated ruthenium complexes incorporating substituted triazoles as the N-heterocycle.

The ^{n}butyl and phenyl substituted triazole ligands by Zhong and co-workers had very low yields of 19% and 5% respectively (Figure 4.1). This was because of the additional nitrogen that is available to bind to the ruthenium, resulting in a range of byproducts and thus lowering the yield. The work by Schulze et al. used methyl groups to successfully block the ruthenium from coordinating to alternate binding sites, which lead to a significant increase in the reaction yield (68%). The MLCT in the visible region of the UV-vis spectra for all three of these complexes are blue shifted compared to [Ru(dpyb)(tpy)](PF_6), with peaks at 490 nm (ε = 10,000) for the ^{n}butyl substituted triazole, 485 nm (ε = 7,900) for the phenyl substituted triazole and 488 nm (ε = 7,300) for the mesityl substituted triazole. The emission spectra for the ^{n}butyl and phenyl substituted triazole complexes have not been completed, but the mesityl substituted triazole shows an emission profile with a peak at 751 nm, which has a lifetime of 4.1 ns and a quantum yield of 6.1 x 10^{-5}.

A range of different aryl groups have been incorporated onto the triazole in addition to the ^{n}butyl, phenyl and mesityl groups shown in Figure 4.1. The original modifications were incorporated to aid formation of the target ruthenium complex, however they can also be used to modify the photophysical properties of these complexes, especially the energy of the MLCT. There are also a range of examples in which substitutions to the side pyridyl rings in [Ru(tpy)$_2$](PF_6)$_2$[180-185] or the pyridyl rings in [Ru(bpy)$_3$](PF_6)$_2$[186-191] result in changes in their photophysical properties. To compare the aryl substituted triazole ligands with the non-substituted pyrazole ligands from chapters two and three, 4-substituted pyrazoles were synthesized to compare the effect of introducing aryl groups onto both types of N-heterocycles (Figure 4.2). Modifying the N-heterocycle from the π-deficient pyridine[118] to the π-excessive pyrazole[118] and triazole[177] has been shown in chapter two and other published work[28] to have a significant effect on the π-acceptor properties. Using extended aryl groups substituted onto the N-heterocycle should further modify the π-acceptor properties of the N-heterocycles used.

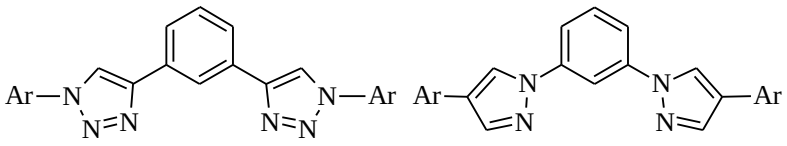

Figure 4.2 Aryl substituted triazole and pyrazole containing cyclometalating ligands, 1,3-di(1-aryl-1,2,3-triazol-4-yl)benzene and1,3-di(4-aryl-pyrazol-1-yl)benzene.

This is due to the significantly different π-acceptor properties of π-excessive pyrazole compared to π-deficient pyridine. Pyrazole is also a better σ-donor than pyridine.

4.2 Chapter four research outline.

In this chapter a series of N^C^N cyclometalated ruthenium complexes have been synthesized which focus on modifications to the N-heterocycle of the cyclometalated ligand. Eleven new N^C^N cyclometalated ruthenium complexes have been synthesized, as shown in Figure 4.3. Previous results from chapters two and three have shown that changes to the N-heterocycle has a substantial impact on the overall properties of the complex and this is explored by using a variety of different substituted N-heterocycles in this chapter.

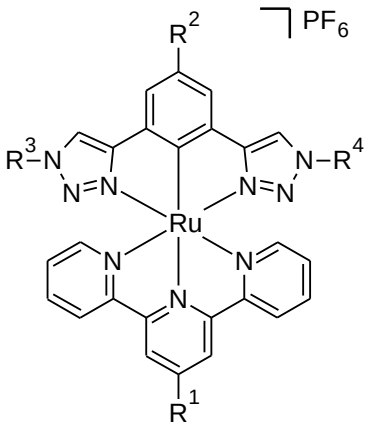

PF_6	R^1 = H	R^2 = Br	R^3/R^4 = 4-Tertbutylbenzyl	**4.1**
	R^1 = 4-Tertbutylphenyl	R^2 = Br	R^3/R^4 = 4-Bromobenzyl	**4.2**
	R^1 = H	R^2 = Br	R^3/R^4 = 4-Tertbutylphenyl	**4.3**
	R^1 = H	R^2 = Br	R^3/R^4 = 4-Methoxyphenyl	**4.4**
	R^1 = 4-Tertbutylphenyl	R^2 = Br	R^3/R^4 = 4-Tolyl	**4.5**
	R^1 = 4-Tertbutylphenyl	R^2 = H	R^3/R^4 = 4-Mesityl	**4.6**
	R^1 = H	R^2 = Br	R^3 = mesityl, R^4 = 4-Tertbutylbenzyl	**4.7**
PF_6	R^1 = 4-Tertbutylphenyl	R^2 = Br	R^3 = mesityl, R^4 = 4-Tertbutylbenzyl	**4.8**

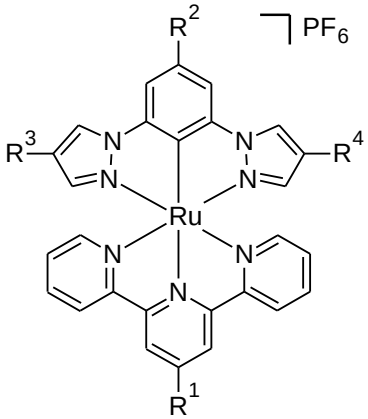

R^1 = 9-Anthracenyl	R^2 = Br	R^3/R^4 = Phenyl	**4.9**
R^1 = 9-Anthracenyl	R^2 = Br	R^3/R^4 = 4-Methoxyphenyl	**4.10**
R^1 = 4-Tertbutylphenyl	R^2 = Br	R^3/R^4 =1-Naphthyl	**4.11**
R^1 = 9-Anthracenyl	R^2 = Br	R^3/R^4 =1-Naphthyl	**4.12**

Figure 4.3: Ruthenium(II) complexes (**4.1-4.12**) investigated in this chapter.

There are several different approaches which can be utilized to incorporate different heterocycles onto the side of the cyclometalated ligand. Two successful substitution routes used in this series

utilized triazoles or pyrazoles. These N-heterocycles can be substituted to incorporate further aryl groups. In the case of triazole, modified aryl systems were substituted onto the triazoles at the N-1 position, either directly or *via* a CH_2 linker. For pyrazole, the aryl system was substituted directly onto the 4' position of the pyrazole.

Changing the N-heterocycle also has a direct impact on the binding of the cyclometalated ligand with the ruthenium, where some modifications promote the formation of the target complex and others cause a range of byproducts. Reasons for a higher level of success for some cyclometalating ligands in forming the target complex compared to various byproducts is also explored in this chapter, with the properties of the successful complexes analyzed and compared.

4.3 Ligand synthesis.

The pathway to the synthesised complexes required several steps, which could be modified at different stages, to achieve a range of different ligands, and complexes. All substituted triazole ligands utilized 1,3-di(ethynyl)-5-bromobenzene (**4.15**), as a precursor, which was prepared from 1,3,5-tribromobenzene in 2 steps. The first step utilizes a palladium catalyzed Sonogashira cross coupling,[192] in which a mono substituted acetylene is substituted with an aryl halide. Both trimethylsilylacetylene (TMSA) and 2-methyl-3-butyn-2-ol (MEBYNOL) are common primary acetylenes used in reactions of this type, with the use of each having independent advantages and disadvantages. TMSA can be deprotected using mild conditions, achieving very high yields, but it is very expensive. MEBYNOL on the other hand is significantly cheaper, but removal of the propyl alcohol protecting group requires high temperatures and that often do not provide high yields. An extra factor to be considered was that the synthesis pathway would produce a range of byproducts which would need to be separated, in this case using column chromatography. This meant that the majority of work was carried out using MEBYNOL as the reaction products were more easily separated and reactions were able to be completed on a large scale because of the significantly cheaper price of MEBYNOL, compared to TMSA.

Removing the TMS was achieved by stirring an aqueous KOH solution at room temperature and the propyl alcohol group was removed by refluxing in a solution of toluene with KOH. Both these methods provided **4.15** in relatively high yield as shown in Scheme 4.1.

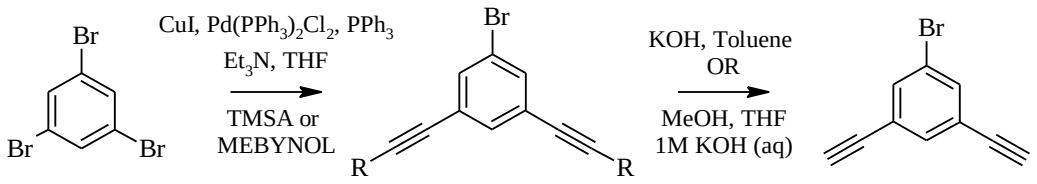

$R_1 = SiCH_3$	**4.13** 83%	**4.15** 98%
$R_2 = C(CH_3)_3OH$	**4.14** 85%	**4.15** 76%

Scheme 4.1: Synthesis of 1,3-di(ethynyl)-5-bromobenzene (**4.15**) *via* 2 different intermediates.

Ligand precursor **4.15** proved to be an important building block as it enabled a range of different substituted triazoles to be synthesised in one step from aryl azides. Following work by Crowley *et al*,[193] who developed a one pot multi-component CuAAC "click" approach to synthesizing substituted 1,2,3-triazole ligands, experimental conditions were used which did not require the isolation of potentially explosive aryl azides. This meant that benzyl bromide derivatives could be reacted with NaN_3 in situ and then with **4.15** as shown in Scheme 4.2.

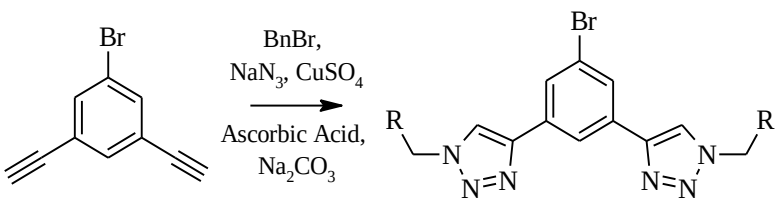

R =

Phenyl	**4.16**	88%
4-^{t}Butylphenyl	**4.17**	91%
4-Bromophenyl	**4.18**	91%
1-Naphthyl	**4.19**	83%

Scheme 4.2: Synthesis of potential ligands **4.16**-**4.19**.

Four potential ligands **4.16**-**4.19** were synthesised using this method, in high yield (Scheme 4.2). Compounds **4.16** and **4.17** were synthesised to explore the impact adding aryl groups onto the triazole N-heterocycle with a benzyl unit. Ligand **4.18** was synthesised with an additional bromine atom on each side, opening up these sites to potential substitution. Following the successful of synthesizing **4.16**-**4.18**, compound **4.19** was synthesised in high yield from **4.15** and 1-chloromethylnaphthalene (**4.22)** using the same CuAAC 'click' reaction conditions. The precursor, **4.22** was synthesised in an interesting three step procedure in which 1-acetylnaphathalene undergoes a modified haloform reaction with bleach and pyridine to achieve 1-naphthoic acid in 84% yield. The acid (**4.20**) was then able to be reduced using lithium aluminum hydride in 73% yield and then treated with thionyl chloride to convert the alcohol into

the **4.22** in 85% yield (Scheme 4.3). This method was based on work by Malashikhin *et al*., who completed a similar procedure using substituted pyrene.[194] These three potential ligands will explore the effect of adding non-conjugated aryl rings onto the N-heterocycle on each side of the cyclometalating ligand.

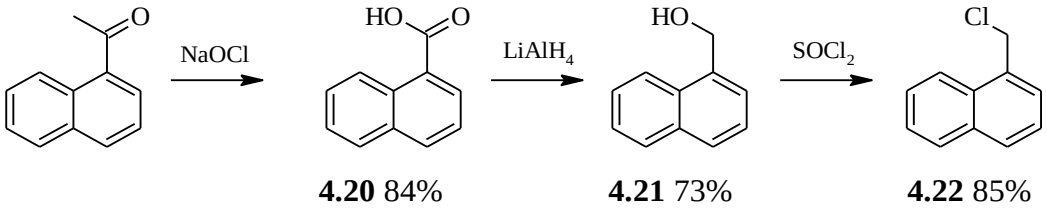

4.20 84% **4.21** 73% **4.22** 85%

Scheme 4.3: Synthesis of 1-chloromethylnaphthalene (**4.22**) in three steps, all in relatively high yield.

One drawback of these ligands (**4.16**-**4.19**) was that aryl groups were unable to be attached directly to the triazole, as an aryl halide does not react *in situ* with the NaN_3 to form the aryl azide. This observation is supported by there being no evidence of reaction of the bromine atom on the **4.15**. To avoid this, aryl halides were converted to aryl boronic acids (Scheme 4.4) using previously optimized conditions.[126-127]

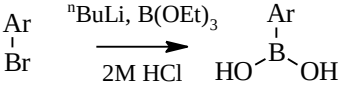

R =

4-Tolyl	**4.23**	71%
4-Tertbutylphenyl	**4.24**	73%
Mesityl	**4.25**	81%
4-Methoxyphenyl	**4.26**	78%
1-Naphthyl	**4.27**	68%
2-Naphthyl	**4.28**	63%
1-Pyrenyl	**4.29**	68%

Scheme 4.4: Synthesis of aryl boronic acids used in this study.

The aryl boronic acids were then converted to aryl azides, which were then reacted in situ with **4.15** to attempt to form **4.30**-**4.34** (Scheme 4.5), **4.35** (Scheme 4.6) and **4.36** (Scheme 4.7). All these reactions occurred with relatively high overall yields, taking into account the number of

steps occurring *in situ* except for **4.35** and **4.36**. For **4.35**, a shorter reaction time was used to synthesize both the mono (**4.35a**) and di (**4.35**) substituted derivatives with the goal of using **4.35a** to form an asymmetric cyclometalating ligand in addition to using **4.35**.

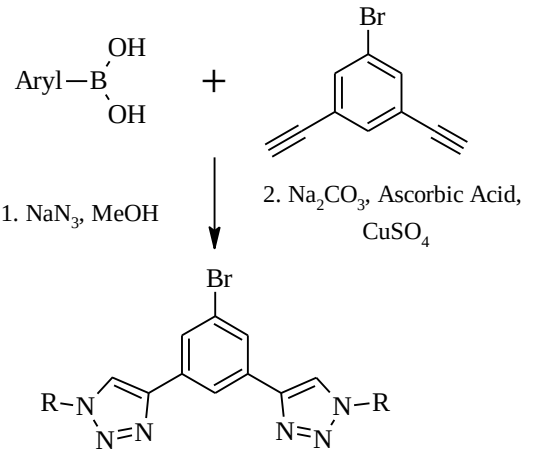

R =	4-Methylphenyl	**4.30**	89%
	4-Tertbutylphenyl	**4.31**	86%
	4-Methoxyphenyl	**4.32**	87%
	1-Naphthyl	**4.33**	79%
	2-Naphthyl	**4.34**	76%

Scheme 4.5: Synthesis of **4.30**-**4.34**.

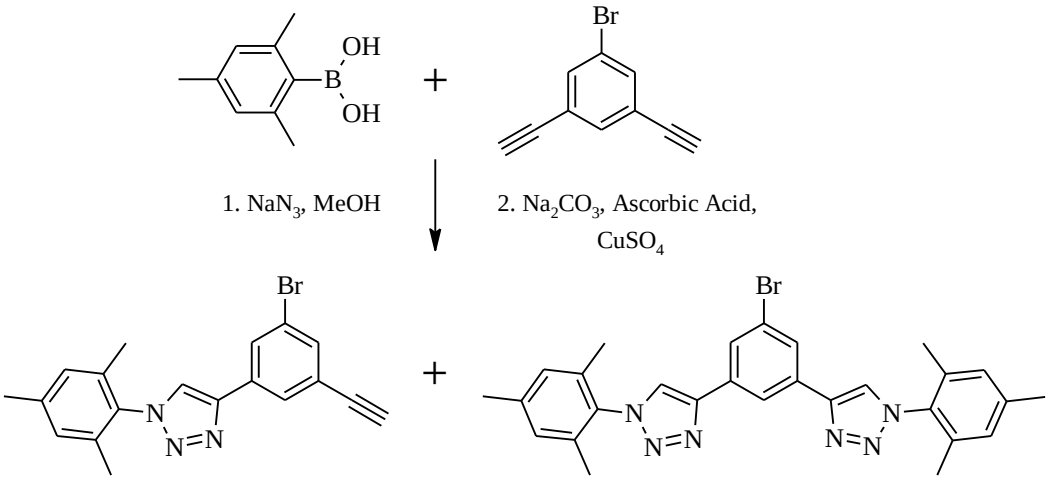

4.35a 29% **4.35** 52%

Scheme 4.6: Synthesis of **4.35** and **4.35a**.

The reaction which attempted to synthesize **4.36** (**Scheme 4.7**) did not show any evidence of the target product by ^{1}H NMR spectroscopy or mass spectrometry. The monosubstituted derivative (**4.36a**) was isolated in 23% yield however. An additional precipitate was also formed during the reaction, although this could not be analysed by ^{1}H and ^{13}C NMR spectroscopy or mass spectrometry as it was insoluble in all available solvents.

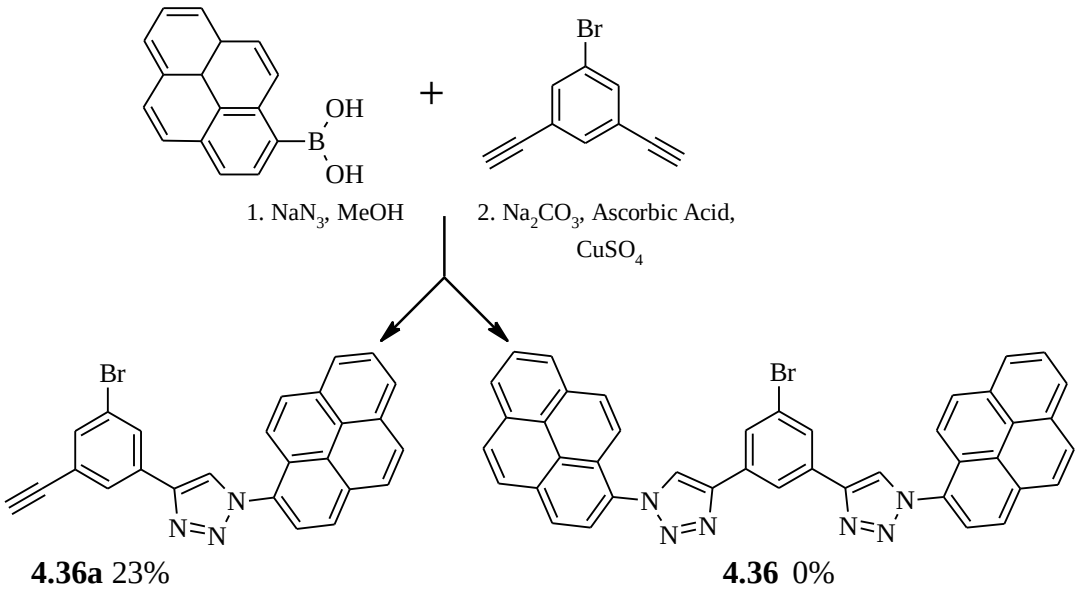

Scheme 4.7: Synthesis of target compound **LX8** and reaction product **LX8a**.

Previous ligands in this series incorporate either non-conjugated aryl groups attached to the triazole N-heterocycle (**4.16**-**4.19**) or conjugated aryl groups (**4.30**-**4.34**). An asymmetric ligand has also been synthesised to analyze the effect of having both types of substituted aryl groups substituted onto the N-heterocycle. Previously synthesised **4.35a** was reacted with 4-tertbutylbenzyl bromide and NaN_3 using previously optimized CuAAC 'click' reaction conditions to give **4.37** in 93% yield (Scheme 4.8). This gave a potential ligand in which one triazole ring was directly substituted with an aryl group and the other side incorporated the non-conjugated aryl group.

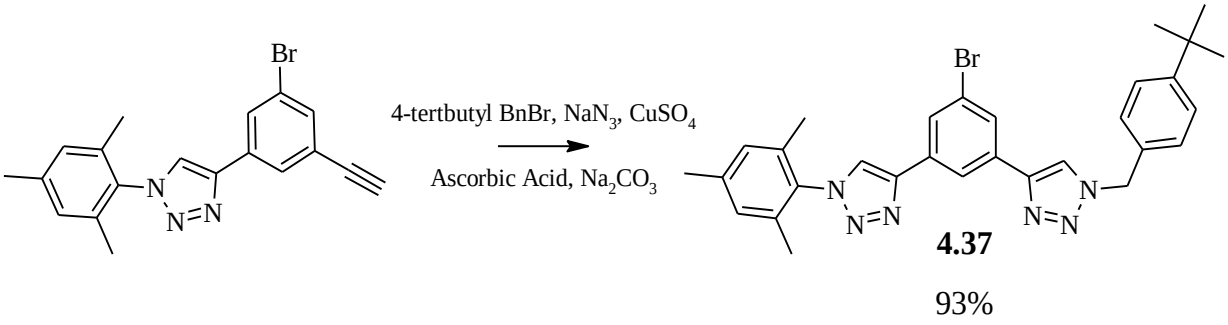

Scheme 4.8: Synthesis of **4.37**.

Another route of potential modification was to synthesize 4-substituted pyrazoles, which could be incorporated into potential ligands to investigate the effect of extending the ring system. Synthesis of 4-substituted pyrazoles was achieved in a one pot three step reaction where 4-substituted phenyl acetic acid was reacted with $POCl_3$/DMF, using Vilsmeyer-Haack-type reaction conditions to give the bis(trimethinium) salt, which was isolated at its perchlorate salt. Hydrolysis of this perchlorate salt gave the corresponding dialdehyde which was then reacted, without isolation, with hydrazine hydrate to form the 4-substituted pyrazole.[195] Compounds 4-phenylpyrazole (**4.38**), 4-(4-methoxyphenyl)pyrazole (**4.39**) and 4-(1-naphthyl)pyrazole (**4.40**) were synthesised using this method in 83%, 85% and 79% yield respectively (Scheme 4.9) and characterized using ^1H and ^{13}C NMR spectroscopy and mass spectrometry.

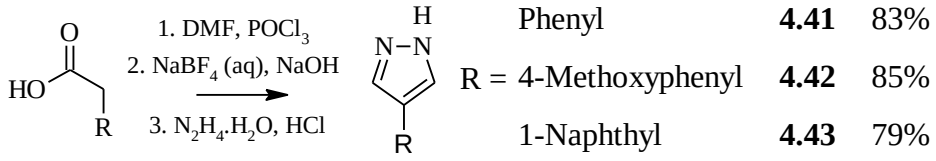

Scheme 4.9: Synthesis of 4-substituted pyrazoles, **4.38**-**4.40**.

Compounds **4.38**-**4.40** were then reacted using previously optimized modified Ullmann coupling conditions to form new potential ligands, **4.41**-**4.43**. These reactions occurred at moderate yield, as shown in Scheme 4.10. The reaction mixtures were purified using column chromatography (SiO_2, 10% EtOAc/DCM) giving the target product as a white solid. All of these new compounds (**4.41**-**4.43**) were characterized by ^1H and ^{13}C NMR spectroscopy and mass spectroscopy.

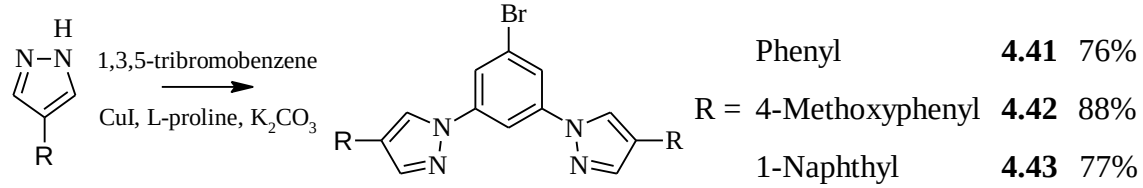

Scheme 4.10: Synthesis of potential ligands **4.41**-**4.43**.

4.4 Synthesis of complexes.

Using previously optimized reaction conditions potential ligand **4.16** was reacted with AgOTf, Et_3N and $Ru(tpy)Cl_3$ in ethanol/water and the crude mixture was separated using column

chromatography to give a range of different complexes. The predominant reaction product was unable to be initially identified by ^{1}H and ^{13}C NMR spectroscopy or by mass spectrometry. To acquire additional structural information crystals were grown from diffusion of diisopropylether into an acetonitrile solution containing a single drop of toluene.

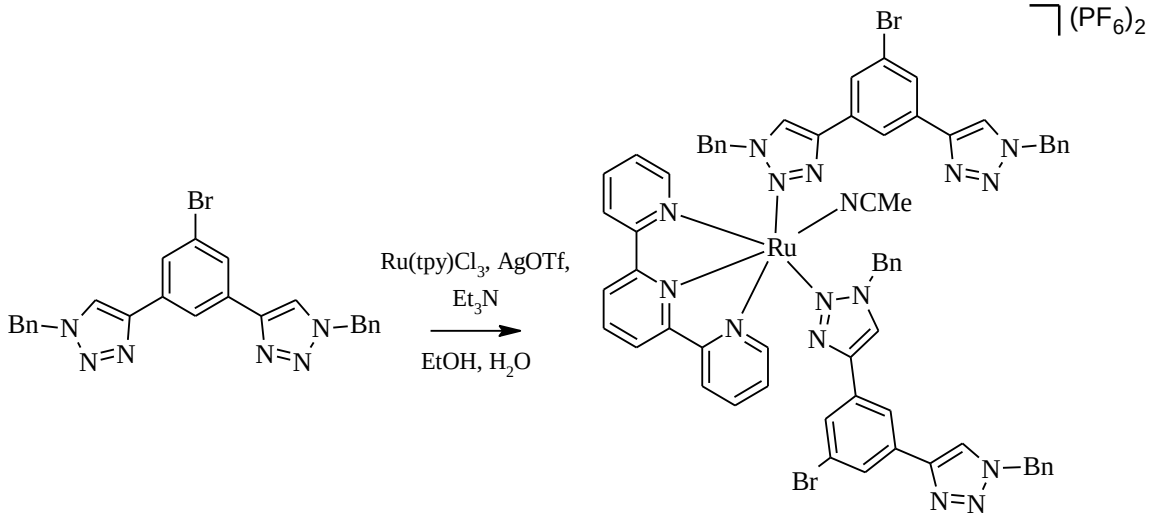

Scheme 4.11: Potential complex formed by reacting **4.16** with $Ru(tpy)Cl_3$ and AgOTf in ethanol/water.

The crystals were examined by X-ray diffraction, but an exact structure was unable to be identified. Despite this, information from the X-ray structure suggested the product was not cyclometalated. ^{1}H NMR spectroscopy, while not providing a complete assignment, did show that there were two equivalents of **4.16**, in addition to the terpyridine ligand. It also showed that the **4.16** was not symmetrical, as the benzyl CH_2 ^{1}H peak was split into two, one moving upfield from 5.57 ppm to 5.18 ppm and the other remaining unshifted. Based on this evidence the complex is likely [Ru(tpy)(**4.16**)$_2$(MeCN)](PF$_6$)$_2$ (Scheme 4.11), for which a peak was observed in the analysis from mass spectrometry.

The target complex [Ru(tpy)(**4.16**)]PF$_6$ (**4.44**) was also identified as part of the remaining crude mixture and single crystals were able to be grown by slowly diffusing ether into a toluene/acetonitrile mixture. While insufficient material was formed for thorough characterization, valuable structural information was able to be obtained from X-ray diffraction, which is discussed in chapter 4.6.1.

Regardless of the exact structure of the reaction byproduct, new methods were needed to promote cyclometalation, and increase the yield of the target complex. Other research groups have found methods to get around this problem, either modifying reaction conditions by carrying out the reaction in a specially designed sealed tube with long reaction times, using a microwave reactor [29] or by using specific ligands which block the extra nitrogen site from binding.[28] Another way to help get around this problem is to run the reaction in two steps, in which $Ru(tpy)Cl_3$ is initially reacted with AgOTf in acetonitrile, to give $[Ru(tpy)(MeCN)_3](PF_6)_2$ (Scheme 4.12), which was then reacted with the cyclometalating ligand (Scheme 4.13). This was beneficial because the ruthenium precursor complex was able to be purified completely using column chromatography before use in the subsequent reaction. It also meant that the cyclometalation reaction was able to be completed without having silver *in situ*, which can cause homocoupling and/or various other byproducts when present in the reaction mixture[196]. The MeCN ligands are also able to be easily replaced by the cyclometalating ligand, meaning shorter reaction times and less chance of byproduct formation.

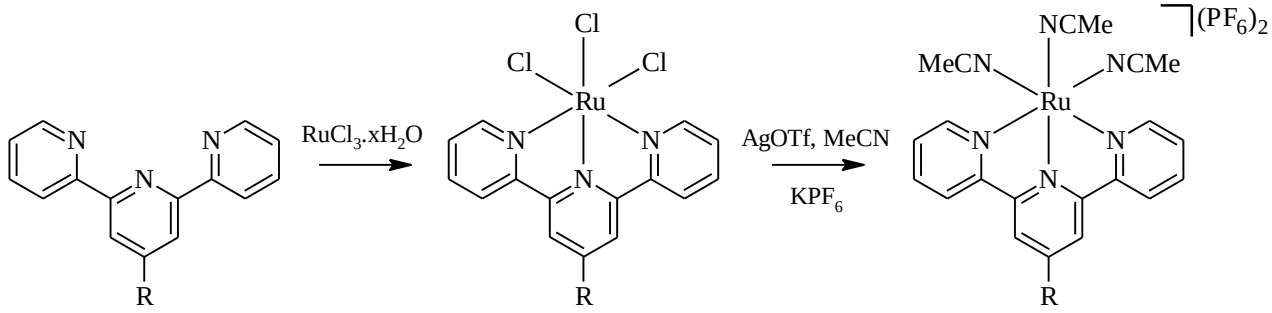

Scheme 4.12: General synthesis pathway for ruthenium precursor complexes used in this chapter.

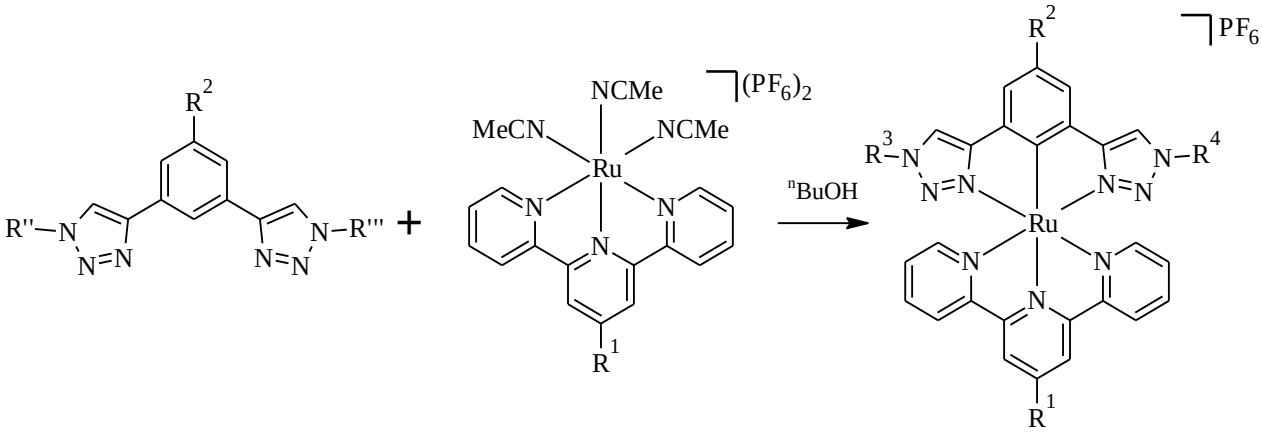

R^1 = H	R^2 = Br	R^3/R^4 = 4-Tertbutylbenzyl	**4.1**	49%
R^1 = 4-Tertbutylphenyl	R^2 = Br	R^3/R^4 = 4-Bromobenzyl	**4.2**	52%
R^1 = H	R^2 = Br	R^3/R^4 = 4-Tertbutylphenyl	**4.3**	56%
R^1 = H	R^2 = Br	R^3/R^4 = 4-Methoxyphenyl	**4.4**	66%
R^1 = 4-Tertbutylphenyl	R^2 = Br	R^3/R^4 = 4-Tolyl	**4.5**	59%
R^1 = 4-Tertbutylphenyl	R^2 = H	R^3/R^4 = 4-Mesityl	**4.6**	76%
R^1 = H	R^2 = Br	R^3 = mesityl, R^4 = 4-Tertbutylbenzyl	**4.7**	71%
R^1 = 4-Tertbutylphenyl	R^2 = Br	R^3 = mesityl, R^4 = 4-Tertbutylbenzyl	**4.8**	73%

Scheme 4.13: General pathway for the synthesis of new cyclometalated ruthenium complexes incorporating substituted triazole derivatives (**4.1**-**4.8**).

Using $[Ru(tpy)(MeCN)_3](PF_6)_2$ allowed a number of previously ineffective reactions to be carried out successfully, although several still resulted in inseparable mixtures (Scheme 4.13). 'Reactions involving the ligands incorporating benzyl substituted triazoles were successful (**4.1** and **4.2**), but gave the desired product in low yields. Only some of the conjugated phenyl substituted triazole ligands were complexed successfully to form complexes (**4.3**-**4.6**), with many of the others including both 1-naphthyl and 2-naphthyl derivatives were not able to be successfully isolated, but were able to be identified using mass spectrometry. As previously reported the mesityl substituted triazoles support product formation and gave a cyclometalated complex in the best yield (76%) of the triazole substituted complexes, although it was not the target complex. Instead a complex formed in which the 4-bromo on the central benzene ring of the cyclometalated ligand was replaced by a hydrogen atom at some stage during the reaction or

workup. Interestingly Schulze *et al*. published work on similar complexes in which they synthesised **4.35** but did not include its corresponding cyclometalated complex in their publication.[28] Mass spectrometry identified the complex as the proposed structure and did not show any indicative bromine pattern, or the expected mass for the target complex. ^{1}H NMR spectroscopy shows characteristic peaks for the complex being 4-H substituted, in which the new hydrogen presents as a triplet at 7.41 ppm (J = 7.5 Hz). A full assignment of the ^{1}H and ^{13}C spectra is included in the experimental section (Chapter 6.7). Complexes **4.7** and **4.8** formed the target complex in 71% and 73% yield, respectively, showing that even having one mesityl substitution has an effect on how well the reaction occurs as the yields for these two complexes are similar to **4.6**. The less polar ligands produced complexes which were more easily separated during column chromatography, increasing the recovered yield for those reactions.

Complexes **4.9**-**4.12**, in which the ligands incorporated substituted pyrazoles instead of substituted triazoles were very successful (Scheme 4.14). They used the previously optimized conditions, in which the ligand and Ru(R-tpy)Cl_3 were combined together with AgOTf and NEt_3 in a single step. The yields for these complexes were all above 83% and at a similar yield to previously synthesised substituted pyrazole complexes from chapter two.

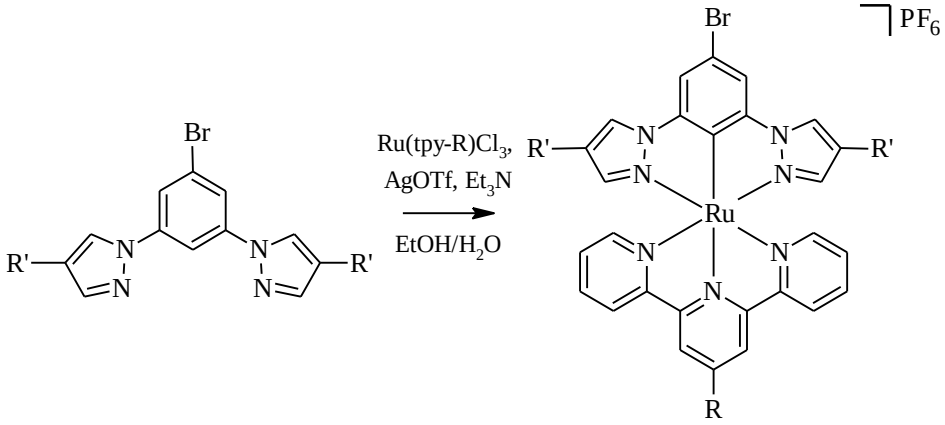

R = 9-Anthracenyl R' = Phenyl	**4.9**	83%	R = 4-^{t}Butylphenyl R' = 1-Naphthyl	**4.11**	91%
R = 9-Anthracenyl R' = 4-Methoxyphenyl	**4.10**	89%	R = 9-Anthracenyl R' = 1-Naphthyl	**4.12**	87%

Scheme 4.14: Synthesis of new cyclometalated ruthenium complexes, **4.9**-**4.12**.

4.5 Structural analysis.

4.5.1 NMR analysis

One of the methods of characterization used in this work is NMR spectroscopy. Most of the ligands and their complexes synthesised had signals for different protons which were well separated, which made assignment straightforward and unambiguous, however ligands and corresponding complexes with naphthalene (**4.11, 4.12**) and anthracene (**4.9**, **4.10** and **4.12**), as well as the two complexes incorporating an asymmetric cyclometalating ligand (**4.7** and **4.8**) were difficult to assign based solely on ^{1}H and ^{13}C spectra. This difficulty was reduced by using a range of two-dimensional techniques, such as COSY, HSQC and HMBC in partnership with the spectral assignments for similar compounds'.

The NMR spectra of these ligands and complexes show significant changes upon cyclometalation of the free ligand to ruthenium and these changes can be examined by analysis of coordination induced shifts (Refer Chapter 2.5.1). Complexes **4.1**-**4.12** and their corresponding unbound N^C^N ligand were all able to be dissolved in acetone-D6 and analysis of their CIS was carried out.

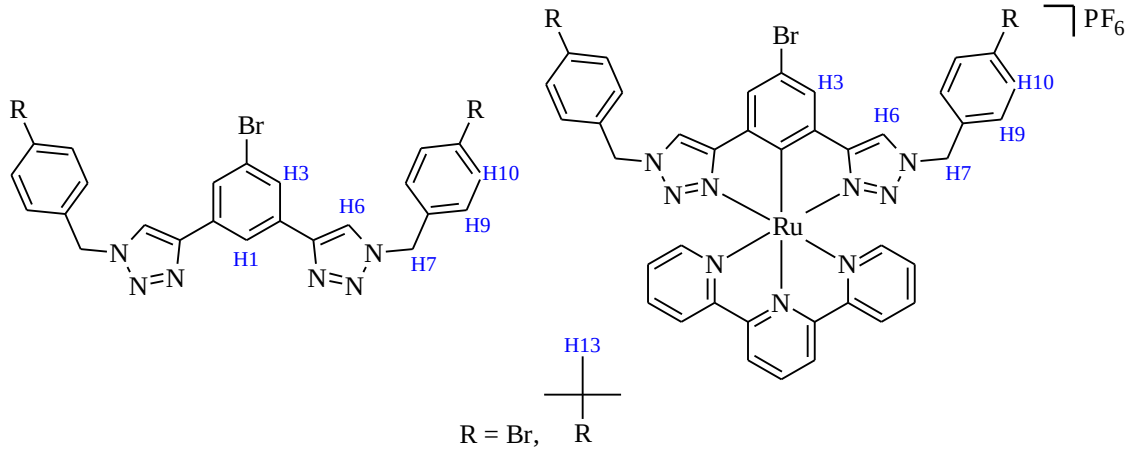

Figure 4.4: Labeling scheme for ^{1}H CIS analysis for complexes **4.1**-**4.2** and the corresponding free ligand.

Analysis of the ^{1}H NMR spectra for **4.1** and **4.2** and their corresponding free ligand show small positive CIS of +0.01 ppm and +0.09 ppm for the H3 proton, respectively (Table 4.1). These small CIS are due to a lack of large conformational changes or large electron donating/withdrawing effects this position. The CIS of H6 shows only small changes as well,

with a small negative CIS for **4.1** and a small positive CIS for **4.2**. The protons on the aryl ring substituted *via* a CH_2 unit onto the triazole on each side, show negative CIS at all positions as a result of increased electron density through metal–to–ligand π back-donation.

	H1	H3	H6	H7	H9	H10	H13
4.17	8.38	8.01	8.52	5.65	7.36	7.42	1.29
4.1	-	8.02	8.46	5.34	6.90	7.24	1.23
CIS	-	+0.01	-0.06	-0.31	-0.46	-0.18	-0.06
4.18	8.38	8.01	8.56	5.71	7.40	7.59	-
4.2	-	8.10	8.61	5.42	6.90	7.23	-
CIS	-	+0.09	+0.05	-0.29	-0.50	-0.36	-

Table 4.1: ^{1}H CIS analysis for complexes **4.1-4.2**.

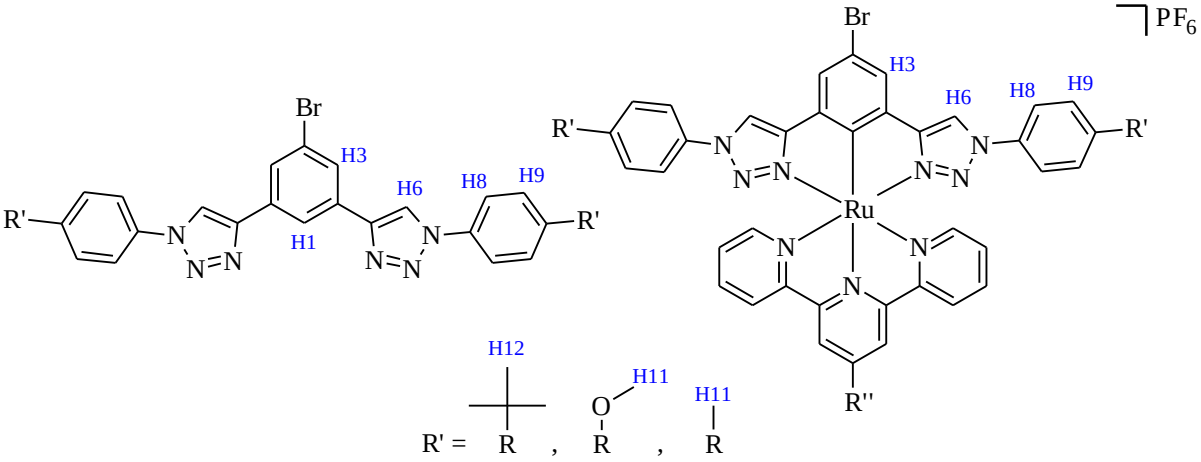

Figure 4.5: Labeling Scheme for ^{1}H CIS analysis for complexes **4.3-4.5** and the corresponding free ligands.

	H1	H3	H6	H8	H9	H11
4.31	8.63	8.15	9.17	7.94	7.71	1.40
4.3	-	8.15	9.10	7.50 [a]	7.50[a]	1.26
CIS	-	0.00	-0.07	-0.44[a]	-0.22[a]	-0.14
4.32	8.61	8.14	9.10	7.91	7.19	3.92
4.4	-	8.04	8.94	7.37	6.91	3.71
CIS	-	-0.10	-0.16	-0.54	-0.28	-0.21
4.30	8.56	8.19	9.08	7.82	7.42	2.42
4.5	-	8.14	9.11	7.45	7.26	2.30
CIS	-	-0.05	+0.03	-0.37	-0.16	-0.12

Table 4.2: [1]H CIS analysis for complexes **4.3-4.5**. (a) Approximate values are taken from the center of the respective multiplet for overlapping/broad peaks.

Analysis of the [1]H NMR spectra for **4.3**, **4.4** and **4.5** and their corresponding free ligand all show either negligible shifts or small negative CIS for the H3 and H6 protons (Table 4.2). The small negative CIS are due to ligand-to-metal σ donation, which results in less electron density at these positions. The aryl ring directly substituted onto the triazole on each side, shows a negative CIS at all positions, showing increased electron density through metal–to–ligand π back-donation. These results show that there is a greater amount of metal–to–ligand π back-donation on the aryl groups on the side compared to the central benzene ring, as a result of the orbitals involved in the π back-donation on the metal being able to donate into the side rings more efficiently.

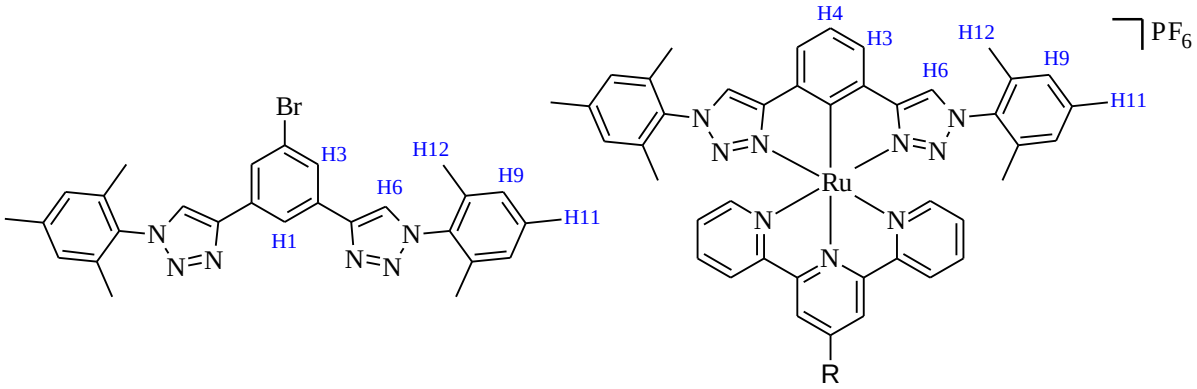

Figure 4.6: Labeling scheme for [1]H CIS analysis for complex **4.6** and the corresponding free ligand **4.35**.

	H1	H3	H4	H6	H9	H11	H12
4.35	8.62	8.16	-	8.71	7.12	2.03	2.38
4.6	-	8.01	7.41	8.57	6.90	1.52	2.22
CIS	-	-0.15	-	-0.14	-0.22	-0.51	-0.16

Table 4.3: [1]H CIS analysis for complex **4.6**.

Analysis of the [1]H NMR spectra for **4.6** and its free ligand show negative CIS for protons H3, H6, H9, H11 and H12, although their shifts are not directly comparable since the free ligand is different to the cyclometalated ligand as the bromine atom was replaced by a proton during the reaction (Table 4.3).

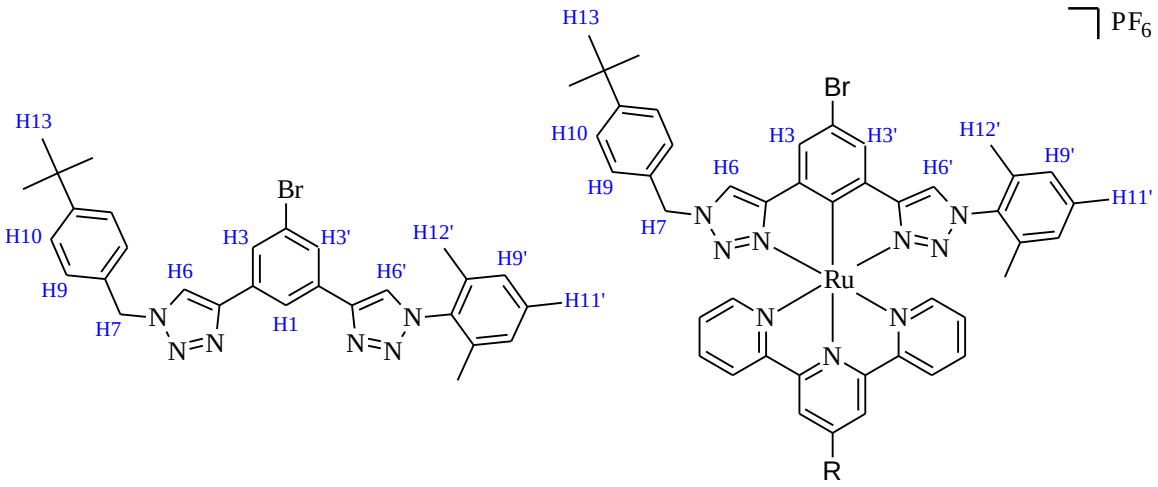

Figure 4.7: Labeling scheme for ^{1}H CIS analysis for complexes **4.7**-**4.8** and the corresponding free ligand.

	H1	H3	H6	H7	H9	H10	H13	H3'	H6'	H9'	H11'	H12'
4.37	8.50	8.06	8.57	5.67	7.37	7.44	1.30	8.11	8.66	7.10	2.37	2.01
4.7	-	8.07	8.52	5.37	6.93	7.25	1.21	8.07	8.59	6.91	2.23	1.48
CIS	-	0.01	-0.05	-0.30	-0.44	-0.19	-0.09	-0.04	-0.07	-0.19	-0.14	-0.53
4.38	8.50	8.06	8.57	5.67	7.37	7.44	1.30	8.11	8.66	7.10	2.37	2.01
4.8	-	8.13	8.64	5.41	6.96	7.19	1.13	8.09	8.61	6.89	2.21	1.48
CIS	-	0.07	0.07	-0.26	-0.41	-0.25	-0.17	-0.02	-0.05	-0.21	-0.16	-0.53

Table 4.4: ^{1}H CIS analysis for complexes **4.7** and **4.8**.

Analysis of the ^{1}H NMR spectra for **4.7** and **4.8** and their corresponding free ligand (Table 4.4) all show small CIS for the H3 and H6 protons, with H6 on **4.7** being slightly negative and H6 on **4.8** and H3 on both **4.7** and **4.8** being slightly positive. The small positive CIS are due to ligand-to-metal σ donation, which results in less electron density at these positions and the small negative CIS are due to metal-to-ligand π back-donation. All the protons on the aryl rings substituted onto the triazole on each side, either directly or *via* a CH_2 unit show negative CIS, showing increased electron density through metal–to–ligand π back-donation. These results show that there is a greater amount of metal–to–ligand π back-donation on the aryl group linked *via* the CH_2 unit compared to the directly linked mesityl group on the opposite triazole. This is a result of the mesityl group being able donate more electron density, which results in the net amount being slightly less. Both sides have a greater amount of electron density compared to the central

benzene ring, as a result of the orbitals involved in the π back-donation on the metal being able to donate into the side rings more efficiently.

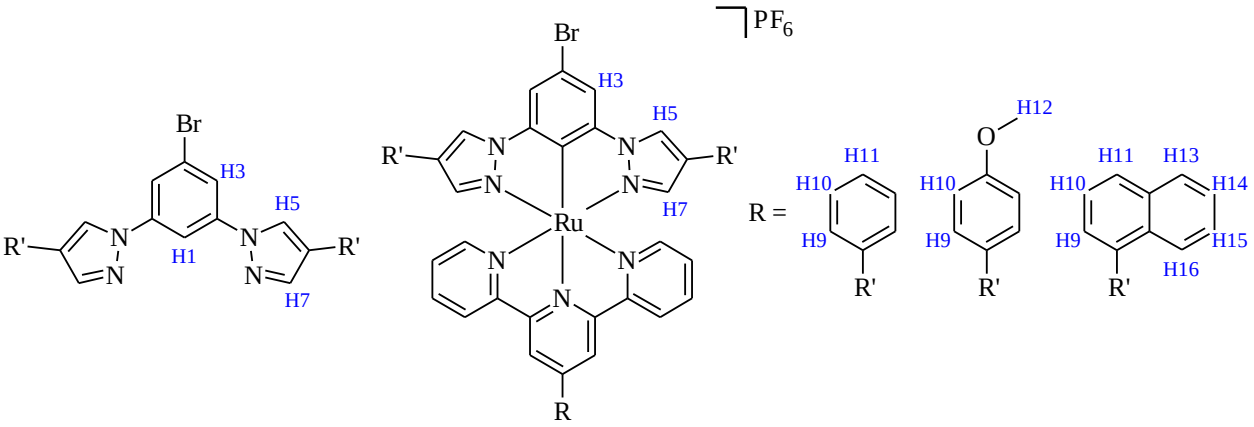

Figure 4.8: Labeling scheme for ^{1}H CIS analysis for complexes **4.9**-**4.12** and their corresponding free ligand.

	H1	H3	H5	H7	H9	H10	H11	H12
4.41	8.49	8.07	8.99	8.23	7.76	7.43	7.29	-
4.9	-	8.22	9.35	7.52	7.48	7.32	7.23	-
CIS	-	0.15	0.36	-0.71	-0.28	-0.11	-0.06	-
4.42	8.45	8.03	8.89	8.15	7.01	7.70	-	3.84
4.10	-	8.18	9.25	7.44	6.89	7.4	-	3.76
CIS	-	0.15	0.36	-0.71	-0.12	-0.30	-	-0.08

Table 4.5: ^{1}H CIS analysis for complexes **4.9** and **4.10**.

Analysis of the ^{1}H NMR spectra for complex **4.9** and **4.10** and the corresponding free ligand for each shows a large negative CIS of -0.71 for H7 (Table 4.5) due to interligand through-space ring-current anisotropy effects in which the H7 proton lies over the shielding plane of the central pyridine ring of the terpyridine ligand as a result of the distorted octahedral geometry (Figure 4.9).

Conformational effects typically occur in 2,6-disubstituted pyridyl ligands and cause significant CIS[146] due to the free ligand preferring a transoid conformation to minimize steric interactions, whereas the ligand in the complex is locked in the cisoid conformation. This leads to neighboring protons (to the central nitrogen) experiencing different shielding effects in the free and complexed environments.

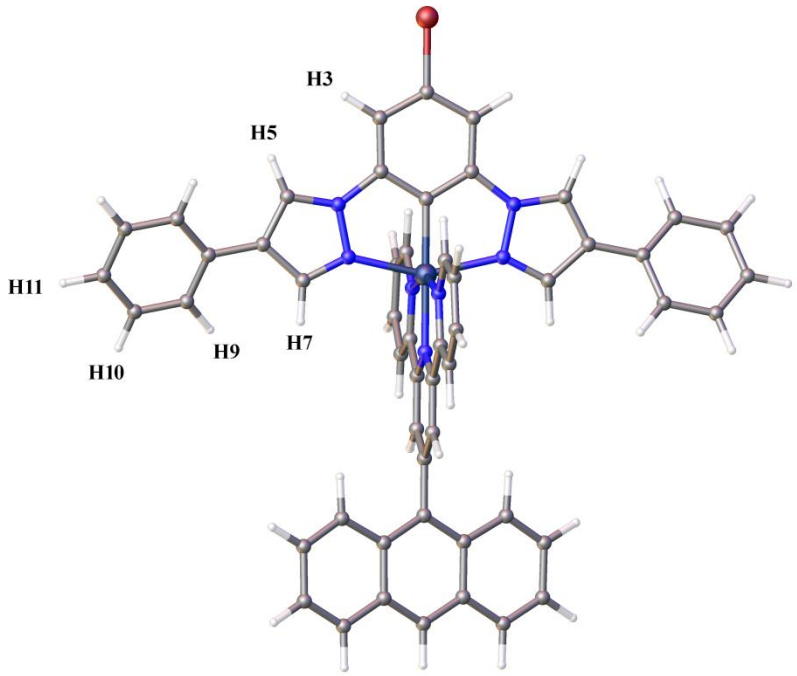

Figure 4.9: Calculated structure of **4.9**, showing H7 proton lying over the shielding plane of the central pyridine ring of the terpyridine ligand.

In 1,3-disubstituted benzene ligands, the N-heterocycle rings are also able to freely rotate, however there is less preference for the transoid conformation because there is less interaction between the C-H compared to the N (and its lone pair of electrons) and thus the CIS resulting from chelation-imposed conformational changes are not as large in these complexes compared to similar 2,6-disubstituted pyridine based ligands/complexes, which have CIS values up to -1.46 ppm for neighboring hydrogens.[145] The CIS values for H5 in **4.9** and **4.10** both have values of 0.36 ppm. This results from a conformational change when the free ligand is locked in the cisoid conformation in the complex. The CIS values for H5 in **4.9** and **4.10** are also impacted by the aryl group introduced onto the pyrazole, which results in these values being larger than for the H5 proton in **2.1** (+0.29 ppm).

Conformation effects have less impact on H3 with pyrazole compared to pyridine because the ring is smaller and the H5 proton (Figure 4.9) is positioned further away from H3. As a result there is less of a preference for a transoid conformer with the benzene core compared to the alternate pyridine core. This is shown by H3 in **4.9** and **4.10** having a smaller CIS value of +0.15

ppm compared to the CIS value of +0.46 ppm for the corresponding proton in $[Ru(tpy)_2]PF_6$[147] and also smaller than the CIS value of +0.36 ppm for H5 in **4.9** and **4.10**.

The CIS values for H9, H10 and H11/H12 for **4.9** and **4.10** are both negative as a result of metal–to–ligand π back-donation. This occurs as a result of the orbitals involved in the π back-donation on the metal being able to donate into the side rings more efficiently.

	H1	H3	H5	H7	H9	H10	H11	H13	H14	H15	H16
4.43	8.59	8.16	8.88	8.1	7.56[a]	8.28[a]	7.98[a]	7.64	7.56[a]	7.56[a]	7.92
4.11	-	8.31	9.25	7.28	7.46	7.85	7.81	7.81	7.37	7.37	7.87
CIS	-	0.15	0.37	-0.82	-0.09	-0.43[a]	-0.17[a]	-0.17	-0.18[a]	-0.19[a]	-0.05
4.43	8.59	8.16	8.88	8.1	7.56[a]	8.28[a]	7.98[a]	7.64	7.56[a]	7.56[a]	7.92
4.12	-	8.34	9.3	7.41	7.45	7.89	7.89	7.35	7.41	7.51	7.89
CIS	-	0.18	0.42	-0.69	-0.11[a]	-0.39[a]	-0.09[a]	-0.34	-0.15[a]	-0.04[a]	-0.03

Table 4.6: ^{1}H CIS analysis for complexes **4.9** and **4.10**. (a) Approximate values are taken from the center of the respective multiplet for overlapping/broad peaks.

Complexes **4.11** and **4.12** have similar CIS (Table 4.6) as for complexes **4.9** and **4.10**. The CIS for H7 in **4.11** and **4.12** are -0.82 ppm and -0.69 ppm due to interligand through-space ring-current anisotropy effects. The CIS of the H3 and H5 protons are due to conformational effects and have values of 0.15 ppm and 0.37 ppm, respectively, for **4.11** and 0.18 ppm and 0.42 ppm, respectively, for **4.12**. The remaining CIS for H9-H11 and H13-H16 are all negative as a result of metal–to–ligand π back-donation. This occurs as a result of the orbitals involved in the π back-donation on the metal being able to donate into the side rings more efficiently.

4.5.2 DFT calculations

Using DFT calculations *in vacuo* for complexes **4.1**-**4.8**, structural information was obtained and selected bond lengths are shown in Table 4.7 and selected bond angles are shown in Table 4.8. For comparison, the equivalent bond lengths/angles from the x-ray crystal structure of **4.45** are shown, which was solved by Schulze *et al*.[28] This crystal structure of **4.45** is similar to **4.6**, except it incorporates terpyridine instead of 4'-(p-^{t}butylphenyl)terpyridine. The results from chapter three showed that changing the hydrogen to 4'-(p-^{t}butylphenyl) at the 4' position on the terpyridine did not affect the structure of **2.1** compared to **3.1**. Thus, **4.45** is compared with **4.6** to analyze the effect of cyclometalation in these complexes.

Complex	Cyclometalated Ligand			Terpyridine Ligand		
	N2-Ru	C-Ru	N4-Ru	N5-Ru	N6-Ru	N7-Ru
4.1	2.07815	2.01034	2.07815	2.09056	2.03315	2.08913
4.2	2.07871	2.00905	2.07898	2.09081	2.03471	2.09187
4.3	2.07657	2.00969	2.07656	2.09088	2.03404	2.09053
4.4	2.07791	2.01015	2.07790	2.09108	2.03357	2.08881
4.5	2.07638	2.00832	2.07623	2.09256	2.03463	2.09164
4.6	2.07841	2.01207	2.07797	2.08883	2.03255	2.08935
4.7	2.07859	2.01053	2.07961	2.08931	2.03283	2.08864
4.8	2.07816	2.00899	2.07921	2.08976	2.03300	2.09080

Table 4.7: Calculated bond lengths for **4.1**-**4.8** from DFT calculations *in vacuo*.

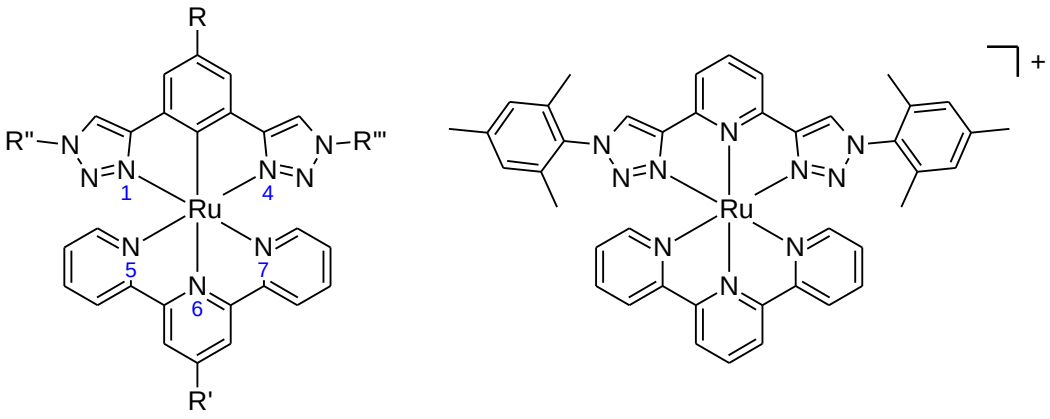

Figure 4.10: Left, general structure of complexes **4.1**-**4.8**, showing the labeling system used in this discussion. Right, Complex **4.45**.

The most important bond length to analyze in cyclometalated complexes compared to the corresponding coordinated complex is the Ru-C bond. In complex **4.6**, the Ru-C bond length is calculated to be 2.01 Å, which is shorter than the corresponding Ru-N bond length in **4.45**, which has a length of 2.06 Å. The Ru-N6 bond in **4.6** has a length of 2.03 Å, which is longer than the comparable Ru-N bond length in **4.45** (2.00 Å). The replacement of the dative Ru-N bond with the Ru-C bond results in a shorter bond due to strong σ-donating, π-donating and electrostatic properties from the anionic, aromatic carbon donor. Due to the increased electron donation ability of the carbanion, the opposite Ru-N6 bond becomes elongated as a result of the trans effect.[149-150]

The Ru-N1 and Ru-N4 bonds from the adjacent triazole to the ruthenium are slightly elongated from 2.06 Å to 2.08 Å, which is most likely due to reduced σ orbital overlap caused by the

smaller bite angle[28]. The Ru-N5 and Ru-N7 bonds between the ruthenium and the peripheral nitrogen atoms on the terpyridine ligand are also shortened upon cyclometalation, with bond lengths of 2.10 Å and 2.09 Å for **4.45** and **4.6** respectively due to increased π back donation from the more electron rich metal onto the terpyridine ligand.

The rest of the calculated structures for the complexes in this series (**4.1**-**4.8**) show only very small differences in the bond lengths (Table 4.48). The Ru-C bond length is 2.01 Å and the opposite Ru-N bond length is 2.03 Å in all of the complexes (**4.1**-**4.8**). The bond lengths between the ruthenium and the two triazoles on the cyclometalated ligand (Ru-N1 and Ru-N4, Figure 4.10) are all 2.03 Å (Table 4.7) and the peripheral bond lengths between the ruthenium and the side pyridines on the terpyridine ligand (Ru-N5 and Ru-N7, Figure 4.10) are all 2.09 Å (Table 4.7).

Complex	C-Ru-N5	C-Ru-N6	C-Ru-N7	N2-Ru-N4	N5-Ru-N7	Dihedral A	Dihedral B
4.1	101.64	179.94	101.52	155.24	156.85	N/A	N/A
4.2	101.69	179.89	101.87	155.31	156.44	N/A	33.21
4.3	101.61	179.97	101.55	155.27	156.84	1.68	N/A
4.4	101.63	179.96	101.51	155.23	156.86	26.65	N/A
4.5	101.95	179.77	101.60	155.37	156.46	22.58	33.24
4.6	101.62	179.89	101.85	155.37	156.53	89.70	33.71
4.7	101.56	179.87	101.55	155.26	156.89	87.23[a]	N/A
4.8	101.47	179.70	102.02	155.36	156.51	88.27[a]	33.79
4.45	100.79	179.88	101.08	156.48	158.12	87.63	N/A

Table 4.8: Calculated bond angles for complexes **4.1**-**4.8** from DFT calculations in vacuo. Dihedral A is the dihedral angle between the substituted aryl group and the triazole ring on the cyclometalated ligand. Dihedral B is the dihedral angle between the central pyridine ring and the substituted aryl group on the terpyridine ligand. (a) Dihedral angle A applies to conjugated mesityl group only due to asymmetric cyclometalated ligand.

The bite angle of the cyclometalated ligand onto the ruthenium (N1-Ru-N4, Figure 4.10) for complex **4.6** is 155.37° and is reduced slightly compared to the corresponding non cyclometalated complex, **4.45**, which has a calculated angle of 156.48°. The bite angle is reduced as the central Ru-N/Ru-C bond length on the substituted triazole ligand increases due to the geometric constraints of the ligand. There is only a small change in the calculated Ru-C bond lengths for **4.1**-**4.8**, which results in only a small change in the bite angle, which range from 155.23°-155.37° (Table 4.8).

The chelate bite angle of the terpyridine ligand onto the ruthenium (N5-Ru-N7, Figure 4.10) for **4.6** is 156.53° and is smaller than the chelate bite angle for the corresponding non cyclometalated complex, **4.45**, which has an angle of 158.12°. This occurs due to the slight elongation of the Ru-N6 bond length, which decreases the chelate bite angle due to geometric constraints of the terpyridine. The chelate bite angle in complexes **4.1**-**4.5 and 4.7**-**4.8** are all within 0.23% of the value for **4.6**, and are thus their chelate bite angles are considered equivalent.

Complex	Cyclometalated Ligand			Terpyridine Ligand		
	N2-Ru	C-Ru	N4-Ru	N5-Ru	N6-Ru	N7-Ru
4.9	2.10563	1.98782	2.10563	2.09392	2.0317	2.09393
4.10	2.10596	1.98813	2.10596	2.09333	2.03112	2.09332
4.11	2.10508	1.98786	2.10465	2.09422	2.03269	2.09313
4.12	2.10427	1.98839	2.10461	2.09413	2.03223	2.09338
2.1	2.10590	1.99121	2.10580	2.0915	2.03081	2.09136

Table 4.9: Calculated bond lengths for **4.9**-**4.12** and parent complex **2.1** from DFT calculations *in vacuo*.

All of the Ru-C bond lengths for complexes **4.9**-**4.12** are shorter than for the parent complex, **2.1**. This indicates that there is more electron density in the bond, making it stronger and thus shorter. The calculated Ru-C bond lengths vary between 1.98839 Å and 1.98782 Å, compared to the value of 1.99121 Å for **2.1**.

This results in the Ru-N6 bond length being slightly elongated in complexes **4.9**-**4.12** compared to **2.1** as a result of the trans effect.[149-150] The Ru-N6 bond length in **4.9**-**4.12** varies from 2.03112 Å to 2.03269 Å and these are all longer than the bond length for **2.1**, which has a calculated value of 2.03081 Å. This shows that there is an inverse relationship between these two bond lengths, as the complexes with the shorter Ru-C bond lengths have longer Ru-N6 bond lengths.

The Ru-N5 and Ru-N7 bonds, which incorporate the peripheral pyridines on the terpyridine ligand are shortened compared the corresponding bond length in similar non-cyclometalated complexes as a result of increased π-back donation from the more electron rich ruthenium in the cyclometalated complex, which supports the observed CIS in the ^{1}H NMR spectra. There is no significant change in the Ru-N5 and Ru-N7 bond lengths for **4.9**-**4.12** however compared to **2.1**, which have values between 2.09136 Å and 2.09313 Å, which are all within 0.09% of the values of Ru-N5 and Ru-N7 for **2.1** (2.09422 Å and 2.09313 Å respectively). There is no significant

change in the Ru-N2 and Ru-N4 bond lengths for **4.9**-**4.12** compared to **2.1** either, which have values between 2.10427 Å 2.10596 Å, which are all within 0.08% of the values of Ru-N5 and Ru-N7 for **2.1** (2.10590 Å and 2.10580 Å respectively).

Complex	C-Ru-N5	C-Ru-N6	C-Ru-N7	N2-Ru-N4	N5-Ru-N7	Dihedral A	Dihedral B
4.9	101.67	180.00	101.67	154.87	156.66	22.07	67.74
4.10	101.66	180.00	101.66	154.81	156.67	20.91	68.45
4.11	101.80	179.75	101.66	154.95	156.54	44.52	33.83
4.12	101.57	179.85	101.80	154.89	156.62	46.09	68.44
2.1	101.53	180.00	101.52	154.94	156.95	N/A	N/A

Table 4.10: Calculated bond angles for complexes **4.9**-**4.12** from DFT calculations *in vacuo*. Dihedral A is the dihedral angle between the substituted aryl group and the triazole ring on the cyclometalated ligand. Dihedral B is the dihedral angle between the central pyridine ring and the substituted aryl group on the terpyridine ligand.

There are only negligible changes that occur in the key bond angles from the calculated structures for **4.9**-**4.12** (Table 4.10), compared to the parent structure **2.1**. The chelate bite angles for the cyclometalated ligand and the ruthenium atom (N2-Ru-N4) in **4.9**-**4.12** are within 0.08% of the value for 154.94° for **2.1**. The chelate bite angles for the terpyridine ligand and the ruthenium atom (N5-Ru-N7) in **4.9**-**4.12** are slightly smaller than **2.1** due to the slight elongation of the Ru-N6 bond length, with values ranging from 156.67° to 156.54°. This relationship is due to the geometric constraints of the terpyridine ligand, in which an elongated Ru-N6 bond length results in a smaller bond angle for N5-Ru-N7.

The angles for dihedral A and dihedral B show the twisting between the core structure and the substituted aryl groups. The phenyl rings substituted to each pyrazole on the cyclometalated ligand in **4.9** and **4.10** are calculated to be twisted by ca. 21-22°. The naphthyl group on each pyrazole on the cyclometalated ligand in **4.11** and **4.12** is calculated to be further twisted, with a value of ca. 45°. The phenyl ring substituted onto the terpyridine ligand in **4.11** is calculated to twist by ca. 34° and the anthracene substituted onto the terpyridine ligand in **4.9**, **4.10** and **4.12** is calculated to twist by ca. 68°. These orientations minimize the steric hindrance by twisting the aryl rings out of the plane.

4.6 Crystal Structure Determination.

*4.6.1 Crystal structure of **4.44***

Dark red crystals suitable for X-ray analysis of **4.44** (Figure 4.11) were grown by slow evaporation of a solution containing a crude reaction mixture of **4.44** dissolved in an acetone/toluene mixture. While only a small quantity of pure **4.44** was obtained, which limited further analysis, a single crystal was successfully characterized by X-ray diffraction. The structure solved in the monoclinic space group $P2_1/n$ and contained one molecule of complex **4.44**, one hexafluorophosphate anion and a toluene solvate molecule in the asymmetric unit.

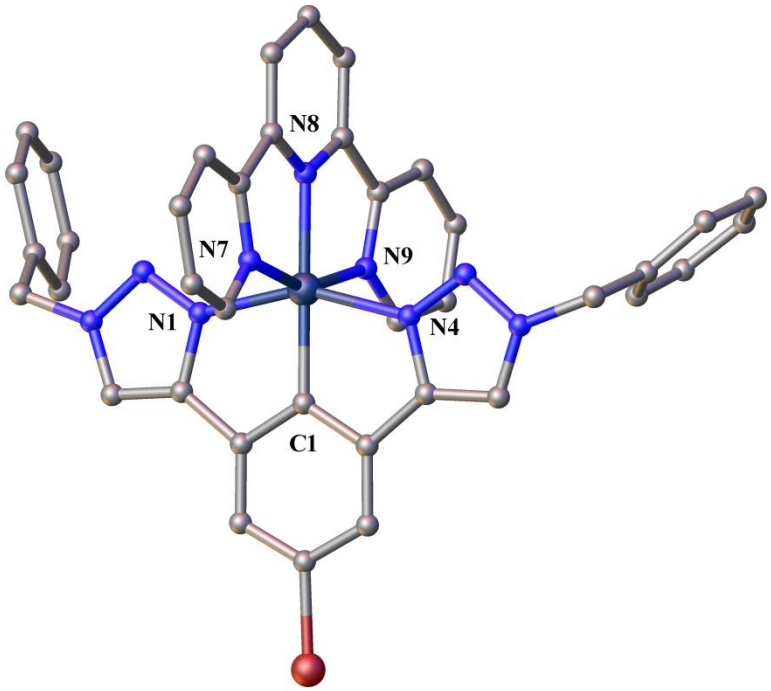

Figure 4.11: Crystal structure of complex **4.44**. Hydrogen atoms, counterions and the solvate molecules are omitted for clarity. Selected bond distances (Å): Ru1-N1 2.091(7), Ru1-C1 1.990(10), Ru1-N4 2.095(8), Ru1-N7 2.083(7), Ru1-N8 2.014(8), Ru1-N9 2.081(8). Selected bond angles (°):C1-Ru1-N7 103.9(3), C1-Ru1-N8 178.7(3), C1-Ru1-N9 99.9(3), N1-Ru1-N4 155.3(3), N7-Ru1-N9 155.9(3).

The replacement of the dative Ru-N bond with a covalent, organometallic Ru-C bond leads to shortening of this bond length, as shown by the Ru-C bond length of 1.990(10) Å. This is a result of σ-donation and additional π-donation, as well as electrostatic interactions with the anionic, aromatic carbon donor. The opposite Ru-N8 bond length is elongated due to the trans effect in

relation to shortened Ru-C bond length and has a value of 2.014(8) Å. The crystal structure of a comparable non-cyclometalated ruthenium complex, **4.45**, shows a bond length of 2.017(3) Å between the central nitrogen on the substituted bis(triazolyl)pyridine ligand and the ruthenium. The crystal structure shows that the Ru-N bond opposite, between the central pyridine on the terpyridine ligand and the ruthenium atom, has a bond length of 1.972(3) Å, showing the elongation of the bond length in **4.44**. The other Ru-N bond lengths only show small changes in bond lengths between **4.45** and **4.44**, but since the structures are not directly comparable these bond lengths may vary due to other effects such as packing effects rather than electronic effects. Previous work by Schulze et al. have shown that in comparable structures the outer pyridine Ru-N bonds are shortened as a result of increased π back donation from the more electron rich ruthenium center in the cyclometalated complex compared to a corresponding non-cyclometalated ruthenium complex. The outer triazole Ru-N bonds are elongated as a result of increased p back donation into p* antibonding orbitals. The bond elongation is also the result reduced σ orbital overlap by the smaller chelate bite angle between each of the triazole nitrogens and the ruthenium.[28] The chelate bite angles for the cyclometalated ligand (N1-Ru-N4) and the terpyridine ligand are 155.3(3)° and 155.9(3)° and these show that each ligand is coordinated in a tridentate, meridional fashion to the ruthenium(II) ion, giving the complex its distorted octahedral geometry.

*4.6.2 Crystal structure of **4.1***

Slow diffusion of petroleum ether into an acetone solution of the complex gave dark red crystals of **4.1** suitable for X-ray crystallography. Complex **4.1** (Figure 4.12) crystallized in the monoclinic space group $P2_1/c$. The asymmetric unit contains one molecule of **4.1** and one hexafluorophosphate anion. The structure is well resolved except for the 4-^{t}butylbenzyl group on one side the cyclometalated ligand being disordered over two positions through the free rotation of the CH_2 between the triazole and aryl group.

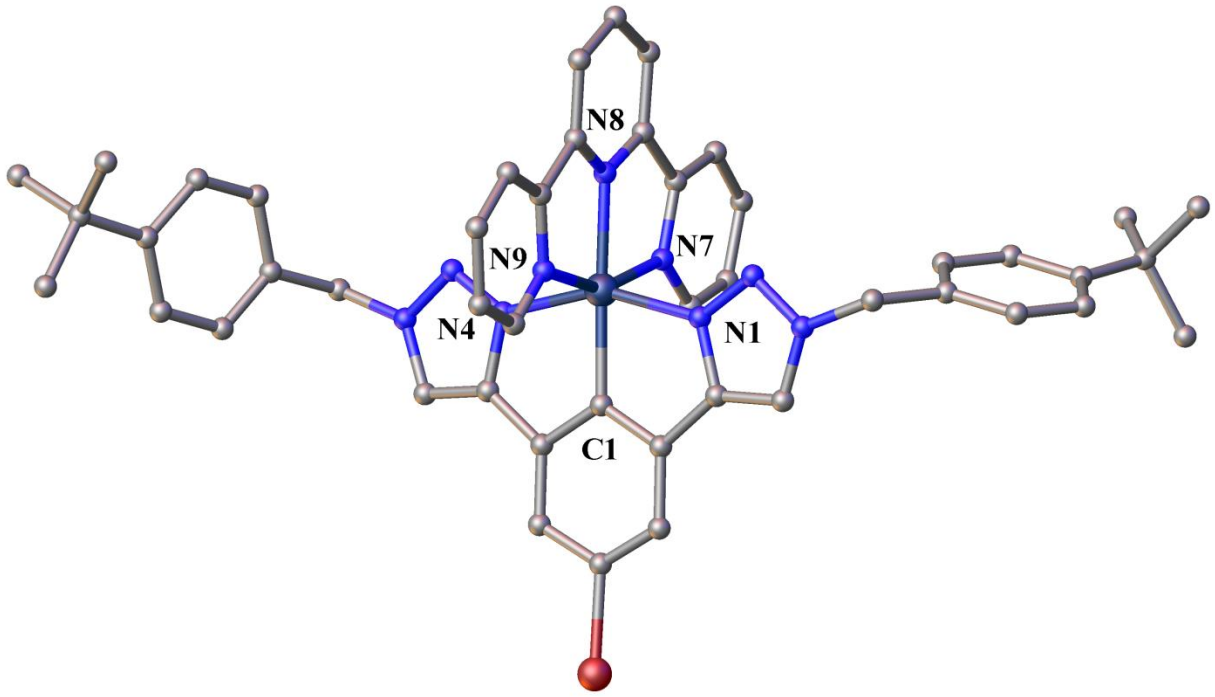

Figure 4.12: Crystal structure of complex **4.1**. Hydrogen atoms, counterions and the solvate molecules are omitted for clarity. Selected bond distances (Å): Ru1-N1 2.060(4), Ru1-C1 1.995(5), Ru1-N4 2.095(4), Ru1-N7 2.071(5), Ru1-N8 2.028(4), Ru1-N9 2.079(4). Selected bond angles (°): C1-Ru1-N7 102.7(2), C1-Ru1-N8 177.3(2), C1-Ru1-N9 101.3(2), N1-Ru1-N4 155.5(2), N7-Ru1-N9 155.9(2).

The crystal structure of **4.1** (Figure 4.12) is very similar to **4.44** due to the large parts of the complex which are the same. This results in all the key bond lengths for the Ru-N and Ru-C bonds being comparable except for the Ru-N8 bond length which is slightly longer and has a value of 2.028(4) Å compared to the 2.014(8) Å bond length in **4.44**. The difference is not large and so it likely results from crystal packing effects.

The structure calculated using DFT calculations for **4.1** shows comparable bond lengths and angles except that the bond lengths are slightly longer than the values from the X-ray structures. This is a result of the DFT calculations tending to slightly overestimate bond lengths, which has been tentatively explained by Hiberty and co-workers as a result of from electron self-interaction in the DFT calculation process, which leads to slightly high energies for the bonds and thus they are expressed as being slightly elongated. In similar structures these factors are observed as a systematic error in the bond lengths and related properties.[151]

4.7 Photophysical properties of ruthenium complexes.

Polypyridine ruthenium(II) complexes are characterized by generally having medium intensity absorptions in the visible region which are traditionally assigned as being MLCT transitions[157]. The transitions are in fact a collection of mixed metal/ligand to ligand charge transfer arising from the HOMO being largely metal based but also mixing with part of one, or both ligands. Despite this, transitions are described as being MLCT as it offers the most concise description. Polypyridine ruthenium(II) complexes are also characterized by their strong $\pi \rightarrow \pi^*$ transitions in the UV region and in the case of these cyclometalated ruthenium complexes there are several strong intraligand absorptions owing to the two substantially different ligands systems.

The ruthenium(II) complexes investigated in this chapter (**4.1**-**4.12**) all show broad MLCT transitions between 450 and 600 nm, with a distinct λ_{max} between 477 nm (**4.4**) and 494 nm (**4.5**). There is also a shoulder between 500 nm and 540 nm, and another much smaller shoulder between 560 nm and 620 nm. A second MLCT envelope is generally seen between 340 nm and 410 nm. This MLCT is also of medium intensity, similar to the lower energy MLCT, although it is not as clearly defined due to a large number of transitions, especially the ligand centered π-π^* transitions resulting from anthracene in complexes **4.9**, **4.10** and **4.12**. Another reason this 2nd MLCT appears less well defined is because of the intense transition at slightly higher energy, obscuring the peak profile. The remaining transitions for these ruthenium complexes are between 200-300 nm and are assigned be being predominantly strong LC ($\pi \rightarrow \pi^*$) transitions.

As there are a large number of overlapping transitions occurring which cannot be easily assigned, computational calculations were carried out to aid understanding. Density functional theory (DFT) calculations were used in parallel with experimental UV-vis analysis (Chapter 2.7.1).

*4.7.1 Complexes **4.1**-**4.2***

Complex	absorption 298 K, MeCN, λ_{max} (nm) ($\varepsilon(10^3\ M^{-1}\ cm^{-1})$)
4.1	528 (5.5), 483 (6.6), 368 (9.4), 315 (26.5), 273 (24.3), 229 (49.4)
4.2	530 (6.8), 489 (7.7), 371 (11.1), 313 (27.3), 284 (31.7), 227 (55.5)

Table 4.11: Electronic absorption data for complexes **4.1**-**4.2**.

The UV-vis spectra for **4.1** and **4.2** are shown in Figure 4.13 along with their corresponding TD-DFT data. The measured UV-vis spectra shows that the lowest energy MLCT has a peak at 483 nm (ε = 6,600) for **4.1** and 489 nm (ε = 7,700) for **4.2**. Both of these peaks are very broad and have distinct shoulders between 520 nm and 550 nm, in which the shoulder for **4.2** is red shifted and at higher intensity compared to **4.1**. Analysis of the TD-DFT calculations for **4.1** shows three transitions in the range of the lowest energy MLCT envelope. The largest transition is calculated to occur at 465.0 nm and corresponds to a HOMO-2 → LUMO transition, which is assigned as corresponding to the experimental λ_{max}. The other two calculated transitions occur at similar energy to the two shoulders, with the HOMO-2 → LUMO+1 transition occurring at 518.9 nm and the HOMO-2 → LUMO transition occurring at 595.2 nm. Analysis of the isodensity plots for **4.1** from the TD-DFT results shows the HOMO-1 is primarily metal based with a small contribution from both ligands, but there is no contribution from the substituted benzyl attached to triazole. The isodensity plot for the HOMO-2 (Figure 4.14) shows that the electron density is also predominantly metal based but a small amount of electron density is also on terpyridine ligand. The isodensity plot for the LUMO (Figure 4.14) shows that electron density is largely based on the terpyridine ligand, with a small amount on the metal and the LUMO+1 is solely based on the terpyridine ligand. This shows all three transitions are all MLCT transitions, but they are different types of mixed metal/ligand to ligand charge transfer.

Analysis of the TD-DFT calculations for the lowest energy MLCT for **4.2** shows three similar transitions compared to **4.1**, at 468.0 nm, 522.7 nm and 581.4 nm, but also an additional transition at 539.5 nm. As was the case with **4.1**, the largest calculated transition is at 468.0 nm and represents the $\lambda_{max,}$ while the transitions at 522.7 nm and 539.5 nm both relate to the large shoulder and the small transition at 581.4 nm relates to the very small 2nd shoulder. The extra transition in **4.2** relates to the first shoulder and explains the extra broad nature that is observed in the measured UV-Vis. The transition relating to the λ_{max} results from a HOMO-2 → LUMO+1 transition in which the HOMO-2 has a dominant contribution from the metal and a small contribution from the cyclometalating ligand and the LUMO+1 only has contribution from the terpyridine ligand. The energy of the HOMO-2 involved in both transitions for **4.1** and **4.2** is very similar and thus does not account for the red shift observed in **4.2**, instead the shift most likely results from a change in the energy for the LUMO as a result of the aryl substituted terpyridine ligand. This follows the result from chapter three in which **3.1** had a red shift

compared to **2.1** when the terpyridine ligand had a 4-^{t}butylphenyl group added in the 4' position of the central pyridine ring. Extending the terpyridine in **4.2** also has the effect of increasing the absorption of the lowest energy MLCT envelope compared to **4.1**.

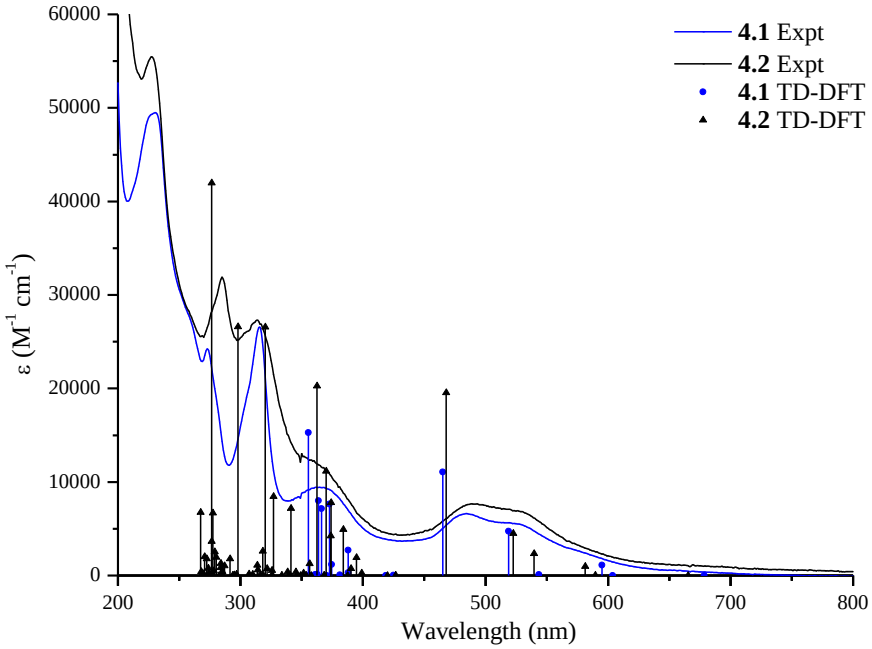

Figure 4.13: Electronic absorption spectra of complexes **4.1**-**4.2** and TD-DFT data for **4.1**-**4.2** *in vacuo*.

S_n	E/nm	f	Dominant Transition			Percentage Contribution
4.1						
S1	678.6	0.000	HOMO	→	LUMO	96
S3	595.2	0.011	HOMO -1	→	LUMO	92
S5	518.9	0.047	HOMO -2	→	LUMO +1	92
S6	465.0	0.111	HOMO -2	→	LUMO	51
4.2						
S1	665.3	0.000	HOMO	→	LUMO	97
S3	581.4	0.010	HOMO-2	→	LUMO	92
S4	539.5	0.023	HOMO-1	→	LUMO	52
S5	522.7	0.045	HOMO-1	→	LUMO+1	91
S6	468.0	0.196	HOMO-2	→	LUMO+1	52

Table 4.12: Selected calculated UV-vis transitions from TD-DFT calculations for **4.1** and **4.2** *in vacuo* over the range of 450-800 nm (1st MLCT).

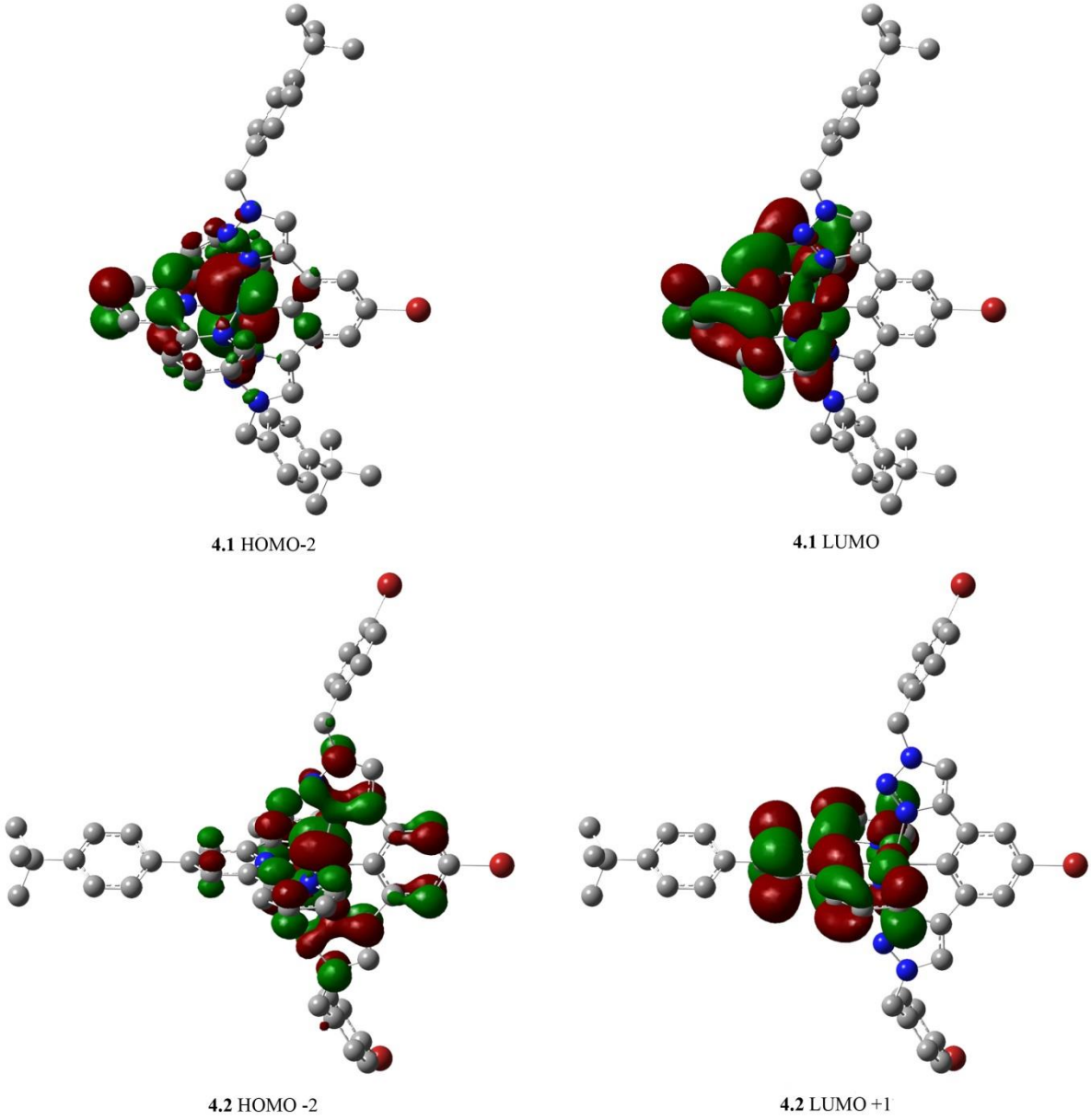

Figure 4.14: Isodensity plots (isovalue 0.02) of selected frontier orbitals that are involved in the dominant transition for the lowest energy MLCT for **4.1** and **4.2** from DFT calculation *in vacuo*.

The 2nd lowest energy peak for complexes **4.1** and **4.2** occurs between 340 nm and 400 nm. In complex **4.1** there is a distinct peak at 368 nm (ε = 9,400) while in **4.2** it appears as a broad shoulder between 350 nm and 380 nm (ε ≈ 13,000-9,500). Due to the obscured peak in **4.2** it is difficult to comment on blue/red shifts however there is a small hyperchromic shift in **4.2** compared to **4.1**. TD-DFT calculations run for these two complexes show five significant

transitions within this range for **4.1** and seven for **4.2**. Also the range of these transitions is greater for **4.2**, with the five transitions spread over 53.5 nm for **4.2**, compared to only 32.6 nm for **4.1**. These two factors result in a distinct peak in **4.1** and a broad peak, which presents as a shoulder due to the neighboring higher energy peak, in **4.2**. Due to the large number of transitions in this small range, assigning specific details of the isodensity plots (Chapter 7.3, Figures 7.3.23-7.3.24) is difficult, although they do show that all the transitions within the range are different types of MLCT transitions.

For the relevant occupied orbitals in **4.1**, the HOMO is predominantly metal based, but extends over the central conjugated part of the cyclometalated ligand, but not the benzyl group on each triazole. The HOMO-1 is also predominantly metal based but has a small contribution from the central part of both ligands, with no contribution from the benzyl groups once again. For the relevant unoccupied orbitals, the LUMO+2 and LUMO+3 are based just on the terpyridine and the LUMO+4 and LUMO+6 are based on the central part of the cyclometalated ligand and not out into the non-conjugated part of the ligand.

The occupied orbitals for **4.2** follow a similar pattern in which all three relevant orbitals, HOMO, HOMO-1 and HOMO-2 are all mainly metal based, with the HOMO having a small contribution from the central part of the cyclometalated ligand, the HOMO-1 having a small contribution from the entire substituted terpyridine ligand and the HOMO-2 having a small contribution from the central parts of both ligands. For the relevant unoccupied orbitals for **4.2**, the LUMO+2 and LUMO+3 both have contribution from just the terpyridine ligand and the LUMO+4, LUMO+5 and LUMO+7 all have contribution from just the central part of the cyclometalating ligand, but no significant contribution from the benzyl group. This shows that despite the large number of calculated transitions, they are all different types of MLCT also, and not LMCT or MC transitions, which can also potentially occur in this wavelength range.[158]

S_n	E/nm	f	Dominant Transition			Percentage Contribution
4.1						
S10	387.9	0.027	HOMO	→	LUMO +4	77
S13	372.6	0.077	HOMO -1	→	LUMO +3	41
S15	366.2	0.072	HOMO -1	→	LUMO +2	44
S16	363.7	0.080	HOMO	→	LUMO +6	39
S20	355.3	0.153	HOMO	→	LUMO +6	44
4.2						
S10	394.7	0.019	HOMO	→	LUMO+5	74
S13	383.8	0.049	HOMO-1	→	LUMO+3	75
S14	374.0	0.078	HOMO-2	→	LUMO+2	58
S15	373.6	0.042	HOMO	→	LUMO+7	52
S16	369.9	0.112	HOMO-2	→	LUMO+3	57
S18	362.5	0.203	HOMO-2	→	LUMO+4	54
S26	341.2	0.072	HOMO-3	→	LUMO	54

Table 4.13: Selected calculated UV-vis transitions from TD-DFT calculations for **4.1**-**4.2** *in vacuo* over the range of 340-400 nm (2nd MLCT).

*4.7.2 Complexes **4.3**-**4.6***

Complex	absorption 298 K, MeCN, λ_{max} (nm) ($\varepsilon(10^3\ M^{-1}\ cm^{-1})$)
4.3	516 (3.7), 476 (4.2), 379 (9.4), 314 (19.0), 300 (17.5), 272 (23.4), 246 (38.0)
4.4	517 (5.2), 479 (6.0), 374 (12.9), 313 (28.3), 301 (27.7), 255 (41.9), 236 (41.7)
4.5	521 (7.2), 489 (7.6), 367 (13.8), 314 (23.9), 285 (35.1), 245 (46.1)
4.6	530 (8.4), 494 (8.8), 363 (14.9), 314 (28.6), 284 (36.8), 276 (32.7), 233 (61.6)

Table 4.14: Electronic absorption data for group two complexes (**4.3**-**4.6**).

The UV-vis spectra for **4.3**, **4.4**, **4.5** and **4.6** are shown in Figure 4.15 and their corresponding TD-DFT data is shown in Figure 4.16. The measured UV-vis spectra shows that the lowest energy MLCT has a peak at 476 nm (ε = 4,200) for **4.3**, 479 nm (ε = 6,000) for **4.4**, 494 nm (ε =8,800) for **4.5** and 489 nm (ε = 7,600) for **4.6**. All four complexes also have a distinct shoulder between 520 nm and 550 nm, which all have an equal systematic shift compared to their main peak. These results show that changing the N-heterocycle from substituted benzyl (**4.1**, 483 nm) to substituted phenyl (**4.3**, 476 nm), in which the aryl ring is directly attached to the triazole results in a blue shift of 7 nm for the lowest energy MLCT in each. There is also a small

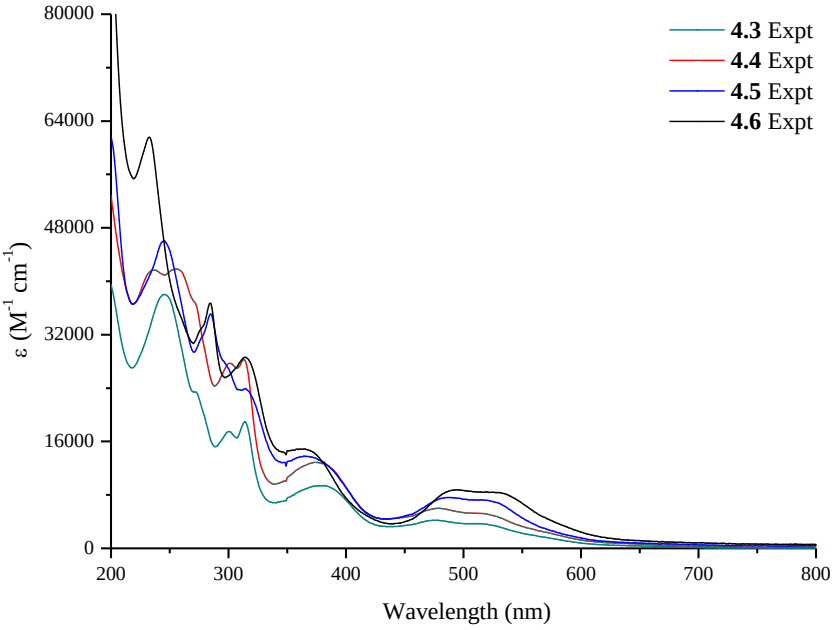

Figure 4.15: Electronic absorption spectra of complexes **4.3**-**4.6**.

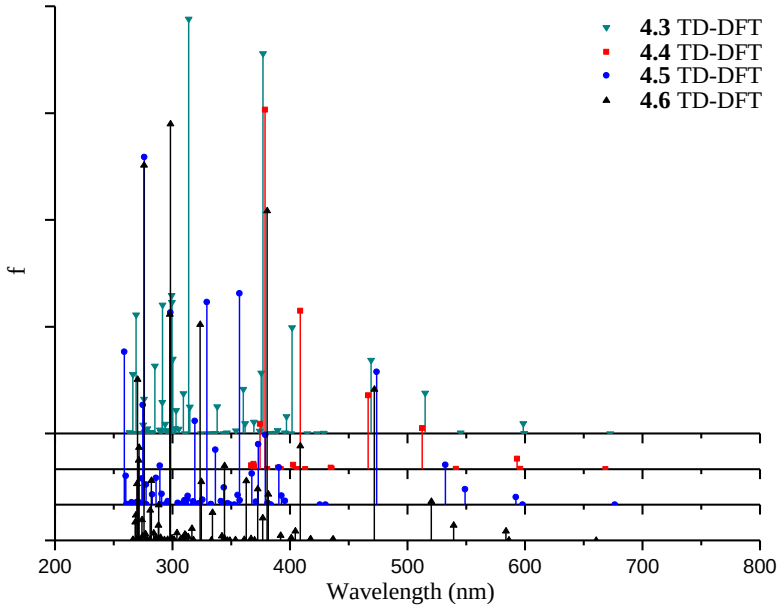

Figure 4.16: Calculated TD-DFT data for **4.3**-**4.6** in vacuo.

hypochromic shift for **4.3** (ε = 4,200) compared to **4.1** (ε = 6,600), showing the effect of using conjugated aryl groups off the N-heterocycle on the cyclometalated ligand.

TD-DFT calculations for **4.3** were run *in vacuo* and show three transitions within the range of the lowest energy peak envelope, the 1st at 469.0 nm which corresponds to the λ_{max}, the 2nd at 515.0 nm which corresponds to the 1st observed shoulder at lower energy and a 3rd transition at 598.4 nm which corresponds to a 2nd much smaller shoulder at even lower energy, which was observed in previous complexes, but is obscured in **4.3**. The transition related to the λ_{max} for **4.3** results from a HOMO-2 → LUMO transition, the same result as **4.1**. The isodensity plot of the HOMO-2 shows electron density is predominately on the metal, with a small amount on the central pyridine of the terpyridine ligand, almost identical to the HOMO-2 in **4.1**. The difference however is that the energy of the HOMO-2 in **4.3** is lower than in **4.1**. The LUMO in **4.3**, which just incorporates the terpyridine ligand, is equivalent to **4.1** and has similar energy to it. The net result of this is a transition with higher energy, resulting in the observed blue shift for **4.3** compared to **4.1**.

Complex **4.4**, in which the 4-tertbutylphenyl (**4.3**) is changed to 4-methoxyphenyl on the substituted triazole, results in a small red shift relative to **4.3** and a small hyperchromic shift. The TD-DFT calculations for **4.4** are very similar to **4.3** and show a negligible difference for the main calculated peak in the lowest energy MLCT, compared to **4.4**. The electron donating methoxy group substituted onto the N-heterocycle does not appear to have a substantial effect on either the HOMO-2 or LUMO, the corresponding orbitals for this transition. This follows previous results which show that when 4-methoxyphenyl is substituted into a system there is only a minimal effect on the lowest energy MLCT.

Complex **4.5** incorporates 4-methylphenyl instead of 4-tertbutylphenyl as the N-heterocycle on the cyclometalated ligand and also has the 4-tertbutylphenyl substituted terpyridine, as was used for **4.2**. This results in both a red shift and a hyperchromic shift for **4.5** compared to **4.3**, a similar result as was seen for **4.2** compared to **4.1** previously, for which a red shift was observed due to the aryl substituted terpyridine ligand. The TD-DFT calculations show four transitions, three transitions similar to those observed for **4.3** and **4.4**, and also another transition which appears to increase broad profile of the lowest energy MLCT envelope even further. The main transition for

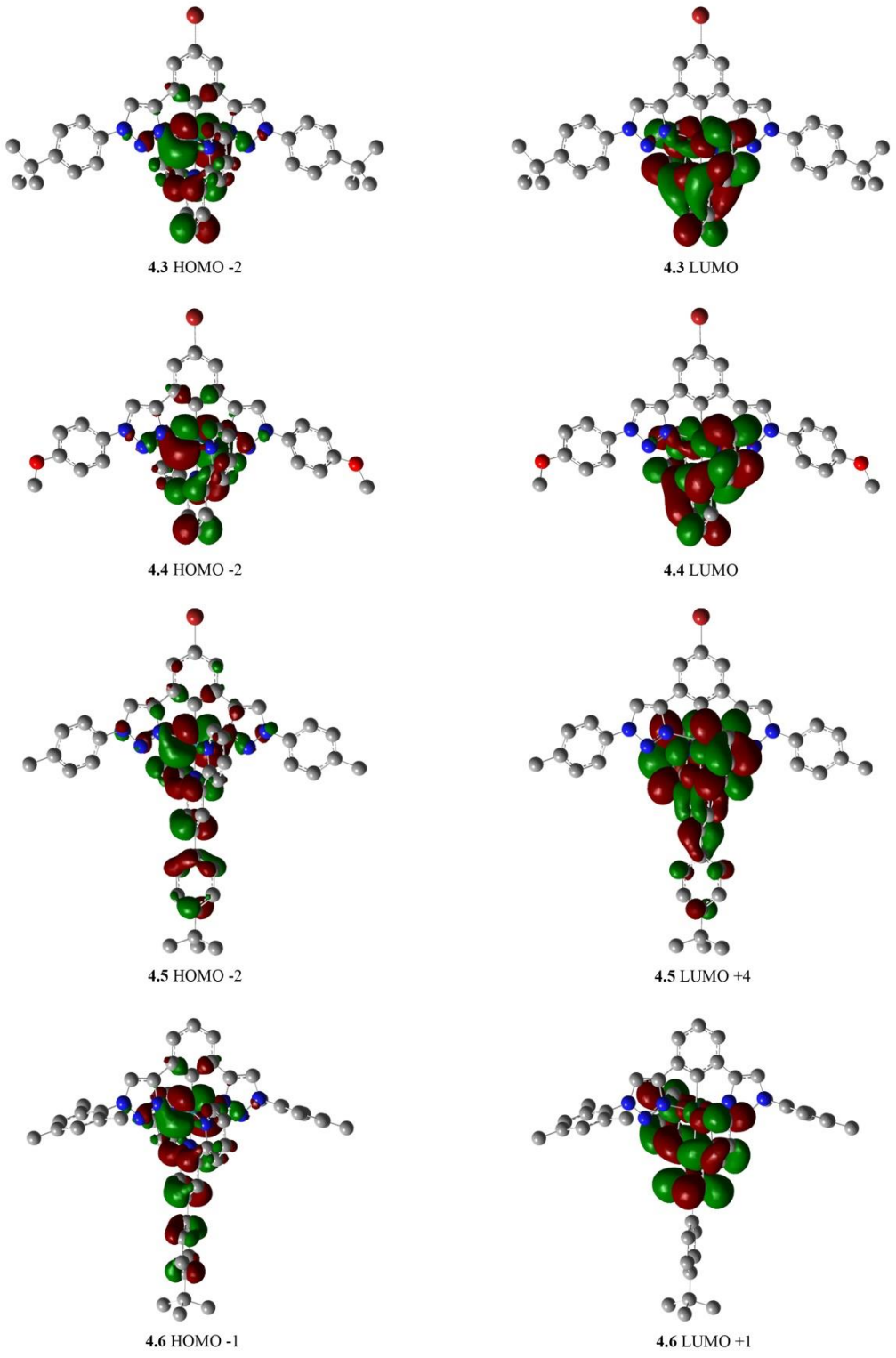

Figure 4.17: Isodensity plots (isovalue 0.02) of selected frontier orbitals that are involved in the dominant transition for the lowest energy MLCT for **4.3-4.6** from DFT calculation *in vacuo*.

4.5 results from a HOMO-2 → LUMO+1 transition, in which the isodensity plots for the terpyridine ligand, not including on the terpyridine ligand, not including on the substituted aryl group. The energy of the HOMO-2 and LUMO+1 are significantly increased compared to previous complexes, which a slightly large increase in the energy of the HOMO-2. This gives a smaller energy difference between the HOMO-2 and LUMO+1, which results in the observed red shift for **4.5** compared to **4.3**.

Complex **4.6**, in which the 4-methylphenyl (**4.5**) is changed to a mesitylene substituted triazole on the cyclometalated ligand, shows a further red shift compared to complexes **4.3**-**4.5** in this series and also another small hyperchromic shift. The TD-DFT calculations for **4.6** are similar to **4.5**, in which there are four transitions making up the broad lowest energy MLCT envelope. The largest calculated transition results from a HOMO-1 → LUMO+1 transition, in which the HOMO-1 has electron density is predominately on the ruthenium atom but also on the central pyridine ring and substituted phenyl ring. The LUMO+1 has electron density only on the terpyridine ligand, without any electron density on the attached aryl ring. The energy of the HOMO-1 is higher in **4.6** compared to **4.3** and **4.4** but lower than **4.5** and the energy of the LUMO+1 is slightly lower than in **4.5**. The net result of this is a transition with lower energy than for the comparable transitions in complexes **4.3**-**4.5**, and thus the observed red shift.

The 2nd lowest MLCT occurs between 340 nm and 440 nm for complexes **4.3**-**4.6**. All four complexes show distinct peaks in this region at 379 nm (ε = 9,400) for **4.3**, 374 nm (ε = 12,900) for **4.4**, 367 nm (ε = 13,800) for **4.5** and 363 nm (ε = 12,900) for **4.6**. This means there is an observed a red shift for the λ_{max} in **4.3** compared to **4.1** and also an increase in absorption at this wavelength. TD-DFT calculations for **4.3** show four transitions within the range of this peak envelope, in which the dominant transition is calculated to occur at 376.9 nm, resulting from a HOMO → LUMO+6 transition. The electron density on the HOMO is predominantly on the metal, but there is also a significant amount spread over the central part of the cyclometalated ligand. The LUMO+6 has a small amount of electron density remaining on the metal, although the majority is spread over the entire cyclometalating ligand. The orbital energy diagram (Chapter 7.4, Figure 7.4.1) shows that the energy of the HOMO is very similar in **4.3** as it is in **4.1**, due to the electron density being predominantly on the metal in both complexes, with only a small amount spread over the core of the cyclometalating ligand, which is similar in both

complexes. The energy of the LUMO+6 on the other hand is significantly lower for **4.3** compared to **4.1** because the energy is spread into the phenyl ring directly attached to the N-heterocycle in **4.3** whereas in **4.1** it is limited to just the two triazole rings on the cyclometalating ligand. This results in the net energy of the transitions being lower, which results in the observed red shift (Chapter 7.4, Figure 7.4.2).

S_n	E/nm	f	Dominant Transition			Percentage Contribution
4.3						
S1	672.5	0.000	HOMO	→	LUMO	93
S3	598.4	0.012	HOMO-1	→	LUMO	89
S5	515.0	0.046	HOMO-2	→	LUMO+1	90
S6	469.0	0.083	HOMO-2	→	LUMO	56
4.4						
S1	668.5	0.000	HOMO	→	LUMO	97
S3	593.2	0.012	HOMO -1	→	LUMO	93
S5	512.6	0.046	HOMO -2	→	LUMO +1	94
S6	466.6	0.083	HOMO -2	→	LUMO	56
4.5						
S1	676.4	0	HOMO	→	LUMO	98
S3	592.2	0.0086	HOMO-2	→	LUMO	90
S4	549.1	0.0173	HOMO-1	→	LUMO	51
S5	532.2	0.0446	HOMO-1	→	LUMO+1	90
S6	473.7	0.1491	HOMO-2	→	LUMO+1	51
4.6						
S1	660.5	0.000	HOMO	→	LUMO	97
S3	583.6	0.011	HOMO-1	→	LUMO	80
S4	539.2	0.017	HOMO-1	→	LUMO+1	40
S5	520.2	0.044	HOMO-2	→	LUMO+1	78
S6	471.8	0.170	HOMO-1	→	LUMO+1	41

Table 4.15: Selected calculated UV-vis transitions from TD-DFT calculations for **4.3**-**4.6** *in vacuo* over the range of 450-800 nm (1^{st} MLCT).

The peak in complex **4.4** (374 nm) is blue shifted compared to **4.3** (379 nm) and also has a greater absorbance at this wavelength. TD-DFT calculations show that it is also the HOMO →

LUMO+6 transition that is dominant, as was the case for **4.1** and **4.3**. The isodensity plots show that the HOMO has electron density predominantly on the metal, with a small amount spread over the core of the cyclometalated ligand, as was the case for **4.1** and **4.3** (Chapter 7.3, Figure 7.3.1). The electron density on the LUMO+6 (Chapter 7.3, Figure 7.3.2) is spread over the entire cyclometalated ligand, similar to **4.2**, but there is negligible electron density on the methoxy group, resulting in the electron donating group having little effect on the energy of the orbital, thus the energy of the LUMO+6 for **4.4** is very similar to the energy of the LUMO+6 for **4.3**. This results in only a small change in the energy of the transition for **4.4**, with the methoxy substituted N-heterocycle, compared to **4.3** (Chapter 7.4, Figure 7.4.3).

The peak in complex **4.5** (367 nm) is blue shifted compared to both **4.3** (379 nm) and **4.4** (374 nm) and there is also a hyperchromic shift. This envelope is the broadest of these four complexes, and the reasons for this are clear upon analysis of the corresponding TD-DFT calculation, which shows five transitions of similar strength and several other smaller transitions. Analysis of these transitions is difficult due to the large number of them and thus rationalizing the blue shift is difficult, however some similarities are present. They all include either the HOMO, HOMO-1 or HOMO-2 which are all predominately metal based with the HOMO also having electron density on the core of the cyclometalated ligand, the HOMO-1 also having electron density on parts of both ligands and the HOMO-2 also having electron density on the central pyridine and benzene ring of the terpyridine ligand (Figure 7.3.30). The unoccupied orbitals involved include the LUMO+2, LUMO+3, LUMO+4 and LUMO+5 which show electron density on either parts of the cyclometalated ligand (LUMO+2), parts of the terpyridine ligand (**4.4**) or a mixture of both ligands (**4.3** and **4.5**). This shows that despite the large number of calculated transitions, they are all different types of MLCT, and not LMCT or MC transitions, which can also potentially occur in this wavelength range.[158]

The peak in complex **4.6** (363 nm) is further shifted towards the blue and has an increased absorption compared to the other complexes in this series. TD-DFT calculations show a range of transitions in this range, with the dominant one being the HOMO → LUMO+6 transition, as was the case for **4.1**, **4.3** and **4.4** previously. The electron density on the HOMO is similar to the previous complexes listed, in which it is predominantly metal based, with a small amount spread over the core of the cyclometalated ligand. Thus the energy of the HOMO is similar to previous

complexes, except it is slightly higher in energy due to the electron withdrawing bromine not being present on the cyclometalated ligand in this complex. The LUMO+6 on the other hand is different to the LUMO+6 in **4.3** and **4.4** as the electron density is spread over the entire terpyridine ligand instead of over the cyclometalated ligand. This results in an increase in the energy of the LUMO+6 for **4.6** compared to **4.3** and **4.4**, but lower than for **4.1** because it is completely different in nature to the previous examples in which the energy is dependent on the terpyridine ligand instead of the cyclometalated ligand. The net difference of this is a larger energy gap and thus the observed blue shift for **4.6** compared to all the others in this series.

S_n	E/nm	f	Dominant Transition			Percentage Contribution
4.3						
S10	401.7	0.119	HOMO-1	→	LUMO+3	72
S18	376.9	0.427	HOMO	→	LUMO+6	62
S19	375.6	0.068	HOMO-1	→	LUMO+4	78
S23	360.4	0.050	HOMO-1	→	LUMO+5	72
4.4						
S10	408.7	0.178	HOMO -1	→	LUMO +2	81
S16	378.8	0.404	HOMO	→	LUMO +6	67
S17	374.4	0.051	HOMO -1	→	LUMO +4	84
4.5						
S11	390.5	0.0418	HOMO-1	→	LUMO+2	90
S14	379.0	0.0783	HOMO-2	→	LUMO+2	88
S15	373.0	0.068	HOMO-2	→	LUMO+3	85
S17	367.5	0.0349	HOMO	→	LUMO+5	47
S19	357.1	0.2373	HOMO-2	→	LUMO+4	47
4.6						
S11	408.7	0.106	HOMO-1	→	LUMO+2	57
S15	381.5	0.052	HOMO-2	→	LUMO+4	68
S16	380.5	0.370	HOMO	→	LUMO+6	63
S18	372.4	0.058	HOMO-1	→	LUMO+4	28
S21	362.8	0.067	HOMO-1	→	LUMO+5	56

Table 4.16: Selected calculated UV-vis transitions from TD-DFT calculations for **4.3**-**4.6** *in vacuo* over the range of 350-410 nm (2nd MLCT).

*4.7.3 Complexes **4.7**-**4.8***

Complex	absorption 298 K, MeCN, λ_{max} (nm) ($\varepsilon(10^3\ M^{-1}\ cm^{-1})$)
4.7	521 (7.7), 481 (8.8), 365 (13.4), 315 (35.4), 272 (35.8), 233 (70.6)
4.8	527 (11.5), 489 (12.6), 361 (19.0), 315 (35.9), 285 (47.0), 232 (72.2)

Table 4.17: Electronic absorption data for complexes **4.7**-**4.8**.

The UV-vis spectra for **4.7** and **4.8** are shown in Figure 4.18 along with their corresponding TD-DFT data. The measured UV-vis spectra show that the lowest energy MLCT has a λ_{max} at 481 nm (ε = 8,800) for **4.7** and at 489 nm (ε = 6,600) for **4.8**. Each of these peak envelopes also have a distinct shoulder at lower energy found at approximately 521 nm (ε = 7,700) for **4.7** and 527 nm (ε = 11,500). The shoulder appears more pronounced than in previous complexes and thus an approximate value is given. Previous results show that substituted phenyl groups directly bound to the triazole resulted in a blue shift compared to substituted benzyl groups, as was the case for **4.1** and **4.3**. Complex **4.7** is a hybrid of both types and the result of this is that the energy of the lowest energy MLCT for complex **4.7** is between both **4.1** (483 nm) and **4.3** (476 nm) at 481 nm. Complex **4.8** is red shifted compared to **4.7** by 6 nm, and also has a hyperchromic shift, a similar result to what was observed for previous complexes which had an aryl substituted terpyridine.

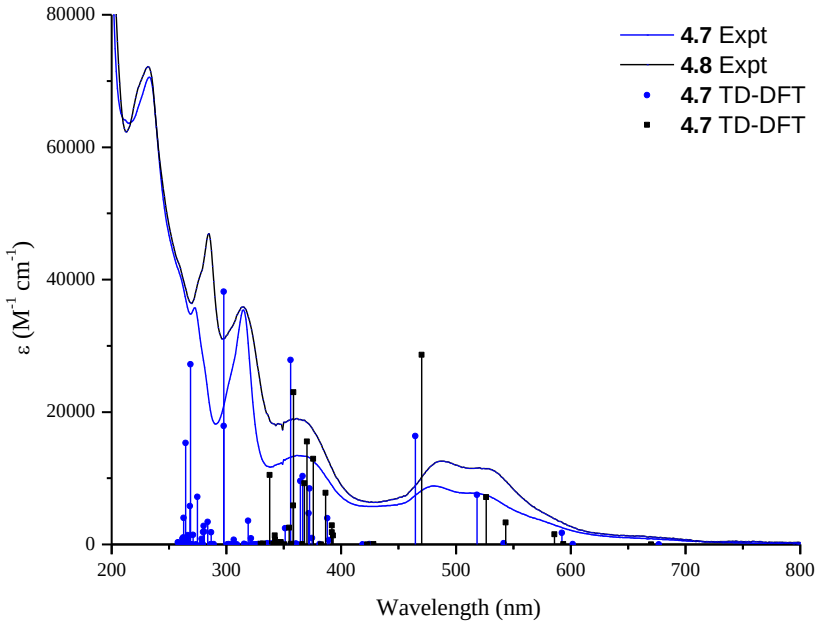

Figure 4.18: Electronic absorption spectra of complexes **4.7**-**4.8** and calculated TD-DFT data for **4.7**-**4.8** *in vacuo*.

TD-DFT calculations for **4.7** and **4.8** show that the main transition for the lowest MLCT is the HOMO-2 → LUMO for **4.7** and HOMO-2 → LUMO+1 for **4.8**. The HOMO-2 for **4.7** is predominantly metal based with a small contribution from the central pyridine on the terpyridine ligand and the HOMO-2 for **4.8** has electron density predominantly on the metal with a small amount on the core of both ligands surrounding the metal. This results in the energy of the HOMO-2 for **4.7** being equivalent to **4.1** and the energy of the HOMO-2 in **4.8** being slightly raised.

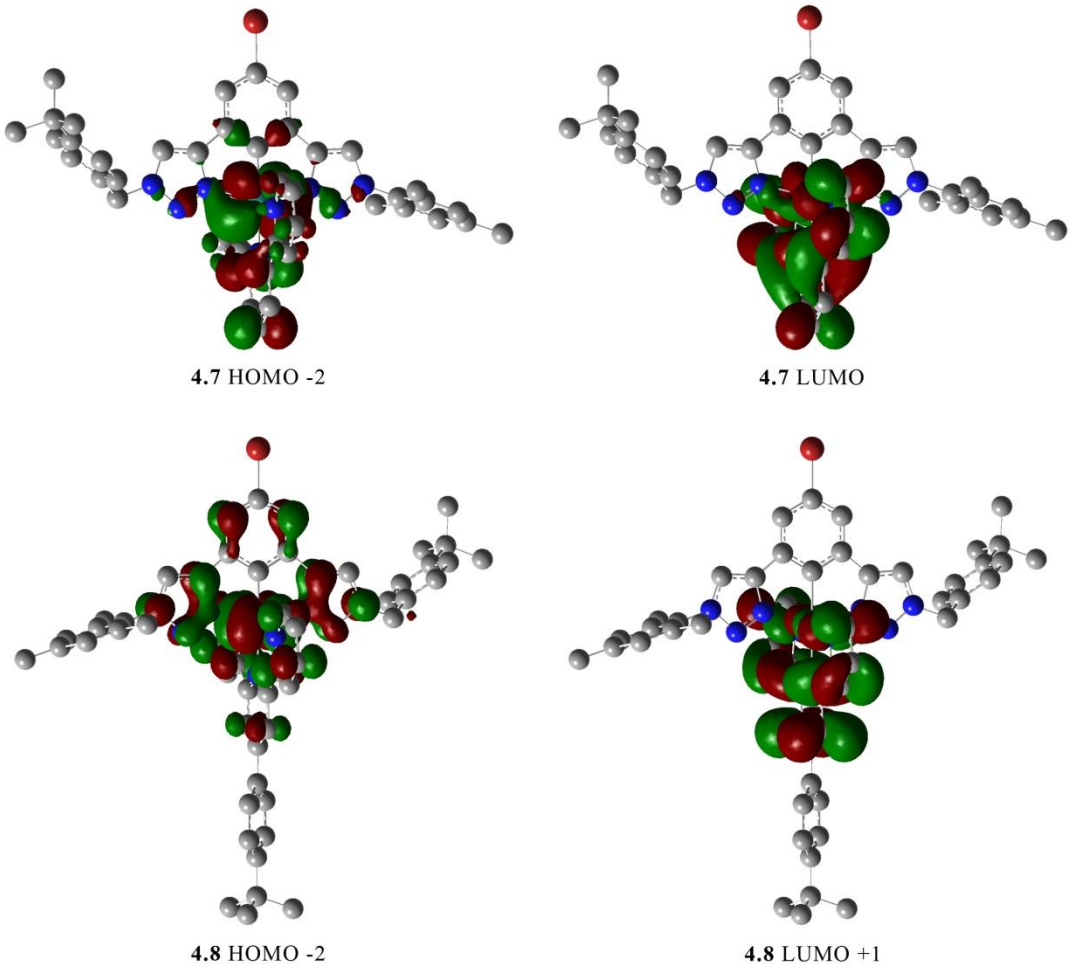

Figure 4.19: Isodensity plots (isovalue 0.02) of selected frontier orbitals that are involved in the dominant transitions for the lowest energy MLCT for **4.7-4.8** from DFT calculation *in vacuo*.

The electron density on the LUMO for **4.7** and the LUMO+1 for **4.8** is only on the terpyridine, not including the substituted phenyl group in **4.8**. This results in the net energy being similar to previous complexes, in which the energy for the transition in **4.7** is similar in energy to **4.1** and the energy of the transition in **4.8** is similar to **4.2**. The calculations also show that the extra broad shoulder in **4.8** compared to **4.7** likely results from the additional transition calculated at 543.3 nm, which means the shoulder is made up of two equally large transitions compared to just the single transition in **4.7**.

S_n	E/nm	f	Dominant Transition			Percentage Contribution
4.7						
S1	676.9	0.000	HOMO	→	LUMO	97
S3	592.2	0.011	HOMO-1	→	LUMO	93
S5	518.3	0.047	HOMO-2	→	LUMO+1	93
S6	464.6	0.102	HOMO-2	→	LUMO	50
4.8						
S1	670.1	0.000	HOMO	→	LUMO	97
S3	586.0	0.009	HOMO-2	→	LUMO	91
S4	543.3	0.021	HOMO-1	→	LUMO	51
S5	526.3	0.045	HOMO-1	→	LUMO+1	91
S6	470.3	0.179	HOMO-2	→	LUMO+1	51

Table 4.18: Selected calculated UV-vis transitions from TD-DFT calculations for **4.7** and **4.8** *in vacuo* over the range of 450-800 nm (1st MLCT).

The 2nd lowest energy peak for complexes **4.7** and **4.8** occurs at 365 nm (ε = 13,400) and at 361 nm (ε = 19,000), respectively. Complex **4.7** is blue shifted compared to **4.1** (368 nm) and complex **4.8** is further blue shifted compared to **4.7**. There are seven large transitions for **4.7** between 350 nm and 390 nm and there are six large transitions for **4.8** over the same range, although there is a dominant transition in each, the HOMO → LUMO+6 transition in **4.7** and the HOMO → LUMO+7 transition in **4.8**. The isodensity plots for the HOMO in both complexes (Chapter 7.3, Figures 7.3.29 and 7.3.30) show that electron density is predominantly on the metal, but also spread over the core of the cyclometalating ligand and the LUMO+6 in **4.7** (Chapter 7.3, Figure 7.3.29) and LUMO+7 in **4.8** (Chapter 7.3, Figure 7.3.30) has electron density predominantly on the triazoles on the cyclometalated ligand in both complexes. The

energy of the HOMO and LUMO+6 in **4.7** is similar in energy compared to **4.1** which means this cannot solely account for the observed blue shift and the shift likely occurs due to the overall effect of the large number of transitions in this range. A similar situation occurs for **4.8**, in which the energy of the HOMO and LUMO+7 are significantly raised compared to **4.7**, but there is no significant net change and thus the small blue shift likely results from a combination of the other transitions within this range.

The remaining higher energy portion of the UV-vis spectrum for **4.7** and **4.8** is likely a mixture of high energy LC ($\pi \rightarrow \pi^*$) transitions and it is typically not very well modeled by TD-DFT calculations, because of the large number of transitions in this range and the difficulty of assigning them to experimental results. They both have a λ_{max} at around 315 nm and around 232 nm, with **4.7** having another low intensity λ_{max} at 272 nm and **4.8** having an additional λ_{max} at 285 nm.

S_n	E/nm	f	Dominant Transition			Percentage Contribution
4.7						
S10	387.9	0.025	HOMO	→	LUMO+5	49
S13	372.5	0.053	HOMO-1	→	LUMO+3	46
S14	371.7	0.029	HOMO-2	→	LUMO+5	37
S15	366.4	0.064	HOMO-1	→	LUMO+2	60
S16	364.6	0.060	HOMO	→	LUMO+6	40
S20	355.9	0.174	HOMO	→	LUMO+6	40
S21	351.3	0.015	HOMO-1	→	LUMO+5	43
4.8						
S12	386.4	0.049	HOMO-1	→	LUMO+2	60
S14	375.8	0.081	HOMO-2	→	LUMO+2	73
S15	370.3	0.097	HOMO-2	→	LUMO+3	65
S16	368.0	0.058	HOMO	→	LUMO+7	45
S18	358.4	0.144	HOMO	→	LUMO+7	31
S19	358.3	0.037	HOMO-6	→	LUMO	50

Table 4.19: Selected calculated UV-vis transitions from TD-DFT calculations for **4.7**-**4.8** *in vacuo* over the range of 350-390 nm (2nd MLCT).

*4.7.4 Complexes **4.9**-**4.12***

Complex	absorption 298 K, MeCN, λ_{max} (nm) ($\varepsilon(10^3\ M^{-1}\ cm^{-1})$)
4.9	519 (7.6), 484 (10.5), 440 (7.9), 385 (15.6), 366 (16.2), 348 (13.1), 316 (32.9), 301 (36.8), 275 (60.8), 252 (108.3)
4.10	519 (7.9), 486 (10.4), 434 (8.0), 385 (15.6), 366 (16.1), 348 (13.1), 316 (42.4), 275 (66.5), 252 (119.9)
4.11	520 (7.4), 490 (8.6), 362 (13.1), 303 (43.4), 286 (49.5), 223 (96.2)
4.12	519 (7.0), 485 (9.3), 438 (7.0), 385 (14.4), 366 (15.6), 348 (14.4), 315 (39.9), 284 (44.5), 276 (45.0), 252 (103.5), 223 (112.1)
2.1	536 (2.7), 487 (4.7), 375 (5.4), 318 (15.2), 259 (19.9), 234 (17.6).
3.9	529 (10.1), 490 (16.2), 385 (28.9), 368 (26.7), 339 (36.7), 320 (45.7), 277 (76.7), 266 (64.8), 251

Table 4.20: Electronic absorption data for group four complexes (**4.9**-**4.12**) and reference complexes **3.9** and **2.1** from previous chapters.

The UV-vis spectra for **4.9**-**4.12** are shown in Figure 4.20 and their corresponding TD-DFT data are shown in Figure 4.21. The measured UV-vis spectra shows that the lowest energy MLCT envelope has a λ_{max} at 484 nm (ε = 10,500) for **4.9**, at 486 nm (ε = 10,400) for **4.10**, at 490 nm (ε = 8,600) for **4.11** and at 485 nm (ε = 9,300) for **4.12**. The three complexes containing anthracene substituted onto the terpyridine (**4.9**, **4.10** and **4.12**) give almost equivalent values, with **4.11** being slightly red shifted compared to the others. All four complexes also have a shoulder between 515 nm and 530 nm of similar intensity to the λ_{max} and another much less intense shoulder between 565 nm and 650 nm.

Complex **3.9** which was previously analysed in chapter three, showed a MLCT at 491 nm (ε = 16,000) and complexes **4.9**, **4.10** and **4.12** are all blue shifted compared to it. Complex **4.11** (490 nm) is blue shifted compared to **3.1** (493 nm), which incorporates the same substituted terpyridine ligand, thus showing the direct effect of the 2-naphthyl group substituted onto each pyrazole. Also, increasing the size of the aryl system typically results in a hyperchromic shift, however the absorbance of the λ_{max} is reduced in this case when the N-heterocycle is expanded, from pyrazole to 4-phenylpyrazole (**4.9**) and then to 4-(1-naphthyl)pyrazole (**4.12**).

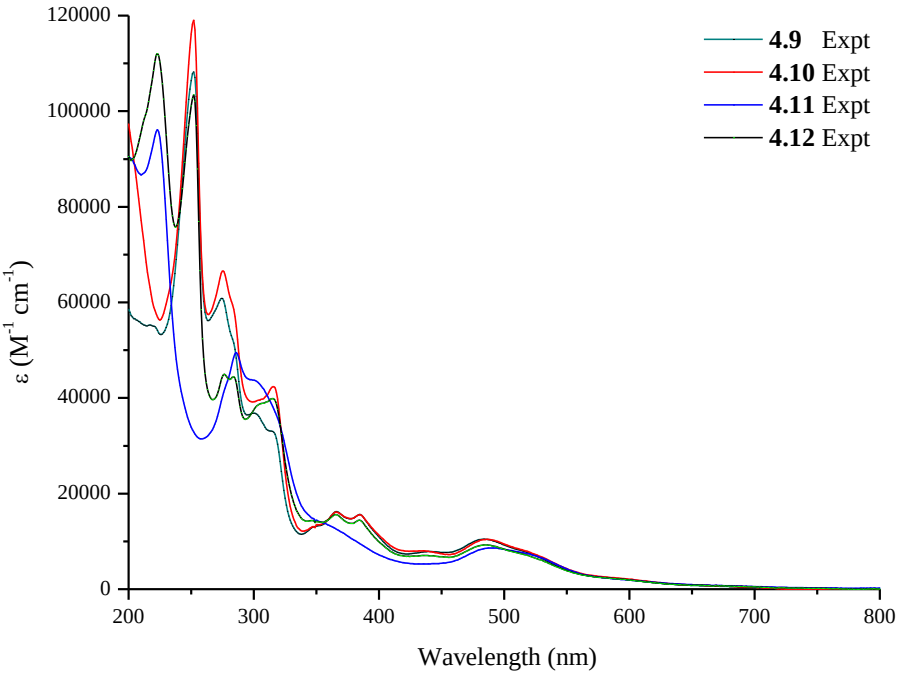

Figure 4.20: Electronic absorption spectra of complexes **4.9**-**4.12**.

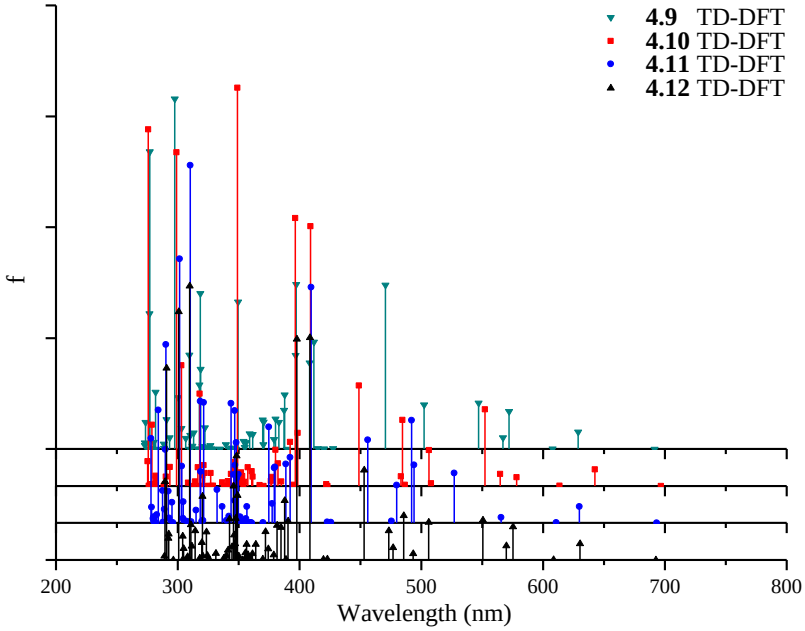

Figure 4.21: Calculated TD-DFT data for **4.9**-**4.12** *in vacuo*.

TD-DFT calculations for these four complexes show up to seven transitions over the range of this lowest energy MLCT. Complex **4.9** has a single large peak at 470.5 nm which results from a HOMO-3 → LUMO transition and has several other minor transitions making up the broad peak envelope. The isodensity plots (Figure 4.22) show electron density for the HOMO-3 predominantly on the metal, with a small amount on the central pyridine on the terpyridine ligand and the LUMO shows electron density only on the three pyridine rings of the aryl substituted terpyridine ligand. The energy of both these two orbitals are increased compared to the relevant orbitals of **3.9**, with the increase in energy of the LUMO in **4.9** being slightly larger and leading to an increase in the energy gap for this transition, resulting in the observed blue shift.

The TD-DFT calculations for Complex **4.10** do not show a single large transition, instead several transitions of similar strength. The three largest transitions are a HOMO-5 → LUMO+1 at 448.7 nm, HOMO-4 → LUMO at 484.5 nm and HOMO-1 → LUMO at 552.3 in order of decreasing energy. The isodensity plot of the HOMO-5 (Figure 4.22) shows electron density spread over both naphthyl substituted pyrazoles and on the metal, the first example thus far in which a significant amount of electron density is shown to be on the aryl group bound to the N-heterocycle. The LUMO+1 is similar to previous complexes in which electron density is only on the three pyridine rings of the aryl substituted terpyridine ligand. The HOMO-4 is similar to previous complexes, in which electron density is predominantly on the metal, with a small amount on the central pyridine of the terpyridine ligand resulting in a transition incorporating different features compared to the main transition involved in the lowest energy MLCT in other complexes. The LUMO is equivalent to the LUMO+1, in which electron density is only on the three pyridine rings of the aryl substituted terpyridine ligand. The HOMO-1 → LUMO transition is different to the others because the HOMO-1 shows electron density only on the anthracene and the LUMO shows electron density only on the three pyridine rings, meaning the transition is not MLCT, but instead LC ($\pi \rightarrow \pi^*$). The strength of these last two transitions likely masks the effect of the first transition, resulting in a negligible change in the λ_{max} for this peak envelope compared to **4.9**. Previous complexes incorporating electron withdrawing methoxy groups, substituted onto either the cyclometalated ligand or onto the 4' position of the terpyridine ligand at the have all resulted in a negligible change in energy of the peaks in the UV-vis.

The TD-DFT calculations for Complex **4.11** show two large transitions at 455.9 nm, corresponding to the HOMO-4 → LUMO+1 transition and at 479.9 nm, corresponding to the HOMO-4 → LUMO transition. The isodensity plot for the HOMO-4 (Figure 4.23) shows electron density predominantly on the metal, with a significant amount also on the pyrazole and the naphthalene. The isodensity plots for the LUMO and LUMO+1 (Figure 4.23) both show electron density only on the terpyridine but not the substituted phenyl group on the terpyridine, as has been commonly observed for previous complexes.

The other transitions for **4.11** involve either the HOMO-1 or HOMO-2, for which the isodensity plots (Chapter 7.3, Figure 7.3.3) show electron density predominantly on the metal and also on the naphthalene, or the HOMO-3 which has electron density on the central pyridine and attached aryl ring. All these others transitions also incorporate the LUMO or LUMO+1, for which the electron density is only terpyridine based, as previously discussed. The energy of the HOMO-3 is significantly higher than the corresponding occupied orbital in **3.1** and the energy of the LUMO and LUMO+1 are equivalent in energy to the LUMO and LUMO+1 for complex **3.1**, which is to be expected since the electron density is solely on the terpyridine ligand, which is the same in both. This should result in an observed red shift, but as the data shows, it is in fact the opposite, which likely results from a combination of all the other transitions in this region. This is not only supported by the number of transitions in this range, but also by the low percentage contributions for several of the listed dominant transitions. For example, the percentage contribution for the highest strength transition, HOMO-2 → LUMO, is only 37% and thus will likely have a large number of other orbital transitions involved instead of having a single dominant transition.

The TD-DFT calculations for complex **4.12** show seven transitions within the range of the lowest energy MLCT, with the largest transition at 453.0 nm, corresponding to the HOMO-4 → LUMO+1 transition. The HOMO-4 and LUMO+1 transitions, which were also the largest for **4.11**, show electron density in similar regions compared to **4.11**, in which the HOMO-4 has electron density predominantly on the metal, with a significant amount also on the pyrazole and naphthalene and the LUMO+1 has electron density only on the terpyridine, not including the substituted anthracene.

The energy of the HOMO-4 is the same as in **4.11**, in which the electron density is also only on the cyclometalated ligand and the metal. The energy of the LUMO+1 is slightly reduced

compared to the LUMO+1 in **4.11**, resulting in an increase in the net energy of these two orbitals, and thus the observed blue shift for the lowest energy MLCT in **4.12** compared to in **4.11**. The energy of the HOMO-4 in **4.12** is higher compared to the corresponding orbital in **4.9**, however the LUMO+1 is increased in energy by the same amount, resulting in a negligible difference in energy for the transition in **4.12** compared to **4.9**. This shows that substitution of the benzene ring with a naphthalene ring onto each pyrazole has an effect on the transition energy, however it is counteracted by a change in energy of the LUMO+1, leading to no distinct blue/red shift.

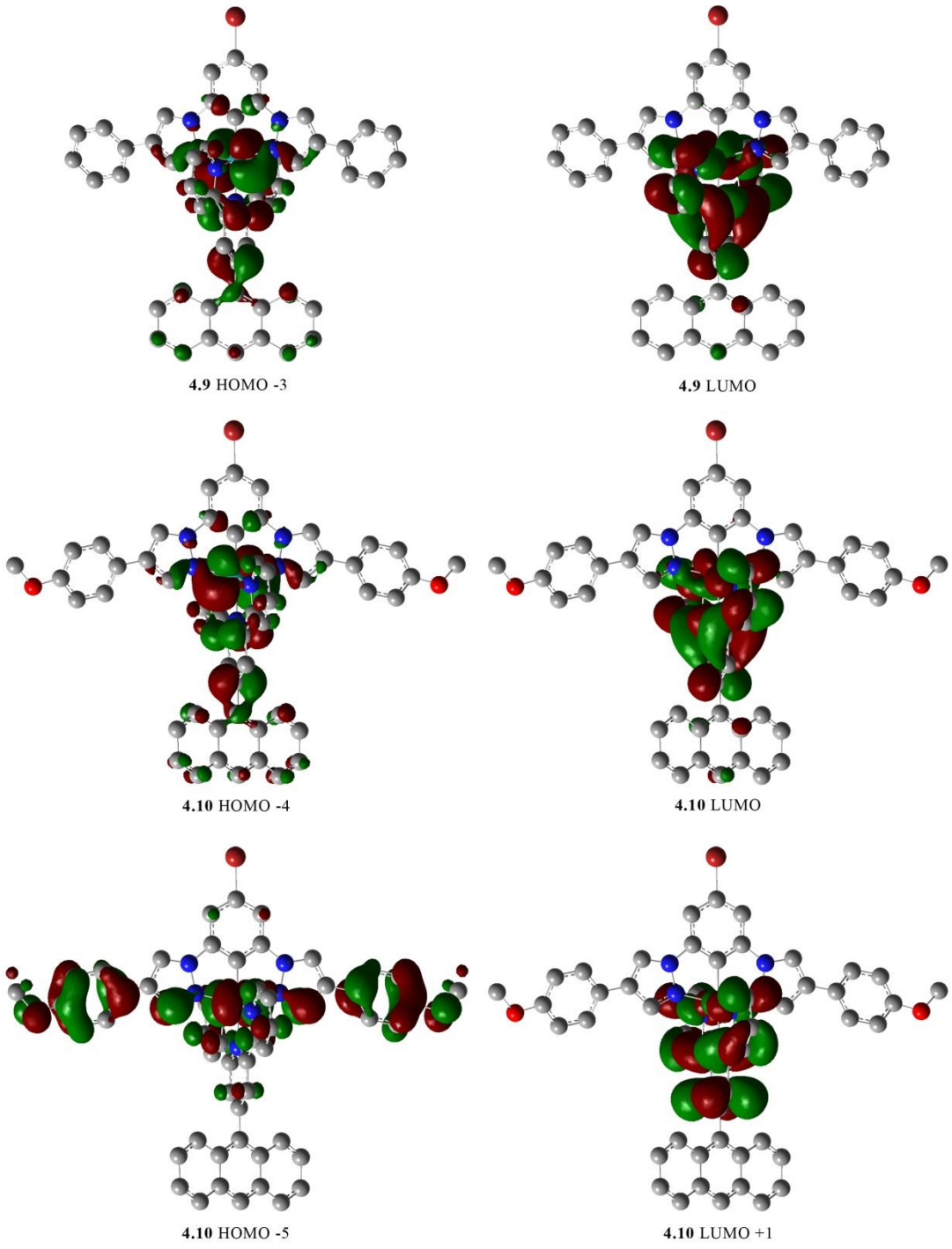

Figure 4.22: Isodensity plots (isovalue 0.02) of selected frontier orbitals that are involved in the dominant transitions for the lowest energy MLCT for **4.9**-**4.10** from DFT calculation *in vacuo*.

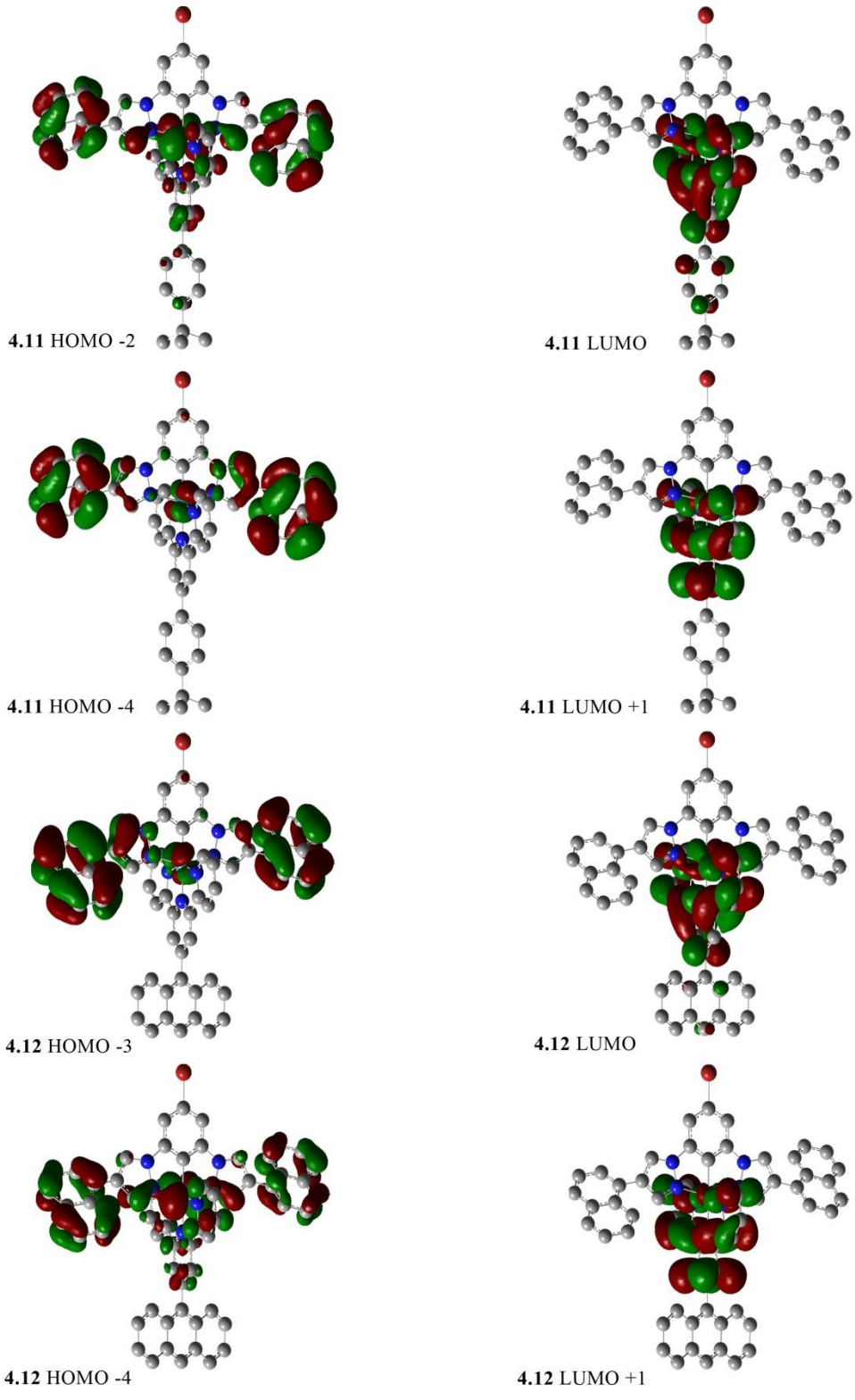

Figure 4.23: Isodensity plots (isovalue 0.02) of selected frontier orbitals that are involved in the dominant transitions for the lowest energy MLCT for **4.11-4.12** from DFT calculation *in vacuo*.

S_n	E/nm	f	Dominant Transition			Percentage Contribution
4.9						
S1	691.4	0.000	HOMO -1	→	LUMO	94
S2	628.7	0.013	HOMO -2	→	LUMO	93
S4	572.0	0.027	HOMO	→	LUMO	61
S6	547.0	0.033	HOMO -2	→	LUMO +1	48
S7	502.3	0.032	HOMO -3	→	LUMO +1	94
S8	470.5	0.118	HOMO -3	→	LUMO	67
4.10						
S1	696.8	0.000	HOMO	→	LUMO	87
S2	642.4	0.012	HOMO -2	→	LUMO	75
S6	552.3	0.055	HOMO -1	→	LUMO	71
S8	506.1	0.026	HOMO -4	→	LUMO +1	79
S10	484.5	0.048	HOMO -4	→	LUMO	56
S12	448.7	0.072	HOMO -5	→	LUMO +1	73
4.11						
S1	693.3	0.000	HOMO	→	LUMO	94
S2	629.8	0.012	HOMO-1	→	LUMO	66
S5	526.9	0.036	HOMO-3	→	LUMO+1	82
S6	494.0	0.042	HOMO-2	→	LUMO	56
S7	491.9	0.074	HOMO-2	→	LUMO	37
S8	479.9	0.027	HOMO-4	→	LUMO	68
S10	455.9	0.060	HOMO-4	→	LUMO+1	75
4.12						
S1	692.5	0.000	HOMO -1	→	LUMO	91
S2	630.2	0.012	HOMO -2	→	LUMO	64
S4	575.3	0.024	HOMO	→	LUMO	59
S6	550.6	0.029	HOMO -2	→	LUMO +1	40
S7	505.9	0.027	HOMO -5	→	LUMO +1	56
S9	485.5	0.032	HOMO -4	→	LUMO	51
S11	473.4	0.021	HOMO -3	→	LUMO +1	63
S12	453.0	0.065	HOMO -4	→	LUMO +1	45

Table 4.21: Selected calculated UV-vis transitions from TD-DFT calculations for **4.9**-**4.12** *in vacuo* over the range of 450-800 nm (1^{st} MLCT).

The higher energy peaks beyond the lowest energy MLCT are significantly more difficult to assign for complexes **4.9**-**4.12**. The complexes incorporating anthracene substituted onto the terpyridine all have a small obscured peak between 420 nm and 460 nm, a region between the lowest energy MLCT and what is typically the 2nd lowest MLCT that normally has no peaks. The peak is observed at 440 nm (ε = 7,900) for **4.9**, 434 nm (ε = 8,000) for **4.10** and at 438 nm (ε = 7,000) for **4.12**. This additional peak is not observed for **4.11**, in which the anthracene is substituted for 4-tertbutylphenyl on the terpyridine, and interestingly it is not observed for **3.9** either, which incorporates the anthracene on the terpyridine and unsubstituted pyrazoles on the cyclometalated ligand. This suggests that the additional peak is a result of having both anthracene substituted terpyridine and phenyl substituted pyrazole on the cyclometalated ligand. The TD-DFT calculations for these complexes do not provide information about specific transitions for this peak in complexes **4.9**, **4.10** and **4.12** because there are too many transitions within a small range. Typically assigning transitions for the lowest energy peak envelope and the 2nd lowest peak envelope is able to be achieved because there is a significant energy gap between the two.

The next section of interest in the measured UV-vis for these complexes is between 335 nm and 420 nm. Previous complexes in this study have shown another MLCT peak envelope in this range and **4.11** shows a distinct peak at 362 nm (ε = 13,100). Complexes **4.9**, **4.10** and **4.11** on the other hand have three peaks at the same wavelength in each, 385 nm, 366 nm and 348 nm, with similar absorbance. These peaks result from the anthracene LC ($\pi \rightarrow \pi^*$) transition and are not affected by the changes to the cyclometalated ligand. The other result of this however is that they mask the MLCT transition which generally occurs in this region. The TD-DFT calculations for complex **4.9**, **4.10** and **4.12** all show six significant transitions within the range of this peak envelope, which are a mixture of both MLCT transitions and the anthracene $\pi \rightarrow \pi^*$ transitions. The remaining higher energy portion of the UV-vis spectrum for each complex (200-355 nm) is likely a mixture of high energy LC transitions and it is typically not very well modeled by TD-DFT calculations, because of the large number of transitions in this range and difficulty assigning them to experimental results. The three complexes incorporating anthracene (**4.9**, **4.10** and **4.12**) all have an intense peak at 252 nm, which likely results from the anthracene.

S_n	E/nm	f	Dominant Transition			Percentage Contribution
4.9						
S13	411.7	0.077	HOMO -1	→	LUMO +3	45
S14	408.4	0.062	HOMO -4	→	LUMO +1	52
S15	397.1	0.119	HOMO -5	→	LUMO +1	55
S16	396.7	0.068	HOMO	→	LUMO +2	46
S18	387.6	0.039	HOMO -2	→	LUMO +4	46
S31	349.5	0.106	HOMO -2	→	LUMO +6	82
4.10						
S15	409.1	0.187	HOMO	→	LUMO +5	56
S16	398.5	0.038	HOMO -2	→	LUMO +2	57
S17	396.4	0.193	HOMO -1	→	LUMO +2	84
S19	392.2	0.032	HOMO -2	→	LUMO +3	73
S22	380.4	0.026	HOMO -1	→	LUMO +4	63
S36	349.0	0.287	HOMO -3	→	LUMO +5	39
4.11						
S13	409.5	0.170	HOMO	→	LUMO+4	59
S14	392.2	0.047	HOMO-1	→	LUMO+2	76
S15	388.6	0.043	HOMO-1	→	LUMO+3	67
S16	379.8	0.040	HOMO-3	→	LUMO+3	23
S17	379.4	0.040	HOMO-3	→	LUMO+2	83
S19	374.7	0.069	HOMO-3	→	LUMO+4	31
S33	348.1	0.058	HOMO	→	LUMO+6	21
S34	347.1	0.042	HOMO-8	→	LUMO	24
S35	346.7	0.081	HOMO-7	→	LUMO+1	54
S38	343.7	0.086	HOMO-8	→	LUMO	24
4.12						
S15	408.6	0.160	HOMO -1	→	LUMO +5	50
S16	397.8	0.159	HOMO	→	LUMO +2	78
S19	387.7	0.043	HOMO -2	→	LUMO +3	37
S40	349.1	0.047	HOMO -2	→	LUMO +6	25
S41	348.2	0.075	HOMO -5	→	LUMO +2	17
S45	345.7	0.053	HOMO -5	→	LUMO +3	17

Table 4.22: Selected calculated UV-vis transitions from TD-DFT calculations for **4.9**-**4.12** *in vacuo* over the range of 340-400 nm (2nd MLCT).

4.8 Emission Studies.

Emission studies were carried out in degassed acetonitrile at ambient temperature and in butyronitrile at 77 K using a continuous flow cryostat from oxford instruments limited. At room temperature none of these complexes (**4.1**-**4.12**) showed distinct emission spectra using the spectrofluorimeter at hand and thus 77 K emission studies were carried out. Emission spectroscopy at low temperature provides greater emission intensity in cases where the dominant non-radiative channels are thermally activated.[159]

Complex	77K Emission λ_{max} (nm) ($\tilde{\nu}$, cm^{-1})	Stokes Shift ($\tilde{\nu}$, cm^{-1})	Quantum Yield
4.1	651 (15,360)	5,340	0.08
4.2	664 (15,060)	5,600	0.83
4.3	677 (14,770)	6,180	0.84
4.4	680 (14,710)	6,020	0.75
4.5	664 (15,060)	5,700	0.89
4.6	663 (15,080)	5,270	0.90
4.7	690 (14,490)	6,300	0.58
4.8	655 (15,270)	5,400	0.88
4.9	694 (14,410)	6,040	0.13
4.10	694 (14,410)	5,960	0.19
4.11	699 (14,310)	6,020	0.41
4.12	692 (14,450)	6,040	0.21

Table 4.23: Luminescence data for complexes incorporating triazole (**4.1**-**4.8)** complexes incorporating pyrazole (**4.9**-**4.12**). Measurements were carried out in ca. 10^{-6} M butyronitrile and quantum yields were calculated using $[Ru(bpy)_3](Cl)_2$ in MeOH/EtOH (1:4, Φ_{PL} = 0.38).[15]

All of the complexes in this series (**4.1**-**4.12**) are emissive at 77 K and show emission profiles with a single peak that are of a similar shape to previously reported spectra for cyclometalated ruthenium complexes.[28] As the measurements are recorded at low temperature the transition is assigned as being an intense 0-0 transition.[160] The luminescence spectra and the corresponding UV-vis data for complexes **4.1**-**4.6** are shown in Figure 4.24 and for complexes **4.7**-**4.12** are shown in Figure 4.25. For each of the triazole containing complexes (**4.1**-**4.8**) there is a distinct λ_{max}, ranging from 651 nm to 690 nm, which gives a Stokes shift between 5,340 cm^{-1} and 6,400 cm^{-1} for each of these complexes. For each of the substituted pyrazole containing complexes (**4.9**-**4.12**) there is a distinct λ_{max}, ranging from 692 nm to 699 nm, which gives a Stokes shift between 5,960 cm^{-1} and 6,040 cm^{-1} for each.

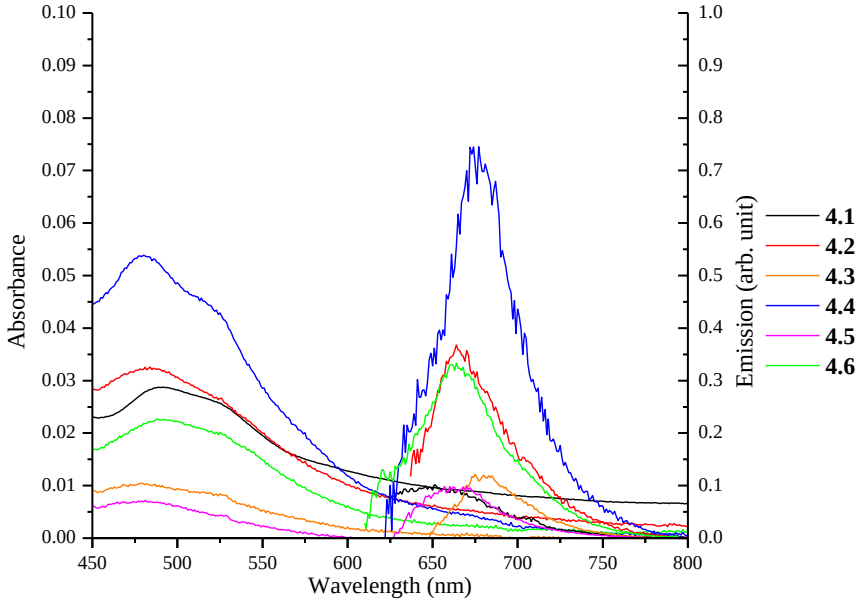

Figure 4.24: UV-vis spectra for **4.1-4.6** in butyronitrile at ca.10^{-6} M at ambient temperature and corresponding emission spectra in butyronitrile at ca. 10^{-6} M at 77 K.

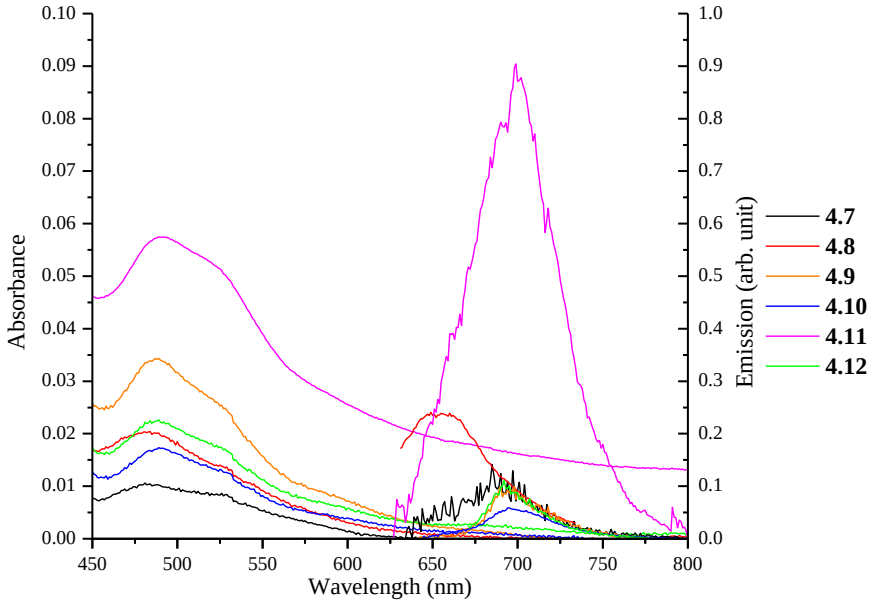

Figure 4.25: UV-vis spectra for **4.7-4.12** in butyronitrile at ca.10^{-6} M at ambient temperature and corresponding emission spectra in butyronitrile at ca. 10^{-6} M at 77 K.

The emission profiles for all the complexes in this series (**4.1**-**4.12**) are significantly red shifted compared to $[Ru(tpy)_2]PF_6$, which shows an emission band at 602 nm at 77 K upon excitation at 475 nm and shows a Stokes shift of 4,440 cm^{-1}.[37] The emission profiles are also red shifted compared to $[Ru(bpy)_3](Cl)_2$, which has an emission band peak at 580 nm and a shoulder at around 630 nm when measured at 77 K and excited at 450 nm. This shows that there is a Stokes shift of 4,980 cm^{-1} for $[Ru(bpy)_3](Cl)_2$. The large Stokes shift for these complexes is a result of the strong HOMO destabilization due to the cyclometalation. The functionalization of cyclometalated ligand has a similar effect on the wavelength of the emission as it did for the absorption, and so for similar complexes the Stokes shift remains relatively unchanged. Similar complexes by Schubert and co-workers have synthesized similar triazole containing cyclometalated ruthenium complexes, for which the Stokes shifts range from 5,700 cm^{-1} to 6,900 cm^{-1}.[28] A smaller Stokes shift results from the ^{1}MLCT and ^{3}MLCT being closer in energy and a similar Stokes shift indicates similar processes are occurring, especially in similar complexes, as for **4.9**-**4.12**.

The quantum yields for complexes **4.1**-**4.12** were found to be between 8% and 90%, using $[Ru(bpy)_3](Cl)_2$ in MeOH/EtOH (1:4, Φ_{PL} = 0.38) at 77 K as a standard.[15] The quantum yield for $[Ru(bpy)_3](Cl)_2$ is relatively high, at 38%, at 77 K[15], but it drops to ca. 4% at room temperature[162] showing the effect of the ^{3}MC state being thermally accessible. The quantum yields were calculated using Equation 2.1 (Section 2.8) and are relative to $[Ru(bpy)_3](Cl)_2$.[162-163]

The quantum yield for complex **4.1** is less than a quarter of the value for standard $[Ru(bpy)_3](Cl)_2$ complex, with a value of 8% at 77 K, the lowest in this series. The quantum yield in complexes **4.2**-**4.8** is very high, with all complexes having a quantum yield above 58%. Despite this high quantum yield at 77 K, emission at room temperature was not able to be detected. A similar triazole containing ruthenium complex (Figure 4.26) by Schulze et al. has a quantum yield of 0.0061%,[28] which is well below the quantum yield of $[Ru(bpy)_3](PF_6)_2$, which has a value of 6.2%.[62]

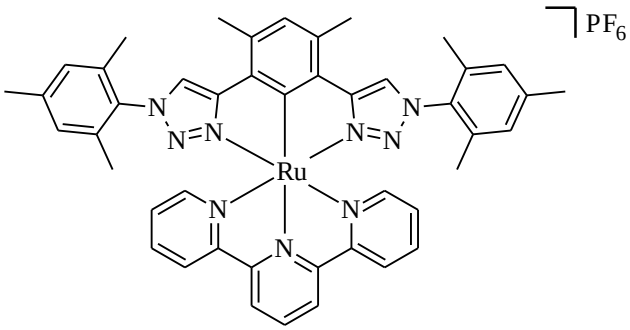

Figure 4.26: Ruthenium complex synthesized by Schulze et al. with an emission quantum yield of 0.0061% at room temperature.

Complexes **4.9**, **4.10** and **4.12** all have a similar quantum yield for emission at 694 nm for **4.9** and **4.10** and **692** nm for **4.12**. Complex **4.11** has a similar emission wavelength has a significantly higher quantum yield. The difference between **4.11** and the other three pyrazole containing ruthenium complexes is that **4.11** does not have anthracene on the terpyridine ligand, but instead a ^{t}butylphenyl group, which indicates that the anthracene likely reduces the quantum yield in complexes **4.9**, **4.10** and **4.12**. The anthracene can also be excited and electronically communicate with the excited state of the ruthenium complex, which may result in lowering of the quantum yield in these complexes.

The high quantum yields and small Stokes shifts for several of these complexes show that the ^{1}MLCT and ^{3}MLCT are closer in energy than in the other complexes in this work and that there are less non-radiative deactivation pathways available to the excited state in these complexes at 77 K. This does not mean that the intersystem crossing process is more efficient in these complexes however, as Demas and co-workers have shown that intersystem crossing to various MLCT excited states occurs with a quantum yield near unity in fluid solution for ruthenium(II) photosensitizers.[164]

The relative quantum yield calculation method provides insight into the quantum yield for new compounds, however there are large errors associated with the method, mostly as a result of poor integration and/or a poor baseline, with typical errors believed to be up to 30%.[165] Errors can be minimized by running multiple measurements at different concentrations, however this was not practical at 77 K using the experimental setup at hand due to large amount of time required to run a single sample. While the relative error associated with each quantum yield is potentially

very high, it is largely a systematic error and the observed trends within a particular series of results are reproducible.[165]

Another important excited state parameter is the lifetime which reflects the stability of the excited state. While emission lifetimes were not able to be measured in this work, it is understood that as the emission energy decreases, the lifetime will also decrease in accordance with the energy gap law.[62-64] The energy gap law shows that as the energy gap is decreased and emission is red shifted, non-radiative decay processes increase which results in shorter emission lifetimes. This has large implications for cyclometalated ruthenium complexes, which show shorter lifetimes compared to their corresponding non-cyclometalated analogues because they have a small band gap.[37, 39] This observation also applies to smaller changes in energy, resulting from modifications to the cyclometalated ligand and terpyridine ligand, such as in complexes **4.1**-**4.12**.

While measuring the lifetime of an excited state is important to gaining further understanding about what factors influence the emission lifetime and thus how to modify the complex so they are luminescent at room temperature, it is less important for these complexes as they are not luminescent at room temperature. An example of luminescence lifetimes not being largely important is their use in dye-sensitized solar cells. Their short lifetimes are less important because the complex is immobilized and there is fast electron injection into the semiconductor, meaning other problems of using cyclometalated ruthenium complexes can be utilized without the short lifetimes being a problem.

The key argument against room temperature emission is that the ^{3}MC state is both thermally assessable to the ^{3}MLCT and has strong coupling to the ground state, which results in rapid relaxation of the ^{3}MC state once populated. While there is no direct spectroscopic evidence to support this, it is widely considered to be the cause of reduced emission. This is supported however by theoretical calculations, which have shown that the ^{3}MC and ^{3}MLCT states are similar in energy, and low temperature luminescence studies which show that there are longer lifetimes and higher quantum yields at 77 K as the ^{3}MC state is no longer thermally accessible. The reason the ^{3}MC state is deactivating is that in the ^{3}MC state antibonding orbitals are occupied and this matches the ground state geometry when there are high energy vibrations.

4.9 Electrochemical Studies.

The electrochemical properties of **4.1**-**4.12** were examined by cyclic voltammetry, using degassed acetonitrile solutions containing 0.1 M Bu_4NPF_6. Measured redox couples for the modified terpyridine series of ruthenium complexes are reported in **Table 4.24**. All complexes exhibit a chemically reversible redox couple for both oxidation and reduction. Ruthenium(II) polypyridine complexes have a predominately metal based HOMO and a ligand based LUMO which leads to oxidation being associated with the metal center, while reduction occurs on the ligand, which is supported by the previously discussed TD-DFT calculations for these complexes.

Complex	$E_{1/2}$ anodic[a]	$E_{1/2}$ cathodic[a]	ΔE[c]
$[Ru(tpy)_2]PF_6$[37]	0.89 (64)	-1.66 (63), -1.90 (63)	2.55
$[Ru(dpyb)(tpy)]PF_6$[37]	0.12 (62), 1.36[b]	-1.95 (63)	2.07
2.1	0.11 (116), 1.05[b]	-1.96 (121)	2.07
4.1	0.17 (76), 1.30[b]	-1.97 (78)	2.14
4.2	0.20 (76), 1.28[b]	-1.90 (126)	2.10
4.3	0.22 (66), 1.38[b]	-1.94 (73), -2.23 (187)	2.16
4.4	0.20 (81), 1.29[b]	-1.96 (78), -2.35[b]	2.16
4.5	0.21 (85), 1.32[b]	-1.97 (86)	2.18
4.6	0.13 (75), 1.30[b]	-1.94 (89), -2.33[b]	2.07
4.7	0.19 (75), 1.34[b]	-1.96 (79)	2.15
4.8	0.19 (65), 1.36[b]	-1.94 (69), -2.28(212)	2.13
4.9	0.19 (77), 1.03[b], 1.22[b]	-1.90 (144), -2.11 (128)	2.09
4.10	0.18 (66), 1.05[b], 1.29[b]	-1.91 (96)	2.09
4.11	0.16 (100), 1.09[b], 1.40[b]	-1.94 (130)	2.10
4.12	0.19 (81), 1.11[b], 1.43[b]	-1.91 (104)	2.10

Table 4.24: Electrochemical data for complexes **4.1**-**4.12**, **2.1** and relevant literature complexes. (a) The potential is reported as the $E_{1/2}$ value vs. Fc/Fc^+. (b) Ep, irreversible. (c) Energy difference between first reversible oxidation and reduction.

The first oxidation process for each of the complexes **4.1**-**4.12** is quasi-reversible under cyclic voltammetry conditions and is assigned as being a $Ru^{2+/3+}$ redox couple. This redox couple has been shown to have a mixed metal/cyclometalated ligand character and thus modifications to the cyclometalated ligand should have an impact on this process. For complex **4.1**, the $E_{1/2}$ for the oxidation process is at 0.17 V (versus Fc) for the $Ru^{2+/3+}$ couple, which shows an anodic shift

compared **2.1** (60 mV) and [Ru(dpyb)(tpy)PF^6] (50 mV). This shift results from the triazole on the cyclometalated ligand, which increases electron density on the mixed Ru^{2+}/cyclometalated ligand HOMO because it is a stronger π donor. It is important to note that there is still a significant cathodic shift compared to [$Ru(tpy)_2$]PF^6 (720 mV) due to the effects of cyclometalation discussed previously.

The $E_{1/2}$ for the oxidation process in **4.2** is 0.20 V, which means it is more difficult to oxidize **4.2** compared to **4.1**, with an anodic shift of 30 mV. The increased size of both ligands results in there being additional electron density available and thus a more electron rich metal. Also, bromine atoms have been shown previously in this work to result in anodic shifts, which could be a factor in the shift in oxidation potential for **4.2** compared to **4.1** as well.

The $E_{1/2}$ for the oxidation processes in **4.3**, **4.4** and **4.5** are very similar, with values of 0.22 V, 0.20 V and 0.21 V, respectively. The value for **4.3** is shifted due to the enhanced delocalization of the cyclometalated ligand, which results in greater electron density on the metal, compared to **4.1** which does not have the substituted phenyl ring conjugated to the triazole. It is difficult to draw conclusions on whether the methoxy group in **4.4** is causing a small cathodic shift compared to **4.3** and **4.5**, as there is only a very small shift. Previous results have also showed that the methoxy group has only a small effect on the complexes in which they have been incorporated, and their corresponding isodensity plots (discussed earlier) show little contribution from the methoxy group in any of the highest occupied molecular orbitals. The negligible change for **4.5** compared to **4.3** and **4.4** shows that the aryl substituted terpyridine ligand does not have a significant effect on the first oxidation process, which is supported by the TD-DFT calculations which show no contribution in any of the highest occupied molecular orbitals.

The $E_{1/2}$ for the oxidation process in **4.6** is significantly different to all the previous complexes in this section however, with a cathodic shift of 40 mV compared to **4.1**, and 80 mV compared to **4.5** (the most similar complex in this series). The notable difference between these complexes is the lack of the bromine on the cyclometalated ligand at the 4' position on central benzene ring, which results in there being less electron density on the mixed metal/cyclometalated ligand HOMO, which means that the metal is easier to oxidize , which results in the observed cathodic shift.

The $E_{1/2}$ for the oxidation process in **4.7** and **4.8** is the same, with a value of 0.19 V, which further supports the observation that the oxidation only depends on the metal and cyclometalated ligand. This $E_{1/2}$ value for **4.7** and **4.8** shows an anodic shift compared to **4.1** of 20 mV and a cathodic shift compared to **4.5** of 20 mV. This shows a stepwise change in potential as the substituted benzyl on the triazole is exchanged for the conjugated substituted phenyl.

The $E_{1/2}$ for the oxidation process in **4.9** is 0.19 V, which has an anodic shift of 20 mV compared to **4.1**, but more importantly has an anodic shift of 80 mV compared to its parent complex, **2.1**. This shows that extending the aromaticity on the pyrazole has the desired effect of increasing the electron density on the mixed metal/cyclometalated ligand HOMO, resulting in the metal being harder to oxidize. The result for **4.10** is comparable, with a value of 0.18 V, which is a slight cathodic shift compared to **4.9**. This is similar to the shift that was observed for **4.4**, compared to **4.3** and **4.5** which also incorporated methoxyphenyl. This is once again a very small cathodic shift (and potentially negligible), which shows the minimal effect that methoxy groups have when incorporated into structures of this type.

The $E_{1/2}$ for the oxidation process in **4.11** and **4.12**, based on previous work, should be the equivalent as they incorporate the same cyclometalated ligand, however the values are 0.16 V and 0.19 V, respectively. The value for **4.12** is comparable to **4.9**, which suggests that the effect of changing the benzene ring on the pyrazole to a naphthalene ring is negligible. The value for **4.11** has a cathodic shift of 30 mV compared to **4.12**, the reason for which is unclear based on these results.

The anodic scan to a more positive potential led to the appearance of a single irreversible oxidation between 1.28 – 1.38 V for **4.1**-**4.8** and two irreversible oxidations for **4.9**-**4.12**, the first of which was observed between 1.03 – 1.11 V and the second observed between 1.22 – 1.43 V. The irreversible oxidation peak in **4.1**-**4.8** and the more positive of the two peaks in **4.9**-**4.12** are most likely attributable to a $Ru^{3+/4+}$ process, or ligand based decomposition,[29] with the additional peak in **4.9**-**4.12** most likely resulting from decomposition of the naphthalene/anthracene unit on the cyclometalated ligand, as seen for previous results which incorporate these large aromatic systems.

The nature of these cyclometalated complexes results in the reduction process being related to the oxidation process because the more electron rich the Ru^{2+}/cyclometalated ligand HOMO becomes due to factors such as increased π donor character, the more electron rich the LUMO becomes through increased π back donation from the electron rich metal onto the terpyridine ligand.[28] Through TD-DFT calculations the LUMO has been shown to have electron density that is generally on the terpyridine ligand and thus the energy of the reduction process is also based on the substituted terpyridine ligand, where larger ligands result in more electron rich terpyridine ligands, which in turn are easier to reduce. Although substituted terpyridines were not the focus of this chapter, several different terpyridine ligands have been used, a more detailed examination of their differences can be found in chapter three.

All of the complexes in this chapter, **4.1**-**4.12** have at least one reduction process, which occurs between -1.90 V and -1.97 V and all of these reduction processes are quasi-reversible under cyclic voltammetry conditions. These are assigned as being reduction of the terpyridine ligand in all of these complexes, based on previous results and TD-DFT calculations. Complexes **4.3**, **4.8** and **4.9** have a second quasi-reversible reduction process and complexes **4.4** and **4.6** have an irreversible reduction process, all of which occur between -2.11 V and -2.35 V and are probably due to reduction of the cyclometalated ligand. These reductions occur very close to the solvent boundary and thus it is highly probable that the other complexes also have this 2nd reduction process, however it is obscured by the solvent boundary. Nevertheless, it is the 1st (LUMO) reduction process which is the most important as it gives information about the HOMO/LUMO energy gap, and will thus be examined in more detail.

For complex **4.1**, the $E_{1/2}$ for the reduction process is at -1.97 V (versus Fc), which is very similar compared to **2.1**, with a value of -1.96 V. The similar value is most likely a result of the terpyridine ligand, which is the same on both complexes, and thus the potential is largely unaffected by the change to the cyclometalated ligand. The $E_{1/2}$ for the reduction process in **4.2** is at -1.90 V, which shows a large anodic shift compared to **4.1** (70 mV). The aryl substituted terpyridine ligand is known to enhance the degree of delocalization, which means that it is easier to be reduced,[166] and thus the observed anodic shift in **4.2**. The shift is potentially further than it would be expected, for a change from terpyridine to 4-(4-tertbutylphenyl)terpyridine and thus it is also probably affected by an increased amount of π back donation from the electron rich metal.

The increased amount of π back donation from the electron rich metal is also the most likely cause of the 1st reduction process of **4.3** having an $E_{1/2}$ of -1.94 V, a shift of 20 mV compared to **4.1**. The terpyridine ligand is unchanged in **4.3** compared to **4.1**, showing the effect of the change in cyclometalated ligand and its effect on the π back donation from the metal onto the terpyridine ligand.

The $E_{1/2}$ for the 1st reduction process in **4.4** is -1.96 V, which shows a similar small shift compared to the oxidation process in **4.3**. Once again, this is a small shift of only 20 mV, but an important observation to make is that the shift between the reduction process and oxidation process in **4.3** is also 20 mV. This means that while both processes are slightly shifted, the energy gap between the two is the same.

The $E_{1/2}$ value for the reduction process in **4.5** is -1.97 V, which goes against the trend of previous complexes in which the aryl substituted terpyridine ligand results in a more positive potential. In this case there is a small cathodic shift of 10 mV compared to **4.4**, but it is a more significant shift compared to the other substituted terpyridine containing complexes.

The $E_{1/2}$ value for the 1st reduction process in **4.6** is -1.94 V, which is more in line with the expected value for this substituted terpyridine ligand, and corresponds to the other complexes **4.8** and **4.11**, which also have a value of -1.94 V.

The $E_{1/2}$ value for the reduction process in **4.7** is -1.96 V and the $E_{1/2}$ value for the 1st reduction in **4.8** is -1.94 V and these values show that impact of the substituted terpyridine versus the parent terpyridine better than any other complex, because they have the same cyclometalated ligand in each case. The value of this reduction process in **4.7** is the same as for **2.1**, showing that the cyclometalated ligand has a limited impact on the reduction potential.

The $E_{1/2}$ value for the 1st reduction in **4.9** (-1.90 V) and the only observed reduction in **4.10** and **4.12** (both -1.91 V) are very similar and show the strong effect that anthracene has in the system, resulting in the LUMO being significantly easier to reduce in these complexes compared to the others in this series. These values are also comparable to **3.9**, which has a value of -1.92 V, with the difference in reduction potential resulting from a small π back donation effect.

All these subtle changes in the oxidation and reduction potentials result in changes to the overall energy gap between the HOMO and LUMO, with all but **4.6** having an E_{gap} that is larger than complex **2.1** from chapter two and also a larger E_{gap} than reference complex [Ru(dpyb)(tpy)]PF^6. The E_{gap} for **4.1** is 2.14 V, which results from a large change in the oxidation potential compared to **2.1**, with the reduction potential almost unchanged. The E_{gap} in **4.2** on the other hand results from a large change in the reduction potential, with only a small change in the oxidation potential and has a value of 2.10 V. Complexes **4.3** and **4.4** both have a E_{gap} of 2.16 V, showing the negligible overall effect of the methoxyphenyl group on the terpyridine. The E_{gap} for **4.5** is the largest of this series, with a value of 2.18 V, resulting from a harder to reduce LUMO compared to **4.4** but also a harder to oxidize HOMO compared to **4.4**. Complex **4.6** has the smallest E_{gap} of complexes in this series, with a value 2.07 V, the same as the two listed reference compounds. This shows the effect of changing the N-heterocycle to substituted triazole from pyrazole/pyridine is counteracted by the loss of the bromine atom on the central ring of the cyclometalated ligand.

The E_{gap} in complexes **4.7** and **4.8** shows the effect of changing the terpyridine ligand once again, with the value for **4.8** (2.13 V) being smaller than for **4.7** (2.15 V). This follows previous results which show that extending the size of the ring system lowers the energy of the overall complex.

Lastly, the E_{gap} for all the substituted pyrazole complexes are very similar, with the value for **4.9** and **4.10** being 2.09 V and the value for **4.11** and **4.12** being 2.10 V. The anthracene has a significant impact on the reduction potential in **4.9**, **4.10** and **4.12**, which results in their values being very similar and the oxidation potential is very similar for **4.9**, **4.10** and **4.12**, showing a negligible effect from the different cyclometalated ligands. The oxidation potential for **4.11** and **4.12** are different however (30 mV), and since these complexes incorporate the same cyclometalated ligand, the substituted terpyridine ligand must be having an effect on this potential. This is supported by the TD-DFT calculations which show several of the highest occupied molecular orbitals having electron density from both ligands.

4.10 Summary.

The synthesis of twelve new cyclometalated ruthenium complexes has been investigated to analyze the result of adding substituted aryl groups onto the side N-heterocycles of the cyclometalating ligand.

The electrochemistry and spectroscopic properties of these complexes have been studied and compared with $[Ru(tpy)_2](PF_6)_2$, literature complex **4.45** and [Ru(1,3-di(pyridyl-2-yl)(terpyridine)]PF_6 to analyze the effect of introducing electron donating groups and large aryl groups onto the 4' position of the N-heterocycle of the cyclometalated ligand. This was achieved by using substituted triazole cyclometalating ligands (**4.1**-**4.8**) or substituted pyrazole cyclometalating ligands (**4.9**-**4.12**). To gain further understanding about the structure of these complexes DFT calculations were used to calculate optimized structures. From these preliminary calculations, TD-DFT calculations were used to gain a more thorough understanding of the photophysical and electrochemical properties to provide further insight into the structure-property relations of these complexes.

The synthesis of the cyclometalating ligands for **4.1**-**4.8** was completed by reacting 1,3-di(ethynyl)-5-bromobenzene with either a benzyl bromide derivatives or an aryl boronic acid utilizing the CuAAC "click" approach. The synthesis of cyclometalating ligands for **4.9**-**4.12** was completed by reacting 1,3,5-tribromobenzene with 4-substituted pyrazoles using modified Ullmann coupling conditions. Synthesis of the complexes was more difficult for triazole containing cyclometalating ligands as there were two nitrogens available to coordinate to the ruthenium. The reaction conditions were optimized, with the key difference being that $[Ru(tpy\text{-}R)(MeCN)_3](PF_6)_2$ was used instead of $Ru(tpy\text{-}R)Cl_3$ for triazole containing cyclometalating ligands (**4.1**-**4.8**). The complexes incorporating pyrazole containing cyclometalating ligands (**4.9**-**4.12**) used optimized conditions from previous sections of this work.

All of the complexes were analyzed using NMR spectroscopy and their ^{1}H and ^{13}C spectra were fully assigned. Analysis of the coordination induced shifts for complexes **4.1**-**4.8** showed only small CIS for the central H3 and H6 protons, but moderate to large negative CIS for the aryl rings substituted onto the N-heterocycle due to metal–to–ligand π back-donation onto the side of the complex. The CIS of complexes **4.9**-**4.12** showed large negative shifts for the H7 proton due to interligand through-space ring-current anisotropy effects in which the H7 proton lies over the

shielding plane of the central pyridine ring of the terpyridine ligand as a result of the distorted octahedral geometry. The aryl rings introduced onto the N-heterocycle in complexes **4.9**-**4.12** all show negative CIS due to metal–to–ligand π back-donation, as for the substituted aryl groups on the triazole containing cyclometalating complexes (**4.1**-**4.8**).

DFT calculations for these complexes (**4.1**-**4.8**) provided optimized geometries which were compared to a similar non-cyclometalated complex, **4.45**. Similar calculations were completed for **4.9**-**4.12** and these were compared to the parent complex, **2.1** and the corresponding non-cyclometalated complex **2.31**. In all of these calculations there was shortening of the Ru-C bond length compared to the corresponding Ru-N bond length in the comparable non-cyclometalated complex. As a result of this the opposite Ru-N bond length was elongated due to the trans effect. The side pyridines were closer to the ruthenium, as the corresponding Ru-N bond lengths for the side pyridines were shorter, due to π back donation from the electron rich ruthenium. The chelate bite angles showed the distorted octahedral geometry for all of the complexes in this series. The crystal structures for **4.44** and **4.1** were obtained and these were comparable with the calculated structures, with experimental bond lengths and angles similar to their calculated values.

The UV-vis spectra for complexes **4.1**-**4.12** were measured in acetonitrile and showed a broad MLCT for all complexes between 440 nm and 600 nm, with a distinct λ_{max} for each complex between 476 nm and 494 nm showing that a large amount of variation in this MLCT can be achieved by modifying the aryl group attached to the N-heterocycle, taking into the account the shift resulting from the three different substituted terpyridine ligands used in this series. The MLCT in complexes **4.1** is at 483 nm and there is a blue shift to 476 nm in **4.3**, which shows the effect of the conjugated aryl group in **4.3** compared to the benzyl group in **4.1**. The lowest energy MLCT for **4.9**, **4.10** and **4.12** are all blue shifted by ca. 5 nm compared to the parent complex **3.9**, showing the effect of substituting aryl groups onto the 4' position of both pyrazoles. The UV-vis spectra also show a 2nd broad MLCT for complexes **4.1**-**4.12** between 340 nm and 440 nm as well as several LC (π→π*) transitions between 200 nm and 340 nm.

TD-DFT calculations showed at least three transitions over the range of the lowest energy MLCT, which explains the broad nature of the peak envelope. The isodensity plots from the TD-DFT calculations enabled assignment of the orbitals involved in all the lowest energy MLCT transitions. The TD-DFT calculations also provided insight into which orbitals were involved for

the 2nd lowest energy MLCT, despite not providing a complete assignment due to the large number of transitions over the range of the peak envelope.

The potential emission of all of these complexes was measured at room temperature in degassed acetonitrile but did not show distinct peaks. At 77 K all complexes were emissive with excitation of the lowest energy MLCT producing broad luminescence profiles with a single λ_{max}, which occurred between 651 nm and 690 nm in complexes **4.1**-**4.8** and between 692 nm and 699 nm in complexes **4.9**-**4.12**.

For each of the triazole containing complexes (**4.1**-**4.8**) there is a large variation in the Stokes shifts, with values between 5,340 cm^{-1} and 6,400 cm^{-1}. For each of the substituted pyrazole containing complexes (**4.9**-**4.12**) there is a distinct λ_{max} between 692 nm and 699 nm, with similar Stokes shifts, ranging from 5,960 cm^{-1} to 6,000 cm^{-1}. These Stokes shifts are all larger than for $[Ru(tpy)_2](PF_6)_2$ and $[Ru(bpy)_3](PF_6)_2$, which have values of 4,400 cm^{-1} and 5,000 cm^{-1}, respectively.

The quantum yields of complexes **4.1**-**4.12** were measured at 77 K and varied between 8% and 90%, with the quantum yield for **4.2, 4.3, 4.4, 4.5**, **4.6** and **4.8** all very high, with values of 83%, 84%, 75%, 89%, 90% and 88%, respectively. While the error associated with these values is very high, the results show that the quantum yield is significantly higher than $[Ru(bpy)_3](PF_6)_2$, which has a quantum yield of 38% at 77 K. These results cannot be directly related to $[Ru(dpyb)(tpy)]PF_6$,[37] as its emission spectrum has not been measured at 77 K and none of these complexes had detectable luminescence at room temperature using the experimental setup at hand. At room temperature $[Ru(dpyb)(tpy)]PF_6$,[37] has emission at 781 nm (12,800 cm^{-1}) with a very low quantum yield of 9.4×10^{-6}.

The electrochemical properties of **4.1**-**4.12** were also examined by cyclic voltammetry. All complexes exhibit a chemically quasi-reversible redox couple for both oxidation and reduction, with the oxidation occurring on the metal center and reduction occurring on the terpyridine ligand. This was supported by the TD-DFT calculations which showed that the HOMO was largely associated with the metal center and the LUMO was largely associated with the terpyridine ligand and not the cyclometalated ligand.

The potential of the quasi-reversible oxidation process was modified between 0.13 V and 0.22 V and the potential of the quasi-reversible reduction process was modified between -1.90 V and -1.97 V for complexes **4.1**-**4.12**. These potentials are slightly modified compared to the values for [Ru(dpyb)(tpy)]PF_6[37] which has quasi-reversible oxidation and reduction processes at 0.12 V and -1.95 V, respectively. These potentials also show the large shift that occurs upon cyclometalation, as [$Ru(tpy)_2$](PF_6)$_2$[37] has quasi-reversible oxidation and reduction processes at 0.89 V and -1.66 V, respectively. These potentials for complexes **4.1**-**4.12** show a ΔE between 2.04 V and 2.16 V, compared to the ΔE for [Ru(dpyb)(tpy)]PF_6[37] and [$Ru(tpy)_2$](PF_6)$_2$[37] of 2.07 V and 2.55 V, respectively. This showed that the electrochemical properties could be modified by introducing various aryl groups onto the 4' position of the N-heterocycle on the cyclometalated ligand, with changes to both the quasi-reversible oxidation and reduction processes, as well as the energy gap between them (ΔE).

CHAPTER 5

SUMMARY, CONCLUSIONS AND FUTURE PERSPECTIVES

5. Summary, conclusions and future perspectives.

5.1 Overall summary.

All thirty three of these cyclometalated ruthenium complexes had not been previously synthesised and were characterized by ^{1}H and ^{13}C NMR spectroscopy and mass spectrometry. Their properties were measured by cyclic voltammetry, UV-vis spectroscopy and Fluorescence spectroscopy at room temperature and at 77K. Their structures were calculated using DFT calculations to be used in parallel with experimental structures obtained using x-ray crystallography. Their UV-vis properties and orbital energies were calculated using TD-DFT calculations.

Analysis of their ^{1}H NMR spectra showed coordination induced shifts (CIS), with significant changes occurring upon coordination due to a range of different effect, including through–space ring–current anisotropy effects, conformational changes due to chelation, ligand–to–metal σ donation and metal–to–ligand π back-donation. The aryl groups attached to the 4' position of the central benzene ring on the cyclometalating ligand in chapter two had small positive CIS as these protons had less electron density due to ligand-to-metal σ donation. Large shifts also occurred for cyclometalated complexes incorporating pyrazole, in which the H7 proton on the pyrazole ring had a CIS between -0.71 ppm and -1.20 ppm and occurred due to interligand through-space ring-current anisotropy effects. The complexes in chapter four also showed small negative CIS for the protons on the aryl groups substituted onto the N-heterocycles bound to the cyclometalated ligand. These were the result of increased electron density due to metal–to–ligand π back-donation. In complexes in which the H4 proton on the central benzene ring on the cyclometalating ligand is not substituted with another group, it has a small negative CIS of ca. 0.15 ppm. There is a point effect at this position resulting from the σ-bond between the metal and the carbon from the aryl system. The polarity of the M-C bond results in a partial negative charge which can be delocalized throughout the aryl ring and the 4' position and can facilitate electrophilic aromatic substitution reactions in this position. The 2' positions can also facilitate electrophilic aromatic substitution reactions, however those are the positions the N-heterocycles are attached.

Crystal structures of ten cyclometalated complexes were successfully solved during this work, eight of which were the target cyclometalated structures. The crystal structure of **2.9** showed a hydrated version of the target structure, with a substituted ketone bound to the 4' position of the central benzene ring on the cyclometalated ligand instead of the target substituted acetylene. This was supported by ^{1}H and ^{13}C NMR spectroscopy as well as mass spectrometry for **2.9**. Based on similar evidence it is likely this also occurred for **2.10**. The other unexpected crystal structure was the structure of **2.5a**, which showed one of the potential byproducts that can form when attempting to form bis-tridentate cyclometalated ruthenium complexes.

Analysis of the optimized calculated structures was completed for all complexes in this work and compared with calculated structures for similar non-cyclometalated complexes as well as comparing the calculated structures with the structures obtained by X-ray crystallography. The calculated structures reflected the experimental data, showing shortening of the Ru-C bond and elongation of the opposite Ru-N bond compared to similar non-cyclometalated ruthenium complexes. Modifications to the 4' position of the central benzene ring on the cyclometalated ligand which were able to donate electron density resulted in further shortening in the Ru-C bond length. This reflected the observed CIS for the complexes in chapter two showing a relationship between the more negative CIS and the Ru-C bond length through ligand to metal σ-donation. This shows changes to the terpyridine ligand do not affect the overall structure of the complex as much as changes to the cyclometalated ligand due to the Ru-C σ-bond.

Analysis of the UV-vis spectra showed a broad MLCT in the visible spectrum for all thirty three complexes, with a distinct λ_{max} varied between 476 nm and 505 nm. $[Ru(dpyb)(tpy)]PF_6$ has a MLCT at 499 nm and this was blue shifted to 487 nm by changing the N-heterocycle from pyridine to pyrazole. Changing the parent pyrazole containing complex, by substitution at the 4' position on the central benzene on the cyclometalating ligand resulted in the lowest energy MLCT shifting between 479 nm and 488 nm for **2.2**-**2.10**, which are almost all blue shifts compared to the lowest energy MLCT in **2.1** (487 nm). The only large red shift in this series occurs when the central benzene unit is replaced with pyrene, for which the lowest energy MLCT shifts to 505 nm (**2.11**). In contrast to the results for **2.1**-**2.10**, modification of the 4' position on the central pyridine on the terpyridine ligand resulted in only red shifts for complexes **3.2**-**3.11**, with the MLCT ranging between 490 nm and 502 nm compared to the MLCT in the

parent complex at 487 nm. Modifications in chapter four were a mixture of changes to the cyclometalating ligand and changes to the terpyridine ligand and these resulted in the lowest energy MLCT varying between 476 nm and 494 nm for the triazole containing cyclometalating ligands (**4.1**-**4.8**) and between 484 nm and 490 nm for the pyrazole containing cyclometalating ligands (**4.9**-**4.12**). This showed introducing various aryl groups attached to the triazole or pyrazole can greatly affect the energy of the MLCT, with both blue and red shifts observed. The changes in **4.9**, **4.10** and **4.12** all resulted in blue shifts for the lowest energy MLCT compared to the parent complex **3.10**, as a result of introducing aryl groups onto the 4' position of the pyrazole on each side of the cyclometalating ligand. In addition to the changes in the wavelength of the MLCT, there is a significant increase in the intensity of the MLCT for complexes incorporating large PAHs, especially those incorporating anthracene and pyrene or in the case of **3.11**, both.

The emission spectra for all of the complexes in this work were measured at room temperature in degassed acetonitrile but did not show distinct emission peaks. At 77 K all complexes were emissive with excitation of the lowest energy MLCT producing luminescence over a wide energy range (666 nm and 753 nm). The Stokes shifts for the pyrazole containing complexes were similar, with values between 6,200 cm^{-1} and 6,600 cm^{-1}, whereas the triazole containing complexes had Stokes shifts over a wider range, with values between 5,300 cm^{-1} and 6,300 cm^{-1}.

The emission quantum yields at 77 K ranged between 4% and 95%, with several complexes having very high values. These results cannot be directly related to $[Ru(dpyb)(tpy)]PF_6$, as its emission spectrum has not been measured at 77 K, and none of these complexes had detectable luminescence at room temperature using the experimental setup at hand. The emission values at 77 K were within a similar range compared to previous studies however. While changes to the complex structure have shown that the emission/absorption wavelengths can be tuned, further changes are needed to prevent ^{3}MC non-radiative decay pathways and thus enable room temperature emission.

The electrochemical properties of all complexes in this work were also examined by cyclic voltammetry. All complexes exhibit a chemically quasi-reversible redox couple for both oxidation and reduction, with the oxidation occurring on the metal center and reduction occurring on the terpyridine ligand. This was supported by the TD-DFT calculations, which were

completed for each complex and show that the HOMO is associated with the metal center and the LUMO was associated with the terpyridine ligand and not the cyclometalated ligand.

The potential of the quasi-reversible oxidation process was modified between 0.09 V and 0.24 V and the potential of the quasi-reversible reduction process was modified between -1.90 V and -2.07 V. The largest changes in the potential of the oxidation process was observed for complexes with significantly modified cyclometalated ligands as the electron density, while predominantly on the metal, is also spread over the cyclometalating ligand as shown by orbital diagrams (isodensity plots) from the TD-DFT calculations. In chapter three, where there were not large changes to the cyclometalated ligand, only a small range of potentials for the oxidation process are observed. Complex **3.5** is significantly different from the others complexes in this work, as the potential of the reduction process is -1.38 V, with a relatively unchanged potential for the oxidation process. This was a result of the electron withdrawing nature of the nitrophenyl group making it more difficult for the LUMO to be reduced, but not affecting the HOMO. This resulted in an energy gap of 1.52 V, significantly lower than the others in this work, which all range from 2.04 V to 2.16 V.

These potentials are slightly modified compared to the values for $[Ru(dpyb)(tpy)]PF_6$[37] which has quasi-reversible oxidation and reduction processes at 0.12 V and -1.95 V respectively. These potentials also show the large shift that occurs upon cyclometalation, as $[Ru(tpy)_2](PF_6)_2$ has quasi-reversible oxidation and reduction processes at 0.89 V and -1.66 V respectively. This results in a ΔE for $[Ru(dpyb)(tpy)]PF_6$[37] and $[Ru(tpy)_2](PF_6)_2$[37] of 2.07 V and 2.55 V respectively. These cyclic voltammetry results show that the electrochemical properties are changed as a result of modifications to either the cyclometalating ligand or the terpyridine as they largely affect the HOMO and LUMO respectively.

5.2 Conclusion.

This thesis highlights the viability of using substituted cyclometalated complexes in photovoltaic applications. Thirty three new cyclometalated ruthenium complexes have been successfully synthesized from forty-four potential ligands, which incorporate modifications to three key areas. The positions of these modifications were specifically chosen to direct electronic effects into the

Ru-C bond, the opposite Ru-N bond or directly into the N-heterocycle to analyze their effect in different positions.

Modifications to the 4' position of the central benzene ring on the cyclometalating ligand had a significant impact on the electronic nature of the complex and predominantly modified the energy of occupied orbitals involved in the MLCT. The work in chapter three used similar groups to those explored in chapter two, but instead incorporated them onto the 4' position of the central pyridine ring of the terpyridine ligand and these changes generally had less impact on the overall electronic nature of the complex as changes to the terpyridine ligand affected both the occupied and unoccupied orbitals in the MLCT to a similar extent, and thus the energy gap between these orbitals was largely unchanged for most complexes. Chapter four used similar aryl substitution as the previous chapters, but in this chapter substituted directly onto the N-heterocycle on each side of the cyclometalating complex.

The electrochemical and spectroscopic properties for all of these complexes show that the wavelength of absorption and emission can be tuned over a wide energy range and the intensity of the absorption for the MLCT can be significantly increased by using large aryl groups. Several complexes show very high quantum yields at 77 K, but did not show room temperature emission due to the ^{3}MC excited state being thermally accessible at room temperature.

5.3 Future perspectives.

The results in this work have shown which areas are important to modifying the energy of the frontier orbitals and this is effectively achieved. What this work does not address however is destabilizing the ^{3}MC excited state, which is preventing room temperature emission. While pyrazole was effective at causing a blue shift in the energy of the MLCT compared to using pyridine as the N-heterocycle, it reduced the chelate bite angle, which results in a more distorted octahedral structure and thus making it less favorable for room temperature emission to occur. Methods to bring the chelate bite angle closer to 180° are needed and this could potentially be achieved by using 2,6-di(quinolin-8-yl)pyridine instead of terpyridine. Using this ligand on one side of the ruthenium and some of the cyclometalated ligands synthesized in this work could lead to a structure with long emission lifetimes at room temperature. Changing the terpyridine in this manner has not been utilized with cyclometalated complexes, although it has been used to form

homoleptic ruthenium complexes, which have then been substituted at the positions para to the central co-coordinating nitrogen atom. These complexes have microsecond ^{3}MLCT excited state lifetimes.[197]

CHAPTER 6

EXPERIMENTAL PROCEDURES

6. Experimental procedures.

6.1 General information.

Unless otherwise specified, all reagents and starting materials were reagent grade, purchased from standard suppliers and used as received. Water was purified by reverse osmosis *in-house*. Where anhydrous solvents were required, the HPLC-grade solvent was either distilled from standard drying agents or dried by passing over a sealed column of activated alumina. All air- and water-sensitive manipulations were carried out under either an argon or nitrogen atmosphere using standard Schlenk techniques. Melting points were recorded on an Electrothermal melting point apparatus and are uncorrected. The following compounds were prepared using literature procedures: 1-bromopyrene,[125] 4-^{t}butylphenyl boronic acid,[129] esityl boronic acid,[128] 4-methoxyphenyl boronic acid,[130] 1-naphthyl boronic acid,[127] 2-naphthyl boronic acid,[131] 1-pyrenyl boronic acid,[126] 1,3-di(3-methyl-1-butyn-3-ol)-5-bromobenzene,[198] 2-^{t}butylpyrene,[199] 1,3-di(trimethylsilylacetylene)-5-bromobenzene,[198] 1,3-di(ethynyl)-5-bromobenzene,[198] 4-phenylpyrazole,[200] 4-(4-methoxy phenyl)pyrazole,[200] [Ru(4′-(chloro)-tpy)Cl_3,[201] [Ru(4′-(4-^{t}butylphenyl)-tpy)Cl_3,[202] [Ru(4′-(4-methoxy phenyl)-tpy)Cl_3,[203] [Ru(4′-(4-nitrophenyl)-tpy)Cl_3,[204] [Ru(4′-(4-bromophenyl)-tpy)Cl_3,[205] [Ru(4′-(2-naphthyl)-tpy)Cl_3,[206] and [Ru(4′-(9-anthracenyl)-tpy)Cl_3.[206] Safety Note: Sodium azide is toxic and appropriate precautions should be taken. As low molecular weight organic azides are potential explosives, care must be taken during their handling.[207] Generally, when the total number of carbon (C) and oxygen (O) atoms is less than the total number of nitrogen atoms (N) by a ratio of three, i.e.,$(C+O)/N < 3$, the compound is considered to be potentially explosive. Additionally, copper azides and acetylides are explosive when dry, and thus their traces were removed before the CuAAC reaction products were dried. This was achieved by pouring the crude reaction mixture into 100 mL of $EDTA_{(aq)}/NH_4OH_{(aq)}$.[193]

Mass spectroscopy (ESI-MS)

Mass spectra were recorded by Dr. Marie Squire and Dr. Meike Holzenkaempfer on either a DIONEX Ultimate 3000 or Bruker MaXis 4G spectrometer, operated in high resolution positive ion electrospray mode. Samples were dissolved and diluted to the required concentration in HPLC grade acetonitrile or methanol.

Nuclear magnetic resonance (NMR)

All spectra were recorded on a Varian INOVA 500, Varian Unity 300, or an Agilent 400-MR instrument operating at 500, 300 and 400 MHz, respectively, for ^{1}H, and 125, 75 and 125 MHz, respectively, for ^{13}C. All samples were dissolved in commercially available deuterated solvents $CDCl_3$, CD_3CN, Acetone-D6 and DMSO-D6. Spectra were referenced to the residual solvent peak. When required, COSY, HSQC and HMBC experiments were employed, using standard Varian and Agilent pulse sequences.

UV/visible spectroscopy (UV-vis)

UV/Visible spectra were recorded on a Varian CARY UV/Visible spectrometer over 200-800 nm in acetonitrile, dichloromethane or butyronitrile. Samples were measured at room temperature in quartz curvettes of path length 1 cm and approximate capacity 2 mL.

Fluorometry

Emission spectra were recorded on a Horiba Fluorolog-3 spectrometer in the range 300-800 nm for acetonitrile and butyronitrile solutions. Degassed acetonitrile samples were measured at room temperature in quartz curvettes with a path length of 1 cm and approximate capacity of 1.6 mL. Butyronitrile samples were measured at 77 K in glass tubes which were cooled using a continuous flow cryostat from oxford instruments limited. Samples had an absorbance of ca. 0.04-0.1 Abs. Quantum yields samples were determined using the quantum yield for $[Ru(bpy)_3](Cl)_2$ in MeOH/EtOH (1:4) as a standard, which has a value of 38% at 77 K.[15]

DFT calculations

DFT calculations were performed using the DZ Dunning basis set[20-21] for all atoms except ruthenium, which used the Stuttgart RSC 1997 ECP relativistic core potential[22] and bromine, which used LAND2DZ ECP.[23-25] Subsequent TD-DFT calculations were run on the optimized geometry at the same level of theory using the Gaussian version 09 program package.[65] Isodensity plots of the frontier molecular orbitals were made using the Gaussview software package.

X-Ray crystallography

Refinement data is presented in chapter 7.1 Crystallography Tables:. X-ray crystallographic data collection and refinement was carried out with either a Bruker APEXII instrument, using

graphite-monochromated Mo Kα (λ = 0.71073 Å) radiation, or an Oxford-Agilent SuperNova instrument with focused microsource Cu Kα (λ = 1.5418 Å) radiation and ATLAS CCD area detector. All structures were solved using direct methods with SHELXS-1 and refined on F2 using all data by full matrix least-squares procedures with SHELXL-972 within OLEX-2.3 Non-hydrogen atoms were refined with anisotropic displacement parameters. Hydrogen atoms were included in calculated positions, or were manually assigned from residual electron density where appropriate, with isotropic displacement parameters 1.2 times the isotropic equivalent of their carrier atoms. The functions minimized were $\Sigma w(F^2o-F^2c)$, with $w=[\sigma^2(F^2o)+aP^2+bP]^{-1}$, where $P=[max(Fo)^2+2F^2c]/3$. Some of the refinements reported may change a little upon preparation for final publication. Crystallographic data for all compounds is available in .cif format if required.

Electrochemical Studies

Electrochemical measurements were performed using a Eco Chemie Autolab PGSTAT302. Measurements were recorded in acetonitrile with 0.1 M $TBAPF_6$ as supporting electrolyte. The working electrode was platinum (Pt), the secondary electrode was also platinum and Ag/AgCl was used as the wire reference electrode. The working electrode was polished using a microcloth and 1μm alumina powder slurry; then sonicated in water and washed thoroughly with water and dried in 60 °C oven and was polished between each scan. Ferrocene was added as an internal standard on completion of each experiment and samples were referenced to it. Cyclic voltammetry was performed with a sweep rate of 100 mVs^{-1}. All experiments were measured in nitrogen sparged solutions at room temperature.

6.2 Synthesis of precursors and ligands - Chapter two.

2.12

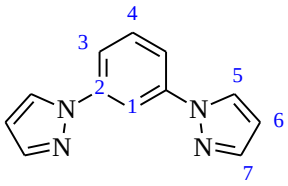

A mixture of 1,3-dibromobenzene (2.5 g, 10.5 mmol), pyrazole (1.6 g, 23.5 mmol), potassium carbonate (6.6 g, 47.8 mmol), copper(I) iodide (100 mg, 0.5 mmol) and L-proline (170 mg, 1.3 mmol) in DMSO (10 mL) was degassed by freeze-pump-thaw (3 times). The mixture was then heated at 140 °C with vigorous stirring under a nitrogen atmosphere for 24 h. After cooling to room temperature, dichloromethane (50 mL) and $NH_4OH_{(aq)}$ (2 M, 50 mL) were added and the organic phase was washed with water (4 x 50 mL). The organic phase was dried over anhydrous

potassium carbonate and the solvent removed under reduced pressure. The residue was purified by column chromatography on silica, gradient elution from dichloromethane to 20% ethyl acetate/dichloromethane, leading to the product as an oil (1.54 g, 70%).

^{1}H NMR ($CDCl_3$, 400 MHz): δ 8.09 (1H, t, J = 2.0 Hz, H1), 7.99 (2H, d, J = 2.3 Hz, H5), 7.72 (2H, m, H7), 7.59 (2H, d, J = 1.7 Hz, H3), 7.48 (1H, t, J = 1.7 Hz, H4), 6.47 (2H, t, J = 1.6 Hz, H6). **^{1}H NMR** (Acetone-D6, 400 MHz): δ 8.43 (2H, d, J = 2.5 Hz, H5), 8.36 (1H, t, J = 2.1 Hz, H1), 7.77 (2H, dd, J = 2.1 Hz, 8.1 Hz, H3), 7.74 (2H, d, J = 1.6 Hz, H7), 7.59 (2H, t, J = 8.1 Hz, H4), 6.54 (2H, t, J = 2.2 Hz, H6). **^{13}C NMR** ($CDCl_3$, 100 MHz): 141.34 (C7), 141.07 (C2), 130.41 (C4), 126.87 (C5), 116.51 (C3), 109.85 (C1), 107.97 (C6). **ESI-MS**: Found MH^+ 211.0971, $C_{12}H_{12}N_4$ requires MH^+ 211.0978. **UV-Vis** (DCM) λ_{max}/nm (ε, 10^3 $M^{-1}cm^{-1}$): 256 (32.6).

2.13

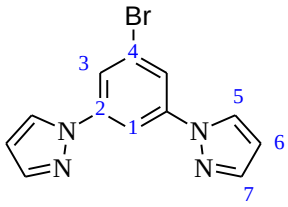

A mixture of 1,3,5-tribromobenzene (3.3 g, 10.5 mmol), pyrazole (1.6 g, 23.5 mmol), potassium carbonate (6.6 g, 47.8 mmol), copper(I) iodide (100 mg, 0.5 mmol) and L-proline (170 mg, 1.3 mmol) in DMSO (15 mL) was degassed by freeze-pump-thaw (3 times). The mixture was then heated at 140 °C with vigorous stirring under a nitrogen atmosphere for 24 h. After cooling to room temperature, dichloromethane (50 mL) and $NH_4OH_{(aq)}$ (2 M, 50 mL) were added and the organic phase was washed with water (4 x 50 mL). The organic phase was dried over anhydrous potassium carbonate and the solvent removed under reduced pressure. The residue was purified by column chromatography on silica, gradient elution from dichloromethane to 20% ethyl acetate/dichloromethane, leading to a white solid (1.82 g, 60%).

^{1}H NMR ($CDCl_3$, 400 MHz): δ 8.05 (1H, s, H1), 8.00 (2H, d, J = 1.3 Hz, H3), 7.80 (2H, s, H5), 7.75 (2H, s, H7), 6.51 (2H, s, H6). **^{1}H NMR** (Acetone-D6, 400 MHz): δ 8.51 (2H, d, J = 2.5 Hz, H5), 8.33 (1H, t, J = 1.9 Hz, H1), 7.97 (2H, d, J = 1.9 Hz, H3), 7.77 (2H, d, J = 1.5 Hz, H7), 6.57 (2H, t, J = 1.9 Hz, H6). **^{13}C NMR** ($CDCl_3$, 100 MHz): δ 141.83 (C5), 141.77 (C2), 126.93 (C7), 123.72 (C4), 119.43 (C3), 108.48 (C6), 108.13 (C1). **ESI-MS**: Found MNa^+ 310.9911, $C_{12}H_9BrN_4Na$ requires MNa^+ 310.9903. **UV-Vis** (DCM) λ_{max}/nm (ε, 10^3 $M^{-1}cm^{-1}$): 260 (71.6).

2.20

A solution of 4-^{t}butylphenyl boronic acid (342 mg, 1 mmol), 1,3-di(pyrazol-1-yl)-5-bromobenzene (145 mg, 0.5 mmol), Na_2CO_3 (2M, 1.5 mL), EtOH (2.2 mL), and toluene (13 mL) was stirred under N_2. After 20 min, $Pd(PPh_3)_4$ (93 mg, 0.08 mmol) was added and the solution was refluxed at 85 °C for 22 h. The solution was allowed to cool to room temperature, added to water (200 mL), and extracted with dichloromethane (2 x 50 mL). The benzene extracts were washed with brine (50 mL) and dried with $MgSO_4$, and solvent was removed to give a light yellow oil. This material was purified by column chromatography on silica, eluting with 10% ethyl acetate /dichloromethane to give the product (133 mg, 78%).

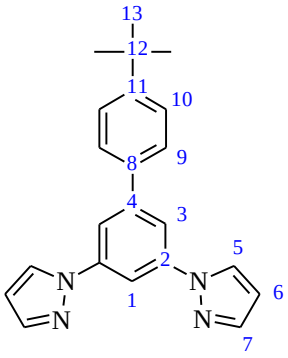

^{1}H NMR ($CDCl_3$, 400 MHz): δ 8.06 (2H, m, H7), 8.04 (1H, s, H1), 7.85 (2H, s, H3), 7.77 (2H, m, H5), 7.65 (2H, d, J = 7.8 Hz, H9), 7.52 (2H, d, J = 7.8 Hz, H10), 6.52 (2H, m, H6), 1.37 (9H, s, H13). **^{1}H NMR** (Acetone-D6, 400 MHz): δ 8.58 (2H, d, J = 2.7 Hz, H5), 8.35 (1H, t, J = 2.0 Hz, H1), 8.04 (2H, d, J = 2.0 Hz, H3), 7.77 (2H, m, H7), 7.76 (2H, m, H9), 7.58 (2H, d, J = 8.5 Hz, H10), 6.58 (2H, t, J = 2.1 Hz, H6), 1.38 (9H, s, H13). **^{13}C NMR** ($CDCl_3$, 100 MHz): δ: 151.46 (C11), 143.88 (C4), 141.55 (C2), 141.39 (C7), 136.67 (C8), 126.99 (C5), 126.90 (C10), 125.88 (C9), 115.32 (C3), 108.42 (C1), 108.01 (C6), 34.63 (C12), 31.31 (C13). **ESI-MS**: Found MH^+ 343.1923, $C_{22}H_{23}N_4$ requires MH^+ 343.1917.

2.21

A solution of mesityl boronic acid (164 mg, 1 mmol), 1,3-di(pyrazol-1-yl)-5-bromobenzene (145 mg, 0.5 mmol), Na_2CO_3 (2M, 1.5 mL), EtOH (2.2 mL), and toluene (13 mL) was stirred under N_2. After 20 min, $Pd(PPh_3)_4$ (93 mg, 0.08 mmol) was added and the solution was refluxed at 85 °C for 22 h. The solution was allowed to cool to room temperature, added to water (200 mL), and extracted with dichloromethane (2 x 50 mL). The benzene extracts were washed with brine (50 mL) and dried with $MgSO_4$, and solvent was removed to give a light yellow oil. This material was purified by column chromatography on silica, eluting with 10% ethyl acetate/dichloromethane to give the product (120 mg, 73%).

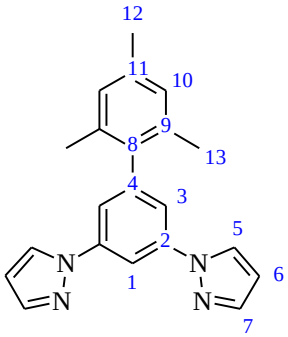

^{1}H NMR ($CDCl_3$, 400 MHz): δ 8.14 (1H, t, J = 1.9 Hz, H1), 8.01 (2H, d, J = 2.1 Hz, H5), 7.74 (2H, m, H7), 7.43 (2H, d, J = 1.9 Hz, H3), 6.96 (2H, s, H10), 6.49 (2H, t, J = 2.1 Hz, H6), 2.34 (3H, s, H12), 2.08 (6H, s, H13). **^{1}H NMR** (Acetone-D6, 400 MHz): δ 8.52 (2H, d, J = 2.5 Hz, H5), 8.41 (1H, t, J = 2.0 Hz, H1), 7.75 (2H, d, J = 1.4 Hz, H7), 7.56 (2H, d, J = 2.0 Hz, H3), 6.98 (2H, s, H10), 6.55 (2H, t, J = 2.0 Hz, H6), 2.32 (3H, s, H12), 2.07 (6H, s, H13). **^{13}C NMR** ($CDCl_3$, 100 MHz): δ 143.99 (C4), 141.44 (C7), 141.37 (C2), 141.24 (C9), 137.33 (C11), 135.74 (C8), 128.21 (C10), 126.88 (C5), 117.29 (C3), 108.10 (C1), 108.00 (C6), 20.74 (C13), 21.09 (C12). **ESI-MS**: Found MH^+ 329.1769, $C_{21}H_{22}N_4$ requires MH^+ 329.1761. **UV-Vis** (DCM) λ_{max}/nm (ε, 10^3 $M^{-1}cm^{-1}$): 257 (33.7).

2.22

A solution of 4-methoxyphenyl boronic acid (152mg, 1 mmol), 1,3-di(pyrazol-1-yl)-5-bromobenzene (145 mg, 0.5 mmol), Na_2CO_3 (2M, 1.5 mL), EtOH (2.2 mL), and toluene (13 mL) was stirred under N_2. After 20 min, $Pd(PPh_3)_4$ (93 mg, 0.08 mmol) was added and the solution was refluxed at 85 °C for 22 h. The solution was allowed to cool to room temperature, added to water (200 mL), and extracted with dichloromethane (2 x 50 mL). The benzene extracts were washed with brine (50 mL) and dried with $MgSO_4$, and solvent was removed to give a light yellow oil. This material was purified by column chromatography on silica, eluting with 10% ethyl acetate /dichloromethane to give the product (130 mg, 82%).

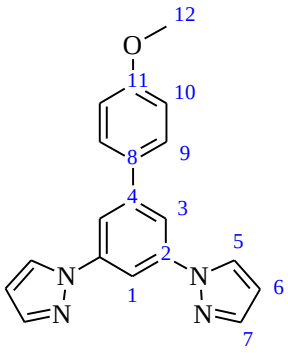

^{1}H NMR ($CDCl_3$, 400 MHz): δ 8.06 (2H, d, J = 2.1 Hz, H5), 7.99 (1H, t, J = 1.9 Hz, H1), 7.82 (2H, d, J = 1.9 Hz, H3), 7.77 (2H, d, J = 2.1 Hz, H7), 7.64 (2H, d, J = 8.8 Hz, H10), 7.01 (2H, d, J = 8.8 Hz, H9), 6.51 (2H, t, J = 2.1 Hz, H6), 3.87 (3H, s, H12). **^{1}H NMR** (Acetone-D6, 400 MHz): δ 8.57 (2H, d, J = 2.5 Hz, H5), 8.31 (1H, t, J = 1.9 Hz, H1), 8.02 (2H, d, J = 2.0 Hz, H3), 7.79 (2H, d, J = 8.8 Hz, H10), 7.77 (2H, d, J = 1.5 Hz, H7), 7.09 (2H, d, J = 8.8 Hz, H9), 6.57 (2H, t, J = 2.0 Hz, H6), 3.88 (3H, s, H12). **^{13}C NMR** ($CDCl_3$, 100 MHz): δ 159.89 (C11), 143.65 (C8), 141.38 (C7), 141.38 (C2), 132.05 (C4), 128.35 (C10), 127.01 (C5), 115.08 (C3), 114.35 (C9), 108.04 (C1), 108.00 (C6), 55.38 (C12). **ESI-MS**: Found MH^+ 317.1399, $C_{19}H_{17}N_4O$ requires MH^+ 317.1397. **UV-Vis** (DCM) λ_{max}/nm (ε, 10^3 $M^{-1}cm^{-1}$): 264 (53.3).

2.23

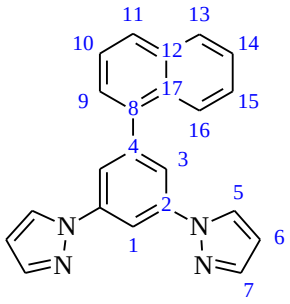

A solution of 1-naphthyl boronic acid (172 mg, 1 mmol), 1,3-di(pyrazol-1-yl)-5-bromobenzene (145 mg, 0.5 mmol), Na_2CO_3 (2M, 1.5 mL), EtOH (2.2 mL), and toluene (13 mL) was stirred under N_2. After 20 min, $Pd(PPh_3)_4$ (93 mg, 0.08 mmol) was added and the solution was refluxed at 85 °C for 22 h. The solution was allowed to cool to room temperature, added to water (200 mL), and extracted with dichloromethane (2 x 50 mL). The benzene extracts were washed with brine (50 mL) and dried with $MgSO_4$, and solvent was removed to give a light yellow oil. This material was purified by column chromatography on silica, eluting with 10% ethyl acetate /dichloromethane to give the product (138 mg, 83%).

^{1}H NMR ($CDCl_3$, 400 MHz): δ 8.21 (1H, m, H1), 8.05 (2H, d, J = 2.5, H5), 7.75 (4H, m, H3, H7), 7.57-7.44 (4H, m, H9, H11, H13, H16), 6.51 (2H, m, H6), 7.96-7.90 (3H, m, H10, H14, H15). **^{1}H NMR** (Acetone-D6, 400 MHz): δ 8.57 (2H, d, J = 2.4 Hz, H5), 8.50 (1H, t, J = 2.2 Hz, H1), 8.07-7.96 (3H, m, H10, H14, H15), 7.90 (2H, d, J = 1.8 Hz, H3), 7.77 (2H, d, J = 2.3 Hz, H7), 7.67-7.49 (4H, m, H9, H11, H13, H16), 6.58 (2H, t, J = 2.3 Hz, H6). **^{13}C NMR** ($CDCl_3$, 100 MHz): δ 141.45 (C7), 141.02 (C2), 138.45 (C4), 128.44/128.45/125.50 (C10, C14, C15), 127.00 (C5), 126.90/126.50/125.99/125.24 (C9, C11, C13, C16), 118.12 (C3), 108.76 (C1), 108.14 (C6), unassigned (C8, C12, C17). **ESI-MS**: Found MH^+ 337.146, $C_{22}H_{17}N_4$ requires MH^+ 337.1448.

2.24

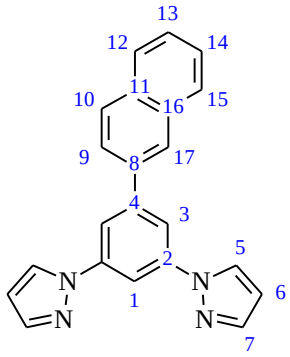

A solution of 2-naphthyl boronic acid (172mg, 1 mmol), 1,3-di(pyrazol-1-yl)-5-bromobenzene (145 mg, 0.5 mmol), Na_2CO_3 (2M, 1.5 mL), EtOH (2.2 mL), and toluene (13 mL) was stirred under N_2. After 20 min, $Pd(PPh_3)_4$ (93 mg, 0.08 mmol) was added and the solution was refluxed at 85 °C for 22 h. The solution was allowed to cool to room temperature, added to water (200 mL), and extracted with dichloromethane (2 x 50 mL). The benzene extracts were washed with brine (50 mL) and dried with $MgSO_4$, and solvent was removed to give a light yellow oil. This material was purified by column chromatography on silica, eluting with 10% ethyl acetate /dichloromethane to give the product (106 mg, 63%).

^{1}H NMR ($CDCl_3$, 400 MHz): δ 8.17 (1H, s, H17), 8.11 (2H, m, H5), 8.07 (1H, s, H1), 8.00 (2H, m, H3), 7.98-7.81 (4H, m, H15, H12, H9, H10), 7.80 (2H, m, H7), 7.57-7.50 (2H, m, H13, H14), 6.54 (2H, m, H6). **^{1}H NMR** (Acetone-D6, 400 MHz): δ 8.61 (2H , d, J = 2.5 Hz, H5), 8.40 (1H, m, H17), 8.40 (1H, m, H1), 8.21 (2H, d, J = 1.8 Hz, H3), 8.09-8.03 (2H, m, H9, H10), 8.02-7.95 (2H, m, H12, H15), 7.80 (2H, d, J = 1.9 Hz, H7), 7.62-7.52 (2H, m, H13, H14), 6.60 (2H, t, J = 2.0 Hz, H6). **^{13}C NMR** ($CDCl_3$, 100 MHz): δ 143.98 (C8), 141.50 (C2), 141.50 (C7), 136.86 (C4), 133.54/133.05 (C16/C11), 128.68/128.22/127.66/125.16 (C15/C12/C9/C10), 127.07 (C5), 126.45/126.57 (C13/C14), 126.30 (C17), 115.72 (C3), 108.58 (C1), 108.11 (C6). **ESI-MS**: Found MH^+ 337.145, $C_{22}H_{17}N_4$ requires MH^+ 337.1448.

2.25

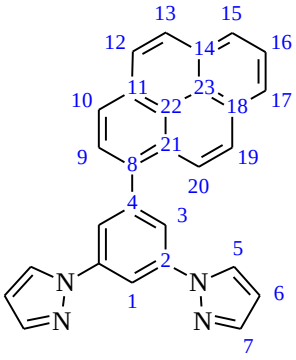

A solution of 1-pyrenyl boronic acid (246 mg, 1 mmol), 1,3-di(pyrazol-1-yl)-5-bromobenzene (145 mg, 0.5 mmol), Na_2CO_3 (2M, 1.5 mL), EtOH (2.2 mL), and toluene (13 mL) was stirred under N_2. After 20 min, $Pd(PPh_3)_4$ (93 mg, 0.08 mmol) was added and the solution was refluxed at 85 °C for 22 h. The solution was allowed to cool to room temperature, added to water (200 mL), and extracted with dichloromethane (2 x 50 mL). The benzene extracts were washed with brine (50 mL) and dried with $MgSO_4$, and solvent was removed under reduced pressure to give a light yellow oil. This material was purified by column chromatography on silica, eluting with 10% ethyl acetate/dichloromethane to give the product (121 mg, 59%).

^{1}H NMR ($CDCl_3$, 400 MHz): δ 8.26 (1H, m, H1), 8.10 (2H, d, J = 2.4 Hz, H5), 8.00-8.30 (9H, m, H9, H10, H12, H13, H15, H16, H17, H19, H20), 7.90 (2H, d, J = 2.0 Hz, H3), 7.79 (2H, d, J = 1.5 Hz, H7), 6.53 (2H, m, H6). **^{1}H NMR** (Acetone-D6, 400 MHz): δ 8.63 (2H, d, J = 2.5 Hz, H5), 8.56 (1H, t, J = 1.9 Hz, H1), 8.09-8.44 (10H, m, H9-H20), 8.07 (2H, d, J = 1.9 Hz, H3), 7.80 (2H, d, J = 1.9 Hz, H7), 6.60 (2H, t, J = 2.0 Hz, H6). **^{13}C NMR** ($CDCl_3$, 100 MHz): δ 141.55(C7), 141.13(C2), 135.76(C4), 127.07(C5), 118.66(C3), 108.76 (C1), 108.16(C6), 144.02/135.77/131.43/131.14/130.88/128.51/128.12/127.84/127.36/127.31/126.18/125.43/125.15/124.91/124.78/124.66 (C8-C24). **ESI-MS**: Found MH^+ 411.1617, $C_{28}H_{19}N_4$ requires MH^+ 411.1610.

2.26

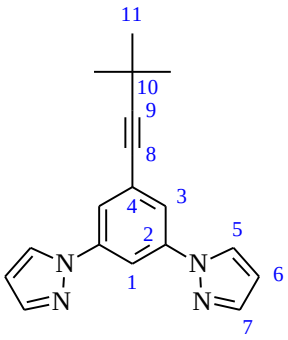

A mixture of ^{t}butylacetylene (50 mmol), 1,3-di(pyrazol-1-yl)-5-bromobenzene (145 mg, 0.5 mmol), triphenylphosphine (26.2 mg, 0.1 mmol), $Pd[(PPh_3)_2](Cl)_2$ (5 mol %) and CuI (2% mol) in THF (30 mL) and triethylamine (10 mL) was stirred at reflux for 20 h (monitored by TLC). Then, an aqueous solution of ammonium hydroxide (30 mL) was added, and the organic layer was separated with dichloromethane and dried over sodium sulfate. Finally solvent was removed under reduced pressure to give an oil. The crude oil was purified by column chromatography, eluting with dichloromethane on silica, giving the target compound (110 mg, 76%).

^{1}H NMR ($CDCl_3$, 400 MHz): δ 8.00 (1H, t, J = 1.8 Hz, H1), 7.98 (2H, d, J = 2.1 Hz, H5), 7.72 (2H, d, J = 2.1 Hz, H7), 7.63 (2H, d, J = 1.8 Hz, H3), 6.46 (2H, t, J = 2.1 Hz, H6), 1.32 (9H, s, H11). **^{1}H NMR** (Acetone-D6, 400 MHz): δ 8.50 (2H, d, J = 2.5 Hz, H5), 8.30 (1H, t, J = 2.0 Hz, H1), 7.78 (2H, d, 2.0 Hz, H3), 7.76 (2H, m, H7), 6.56 (2H, t, J = 1.9 Hz, H6), 1.36 (9H, s, H11). **^{13}C NMR** ($CDCl_3$, 100 MHz): δ 141.42 (C7), 126.91 (C5), 126.59 (C4), 119.4 (C3), 119.4 (C2), 108.8 (C1), 108.06 (C6), 100.46 (C9), 77.85 (C8), 30.82 (C11), 27.97 (C10). **ESI-MS**: Found MH^+ 291.1608, $C_{18}H_{19}N_4$ requires MH^+ 291.1604.

2.27

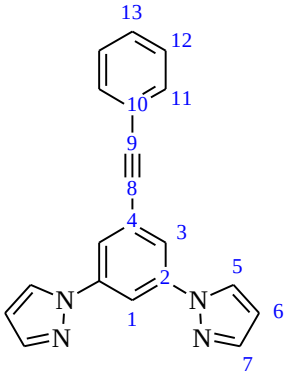

A mixture of phenylacetylene (5.10 g, 50 mmol), 1,3-di(pyrazol-1-yl)-5-bromobenzene (145 mg, 0.5 mmol), triphenylphosphine (26.2 mg, 0.1 mmol), $Pd[(PPh_3)_2](Cl)_2$ (5 mol %) and CuI (2% mol) in THF (30 mL) and triethylamine (10 mL) was stirred at reflux for 20 h (monitored by TLC). Then, an aqueous solution of ammonium hydroxide (30 mL) was added, and the organic layer was separated with dichloromethane and dried over sodium sulfate. Finally solvent was removed under reduced pressure to give an oil. The crude oil was purified by column chromatography, eluting with dichloromethane on silica, giving the target compound (129 mg, 83%).

^{1}H NMR ($CDCl_3$, 400 MHz): δ 8.12 (1H, s, H1), 8.04 (2H, m, H5), 7.80 (2H, s, H3), 7.77 (2H, m, H7), 7.56 (2H, m, H11), 7.38 (3H, m, H12, H13), 6.52 (2H, m, H6). **^{13}C NMR** ($CDCl_3$, 100 MHz): δ 141.6 (C7), 141.09 (C2), 131.53 (C11), 128.8 (C10), 128.26 (C13), 128.26 (C12),

126.43 (C5), 118.99 (C3), 109.55 (C1), 108.20 (C6), 88.01 (C8), 77.19 (C9), unassigned (C4). **ESI-MS**: Found MH^+ 311.1293, $C_{20}H_{15}N_4$ requires MH^+ 311.1297.

1-bromo-7-^{t}butylpyrene

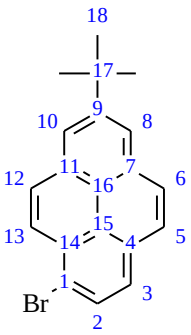

NBS (2.76 g, 15.48 mmol) in anhydrous DCM (80 mL) was slowly added to a degassed solution of 2-^{t}butylpyrene (4 g, 15.48 mmol) in anhydrous DCM (30 mL) at -78 ºC under argon atmosphere. The resulting mixture was allowed to slowly warm up to room temperature and stirred overnight. The organic layer was washed with NaCl saturated solution, after H_2O, dried over $MgSO_4$, filtered and evaporated to dryness. Recrystallization from pure hexane afforded 1-bromo-7-^{t}butylpyrene as white silver flakes (3.9 g, 75%).

^{1}H NMR (400 MHz, $CDCl_3$): δ 8.39 (1H, d, J = 9Hz, H2), 8.30 (2H, m, H8, H10), 8.20 (1H, d, J = 9.0 Hz, H13), 8.17 (1H, d, J = 9.0 Hz, H3), 8.10 (1H, d, J = 9.0 Hz, H12), 8.01 (1H, d, J = 9.0 Hz, H6), 8.00 (1H, d, J = 9.0 Hz, H5), 1.60 (s, 9H, H18). **ESI-MS**: Found MH^+ 337.0526, $C_{20}H_{18}Br$ requires MH^+ 337.0519.

2.29

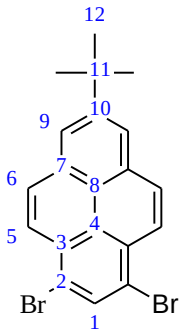

NBS (345 mg, 1.94 mmol) in anhydrous DCM (20 mL) was slowly added to a degassed solution of 2-^{t}butylpyrene (0.5 g, 1.94 mmol) in anhydrous DCM (10 mL) at -78 ºC under argon atmosphere. The resulting mixture was allowed to slowly warm up to room temperature and stirred overnight. The organic layer was washed with NaCl saturated solution, after H_2O, dried over $MgSO_4$, filtered and evaporated to dryness. Recrystallization from pure hexane gave **2.29** (0.71 g, 0.81 %).

^{1}H NMR (500 MHz, $CDCl_3$): δ 8.48 (1H, s, H1), 8.36 (2H, d, *J* = 9.0 Hz, H5), 8.35 (2H, s, H9), 8.21 (2H, d, *J* = 9.0 Hz, H6), 1.59 (9H, s, H12). **ESI-MS**: Found MH^+ 416.9683, $C_{20}H_{17}Br_2$ requires MH^+ 416.9677.

2.30

A mixture of 1,3-dibromo-7-^{t}butylpyrene (1.0 g, 2.56 mmol), pyrazole (383 mg, 5.63 mmol), potassium carbonate (1.55 g, 11.3 mmol), copper(I) iodide (107 mg, 0.56 mmol) and L-proline (170 mg, 5.63 mmol) in DMSO (10 mL) was degassed by freeze-pump-thaw (3 times). The

mixture was then heated at 140 °C with vigorous stirring under a nitrogen atmosphere for 24 h. After cooling to room temperature, dichloromethane (50 mL) and $NH_4OH_{(aq)}$ (2 M, 50 mL) were added and the organic phase was washed with water (4 x 50 mL). The organic phase was dried over anhydrous potassium carbonate and the solvent removed under reduced pressure. The residue was purified by column chromatography on silica, gradient elution from dichloromethane to 20% ethyl acetate/dichloromethane, leading to a white solid (1.82 g, 60%).

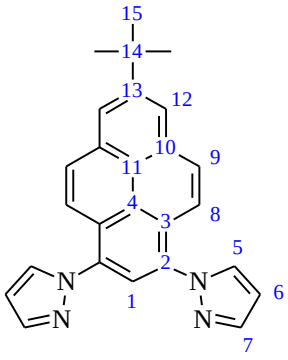

^{1}H NMR (300 MHz, $CDCl_3$): δ 8.31 (2H, s, H12), 8.14 (1H, s, H1), 8.08-8.18 (4H, m, H8, H9), 7.97 (2H, d, J = 2.1 Hz, H5), 7.93 (2H, d, J = 1.7 Hz, H7), 6.63 (2H, t, J = 1.9 Hz, H6), 1.60 (9H, s, H15). **^{13}C NMR** (125 MHz, $CDCl_3$): δ 150.36 (C13), 141.34 (C7), 133.91/130.92/ 125.96/122.54 (C3/C4/C10/C11), 132.18 (C5), 129.73 (C8), 129.73 (C9), 123.75 (C12), , 121.76 (C1), 121.08 (C2), 107.09 (C6), 35.33 (C14), 31.84 (C15). **ESI-MS**: Found MH^+ 390.1853, $C_{26}H_{23}N_4$ requires MH^+ 390.1845.

6.3 Ruthenium complexes - Chapter two.

2.1

A mixture of $Ru(tpy)Cl_3$ (86 mg, 0.196 mmol), 1,3-di(pyrazol-1-yl)benzene (33 mg, 0.157 mmol), silver triflate (160 mg, 0.62 mmol) and Et_3N (3 drops) in $EtOH/H_2O$ (3:1, 12 mL) was refluxed for 12 h. After cooling and filtering, the solvent was removed under reduced pressure. The solid was slowly dropped into an excess of $NH_4PF_{6(aq)}$. The fine precipitate was filtered, washed with water, rinsed with CH_3CN, dried over Na_2SO_4 and the solvent was removed in vacuo. The crude product was purified using column chromatography, eluting with 10% acetonitrile/ethyl acetate on silica to give the pure complex (82 mg, 76%).

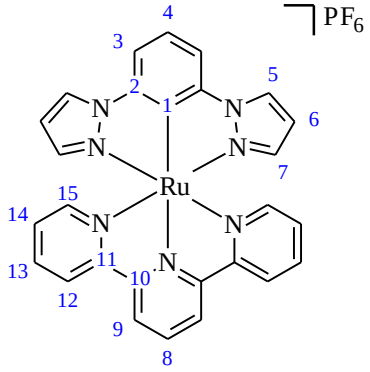

^{1}H NMR (CD_3CN, 400 MHz): δ 8.90 (2H, d, J = 8.1 Hz, H9), 8.72 (2H, d, J = 2.7 Hz, H5), 8.63 (2H, d, J = 8.1 Hz, H15), 8.33 (1H, t, J = 8.1 Hz, H8), 7.90 (2H, d, J = 7.8 Hz, H3), 7.83 (2H, dt, J = 1.3 Hz, 8.1 Hz, H14), 7.44 (1H, t, J = 7.8 Hz, H4), 7.37 (2H, d, J = 5.4 Hz, H12), 7.15 (2H, dt, J = 1.5 Hz, 6.6 Hz, H13), 6.69 (2H, d, J = 2.1 Hz, H7), 6.24 (2H, t, J = 2.6 Hz, H6). **^{13}C NMR** (CD_3CN, 100 MHz): δ 181.28 (C1), 159.89 (C11), 154.96 (C10), 154.16 (C12), 143.25 (C2),

141.62 (C7), 135.27 (C14), 132.54 (C8), 127.91 (C5), 126.34 (C13), 123.20 (C15), 121.81 (C9), 121.81 (C4), 108.65 (C3), 107.03 (C6). **ESI-MS**: Found $[M\text{-}PF_6+H]^{2+}$ 544.0827, $C_{27}H_{20}N_7Ru$ requires $[M\text{-}PF_6+H]^{2+}$ 544.0825. **ESI-MS**: Found $[M\text{-}PF_6]^+$ 272.5437, $C_{27}H_{20}N_7Ru$ requires $[M\text{-}PF_6]^+$ 272.5452. **UV-Vis** (CH_3CN) λ_{max}/nm (ε, 10^3 $M^{-1}cm^{-1}$): 536 (2.7), 487 (4.7), 375 (5.4), 318 (15.2), 259 (19.9), 234 (17.6). **Fluorometry** (Butyronitrile, 77K) λ_{max}: 712 nm.

2.2

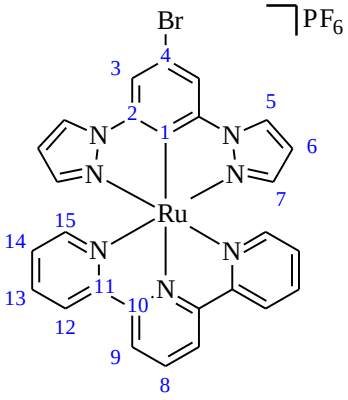

A mixture of $Ru(tpy)Cl_3$ (86 mg, 0.196 mmol), 1,3-di(pyrazol-1-yl)-5-bromobenzene (45 mg, 0.157 mmol), silver triflate (160 mg, 0.62 mmol) and Et_3N (3 drops) in $EtOH/H_2O$ (3:1, 12 mL) was refluxed for 12 h. After cooling and filtering, the solvent was removed under reduced pressure. The solid was slowly dropped into an excess of $NH_4PF_{6(aq)}$. The fine precipitate was filtered, washed with water, rinsed with CH_3CN, dried over Na_2SO_4 and the solvent was removed in vacuo. The crude product was purified using column chromatography, eluting with 10% acetonitrile/ethyl acetate on silica to give the pure complex (89 mg, 74%).

^{1}H NMR (CD_3CN, 400 MHz): δ 8.67 (2H, d, J = 8.1 Hz, H9), 8.46 (2H, d, J = 2.5 Hz, H5), 8.40 (2H, d, J = 8.1 Hz, H15), 8.25 (1H, t, J = 8.1 Hz, H8), 7.97 (2H, s, H3), 7.74 (2H, m, H14), 7.30 (2H, m, H12), 7.02 (2H, m, H13), 6.57 (2H, d, J = 2.5 Hz, H7), 6.21 (2H, t, J = 2.5 Hz, H6). **^{13}C NMR** (CD_3CN, 100 MHz): δ 180.78 (C1), 159.83 (C11), 154.93 (C10), 154.29 (C12), 144.11 (C2), 142.17 (C7), 135.58 (C14), 133.08 (C8), 128.52 (C5), 126.45 (C13), 123.36 (C15), 121.99 (C9), 111.65 (C3), 107.50 (C6), unassigned (C4). **ESI-MS**: Found $[M\text{-}PF_6]^+$ 621.9929, $C_{27}N_7H_{19}RuBr$ requires $[M\text{-}PF_6]^+$ 621.9925. Found $[M\text{-}PF_6+H]^{2+}$ 311.4991, $C_{27}H_{19}N_7RuBr$ requires $[M\text{-}PF_6+H]^{2+}$ 311.4999. **UV-Vis** (CH_3CN) λ_{max}/nm (ε, 10^3 $M^{-1}cm^{-1}$): 590 (sh), 530 (sh), 482 (9.4), 361 (9.8), 317 (31.5), 263 (40.2), 233 (35.0). **Fluorometry** (Butyronitrile, 77K) λ_{max}: 700 nm.

2.3

A mixture of Ru(tpy)Cl_3 (43 mg, 0.098 mmol), 1,3-di(pyrazol-1-yl)-5-(4-^{t}butylphenyl)benzene (27 mg, 0.079 mmol), silver triflate (80 mg, 0.31 mmol) and Et_3N (3 drops) in EtOH/H_2O (3:1, 12 mL) was refluxed for 12 h. After cooling and filtering, the solvent was removed under reduced pressure. The solid was slowly dropped into an excess of $NH_4PF_{6(aq)}$. The fine precipitate was filtered, washed with water, rinsed with CH_3CN, dried over Na_2SO_4 and the solvent was removed in vacuo. The crude product was purified using column chromatography, eluting with 10% acetonitrile/ethyl acetate on silica to give the pure complex (47 mg, 60% yield).

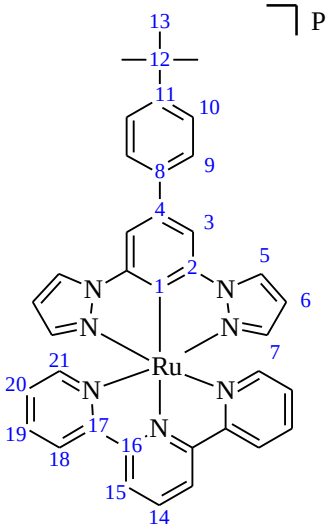

^{1}H NMR (Acetone-*d6*, 400 MHz): δ 8.90 (2H, d, J = 2.8 Hz, H5), 8.28 (2H, s, H3), 7.95 (2H, d, J = 8.7 Hz, H8), 7.64 (2H, d, 8.7 Hz, H9), 6.73 (2H, d, J = 2.0 Hz, H7), 6.29 (2H, t, J = 2.4 Hz, H6), 1.44 (9H, s, H13). **^{13}C NMR** (Acetone-*d6*, 100 MHz): δ 181.1 (C1), 159.89 (C17), 154.98 (C16), 154.20 (C18), 149.67 (C11), 143.17 (C2), 141.81 (C7), 138.94 (C4), 135.37 (C8), 135.36 (C20), 132.62 (C14), 128.14 (C5), 126.60 (C9), 126.41 (C19), 125.78 (C10), 123.25 (C21), 121.85 (C15), 107.37 (C3), 107.11 (C6), 34.21 (C12), 30.82 (C13). **ESI-MS**: Found $[M\text{-}PF_6]^+$ 676.1793, $C_{37}H_{32}N_7Ru$ requires $[M\text{-}PF_6]^+$ 676.1767. Found $[M\text{-}PF_6\text{+}H]^{2+}$ 338.0897, $C_{37}H_{33}N_7Ru$ requires $[M\text{-}PF_6\text{+}H]^{2+}$ 338.0881. **UV-Vis** (CH_3CN) λ_{max}/nm (ε, 10^3 $M^{-1}cm^{-1}$): 600 (sh), 534 (sh), 488 (6.0), 373 (6.9), 317 (24.5), 270 (sh), 263 (33.9), 232 (32.6). **Fluorometry** (Butyronitrile, 77K) λ_{max}: 718 nm.

2.4

A mixture of Ru(tpy)Cl_3 (43 mg, 0.098 mmol), 1,3-di(pyrazol-1-yl)-5-bromobenzene (26 mg, 0.079 mmol), silver triflate (80 mg, 0.31 mmol) and Et_3N (3 drops) in EtOH/H_2O (3:1, 12 mL) was refluxed for 12 h. After cooling and filtering, the solvent was removed under reduced pressure. The solid was slowly dropped into an excess of $NH_4PF_{6(aq)}$. The fine precipitate was filtered, washed with water, rinsed with CH_3CN, dried over Na_2SO_4 and the solvent was removed in vacuo. The crude product was purified using column chromatography, eluting with 10% acetonitrile/ethyl acetate on silica to give the pure complex (40 mg, 64%).

^{1}H NMR (Acetone-*d6*, 400 MHz): δ 8.93 (2H, d, J = 8.1 Hz, H15), 8.75 (2H, d, J = 2.6, H5), 8.64 (2H, d, J = 8.0 Hz, H21), 8.35 (1H, t, J = 8.1 Hz, H14), 7.86 (2H, t, J = 8.0 Hz, H20), 7.69 (2H, s, H3), 7.50 (2H, d, J = 5.4 Hz, H18), 7.18 (2H, t, J = 6.8 Hz, H19), 7.08 (2H, s, H10), 6.74 (2H, d, J = 2.6 Hz, H7), 6.26 (2H, m, H6), 2.38 (3H, s, H12), 2.31 (6H, s, H13). **^{13}C NMR** (Acetone-*d6*, 100 MHz): δ 179.25 (C1), 159.98 (C16), 155.02 (C17), 154.10 (C18), 143.17 (C2), 141.78 (C7), 139.45 (C4), 136.40 (C9), 136.31 (C11), 135.30 (C20), 134.79 (C8), 132.50 (C14), 128.07 (C5), 128.01 (C10), 126.43 (C19), 123.26 (C21), 121.86 (C15), 109.76 (C3), 107.06 (C6), 20.40 (C13), 20.29 (C12). **ESI-MS**: Found $[M\text{-}PF_6]^+$ 662.1639, $C_{36}H_{30}N_7Ru$ requires $[M\text{-}PF_6]^+$ 662.1610. Found $[M\text{-}PF_6{+}H]^{2+}$ 331.0823, $C_{36}H_{31}N_7Ru$ requires $[M\text{-}PF_6{+}H]^{2+}$ 331.0802. **UV-Vis** (CH_3CN) λ_{max}/nm (ε, 10^3 $M^{-1}cm^{-1}$): 606 (sh), 530 (sh), 487 (7.1), 363 (10.7), 317 (29.7), 272 (37.3), 262 (37.0), 235 (31.7). **Fluorometry** (Butyronitrile, 77K) λ_{max}: 715 nm.

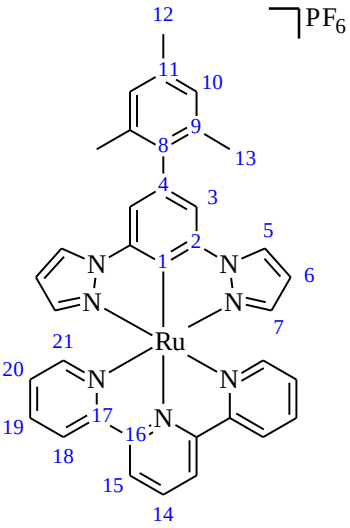

2.5

A mixture of $Ru(tpy)Cl_3$ (86 mg, 0.196 mmol), 1,3-di(pyrazol-1-yl)-5-(4-methoxyphenyl)benzene (50 mg, 0.157 mmol), silver triflate (160 mg, 0.62 mmol) and Et_3N (3 drops) in EtOH/H_2O (3:1, 12 mL) was refluxed for 12 h. After cooling and filtering, the solvent was removed under reduced pressure. The solid was slowly dropped into an excess of $NH_4PF_{6(aq)}$. The fine precipitate was filtered, washed with water, rinsed with CH_3CN, dried over Na_2SO_4 and the solvent was removed in vacuo. The crude product was purified using column chromatography, eluting with 10% acetonitrile/ethyl acetate on silica to give the pure complex (77 mg, 62% yield).

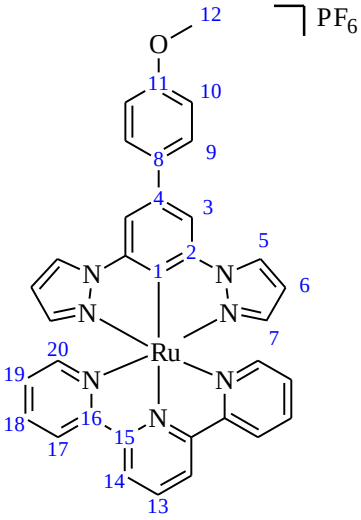

^{1}H NMR (Acetone-*d6*, 400 MHz): δ 8.92 (2H, m, H14), 8.90 (2H, m, H5), 8.64 (2H, d, 8.2 Hz, H20), 8.34 (1H, t, J = 8.1 Hz, H13), 8.26 (2H, s, H3), 7.96 (2H, d, 5.4 Hz, H9), 7.83 (2H, t, 8.2 Hz, H19), 7.46 (2H, d, 5.4 Hz, H17), 7.17 (2H, m, H10), 7.15 (2H, m, H18), 6.73 (2H, m, H7), 6.27 (2H, m, H6), 3.92 (3H, s, H12). **^{13}C NMR** (Acetone-*d6*, 100 MHz): δ 180.36 (C1), 159.88

(C16), 159.08 (C11), 154.94 (C15), 154.18 (C9), 143.71 (C2), 141.82 (C7), 135.33 (C19), 135.18 (C8), 134.20 (C4), 132.61 (C13), 128.14 (C5), 127.90 (C17), 126.40 (C18), 123.24 (C20), 121.86 (C14), 114.35 (C10), 107.10 (C6), 107.08 (C3), 54.82 (C12). ESI-MS: Found $[M\text{-}PF_6]^+$ 650.1272, $C_{34}H_{26}N_7ORu$ requires $[M\text{-}PF_6]^+$ 650.1246. Found $[M\text{-}PF_6\text{+}H]^{2+}$ 325.0636, $C_{34}H_{27}N_7ORu$ requires $[M\text{-}PF_6\text{+}H]^{2+}$ 325.0620. **UV-Vis** (CH_3CN) λ_{max}/nm (ε, 10^3 $M^{-1}cm^{-1}$): 603 (sh), 532 (sh), 487 (6.7), 362 (9.4), 318 (29.2), 271 (38.4), 263 (sh), 234 (26.6). **Fluorometry** (Butyronitrile, 77K) λ_{max}: 729 nm.

2.6

A mixture of $Ru(tpy)Cl_3$ (86 mg, 0.196 mmol), 1,3-di(pyrazol-1-yl)-5-(1-naphthyl)benzene (53 mg, 0.157 mmol), silver triflate (160 mg, 0.62 mmol) and Et_3N (3 drops) in $EtOH/H_2O$ (3:1, 12 mL) was refluxed for 12 h. After cooling and filtering, the solvent was removed under reduced pressure. The solid was slowly dropped into an excess of $NH_4PF_{6(aq)}$. The fine precipitate was filtered, washed with water, rinsed with CH_3CN, dried over Na_2SO_4 and the solvent was removed in vacuo. The crude product was purified using column chromatography, eluting with 10% acetonitrile/ethyl acetate on silica to give the pure complex (68 mg, 53% yield).

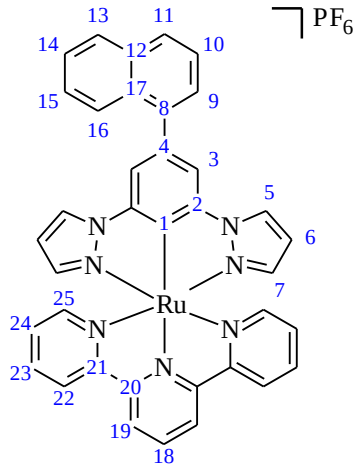

^{1}H NMR (Acetone-*d6*, 400 MHz): δ 8.86 (2H, m, H5), 8.38 (1H, m, H9), 8.09 (1H, m, H11), 8.05 (2H, s, H3), 8.05 (1H, m, H13), 7.80 (1H, d, J = 7.1 Hz, H16), 7.72 (1H, m, H14), 7.54-7.67 (1H, m, H15), 7.54-7.67 (1H, m, H10), 6.76 (2H, m, H7), 6.29 (2H, m, H6). **^{13}C NMR** (Acetone-*d6*, 100 MHz): δ 181.05 (C1), 143.06 (C2), 141.84 (C7), 140.98 (C4), 128.40 (C5), 128.21 (C11), 127.47 (C13), 127.30 (C16), 126.34 (C9), 126.18 (C10/C15), 125.90 (C10/C15), 125.55 (C14), 110.54 (C3), 107.14 (C6), unassigned (C8, C12, C17). **ESI-MS**: Found $[M\text{-}PF_6]^+$ 670.1308, C37H26N7Ru requires $[M\text{-}PF_6]^+$ 670.1297. Found $[M\text{-}PF_6\text{+}H]^{2+}$ 335.0660, C37H27N7Ru requires $[M\text{-}PF_6\text{+}H]^{2+}$ 335.0646. **UV-Vis** (CH_3CN) λ_{max}/nm (ε, 10^3 $M^{-1}cm^{-1}$): 601 (sh), 531 (sh), 486 (8.5), 366 (12.9), 318 (31.7), 271 (43.3), 266 (43.3), 221 (78.1). **Fluorometry** (Butyronitrile, 77K) λ_{max}: 705 nm.

2.7

A mixture of $Ru(tpy)Cl_3$ (43 mg, 0.098 mmol), 1,3-di(pyrazol-1-yl)-5-(2-naphthyl)benzene (26 mg, 0.079 mmol), silver triflate (80 mg, 0.31 mmol) and Et_3N (3 drops) in $EtOH/H_2O$ (3:1, 12 mL) was refluxed for 12 h. After cooling and filtering, the solvent was removed under reduced pressure. The solid was slowly dropped into an excess of $NH_4PF_{6(aq)}$. The fine precipitate was filtered, washed with water, rinsed with CH_3CN, dried over Na_2SO_4 and the solvent was removed in vacuo. The crude product was purified using column chromatography, eluting with 10% acetonitrile/ethyl acetate on silica to give the pure complex (40 mg, 63% yield).

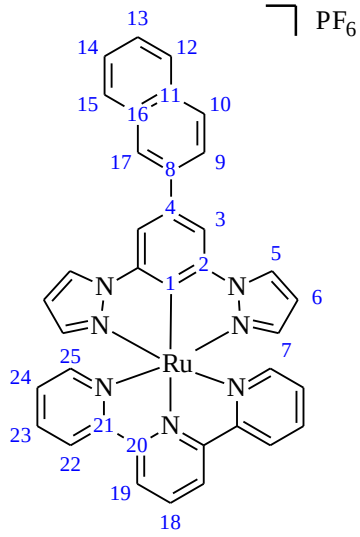

^{1}H NMR (Acetone-*d6*, 400 MHz): δ 8.94 (2H, m, H5), 8.92 (2H, m, H19), 8.64 (2H, d, J = 8.1 Hz, H25), 8.53 (1H, s, H17), 8.46 (2H, s, H3), 8.36 (1H, t, J = 8.1 Hz, H18), 8.23 (1H, d, J = 8.51 Hz, H10), 8.13 (1H, d, J = 8.51 Hz, H9), 8.06 (1H, d, 8.00 Hz, H15), 8.02 (1H, d, J = 8.00 Hz, H12), 7.86 (2H, d, J = 8.4 Hz, H24), 7.61 (1H, m, H13), 7.56 (1H, m, H14), 7.51 (2H, d, J = 5.53 Hz, H22), 7.19 (2H, t, J = 6.9 Hz, H23), 6.75 (2H, d, 2.2 Hz, H7), 6.30 (2H, t, J = 2.2 Hz, H6). **^{13}C NMR** (Acetone-*d6*, 100 MHz): δ 182.00 (C1), 159.86 (C21), 154.92 (C20), 154.27 (C22), 143.95 (C2), 141.90 (C5), 139.18 (C4), 135.43 (C24), 135.05 (C8), 134.23 (C11), 132.73 (C18), 132.63 (C16), 128.58 (C9), 128.24 (C7), 128.02 (C15), 127.71 (C12), 126.46 (C23), 125.75 (C14), 125.75 (C13), 125.68 (C10), 124.99 (C17), 123.26 (C25), 121.87 (C19), 107.69 (C3), 107.17 (C6). ESI-MS: Found $[M\text{-}PF_6]^+$670.1325, $C_{37}H_{26}N_7Ru$ requires $[M\text{-}PF_6]^+$ 670.1328. Found $[M\text{-}PF_6+H]^{2+}$ 335.0664, $C_{37}H_{26}N_7Ru$ requires $[M\text{-}PF_6+H]^{2+}$ 335.0646. **UV-Vis** (CH_3CN) λ_{max}/nm (ε, 10^3 $M^{-1}cm^{-1}$): 602 (sh), 527 (sh), 484 (7.6), 372 (13.4), 318 (28.1), 271 (43.7), 263 (42.4), 254 (42.2), 234 (41.5), 211 (37.5). **Fluorometry** (Butyronitrile, 77K) λ_{max}: 714 nm.

2.8

A mixture of $Ru(tpy)Cl_3$ (86 mg, 0.196 mmol), 1,3-di(pyrazol-1-yl)-5-(1-pyrenyl)benzene (64 mg, 0.157 mmol), silver triflate (160 mg, 0.62 mmol) and Et_3N (3 drops) in $EtOH/H_2O$ (3:1, 12 mL) was refluxed for 12 h. After cooling and filtering, the solvent was removed under reduced pressure. The solid was slowly dropped into an excess of $NH_4PF_{6(aq)}$. The fine precipitate was filtered, washed with water, rinsed with CH_3CN, dried over Na_2SO_4 and the solvent was removed

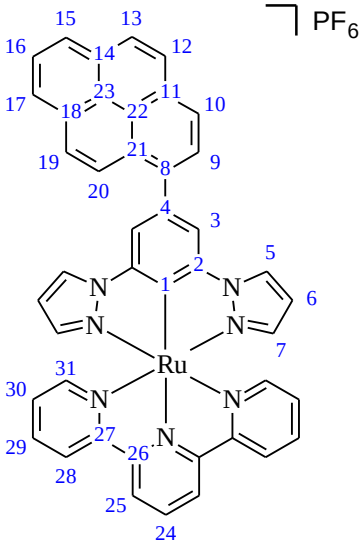

in vacuo. The crude product was purified using column chromatography, eluting with 10% acetonitrile/ethyl acetate on silica to give the pure complex (67 mg, 48% yield).

^{1}H NMR (Acetone-*d6*, 400 MHz): δ 8.96 (2H, d, J = 8.1 Hz, H25), 8.90 (2H, d, J = 2.9 Hz, H5), 8.70 (1H, m, H20), 8.69 (2H, m, H31), 8.51 (1H, m, H9), 8.43 (1H, m, H10), 8.37 (1H, m, H24), 8.36 (1H, m, H17), 8.36 (1H, m, H15), 8.30 (1H, m, H12), 8.29 (1H, m, H13), 8.26 (1H, m, H19), 8.22 (2H, s, H3), 8.14 (1H, t, J = 7.6 Hz, H16), 7.90 (2H, m, H30), 7.66 (2H, m, H28), 7.25 (2H, t, J = 6.6 Hz, H29), 6.79 (2H, d, J = 2.1 Hz, H7), 6.31 (2H, t, J = 2.5 Hz, H6). **^{13}C NMR** (Acetone-*d6*, 100 MHz): δ 181.95 (C1), 159.92 (C27), 155.02 (C26), 154.43 (C28), 143.42 (C2), 141.91 (C7), 138.65 (C4), 135.43 (C30), 132.69 (C24), 128.45 (C10), 128.28 (C5), 128.28 (C17), 128.28 (C15), 127.56 (C12), 127.40 (C19), 127.40 (C13), 126.50 (C29), 126.36 (C16), 125.77 (C20), 124.86 (C9), 123.27 (C31), 121.87 (C25), 111.06 (C3), 107.19 (C6), 131.69/131.18/130.56/128.72/125.29/124.92 (C8, C11, C14, C20, C21, C22). **ESI-MS**: Found $[M\text{-}PF_6]^+$ 744.1468, $C_{43}H_{28}N_7Ru$ requires $[M\text{-}PF_6]^+$ 744.1456. Found $[M\text{-}PF_6\text{+}H]^{2+}$ 372.0729, $C_{43}H_{29}N_7Ru$ requires $[M\text{-}PF_6\text{+}H]^{2+}$ 372.0725. **UV-Vis** (CH_3CN) λ_{max}/nm (ε, 10^3 $M^{-1}cm^{-1}$): 598 (sh), 528 (sh), 482 (11.2), 377 (18.1), 339 (26.1), 318 (40.2), 276 (59.4), 266 (sh), 237 (62.5). **Fluorometry** (Butyronitrile, 77K) λ_{max}: 670 nm.

2.9

A mixture of $Ru(tpy)Cl_3$ (86 mg, 0.196 mmol), 1,3-di(pyrazol-1-yl)-5-(^{t}butylacetylene)benzene (46 mg, 0.157 mmol), silver triflate (160 mg, 0.62 mmol) and Et_3N (3 drops) in $EtOH/H_2O$ (3:1, 12 mL) was refluxed for 12 h. After cooling and filtering, the solvent was removed under reduced pressure. The solid was slowly dropped into an excess of $NH_4PF_{6(aq)}$. The fine precipitate was filtered, washed with water, rinsed with CH_3CN, dried over Na_2SO_4 and the solvent was removed in vacuo. The crude product was purified using column chromatography, eluting with 10% acetonitrile/ethyl acetate on silica to give the pure complex (51 mg, 41% yield).

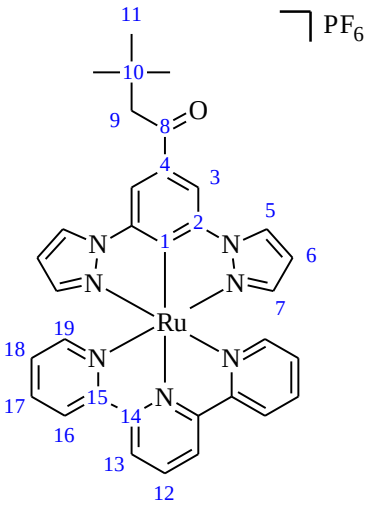

^{1}H NMR (Acetone-D6, 400 MHz): δ 8.68 (2H, d, J = 8.1 Hz, H13), 8.63 (2H, m, H5), 8.41 (2H, m, H19), 8.40 (2H, s, H3), 8.28 (1H, t, J = 8.1 Hz, H12), 7.74 (2H, t, J = 5.6 Hz, H18), 7.25 (2H, d, J = 6.3 Hz, H16), 6.99 (2H, t, J = 5.6 Hz, H17), 6.59 (2H, m, H7), 6.24 (2H, m, H6), 1.24 (9H, s, H11). **^{13}C NMR** (Acetone-D6, 100 MHz): δ 198.48 (C8), 196.03 (C1), 159.46 (C16), 159.46 (C15), 154.65 (C14), 143.29 (C2), 143.19 (C4), 141.87 (C5), 135.77 (C18), 133.37 (C12), 128.37 (C7), 126.27 (C17), 123.31 (C19), 121.91 (C13), 109.59 (C3), 108.59 (C6), 50.88 (C9), 32.53 (C10), 30.84 (C11). **ESI-MS**: Found $[M\text{-}PF_6]^+$ 642.1569, $C_{33}H_{30}N_7ORu$ requires $[M\text{-}PF_6]^+$ 642.1558. Found $[M\text{-}PF_6\text{+}H]^{2+}$ 321.0778, $C_{33}H_{31}N_7ORu$ requires $[M\text{-}PF_6\text{+}H]^{2+}$ 321.0776. **UV-Vis** (CH_3CN) λ_{max}/nm (ε, 10^3 $M^{-1}cm^{-1}$): 596 (0.9), 517 (2.8), 479 (4.3), 388 (5.5), 316 (12.1), 272 (14.9), 262 (15.7), 234 (12.8). **Fluorometry** (Butyronitrile, 77K) λ_{max}: 674 nm.

2.10

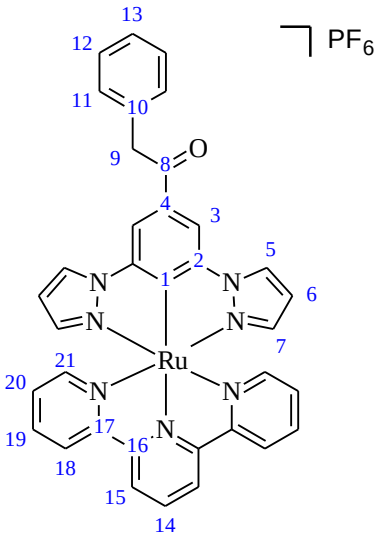

A mixture of $Ru(tpy)Cl_3$ (86 mg, 0.196 mmol), 1,3-di(pyrazol-1-yl)-5-(phenylacetylene)benzene (49 mg, 0.157 mmol), silver triflate (160 mg, 0.62 mmol) and Et_3N (3 drops) in $EtOH/H_2O$ (3:1, 12 mL) was refluxed for 12 h. After cooling and filtering, the solvent was removed under reduced pressure. The solid was slowly dropped into an excess of $NH_4PF_{6(aq)}$. The fine precipitate was filtered, washed with water, rinsed with CH_3CN, dried over Na_2SO_4 and the solvent was removed in vacuo. The crude product was purified using column chromatography, eluting with 10% acetonitrile/ethyl acetate on silica to give the pure complex (46 mg, 36% yield).

^{1}H NMR (Acetone-D6, 400 MHz): δ 9.00 (2H, d, J = 2.9 Hz, H5), 8.96 (2H, m, H15), 8.66 (2H, d, J = 8.1 Hz, H21), 8.43 (1H, m, H14), 8.42 (2H, s, H3), 8.14 (2H, d, J = 7.4, H11), 7.89 (2H, m, H12), 7.71 (2H, t, J = 8.1 Hz, H20), 7.47 (2H, d, J = 6.3 Hz, H18), 7.33 (1H, t, J = 7.5 Hz, H13), 7.17 (2H, m, H19), 6.88 (2H, d, J = 2.1 Hz, H7), 6.33 (2H, t, J = 2.8 Hz, H6), 2.85 (2H, s, H9). **^{13}C NMR** (Acetone-D6, 100 MHz): δ 198.23 (C8), 196.24 (C1), 159.64 (C18), 159.37 (C17), 154.54 (C16), 144.01 (C4), 143.19 (C2), 141.54 (C5), 135.80 (C20), 133.32 (C14), 129.60

(C11), 129.23 (C12), 128.22 (C7), 126.84 (C13), 126.34 (C19), 123.19 (C21), 121.99 (C15), 109.69 (C3), 108.12 (C6), 50.31 (C9), Unassigned (C10). **ESI-MS**: Found $[M\text{-}PF_6]^+$ 662.1248, $C_{35}H_{26}N_7ORu$ requires $[M\text{-}PF_6]^+$ 622.1242. Found $[M\text{-}PF_6\text{+}H]^{2+}$ 331.5668, $C_{35}H_{27}N_7ORu$ requires $[M\text{-}PF_6\text{+}H]^{2+}$ 331.5660. **UV-Vis** (CH_3CN) λ_{max}/nm (ε, 10^3 $M^{-1}cm^{-1}$): 595 (0.9), 481 (4.9), 361 (4.1), 316 (9.2), 271 (12.5), 264 (12.5), 226 (13.3). **Fluorometry** (Butyronitrile, 77K) λ_{max}: 666 nm.

2.11

A mixture of Ru(**3.13**)Cl_3 (36 mg, 0.098 mmol), 1,3-di(pyrazol-1-yl)-7-^{t}butylpyrene (31 mg, 0.079 mmol), silver triflate (80 mg, 0.31 mmol) and Et_3N (3 drops) in EtOH/H_2O (3:1, 12 mL) was refluxed for 12 h. After cooling and filtering, the solvent was removed under reduced pressure. The solid was slowly dropped into an excess of $NH_4PF_{6(aq)}$. The fine precipitate was filtered, washed with water, rinsed with CH_3CN, dried over Na_2SO_4 and the solvent was removed in vacuo. The crude product was purified using column chromatography, eluting with 10% acetonitrile/ethyl acetate on silica to give the pure complex (39 mg, 49% yield).

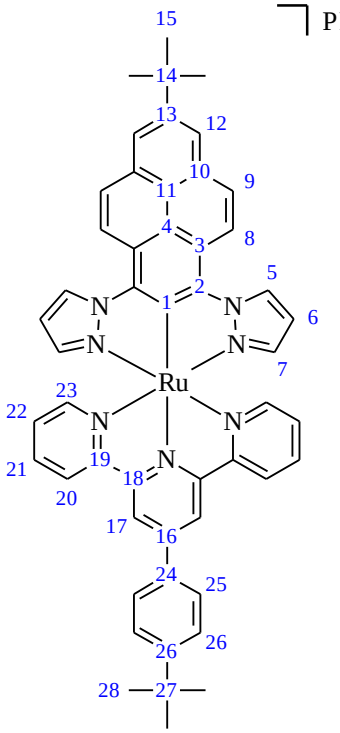

^{1}H NMR (Acetone-D6, 400 MHz): δ 9.48 (2H, d, H5), 9.29 (2H, s, H17), 9.04 (2H, d, J = 9.3 Hz, H8), 8.89 (2H, d, J = 7.8 Hz, H23), 8.52 (2H, s, H12), 8.47 (2H, d, J = 9.3 Hz, H9), 8.27 (2H, d, J = 8.1 Hz, H26), 7.84 (2H, t, J = 7.3 Hz, H22), 7.78 (2H, d, J = 8.1 Hz, H25), 7.32 (2H, d, J = 5.5 Hz, H20), 7.02 (2H, t, J = 6.8 Hz, H21), 6.97 (2H, d, J = 1.4 Hz, H7), 6.51 (2H, t, J = 2.2 Hz, H6), 1.68 (9H, s, H15), 1.47 (9H, s, H28). **ESI-MS**: Found $[M\text{-}PF_6]^+$ 856.2709, $C_{51}H_{44}N_7Ru$ requires $[M\text{-}PF_6]^+$ 856.2702. Found $[M\text{-}PF_6\text{+}H]^{2+}$ 428.6399, $C_{51}H_{45}N_7Ru$ requires $[M\text{-}PF_6\text{+}H]^{2+}$ 428.6390. **UV-Vis** (CH_3CN) λ_{max}/nm (ε, 10^3 $M^{-1}cm^{-1}$): 505 (12.6), 375 (40.5), 358 (46.5), 315 (65.4), 285 (92.7), 239 (83.7). **Fluorometry** (Butyronitrile, 77K) λ_{max}: 702 nm.

6.4 Synthesis of precursors and ligands - Chapter three.

3.14

To 3,4,5-trimethylbenzaldehyde (799 mg, 5.40 mmol) in 120 mL EtOH was added 2-acetylpyridine (1.3 g, 10.80 mmol), NaOH (0.44 g, 10.8 mmol) and 30 mL concentrated $NH_4OH_{(aq)}$. The reaction mixture was refluxed for 72 h, and then stirred at room temperature for another 3 h. The formed off white precipitate was filtered and washed sequentially with H_2O and EtOH. White powder could be obtained after recrystallization from EtOH (1.52 g, 80% yield).

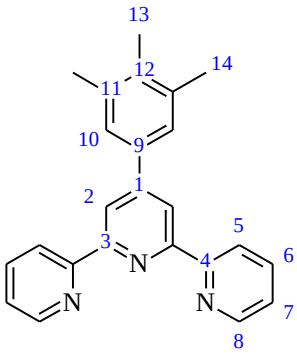

^{1}H NMR (DMSO-D6, 400 MHz): δ 8.77 (2H, d, J = 4.5 Hz, H8), 8.66 (2H, d, J = 8.1 Hz, H5), 8.64 (2H, s, H2), 8.02 (2H, t, J = 6.0 Hz, H7), 7.52 (2H, t, J = 7.3 Hz, H6), 7.12 (2H, s, H10), 3.92 (6H, s, H14), 3.74 (3H, s, H13). **^{13}C NMR** (DMSO-D6, 100 MHz): δ 156.01 (C4), 155.55 (C3), 153.98 (C11), 150.61 (C9), 149.79 (C8), 139.32 (C12), 137.89 (C7), 133.93 (C1), 124.93 (C6), 121.50 (C5), 118.75 (C2), 104.93 (C10), 60.60 (C13), 56.66 (C14). **ESI-MS**: Found MH^+ 352.1819, $C_{24}H_{22}N_3$ requires MH^+ 352.1814.

Ru(3.14)Cl_3

A mixture of **3.14** (109 mg, 0.31 mmol) and $RuCl_3.xH_2O$ (82 mg, 0.31 mmol) in absolute EtOH (50 mL) was heated at reflux for 3 h. The solid was isolated by filtration and washed with EtOH (2 x 20 mL) and diethyl ether and dried to yield a red/brown solid product. The solid was used in the next step as a crude product without further purification (151 mg, 87% yield).

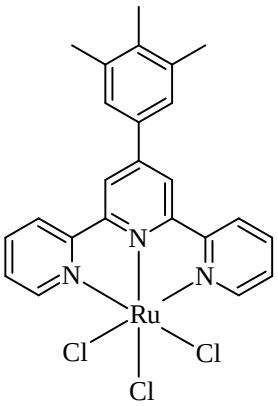

6.5 Ruthenium complexes - Chapter three.

3.2

A mixture of Ru(**3.13**)Cl_3 (72 mg, 0.196 mmol), 1,3-di(pyrazol-1-yl)benzene (0.157 mmol), silver triflate (160 mg, 0.62 mmol) and Et_3N (3 drops) in EtOH/H_2O (3:1, 12 mL) was refluxed for 12 h. After cooling and filtering, the solvent was removed under reduced pressure. The solid was slowly dropped into an excess of $NH_4PF_{6(aq)}$. The fine precipitate was filtered, washed with

water, rinsed with CH_3CN, dried over Na_2SO_4 and the solvent was removed in vacuo. The crude product was purified using column chromatography, eluting with 10% acetonitrile/ethyl acetate on silica to give the pure complex (101 mg, 78% yield).

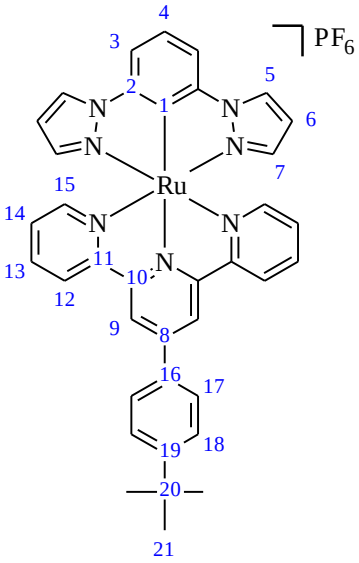

^{1}H NMR (Acetone-D6, 400 MHz): δ 9.23 (2H, s, H9), 8.85 (2H, d, J = 8.1 Hz, H15), 8.73 (2H, m, H5), 8.24 (2H, d, J = 7.9 Hz, H18), 7.94 (2H, d, J = 7.8 Hz, H3), 7.86 (2H, t, J = 7.8 Hz, H14), 7.76 (2H, d, J = 8.0 Hz, H17), 7.43 (1H, t, J = 7.9 Hz, H4), 7.40 (2H, d, J = 5.3 Hz, H12), 7.16 (2H, t, J = 5.9 Hz, H13), 6.75 (2H, m, H7), 6.26 (2H, m, H6), 1.47 (9H, s, H21). **^{13}C NMR** (Acetone-D6, 100 MHz): δ 180.45 (C1), 160.10 (C11), 155.22 (C10), 154.59 (C12), 152.73 (C19), 144.85 (C16), 143.80 (C2), 141.85 (C7), 135.27 (C14), 135.00 (C8), 128.10 (C5), 127.30 (C18), 126.48 (C13), 126.30 (C17), 123.45 (C15), 119.47 (C9), 107.01 (C6), 34.52 (C20), 30.69 (C21), unassigned (C4). **ESI-MS**: Found $[M\text{-}PF_6]^+$ 676.1779, $C_{37}H_{32}N_7Ru$ requires $[M\text{-}PF_6]^+$ 676.1767. Found $[M - PF_6+H]^{2+}$ 338.5919, $C_{37}H_{32}N_7RuH$ requires $[M - PF_6+H]^{2+}$ 338.5920. **UV-Vis** (CH_3CN) λ_{max}/nm (ε, 10^3 $M^{-1}cm^{-1}$): 530 (9.0), 493 (11.9), 361 (14.5), 317 (29.5), 285 (40.1), 260 (40.5). **Fluorometry** (Butyronitrile, 77K) λ_{max}: 718 nm.

3.3

A mixture of Ru(**3.14**)Cl_3 (69 mg, 0.124 mmol), 1,3-di(pyrazol-1-yl)benzene (11 mg, 0.099 mmol), silver triflate (129 mg, 0.5 mmol) and Et_3N (3 drops) in EtOH/H_2O (3:1, 12 mL) was refluxed for 12 h. After cooling and filtering, the solvent was removed under reduced pressure. The solid was slowly dropped into an excess of $NH_4PF_{6(aq)}$. The fine precipitate was filtered, washed with water, rinsed with CH_3CN, dried over Na_2SO_4 and the solvent was removed in vacuo. The crude product was purified using column chromatography, eluting with 10% acetonitrile/ethyl acetate on silica to give the pure complex (63 mg, 79% yield).

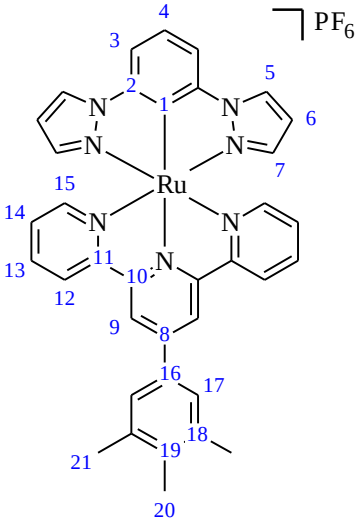

^{1}H NMR (Acetone-D6, 400 MHz): δ 9.22 (2H, s, H9), 8.78 (2H, d, J = 7.9 Hz, H15), 8.75 (2H, d, J = 2.6 Hz, H5), 7.92 (2H, d, J = 7.8 Hz, H3), 7.85 (2H, t, J = 7.9 Hz, H14), 7.58 (2H, s, H17), 7.46 (1H, t, J = 7.8 Hz, H4), 7.40 (2H, d, J = 5.2 Hz, H12), 7.16 (2H, t, J = 6.5 Hz, H13), 6.75 (2H, d, J= 1.9 Hz, H7), 6.27 (2H, t, J = 2.2 Hz, H6), 4.04 (6H, s, H21), 3.89 (3H, s, H20). **^{13}C NMR** (Acetone-D6, 100 MHz): δ 181.43 (C1), 160.07 (C11), 155.09 (C10), 154.30 (C18), 154.04 (C12), 145.06 (C16), 143.17 (C2), 141.56 (C7), 139.83 (C19), 135.11 (C14), 133.44 (C8), 127.85 (C5), 126.26 (C13), 123.36 (C15), 121.22 (C4), 119.59 (C9), 108.62 (C3), 107.99 (C6), 105.22 (C17), 59.83 (C20), 55.97 (C21). **ESI-MS**: Found $[M\text{-}PF_6]^+$ 661.7397, $C_{36}H_{30}N_7Ru$ requires $[M\text{-}PF_6]^+$ 661.7392. Found $[M\text{-}PF_6+H]^{2+}$ 331.3742, $C_{36}H_{31}N_7Ru$ requires MH^+ 331.3738. **UV-Vis** (CH_3CN) λ_{max}/nm (ε, 10^3 $M^{-1}cm^{-1}$): 530 (7.6), 494 (9.7), 361 (sh, 11.0), 316 (27.7), 279 (27.1), 259 (33.1), 211 (51.9). **Fluorometry** (Butyronitrile, 77K) λ_{max}: 717 nm.

3.4

A mixture of Ru(**3.15**)Cl_3 (79 mg, 0.232 mmol), 1,3-di(pyrazol-1-yl)benzene (39 mg, 0.186 mmol), silver triflate (184 mg, 0.716 mmol) and Et_3N (3 drops) in EtOH/H_2O (3:1, 12 mL) was refluxed for 12 h. After cooling and filtering, the solvent was removed under reduced pressure. The solid was slowly dropped into an excess of $NH_4PF_{6(aq)}$. The fine precipitate was filtered, washed with water, rinsed with CH_3CN, dried over Na_2SO_4 and the solvent was removed in vacuo. The crude product was purified using column chromatography, eluting with 10% acetonitrile/ethyl acetate on silica to give the pure complex (106 mg, 72% yield).

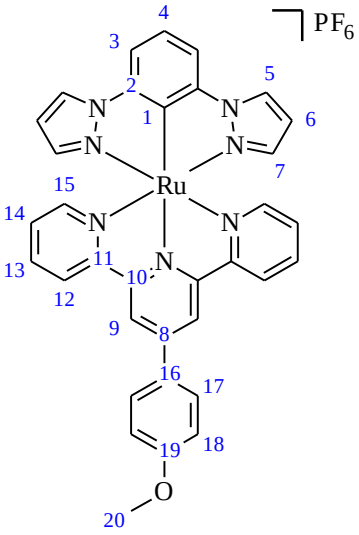

^{1}H NMR (Acetone-D6, 400 MHz): δ 9.21 (2H, s, H9), 8.84 (2H, d, J = 8.1 Hz, H15), 8.74 (2H, d, J = 2.3 Hz, H5), 8.29 (2H, d, J = 8.6 Hz, H18), 7.92 (2H, d, J = 7.8 Hz, H3), 7.85 (2H, t, J = 7.8 Hz, H14), 7.45 (1H, t, J = 7.8 Hz, H4), 7.39 (2H, d, J = 5.2 Hz, H12), 7.26 (2H, d, J = 8.6 Hz, H17), 7.15 (2H, t, J = 6.6 Hz, H13), 6.78 (2H, d, J = 1.7 Hz, H7), 6.26 (2H, t, J = 2.0 Hz, H6), 3.97 (3H, s, H20). **^{13}C NMR** (Acetone-D6, 100 MHz): δ 181.56 (C1), 143.25 (C2), 161.18 (C19), 160.18 (C11), 155.16 (C10), 154.01 (C12), 144.64 (C16), 141.59 (C7), 135.07 (C14), 129.90 (C8), 128.84 (C18), 127.78 (C5), 126.18 (C13), 123.30 (C15), 121.12 (C4), 118.78 (C9), 114.62 (C17), 108.57 (C3), 106.97 (C6), 54.952 (C20). **ESI-MS**: Found $[M\text{-}PF_6]^+$ 650.1261,

$C_{34}H_{26}N_7ORu$ requires $[M\text{-}PF_6]^+$ 650.1246. Found $[M\text{-}PF_6+H]^{2+}$ 325.5659, $C_{34}H_{27}N_7ORu$ requires $[M\text{-}PF_6+H]^{2+}$ 325.5659. **UV-Vis** (CH_3CN) λ_{max}/nm (ε, 10^3 $M^{-1}cm^{-1}$): 531 (9.6), 493 (12.6), 361 (sh, 15.6), 315 (36.8), 282 (35.0), 260 (42.5), 234 (41.0). **Fluorometry** (Butyronitrile, 77K) λ_{max}: 715 nm.

3.5

A mixture of Ru(**3.16**)Cl_3 (85 mg, 0.151 mmol), 1,3-di(pyrazol-1-yl)benzene (25 mg, 0.119 mmol), silver triflate (116 mg, 0.45 mmol) and Et_3N (3 drops) in EtOH/H_2O (3:1, 12 mL) was refluxed for 12 h. After cooling and filtering, the solvent was removed under reduced pressure. The solid was slowly dropped into an excess of $NH_4PF_{6(aq)}$. The fine precipitate was filtered, washed with water, rinsed with CH_3CN, dried over Na_2SO_4 and the solvent was removed in vacuo. The crude product was purified using column chromatography, eluting with 10% acetonitrile/ethyl acetate on silica to give the pure complex (67 mg, 70% yield).

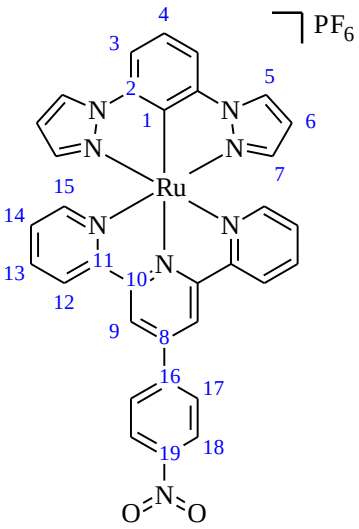

^{1}H NMR (Acetone-D6, 400 MHz): δ 9.40 (2H, s, H9), 8.89 (2H, d, J = 8.1 Hz, H15), 8.76 (2H, d, J = 2.8 Hz, H5), 8.62 (2H, d, J = 8.7 Hz, H18), 8.54 (2H, d, J = 8.7 Hz, H17), 7.94 (2H, d, J = 7.8 Hz, H3), 7.89 (2H, t, J = 8.1 Hz, H14), 7.49 (1H, t, J = 7.8 Hz, H4), 7.44 (2H, d, J = 5.2 Hz, H12), 7.21 (2H, t, J = 8.1 Hz, H13), 6.78 (2H, d, J = 2.1 Hz, H7), 6.27 (2H, t, J = 2.5 Hz, H6). **^{13}C NMR** (Acetone-D6, 100 MHz): δ 181.01 (C1), 159.91 (C11), 155.56 (C10), 154.18 (C12), 148.33 (C19), 144.24 (C8), 142.92 (C2), 141.89 (C16), 141.72 (C7), 135.40 (C14) 128.72 (C18), 128.08 (C5), 126.57 (C13) 124.39 (C17), 123.63 (C15), 121.75 (C4), 120.10 (C9), 108.85 (C3), 107.16 (C6). **ESI-MS**: Found $[M\text{-}PF_6+H]^{2+}$ 333.0525, $C_{33}H_{24}N_8O_2Ru$ requires $[M\text{-}PF_6+H]^{2+}$ 333.0532. Found $[M\text{-}PF_6]^+$ 665.1002, $C_{33}H_{23}N_8O_2Ru$ requires $[M\text{-}PF_6]^+$ 665.0991. **UV-Vis** (CH_3CN) λ_{max}/nm (ε, 10^3 $M^{-1}cm^{-1}$): 537 (13.3), 502 (14.8), 393 (13.8), 321 (29.0), 279 (44.4), 260 (44.9), 241 (37.5). **Fluorometry** (Butyronitrile, 77K) λ_{max}: 753 nm.

3.6

A mixture of Ru(**3.12**)Cl_3 (72 mg, 0.151 mmol), 1,3-di(pyrazol-1-yl)benzene (25 mg, 0.119 mmol), silver triflate (116 mg, 0.45 mmol) and Et_3N (3 drops) in EtOH/H_2O (3:1, 12 mL) was

refluxed for 12 h. After cooling and filtering, the solvent was removed under reduced pressure. The solid was slowly dropped into an excess of $NH_4PF_{6(aq)}$. The fine precipitate was filtered, washed with water, rinsed with CH_3CN, dried over Na_2SO_4 and the solvent was removed in vacuo. The crude product was purified using column chromatography, eluting with 10% acetonitrile/ethyl acetate on silica to give the pure complex (61 mg, 71% yield).

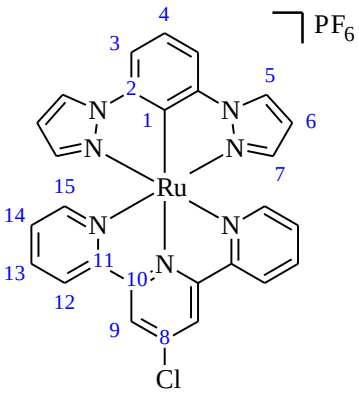

^{1}H NMR (Acetone-D6, 400 MHz): δ 9.00 (2H, s, H9), 8.73 (2H, d, J = 1.9 Hz, H5), 8.71 (2H, m, H14), 7.92 (2H, d, J = 7.8 Hz, H3), 7.86 (2H, t, J = 7.8 Hz, H13), 7.46 (1H, t, J = 7.8 Hz, H4), 7.42 (2H, d, J = 5.2 Hz, H11), 7.19 (2H, t, J = 6.5 Hz, H12), 6.80 (2H, d, J = 1.9 Hz, H7), 6.25 (2H, t, J = 1.9 Hz, H6). **^{13}C NMR** (Acetone-D6, 100 MHz): δ 180.80 (C1), 159.01 (C11), 156.02 (C10), 154.45 (C12), 143.08 (C2), 141.96 (C5), 138.77 (C8), 135.52 (C14), 127.93 (C5), 126.73 (C13), 123.75 (C15), 122.15 (C7), 121.88 (C4), 108.90 (C3), 106.98 (C6). **ESI-MS**: Found $[M\text{-}PF_6+H]^{2+}$ 289.5251, $C_{27}H_{20}N_7ClRu$ requires $[M\text{-}PF_6+H]^{2+}$ 289.5252. Found $[M\text{-}PF_6]^{+}$ 578.0442, $C_{27}H_{19}N_7ClRu$ requires $[M\text{-}PF_6]^{+}$ 578.0432. **UV-Vis** (CH_3CN) λ_{max}/nm (ε, 10^3 $M^{-1}cm^{-1}$): 545 (4.7), 494 (8.0), 368 (8.8) 317 (24.7), 275 (28.2), 258 (36.4), 239 (40.0). **Fluorometry** (Butyronitrile, 77K) λ_{max}: 728 nm.

3.7

A mixture of Ru(**3.17**)Cl_3 (90 mg, 0.150 mmol), 1,3-di(pyrazol-1-yl)benzene (25 mg, 0.125 mmol), silver triflate (116 mg, 0.45 mmol) and Et_3N (3 drops) in EtOH/H_2O (3:1, 12 mL) was refluxed for 12 h. After cooling and filtering, the solvent was removed under reduced pressure. The solid was slowly dropped into an excess of $NH_4PF_{6(aq)}$. The fine precipitate was filtered, washed with water, rinsed with CH_3CN, dried over Na_2SO_4 and the solvent was removed in vacuo. The crude product was purified using column chromatography, eluting with 10% acetonitrile/ethyl acetate on silica to give the pure complex (82 mg, 81% yield).

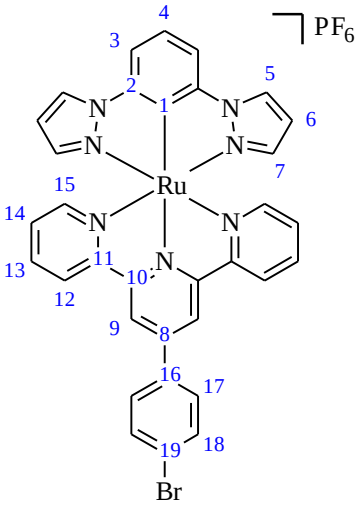

^{1}H NMR (Acetone-D6, 400 MHz): δ 9.27 (2H, s, H9), 8.85 (2H, d, J = 8.1 Hz, H12), 8.73 (2H, d, J = 2.8 Hz, H5), 8.30 (2H, d, J = 8.5 Hz, H18), 7.93 (2H, d, J = 7.8 Hz, H3), 7.88 (2H, d, J = 8.5 Hz, H17), 7.85 (2H, t, J = 8.1 Hz, H13), 7.44 (1H, t, J = 7.8 Hz, H4), 7.41 (2H, d, J = 5.4 Hz, H15), 7.16 (2H, t, J = 6.2 Hz, H14), 6.76 (2H, d, J = 2.6 Hz, H7), 6.25 (2H, t, J = 2.5 Hz, H6). **^{13}C NMR** (Acetone-D6, 100 MHz): δ 180.85 (C1), 160.00 (C11), 155.40 (C10), 154.32 (C12), 143.32 (C2), 143.29 (C8), 141.83 (C7), 137.07 (C16), 135.29 (C13), 132.46 (C17), 129.45 (C18), 128.04 (C5), 126.48 (C14), 123.54 (C15), 123.34 (C19), 121.83 (C4), 119.45 (C9), 108.56 (C3), 107.09 (C6). **ESI-MS**: Found $[M\text{-}PF_6+H]^{2+}$ 350.5150, $C_{33}H_{24}N_7BrRu$ requires $[M\text{-}PF_6+H]^{2+}$ 350.5146. Found $[M\text{-}PF_6]^{+}$ 700.0243, $C_{33}H_{23}N_7BrRu$ requires $[M\text{-}PF_6]^{+}$ 700.0219. **UV-Vis** (CH_3CN) λ_{max}/nm (ε, 10^3 $M^{-1}cm^{-1}$): 530 (9.9), 494 (13.0), 364 (16.3), 319 (29.7), 285 (44.8), 278 (43.7), 260 (44.2), 233 (39.8). **Fluorometry** (Butyronitrile, 77K) λ_{max}: 727 nm.

3.8

A mixture of Ru(**3.17**)Cl_3 (60 mg, 0.1 mmol), 1,3-(dipyrazol-1-yl)-5-bromobenzene (22 mg, 0.075 mmol), silver triflate (77 mg, 0.77 mmol) and Et_3N (3 drops) in EtOH/H_2O (3:1, 12 mL) was refluxed for 12 h. After cooling and filtering, the solvent was removed under reduced pressure. The solid was slowly dropped into an excess of $NH_4PF_{6(aq)}$. The fine precipitate was filtered, washed with water, rinsed with CH_3CN, dried over Na_2SO_4 and the solvent was removed in vacuo. The crude product was purified using column chromatography, eluting with 10% acetonitrile/ethyl acetate on silica to give the pure complex (53 mg, 76% yield).

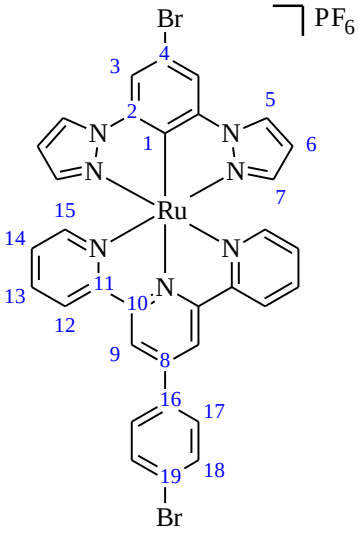

^{1}H NMR (Acetone-D6, 400 MHz): δ 9.30 (2H, s, H9), 8.86 (2H, t, J = 8.1 Hz, H15), 8.82 (2H, m, H5), 8.28 (2H, d, J = 8.5 Hz, H18), 8.13 (2H, s, H3), 7.90 (2H, m, H17), 7.89 (2H, m, H14), 7.48 (2H, d, J = 5.6 Hz, H12), 7.21 (2H, t, J = 6.3 Hz, H13), 6.83 (2H, m, H7), 6.31 (2H, m, H6). **^{13}C NMR** (Acetone-D6, 100 MHz): δ 180.67 (C1), 159.94 (C11), 155.39 (C10), 154.42 (C12), 144.01 (C4), 143.81 (C19), 142.30 (C7), 141.98 (C2), 137.01 (C8), 135.55 (C14), 132.47 (C17), 129.42 (C18), 128.58 (C5), 126.59 (C13), 123.58 (C15), 123.45 (C16), 119.55 (C9), 111.65 (C3), 107.52 (C6). **ESI-MS**: Found $[M\text{-}PF_6+H]^{2+}$ 389.4700, $C_{33}H_{23}N_7Br_2Ru$ requires $[M\text{-}PF_6+H]^{2+}$ 389.4703. Found $[M\text{-}PF_6]^{+}$ 777.9340, $C_{33}H_{22}N_7Br_2Ru$ requires $[M\text{-}PF_6]^{+}$ 777.9332.

UV-Vis (CH_3CN) λ_{max}/nm (ε, 10^3 $M^{-1}cm^{-1}$): 525 (9.5), 490 (12.3), 359 (15.2), 317 (27.8), 285 (41.7), 277 (40.1), 266 (41.2), 226 (36.0). **Fluorometry** (Butyronitrile, 77K) λ_{max}: 712 nm.

3.9

A mixture of Ru(**3.18**)Cl_3 (68 mg, 0.119 mmol), 1,3-di(pyrazol-1-yl)benzene (20 mg, 0.19 mmol), silver triflate (91 mg, 0.36 mmol) and Et_3N (3 drops) in EtOH/H_2O (3:1, 12 mL) was refluxed for 12 h. After cooling and filtering, the solvent was removed under reduced pressure. The solid was slowly dropped into an excess of $NH_4PF_{6(aq)}$. The fine precipitate was filtered, washed with water, rinsed with CH_3CN, dried over Na_2SO_4 and the solvent was removed in vacuo. The crude product was purified using column chromatography, eluting with 10% acetonitrile/ethyl acetate on silica to give the pure complex (105 mg, 68% yield).

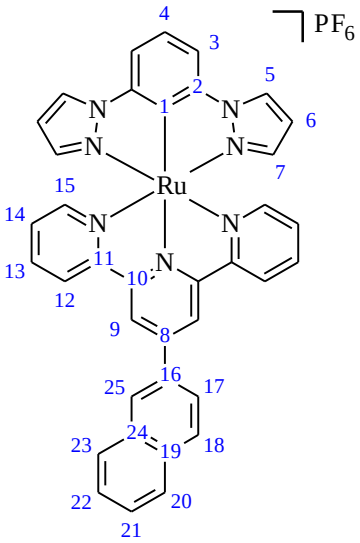

^{1}H NMR (Acetone-D6, 400 MHz): δ 9.43 (2H, s, H9), 8.90 3H, m, H15, H17), 8.75 (2H, d, J = 2.7 Hz, H5), 8.45 (1H, d, J = 8.6 Hz, H25), 8.26 (1H, d, J = 8.6 Hz, H24), 8.17 (1H, m, H19), 8.09 (1H, m, H22), 7.94 (2H, d, J = 7.8 Hz, H3), 7.89 (2H, t, J = 7.9 Hz, H14), 7.68 (2H, t, J = 3.8 Hz, H20, H21), 7.48 (1H, t, J = 7.8 Hz, H4), 7.42 (2H, t, J = 6.6 Hz, H12), 7.19 (2H, t, J = 6.2 Hz, H13), 6.81 (2H, d, J = 1.9 Hz, H7), 6.28 (2H, d, J = 2.2 Hz, H6). **^{13}C NMR** (Acetone-D6, 100 MHz): δ 181.39 (C1), 160.15 (C11), 155.37 (C10), 154.24 (C12), 144.61 (C18), 143.17 (C2), 141.75 (C7), 135.27 (C14), 135.16 (C8), 133.86 (C23), 133.79 (C16), 129.17 (C24), 128.64 (C19), 127.96 (C5), 127.82 (C22), 127.19 (C20), 127.06 (C21), 126.97 (C17), 126.40 (C13), 124.87 (C25), 123.50 (C15), 121.46 (C4), 119.83 (C9), 108.75 (C3), 107.12 (C6). **ESI-MS**: Found $[M\text{-}PF_6+H]^{2+}$ 335.5684, $C_{37}H_{27}N_7Ru$ requires $[M\text{-}PF_6+H]^{2+}$ 335.5685. Found $[M\text{-}PF_6]^+$ 670.1311, $C_{37}H_{26}N_7Ru$ requires $[M\text{-}PF_6]^+$ 670.1297. **UV-Vis** (CH_3CN) λ_{max}/nm (ε, 10^3 $M^{-1}cm^{-1}$): 531 (10.1), 495 (13.0), 372 (sh, 16.0), 319 (31.7), 278 (45.9), 261 (48.1), 226 (63.2), 204 (67.6). **Fluorometry** (Butyronitrile, 77K) λ_{max}: 724 nm.

3.10

A mixture of Ru(**3.19**)Cl_3 (136 mg, 0.22 mmol), 1,3-di(pyrazol-1-yl)benzene (37 mg, 0.176 mmol), silver triflate (170 mg, 0.66 mmol) and Et_3N (3 drops) in EtOH/H_2O (3:1, 12 mL) was

refluxed for 12 h. After cooling and filtering, the solvent was removed under reduced pressure. The solid was slowly dropped into an excess of NH_4PF_6. The fine precipitate was filtered, washed with water, rinsed with CH_3CN, dried over Na_2SO_4 and the solvent was removed in vacuo. The crude product was purified using column chromatography, eluting with 10% acetonitrile/ethyl acetate on silica to give the pure complex (107 mg, 70% yield).

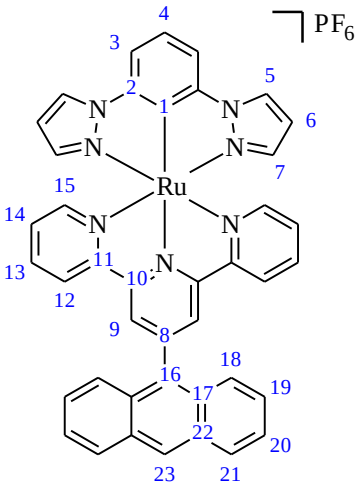

^{1}H NMR (Acetone-D6, 400 MHz): δ 9.01 (2H, s, H9), 8.89 (1H, s, H23), 8.79 (2H, m, H5), 8.75 (2H, d, J = 8.1 Hz, H15), 8.32 (2H, d, J = 8.5 Hz, H21), 8.16 (2H, d, J = 7.8 Hz, H18), 7.96 (2H, d, J = 7.8 Hz, H3), 7.83 (2H, t, J = 7.6 Hz, H14), 7.66 (2H, t, J = 8.8 Hz, H20), 7.57 (2H, t, J = 7.0 Hz, H19), 7.50 (1H, m, H4), 7.48 (2H, d, J = 5.2 Hz, H12), 7.20 (2H, t, J = 6.2 Hz, H13), 6.96 (2H, m, H7), 6.34 (2H, m, H6). **^{13}C NMR** (Acetone-D6, 100 MHz): δ 181.37 (C1), 160.11 (C11), 155.32 (C10), 154.29 (C12), 143.42 (C2), 143.26 (C8), 141.97 (C7), 135.27 (C14), 133.56 (C16), 131.61 (C17), 130.05 (C22), 128.72 (C21), 128.18 (C23), 128.01 (C15), 126.64 (C19), 126.47 (C13), 126.23 (C18), 125.66 (C20), 124.47 (C9), 123.57 (C5), 121.50 (C4), 108.76 (C3), 107.09 (C6). **ESI-MS**: Found $[M\text{-}PF_6]^+$ 720.1464, $C_{41}H_{28}N_7Ru$ requires $[M\text{-}PF_6]^+$ 720.1455. **ESI-MS**: Found $[M\text{-}PF_6+H]^{2+}$ 360.5760, $C_{41}H_{29}N_7Ru$ requires $[M\text{-}PF_6+H]^{2+}$ 360.5764. **UV-Vis** (CH_3CN) λ_{max}/nm (ε, 10^3 $M^{-1}cm^{-1}$): 533 (6.7), 491 (10.4), 385 (16.9), 366 (16.2), 348 (12.4), 318 (28.7), 276 (33.3), 252 (110). **Fluorometry** (Butyronitrile, 77K) λ_{max}: 715 nm.

3.11

A mixture of Ru(**3.19**)Cl_3 (62 mg, 0.1 mmol), 1,3-(dipyrazol-1-yl)-(5-(pyren-1-yl)benzene (31mg, 0.075 mmol), silver triflate (77 mg, 0.3 mmol) and Et_3N (3 drops) in EtOH/H_2O (3:1, 12 mL) was refluxed for 12 h. After cooling and filtering, the solvent was removed under reduced pressure. The solid was slowly dropped into an excess of $NH_4PF_{6(aq)}$. The fine precipitate was filtered, washed with water, rinsed with CH_3CN, dried over Na_2SO_4 and the solvent was removed in vacuo. The crude product was purified using column chromatography, eluting with 10% acetonitrile/ethyl acetate on silica to give the pure complex (50 mg, 63% yield).

^{1}H NMR (Acetone-D6, 400 MHz): δ 9.06 (2H, s, H25), 8.97 (2H, m, H5), 8.92 (1H, ,s, H39), 8.80 (2H, d, J = 8.1 Hz, H31), 8.75 (1H, d, J = 9.2 Hz, H10), 8.52 (1H, d, J = 7.7 Hz, H12), 8.44 (1H, d, J = 7.7 Hz, H13), 8.41-8.35 (1H, m , H15), 8.41-8.35 (1H, m, H17), 8.33 (2H, m, H19), 8.33 (2H, m, H37), 8.28 (2H, s, H3), 8.28 (1H, m, H9), 8.28 (1H, m, H20), 8.19 (2H, d, J = 8.7 Hz, H34), 8.15 (1H, d, J = 7.7 Hz, H16), 7.90 (2H, t, J = 8.3 Hz, H30), 7.75 (2H, d, J = 5.1 Hz, H28), 7.68 (2H, t, J = 7.0 Hz, H36), 7.59 (2H, t, J = 8.4 Hz, H35), 7.30 (2H, t, J = 6.4 Hz, H29), 7.05 (2H, m, H7), 6.40 (2H, m, H6). **^{13}C NMR** (Acetone-D6, 100 MHz): δ 181.33 (C1), 160.17 (C27), 155.35 (C26), 154.57 (C28), 143.64 (C2), 143.47 (C8), 142.26 (C7), 138.68 (C4), 135.43 (C30), 134.78 (C14), 133.57 (C32), 131.72 (C33), 131.63 (C18), 131.21 (C11), 130.59 (C23), 130.08 (C38), 128.92 (C19), 128.73 (C37), 128.48 (C13), 128.38 (C5), 128.21 (C39), 127.58 (C9), 127.42 (C20), 126.66 (C35), 126.62 (C3), 126.38 (C21), 126.26 (C34), 125.80 (C36), 125.68 (C10), 125.30 (C22), 125.15 (C12), 124.94 (C15), 124.88 (C17), 124.56 (C25), 123.65 (C31), 111.12 (C29), 107.23 (C6), unassigned (C16, C24). **ESI-MS**: Found $[M\text{-}PF_6]^+$ 920.2085, $C_{57}H_{36}N_7Ru$ requires $[M\text{-}PF_6]^+$ 920.2107. **ESI-MS**: Found $[M\text{-}PF_6\text{+}H]^{2+}$ 460.1047, $C_{57}H_{37}N_7Ru$ requires $[M\text{-}PF_6\text{+}H]^{2+}$ 460.1040. **UV-Vis** (CH_3CN) λ_{max}/nm (ε, 10^3 $M^{-1}cm^{-1}$): 529 (10.1), 490 (16.2), 385 (28.9), 368 (26.7), 339 (36.7), 320 (45.7), 277 (76.7), 266 (64.8), 251 (114). **Fluorometry** (Butyronitrile, 77K) λ_{max}: 720 nm.

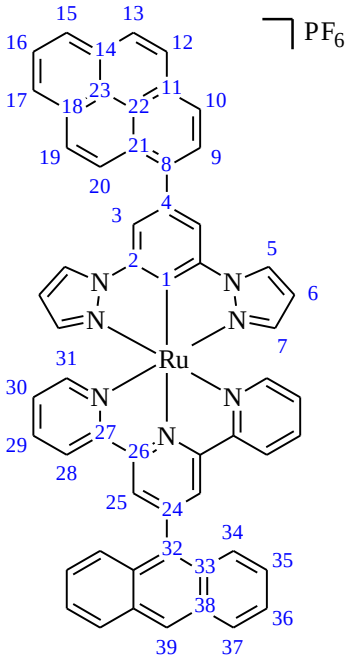

6.6 Synthesis of precursors and ligands - Chapter three.

4.16

1,3-di(ethynyl)-5-bromobenzene (150 mg, 0.75 mmol), benzyl bromide (0.26 g, 1.51 mmol), NaN_3 (110 mg, 1.62 mmol), $CuSO_4.5H_2O$ (40 mg, 0.15 mmol), sodium carbonate (160 mg, 0.75 mmol) and ascorbic acid (110 mg, 0.75 mmol) were added to a solution of DMF (8 mL) and H_2O (2 mL). The mixture was stirred vigorously for 18 h. Then $NH_4OH_{(aq)}$ (2M, 100 mL) was added to the solution and it was extracted with DCM and dried with anhydrous $MgSO_4$. After the solvent was

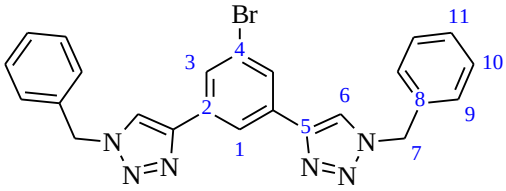

removed, the residue was purified by column chromatography on silica gel using DCM followed by 5% EtOAc/DCM as the eluent. Removal of solvent under reduced pressure gave the pure product (311 mg, 88%).

^{1}H NMR ($CDCl_3$, 400 MHz): δ 8.09 (1H, s, H1), 7.89 (2H, s, H3), 7.73 (2H, s, H6), 7.28-7.40 (5H, m, H9, H10, H11), 5.55 (4H, s, H7). **^{13}C NMR** ($CDCl_3$): δ 146.41 (C5), 134.32 (C8), 132.86 (C4), 128.93/128.13/129.36 (C9, C10, C11), 128.17 (C3), 123.38 (C2), 121.31 (C1), 120.23 (C6), 54.38 (C7). **ESI-MS**: Found MH^+ 471.0939, $C_{24}H_{20}BrN_6$ requires MH^+ 471.0933.

4.17

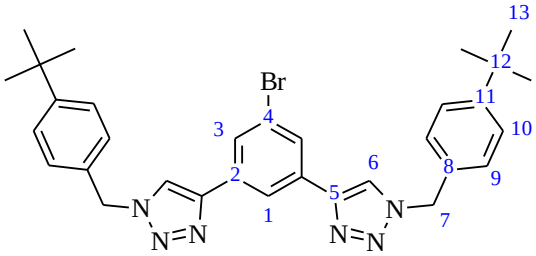

1,3-di(ethynyl)-5-bromobenzene (150 mg, 0.75 mmol), 4-tertbutylbenzyl bromide (0.34 g, 1.51 mmol), NaN_3 (110 mg, 1.62 mmol), $CuSO_4.5H_2O$ (40 mg, 0.15 mmol), sodium carbonate (160 mg, 0.75 mmol) and ascorbic acid (110 mg, 0.75 mmol) were added to a solution of DMF (8 mL) and H_2O (2 mL). The mixture was stirred vigorously for 18 h. Then $NH_4OH_{(aq)}$ (2M, 100 mL) was added to the solution and it was extracted with DCM and dried with anhydrous $MgSO_4$. After the solvent was removed, the residue was purified by column chromatography on silica gel using DCM followed by 5% EtOAc/DCM as the eluent. Removal of solvent under reduced pressure gave the pure product (399 mg, 91%).

^{1}H NMR ($CDCl_3$, 400 MHz): δ 8.13 (1H, s, H1), 7.91 (2H, s, H3), 7.74 (2H, s, H6), 7.42 (4H, d, J = 8.1 Hz, H10), 7.26 (4H, d, J = 8.1 Hz, H9), 5.54 (4H, s, H7), 1.33 (9H, s, H13). **^{1}H NMR** (Acetone-D6, 400 MHz): δ 8.52 (2H, s, H6), 8.38 (1H, s, H1), 8.01 (2H, s, H3), 7.42 (4H, d, J = 8.4 Hz, H9), 7.36 (4H, d, J = 8.4 Hz, H10), 5.65 (2H, s, H7), 1.29 (18H, s, H13). **^{13}C NMR** ($CDCl_3$): δ 152.14 (C11), 146.41 (C5), 132.89 (C2), 131.18 (C8), 128.06 (C10), 127.97 (C3), 126.2 (C9), 123.35 (C4), 121.34 (C1), 120.25 (C6), 54.16 (C7), 34.67 (C12), 31.25 (C13). **ESI-MS**: Found MH^+ 583.2178, $C_{32}H_{36}BrN_6$ requires MH^+ 583.2185.

4.18

1,3-di(ethynyl)-5-bromobenzene (150 mg, 0.75 mmol), 4-bromobenzyl bromide (0.38 g, 1.51 mmol), NaN_3 (110 mg, 1.62 mmol), $CuSO_4.5H_2O$ (40 mg, 0.15 mmol), sodium carbonate (160

mg, 0.75 mmol) and ascorbic acid (110 mg, 0.75 mmol) were added to a solution of DMF (8 mL) and H_2O (2 mL). The mixture was stirred vigorously for 18 h. Then $NH_4OH_{(aq)}$ (2M, 100 mL) was added to the solution and it was extracted with DCM and dried with anhydrous $MgSO_4$. After the solvent was removed, the residue was purified by column chromatography on silica gel using DCM followed by 5% EtOAc/DCM as the eluent. Removal of solvent under reduced pressure gave the pure product (399 mg, 91%).

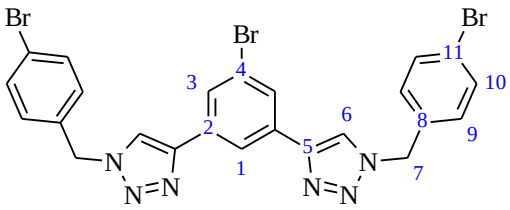

^{1}H NMR (Acetone-D6, 400 MHz): δ 8.56 (2H, s), 8.38 (1H, s), 8.01 (2H, s), 7.59 (4H, d, J = 8.1 Hz), 7.40 (4H, d, J = 8.1 Hz), 5.73 (2H, s). **^{1}H NMR** (Acetone-D6, 400 MHz): δ 8.56 (2H, s, H6), 8.38 (1H, s, H1), 8.01 (2H, s, H3), 7.59 (4H, d, J = 8.4 Hz, H9), 7.40 (4H, d, J = 8.4 Hz, H10), 5.71 (2H, s, H7). **^{13}C NMR** (Acetone-D6, 100 MHz): δ 145.73 (C2), 135.28 (C8), 133.90 (C4), 131.91 (C10), 130.17 (C9), 127.12 (C3), 122.85 (C5), 121.88 (C11), 121.66 (C6), 120.98 (C1), 52.86 (C7). **ESI-MS**: Found MH^+ 469.0771, $C_{24}H_{18}BrN_6$ requires MH^+ 469.0776.

1-Naphthoic acid

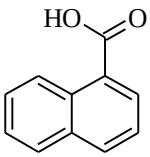

To a mixture of 1-acetylnaphthalene (1.6 g, 9.38 mmol) and pyridine (2 mL) in a 100 mL round-bottomed flask equipped with a condenser, heated to 85 °C, was added NaOCl solution (70 mL, 3.8%, 37.6 mol). After heating at the same temperature for 1 h, the reaction mixture was concentrated and filtered. The white precipitate obtained was dissolved in hot water and filtered to remove insolubles. The filtrate was cooled and acidified with 2 M HCl to obtain a white solid, that after filtration and drying, was sufficiently pure (1.16 g, 72%).

^{1}H NMR (DMSO-D6, 400 MHz): δ 13.18 (1H, s), 8.90 (1H, d, J = 8.5 Hz), 8.19–8.12 (2H, m), 8.10–7.98 (1H, m), 7.7–7.4 (3H, m). **^{13}C NMR** (DMSO-D6, 400 MHz): δ 169.0, 133.8, 133.3, 131.0, 130.2, 129.0, 128.1, 127.9, 126.5, 125.9, 125.2. **ESI-MS**: Found MH^+ 173.0600, $C_{11}H_8O_2$ requires 173.0597. Found MNa^+ 195.0418, $C_{11}H_8O_2Na$ requires 195.0417. **M.p**: 271 °C. (lit[208] 271 °C).

1-Hydroxymethyl naphthalene

To 1-naphthoic acid (463 mg, 2.69 mmol) in dry THF (140 mL) under N_2 was added $LiAlH_4$ (238 mg, 6.25 mmol) portionwise. The mixture was heated at reflux for 6 hours and then cooled to room temperature at which point ammonium chloride was added. The slurry was filtered and the filtrate was collected and concentrated under reduced pressure to give a pure product (174 mg, 41%).

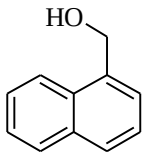

^{1}H NMR ($CDCl_3$, 400 MHz): δ 8.13 (1H, d, J = 8.0 Hz), 7.88 (1H, d, J = 8.0 Hz), 7.81 (1H, d, J = 8.0 Hz), 7.45-7.56 (4H, m), 5.16 (2H, s), 1.68 (1H, s). **^{13}C NMR** ($CDCl_3$, 100 MHz): δ 136.3, 133.8, 131.2, 128.7, 128.6, 126.3, 125.9, 125.4, 125.3, 123.7, 63.6. **M.p**: 60 °C (Lit[209] 60–62 °C. **ESI-MS**: Found M^+ 158.0725, $C_{11}H_{10}O$ requires M^+ 158.0732.

1-Chloromethylnapthalene

Previously synthesised 1-hydroxymethyl naphthalene (0.45g, 2.85 mmol) was dissolved in dry chloroform (10 mL) and cooled to 5 °C. Thionyl chloride (4.28 mmol) was added to this solution at such a rate that the temperature of the reaction mixture did not rise above 10 °C. After the addition was over, the temperature of the reaction mixture was allowed to rise to room temperature and stirred for a further 30 min. The reaction mixture was basified to pH 8 by slow and careful addition of saturated sodium bicarbonate solution, extracted with chloroform (3 x 30 mL); the combined organic layer was washed with water (3 x 20 mL), dried over anhydrous sodium sulfate, and the solvent removed to give the target product as a yellow oil (0.38 g, 85%).

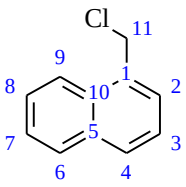

^{1}H NMR ($CDCl_3$, 400 MHz): δ 8.20 (1H, d, J = 8.4 Hz), 7.93 (H, d, J = 7.0 Hz), 7.88 (1H, d, J = 8.2 Hz), 7.64 (1H, m), 7.56 (2H, m), 7.46 (1H, m), 5.08 (2H, s). **^{13}C NMR** ($CDCl_3$, 400 MHz): δ 133.81 (C1), 132.87 (C5), 130.99 (C10), 129.64 (C4), 128.74 (C6), 127.56 (C2), 126.60 (C8), 126.03 (C7), 125.16 (C3), 123.53 (C9), 44.46 (C11).

4.19

1,3-di(ethynyl)-5-bromobenzene (150 mg, 0.75 mmol), 1-chloromethylnaphthalene (0.27 g, 1.51 mmol), NaN_3 (110 mg, 1.62 mmol), $CuSO_4.5H_2O$ (40 mg, 0.15 mmol), sodium carbonate (160 mg, 0.75 mmol) and ascorbic acid (110 mg, 0.75 mmol) were added to a solution of DMF (8 mL) and H_2O (2 mL). The mixture was stirred vigorously for 18 h. Then $NH_4OH_{(aq)}$ (2M, 100 mL)

was added to the solution and it was extracted with DCM and dried with anhydrous $MgSO_4$. After the solvent was removed, the residue was purified by column chromatography on silica gel using DCM followed by 5% EtOAc/DCM as the eluent. Removal of solvent under reduced pressure gave the pure product (355 mg, 83%).

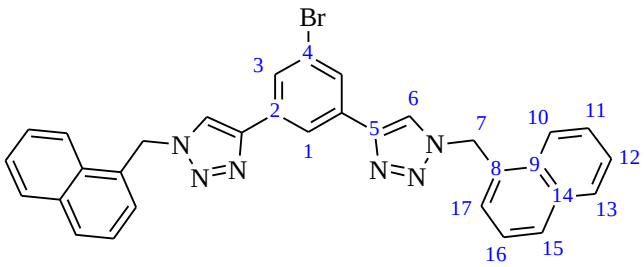

^{1}H NMR ($CDCl_3$, 400 MHz): δ 7.93 (4H, m, H12, H12), 7.74 (2H, s, H6), 7.66 (5H, m, H1, H15, H17), 7.54 (2H, m, H16), 7.26 (2H, s, H3), 7.08 (4H, m, H10, H13), 5.19 (4H, s, H7). **^{13}C NMR** ($CDCl_3$, 100 MHz): δ 163.05 (C8), 158.52/132.06/131.43 (C1/C15/C17), 137.12 (C9), 133.41 (C11, C12), 130.71 (C6), 129.64 (C16), 124.69 (C4), 118.29 (C5), 114.15 (C2), 113.11 (C14), 69.05 (C7). **ESI-MS**: Found MH^+ 492.2069, $C_{32}H_{24}N_6$ requires MH^+ 492.2062.

4.30

4-methylphenylboronic acid (0.39 g, 2.9 mmol), NaN_3 (0.8 g, 12.31 mmol), $Cu(OAc)_2$ (0.14 g, 0.82 mmol) were stirred in dry methanol (5 mL) for 2 hrs at 55°C. The reaction mixture was cooled to room temperature and 1,3-di(ethynyl)-5-bromobenzene (0.248 g, 1.21 mmol) and sodium-L-ascorbate (0.174 g, 0.88 mmol) were added and the resulting mixture was stirred for 16 hrs. The reaction was quenched with NH_4OH (2M, 250 mL) and a precipitate was extracted with chloroform (3 x 30 mL); the combined organic layer was washed with water (3 x 20 mL), dried over anhydrous sodium sulfate, and the solvent removed to give a crude oil. The oil was purified by column chromatography to give the target product as an off white solid (0.51 g, 89%).

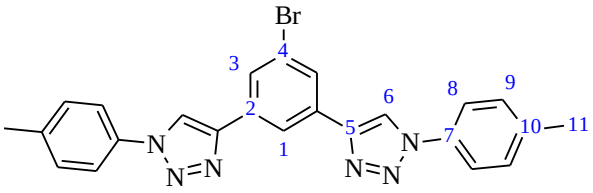

^{1}H NMR ($CDCl_3$, 400 MHz): δ 8.40 (1H, s, H1), 8.29 (2H, s, H6), 8.07 (2H, s, H3), 7.66 (4H, d, J = 8.2 Hz, H8), 7.36 (4H, d, J = 8.2 Hz, H9), 2.44 (6H, s, H11). **^{1}H NMR** (Acetone-D6, 400 MHz): δ 9.08 (2H, s, H6), 8.56 (1H, s, H1), 8.19 (2H, s, H3), 7.82 (4H, d, J = 8.4 Hz, H8), 7.42 (4H, d, J = 8.4 Hz, H9), 2.42 (6H, s, H11). **^{13}C NMR** ($CDCl_3$): δ 146.71 (C5), 139.20 (C10), 134.65 (C7), 132.84 (C2), 130.36 (C9), 128.34 (C3), 123.62 (C4), 121.60 (C1), 120.50 (C8), 118.35 (C6), 21.20 (C11). **ESI-MS**: Found MH^+ 471.0925, $C_{24}H_{20}BrN_6$ requires MH^+ 471.0933.

4.31

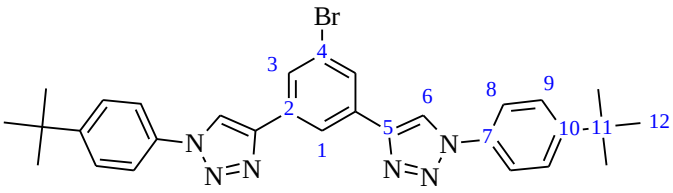

4-tert-Butylphenylboronic acid (0.52 g, 2.9 mmol), NaN_3 (0.8 g, 12.31 mmol), $Cu(OAc)_2$ (0.14 g, 0.82 mmol) were stirred in dry methanol (5 mL) for 2 hrs at 55 °C. The reaction mixture was cooled to room temperature and 1,3-di(ethynyl)-5-bromobenzene (0.248 g, 1.21 mmol) and sodium-L-ascorbate (0.174 g, 0.88 mmol) were added and the resulting mixture was stirred for 16 hrs. The reaction was quenched with $NH_4OH_{(aq)}$ (2M, 250 mL) and a precipitate was extracted with chloroform (3 x 30 mL); the combined organic layer was washed with water (3 x 20 mL), dried over anhydrous sodium sulfate, and the solvent removed to give a crude oil. The oil was purified by column chromatography to give the target product as an off white solid (0.58 g, 86%).

^{1}H NMR ($CDCl_3$, 400 MHz): δ 8.41 (1H, s, H1), 8.29 (2H, s, H6), 8.09 (2H, s, H3), 7.73 (4H, d, J = 8.6 Hz, H9), 7.59 (4H, d, J = 8.6 Hz, H8), 1.39 (18H, s, H12). **^{1}H NMR** (Acetone-D6, 400 MHz): δ 9.17 (2H, s, H6), 8.63 (1H, s, H1), 8.15 (2H, s, H3), 7.94 (4H, d, J = 8.7 Hz, H8), 7.71 (4H, d, J = 8.7 Hz, H9), 1.40 (18H, s, H12). **^{13}C NMR** ($CDCl_3$): δ 152.46 (C10), 146.53 (C2), 134.42 (C7), 132.77 (C5), 128.33 (C3), 126.75 (C8), 123.60 (C4), 121.62 (C1), 120.24 (C9), 118.35 (C6), 34.831 (C11), 31.261 (C12). **ESI-MS**: Found MH^+ 555.1877, $C_{30}H_{32}BrN_6$ requires MH^+ 555.1872.

4.35 and 4.35

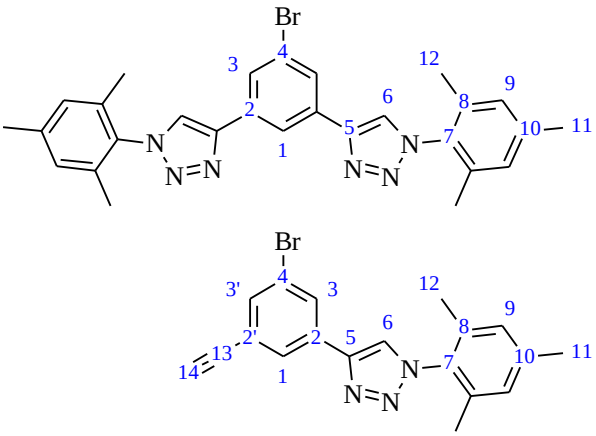

Mesityl boronic acid (0.48 g, 2.9 mmol), NaN_3 (0.8 g, 12.31 mmol), $Cu(OAc)_2$ (0.14 g, 0.82 mmol) were stirred in dry methanol (5 mL) for 2 hrs at 55 °C. The reaction mixture was cooled to room temperature and 1,3-di(ethynyl)-5-bromobenzene (0.248 g, 1.21 mmol) and sodium-L-ascorbate (0.174 g, 0.88 mmol) were added and the resulting mixture was stirred for 16 hrs. The reaction was quenched with

$NH_4OH_{(aq)}$ (2M, 250 mL) and a precipitate was extracted with chloroform (3 x 30 mL); the combined organic layer was washed with water (3 x 20 mL), dried over anhydrous sodium sulfate, and the solvent removed to give a crude oil. The oil was purified by column chromatography to give the target product as an off white solid (0.33 g, 52%) and the mono substituted intermediate as a white solid (0.18 g, 29%) .

4.35: **^{1}H NMR** ($CDCl_3$, 400 MHz): δ 8.40 (1H, t, J = 1.4 Hz, H1), 8.10 (2H, d, J = 1.4 Hz, H3), 7.95 (2H, s, H6), 7.02 (4H, s, H9), 2.38 (6H, s, H11), 2.02 (12H, s, H12). **^{1}H NMR** (Acetone-D6, 400 MHz): δ 8.71 (2H, s, H6), 8.62 (1H, s, H1), 8.16 (2H, s, H3), 7.12 (4H, s, H9), 2.38 (6H, s, H11), 2.03 (12H, s, H12). **^{13}C NMR** ($CDCl_3$, 125 MHz): δ 145.93 (C5), 140.27 (C10), 135.00 (C7), 133.27 (C8), 132.98 (C2), 129.19 (C9), 128.28 (C3), 123.61 (C4), 122.27 (C6), 121.57 (C1), 21.19 (C11), 17.35 (C12). **ESI-MS**: Found MH^+ 526.1489, $C_{28}H_{27}N_6Br$ requires MH^+ 526.1481.

4.35a: **^{1}H NMR** ($CDCl_3$, 400 MHz): δ 8.67 (1H, s, H6), 8.21 (1H, t, J = 1.6 Hz, H3), 8.09 (1H, t, J = 1.6 Hz, H1), 7.63 (1H, t, J = 1.6 Hz, H3a), 7.11 (2H, s, H9), 3.86 (1H, s, H14), 2.37 (3H, s, H11), 2.00 (6H, s, H12). **^{13}C NMR** ($CDCl_3$, 125 MHz): δ 122.31 (C4), 123.86 (C6), 124.92 (C2a), 127.60 (C1), 128.60 (C3), 129.01 (C9), 133.34 (C3a), 133.63 (C7), 133.67 (C2), 134.90 (C8), 140.10 (C10), 144.61 (C5), 80.23 (C14), 81.42 (C13), 20.20 (C11), 16.44 (C12). **ESI-MS**: Found MH^+ 365.0532, $C_{19}H_{16}N_3Br$ requires MH^+ 365.0528.

4.32

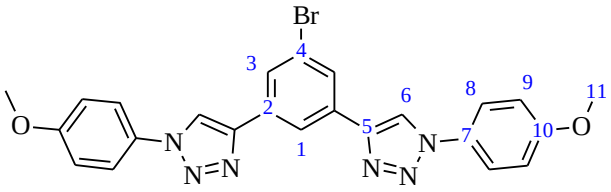

4-Methoxyphenylboronic acid (0.44 g, 2.9 mmol), NaN_3 (0.8 g, 12.31 mmol), $Cu(OAc)_2$ (0.14 g, 0.82 mmol) were stirred in dry methanol (5 mL) for 2 hrs at 55 °C. The reaction mixture was cooled to room temperature and 1,3-di(ethynyl)-5-bromobenzene (0.248 g, 1.21 mmol) and sodium-L-ascorbate (0.174 g, 0.88 mmol) were added and the resulting mixture was stirred for 16 hrs. The reaction was quenched with $NH_4OH_{(aq)}$ (2M, 250 mL) and a precipitate was extracted with chloroform (3 x 30 mL); the combined organic layer was washed with water (3 x 20 mL), dried over anhydrous sodium sulfate, and the solvent removed to give a

crude oil. The oil was purified by column chromatography to give the target product as an off white solid (0.53 g, 87%).

^{1}H NMR ($CDCl_3$, 400 MHz): δ 8.39 (1H, s, H1), 8.24 (2H, s, H6), 8.08 (2H, s, H3), 7.72 (4H, d, J = 8.9 Hz), 7.08 (4H, d, J = 8.9 Hz) 3.90 (6H, s, H11). **^{1}H NMR** (Acetone-D6, 400 MHz): δ 9.10 (2H, s, H6), 8.61 (1H, s, H1), 8.14 (2H, s, H3), 7.91 (4H, d, J = 8.4 Hz, H8), 7.19 (4H, d, J = 8.4 Hz, H9), 3.92 (6H, s, H11). **^{13}C NMR** ($CDCl_3$, 125 MHz): δ 160.03 (C10), 146.51 (C5), 132.85 (C2), 130.33 (C7), 128.28 (C3), 123.59 (C4), 122.21 (C9), 121.54 (C1), 118.53 (C6), 114.89 (C8), 55.66 (C11). **ESI-MS**: Found MH^+ 503.0839, $C_{24}H_{20}BrN_6O_2$ requires MH^+ 503.0831.

4.33

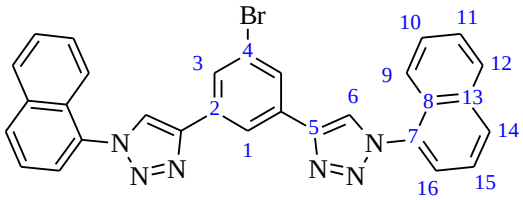

1-naphthyl boronic acid (0.49 g, 2.9 mmol), NaN_3 (0.8 g, 12.31 mmol), $Cu(OAc)_2$ (0.14 g, 0.82 mmol) were stirred in dry methanol (5 mL) for 2 hrs at 55 °C. The reaction mixture was cooled to room temperature and 1,3-di(ethynyl)-5-bromobenzene (0.248 g, 1.21 mmol) and sodium-L-ascorbate (0.174 g, 0.88 mmol) were added and the resulting mixture was stirred for 16 hrs. The reaction was quenched with $NH_4OH_{(aq)}$ (2M, 250 mL) and a precipitate was extracted with chloroform (3 x 30 mL); the combined organic layer was washed with water (3 x 20 mL), dried over anhydrous sodium sulfate, and the solvent removed to give a crude oil. The oil was purified by column chromatography to give the target product as an off white solid (0.52 g, 79%).

^{1}H NMR ($CDCl_3$, 400 MHz): δ 8.48 (1H, s, H1), 8.28 (2H, s, H6), 8.16 (2H, s, H3), 8.06 (2H, m, H12), 7.99 (2H, m, H15), 7.70 (2H, m, H9), 7.65 (2H, m, H13), 7.64 (2H, m, H10), 7.61 (2H, m, H8), 7.58 (2H, m, H14). **^{13}C NMR** ($CDCl_3$, 125 MHz): δ 146.09 (C5), 134.20 (C16), 133.50 (C11), 132.88 (C4), 130.65 (C12), 128.52 (C3), 128.43 (C7), 128.36 (C15), 128.07 (C14), 127.19 (C8), 125.02 (C10), 123.72 (C2), 123.58 (C13), 122.97 (C6), 122.21 (C9), 121.76 (C1). **ESI-MS**: Found MH^+ 543.0937, $C_{31}H_{20}BrN_6$ requires MH^+ 543.0933.

4.34

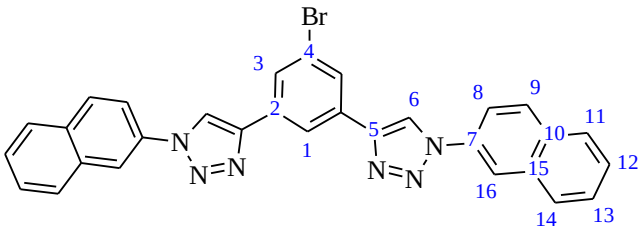

2-Naphthyl boronic acid (0.49 g, 2.9 mmol), NaN_3 (0.8 g, 12.31 mmol), $Cu(OAc)_2$ (0.14 g, 0.82 mmol) were stirred in dry methanol (5 mL) for 2 hrs at 55 °C. The reaction mixture was cooled to room temperature and 1,3-di(ethynyl)-5-bromobenzene (0.248 g, 1.21 mmol) and sodium-L-ascorbate (0.174 g, 0.88 mmol) were added and the resulting mixture was stirred for 16 hrs. The reaction was quenched with $NH_4OH_{(aq)}$ (2M, 250 mL) and a precipitate was extracted with chloroform (3 x 30 mL); the combined organic layer was washed with water (3 x 20 mL), dried over anhydrous sodium sulfate, and the solvent removed to give a crude oil. The oil was purified by column chromatography to give the target product as an off white solid (0.50 g, 76%).

^{1}H NMR (CD_3CN, 400 MHz): δ 8.47 (2H, s, H8), 8.46 (1H, s, H1), 8.25 (2H, s, H6), 8.12 (2H, s, H3), 8.05 (2H, d, J = 8.8 Hz, H16), 7.91-8.00 (6H, m, H10, H13, H15), 7.56-7.64 (4H, m, H11, H12). **^{13}C NMR** ($CDCl_3$, 125 MHz): δ 146.78 (C2), 134.25 (C7), 133.23 (C14), 133.01 (C9), 132.77 (C5), 130.18 (C16), 128.45 (C3), 128.32 (C10), 127.98 (C13), 127.58 (C11), 127.15 (C12), 123.70 (C4), 121.67 (C1), 118.81 (C8), 118.52 (C15), 118.51 (C6). **ESI-MS**: Found MH^+ 543.0939, $C_{31}H_{20}BrN_6$ requires MH^+ 543.0933.

4.37

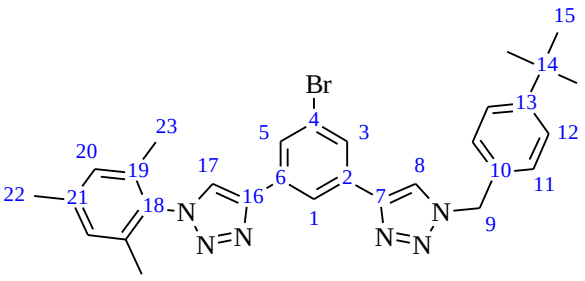

4.35a (0.14 g, 0.38 mmol), 4-tertbutylbenzyl bromide (0.09 g, 0.38 mmol), NaN_3 (28 mg, 0.41 mmol), $CuSO_4.5H_2O$ (10 mg, 0.04 mmol), sodium carbonate (40 mg, 0.38 mmol) and ascorbic acid (55 mg, 0.38 mmol) were added to a solution of DMF (8 mL) and H_2O (2 mL). The mixture was stirred vigorously for 18 h. Then NH_4OH (2M, 100 mL) was added to the solution and it was extracted with DCM and dried with anhydrous $MgSO_4$. After the solvent was removed, the residue was purified by column chromatography on silica gel using DCM followed

by 5% EtOAc/DCM as the eluent. Removal of solvent under reduced pressure gave the pure product (196 mg, 93%).

^{1}H NMR ($CDCl_3$, 400 MHz): δ 8.28 (1H, s, H1), 8.02 (1H, s, H5), 7.98 (1H, s, H3), 7.92 (1H, s, H17), 7.80 (1H, s, H8), 7.42 (2H, d, J = 8.1 Hz, H12), 7.26 (2H, d, J = 8.1 Hz, H11), 7.01 (2H, s, H20), 5.55 (2H, s), 2.36 3H, s, H23), 2.00 (6H, s, H22), 1.32 (9H, s, H15). **^{1}H NMR** (Acetone-D6, 400 MHz): δ 8.66 (1H, s, H17), 8.57 (1H, s, H8), 8.50 (1H, s, H1), 8.11 (1H, s, H5), 8.06 (1H, s, H3), 7.44 (2H, d, J = 8.4 Hz, H11), 7.37 (2H, d, J = 8.4 Hz, H12), 7.10 (2H, s, H20), 5.67 (2H, s, H9), 2.37 (3H, s, H22), 2.01 (6H, s, H23), 1.30 (9H, s, H15). **^{13}C NMR** ($CDCl_3$, 125 MHz): δ 152.15 (C13), 146.13 (C16), 146.08 (C7), 140.24 (C21), 134.98 (C18), 133.28 (C19), 133.13 (C6), 132.86 (C2), 131.20 (C10), 129.17 (C20), 128.07 (C3), 128.07 (C5), 128.07 (C11), 126.21 (C12), 123.48 (C4), 122.31 (C17), 121.41 (C1), 120.26 (C8), 54.16 (C9), 34.68 (C14), 31.25 (C15), 21.13 (C23), 17.31 (C22). **ESI-MS**: Found MH^+ 555.1878, $C_{30}H_{32}BrN_6$ requires MH^+ 555.1872.

4-(1-Naphthyl)pyrazole

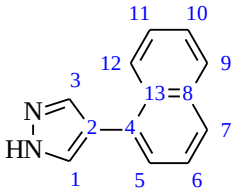

$POCl_3$ (20 mL, 0.21 mmol) was added dropwise to 45 mL of dry DMF at 5-10 °C with constant stirring. The mixture was stirred for an additional hour at room temperature. Then 1-naphthylacetic acid (13.8 g, 74 mmol) was added at once and the clear solution formed was stirred for 4 h at 90-95 °C and then at room temperature overnight. The resulting black mixture was poured on crushed ice. After decomposition of the excess Vilsmeyer reagent, a saturated solution of $NaBF_4$ (10 g, 0.039 mmol, in 15 mL H_2O) was added with stirring. The resulting nearly white crystalline deposit of the perchlorate salt was filtered and washed with two 20 mL portions of water. This compound was used in the next step without further purification. The salt was added to a warm solution of 6.0 g NaOH in 100 mL water, and the mixture was heated with stirring for 15 min (bath temperature 90 °C) until total dissolution of the organic salt was observed. The yellow-colored mixture was cooled to room temperature, diluted with 30 mL water and 10% HCl solution was added to pH = 5, leading to precipitation of the 1,3-dialdehyde. Then hydrazine hydrate (8 mL, 0.26 mmol) was added at once with stirring, which effects dissolution of 1,3-dialdehydes compound and after 15-20 min stirring at room temp. The 4-substituted pyrazole compound

deposits as thin white needles. The mixture was left overnight and the precipitate was collected by filtration and oven-dried in vacuo (11.2 g, 79%).

^{1}H NMR (DMSO-D6, 400 MHz): δ 8.12 (1H, s, H1), 7.84 (1H, m, H3), 7.93 (3H, m, H6, H10, H11), 7.50 (4H, m, H5, H7, H9, H13). **^{13}C NMR** (DMSO-D6, 100 MHz): δ 134.01 (C4), 131.41 (C2), 128.79 (C6), 127.23 (C3), 126.98/126.71/126.26/126.13 (C5/C7/C9/C13), 125.64 (C1), 119.53 (C8), unassigned (C10, C11). **ESI-MS**: Found MH^+ 195.0928, $C_{13}H_{11}N_2$ requires MH^+ 195.0922.

4.41

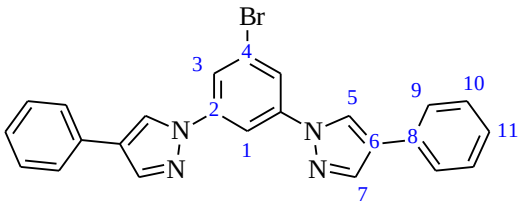

A mixture of 1,3,5-tribromobenzene (3.3 g, 10.5 mmol), 4-phenylpyrazole (3.4 g, 23.5 mmol), potassium carbonate (6.6 g, 47.8 mmol), copper(I) iodide (100 mg, 0.5 mmol) and L-proline (170 mg, 1.3 mmol) in DMSO (15 mL) was degassed by freeze-pump-thaw (3 times). The mixture was then heated at 140 °C with vigorous stirring under a nitrogen atmosphere for 24 h. After cooling to room temperature, dichloromethane (50 mL) and $NH_4OH_{(aq)}$ (2 M, 50 mL) were added and the organic phase was washed with water (4 x 50 mL). The organic phase was dried over anhydrous potassium carbonate and the solvent removed under reduced pressure. The residue was purified by column chromatography on silica, gradient elution from dichloromethane to 20% ethyl acetate/dichloromethane, leading to a white solid (3.52 g, 76%).

^{1}H NMR ($CDCl_3$, 400 MHz): δ 9.18 (2H, s, H5), 8.44 (1H, s, H1), 8.31 (2H, s, H7), 8.05 (2H, s, H3), 7.74 (4H, d, J = 7.2 Hz, H9), 7.41 (4H, t, J = 7.2 Hz, H10), 7.26 (2H, t, J = 7.2 Hz, H11). **^{1}H NMR** (Acetone-D6, 400 MHz): δ 8.99 (2H, s, H5), 8.49 (1H, t, J = 1.9 Hz, H1), 8.23 (2H, s, H7), 8.07 (2H, d, J = 1.9 Hz, H3), 7.76 (4H, d, J = 7.4 Hz, H9), 7.43 (4H, t, J = 7.4 Hz, H10), 7.29 (2H, t, J = 7.4 Hz, H11). **^{13}C NMR** (125 MHz, $CDCl_3$): δ 141.85 (C2), 139.99 (C7), 131.86 (C9), 129.37 (C10), 127.34 (C11), 125.80 (C8), 125.62 (C5), 125.25 (C6), 123.67 (C4), 118.26 (C3), 107.09 (C1). **ESI-MS**: Found MH^+ 441.0723, $C_{24}H_{18}BrN_4$ requires MH^+ 441.0715.

4.42

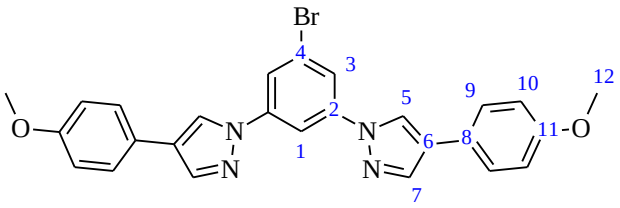

A mixture of 1,3,5-tribromobenzene (3.3 g, 10.5 mmol), 4-(4-methoxyphenyl)pyrazole (4.1 g, 23.5 mmol), potassium carbonate (6.6 g, 47.8 mmol), copper(I) iodide (100 mg, 0.5 mmol) and L-proline (170 mg, 1.3 mmol) in DMSO (15 mL) was degassed by freeze-pump-thaw (3 times). The mixture was then heated at 140 °C with vigorous stirring under a nitrogen atmosphere for 24 h. After cooling to room temperature, dichloromethane (50 mL) and $NH_4OH_{(aq)}$ (2 M, 50 mL) were added and the organic phase was washed with water (4 x 50 mL). The organic phase was dried over anhydrous potassium carbonate and the solvent removed under reduced pressure. The residue was purified by column chromatography on silica, gradient elution from dichloromethane to 20% ethyl acetate/dichloromethane, leading to a white solid (4.63 g, 88%).

^{1}H NMR (300 MHz, $CDCl_3$): δ 8.15 (2H, s, H5), 8.09 (1H, t, J = 1.8 Hz, H1), 7.96 (2H, s, H7), 7.81 (2H, d, J = 1.8 Hz, H3), 7.49 (4H, d, J = 8.7 Hz, H10), 6.96 (4H, d, J = 8.7 Hz, H9), 3.85 (6H, s). **^{1}H NMR** (Acetone-D6, 400 MHz): δ 8.89 (2H, s, H5), 8.45 (1H, s, H1), 8.15 (2H, s, H7), 8.03 (2H, s, H3), 7.70 (4H, d, J = 8.7 Hz, H9), 7.01 (4H, d, J = 8.7 Hz, H10), 3.84 (6H, s, H12). **^{13}C NMR** (125 MHz, $CDCl_3$): δ 158.94 (C11), 141.65 (C2), 139.42 (C7), 126.98 (C10), 125.52 (C8), 124.01 (C6), 123.82 (C4), 122.66 (C5) 118.98 (C3), 114.45 (C9) 107.43 (C1) 55.35 (C12). **ESI-MS**: Found MH^+ 501.0936, $C_{26}H_{21}BrN_4O_2$ requires MH^+ 501.0926.

4.43

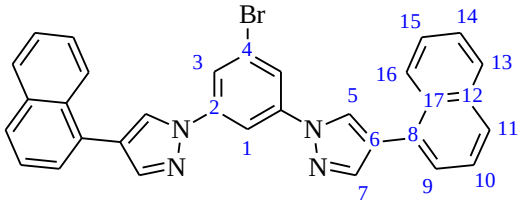

A mixture of 1,3,5-tribromobenzene (3.3 g, 10.5 mmol), 4-(1-naphthyl)pyrazole (4.6 g, 23.5 mmol), potassium carbonate (6.6 g, 47.8 mmol), copper(I) iodide (100 mg, 0.5 mmol) and L-proline (170 mg, 1.3 mmol) in DMSO (15 mL) was degassed by freeze-pump-thaw (3 times). The mixture was then heated at 140 °C with vigorous stirring under a nitrogen atmosphere for 24 h. After cooling to room temperature, dichloromethane (50 mL) and $NH_4OH_{(aq)}$ (2 M, 50 mL) were added and the organic phase was washed with water (4 x 50 mL). The organic phase was dried over anhydrous

potassium carbonate and the solvent removed under reduced pressure. The residue was purified by column chromatography on silica, gradient elution from dichloromethane to 20% ethyl acetate/dichloromethane, leading to a white solid (4.39 g, 77%).

^{1}H NMR (CD_3Cl, 400 MHz): δ 8.24 (2H, m, H5), 8.23 (1H, m, H1), 8.19-8.14 (2H, m, H16), 8.02 (2H, s, H7), 7.95-7.90 (4H, m, H3, H9), 7.89-7.51 (10H, m, H10, H13, H14, H15). **^{1}H NMR** (Acetone-D6, 400 MHz): δ 8.88 (2H, s, H5), 8.59 (1H, s, H1), 8.30-8.26 (2H, m, H5), 8.16 (2H, s, H3), 8.10 (2H, s, H7), 7.95-8.00 (2H, m, H7), 7.92 (2H, d, J = 8.1 Hz, H11), 7.64 (2H, d, J = 6.7 Hz, H8), 7.52-7.59 (6H, m, H6, H9, H10). **^{13}C NMR** (CD_3Cl, 100 MHz): δ 142.41 (C7), 141.75 (C2), 133.90 (C12), 131.61 (C17), 129.52 (C8), 128.56 (C9), 128.08/126.52/126.06/125.47 (C10/C13/C14/C15), 127.05 (C17), 126.04 (C5), 125.21 (C16), 124.00 (C6), 123.95 (C4), 119.36 (C3), 107.81 (C1). **ESI-MS**: Found MH^+ 540.0959, $C_{32}H_{21}BrN_4$ requires MH^+ 540.0950.

[Ru(tpy)(MeCN)$_3$](PF$_6$)$_2$

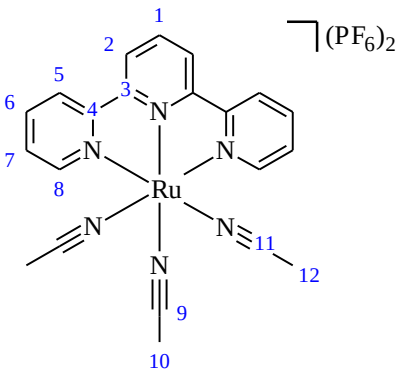

A suspension of Ru(III)(2,2′:6′,2″-tpy)Cl_3 (0.50 g, 1.14 mmol), $AgNO_3$ (585 mg, 3.44 mmol) and $CH_3CN/EtOH/H_2O$ (6:1:1; 40 mL) was heated to 80 °C for 24 h. The mixture was cooled to ambient temperature, filtered through a pad of celite and rinsed with additional CH_3CN. The solvent was removed under reduced pressure and the concentrated solution was slowly dropped into an excess of $KPF_{6(aq)}$. The fine precipitate was filtered, washed with water, rinsed with CH_3CN and dried over Na_2SO_4 to give the target product. (1.27 g, 75%).

^{1}H NMR (CD_3CN, 400 MHz): δ 8.94 (2H, d, 5.4 Hz, H5), 8.42 (4H, m, H2, H8), 8.20 (3H, m, H1, H7), 7.76 (2H, m, J = 6.5 Hz, H6), 1.94 (9H, s, H10). **^{13}C NMR** (100 MHz, CD_3CN, ppm): δ 159.74 (C4), 159.36 (C3), 155.27 (C8), 139.92 (C6), 138.32 (C1), 128.90 (C9), 128.22 (C7), 124.85 (C11), 124.22 (C5), 123.70 (C2), 4.55 (C10), 3.83 (C12). **ESI-MS**: Found $[M\text{-}PF_6]^+$ 603.0418, $C_{21}H_{20}F_6N_6PRu$ requires $[M\text{-}PF_6]^+$ 603.0429. **UV-vis** (CH_3CN) λ_{max}/nm (ε, 10^3 $M^{-1}cm^{-1}$): 201 (47,000), 216 (43,000), 229 (sh, 28,000), 239 (sh, 20,000), 251 (sh 13,000), 272 (19,000),

299 (31,000), 318 (sh, 15,000), 330 (17,000), 413 (sh, 4,500), 436 (sh, 4,800), 487 (sh, 1,400), 580 (400).

[Ru(3.13)(MeCN)$_3$](PF$_6$)$_2$

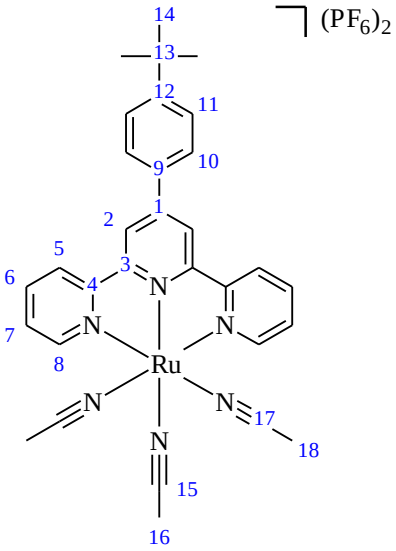

A suspension of Ru(**3.13**)Cl$_3$ (0.66 g, 1.14 mmol), AgNO$_3$ (585 mg, 3.44 mmol) and CH$_3$CN/EtOH/H$_2$O (6:1:1; 40 mL) was heated to 80 °C for 24 h. The mixture was cooled to ambient temperature, filtered through a pad of celite and rinsed with additional CH$_3$CN. The solvent was removed under reduced pressure and the concentrated solution was slowly dropped into an excess of KPF$_{6(aq)}$. The fine precipitate was filtered, washed with water, rinsed with CH$_3$CN and dried over Na$_2$SO$_4$ to give the target product. (0.79 g, 79%).

^{1}H NMR (CD$_3$CN, 400 MHz): δ 8.97 (2H, d, J = 5.3 Hz, H8), 6.68 (2H, s, H2), 8.58 (2H, d, J = 6.9 Hz, H5), 8.23 (2H, t, J = 7.8 Hz, H6), 8.03 (2H, d, J = 8.5 Hz, H11), 7.80-7.74 (4H, m, H10, H7), 2.7 (3H, s, H16), 1.99 (6H, s, H18), 1.44 (9H, s, H14). **^{13}C NMR** (100 MHz, CD$_3$CN): δ 160.21 (C4), 160.01 (C3), 155.82 (C8), 155.60 (C12), 151.17 (C9), 140.34 (C6), 134.79 (C1), 129.37 (C10), 128.83 (C11), 128.65 (C15), 127.95 (C7), 125.47 (C5), 124.78 (C17), 121.91 (C2), 35.99 (C13), 31.82 (C14), 5.10 (C16), 4.38 (C18). **ESI-MS**: Found [M-PF$_6$]$^+$ 735.1382, C$_{31}$H$_{32}$N$_6$Ru requires [M-PF$_6$]$^+$ 735.1373.

6.7 Ruthenium complexes - Chapter four.

4.1

A mixture of [Ru(tpy)(MeCN)$_3$](PF$_6$)$_2$ (75 mg, 0.10 mmol) and 1,3-bis(1-(4-tertbutylbenzyl)-1*H*-1,2,3-triazol-4-yl)-5-bromobenzene (73 mg, 0.10 mmol) in n-butanol (20 mL) were refluxed for 16 h. After cooling and filtering, the solvent was removed under reduced pressure. The solid was slowly dropped into an excess of NH$_4$PF$_{6(aq)}$. The fine precipitate was filtered, washed with water, rinsed with CH$_3$CN, dried over Na$_2$SO$_4$ and the solvent was removed in vacuo. The crude product was purified using column chromatography, eluting with 10% acetonitrile/ethyl acetate on silica to give the pure complex (52 mg, 49% yield).

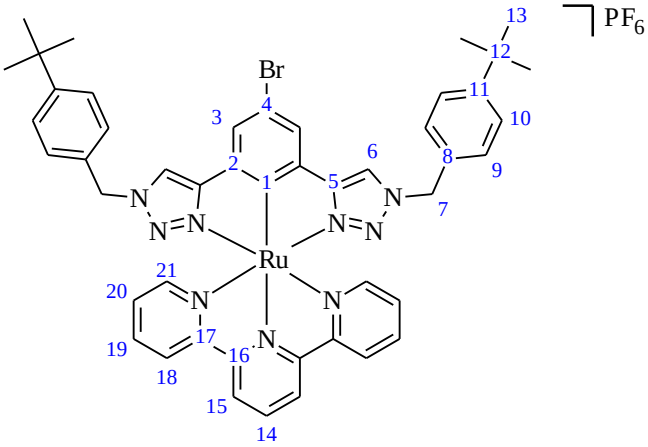

^{1}H NMR (Acetone-D6, 400 MHz): δ 8.85 (2H, d, J = 8.3 Hz, H15), 8.61 (2H, d, J = 8.0 Hz, H18), 8.46 (2H, s, H6), 8.30 (1H, t, J = 8.3 Hz, H14), 8.02 (2H, s, H3), 7.88 (2H, t, J = 8.0 Hz, H19), 7.37 (2H, d, J = 5.3 Hz, H21), 7.24 (4H, d, J = 7.4 Hz, H10), 7.18 (2H, t, J = 6.8 Hz, H20), 6.90 (4H, d, J = 7.4 Hz, H9), 5.34 (4H, s, H7), 1.23 (18H, s, H13). **^{13}C NMR** (Acetone-D6, 100 MHz): δ 209.21 (C1), 159.84 (C17), 158.14 (C5), 154.70 (C16), 154.43 (C18), 151.33 (C11), 137.08 (C2), 135.28 (C19), 132.81 (C14), 131.97 (C8), 127.38 (C9), 126.45 (C20), 125.62 (C10), 123.16 (C21), 122.68 (C3), 121.62 (C15), 119.14 (C6), 112.73 (C4), 54.21(C7), 34.13(C12), 30.53 (C13). **ESI-MS:** Found $[M\text{-}PF_6]^+$ 916.2028, $C_{47}H_{45}BrN_9Ru$ requires $[M\text{-}PF_6]^+$ 916.2025. Found $[M\text{-}PF_6+H]^{2+}$ 458.1018, $C_{47}H_{46}BrN_9Ru$ requires $[M\text{-}PF_6+H]^{2+}$ 458.1012. **UV-Vis** (CH_3CN) λ_{max}/nm (ε, 10^3 $M^{-1}cm^{-1}$): 528 (5.5), 483 (6.6), 368 (9.4), 315 (26.5), 273 (24.3), 229 (49.4). **Fluorometry** (Butyronitrile, 77K) λ_{max}: 651 nm.

4.2

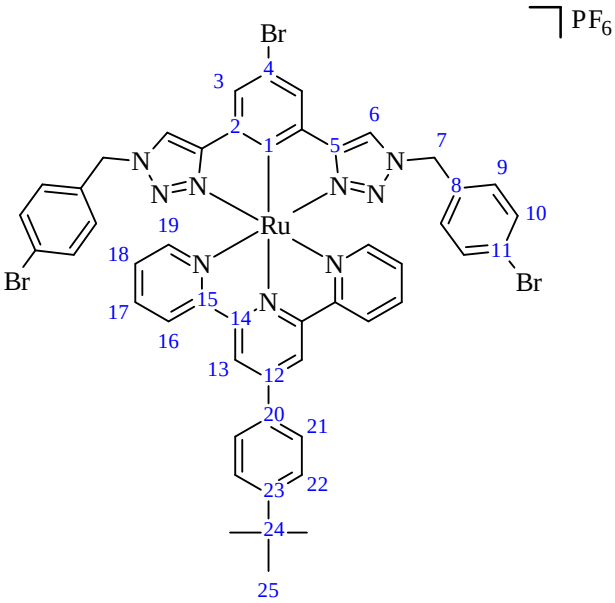

A mixture of [Ru(**3.13**)$(MeCN)_3$]$(PF_6)_2$ (88 mg, 0.10 mmol) and 1,3-bis(1-(4-bromobenzyl)-1H-1,2,3-triazol-4-yl)-5-bromobenzene (63 mg, 0.10 mmol) in n-butanol (20 mL) were refluxed for 16 h. After cooling and filtering, the solvent was removed under reduced pressure. The solid was slowly dropped into an excess of $NH_4PF_{6(aq)}$. The fine precipitate was filtered, washed with water, rinsed with CH_3CN, dried over Na_2SO_4 and the solvent was removed in vacuo. The crude product was purified using column chromatography, eluting with 10% acetonitrile/ethyl acetate on silica to give the pure complex (65 mg, 52% yield).

^{1}H NMR (Acetone-D6, 400 MHz): δ 8.83 (2H, s, H13), 8.61 (2H, s, H6), 8.57 (2H, d, J = 5.9 Hz, H19), 8.10 (2H, S, H3), 7.87 (2H, t, J = 8.0 Hz, H18), 7.61 (2H, d, J = 8.3 Hz, H21), 7.74 (2H, d, J = 8.3 Hz, H22), 7.35 (2H, d, J = 8.3 Hz, H16), 7.23 (4H, d, J = 8.3 Hz, H10), 7.12 (2H, m, H17), 6.90 (4H, d, J = 8.3 Hz, H9), 5.42 (4H, s, H7), 1.45 (9H, s, H25). **^{13}C NMR** (Acetone-D6, 100 MHz): δ 180.25 (C1), 121.94 (C3), 119.67 (C6), 53.84 (C7), 129.70 (C9), 131.75 (C10), 134.27 (C12), 119.13 (C13), 155.10 (C14), 159.93 (C15), 154.83 (C16), 126.58 (C17), 135.22 (C18), 123.27 (C19), 144.30 (C20), 126.20 (C21), 127.19 (C22), 126.20 (C23), 152.73 (C24), 34.50 (C25), 30.67 (C26). **ESI-MS:** Found $[M\text{-}PF_6+H]^{2+}$ 547.4993, $C_{49}H_{40}Br_3N_9Ru$ requires $[M\text{-}PF_6+H]^{2+}$ 547.4990. **UV-Vis** (CH_3CN) λ_{max}/nm (ε, 10^3 $M^{-1}cm^{-1}$): 530 (6.8), 489 (7.7), 371 (11.1), 313 (27.3), 284 (31.7), 227 (55.5). **Fluorometry** (Butyronitrile, 77K) λ_{max}: 664 nm.

4.3

A mixture of $[Ru(tpy)(MeCN)_3](PF_6)_2$ (75 mg, 0.10 mmol) and 1,3-bis(1-(4-tertbutylphenyl)-1H-1,2,3-triazol-4-yl)-5-bromobenzene (56 mg, 0.10 mmol) in ^{n}butanol (20 mL) were refluxed for 16 h. After cooling and filtering, the solvent was removed under reduced pressure. The solid was slowly dropped into an excess of $NH_4PF_{6(aq)}$. The fine precipitate was filtered, washed with water, rinsed with CH_3CN, dried over Na_2SO_4 and the solvent was removed in vacuo. The crude product was purified using column chromatography, eluting with 10% acetonitrile/ethyl acetate on silica to give the pure complex (58 mg, 56% yield).

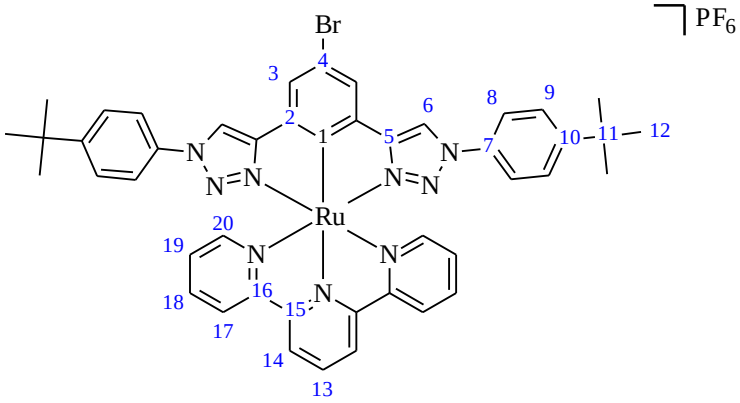

^{1}H NMR (Acetone-D6, 400 MHz): δ 9.10 (2H, s, H6), 8.89 (2H, d, J = 8.1 Hz, H14), 8.63 (2H, d, J = 7.8 Hz, H20), 8.37 (1H, t, J = 8.1 Hz, H13), 8.15 (2H, s, H3), 7.85 (2H, t, J = 7.7 Hz, H19), 7.54–7.45 (10H, m, H8, H9, H17), 7.19 (2H, t, J = 6.9 Hz, H18), 1.26 (18H, s, H12). **^{13}C NMR** (Acetone-D6, 125 MHz): δ 209.46 (C1), 159.82 (C16), 158.70 (C5), 154.67 (C17), 154.34 (C15), 152.32 (C10), 136.88 (C4), 135.56 (C19), 134.11 (C7), 133.30 (C13), 126.73 (C8), 126.50 (C18), 123.18 (C20), 123.05 (C3), 121.61 (C14), 119.24 (C9), 116.40 (C6), 112.82 (C2),

34.45 (C11), 30.36 (C12). **ESI-MS:** Found $[M\text{-}PF_6]^+$ 888.1717, $C_{45}H_{41}BrN_9Ru$ requires $[M\text{-}PF_6]^+$ 888.1712. Found $[M\text{-}PF_6\text{+}H]^{2+}$ 444.0853, $C_{45}H_{42}BrN_9Ru$ requires $[M\text{-}PF_6\text{+}H]^{2+}$ 444.0856. **UV-Vis** (CH_3CN) λ_{max}/nm (ε, 10^3 $M^{-1}cm^{-1}$): 516 (3.7), 476 (4.2), 379 (9.4), 314 (19.0), 300 (17.5), 272 (23.4), 246 (38.0). **Fluorometry** (Butyronitrile, 77K) λ_{max}: 677 nm.

4.4

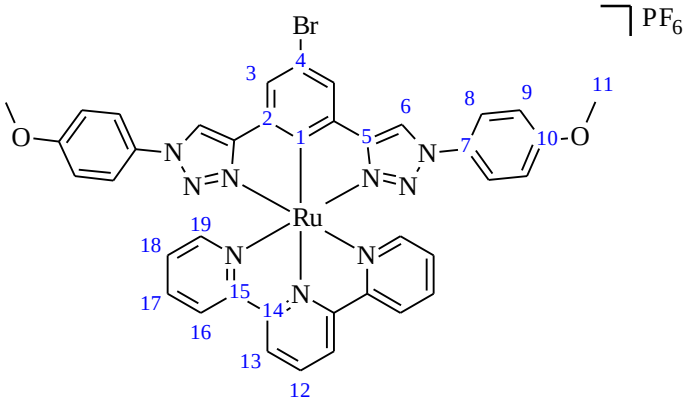

A mixture of $[Ru(tpy)(MeCN)_3](PF_6)_2$ (75 mg, 0.10 mmol) and 1,3-bis(1-(4-methoxyphenyl)-1H-1,2,3-triazol-4-yl)-5-bromobenzene (50 mg, 0.10 mmol) in ^{n}butanol (20 mL) were refluxed for 16 h. After cooling and filtering, the solvent was removed under reduced pressure. The solid was slowly dropped into an excess of $NH_4PF_{6(aq)}$. The fine precipitate was filtered, washed with water, rinsed with CH_3CN, dried over Na_2SO_4 and the solvent was removed in vacuo. The crude product was purified using column chromatography, eluting with 10% acetonitrile/ethyl acetate on silica to give the pure complex (65 mg, 66% yield).

^{1}H NMR (Acetone-D6, 400 MHz): δ 8.94 (2H, s, H6), 8.77 (2H, d, J = 8.1 Hz, H13), 8.51 (2H, d, J = 8.1 Hz, H19), 8.29 (1H, t, J = 8.1 Hz, H12), 8.04 (2H, s, H3), 7.78 (2H, t, J = 8.1 Hz, H18), 7.37 (4H, d, J = 9.1 Hz, H9), 7.31 (2H, d, J = 5.4 Hz, H16), 7.07 (2H, t, J = 6.1 Hz, H17), 6.91 (4H, d, J = 9.1 Hz, H8), 3.71 (6H, s, H11). **^{13}C NMR** (Acetone-D6, 100 MHz): δ 209.59 (C1), 160.08 (C10), 159.55 (C15), 158.36 (C5), 154.54 (C16), 136.92 (C2), 154.52 (C14), 135.52 (C7), 133.07 (C12), 129.81 (C18), 126.45 (C17), 123.21 (C19), 122.81 (C3), 122.71 (C9), 121.61 (C13), 117.31 (C4), 116.85 (C6), 114.77 (C8), 55.37(C11). **ESI-MS:** Found $[M\text{-}PF_6]^+$ 836.0676, $C_{39}H_{29}BrN_9O_2Ru$ requires $[M\text{-}PF_6]^+$ 836.0671. Found $[M\text{-}PF_6\text{+}H]^{2+}$ 418.0335, $C_{39}H_{30}BrN_9O_2Ru$ requires $[M\text{-}PF_6\text{+}H]^{2+}$ 418.0336. **UV-Vis** (CH_3CN) λ_{max}/nm (ε, 10^3 $M^{-1}cm^{-1}$): 517 (5.2), 479 (6.0), 374 (12.9), 313 (28.3), 301 (27.7), 255 (41.9), 236 (41.7). **Fluorometry** (Butyronitrile, 77K) λ_{max}: 680 nm.

4.5

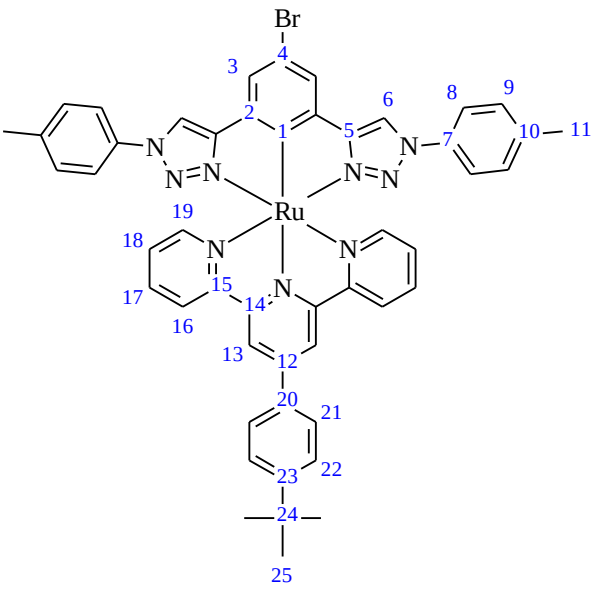

A mixture of [Ru(**3.13**)(MeCN)$_3$](PF$_6$)$_2$ (88 mg, 0.10 mmol) and 1,3-bis(1-(4-methylphenyl)-1H-1,2,3-triazol-4-yl)-5-bromobenzene (47 mg, 0.10 mmol) in ^{n}butanol (20 mL) were refluxed for 16 h. After cooling and filtering, the solvent was removed under reduced pressure. The solid was slowly dropped into an excess of $NH_4PF_{6(aq)}$. The fine precipitate was filtered, washed with water, rinsed with CH_3CN, dried over Na_2SO_4 and the solvent was removed in vacuo. The crude product was purified using column chromatography, eluting with 10% acetonitrile/ethyl acetate on silica to give the pure complex (64 mg, 59% yield).

^{1}H NMR (Acetone-D6, 400 MHz): δ 9.21 (2H, s, H13), 9.11 (2H, s, H6), 8.83 (2H, d, J = 8.0 Hz, H19), 8.25 (2H, d, J = 8.3 Hz, H22), 8.14 (2H, s, H3), 7.88 (2H, t, J = 8.4 Hz, H21), 7.50 (2H, d, J = 5.1 Hz, H16), 7.45 (4H, d, J = 8.4 Hz, H9), 7.26 (4H, d, J = 8.2 Hz, H8), 7.21 (2H, t, J = 6.9 Hz, H17), 2.30 (6H, s, H11), 1.46 (9H, s, H25). **^{13}C NMR** (Acetone-D6, 100 MHz): δ 209.52 (C1), 160.06 (C15), 158.64 (C5), 154.62 (C16), 152.98 (C23), 139.29 (C10), 135.63 (C18), 134.92 (C12), 130.23 (C8), 127.36 (C22), 126.61 (C17), 126.32 (C21), 123.54 (C19), 123.07 (C3), 119.61 (C9), 119.42 (C13), 112.81 (C6), 33.42 (C24), 30.62 (C25), 19.95 (C11), unassigned (C2, C4, C7, C14, C20). **ESI-MS:** Found $[M\text{-}PF_6]^+$ 936.1714, $C_{49}H_{41}BrN_9Ru$ requires $[M\text{-}PF_6]^+$ 936.1711. Found $[M\text{-}PF_6\text{+}H]^{2+}$ 468.5893, $C_{49}H_{42}BrN_9Ru$ requires $[M\text{-}PF_6\text{+}H]^{2+}$ 468.5921. **UV-Vis** (CH_3CN) λ_{max}/nm (ε, 10^3 $M^{-1}cm^{-1}$): 521 (7.2), 489 (7.6), 367 (13.8), 314 (23.9), 285 (35.1), 245 (46.1). **Fluorometry** (Butyronitrile, 77K) λ_{max}: 664 nm.

4.6

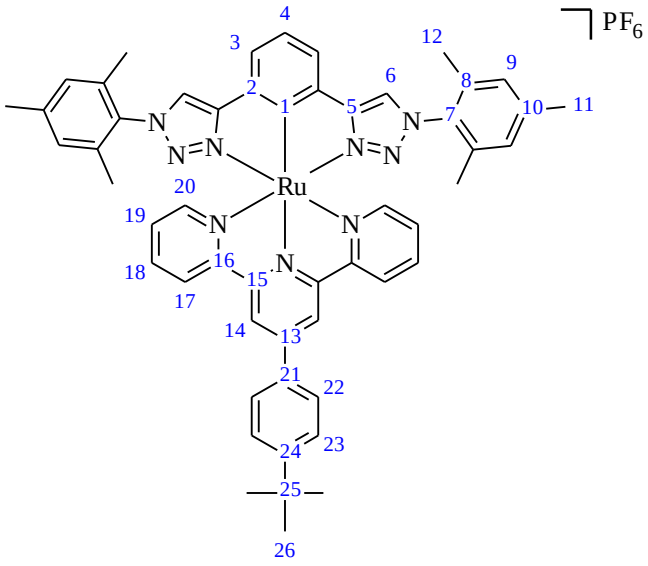

A mixture of [Ru(**3.13**)(MeCN)$_3$](PF$_6$)$_2$ (88 mg, 0.10 mmol) and 1,3-bis(1-(mesityl)-1H-1,2,3-triazol-4-yl)-5-bromobenzene (53 mg, 0.10 mmol) in ^{n}butanol (20 mL) were refluxed for 16 h. After cooling and filtering, the solvent was removed under reduced pressure. The solid was slowly dropped into an excess of NH_4PF_6 . The fine precipitate was filtered, washed with water, rinsed with CH_3CN, dried over Na_2SO_4 and the solvent was removed in vacuo. The crude product was purified using column chromatography, eluting with 10% acetonitrile/ethyl acetate on silica to give the pure complex (80.5 mg, 76% yield).

^{1}H NMR (Acetone-D6, 400 MHz): δ 8.89 (2H, s, H14), 8.68 (2H, d, J = 7.9 Hz, H20), 8.57 (2H, s, H6), 8.01 (2H, m H3), 8.01 (2H, m, H23), 7.82 (2H, t, J = 7.9 Hz, H19), 7.56 (2H, d, J = 8.2 Hz, H22), 7.54 (2H, d, J = 5.1 Hz, H17), 7.41 (1H, t, J = 7.5 Hz, H4), 7.21 (2H, t, J = 6.9 Hz, H18), 6.90 (4H, s, H9), 2.22 (6H, s, H12), 1.52 (12H, s, H11), 1.40 (9H, s, H26). **^{13}C NMR** (Acetone-D6, 100 MHz): δ 210.82 (C1), 159.46 (C2), 160.15 (C16), 159.46 (C6), 154.86 (C15), 154.44 (C17), 154.44 (C24), 144.83 (C21), 140.34 (C10), 134.65 (C8), 134.65 (C13), 134.65 (C19), 132.32 (C7), 128.95 (C9), 127.22 (C23), 126.19 (C18), 126.19 (C22), 123.23 (C20), 120.90 (C3), 120.80 (C4), 120.33 (C5), 119.22 (C14), 34.432 (C25), 30.632 (C26), 20.031 (C12), 15.861 (C11). **ESI-MS:** Found $[M\text{-}PF_6]^+$ 914.3231, $C_{53}H_{50}N_9Ru$ requires $[M\text{-}PF_6]^+$ 914.3233. Found $[M\text{-}PF_6\text{+}H]^{2+}$ 457.1615, $C_{53}H_{51}N_9Ru$ requires $[M\text{-}PF_6\text{+}H]^{2+}$ 457.1616. **UV-Vis** (CH_3CN) λ_{max}/nm (ε, 10^3 $M^{-1}cm^{-1}$): 530 (8.4), 494 (8.8), 363 (14.9), 314 (28.6), 284 (36.8), 276 (32.7), 233 (61.6). **Fluorometry** (Butyronitrile, 77K) λ_{max}: 663 nm.

4.7

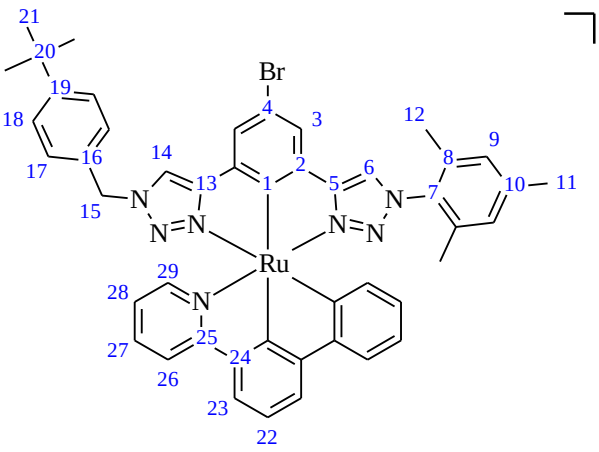

A mixture of $[Ru(tpy)(MeCN)_3](PF_6)_2$ (75 mg, 0.10 mmol) and 1-(1-(mesityl)-1H-1,2,3-triazol-4-yl)-3-(1-benzyl-1H-1,2,3-triazol-4-yl)-5-bromobenzene (56 mg, 0.10 mmol) in n-butanol (20 mL) were refluxed for 16 h. After cooling and filtering, the solvent was removed under reduced pressure. The solid was slowly dropped into an excess of $NH_4PF_{6(aq)}$. The fine precipitate was filtered, washed with water, rinsed with CH_3CN, dried over Na_2SO_4 and the solvent was removed in vacuo. The crude product was purified using column chromatography, eluting with 10% acetonitrile/ethyl acetate on silica to give the pure complex (73 mg, 71% yield).

^{1}H NMR (Acetone-D6, 400 MHz): δ 8.78 (2H, d, J = 8.1 Hz, H23), 8.60 (2H, d, J = 8.1 Hz, H29), 8.59 (1H, s, H6), 8.52 (1H, s, H14), 8.21 (1H, t, J = 8.1 Hz, H22), 8.07 (2H, m, H3), 7.89 (2H, t, J = 7.7 Hz, H28), 7.44 (2H, d, J = 5.5 Hz, H26), 7.25 (2H, d, J = 8.4 Hz, H18), 7.20 (2H, t, J = 6.6 Hz, H27), 6.93 (2H, d, J = 8.4 Hz, H17), 6.91 (2H, s, H9), 5.37 (2H, s, H15), 2.23 (3H, s, H11), 1.48 (6H, s, H12), 1.21 (9H, s, H21). **^{13}C NMR** (Acetone-D6, 100 MHz): δ 209.35 (C1), 159.82 (C25), 158.18 (C13), 158.04 (C5), 154.63 (C26), 154.20 (C24), 151.35 (C19), 140.45 (C10), 137.02 (C4), 135.27 (C28), 134.60 (C7), 133.21 (C8), 132.84 (C22), 131.98 (C16), 128.97 (C9), 127.44 (C17), 126.30 (C27), 125.50 (C18), 123.05 (C29), 122.74 (C3), 121.47 (C23), 120.88 (C6), 119.31 (C14), 112.73 (C2), 54.25 (C15), 34.14 (C20), 30.44 (C21), 19.96 (C11), 15.69 (C12). **ESI-MS:** Found $[M\text{-}PF_6]^+$ 888.1714, $C_{45}H_{41}BrN_9Ru$ requires $[M\text{-}PF_6]^+$ 888.1712. Found $[M\text{-}PF_6\text{+}H]^{2+}$ 444.0859, $C_{45}H_{42}BrN_9Ru$ requires $[M\text{-}PF_6\text{+}H]^{2+}$ 444.0856. **UV-Vis** (CH_3CN) λ_{max}/nm (ε, 10^3 $M^{-1}cm^{-1}$): 521 (7.7), 481 (8.8), 365 (13.4), 315 (35.4), 272 (35.8), 233 (70.6). **Fluorometry** (Butyronitrile, 77K) λ_{max}: 690 nm.

4.8

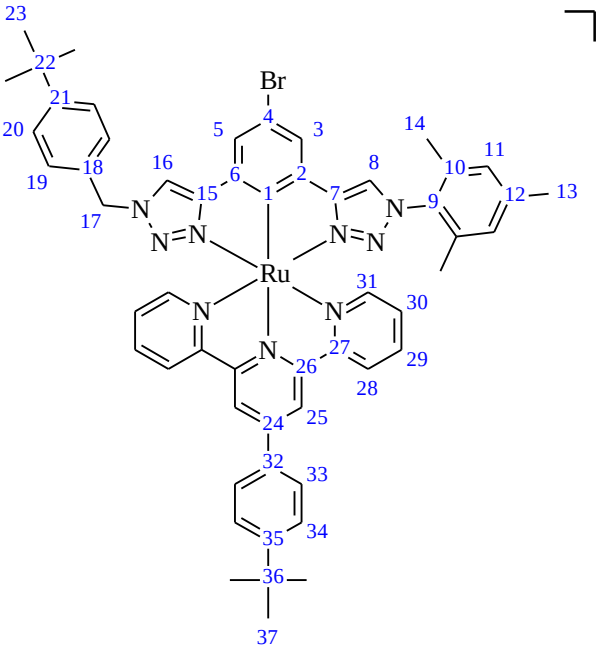

A mixture of [Ru(**3.13**)(MeCN)$_3$](PF$_6$)$_2$ (44 mg, 0.05 mmol) and 1-(1-(mesityl)-1H-1,2,3-triazol-4-yl)-3-(1-benzyl-1H-1,2,3-triazol-4-yl)-5-bromobenzene (28 mg, 0.05 mmol) in ^{n}butanol (20 mL) were refluxed for 16 h. After cooling and filtering, the solvent was removed under reduced pressure. The solid was slowly dropped into an excess of NH_4PF_{6c}. The fine precipitate was filtered, washed with water, rinsed with CH_3CN, dried over Na_2SO_4 and the solvent was removed in vacuo. The crude product was purified using column chromatography, eluting with 10% acetonitrile/ethyl acetate on silica to give the pure complex (42 mg, 73% yield).

^{1}H NMR (Acetone-D6, 400 MHz): δ 8.95 (2H, s, H25), 8.78 (2H, d, J = Hz, H31), 8.64 (1H, s, H16), 8.61 (1H, s, H8), 8.13 (1H, s, H5), 8.09 (1H, s, H3), 7.94 (2H, d, J = Hz, H34), 7.84 (2H, t, J = Hz, H30), 7.66 (2H, d, J = Hz, H33), 7.43 (2H, d, J = Hz, H28), 7.19 (2H, d, J = Hz, H20), 7.17 (2H, t, J = Hz, H29), 6.96 (2H, d, J = Hz, H19), 6.89 (2H, s, H11), 5.41 (2H, s, H17), 2.21 (3H, s, H13), 1.48 (6H, s, H14), 1.43 (9H, s, H23), 1.13 (9H, s, H37).**^{13}C NMR** (Acetone-D6, 100 MHz): δ 209.53 (C1), 160.16 (C27), 158.56 (C15), 158.11 (C7), 154.81 (C26), 154.41 (C28), 152.69 (C21), 151.51 (C35), 145.13 (C32), 135.28 (C30), 134.89 (C24), 134.72 (C9), 133.32 (C10), 131.82 (C18), 129.05 (C12), 128.96 (C11), 127.51 (C19), 127.24 (C34), 126.26 (C33), 126.12 (C20), 125.61 (C29), 123.34 (C31), 122.75 (C5), 122.46 (C3), 120.73 (C8), 119.23 (C25), 119.19 (C16), 113.22 (C6), 113.01 (C2), 53.97 (C17), 34.58 (C36), 34.17 (C22), 30.63 (C37), 30.44 (C23), 20.03 (C13), 15.74 (C14), unassigned (C4). **ESI-MS:** Found $[M\text{-}PF_6]^+$ 1020.2653, $C_{55}H_{53}BrN_9Ru$ requires $[M\text{-}PF_6]^+$ 1020.2651. Found $[M\text{-}PF_6\text{+}H]^{2+}$ 510.1321, $C_{55}H_{54}BrN_9Ru$ requires $[M\text{-}PF_6\text{+}H]^{2+}$ 510.1325. **UV-Vis** (CH_3CN) λ_{max}/nm (ε, 10^3 $M^{-1}cm^{-1}$): 527 (11.5), 489 (12.6), 361 (19.0), 315 (35.9), 285 (47.0), 232 (72.2). **Fluorometry** (Butyronitrile, 77K) λ_{max}: 655 nm.

4.9

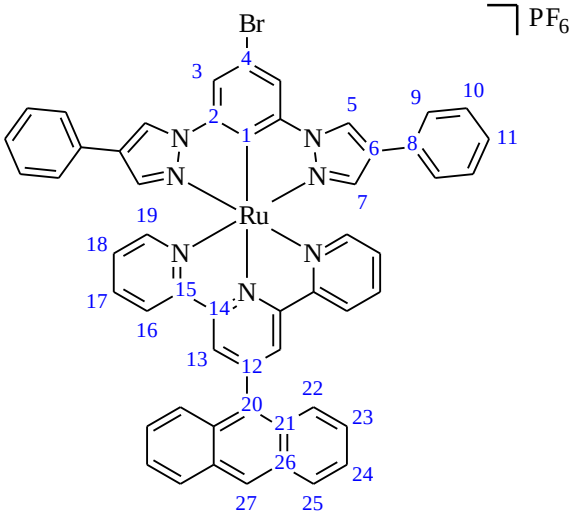

A mixture of Ru(**3.19**)Cl_3 (123 mg, 0.20 mmol), **4.41** (69 mg, 0.16 mmol), silver triflate (160 mg, 0.62 mmol) and Et_3N (3 drops) in EtOH/H_2O (3:1, 12 mL) was refluxed for 12 h. After cooling and filtering, the solvent was removed under reduced pressure. The solid was slowly dropped into an excess of $NH_4PF_{6(aq)}$. The fine precipitate was filtered, washed with water, rinsed with CH_3CN, dried over Na_2SO_4 and the solvent was removed in vacuo. The crude product was purified using column chromatography, eluting with 10% acetonitrile/ethyl acetate on silica to give the pure complex (146 mg, 83% yield).

^{1}H NMR (Acetone-D6, 400 MHz): δ 9.35 (2H, s, H5), 9.06 (2H, s, H13), 8.92 (1H, s, H27), 8.78 (2H, d, J = 7.9 Hz, H19), 8.35 (2H, d, J = 8.2 Hz, H25), 8.22 (2H, s, H3), 8.22 (2H, m, H22), 7.86 (2H, t, J = 7.9 Hz, H18), 7.69 (2H, t, J = 6.8 Hz, H24), 7.63 (2H, m, H16), 7.62 (2H, m, H23), 7.52 (2H, s, H7), 7.48 (2H, d, J = 7.9 Hz, H9), 7.32 (4H, t, J = 7.3 Hz, H10), 7.23 (2H, m, H11), 7.23 (2H, m, H17). **^{13}C NMR** (Acetone-D6, 100 MHz): δ 181.33 (C1), 144.08 (C2), 160.16 (C15), 155.35 (C14), 154.57 (C16), 145.58 (C12), 140.01 (C5), 135.78 (C18), 133.49 (C20), 131.62 (C21), 130.65 (C4), 130.03 (C26), 128.88 (C10), 128.74 (C25), 128.30 (C27), 127.19 (C11), 126.74 (C17), 126.73 (C23), 126.34 (C22), 125.78 (C8), 125.65 (C24), 125.17 (C9), 125.08 (C7), 124.75 (C13), 124.33 (C6), 123.74 (C19), 111.69 (C3). **ESI-MS:** Found $[M\text{-}PF_6]^+$ 950.1183, $C_{53}H_{35}BrN_7Ru$ requires $[M\text{-}PF_6]^+$ 950.1181. Found $[M\text{-}PF_6\text{+}H]^{2+}$ 475.0591, $C_{53}H_{36}BrN_7Ru$ requires $[M\text{-}PF_6\text{+}H]^{2+}$ 475.0590. **UV-Vis** (CH_3CN) λ_{max}/nm (ε, 10^3 $M^{-1}cm^{-1}$): 519 (7.6), 484 (10.5), 440 (7.9), 385 (15.6), 366 (16.2), 348 (13.1), 316 (32.9), 301 (36.8), 275 (60.8), 252 (108.3). **Fluorometry** (Butyronitrile, 77K) λ_{max}: 694 nm.

4.10

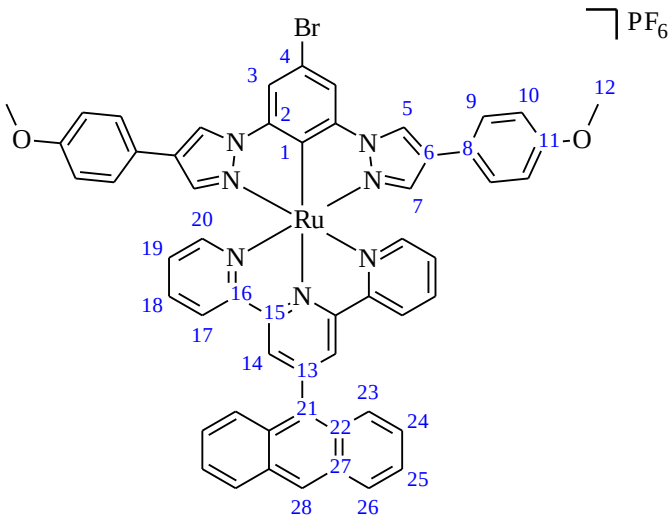

A mixture of Ru(**3.19**)Cl_3 (62 mg, 0.10 mmol), **4.42** (38 mg, 0.08 mmol), silver triflate (80 mg, 0.31 mmol) and Et_3N (3 drops) in EtOH/H_2O (3:1, 12 mL) was refluxed for 12 h. After cooling and filtering, the solvent was removed under reduced pressure. The solid was slowly dropped into an excess of $NH_4PF_{6(aq)}$. The fine precipitate was filtered, washed with water, rinsed with CH_3CN, dried over Na_2SO_4 and the solvent was removed in vacuo. The crude product was purified using column chromatography, eluting with 10% acetonitrile/ethyl acetate on silica to give the pure complex (83 mg, 89% yield).

^{1}H NMR (Acetone-D6, 400 MHz): δ 9.25 (2H, s, H5), 9.05 (2H, s, H14) 8.91 (2H, s, H28), 8.78 (2H, d, J = 7.8 Hz, H20), 8.33 (2H, d, J = 8.4 Hz, H23), 8.22 (2H, d, J = 8.7 Hz, H26), 8.18 (2H, s, H3), 7.85 (2H, t, J = 7.5 Hz, H19), 7.69 (2H, t, J = 7.6 Hz, H24), 7.61 (4H, m H17, H25), 7.44 (2H, s, H7), 7.40 (4H, m, H10), 7.23 (2H, t, 5.9 Hz, H18), 6.89 (4H, d, J = 8.4 Hz, H9), 3.76 (6H, s, H12). **^{13}C NMR** (Acetone-D6, 100 MHz): δ 181.14 (C1), 160.15 (C16), 159.10 (C11), 155.33 (C15), 154.61 (C17), 144.07 (C2), 139.69 (C7), 135.65 (C19), 133.50 (C13), 131.62 (C22), 130.03 (C27), 128.74 (C23), 128.25 (C28), 126.67 (C18), 126.49 (C25), 126.40 (C10), 126.22 (C26), 125.71 (C24), 124.75 (C14), 124.36 (C6), 124.24 (C5), 123.70 (C20), 123.08 (C8), 114.28 (C9), 111.84 (C21), 111.44 (C3), 54.66 (C12), unassigned (C4). **ESI-MS:** Found $[M\text{-}PF_6]^+$ 1010.1394, $C_{55}H_{39}BrN_7O_2Ru$ requires $[M\text{-}PF_6]^+$ 1010.1392. Found $[M\text{-}PF_6+H]^{2+}$ 505.0699, $C_{55}H_{40}BrN_7O_2Ru$ requires $[M\text{-}PF_6+H]^{2+}$ 505.0696. **UV-Vis** (CH_3CN) λ_{max}/nm (ε, 10^3 $M^{-1}cm^{-1}$): 519 (7.9), 486 (10.4), 434 (8.0), 385 (15.6), 366 (16.1), 348 (13.1), 316 (42.4), 275 (66.5), 252 (119.9). **Fluorometry** (Butyronitrile, 77K) λ_{max}: 694 nm.

4.11

A mixture of Ru(**3.13**)Cl_3 (56 mg, 0.10 mmol), **4.43** (44 mg, 0.08 mmol), silver triflate (80 mg, 0.31 mmol) and Et_3N (3 drops) in EtOH/H_2O (3:1, 12 mL) was refluxed for 12 h. After cooling and filtering, the solvent was removed under reduced pressure. The solid was slowly dropped into an excess of $NH_4PF_{6(aq)}$. The fine precipitate was filtered, washed with water, rinsed with CH_3CN, dried over Na_2SO_4 and the solvent was removed in vacuo. The crude product was purified using column chromatography, eluting with 10% acetonitrile/ethyl acetate on silica to give the pure complex (84 mg, 91% yield).

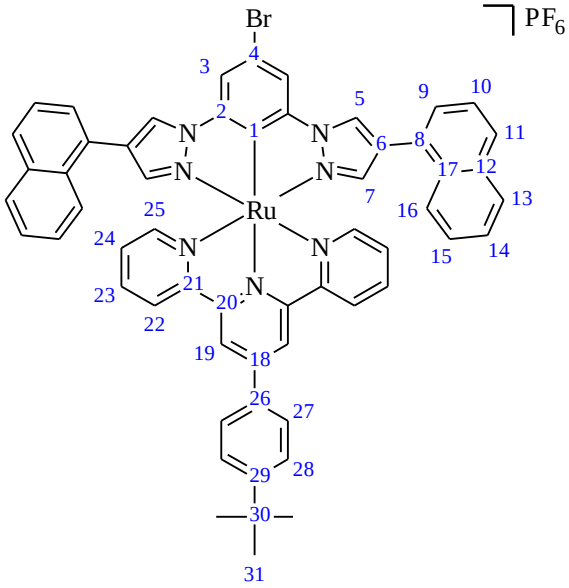

^{1}H NMR (Acetone-D6, 400 MHz): δ 9.25 (4H, m, H5, H19), 8.91 (2H, d, J = 7.7 Hz, H25), 8.31 (2H, s, H3), 8.20 (2H, d, J = 8.3 Hz, H28), 7.94 (2H, t, J = 8.0 Hz, H24), 7.87 (2H, m, H16), 7.85 (2H, m, H9), 7.81 (4H, m, H11, H13), 7.71 (2H, d, J = 8.3 Hz, H27), 7.66 (2H, d, J = 8.3 Hz, H22), 7.46 (2H, t, J = 7.3 Hz, H10), 7.37 (4H, t, J = 7.3 Hz, H14, H15), 7.28 (4H, m, H7, H23), 1.42 (9H, s, H31). **^{13}C NMR** (Acetone-D6, 100 MHz): δ 181.34 (C1), 160.28 (C21), 155.30 (C20), 154.66 (C22), 152.79 (C29), 145.55 (C26), 144.36 (C2), 142.25 (C7), 135.75 (C24), 135.49 (C4), 134.85 (C18), 133.95 (C12), 130.84 (C8), 128.48 (C16), 128.01 (C11), 128.01 (C13), 127.90 (C5), 127.28 (C28), 126.94 (C17), 126.58 (C23), 126.43 (C27), 126.25 (C15), 125.93 (C10), 125.36 (C14), 124.64 (C9), 123.68 (C25), 122.44 (C6), 119.64 (C19), 111.90 (C3), 34.48 (C30), 30.65 (C31). **ESI-MS:** Found $[M\text{-}PF_6]^+$ 1006.1809, $C_{57}H_{43}BrN_7Ru$ requires $[M\text{-}PF_6]^+$ 1006.1807. Found $[M\text{-}PF_6\text{+}H]^{2+}$ 503.0905, $C_{57}H_{44}BrN_7Ru$ requires $[M\text{-}PF_6\text{+}H]^{2+}$ 503.0903. **UV-Vis** (CH_3CN) λ_{max}/nm (ε, 10^3 $M^{-1}cm^{-1}$): 520 (7.4), 490 (8.6), 362 (13.1), 303 (43.4), 286 (49.5), 223 (96.2). **Fluorometry** (Butyronitrile, 77K) λ_{max}: 699 nm.

4.12

A mixture Ru(**3.19**)Cl_3 (62 mg, 0.10 mmol), **4.43**, 0.08 mmol), silver triflate (80 mg, 0.31 mmol) and Et_3N (3 drops) in EtOH/H_2O (3:1, 12 mL) was refluxed for 12 h. After cooling and filtering, the solvent was removed under reduced pressure. The solid was slowly dropped into an excess of $NH_4PF_{6(aq)}$. The fine precipitate was filtered, washed with water, rinsed with CH_3CN, dried over Na_2SO_4 and the solvent was removed in vacuo. The crude product was purified using column chromatography, eluting with 10% acetonitrile/ethyl acetate on silica to give the pure complex (83 mg, 87% yield).

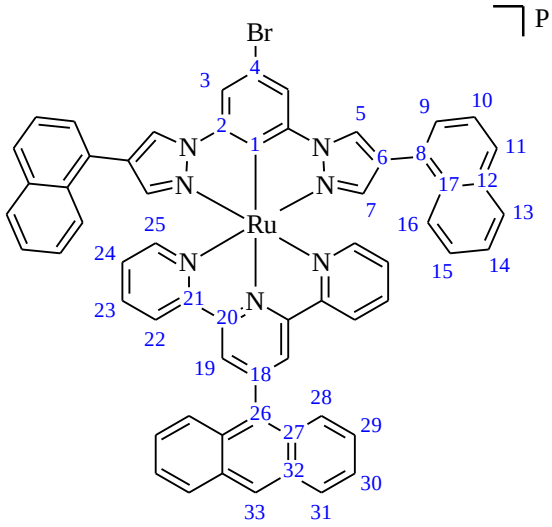

^{1}H NMR (Acetone-D6, 400 MHz): δ 9.30 (2H, s, H5), 9.01 (2H, s, H19), 8.83 (1H, s, H33), 8.77 (2H, d, J = 8.1 Hz, H25), 8.34 (2H, s, H3), 8.25 (2H, d, J = 8.7 Hz, H31), 8.08 (2H, d, J = 8.7 Hz, H28), 7.94 (2H, d, J = 8.2 Hz, H16), 7.89 (2H, m, H11), 7.89 (2H, m , H13), 7.89 (2H, m, H24), 7.74 (2H, d, J = 5.5 Hz, H22), 7.59 (2H, t, J = 6.8 Hz, H30), 7.51 (2H, t, J = 7.2 Hz, H15), 7.45 (2H, t, J = 7.8 Hz, H9), 7.42 (2H, s, H7), 7.38-7.44 (4H, m, H14, H29), 7.35 (2H, m, H10), 7.31 (2H, t, J = 6.2 Hz, H23). **^{13}C NMR** (Acetone-D6, 100 MHz): δ 209.25 (C1), 160.24 (C21), 155.37 (C20), 154.54 (C22), 144.11 (C2), 142.33 (C7), 135.89 (C4), 135.64 (C24), 134.00 (C12), 133.44 (C18), 131.54 (C27), 131.01 (C8), 129.96 (C32), 128.65 (C26), 128.62 (C31), 128.45 (C16), 128.09 (C11), 128.09 (C13), 127.99 (C33), 127.86 (C5), 127.20 (C17), 126.87 (C10), 126.69 (C23), 126.34 (C29), 126.19 (C14), 126.10 (C28), 125.86 (C15), 125.60 (C30), 125.45 (C9), 124.57 (C19), 123.69 (C25), 122.40 (C6), 111.89 (C3). **ESI-MS:** Found $[M\text{-}PF_6]^+$ 1050.1490, $C_{61}H_{39}BrN_7Ru$ requires $[M\text{-}PF_6]^+$ 1050.1494. Found $[M\text{-}PF_6\text{+}H]^{2+}$ 525.5786, $C_{61}H_{40}BrN_7Ru$ requires $[M\text{-}PF_6\text{+}H]^{2+}$ 525.5786. **UV-Vis** (CH_3CN) λ_{max}/nm (ε, 10^3 $M^{-1}cm^{-1}$): 519 (7.0), 485 (9.3), 438 (7.0), 385 (14.4), 366 (15.6), 348 (14.4), 315 (39.9), 284 (44.5), 276 (45.0), 252 (103.5), 223 (112.1). **Fluorometry** (Butyronitrile, 77K) λ_{max}: 692 nm.

APPENDIX

7.1 Crystallography tables.

Complex	**2.1**	**2.2**	**2.5a**
Identification code	5RBC10	5RBC7	5rbc8
Empirical formula	$C_{119}H_{99}F_{24}N_{30}O_4P_4Ru_4$	$C_{63}H_{38}Br_2F_6N_{14}O_6Ru_2S_2$	$C_{36}H_{29}F_6N_8OPRu$
Formula weight	2997.44	1627.15	835.71
Temperature (K)	120 (1)	120 (1)	120 (1)
Crystal system	monoclinic	triclinic	monoclinic
Space group	$P2_1/n$	P-1	$P2_1/c$
a (Å)	19.8933(5)	9.0141(5)	9.08460(9)
b (Å)	14.8060(4)	12.2561(8)	16.10495(16)
c (Å)	20.2343(5)	14.6759(7)	23.1412(2)
α (°)	90	84.642(5)	90
β (°)	89.995(2)	75.453(4)	92.9712(8)
γ (°)	90	88.351(5)	90
Volume ($Å^3$)	5959.8(3)	1562.49(15)	3381.17(6)
Z	2	1	4
Density (calculated) mg/m^3	1.670	1.729	1.642
μ (mm^{-1})	0.657	6.75	4.887
F (000)	3014	806	1688
Crystal size (mm^3)	0.73 × 0.17 × 0.11	0.38 × 0.16 × 0.05	0.27 × 0.15 × 0.08
Radiation	MoKα (λ = 0.71073)	CuKα (λ = 1.54184)	CuKα (λ = 1.54184)
2θ range for data collection (°)	5.29 to 55	6.246 to 150	6.69 to 150
Reflections collected	54390	10973	62727
Independent reflections [R(int)]	13645 [0.0416]	6234 [0.0347]	6883 [0.0377]
Data/restraints/parameters	13645/0/972	6234/0/442	6883/0/480
Goodness-of-fit on F^2	1.286	1.032	1.069
Final R indexes [I > 2σ (I)]	R_1 = 0.1272, wR_2 = 0.2504	R_1 = 0.0376, wR_2 = 0.0997	R_1 = 0.0344, wR_2 = 0.0887
Final R indexes [all data]	R_1 = 0.1552, wR_2 = 0.2610	R_1 = 0.0437, wR_2 = 0.1051	R_1 = 0.0365, wR_2 = 0.0906
Largest diff. peak/hole / (e. $Å^{-3}$)	0.97/-1.12	1.19/-0.83	1.06/-0.89
Flack parameter	-	-	

Table 7.1.1: Crystal data and X-ray experimental data for complexes **2.1**, **2.2** and **2.7**.

Complex	**2.7**	**2.9**
Identification code	5rbc6	exp_2918
Empirical formula	$C_{37}H_{26}F_6N_7PRu$	$C_{34}H_{30}F_3N_7O_4RuS$
Formula weight	814.69	790.78
Temperature (K)	120(1)	120(1)
Crystal system	orthorhombic	monoclinic
Space group	$P2_12_12_1$	$P2_1/c$
a (Å)	12.6312(4)	19.4504(16)
b (Å)	12.6200(3)	13.6775(7)
c (Å)	20.5233(6)	13.4220(10)
α (°)	90	90
β (°)	90	103.293(9)
γ (°)	90	90
Volume ($Å^3$)	3271.53(17)	3475.0(5)
Z	4	4
Density (calculated) mg/m^3	1.654	1.511
μ (mm^{-1})	0.604	4.773
F (000)	1640	1608
Crystal size (mm^3)	0.48 × 0.32 × 0.26	0.59 × 0.26 × 0.05
Radiation	MoKα (λ = 0.71073)	CuKα (λ = 1.54184)
2θ range for data collection (°)	6.048 to 66.374	7.974 to 150
Reflections collected	24718	13642
Independent reflections [R(int)]	10646 [0.0243]	6839 [0.0503]
Data/restraints/parameters	10646/0/469	6839/0/454
Goodness-of-fit on F^2	1.035	1.168
Final R indexes [I > 2σ (I)]	R1 = 0.0432, wR2 = 0.1071	R_1 = 0.0797, wR_2 = 0.1841
Final R indexes [all data]	R1 = 0.0500, wR2 = 0.1126	R_1 = 0.1086, wR_2 = 0.2018
Largest diff. peak/hole / (e. $Å^{-3}$)	1.41/-1.03	1.92/-2.05
Flack parameter	-0.011(9)	-

Table 7.1.2: Crystal data and X-ray experimental data for complexes **2.5a** and **2.9**.

Complex	**3.5**	**3.6**	**3.8**
Identification code	5rbc12	55rbc14	5rbc13
Empirical formula	$C_{34}H_{19}ClF_6N_7PRu$	$C_{43}H_{31}BrF_6N_7OPRu$	$C_{40}H_{32}F_6N_7OPRu$
Formula weight	807.05	987.7	872.76
Temperature (K)	120(1)	286(1)	286(1)
Crystal system	orthorhombic	monoclinic	orthorhombic
Space group	*P*nna	*C*2/c	*P*bca
a (Å)	17.8855(8)	21.7970(11)	14.3712(3)
b (Å)	20.8050(8)	22.2996(9)	20.3973(6)
c (Å)	9.2562(3)	16.8369(7)	25.3035(7)
α (°)	90	90	90
β (°)	90	91.750(4)	90
γ (°)	90	90	90
Volume ($Å^3$)	3444.3(2)	8180.0(6)	7417.3(3)
Z	4	8	8
Density (calculated) mg/m^3	1.556	1.604	1.563
μ (mm^{-1})	0.648	5.239	0.54
F (000)	1608	3952	3536
Crystal size (mm^3)	0.46 × 0.46 × 0.09	0.39 × 0.03 × 0.03	0.45 × 0.14 × 0.08
Radiation	MoKα (λ = 0.71073)	CuKα (λ = 1.54184)	MoKα (λ = 0.71073)
2θ range for data collection (°)	5.328 to 76	5.672 to 135	5.67 to 60
Reflections collected	45108	20744	27752
Independent reflections [R(int)]	9025 [0.0363]	7304 [0.1541]	10627 [0.0377]
Data/restraints/parameters	9025/0/243	7304/0/573	10627/0/611
Goodness-of-fit on F^2	1.084	1.029	1.062
Final R indexes [I > 2σ (I)]	R_1 = 0.0461, wR_2 = 0.1085	R1 = 0.0816, wR2 = 0.2174	R_1 = 0.0442, wR_2 = 0.0956
Final R indexes [all data]	R_1 = 0.0782, wR_2 = 0.1284	R1 = 0.1252, wR2 = 0.2511	R_1 = 0.0658, wR_2 = 0.1074
Largest diff. peak/hole / (e. $Å^{-3}$)	1.55/-0.88	1.64/-1.65	0.88/-1.06

Table 7.1.3: Crystal data and X-ray experimental data for complexes **3.5**, **3.6** and **3.8**.

Complex	**4.1**	**4.44**
Identification code	5rbc11	exp_1546
Empirical formula	$C_{47}H_{45.35}BrF_6N_9PRu$	$C_{46}H_{37}BrF_6N_9PRu$
Formula weight	1062.22	1041.80
Temperature (K)	120(1)	287(1)
Crystal system	monoclinic	monoclinic
Space group	$P2_1/n$	$P2_1/n$
a (Å)	14.6201(6)	11.3846(3)
b (Å)	22.1871(7)	13.3166(4)
c (Å)	19.5238(8)	28.3254(11)
α (°)	90	90
β (°)	93.756(4)	98.466(3)
γ (°)	90	90
Volume ($Å^3$)	6319.5(4)	4247.5(2)
Z	4	4
Density (calculated) mg/m^3	1.116	1.629
μ (mm^{-1})	3.417	5.075
F (000)	2153.0	2101.1
Crystal size (mm^3)	0.14 × 0.08 × 0.06	0.22 × 0.02 × 0.02
Radiation	CuKα (λ = 1.54184)	Cu Kα (λ = 1.54184)
2θ range for data collection (°)	6.038 to 155	6.3 to 150
Reflections collected	40234	15952
Independent reflections [R(int)]	13157 [0.0827]	8314 [0.0712]
Data/restraints/parameters	13157/0/638	8314/0/576
Goodness-of-fit on F^2	0.949	1.058
Final R indexes [I > 2σ (I)]	R_1 = 0.0718, wR_2 = 0.1924	R_1 = 0.1087, wR_2 = 0.2916
Final R indexes [all data]	R_1 = 0.1012, wR_2 = 0.2123	R_1 = 0.1381, wR_2 = 0.3210
Largest diff. peak/hole / (e. $Å^{-3}$)	1.08/-1.95	3.09/-3.55

Table 7.1.4: Crystal data and X-ray experimental data for complexes **4.44** and **4.1**.

7.2 DFT calculation coordinates.

2.1

Atom	X	Y	Z	Atom	X	Y	Z
C	-0.098430	-4.416120	-0.000140	N	0.421073	-2.049080	0.000347
C	-0.481920	-3.069280	0.000153	Ru	0.002003	-0.000003	0.000167
C	1.778060	-2.357650	0.000376	C	0.163664	-0.000230	3.260332
C	2.212266	-3.695400	0.000147	C	-0.788480	-0.000830	4.313091
C	1.272808	-4.737650	-0.000160	H	1.241419	0.000147	3.320688
H	-0.859400	-5.189230	-0.000370	C	-2.040830	-0.001080	3.692172
H	-1.525310	-2.778000	0.000307	H	-0.590990	-0.001080	5.373293
H	3.273440	-3.919590	0.000195	H	-3.032560	-0.001560	4.116857
H	1.600411	-5.772560	-0.000400	C	-2.710710	-0.001050	1.204301
C	2.694195	-1.198850	0.000502	C	-4.115690	-0.001290	1.235476
C	4.100638	-1.220380	0.000667	C	-4.803440	-0.001580	-0.000530
C	4.800618	0.002903	0.000669	H	-4.677720	-0.001200	2.165673
H	4.645778	-2.157820	0.000826	C	-2.710370	-0.001390	-1.204790
C	2.692718	1.202094	0.000285	C	-4.115330	-0.001650	-1.236350
C	4.099126	1.225333	0.000454	H	-4.677140	-0.001860	-2.166680
H	5.885965	0.003578	0.000830	C	-2.039610	-0.001910	-3.692460
H	4.643144	2.163422	0.000453	C	-0.787020	-0.001830	-4.312930
C	1.775147	2.359742	-0.000061	H	-3.031190	-0.002380	-4.117510
C	2.207654	3.698016	-0.000440	C	0.164739	-0.001080	-3.259820
C	1.266900	4.739109	-0.000920	H	-0.589180	-0.002240	-5.373060
H	3.268544	3.923563	-0.000360	H	1.242519	-0.000770	-3.319750
C	-0.485740	3.068554	-0.000520	N	-0.454510	-0.000650	-2.055560
C	-0.103920	4.415875	-0.000960	N	-0.455160	-0.000040	2.055851
H	1.593238	5.774412	-0.001260	C	-1.989210	-0.001040	-0.000140
H	-1.528760	2.775962	-0.000420	N	-1.836130	-0.000620	2.337232
H	-0.865860	5.188032	-0.001330	N	-1.835440	-0.001260	-2.337460
N	0.418494	2.049461	-0.000110	H	-5.889460	-0.001740	-0.000700
N	2.032816	0.001204	0.000392				

2.2

Atom	X	Y	Z	Atom	X	Y	Z
C	0.647240	-4.417520	-0.000550	N	1.166520	-2.050340	-0.000130
C	0.263772	-3.070570	-0.000290	Ru	0.747532	0.000009	0.000042
C	2.523384	-2.358760	-0.000200	C	0.905553	-0.000590	3.261773
C	2.957757	-3.696340	-0.000460	C	-0.048380	-0.000900	4.313645
C	2.018366	-4.738810	-0.000660	H	1.983187	-0.000550	3.324346
H	-0.113750	-5.190590	-0.000670	C	-1.299600	-0.000740	3.692102
H	-0.779840	-2.780250	-0.000170	H	0.147934	-0.001170	5.374042
H	4.018889	-3.920590	-0.000520	H	-2.291520	-0.000880	4.116535
H	2.346087	-5.773650	-0.000890	C	-1.963560	-0.000250	1.203465
C	3.439841	-1.199910	-0.000026	C	-3.368520	-0.000220	1.240291
C	4.846311	-1.222280	0.000121	C	-4.042400	-0.000140	0.000037
C	5.546783	0.000650	0.000314	H	-3.931850	-0.000270	2.168101
H	5.391069	-2.159890	0.000121	C	-1.963550	-0.000056	-1.203370
C	3.439519	1.200651	0.000145	C	-3.368510	-0.000024	-1.240210
C	4.845979	1.223389	0.000307	H	-3.931840	0.000066	-2.168030

H	6.632120	0.000801	0.000463	C	-1.299640	-0.000033	-3.692010
H	5.390490	2.161147	0.000462	C	-0.048430	-0.000067	-4.313580
C	2.522749	2.359242	0.000122	H	-2.291560	-0.000062	-4.116440
C	2.956748	3.696936	0.000013	C	0.905525	-0.000007	-3.261720
C	2.017074	4.739150	-0.000055	H	0.147856	-0.000120	-5.373980
H	4.017819	3.921485	-0.000029	H	1.983158	0.000014	-3.324320
C	0.262938	3.070436	0.000146	N	0.289667	0.000079	-2.056400
C	0.646040	4.417494	0.000032	N	0.289662	-0.000260	2.056469
H	2.344523	5.774078	-0.000160	Br	-6.005960	-0.000083	0.000031
H	-0.780590	2.779833	0.000251	C	-1.241040	-0.000150	0.000047
H	-0.115160	5.190348	0.000009	N	-1.092850	-0.000350	2.336749
N	1.165955	2.050442	0.000163	N	-1.092860	0.000044	-2.336670
N	2.779436	0.000278	0.000028				

2.3

Atom	X	Y	Z	Atom	X	Y	Z
C	1.885318	-4.405570	0.354772	H	-2.722060	0.131671	2.154342
C	1.498271	-3.069490	0.249864	C	-0.764830	-0.117790	-1.22192
C	3.762003	-2.339220	0.190444	C	-2.157090	-0.122040	-1.24781
C	4.195134	-3.678280	0.295506	H	-2.709580	-0.164920	-2.18079
C	3.266301	-4.719680	0.377529	C	-0.094750	-0.303620	-3.70006
H	1.128223	-5.179630	0.417496	C	1.155095	-0.343260	-4.3141
H	0.451483	-2.792480	0.231057	H	-1.085120	-0.340360	-4.12685
H	5.258226	-3.892560	0.312060	C	2.109328	-0.258390	-3.25921
H	3.598938	-5.749840	0.457915	H	1.356797	-0.421940	-5.37048
C	4.660323	-1.184870	0.101079	H	3.187197	-0.257140	-3.31753
C	6.060608	-1.199080	0.106984	N	1.496191	-0.169830	-2.063
C	6.756280	0.034107	0.013256	N	1.483818	0.163041	2.059576
H	6.612762	-2.129590	0.182362	C	-0.037450	-0.012740	-0.00576
C	4.639159	1.225647	-0.087530	N	0.093985	0.179185	2.332816
C	6.047378	1.247333	-0.083840	N	0.108041	-0.198810	-2.34383
H	7.841591	0.041936	0.016530	C	-4.355920	-0.018250	-0.01768
H	6.588643	2.184924	-0.155590	C	-5.093740	-0.679550	-1.03177
C	3.733799	2.357342	-0.180560	C	-5.100060	0.644482	0.995965
C	4.145863	3.709683	-0.283070	C	-6.496050	-0.682890	-1.03167
C	3.205121	4.734092	-0.369340	H	-4.573580	-1.233450	-1.80903
H	5.205815	3.941217	-0.293780	C	-6.497700	0.644015	0.98639
C	1.454032	3.061583	-0.252550	H	-4.583780	1.199178	1.775026
C	1.821912	4.401597	-0.354460	C	-7.238970	-0.021430	-0.02559
H	3.523710	5.768963	-0.447370	H	-7.011430	-1.216240	-1.82242
H	0.410266	2.771963	-0.239730	H	-7.021670	1.178286	1.773601
H	1.055381	5.165680	-0.421000	C	-8.781220	0.001494	0.004617
N	2.362152	2.044032	-0.164620	C	-9.273560	1.478866	-0.06646
N	3.988445	0.008956	0.005044	H	-10.370100	1.508442	-0.03643
N	2.395991	-2.041630	0.166485	H	-8.901230	2.077186	0.773791
Ru	1.889743	-0.002410	-0.000610	H	-8.944230	1.959564	-0.99648
C	2.089589	0.257979	3.259064	C	-9.277190	-0.643360	1.33456
C	1.128835	0.334882	4.308641	H	-10.373700	-0.622820	1.373184
H	3.167073	0.268309	3.323325	H	-8.952420	-1.688820	1.411199
C	-0.117210	0.283333	3.687811	H	-8.903100	-0.106940	2.214832

H	1.324041	0.416877	5.365985	C	-9.406530	-0.777940	-1.17847
H	-1.110210	0.311780	4.109071	H	-9.119050	-0.351460	-2.14835
C	-0.771970	0.090011	1.206246	H	-9.122860	-1.838410	-1.16609
C	-2.164390	0.088986	1.224434	H	-10.499900	-0.729990	-1.11023
C	-2.878250	-0.017660	-0.013680				

2.4

Atom	X	Y	Z	Atom	X	Y	Z
C	-1.544940	4.425416	0.327786	C	2.625489	-0.094550	1.242104
C	-1.122810	3.103888	0.193839	C	3.335462	0.020012	0.010963
C	-3.368650	2.302092	0.200834	H	3.193199	-0.171150	2.164964
C	-3.834930	3.631179	0.334245	C	1.239534	0.125006	-1.21428
C	-2.936640	4.696586	0.398581	C	2.637467	0.131351	-1.22725
H	-0.810300	5.221665	0.375079	H	3.213993	0.209412	-2.14451
H	-0.069030	2.860169	0.136640	C	0.592644	0.340096	-3.69477
H	-4.902750	3.815483	0.386983	C	-0.651070	0.390221	-4.32156
H	-3.297120	5.715346	0.501505	H	1.587550	0.379301	-4.11057
C	-4.230240	1.128572	0.123997	C	-1.615960	0.295573	-3.27783
C	-5.633060	1.092971	0.153785	H	-0.841030	0.481479	-5.37912
C	-6.291710	-0.155050	0.063904	H	-2.693190	0.297830	-3.34637
H	-6.212800	2.005595	0.243884	N	-1.013820	0.192809	-2.07636
C	-4.143920	-1.279620	-0.082460	N	-1.033460	-0.180660	2.055785
C	-5.545380	-1.350120	-0.055800	C	0.510626	0.015654	-0.00315
H	-7.375880	-0.195800	0.085538	N	0.353580	-0.193940	2.334793
H	-6.057910	-2.303750	-0.126380	N	0.375548	0.221496	-2.34196
C	-3.199200	-2.383430	-0.202280	C	4.836378	0.024300	0.018949
C	-3.566460	-3.746220	-0.299770	C	5.548658	-1.191600	0.20006
C	-2.592290	-4.738310	-0.413970	C	5.543289	1.247165	-0.15192
H	-4.617560	-4.014360	-0.284220	C	6.958556	-1.163820	0.202382
C	-0.901090	-3.005390	-0.336550	C	6.950828	1.230118	-0.13336
C	-1.224770	-4.357650	-0.432930	C	7.680003	0.034606	0.037385
H	-2.876590	-5.783370	-0.487660	H	7.502382	-2.096900	0.334072
H	0.131531	-2.678770	-0.350050	H	7.489908	2.168194	-0.25218
H	-0.433770	-5.094140	-0.521440	C	4.827436	-2.519230	0.372559
N	-1.843780	-2.021540	-0.222320	H	4.244751	-2.551160	1.303273
N	-3.526190	-0.051060	0.010540	H	4.127567	-2.711750	-0.45183
N	-1.990500	2.049199	0.127211	H	5.542275	-3.347760	0.403498
Ru	-1.425990	0.023904	-0.013430	C	4.813057	2.569239	-0.32906
C	-1.646110	-0.286640	3.251589	H	4.238117	2.597463	-1.26467
C	-0.690360	-0.369710	4.304695	H	4.104588	2.755432	0.489461
H	-2.723870	-0.299590	3.309751	H	5.521652	3.403389	-0.35314
C	0.558779	-0.309210	3.689746	C	9.196974	0.043431	0.02952
H	-0.889580	-0.461020	5.360543	H	9.595504	0.846535	0.661966
H	1.549969	-0.338770	4.115125	H	9.607291	-0.905890	0.390429
C	1.227703	-0.093040	1.215308	H	9.585163	0.207756	-0.98538

2.5

Atom	X	Y	Z	Atom	X	Y	Z
C	-1.477210	4.387629	-0.473450	H	1.474272	0.489950	4.133524
C	-1.066960	3.056621	-0.328540	C	1.203432	0.182620	1.230722

C	-3.312390	2.301719	-0.275050	C	2.604656	0.206200	1.284609
C	-3.773060	3.622791	-0.419460	C	3.343732	0.089009	0.074263
C	-2.854550	4.678820	-0.519320	H	3.139669	0.281044	2.22716
H	-0.731700	5.172159	-0.548170	C	1.248200	-0.077330	-1.15344
H	-0.018240	2.788106	-0.289840	C	2.650463	-0.051410	-1.16032
H	-4.838430	3.823275	-0.453490	H	3.219297	-0.106570	-2.08427
H	-3.202500	5.701033	-0.630500	C	0.627558	-0.343640	-3.64117
C	-4.205320	1.130216	-0.164210	C	-0.612100	-0.433410	-4.28134
C	-5.611800	1.121821	-0.182000	H	1.627390	-0.364040	-4.04584
C	-6.287130	-0.109580	-0.063380	C	-1.584490	-0.347090	-3.25104
H	-6.175210	2.042624	-0.285220	H	-0.788640	-0.544490	-5.33942
C	-4.155930	-1.257630	0.083850	H	-2.660700	-0.375970	-3.32911
C	-5.561440	-1.310420	0.070724	N	-0.989710	-0.211590	-2.04219
H	-7.372170	-0.133260	-0.075060	N	-1.066240	0.222864	2.044909
H	-6.086630	-2.254740	0.162509	C	0.499403	0.039599	0.02641
C	-3.215100	-2.388890	0.214239	N	0.309713	0.281112	2.345711
C	-3.619750	-3.729620	0.343882	N	0.396611	-0.210590	-2.29747
C	-2.657830	-4.744170	0.462975	C	4.832921	0.109304	0.101186
H	-4.675630	-3.977620	0.351559	C	5.539065	0.927620	1.021189
C	-0.940100	-3.043730	0.319596	C	5.594520	-0.685250	-0.78386
C	-1.294050	-4.392230	0.450679	C	6.936250	0.948467	1.055482
H	-2.962750	-5.781150	0.563176	H	4.990399	1.578749	1.697468
H	0.096058	-2.728010	0.306609	C	7.000575	-0.675240	-0.76579
H	-0.516510	-5.143280	0.541158	H	5.090242	-1.350570	-1.48108
N	-1.865150	-2.050550	0.201691	C	7.678083	0.145612	0.160525
N	-3.520110	-0.049280	-0.032830	H	7.476118	1.581941	1.752307
N	-1.949530	2.023521	-0.228710	H	7.546891	-1.309360	-1.45651
Ru	-1.490400	-0.004090	-0.006110	O	9.060092	0.238989	0.275504
C	-1.705850	0.334178	3.233099	C	9.900294	-0.552650	-0.61691
C	-0.772610	0.462952	4.294675	H	10.925990	-0.302700	-0.34105
H	-2.784330	0.318014	3.275142	H	9.729281	-1.627990	-0.47106
C	0.490240	0.425415	3.695994	H	9.723818	-0.285320	-1.66775
H	-0.988410	0.568106	5.346049				

2.6

Atom	X	Y	Z	Atom	X	Y	Z
C	1.889511	-4.274010	-1.060020	C	-1.042000	-0.610220	1.315051
C	1.377652	-3.019470	-0.706350	C	-2.431260	-0.787410	1.413039
C	3.548686	-2.070840	-0.669550	C	-3.232390	-0.581510	0.257863
C	4.109870	-3.310850	-1.023920	H	-2.915690	-1.061240	2.34635
C	3.280425	-4.425130	-1.222320	C	-1.229670	-0.039880	-1.00955
H	1.210655	-5.107860	-1.203800	C	-2.621860	-0.204100	-0.96953
H	0.314953	-2.858610	-0.571570	H	-3.243120	-0.076740	-1.85145
H	5.183831	-3.404300	-1.143310	C	-0.760010	0.619061	-3.4571
H	3.706404	-5.385290	-1.496100	C	0.433145	0.915498	-4.12257
C	4.343650	-0.846980	-0.440700	H	-1.776340	0.596953	-3.81857
C	5.739904	-0.703840	-0.533360	C	1.459085	0.785933	-3.15022
C	6.314109	0.556964	-0.274130	H	0.546000	1.186716	-5.16021
H	6.371939	-1.544060	-0.798990	H	2.522971	0.930829	-3.26122
C	4.107526	1.467526	0.153443	N	0.939622	0.429943	-1.95177

C	5.499367	1.653865	0.071529	N	1.260284	-0.544420	2.029265
H	7.389923	0.683944	-0.341240	C	-0.416810	-0.235600	0.117364
H	5.946685	2.621747	0.269192	N	-0.088390	-0.773070	2.370766
C	3.084518	2.475742	0.498583	N	-0.451650	0.328495	-2.15415
C	3.382860	3.813937	0.812283	C	-4.707810	-0.823040	0.332052
C	2.348806	4.706365	1.133605	C	-5.675680	0.168620	-0.08186
H	4.412694	4.154233	0.806180	C	-5.158820	-2.058150	0.803094
C	0.774027	2.895037	0.814050	C	-5.315220	1.491669	-0.49999
C	1.021243	4.235714	1.134005	C	-7.080050	-0.167490	-0.03684
H	2.571426	5.740375	1.377728	C	-6.544970	-2.376860	0.862057
H	-0.231080	2.491360	0.802591	H	-4.432590	-2.810600	1.101282
H	0.190683	4.889882	1.377070	C	-6.280040	2.414242	-0.88509
N	1.769666	2.019528	0.500953	H	-4.270110	1.784534	-0.49319
N	3.570932	0.233115	-0.103100	C	-8.049530	0.800732	-0.44994
N	2.173100	-1.930930	-0.511190	C	-7.487890	-1.453280	0.436746
Ru	1.557060	-0.002830	0.014376	H	-6.853910	-3.353130	1.225535
C	1.966131	-0.754730	3.165280	C	-7.662980	2.064381	-0.87262
C	1.102488	-1.112920	4.233243	H	-5.984650	3.414906	-1.19096
H	3.039781	-0.643340	3.167746	H	-9.102700	0.530221	-0.41824
C	-0.187360	-1.113890	3.693973	H	-8.548430	-1.693050	0.462883
H	1.379419	-1.338220	5.250868	H	-8.407300	2.793550	-1.18131
H	-1.138910	-1.327820	4.155256				

2.7

Atom	X	Y	Z	Atom	X	Y	Z
C	-1.407920	4.326129	0.868054	C	0.906954	-0.390510	1.291556
C	-1.094800	2.984296	0.618300	C	2.303609	-0.478260	1.383822
C	-3.385400	2.424661	0.386368	C	3.084940	-0.278040	0.212109
C	-3.749460	3.760783	0.632150	H	2.804161	-0.664140	2.329943
C	-2.758960	4.724204	0.876061	C	1.040250	0.080249	-1.05776
H	-0.609020	5.036757	1.051383	C	2.439853	-0.000075	-1.02489
H	-0.069340	2.635614	0.602375	H	3.042160	0.116453	-1.92149
H	-4.796260	4.044753	0.632860	C	0.511359	0.590053	-3.52884
H	-3.032320	5.757227	1.067020	C	-0.702740	0.785469	-4.19379
C	-4.358940	1.346269	0.119744	H	1.523786	0.607579	-3.90116
C	-5.760480	1.452599	0.065555	C	-1.710620	0.645013	-3.20424
C	-6.521160	0.297537	-0.205930	H	-0.840460	0.998669	-5.24193
H	-6.256140	2.403165	0.228930	H	-2.782060	0.723010	-3.30955
C	-4.480480	-1.004060	-0.355570	N	-1.160820	0.377776	-1.99633
C	-5.884300	-0.941590	-0.418960	N	-1.388460	-0.415510	2.030211
H	-7.603640	0.362591	-0.250820	C	0.249393	-0.111230	0.084764
H	-6.474620	-1.827110	-0.627120	N	-0.026180	-0.554240	2.365593
C	-3.624520	-2.192730	-0.546600	N	0.232187	0.345974	-2.20994
C	-4.124570	-3.475940	-0.832110	C	4.572353	-0.352350	0.283555
C	-3.240040	-4.552050	-1.000370	C	5.378434	0.496564	-0.47656
H	-5.194100	-3.632090	-0.922080	C	5.209134	-1.306970	1.147546
C	-1.406270	-3.024230	-0.592880	C	6.803915	0.434372	-0.41711
C	-1.856310	-4.319180	-0.878470	H	4.923926	1.253131	-1.11343
H	-3.618600	-5.545180	-1.221080	C	6.589872	-1.389850	1.229333
H	-0.351170	-2.800920	-0.491830	H	4.595866	-1.996600	1.722154

H	-1.136040	-5.120990	-1.001570	C	7.633611	1.306398	-1.19168
N	-2.255660	-1.972020	-0.426750	C	7.428278	-0.527590	0.455126
N	-3.760950	0.131493	-0.090300	H	7.053067	-2.127100	1.881517
N	-2.047940	2.040003	0.381336	C	9.017660	1.225025	-1.11012
Ru	-1.735000	0.008607	-0.003400	H	7.165441	2.036884	-1.84833
C	-2.070950	-0.607880	3.183450	C	8.855092	-0.589930	0.518111
C	-1.178980	-0.867230	4.256638	C	9.635052	0.267413	-0.24781
H	-3.148970	-0.554200	3.193641	H	9.640699	1.890402	-1.70209
C	0.103709	-0.824920	3.702265	H	9.323536	-1.318480	1.176302
H	-1.433500	-1.057590	5.287165	H	10.719350	0.215756	-0.19499
H	1.069606	-0.965110	4.161974				

2.8							
Atom	X	Y	Z	Atom	X	Y	Z
C	2.839860	-3.941720	-1.954740	C	-0.316490	0.138952	-0.85374
C	2.342224	-2.798800	-1.325640	C	-1.691000	-0.059250	-0.75481
C	4.506470	-1.832270	-1.210230	H	-2.367390	0.212318	-1.5589
C	5.051105	-2.965200	-1.842500	C	-0.016230	1.293109	-3.13686
C	4.223703	-4.030820	-2.221100	C	1.126039	1.747964	-3.79296
H	2.159172	-4.740750	-2.228960	H	-1.052870	1.323134	-3.43504
H	1.287036	-2.695480	-1.106000	C	2.217290	1.443762	-2.92918
H	6.117340	-3.006670	-2.034690	H	1.172485	2.231890	-4.75557
H	4.640684	-4.906070	-2.709350	H	3.269597	1.638508	-3.06984
C	5.303782	-0.668140	-0.777280	N	1.787375	0.837894	-1.80456
C	6.683751	-0.500210	-0.916530	N	2.379480	-0.920170	1.880537
C	7.267780	0.706124	-0.427820	C	0.580666	-0.272970	0.168265
H	7.303422	-1.258950	-1.381040	N	1.052224	-1.254570	2.25113
C	5.076151	1.485133	0.298509	N	0.378927	0.744862	-1.93968
C	6.471511	1.689772	0.174617	C	-3.658460	-1.000780	0.53055
H	8.337773	0.862324	-0.523140	C	-4.700100	-0.070300	0.16602
H	6.928663	2.602414	0.542803	C	-4.038640	-2.291330	0.99761
C	4.095636	2.369505	0.881425	C	-6.073440	-0.501980	0.190198
C	4.393354	3.639407	1.449164	C	-4.440780	1.312712	-0.1527
C	3.384837	4.428955	1.990948	C	-5.366620	-2.703460	1.030408
H	5.420530	3.989361	1.457325	H	-3.261600	-2.999080	1.269818
C	1.785459	2.699641	1.407174	C	-7.125270	0.396664	-0.18883
C	2.040520	3.947825	1.970954	C	-6.409680	-1.833390	0.6108
H	3.618182	5.397135	2.423517	C	-5.454870	2.179173	-0.50891
H	0.778174	2.301524	1.375223	H	-3.428440	1.690145	-0.07283
H	1.224026	4.529713	2.383834	H	-5.613650	-3.710930	1.354815
N	2.758540	1.907817	0.869739	C	-6.823700	1.746691	-0.56225
N	4.541449	0.299353	-0.189100	C	-8.491520	-0.044930	-0.1873
N	3.139570	-1.752700	-0.952310	C	-7.782850	-2.254080	0.608208
Ru	2.481098	0.009604	-0.001490	H	-5.227930	3.217653	-0.73765
C	3.152466	-1.324180	2.907638	C	-7.876110	2.622080	-0.93922
C	2.363950	-1.914610	3.937120	C	-9.514330	0.857292	-0.57604
H	4.221154	-1.177150	2.870383	C	-8.788810	-1.394180	0.216151
C	1.045709	-1.849920	3.490478	H	-8.017100	-3.267290	0.923956
H	2.713277	-2.323430	4.871888	C	-9.207090	2.177185	-0.95032
H	0.131296	-2.177250	3.960695	H	-7.642440	3.646684	-1.2176

C	0.035146	-0.914970	1.313757	H	-10.547600	0.519169	-0.57964
C	-1.329960	-1.151490	1.445696	H	-9.824990	-1.723060	0.214844
C	-2.218160	-0.707740	0.411218	H	-10.003100	2.855294	-1.24271
H	-1.746880	-1.622490	2.331429				

2.9

Atom	X	Y	Z	Atom	X	Y	Z
C	-1.123660	-4.415930	0.000078	H	1.821434	-0.005110	-4.11273
C	-0.738440	-3.069620	0.000173	C	1.496194	-0.004320	-1.20118
C	-2.997740	-2.355210	-0.000610	C	2.896493	-0.004820	-1.23465
C	-3.433560	-3.692410	-0.000740	C	3.607123	-0.005110	0.000937
C	-2.495300	-4.735770	-0.000380	H	3.461352	-0.004860	-2.16228
H	-0.363560	-5.189890	0.000352	C	1.495867	-0.004470	1.202458
H	0.305291	-2.779450	0.000491	C	2.896208	-0.004920	1.2363
H	-4.495010	-3.915300	-0.001100	H	3.460780	-0.004970	2.164081
H	-2.824140	-5.770290	-0.000450	C	0.827756	-0.004580	3.691026
C	-3.912320	-1.195140	-0.000870	C	-0.424000	-0.003100	4.31324
C	-5.318780	-1.214450	-0.001540	H	1.820160	-0.006190	4.114127
C	-6.016780	0.009992	-0.001690	C	-1.376960	-0.001380	3.261259
H	-5.865420	-2.151020	-0.001950	H	-0.620430	-0.003270	5.373626
C	-3.907090	1.205981	-0.000580	H	-2.454690	0.000054	3.32241
C	-5.313450	1.231377	-0.001210	N	-0.759210	-0.001690	2.056289
H	-7.102130	0.012359	-0.002190	N	-0.758600	-0.001240	-2.05572
H	-5.856040	2.170297	-0.001340	C	0.770629	-0.004030	0.000544
C	-2.987460	2.362046	-0.000087	N	0.622749	-0.003230	-2.33568
C	-3.417390	3.701144	-0.000140	N	0.622064	-0.003630	2.336692
C	-2.474580	4.740380	0.000328	C	5.040558	-0.004560	0.00099
H	-4.477850	3.928731	-0.000530	C	6.266545	-0.003560	0.000239
C	-0.725040	3.066571	0.000918	C	7.751389	-0.000640	-0.00082
C	-1.104350	4.414562	0.000880	C	8.269210	-1.038830	1.03673
H	-2.798900	5.776318	0.000264	H	9.366855	-1.041930	1.042808
H	0.317388	2.771772	0.001374	H	7.920624	-0.793240	2.04724
H	-0.340870	5.185194	0.001288	H	7.923162	-2.049570	0.789211
N	-1.631410	2.049363	0.000419	C	8.264648	-0.377820	-1.42053
N	-3.249210	0.003988	-0.000410	H	7.914292	0.342402	-2.16987
N	-1.640350	-2.048440	-0.000130	H	9.362137	-0.378460	-1.43116
Ru	-1.218280	-0.000490	0.000210	H	7.917293	-1.376350	-1.71218
C	-1.375970	-0.000470	-3.260890	C	8.263219	1.419475	0.38064
C	-0.422660	-0.001890	-4.312570	H	7.913072	2.170473	-0.33769
H	-2.453670	0.000995	-3.322410	H	7.913660	1.708888	1.379017
C	0.828890	-0.003560	-3.689950	H	9.360821	1.430385	0.383466
H	-0.618750	-0.001780	-5.373020				

2.9a

Atom	X	Y	Z	Atom	X	Y	Z
C	-1.255050	4.416769	0.026860	C	1.241338	-0.001250	1.433127
C	-0.873490	3.069551	0.053571	C	2.629525	-0.001350	1.579769
C	-3.124880	2.359736	-0.145010	C	3.439907	-0.001270	0.410857
C	-3.557080	3.697595	-0.176600	H	3.136483	-0.001510	2.540671
C	-2.620770	4.739305	-0.090460	C	1.444901	-0.000920	-0.96678

H	-0.496650	5.189155	0.097531	C	2.843598	-0.000990	-0.87903
H	0.165945	2.778554	0.144061	H	3.466682	-0.000850	-1.76758
H	-4.614180	3.922661	-0.266660	C	0.988182	-0.000760	-3.50446
H	-2.946820	5.774413	-0.113400	C	-0.207220	-0.000510	-4.22854
C	-4.039170	1.201918	-0.226610	H	2.011643	-0.001050	-3.84581
C	-5.440390	1.225898	-0.349300	C	-1.244660	-0.000150	-3.25972
C	-6.139130	0.003524	-0.410610	H	-0.314700	-0.000550	-5.3016
H	-5.982200	2.163992	-0.396700	H	-2.313450	0.000157	-3.41074
C	-4.041010	-1.198130	-0.226990	N	-0.729760	-0.000270	-2.00768
C	-5.442250	-1.219940	-0.349700	N	-1.077580	-0.000770	2.090973
H	-7.220360	0.004363	-0.505030	C	0.619571	-0.001060	0.170458
H	-5.985500	-2.157190	-0.397420	N	0.274622	-0.001230	2.488436
C	-3.128490	-2.357390	-0.145780	N	0.670501	-0.000650	-2.17145
C	-3.562770	-3.694570	-0.177730	C	4.934125	-0.001230	0.612998
C	-2.628080	-4.737760	-0.091940	C	7.377603	-0.000077	-0.41305
H	-4.620230	-3.917970	-0.267800	C	8.024756	0.000592	-1.82479
C	-0.878190	-3.070770	0.052477	H	9.118812	0.000921	-1.74163
C	-1.261840	-4.417390	0.025393	H	7.734610	-0.889720	-2.40121
H	-2.955740	-5.772350	-0.115140	H	7.734038	0.891106	-2.40061
H	0.161702	-2.781400	0.142958	C	7.833383	1.271639	0.348548
H	-0.504650	-5.190970	0.095786	H	7.427789	1.292175	1.364135
N	-1.776510	-2.050010	-0.030280	H	8.928922	1.297024	0.416396
N	-3.383010	0.001390	-0.170220	H	7.512201	2.184039	-0.17513
N	-1.773380	2.050203	-0.029550	C	7.834355	-1.271850	0.347849
Ru	-1.354520	-0.000240	0.002739	H	7.428581	-1.293320	1.363346
C	-1.795660	-0.000880	3.238156	H	7.514049	-2.184210	-0.17642
C	-0.935670	-0.001450	4.367916	H	8.929897	-1.296330	0.415877
H	-2.874630	-0.000540	3.205825	O	5.386866	-0.001640	1.78413
C	0.364661	-0.001660	3.855572	C	5.834476	-0.000610	-0.62291
H	-1.221860	-0.001640	5.407652	H	5.561832	0.878907	-1.22953
H	1.317730	-0.002070	4.361618	H	5.562483	-0.880120	-1.22988

2.10

Atom	X	Y	Z	Atom	X	Y	Z
C	1.436629	4.415677	-0.000350	H	0.942741	0.000028	-5.37359
C	1.054139	3.068536	-0.000280	H	-1.497770	0.000007	-4.11463
C	3.314784	2.358640	-0.000058	C	-1.173310	0.000026	-1.20264
C	3.747941	3.696663	-0.000130	C	-2.572910	0.000031	-1.23669
C	2.807580	4.738189	-0.000280	C	-3.283750	0.000096	3.82E-05
H	0.674944	5.188070	-0.000460	H	-3.137600	-0.000014	-2.16436
H	0.010935	2.776554	-0.000330	C	-1.173240	0.000124	1.202592
H	4.808926	3.921750	-0.000075	C	-2.572840	0.000144	1.236727
H	3.134370	5.773347	-0.000340	H	-3.137470	0.000190	2.164432
C	4.231805	1.200376	0.000091	C	-0.505290	0.000209	3.691152
C	5.638245	1.222756	0.000294	C	0.746434	0.000195	4.313084
C	6.338826	-0.000190	0.000442	H	-1.497560	0.000258	4.114599
H	6.182915	2.160459	0.000338	C	1.699385	0.000109	3.260947
C	4.231707	-1.200590	0.000183	H	0.943007	0.000231	5.373442
C	5.638145	-1.223080	0.000394	H	2.777107	0.000068	3.322183
H	7.424180	-0.000240	0.000602	N	1.081724	0.000119	2.05611

H	6.182740	-2.160830	0.000531	N	1.081616	-0.000064	-2.05626
C	3.314593	-2.358780	0.000101	C	-0.447730	0.000067	-4.20E-05
C	3.747644	-3.696840	0.000150	N	-0.299760	-0.000035	-2.33671
C	2.807200	-4.738290	0.000051	N	-0.299640	0.000162	2.336622
H	4.808611	-3.922010	0.000262	C	-4.713590	0.000091	8.13E-05
C	1.053892	-3.068500	-0.000150	C	-5.941500	0.000057	0.000108
C	1.436275	-4.415670	-0.000100	C	-8.096180	-0.000270	-1.22298
H	3.133909	-5.773470	0.000095	C	-9.500040	-0.000300	-1.21907
H	0.010711	-2.776430	-0.000260	C	-10.207400	-0.000046	0.000151
H	0.674529	-5.188000	-0.000190	C	-9.500010	0.000248	1.21936
N	1.957894	-2.049240	-0.000040	C	-8.096150	0.000284	1.223245
N	3.571456	-0.000081	0.000039	C	-7.375680	0.000025	0.000123
N	1.958060	2.049206	-0.000140	H	-7.550630	-0.000460	-2.16281
Ru	1.539808	0.000003	-0.000085	H	-10.042500	-0.000530	-2.16098
C	1.699218	-0.000039	-3.261130	H	-11.294300	-0.000075	0.00017
C	0.746216	0.000006	-4.313220	H	-10.042500	0.000448	2.161277
H	2.776937	-0.000069	-3.322410	H	-7.550580	0.000509	2.163057
C	-0.505480	-0.000006	-3.691230				

2.10a

Atom	X	Y	Z	Atom	X	Y	Z
C	-1.396740	4.398913	0.340453	H	1.087146	-0.416440	4.293474
C	-1.063410	3.040892	0.261536	C	0.962258	-0.188720	1.375637
C	-3.342770	2.424587	0.068804	C	2.351859	-0.234250	1.497069
C	-3.726990	3.775144	0.143509	C	3.142507	-0.164510	0.316458
C	-2.752240	4.775328	0.280405	H	2.874496	-0.318570	2.445877
H	-0.609730	5.137756	0.447341	C	1.127130	-0.014370	-1.02198
H	-0.033500	2.708368	0.305064	C	2.526795	-0.055200	-0.95953
H	-4.776980	4.042673	0.095789	H	3.134508	-0.005700	-1.85753
H	-3.041580	5.819869	0.339311	C	0.628412	0.187874	-3.54379
C	-4.299450	1.307566	-0.073520	C	-0.578270	0.280918	-4.24256
C	-5.701500	1.387292	-0.155600	H	1.645273	0.178451	-3.90426
C	-6.444220	0.196958	-0.288870	C	-1.598660	0.243720	-3.25639
H	-6.211110	2.343647	-0.117290	H	-0.703790	0.363128	-5.3105
C	-4.385940	-1.084070	-0.252810	H	-2.669240	0.289847	-3.38626
C	-5.789730	-1.050140	-0.338390	N	-1.063280	0.134325	-2.01793
H	-7.526770	0.240992	-0.353110	N	-1.344310	-0.166210	2.075264
H	-6.366370	-1.962690	-0.440850	C	0.320840	-0.077890	0.127371
C	-3.513270	-2.275960	-0.284830	N	0.013722	-0.238970	2.445779
C	-3.995740	-3.591040	-0.409010	N	0.333375	0.099729	-2.20831
C	-3.097270	-4.668780	-0.430030	C	4.636008	-0.211440	0.49288
H	-5.062380	-3.770780	-0.487620	O	5.120381	-0.343140	1.640005
C	-1.285990	-3.078070	-0.203660	C	5.526604	-0.106300	-0.75677
C	-1.718060	-4.404680	-0.325490	H	5.309652	-0.989010	-1.38064
H	-3.462090	-5.686700	-0.524900	H	5.200993	0.765866	-1.34001
H	-0.234370	-2.832580	-0.120270	C	7.016040	-0.010100	-0.47975
H	-0.987360	-5.206350	-0.336680	C	7.726165	-1.104620	0.059297
N	-2.148800	-2.024080	-0.181640	C	7.717927	1.177598	-0.77297
N	-3.684980	0.085010	-0.124320	C	9.108405	-1.013650	0.297974
N	-2.000860	2.061678	0.127925	H	7.197902	-2.022980	0.305578

Ru	-1.654260	0.001732	-0.000950	C	9.102916	1.273530	-0.53476
C	-2.042740	-0.231720	3.232539	H	7.185387	2.032011	-1.18801
C	-1.164510	-0.345510	4.342447	C	9.802445	0.176400	0.000767
H	-3.121530	-0.195810	3.221000	H	9.642419	-1.863790	0.715354
C	0.126372	-0.347090	3.807098	H	9.630119	2.195736	-0.76678
H	-1.433260	-0.416440	5.384402	H	10.871670	0.246265	0.18488

2.11

Atom	X	Y	Z	Atom	X	Y	Z
C	0.176192	4.346160	0.770205	C	-5.978920	-0.004620	-0.01072
C	-0.203110	3.019906	0.529791	C	-6.720290	0.032551	-1.2362
C	2.059367	2.325657	0.403399	C	-4.614430	-0.094590	2.472133
C	2.488713	3.643236	0.642767	H	-4.113550	-0.059540	3.429973
C	1.546550	4.666330	0.828211	C	-5.986720	-0.057550	2.456211
H	-0.587420	5.104328	0.908010	H	-6.541180	-0.031330	3.391442
H	-1.245330	2.729058	0.478766	C	-5.988620	0.048600	-2.47453
H	3.549242	3.866156	0.685439	H	-6.544120	0.023868	-3.40924
H	1.871371	5.685392	1.013776	C	-4.615360	0.084941	-2.49239
C	2.979011	1.186063	0.199032	H	-4.116050	0.050772	-3.45103
C	4.381457	1.210832	0.209340	C	-8.131250	-0.035640	1.193418
C	5.117590	0.015119	0.000126	H	-8.655260	-0.057340	2.145837
H	4.911105	2.136507	0.403303	C	-8.135520	0.029013	-1.21399
C	2.987059	-1.168680	-0.208810	H	-8.656170	0.051956	-2.16575
C	4.389730	-1.185050	-0.212230	C	-8.867810	-0.002330	-0.01211
H	4.925729	-2.107740	-0.402990	C	-10.413100	-0.000520	0.02905
C	2.075203	-2.313780	-0.417250	C	-10.906000	1.250563	0.815387
C	2.513502	-3.628500	-0.656160	H	-12.002600	1.256873	0.864632
C	1.578321	-4.657120	-0.846260	H	-10.526500	1.263154	1.844399
H	3.575530	-3.844870	-0.695070	H	-10.580600	2.176830	0.324565
C	-0.182500	-3.021630	-0.553340	C	-11.042600	0.038731	-1.38586
C	0.205821	-4.345320	-0.793510	H	-10.755600	0.943801	-1.93718
H	1.910061	-5.674010	-1.031520	H	-10.760600	-0.837450	-1.98442
H	-1.226670	-2.737110	-0.506480	H	-12.135900	0.039294	-1.29827
H	-0.552600	-5.107960	-0.935210	C	-10.911500	-1.290050	0.746662
N	0.716595	-2.015140	-0.366390	H	-10.590300	-2.189650	0.206003
N	2.315742	0.006680	-0.006610	H	-10.532000	-1.360310	1.773205
N	0.702819	2.018703	0.347582	H	-12.008100	-1.294160	0.79572
Ru	0.285833	0.000347	-0.009610	C	6.602446	0.019843	0.002757
C	0.515803	0.694334	-3.143450	C	7.339135	-1.096270	0.469877
C	-0.399040	1.000862	-4.179860	C	7.332918	1.136320	-0.46195
H	1.595000	0.701388	-3.160310	C	8.739392	-1.087690	0.470314
C	-1.669190	0.843819	-3.622450	H	6.818027	-1.963820	0.868731
H	-0.170940	1.301323	-5.190150	C	8.737844	1.138082	-0.46198
H	-2.629770	1.025084	-4.067950	H	6.808395	2.001240	-0.8623
C	-2.418690	0.185676	-1.212790	C	9.479031	0.028553	0.003686
C	-3.836150	0.096438	-1.274250	H	9.262446	-1.961960	0.848464
C	-4.540660	-0.004950	-0.010850	H	9.252668	2.014445	-0.84005
C	-2.419370	-0.196240	1.190948	C	11.023070	-0.004500	0.022469
C	-3.835590	-0.106880	1.252386	C	11.523280	-1.199260	-0.84323
C	-1.669560	-0.856920	3.599626	H	12.620040	-1.239170	-0.83018

C	-0.399440	-1.009870	4.158080	H	11.150790	-2.160550	-0.46912
H	-2.629930	-1.044230	4.043156	H	11.197970	-1.093050	-1.88608
C	0.515279	-0.696690	3.123443	C	11.513460	-0.189990	1.489892
H	-0.171150	-1.312120	5.167796	H	11.136920	-1.119870	1.932777
H	1.594477	-0.699270	3.141517	H	12.610090	-0.227230	1.51799
N	-0.144760	-0.370130	1.989410	H	11.183910	0.643964	2.122828
N	-0.144150	0.367763	-2.009300	C	11.647470	1.297279	-0.53786
C	-1.711960	-0.004870	-0.011230	H	11.362570	1.471059	-1.58379
N	-1.521410	0.446209	-2.312520	H	11.359140	2.176974	0.0523
N	-1.521930	-0.455040	2.290929	H	12.741070	1.222701	-0.50318
C	-6.720580	-0.041380	1.217511				

2.31							
Atom	X	Y	Z	Atom	X	Y	Z
C	-0.09431	-4.43486	2.86E-05	N	0.416752	-2.06734	0.000203
C	-0.48205	-3.08759	0.000146	Ru	0.01656	1.23E-05	8.81E-05
C	1.771973	-2.3676	0.000172	C	0.170038	0.000446	3.259321
C	2.214104	-3.70105	0.000108	C	-0.81225	0.000332	4.293607
C	1.277317	-4.74836	1.31E-05	H	1.245665	0.000662	3.354005
H	-0.8503	-5.21252	-5.2E-05	C	-2.04434	0.000178	3.654679
H	-1.5298	-2.81012	0.000267	H	-0.63554	0.000495	5.357669
H	3.275094	-3.92432	0.000143	H	-3.04263	0.000127	4.064701
H	1.609841	-5.78145	-4.1E-05	C	-2.67819	0.00005	1.184078
C	2.679345	-1.19965	0.00014	C	-4.07827	2.8E-06	1.229234
C	4.085483	-1.22119	9.39E-05	C	-4.77047	-0.00022	0.000264
C	4.786303	0.000304	-1.9E-05	H	-4.6191	0.000131	2.168096
H	4.629911	-2.15843	0.000166	C	-2.67833	-0.00027	-1.18376
C	2.679187	1.199981	-7E-05	C	-4.07841	-0.00034	-1.22878
C	4.085318	1.221712	-0.00013	H	-4.61933	-0.00051	-2.16759
H	5.871416	0.000379	-5E-05	C	-2.04476	-0.00065	-3.65445
H	4.629628	2.159015	-0.00024	C	-0.81275	-0.00057	-4.29352
C	1.771662	2.36781	-0.00025	H	-3.04312	-0.00075	-4.06431
C	2.213591	3.701313	-0.00042	C	0.169663	-0.00038	-3.25935
C	1.276651	4.748494	-0.00069	H	-0.63617	-0.00061	-5.35761
H	3.274547	3.924751	-0.00034	H	1.245277	-0.00021	-3.35419
C	-0.48247	3.087466	-0.00053	N	-0.40894	-0.00034	-2.04378
C	-0.09492	4.434797	-0.00076	N	-0.40871	0.000279	2.043809
H	1.609033	5.781623	-0.00082	N	-1.80609	0.000216	2.291538
H	-1.53019	2.809849	-0.00051	N	-1.80635	-0.00043	-2.29134
H	-0.85103	5.212344	-0.001	H	-5.85551	-0.00025	0.000324
N	0.416468	2.067343	-0.00026	N	-2.00562	-7.9E-05	0.000108
N	2.019495	0.000118	9.29E-05				

2.32							
Atom	X	Y	Z	Atom	X	Y	Z
Ru	-0.07364	9E-07	-1.5E-05	C	4.106638	-6.9E-05	1.227374
C	-1.23909	-4.78459	-0.00041	N	0.430994	0.000159	-2.04333
H	-4.68917	2.161628	-7E-07	H	4.654203	0.000161	-2.16361
N	2.039085	1.62E-05	0.000115	C	4.106778	9.79E-05	-1.22692
C	0.124854	4.441919	0.000257	C	1.278071	-0.00031	4.738179

H	-3.25971	4.003099	0.000125	H	3.277383	-0.00024	3.932258
C	-2.00463	-1.3E-05	-8.6E-05	C	4.809126	1.55E-05	0.000259
C	0.124911	-4.44192	-0.00036	C	1.278606	0.000337	-4.73805
H	-3.25966	-4.00314	-0.0004	H	3.277824	0.000275	-3.93191
C	-2.70403	1.2449	-1.7E-05	C	-1.79712	2.414642	8.44E-05
C	0.480264	3.083972	0.000196	C	-0.47703	-0.00023	3.066986
H	-1.54751	5.825746	0.000278	H	1.599999	-0.00037	5.774858
C	-2.70401	-1.24493	-0.00019	C	-1.79708	-2.41466	-0.00025
C	0.480305	-3.08397	-0.00026	C	-0.4767	0.000235	-3.06706
H	-1.54744	-5.82577	-0.00049	H	1.60065	0.000404	-5.77469
C	-4.10991	1.241578	-5E-05	C	-2.20225	3.760147	0.000146
C	1.798952	-0.00015	2.354151	C	-0.10283	-0.00031	4.409763
H	0.899518	5.201036	0.000322	H	-0.86744	-0.00037	5.178718
C	-4.10989	-1.24163	-0.00022	C	-2.2022	-3.76017	-0.00035
C	1.799219	0.000175	-2.35396	C	-0.10234	0.000324	-4.40979
H	0.899585	-5.20102	-0.00041	H	-0.86687	0.000381	-5.17883
C	-4.79507	-3.2E-05	-0.00015	N	-0.44194	2.089952	0.000113
C	2.216493	-0.00024	3.705211	H	5.894381	1.58E-05	0.000318
H	1.51795	2.770725	0.000211	H	-1.52138	-0.00023	2.78008
C	2.702772	9.66E-05	-1.20932	N	-0.44192	-2.08996	-0.0002
C	2.216908	0.000264	-3.70498	H	-5.88184	-3.9E-05	-0.00017
H	1.517988	-2.77071	-0.00022	H	-1.52108	0.000224	-2.78027
C	2.702647	-6.8E-05	1.2096	C	-1.23916	4.78457	0.000233
N	0.430777	-0.00015	2.043363	H	-4.68914	-2.16169	-0.0003
H	4.653958	-0.00013	2.16413				

3.1							
Atom	X	Y	Z	Atom	X	Y	Z
C	-2.053611	-4.402606	0.344117	C	-4.653091	-0.084822	-1.20905
C	-2.433119	-3.058553	0.241922	C	-6.057926	-0.082731	-1.24487
C	-0.170998	-2.354591	0.182350	H	-6.617236	-0.153680	-2.17407
C	0.258602	-3.689617	0.284443	C	-3.974068	-0.280844	-3.68697
C	-0.683292	-4.726621	0.365811	C	-2.719459	-0.333252	-4.3012
H	-2.816827	-5.171123	0.405188	H	-4.964268	-0.310322	-4.11422
H	-3.475539	-2.764418	0.223207	C	-1.771014	-0.255169	-3.24781
H	1.319154	-3.915750	0.301047	H	-2.518218	-0.415545	-5.35751
H	-0.358002	-5.759275	0.444705	H	-0.693008	-0.263022	-3.3026
C	0.748792	-1.200016	0.091673	N	-2.393841	-0.159980	-2.04937
C	2.151212	-1.226168	0.096249	N	-2.406363	0.163784	2.048648
C	2.887326	-0.015624	0.005170	C	-3.935354	0.006866	-0.00546
H	2.681502	-2.166404	0.195526	N	-3.788588	0.188972	2.325274
C	0.756881	1.183280	-0.079614	N	-3.774267	-0.176477	-2.33518
C	2.159525	1.199980	-0.084442	H	-7.835698	0.018736	-0.0184
H	2.695953	2.136687	-0.184200	C	4.371974	-0.021012	0.00115
C	-0.155027	2.343927	-0.172173	C	5.111537	1.039981	0.579076
C	0.283657	3.676218	-0.271524	C	5.098881	-1.082933	-0.58192
C	-0.651144	4.719420	-0.355370	C	6.511726	1.030947	0.571182
H	1.345721	3.895387	-0.283984	H	4.592979	1.860756	1.069722
C	-2.412258	3.062673	-0.239302	C	6.503722	-1.084407	-0.59058
C	-2.023618	4.404292	-0.338961	H	4.571414	-1.901020	-1.06776

H	-0.318870	5.750009	-0.432130	H	7.038399	1.859244	1.037331
H	-3.456676	2.775441	-0.224930	H	7.016047	-1.915538	-1.06225
H	-2.781596	5.177805	-0.402201	C	7.247870	-0.029843	-0.01505
N	-1.513797	2.042024	-0.155783	C	8.791928	0.003715	-0.00397
N	0.086122	-0.006095	0.005798	C	9.413947	-1.236882	-0.69165
N	-1.527714	-2.043879	0.160868	H	9.130773	-2.170025	-0.18732
Ru	-1.945718	0.000499	0.001158	H	9.122097	-1.309095	-1.7475
C	-1.790995	0.254542	3.251279	H	10.507708	-1.163895	-0.65733
C	-2.745949	0.338234	4.298349	C	9.293180	0.048791	1.470759
H	-0.713355	0.255661	3.313337	H	8.920115	0.932000	2.003258
C	-3.996734	0.294052	3.675743	H	8.968351	-0.841597	2.024274
H	-2.551228	0.418824	5.356014	H	10.389947	0.083942	1.493685
H	-4.989559	0.329606	4.096399	C	9.282795	1.277118	-0.75566
C	-4.660486	0.102908	1.193344	H	8.907185	2.197187	-0.29185
C	-6.065528	0.109447	1.219865	H	10.379383	1.321240	-0.7438
C	-6.749635	0.015469	-0.014783	H	8.953096	1.267094	-1.80256
H	-6.630498	0.183694	2.145368				

3.2

Atom	X	Y	Z	Atom	X	Y	Z
C	-1.716945	4.333556	-0.856566	C	-6.429796	-0.004273	-0.001736
C	-2.101251	3.012747	-0.594449	H	-6.302912	-0.421248	-2.127503
C	0.158044	2.312055	-0.454494	C	-4.337578	0.229548	1.181436
C	0.592459	3.623794	-0.715275	C	-5.742566	0.234367	1.211567
C	-0.345504	4.647431	-0.918749	H	-6.305252	0.412873	2.124137
H	-2.477527	5.092243	-1.007554	C	-3.666483	0.708533	3.622843
H	-3.144844	2.727744	-0.539131	C	-2.413757	0.829524	4.231259
H	1.653874	3.841852	-0.759917	H	-4.657943	0.789005	4.040562
H	-0.016555	5.662011	-1.120812	C	-1.462061	0.628335	3.197273
C	1.074257	1.173660	-0.227127	H	-2.215793	1.033429	5.271599
C	2.476770	1.194935	-0.235606	H	-0.384217	0.640492	3.253556
C	3.210322	0.002229	-0.000354	N	-2.081115	0.396026	2.015904
H	3.009475	2.115015	-0.446643	N	-2.078912	-0.396798	-2.016166
C	1.075343	-1.171043	0.227392	C	-3.615642	-0.001598	-0.000713
C	2.477848	-1.191083	0.235159	N	-3.459979	-0.451480	-2.294127
H	3.011381	-2.110816	0.445594	N	-3.462483	0.448334	2.292843
C	0.160307	-2.310317	0.455015	H	-7.515876	-0.005296	-0.002133
C	0.596079	-3.621532	0.716176	C	4.695298	0.002426	-0.001022
C	-0.340815	-4.646073	0.919994	C	5.422897	-1.124216	-0.444251
H	1.657719	-3.838477	0.760883	C	5.422432	1.128197	0.443313
C	-2.098251	-3.013287	0.595273	C	6.828823	-1.136222	-0.451089
C	-1.712579	-4.333616	0.857787	H	4.894357	-1.994839	-0.826379
H	-0.010816	-5.660253	1.122355	C	6.830899	1.147272	0.453270
H	-3.142139	-2.729387	0.539906	H	4.891162	1.996752	0.826459
H	-2.472376	-5.093035	1.009048	C	7.548782	0.006088	0.000652
N	-1.197679	-2.010641	0.395602	C	9.066714	-0.024519	-0.005668
N	0.407804	0.001025	0.000306	H	9.450073	-0.791166	0.682853
N	-1.199642	2.010970	-0.395139	H	9.454452	-0.276336	-1.001932
Ru	-1.625492	-0.000099	0.000043	H	9.505993	0.930597	0.288093
C	-1.458580	-0.627964	-3.197089	C	7.562671	-2.366845	-0.951640

C	-2.409161	-0.830755	-4.231785	H	8.186385	-2.138350	-1.826704
H	-0.380676	-0.638270	-3.252579	H	8.232921	-2.778374	-0.184866
C	-3.662544	-0.711976	-3.624287	H	6.861311	-3.156583	-1.240965
H	-2.210075	-1.034253	-5.271990	C	7.543618	2.390168	0.961744
H	-4.653554	-0.794143	-4.042744	H	8.192979	2.166534	1.818116
C	-4.336276	-0.234152	-1.183381	H	8.175880	2.842665	0.186304
C	-5.741229	-0.241634	-1.214532	H	6.822980	3.149359	1.283918

3.3

Atom	X	Y	Z	Atom	X	Y	Z
C	-1.6661670	4.3951840	-0.3607333	C	-4.1612387	-0.1756715	-1.2700591
C	-2.0234212	3.0449154	-0.2596545	C	-5.5642785	-0.2147488	-1.3390739
C	0.2496941	2.3812550	-0.1615142	C	-6.2878187	-0.1263781	-0.1266409
C	0.6570312	3.7233101	-0.2618186	H	-6.0990371	-0.3094690	-2.2805305
C	-0.3016220	4.7431771	-0.3622152	C	-4.2316805	0.0317638	1.1298644
H	-2.4417092	5.1499190	-0.4365258	C	-5.6365805	-0.0022570	1.1230428
H	-3.0605429	2.7320288	-0.2563300	H	-6.2254697	0.0635169	2.0341653
H	1.7134686	3.9686084	-0.2614332	C	-3.6330980	0.2664353	3.6250962
H	0.0067338	5.7811218	-0.4396576	C	-2.3993701	0.3535099	4.2765038
C	1.1881433	1.2433103	-0.0497290	H	-4.6363021	0.2775242	4.0218018
C	2.5896498	1.2927789	-0.0435031	C	-1.4175875	0.2868401	3.2532668
C	3.3468306	0.0955804	0.0657453	H	-2.2323329	0.4507513	5.3375025
H	3.1029888	2.2413246	-0.1516979	H	-0.3422259	0.3196776	3.3408453
C	1.2341235	-1.1369639	0.1452182	N	-2.0010137	0.1657791	2.0374739
C	2.6363657	-1.1306079	0.1639168	N	-1.8812989	-0.1909441	-2.0558720
H	3.1848674	-2.0582497	0.2810171	C	-3.4756273	-0.0535455	-0.0505386
C	0.3409755	-2.3122456	0.2383095	N	-3.2533511	-0.2499773	-2.3742169
C	0.8011335	-3.6348646	0.3661441	N	-3.3897939	0.1534468	2.2811552
C	-0.1162615	-4.6934200	0.4491945	H	-7.3731390	-0.1542616	-0.1560870
H	1.8664858	-3.8345620	0.4020341	C	4.8291051	0.1264498	0.0746632
C	-1.9039290	-3.0705047	0.2752716	C	5.5885234	-0.9388699	-0.4609317
C	-1.4935402	-4.4031702	0.4028826	C	5.5353856	1.2315198	0.6208252
H	0.2325977	-5.7165901	0.5483333	C	6.9924215	-0.9170446	-0.4621941
H	-2.9528689	-2.8028210	0.2369381	H	5.0860282	-1.7867998	-0.9203743
H	-2.2388434	-5.1890519	0.4643258	C	6.9305762	1.2678049	0.6317684
N	-1.0224026	-2.0349441	0.1927206	H	4.9905522	2.0558396	1.0743128
N	0.5442159	0.0397868	0.0413242	C	7.6715343	0.1927058	0.0880242
N	-1.1016339	2.0467632	-0.1606833	H	7.5384908	-1.7477121	-0.8967956
Ru	-1.4874550	-0.0038148	0.0030975	H	7.4725634	2.1043265	1.0609677
C	-1.2273483	-0.2756485	-3.2383379	O	9.0476645	0.3284834	0.1451665
C	-2.1475095	-0.3885006	-4.3134267	C	9.8969222	-0.7351815	-0.3876767
H	-0.1485695	-0.2524416	-3.2668038	H	9.7258560	-0.8732980	-1.4635093
C	-3.4175061	-0.3689893	-3.7295999	H	10.9191264	-0.3946986	-0.2175913
H	-1.9187825	-0.4716906	-5.3640535	H	9.7265590	-1.6796696	0.1458932
H	-4.3958286	-0.4302799	-4.1802220				

3.4

Atom	X	Y	Z	Atom	X	Y	Z
C	1.749621	4.392701	0.457454	H	4.685194	-0.424562	4.095647
C	2.133051	3.052904	0.319505	C	4.364652	-0.124163	1.197512

C	-0.127150	2.345588	0.240721	C	5.769661	-0.127279	1.228356
C	-0.560913	3.676147	0.378711	C	6.457056	0.000009	-0.001227
C	0.378486	4.712780	0.487878	H	6.331953	-0.223410	2.153349
H	2.510578	5.161483	0.539146	C	4.363980	0.124270	-1.198789
H	3.176201	2.762199	0.293295	C	5.768972	0.127341	-1.230419
H	-1.621775	3.900510	0.401856	H	6.330753	0.223396	-2.155731
H	0.050890	5.742114	0.594580	C	3.691848	0.380447	-3.673270
C	-1.041943	1.190929	0.118525	C	2.438814	0.444849	-4.289653
C	-2.444573	1.211693	0.121146	H	4.683002	0.423570	-4.097172
C	-3.171542	0.000049	0.000297	C	1.487871	0.337720	-3.241492
H	-2.976935	2.148035	0.244362	H	2.240308	0.553223	-5.344099
C	-1.041965	-1.190896	-0.117756	H	0.410061	0.344133	-3.299629
C	-2.444595	-1.211621	-0.120448	N	2.108131	0.213893	-2.044236
H	-2.976984	-2.147949	-0.243664	N	2.109268	-0.213909	2.044138
C	-0.127186	-2.345569	-0.239954	C	3.643560	0.000049	-0.000440
C	-0.560970	-3.676151	-0.377664	N	3.489869	-0.241724	2.324468
C	0.378407	-4.712797	-0.486879	N	3.488584	0.241686	-2.325280
H	-1.621837	-3.900517	-0.400538	H	7.543055	-0.000043	-0.001536
C	2.133007	-3.052894	-0.319096	C	-4.659115	0.000044	0.000249
C	1.749549	-4.392706	-0.456776	C	-5.382391	-1.071570	0.580123
H	0.050796	-5.742147	-0.593369	C	-5.382358	1.071616	-0.579824
H	3.176160	-2.762176	-0.293135	C	-6.783295	-1.080232	0.584498
H	2.510491	-5.161498	-0.538514	H	-4.852249	-1.888138	1.061958
N	1.230010	-2.038715	-0.210922	C	-6.783235	1.080207	-0.584458
N	-0.375163	0.000016	0.000390	H	-4.852152	1.888172	-1.061603
N	1.230037	2.038750	0.211364	H	-7.346743	-1.890400	1.033403
Ru	1.650321	0.000001	0.000096	H	-7.346694	1.890301	-1.033487
C	1.489620	-0.337161	3.241770	C	-7.464792	-0.000034	-0.000040
C	2.441104	-0.444878	4.289380	N	-8.944890	-0.000099	-0.000185
H	0.411840	-0.343005	3.300518	O	-9.541642	0.999047	-0.527554
C	3.693822	-0.381022	3.672297	O	-9.541664	-0.999252	0.527132
H	2.243148	-0.553183	5.343937				

3.5							
Atom	X	Y	Z	Atom	X	Y	Z
C	0.461726	-4.416604	-0.000473	Ru	0.362987	-0.000009	0.000078
C	0.845588	-3.069808	-0.000216	C	0.201841	0.000329	-3.260580
C	-1.414090	-2.359520	-0.000404	C	1.154019	0.000428	-4.313089
C	-1.849020	-3.696748	-0.000659	H	-0.875882	0.000387	-3.321846
C	-0.909307	-4.738791	-0.000699	C	2.406311	0.000360	-3.692021
H	1.222768	-5.189640	-0.000502	H	0.956546	0.000558	-5.373277
H	1.889051	-2.778886	-0.000024	H	3.398015	0.000421	-4.116807
H	-2.909929	-3.922166	-0.000826	C	3.076042	0.000096	-1.204144
H	-1.236621	-5.773680	-0.000909	C	4.481027	0.000107	-1.235321
C	-2.328104	-1.199462	-0.000372	C	5.168695	-0.000008	0.000634
C	-3.733538	-1.227972	-0.000565	H	5.043076	0.000214	-2.165457
C	-4.417358	0.000045	-0.000520	C	3.075758	-0.000165	1.204921
H	-4.286355	-2.159637	-0.000738	C	4.480736	-0.000150	1.236428
C	-2.328064	1.199492	-0.000128	H	5.042565	-0.000229	2.166695
C	-3.733497	1.228041	-0.000310	C	2.405436	-0.000358	3.692642

H	-4.286287	2.159721	-0.000286	C	1.152994	-0.000507	4.313410
C	-1.414020	2.359526	0.000063	H	3.397036	-0.000360	4.117671
C	-1.848916	3.696763	0.000054	C	0.201065	-0.000389	3.260678
C	-0.909182	4.738789	0.000201	H	0.955272	-0.000645	5.373552
H	-2.909821	3.922204	-0.000073	H	-0.876673	-0.000392	3.321684
C	0.845676	3.069767	0.000378	N	0.820193	-0.000204	2.056227
C	0.461841	4.416571	0.000367	N	0.820680	0.000252	-2.055980
H	-1.236478	5.773684	0.000181	C	2.354912	0.000003	0.000302
H	1.889134	2.778829	0.000522	N	2.201554	0.000248	-2.337188
H	1.222904	5.189587	0.000479	N	2.201006	-0.000257	2.337762
N	-0.057116	2.049320	0.000228	H	6.254691	0.000010	0.000762
N	-1.665655	0.000002	-0.000141	Cl	-6.223543	0.000076	-0.000753
N	-0.057187	-2.049344	-0.000177				

3.6

Atom	X	Y	Z	Atom	X	Y	Z
C	2.079602	4.402774	0.348609	H	5.012913	-0.325511	4.107349
C	2.463400	3.060027	0.245136	C	4.695270	-0.096065	1.203013
C	0.203477	2.349840	0.180848	C	6.100214	-0.098918	1.235499
C	-0.230496	3.683397	0.284371	C	6.789207	-0.001444	0.003948
C	0.708318	4.722915	0.368716	H	6.661441	-0.173042	2.163240
H	2.840324	5.173546	0.412010	C	4.697494	0.094956	-1.198837
H	3.506716	2.769056	0.227944	C	6.102497	0.096626	-1.228830
H	-1.291609	3.907096	0.299907	H	6.665433	0.170218	-2.155579
H	0.380107	5.754525	0.448723	C	4.028564	0.292460	-3.679362
C	-0.711858	1.192436	0.086909	C	2.776432	0.342269	-4.298894
C	-2.114548	1.213466	0.091233	H	5.020416	0.325181	-4.102534
H	-2.647333	2.152125	0.193244	C	1.823830	0.260200	-3.249741
C	-0.711770	-1.192104	-0.089353	H	2.579462	0.425385	-5.355936
C	-2.114460	-1.213244	-0.093408	H	0.746078	0.265121	-3.309560
H	-2.647184	-2.151956	-0.195222	N	2.442007	0.164963	-2.048832
C	0.203603	-2.349482	-0.183170	N	2.438247	-0.164659	2.049013
C	-0.230347	-3.682984	-0.287491	C	3.975202	-0.000282	0.001441
C	0.708482	-4.722498	-0.371720	N	3.819040	-0.186137	2.331302
H	-1.291455	-3.906648	-0.303788	N	3.823319	0.185700	-2.328673
C	2.463538	-3.059712	-0.246404	H	7.875248	-0.001917	0.004909
C	2.079761	-4.402403	-0.350685	C	-2.844085	0.000074	-0.000999
H	0.380283	-5.754061	-0.452377	C	-4.330321	-0.000015	-0.000712
H	3.506855	-2.768807	-0.228388	C	-7.156658	-0.000180	-0.000065
H	2.840503	-5.173165	-0.413974	C	-5.057385	-1.056975	0.598019
N	1.561128	-2.042622	-0.162532	H	-4.533722	-1.868469	1.096944
N	-0.045205	0.000192	-0.001277	C	-6.461497	-1.062571	0.603278
N	1.561001	2.042930	0.161151	H	-7.001973	-1.875061	1.078222
Ru	1.984175	0.000145	-0.000325	C	-5.057777	1.056856	-0.599114
C	1.817890	-0.258578	3.248898	H	-4.534434	1.868413	-1.098273
C	2.768580	-0.340781	4.299771	C	-6.461894	1.062288	-0.603730
H	0.740031	-0.262766	3.306801	H	-7.002684	1.874714	-1.078426
C	4.021834	-0.292285	3.682409	Br	-9.114862	-0.000290	0.000399
H	2.569703	-0.423159	5.356513				

3.7							
Atom	X	Y	Z	Atom	X	Y	Z
C	1.299407	4.404825	0.344039	H	4.242177	-0.318937	4.105475
C	1.683882	3.062099	0.241567	C	3.916662	-0.093597	1.200524
C	-0.575293	2.350378	0.178601	C	5.321610	-0.096481	1.237882
C	-1.010131	3.683631	0.281116	C	5.995945	-0.000622	0.001516
C	-0.071953	4.723956	0.364307	H	5.884705	-0.168566	2.163042
H	2.059739	5.176023	0.406541	C	3.917830	0.093600	-1.199410
H	2.727588	2.772689	0.224352	C	5.322812	0.095638	-1.235476
H	-2.071332	3.906763	0.296821	H	5.886804	0.167329	-2.160120
H	-0.400837	5.755387	0.443565	C	3.254142	0.287650	-3.680783
C	-1.490353	1.192316	0.085964	C	2.002991	0.336727	-4.300647
C	-2.893042	1.213453	0.090488	H	4.246075	0.319720	-4.104000
H	-3.425815	2.152161	0.191675	C	1.048866	0.256236	-3.252005
C	-1.490139	-1.191937	-0.087878	H	1.806903	0.418429	-5.357942
C	-2.892828	-1.213350	-0.091873	H	-0.028786	0.261316	-3.313729
H	-3.425449	-2.152169	-0.192808	N	1.664395	0.162558	-2.050300
C	-0.574909	-2.349850	-0.180659	N	1.662429	-0.161746	2.049350
C	-1.009564	-3.683128	-0.283595	C	3.194898	0.000191	0.000220
C	-0.071247	-4.723317	-0.366927	N	3.044973	-0.182314	2.329790
H	-2.070733	-3.906394	-0.299554	N	3.047206	0.182734	-2.329472
C	1.684360	-3.061277	-0.243447	C	-3.622660	-0.000028	-0.000543
C	1.300068	-4.404024	-0.346362	C	-5.108761	-0.000195	-0.000175
H	-0.399997	-5.754764	-0.446543	C	-7.935048	-0.000515	0.000596
H	2.728032	-2.771763	-0.225921	C	-5.835644	-1.057461	0.598289
H	2.060510	-5.175105	-0.408968	H	-5.312078	-1.869115	1.097068
N	0.782607	-2.043693	-0.160513	C	-7.239692	-1.063018	0.603692
N	-0.823981	0.000255	-0.001076	H	-7.780116	-1.875604	1.078512
N	0.782260	2.044379	0.158766	C	-5.836206	1.056903	-0.598246
Ru	1.206596	0.000373	-0.000695	H	-5.313095	1.868676	-1.097310
C	1.045776	-0.254306	3.250564	C	-7.240259	1.062142	-0.602883
C	1.998914	-0.334721	4.300107	H	-7.781127	1.874605	-1.077411
H	-0.031934	-0.258925	3.311307	Br	-9.892841	-0.000738	0.001141
C	3.250644	-0.286608	3.681340	Br	7.959728	-0.001248	0.002404
H	1.801841	-0.415768	5.357269				

3.8							
Atom	X	Y	Z	Atom	X	Y	Z
C	2.100081	4.345332	0.658221	C	6.517959	-0.366380	0.212792
C	2.399125	2.990275	0.469618	H	6.272553	-0.677335	2.346235
C	0.101370	2.439367	0.288117	C	4.500343	-0.029834	-1.070773
C	-0.248133	3.788572	0.474504	C	5.901665	-0.131597	-1.038702
C	0.752509	4.754260	0.662269	H	6.513446	-0.036445	-1.931944
H	2.906765	5.056958	0.798551	C	3.968416	0.393526	-3.556552
H	3.421391	2.632161	0.459422	C	2.754670	0.582673	-4.223734
H	-1.292431	4.081364	0.473421	H	4.979445	0.382442	-3.932911
H	0.489083	5.797278	0.807501	C	1.748702	0.496266	-3.225788
C	-0.884097	1.356507	0.079972	H	2.615750	0.757821	-5.278761
C	-2.281862	1.471922	0.042273	H	0.678148	0.586622	-3.330056
H	-2.755456	2.434561	0.197275	N	2.299194	0.267006	-2.010403

C	-1.031846	-1.001269	-0.279899	N	2.070872	-0.342725	2.047261
C	-2.431408	-0.927744	-0.329975	C	3.715182	-0.153810	0.086843
H	-3.020339	-1.817477	-0.521479	N	3.431050	-0.488335	2.387978
C	-0.190567	-2.207571	-0.434383	N	3.690716	0.204211	-2.227932
C	-0.706362	-3.494785	-0.667351	H	7.599875	-0.447897	0.261511
C	0.164264	-4.586879	-0.802613	C	-3.086414	0.320556	-0.162688
H	-1.778164	-3.641575	-0.744162	C	-4.568458	0.418649	-0.197749
C	2.017847	-3.066326	-0.467240	C	-5.205267	1.592096	-0.727616
C	1.551299	-4.365993	-0.699846	C	-6.794888	-0.538782	0.258475
H	-0.227581	-5.582853	-0.983904	C	-6.585752	1.696420	-0.767695
H	3.076206	-2.851929	-0.382075	H	-4.597451	2.394339	-1.137933
H	2.261634	-5.180070	-0.797628	C	-7.421092	0.643146	-0.278454
N	1.182059	-1.998460	-0.335463	H	-7.051607	2.585425	-1.186504
N	-0.293203	0.132861	-0.078025	C	-8.847445	0.724612	-0.306627
N	1.436121	2.043938	0.288239	C	-9.624038	-0.319317	0.180736
Ru	1.732292	-0.007769	-0.001788	H	-9.318575	1.615958	-0.714464
C	1.386545	-0.473566	3.207979	H	-10.708319	-0.251526	0.157374
C	2.275467	-0.700637	4.291231	C	-5.370655	-0.618860	0.283052
H	0.309603	-0.401516	3.215806	H	-4.916008	-1.504054	0.723798
C	3.558132	-0.703489	3.735481	C	-7.620851	-1.596083	0.756983
H	2.018866	-0.841841	5.329137	H	-7.151012	-2.487268	1.167648
H	4.521869	-0.840656	4.200623	C	-9.004764	-1.489695	0.718010
C	4.366284	-0.386548	1.309052	H	-9.626423	-2.296352	1.096980
C	5.764077	-0.497310	1.402683				

3.9							
Atom	X	Y	Z	Atom	X	Y	Z
C	-2.058149	-2.574554	3.588369	C	-6.080885	-1.002316	-0.722349
C	-2.442181	-1.791262	2.492856	H	-6.643372	-1.756876	-1.265901
C	-0.182588	-1.372249	1.915730	C	-4.005268	-2.993245	-2.161041
C	0.252130	-2.150004	3.003702	C	-2.752876	-3.494952	-2.526799
C	-0.686672	-2.758431	3.850869	H	-4.996915	-3.338119	-2.409271
H	-2.818852	-3.026145	4.216251	C	-1.800912	-2.641372	-1.910242
H	-3.485265	-1.623520	2.253737	H	-2.555462	-4.353181	-3.149309
H	1.313505	-2.277866	3.186428	H	-0.723199	-2.687638	-1.947169
H	-0.358084	-3.359600	4.692879	N	-2.419422	-1.666577	-1.202773
C	0.733042	-0.696629	0.972653	N	-2.418654	1.666530	1.202818
C	2.137727	-0.707596	0.989756	C	-3.954673	0.000263	0.000121
H	2.681621	-1.245797	1.758310	N	-3.799818	1.895998	1.366918
C	0.733017	0.696244	-0.972922	N	-3.800693	-1.895556	-1.366651
C	2.137703	0.707309	-0.989982	H	-7.854480	0.000977	0.000380
H	2.681580	1.245578	-1.758501	C	2.862036	-0.000125	-0.000111
C	-0.182630	1.371849	-1.915990	C	4.359288	-0.000033	-0.000062
C	0.252071	2.149437	-3.004087	C	5.065566	1.204623	0.287718
C	-0.686739	2.757788	-3.851300	C	5.065757	-1.204586	-0.287799
H	1.313443	2.277209	-3.186890	C	4.406788	2.443515	0.622092
C	-2.442232	1.790927	-2.493045	C	6.519348	1.197025	0.278300
C	-2.058212	2.574021	-3.588700	C	6.519538	-1.196783	-0.278272
H	-0.358161	3.358802	-4.693423	C	4.407180	-2.443568	-0.622245
H	-3.485312	1.623331	-2.253808	C	5.128985	3.590256	0.898365

H	-2.818924	3.025554	-4.216613	H	3.322700	2.473151	0.672892
N	-1.540118	1.194749	-1.664559	C	7.234963	2.411753	0.566346
N	0.068682	-0.000213	-0.000139	C	7.205163	0.000169	0.000043
N	-1.540074	-1.195032	1.664407	C	7.235347	-2.411409	-0.566270
Ru	-1.963614	-0.000062	-0.000034	H	3.323102	-2.473354	-0.673145
C	-1.799680	2.640919	1.910437	C	5.129562	-3.590206	-0.898468
C	-2.751240	3.494744	2.527278	C	6.563442	3.580980	0.863878
H	-0.721944	2.686781	1.947208	H	4.610382	4.511425	1.152192
C	-4.003871	2.993571	2.161605	H	8.322171	2.388820	0.549378
H	-2.553425	4.352787	3.149917	H	8.293480	0.000246	0.000081
H	-4.995352	3.338781	2.410027	C	6.564014	-3.580728	-0.863862
C	-4.675471	0.977936	0.704520	H	8.322550	-2.388324	-0.549220
C	-6.080422	1.003616	0.722878	H	4.611110	-4.511445	-1.152350
C	-6.768416	0.000775	0.000311	H	7.111424	4.493475	1.081471
H	-6.642562	1.758382	1.266503	H	7.112142	-4.493143	-1.081420
C	-4.675921	-0.977148	-0.704168				

3.10							
Atom	X	Y	Z	Atom	X	Y	Z
C	-0.080391	-1.759705	-3.794353	C	-5.311124	-0.195161	-0.066782
C	0.199903	-1.110822	-2.585511	C	4.292482	0.737924	0.297291
C	-2.102567	-0.994283	-2.038054	C	-6.802372	-0.316599	-0.134317
C	-2.433886	-1.643562	-3.240780	C	-7.479032	-1.219395	0.736052
C	-1.420750	-2.032126	-4.130417	C	-7.531080	0.473008	-1.070839
H	0.734985	-2.041588	-4.452068	C	-6.791604	-2.065188	1.680725
H	1.215863	-0.881337	-2.287903	C	-8.927101	-1.327282	0.663783
H	-3.473074	-1.843238	-3.478407	C	-8.977706	0.344644	-1.136936
H	-1.669214	-2.533826	-5.060424	C	-6.903661	1.427232	-1.951774
C	-3.101522	-0.551188	-1.043351	C	-7.484725	-2.933479	2.504406
C	-4.498312	-0.681733	-1.118830	H	-5.707800	-2.029725	1.736736
H	-4.968867	-1.156564	-1.972877	C	-9.612347	-2.239296	1.540808
C	-3.282996	0.528392	1.084439	C	-9.635209	-0.547223	-0.269342
C	-4.682884	0.414680	1.045569	C	-9.715374	1.140745	-2.081860
H	-5.296148	0.798576	1.853553	H	-5.828055	1.568071	-1.904740
C	-2.460182	1.137446	2.150198	C	-7.646938	2.178806	-2.843671
C	-2.994457	1.699226	3.323499	C	-8.915736	-3.020749	2.441271
C	-2.139948	2.258650	4.285714	H	-6.945308	-3.564904	3.206020
H	-4.067274	1.698943	3.482588	H	-10.696110	-2.304052	1.476789
C	-0.266545	1.673193	2.868160	H	-10.718701	-0.635606	-0.321085
C	-0.751235	2.243942	4.051511	C	-9.072494	2.032122	-2.917836
H	-2.545555	2.694089	5.193588	H	-10.796479	1.028819	-2.121265
H	0.793615	1.640263	2.648046	H	-7.152804	2.895500	-3.494901
H	-0.053332	2.664368	4.767794	H	-9.440631	-3.708276	3.098621
N	-1.086311	1.127520	1.926833	H	-9.637183	2.630665	-3.627192
N	-2.530719	0.047055	0.047291	C	5.771586	0.936211	0.397706
N	-0.775020	-0.728891	-1.713987	C	6.718483	-0.022431	-0.077284
Ru	-0.509685	0.241802	0.120922	C	6.243643	2.123547	1.003652
C	-0.909803	3.114816	-1.375905	C	8.126092	0.223797	0.109466
C	-0.041100	4.143833	-1.824341	C	6.332699	-1.227929	-0.784447
H	-1.985843	3.058479	-1.438850	C	7.610241	2.372153	1.177406

C	1.250027	3.720129	-1.495673	H	5.520205	2.846123	1.373339
H	-0.315435	5.063213	-2.316787	C	9.098292	-0.729310	-0.350326
H	2.205013	4.195695	-1.656344	C	8.572187	1.430693	0.748316
C	2.099248	1.583808	-0.330244	C	7.264474	-2.134211	-1.229213
C	3.491400	1.755231	-0.289167	H	5.280519	-1.400110	-0.985457
H	3.978518	2.632258	-0.706808	H	7.938702	3.289010	1.660814
C	2.279858	-0.544713	0.765428	C	8.677670	-1.928333	-1.016786
C	3.675894	-0.425647	0.834275	C	10.500829	-0.486508	-0.152282
H	4.296488	-1.180891	1.308198	C	9.988492	1.652136	0.935186
C	1.800864	-2.815704	1.886963	H	6.948478	-3.026593	-1.765506
C	0.602599	-3.494789	2.127083	C	9.647538	-2.857154	-1.460924
H	2.818772	-3.088651	2.118095	C	11.439923	-1.440594	-0.608834
C	-0.422883	-2.661407	1.608572	C	10.913285	0.732371	0.506920
H	0.486481	-4.453552	2.607018	H	10.306958	2.569123	1.425345
H	-1.489886	-2.824008	1.595464	C	11.015979	-2.614238	-1.255344
N	0.101159	-1.531730	1.077618	H	9.325050	-3.763976	-1.967408
N	-0.205971	2.110076	-0.803071	H	12.500894	-1.256641	-0.456657
C	1.468291	0.444067	0.188762	H	11.976559	0.907919	0.653104
N	1.146693	2.499397	-0.882356	H	11.751334	-3.335907	-1.600735
N	1.495784	-1.638167	1.256717				

4.1							
Atom	X	Y	Z	Atom	X	Y	Z
Ru	0.000026	1.383951	0.328315	C	0.000085	1.977173	-3.933465
Br	-0.000107	-4.865373	2.981020	H	0.000083	2.866675	-4.554073
N	-4.190587	0.857292	0.551960	C	-0.000067	-3.051545	2.208292
N	2.029851	0.974505	0.504020	C	7.236262	-1.098758	-2.050615
N	-2.029814	0.974564	0.503951	H	7.070199	-1.442953	-3.065410
N	0.000060	0.972333	-1.719866	C	-5.579501	1.359643	0.394297
C	0.000020	4.329777	0.381998	H	-5.490014	2.242765	-0.246396
N	0.000035	3.256342	-0.464052	H	-5.938317	1.688924	1.376582
N	3.138137	1.675762	0.206546	C	1.236450	-2.429834	1.944451
N	4.190620	0.857203	0.552167	H	2.164778	-2.949110	2.166243
N	0.000017	2.568595	2.050833	C	-8.502576	-1.095007	0.006712
C	-2.364399	-0.286151	1.037126	H	-9.336191	-1.438952	0.612969
C	0.000016	2.133332	3.341793	C	6.520796	0.323065	-0.192691
H	0.000011	1.058691	3.477694	C	-6.520767	0.323133	-0.192869
C	-3.756114	-0.343574	1.060565	C	-7.612245	-0.159047	0.557819
H	-4.437380	-1.118343	1.368063	H	-7.775240	0.202570	1.571877
C	-0.000010	-0.468189	1.110011	C	-7.236027	-1.099144	-2.050524
C	0.000007	5.803337	-1.542125	H	-7.069790	-1.443676	-3.065176
H	-0.000005	6.802984	-1.965069	C	-6.345581	-0.157917	-1.505619
N	-3.138070	1.675823	0.206375	H	-5.514509	0.204780	-2.109091
C	0.000017	3.937428	1.805447	C	8.337201	-1.589174	-1.309711
C	0.000039	3.396175	-1.823775	C	7.611997	-0.159559	0.558124
C	1.224209	-1.131595	1.392238	H	7.774796	0.201713	1.572337
C	0.000060	2.100918	-2.532679	C	8.502291	-1.095507	0.006947
C	0.000018	3.011057	4.433033	H	9.335679	-1.439825	0.613302
H	0.000017	2.611108	5.441502	C	-9.346963	-2.609066	-1.883487
C	3.756099	-0.343691	1.060660	C	-9.378837	-3.874982	-0.976316

H	4.437331	-1.118479	1.368181	H	-9.671906	-3.634588	0.052722
C	2.364385	-0.286226	1.037184	H	-10.104154	-4.599852	-1.367867
C	-1.236557	-2.429786	1.944436	H	-8.394890	-4.360531	-0.943350
H	-2.164908	-2.949026	2.166219	C	-10.764358	-1.962299	-1.913480
C	6.345845	-0.157546	-1.505630	H	-10.776788	-1.070375	-2.552980
H	5.514988	0.205492	-2.109193	H	-11.496273	-2.677855	-2.310047
C	0.000005	5.634164	-0.143435	H	-11.097702	-1.663498	-0.912358
H	-0.000010	6.500439	0.508951	C	-8.984772	-3.052901	-3.322868
C	-1.224259	-1.131552	1.392213	H	-8.985973	-2.208796	-4.024857
C	0.000019	4.399187	4.194322	H	-8.001382	-3.539584	-3.366329
H	0.000021	5.104506	5.019638	H	-9.726976	-3.777396	-3.679495
C	5.579560	1.359545	0.394561	C	9.346914	-2.609065	-1.883561
H	5.938359	1.688723	1.376887	C	10.764363	-1.962412	-1.913177
H	5.490086	2.242725	-0.246049	H	11.097546	-1.663828	-0.911937
C	0.000087	-0.258227	-2.304711	H	11.496298	-2.677933	-2.309769
H	0.000085	-1.102661	-1.626110	H	10.776976	-1.070353	-2.552491
C	0.000024	4.681475	-2.394442	C	8.984873	-3.052513	-3.323096
H	0.000025	4.816444	-3.470465	H	8.001451	-3.539110	-3.366791
C	0.000113	0.705125	-4.525784	H	8.986221	-2.208239	-4.024882
H	0.000132	0.602649	-5.606611	H	9.727077	-3.776960	-3.679821
C	0.000018	4.858033	2.868410	C	9.378547	-3.875225	-0.976716
H	0.000019	5.922554	2.660953	H	10.103823	-4.600067	-1.368394
C	-8.337236	-1.589138	-1.309735	H	9.671576	-3.635137	0.052406
C	0.000116	-0.431909	-3.694245	H	8.394549	-4.360676	-0.943963
H	0.000138	-1.434845	-4.107920				

4.2							
Atom	X	Y	Z	Atom	X	Y	Z
Ru	-0.015644	-0.204578	0.882929	C	0.016537	1.460626	-3.086962
Br	-0.144942	-6.924639	1.839395	H	0.036345	2.479099	-3.458907
N	-4.218114	-0.692362	0.977868	C	-0.107409	-4.973536	1.563607
N	2.006161	-0.682664	0.951927	C	6.998873	-1.836999	-2.276070
N	-2.054673	-0.604460	0.951001	H	6.780550	-1.839617	-3.339252
N	-0.012473	-0.076015	-1.203922	C	-5.594627	-0.145273	0.946496
C	0.041490	2.637860	1.675670	H	-5.474935	0.907224	0.670331
N	0.026059	1.808738	0.591588	H	-6.006869	-0.184490	1.961361
N	3.129378	0.049209	0.851958	C	1.141429	-4.327918	1.470178
N	4.164642	-0.851692	0.986302	H	2.058871	-4.904671	1.549881
N	-0.001985	0.511915	2.848224	C	-8.505086	-2.228092	-0.450631
C	-2.413414	-1.954826	1.145382	H	-9.386084	-2.743119	-0.081356
C	-0.016496	-0.235325	3.987077	C	6.447353	-1.129801	0.002305
H	-0.038280	-1.309187	3.846312	C	-6.501267	-0.883916	-0.024331
C	-3.805320	-1.991556	1.159739	C	-7.645592	-1.559701	0.443181
H	-4.498357	-2.809030	1.264049	H	-7.881306	-1.566576	1.505478
C	-0.053808	-2.192879	1.168375	C	-7.070164	-1.546233	-2.311910
C	0.096232	4.576752	0.188423	H	-6.853465	-1.537497	-3.375389
N	-3.149364	0.169124	0.847604	C	-6.224458	-0.881206	-1.409125
C	0.027141	1.898456	2.955960	H	-5.349447	-0.357238	-1.789010
C	0.042293	2.294566	-0.683625	C	8.122064	-2.523020	-1.777911
C	1.155891	-2.931135	1.272127	C	7.577937	-1.822523	0.478265

C	0.015137	1.222725	-1.701083	H	7.814682	-1.819456	1.540328
C	-0.003329	0.337304	5.265115	C	8.422212	-2.521207	-0.406836
H	-0.015751	-0.304780	6.139512	H	9.292743	-3.049194	-0.031085
C	3.702706	-2.134400	1.167409	C	0.139511	6.045343	-0.029322
H	4.364206	-2.977150	1.275377	C	-0.499665	6.940925	0.862456
C	2.313184	-2.045427	1.148252	C	0.821574	6.600328	-1.134903
C	-1.330412	-4.280371	1.468931	C	-0.456440	8.324693	0.649720
H	-2.269418	-4.821450	1.548027	H	-1.064296	6.555175	1.708462
C	6.168408	-1.141713	-1.382006	C	0.864015	7.989248	-1.341658
H	5.303505	-0.605811	-1.768344	H	1.356625	5.951404	-1.824901
C	0.079653	4.028694	1.497053	C	0.226724	8.888652	-0.457480
H	0.124717	4.691416	2.353740	H	-0.971346	8.973126	1.353765
C	-1.291026	-2.884097	1.270810	H	1.410449	8.366513	-2.199082
C	0.026223	1.740131	5.384601	C	0.247820	10.420123	-0.656408
H	0.037552	2.214096	6.361253	C	1.058871	10.840659	-1.907193
C	5.560223	-0.355584	0.963438	H	2.109613	10.530031	-1.837437
H	5.963340	-0.405529	1.981509	H	0.633582	10.424816	-2.829940
H	5.481032	0.699645	0.682833	H	1.044635	11.933131	-2.002168
C	-0.036625	-1.115483	-2.084685	C	-1.213234	10.934805	-0.825350
H	-0.057017	-2.105760	-1.646143	H	-1.832203	10.703380	0.049868
C	0.073613	3.678221	-0.909235	H	-1.215184	12.024565	-0.956854
H	0.055884	4.070475	-1.919544	H	-1.689539	10.483883	-1.705418
C	-0.009152	0.383082	-3.985472	C	0.890856	11.094032	0.592215
H	-0.008732	0.560597	-5.056531	H	0.336520	10.867596	1.510981
C	0.041367	2.519038	4.217417	H	1.926553	10.758048	0.730563
H	0.064795	3.601118	4.285910	H	0.899081	12.184605	0.468094
C	-8.206470	-2.216404	-1.822013	Br	-9.393854	-3.144529	-3.078500
C	-0.035759	-0.928434	-3.472513	Br	9.288402	-3.493221	-3.022297
H	-0.055873	-1.792149	-4.128774				

4.3							
Atom	X	Y	Z	Atom	X	Y	Z
Ru	-0.000065	-0.299069	-0.043366	H	0.000017	-2.115026	5.660504
Br	-0.000148	6.484927	0.211079	C	0.000197	-2.361795	-3.820648
N	-4.195489	0.272384	-0.017807	H	0.000363	-3.413221	-4.086729
N	2.029485	0.146309	-0.026319	C	-0.000237	-0.366077	4.369432
N	-2.029612	0.146265	-0.026319	H	-0.000408	0.365682	5.170326
N	-0.000047	-0.797296	1.985160	C	0.000213	-2.648001	3.561469
C	0.000388	-2.942416	-1.345624	H	0.000389	-3.716999	3.744662
N	0.000209	-2.331067	-0.123232	C	-0.000134	4.515858	0.139550
N	3.134805	-0.616731	-0.055217	C	1.235968	3.840121	0.114330
N	4.195354	0.272545	-0.017832	H	2.164364	4.404411	0.133878
N	-0.000034	-0.638613	-2.106698	C	-5.546573	-0.213081	-0.027374
C	-2.362745	1.514112	0.025101	C	-5.831801	-1.495967	0.468289
C	-0.000234	0.305007	-3.088927	C	-6.581639	0.600934	-0.535965
H	-0.000382	1.335156	-2.753894	C	-7.153095	-1.971545	0.467515
C	-3.751909	1.578414	0.032190	H	-5.026968	-2.114856	0.850048
H	-4.420919	2.418243	0.101037	C	-7.898578	0.135309	-0.527143
C	-0.000107	1.709480	0.036826	H	-6.366961	1.580478	-0.953737
C	0.000944	-5.094027	-0.229907	C	-8.194071	-1.153134	-0.025111

H	0.001229	-6.178688	-0.272202	H	-7.357563	-2.963610	0.855330
N	-3.134891	-0.616835	-0.055217	H	-8.712144	0.740737	-0.912690
C	0.000188	-1.981524	-2.467159	C	5.546465	-0.212849	-0.027377
C	0.000393	-3.035265	1.048281	C	5.831757	-1.495707	0.468321
C	1.223420	2.430261	0.062334	C	6.581490	0.601200	-0.535999
C	0.000190	-2.164183	2.240978	C	7.153076	-1.971216	0.467563
C	-0.000236	-0.024432	-4.450157	H	5.026958	-2.114636	0.850088
H	-0.000404	0.766739	-5.192368	C	7.898453	0.135646	-0.527157
C	3.751706	1.578553	0.032079	H	6.366757	1.580718	-0.953804
H	4.420666	2.418426	0.100890	C	8.194013	-1.152756	-0.025057
C	2.362542	1.514171	0.025046	H	7.357588	-2.963275	0.855371
C	-1.236223	3.840100	0.114353	H	8.711988	0.741096	-0.912733
H	-2.164629	4.404370	0.133930	C	-9.933398	-2.826966	0.433089
C	0.000764	-4.346382	-1.424165	H	-9.692594	-2.934135	1.499136
H	0.000931	-4.853620	-2.382586	H	-11.014631	-2.864130	0.293887
C	-1.223648	2.430237	0.062356	H	-9.457256	-3.630829	-0.144058
C	-0.000018	-1.381860	-4.824867	C	9.933394	-2.826522	0.433126
H	-0.000014	-1.668725	-5.871894	H	9.457241	-3.630399	-0.143996
C	-0.000253	0.067567	3.037966	H	11.014623	-2.863664	0.293886
H	-0.000426	1.120727	2.784411	H	9.692639	-2.933699	1.499183
C	0.000766	-4.441262	1.018671	O	-9.530499	-1.513769	-0.065355
H	0.000927	-5.020783	1.935340	O	9.530452	-1.513344	-0.065310
C	0.000001	-1.748625	4.638572				

4.4							
Atom	X	Y	Z	Atom	X	Y	Z
Ru	0.000002	-0.169783	-0.014792	C	1.236090	3.971906	0.006733
Br	-0.000019	6.618447	0.018764	H	2.164394	4.536680	0.009575
N	-4.195313	0.399774	-0.003292	C	-5.544782	-0.098824	0.001794
N	2.028396	0.274883	-0.011373	C	-5.775245	-1.488292	0.031342
N	-2.028395	0.274871	-0.011535	C	-6.631801	0.790463	-0.021514
N	-0.000089	-0.599139	2.031174	C	-7.090302	-1.967742	0.038608
C	0.000054	-2.856277	-1.225519	H	-4.934909	-2.172487	0.048443
N	0.000006	-2.203803	-0.024591	C	-7.944638	0.288172	-0.012081
N	3.132163	-0.487275	-0.011647	H	-6.482989	1.865936	-0.047882
N	4.195314	0.399800	-0.003211	C	-8.210062	-1.098370	0.018470
N	0.000095	-0.579778	-2.065078	H	-7.242958	-3.042957	0.061558
C	-2.362420	1.643961	-0.003287	H	-8.763123	0.998728	-0.029536
C	0.000139	0.329819	-3.078995	C	5.544786	-0.098797	0.001890
H	0.000131	1.370911	-2.779596	C	5.775241	-1.488325	0.028577
C	-3.750751	1.706796	0.002148	C	6.631817	0.790545	-0.018535
H	-4.412583	2.553969	0.012333	C	7.090297	-1.967777	0.035876
C	-0.000005	1.839879	-0.004193	H	4.934903	-2.172565	0.043512
C	0.000009	-4.968639	-0.037502	C	7.944651	0.288242	-0.009314
H	0.000009	-6.054103	-0.042612	H	6.483031	1.866081	-0.042364
N	-3.132159	-0.487294	-0.011952	C	8.210066	-1.098360	0.018411
C	0.000102	-1.934212	-2.379438	H	7.242946	-3.043036	0.056637
C	-0.000041	-2.867541	1.170191	H	8.763142	0.998841	-0.024616
C	1.223643	2.561132	-0.000131	C	-9.640211	-1.680937	0.030356
C	-0.000090	-1.956451	2.332786	C	9.640208	-1.680942	0.030300

C	0.000190	-0.045878	-4.428105	C	-10.726605	-0.577139	0.010030
H	0.000223	0.719571	-5.196817	H	-10.664750	0.042962	-0.893827
C	3.750742	1.706819	0.002034	H	-11.719770	-1.042174	0.021047
H	4.412563	2.554005	0.011736	H	-10.661560	0.078884	0.887933
C	2.362411	1.643975	-0.003306	C	-9.838206	-2.584138	-1.223523
C	-1.236111	3.971898	0.006786	H	-9.122966	-3.415464	-1.248104
H	-2.164420	4.536667	0.009664	H	-10.848318	-3.013481	-1.220518
C	0.000055	-4.262196	-1.256565	H	-9.716025	-2.005784	-2.148320
H	0.000087	-4.801762	-2.197219	C	-9.836931	-2.535205	1.318335
C	-1.223656	2.561124	-0.000081	H	-9.124604	-3.367582	1.372510
C	0.000195	-1.415348	-4.756352	H	-9.709872	-1.922521	2.220096
H	0.000232	-1.737649	-5.793022	H	-10.848454	-2.960889	1.334808
C	-0.000136	0.300868	3.053680	C	9.836209	-2.536660	1.317437
H	-0.000132	1.344780	2.764264	H	9.123703	-3.368969	1.370349
C	-0.000038	-4.273692	1.188141	H	10.847664	-2.962505	1.333925
H	-0.000071	-4.821977	2.123752	H	9.708808	-1.924939	2.219802
C	-0.000183	-1.460020	4.714551	C	10.726614	-0.577123	0.011768
H	-0.000217	-1.791992	5.748163	H	11.719773	-1.042180	0.022436
C	0.000151	-2.360530	-3.719273	H	10.664988	0.044198	-0.891266
H	0.000151	-3.420470	-3.949001	H	10.661355	0.077709	0.890543
C	-0.000184	-0.087502	4.399156	C	9.838932	-2.582713	-1.224481
H	-0.000219	0.670725	5.175001	H	9.717125	-2.003348	-2.148695
C	-0.000136	-2.395387	3.668596	H	10.849109	-3.011902	-1.221457
H	-0.000131	-3.457455	3.888233	H	9.123871	-3.414150	-1.250376
C	-0.000013	4.648121	0.009789				

4.5							
Atom	X	Y	Z	Atom	X	Y	Z
Ru	-0.014438	-1.541918	0.004077	C	5.546128	-1.680882	-0.026154
N	-4.214893	-2.069815	0.020170	C	6.198238	-1.452973	1.207891
N	2.011530	-2.003845	-0.002817	C	6.181537	-1.470773	-1.270574
N	-2.048992	-1.966487	0.014241	C	7.533958	-1.012291	1.169827
N	-0.018696	-1.126119	-2.043472	C	7.519316	-1.029733	-1.255909
C	0.017150	1.160516	1.183948	C	8.213483	-0.801228	-0.049642
N	0.003401	0.490534	-0.005533	H	8.053445	-0.827947	2.107682
N	3.121973	-1.247360	-0.014296	H	8.026434	-0.859816	-2.202823
N	4.175137	-2.146395	-0.013781	C	-9.670148	-0.180902	0.021478
N	-0.002254	-1.108078	2.047325	H	-9.955186	0.251309	-0.943813
C	-2.395179	-3.334092	0.025361	H	-10.355634	-1.015783	0.224364
C	-0.007601	-2.007586	3.070932	H	-9.841863	0.575343	0.796794
H	-0.017185	-3.051303	2.780375	C	9.662200	-0.352270	-0.058125
C	-3.785650	-3.380296	0.029229	H	10.335753	-1.199829	0.131771
H	-4.475684	-4.206868	0.037244	H	9.944147	0.081834	-1.023468
C	-0.033068	-3.553855	0.017180	H	9.854797	0.395631	0.720373
C	0.025792	3.288350	-0.017501	C	-5.488830	-1.544317	2.574887
N	-3.145648	-1.190016	0.010912	H	-5.174021	-2.588476	2.704301
C	0.010734	0.250308	2.348235	H	-4.585758	-0.923280	2.634790
C	0.000330	1.150400	-1.200750	H	-6.135798	-1.284232	3.418281
C	1.185625	-4.285722	0.017334	C	-5.509424	-1.609004	-2.537149
C	-0.008405	0.229564	-2.356748	H	-4.603643	-0.994281	-2.617678

C	-0.001546	-1.619010	4.416139	H	-5.201107	-2.657399	-2.646192
H	-0.006452	-2.377100	5.192280	H	-6.161660	-1.364102	-3.381006
C	3.722231	-3.448926	-0.001971	C	5.451514	-1.693661	-2.581635
H	4.397221	-4.287872	0.000003	H	5.117025	-2.734029	-2.690329
C	2.332802	-3.377491	0.005232	H	4.560098	-1.057074	-2.652237
C	-1.283190	-5.673839	0.038797	H	6.101547	-1.462058	-3.430906
H	-2.220344	-6.227512	0.047208	C	5.484470	-1.658902	2.530643
C	0.025514	2.562732	1.201361	H	4.589022	-1.027982	2.600876
H	0.005385	3.100300	2.142580	H	5.159124	-2.699785	2.660416
C	-1.264872	-4.263226	0.027937	H	6.142409	-1.408554	3.368489
C	0.010410	-0.246037	4.730976	H	-0.068736	-7.465910	0.046887
H	0.014410	0.086762	5.764424	C	0.037359	4.773871	-0.022748
C	-0.028533	-2.034939	-3.058700	C	-0.632758	5.509341	-1.025244
H	-0.036984	-3.075927	-2.758406	C	0.720084	5.505054	0.979682
C	0.014491	2.552498	-1.230213	C	-0.623103	6.914620	-1.026406
H	0.043419	3.081867	-2.175873	H	-1.199284	4.988003	-1.793688
C	-0.016191	-0.288678	-4.734792	C	0.727910	6.905473	0.972324
H	-0.014402	0.034702	-5.771236	H	1.279036	4.978540	1.749980
C	0.016731	0.688482	3.684386	C	0.056416	7.650282	-0.029615
H	0.025165	1.750702	3.902894	H	-1.162245	7.433578	-1.811230
C	-0.027702	-1.658704	-4.407478	H	1.275172	7.424724	1.754307
H	-0.035599	-2.423814	-5.176671	C	0.090748	9.194237	0.002778
C	-0.006736	0.655422	-3.696842	C	-0.537553	9.694798	1.337877
H	0.002908	1.715572	-3.925203	H	0.004206	9.314618	2.212507
C	-0.058800	-6.379251	0.038683	H	-0.509403	10.791432	1.378656
C	1.178275	-5.696413	0.028052	H	-1.584267	9.375981	1.423910
H	2.105208	-6.267092	0.028210	C	-0.696123	9.826433	-1.172078
C	-5.577397	-1.579831	0.019086	H	-0.281784	9.534747	-2.146016
C	-6.212668	-1.333672	1.258400	H	-1.758284	9.549691	-1.149161
C	-6.221808	-1.365622	-1.219995	H	-0.639421	10.919783	-1.104616
C	-7.540876	-0.870088	1.231410	C	1.569557	9.677552	-0.082626
C	-7.551450	-0.901144	-1.194239	H	1.609369	10.774131	-0.051323
C	-8.229172	-0.654183	0.017734	H	2.173040	9.298020	0.750837
H	-8.047330	-0.671374	2.173433	H	2.038030	9.344789	-1.017727
H	-8.065279	-0.727540	-2.136871				

4.6							
Atom	X	Y	Z	Atom	X	Y	Z
Ru	1.071212	-0.003924	0.005083	C	-0.231070	-5.795914	-0.469324
Br	7.858137	-0.088585	-0.067170	C	1.888555	-6.607644	0.433324
N	1.587864	-4.205334	-0.013842	C	-0.719269	-7.110030	-0.473512
N	1.539417	2.018816	0.010438	H	-0.848183	-4.970074	-0.805680
N	1.488563	-2.037906	-0.004408	C	1.385583	-7.919516	0.411181
N	0.631725	0.007039	-2.039830	H	2.888086	-6.424458	0.817739
C	-1.620273	0.013271	1.214761	C	0.077739	-8.197068	-0.042570
N	-0.963284	0.015734	0.018425	H	-1.732138	-7.296565	-0.823185
N	0.790568	3.132306	0.023477	H	2.015526	-8.733131	0.761467
N	1.692845	4.183155	0.018841	C	1.217580	5.539076	0.027463
N	0.657114	-0.004477	2.056265	C	-0.090749	5.820153	-0.410838
C	2.854444	-2.388986	-0.018908	C	2.056026	6.575247	0.476138

C	1.566676	-0.012252	3.069995	C	-0.547341	7.145550	-0.402789
H	2.607664	-0.021995	2.770184	H	-0.730797	5.011258	-0.745395
C	2.900614	-3.778255	-0.026921	C	1.584357	7.898834	0.466613
H	3.734566	-4.456430	-0.070505	H	3.054583	6.366391	0.849779
C	3.079284	-0.029091	-0.013662	C	0.279363	8.210579	0.027053
C	-3.760867	0.030477	0.035391	H	-1.558900	7.358207	-0.741183
N	0.712080	-3.132441	-0.000070	H	2.236927	8.694865	0.815947
C	-0.697620	0.007125	2.370181	C	-0.458999	-9.614748	-0.077359
C	-1.634796	0.025351	-1.169727	H	0.197404	-10.307590	0.459642
C	3.816377	1.185556	-0.016879	H	-1.456759	-9.675311	0.374988
C	-0.727013	0.018656	-2.336719	H	-0.548900	-9.976703	-1.110921
C	1.191723	-0.007906	4.419278	C	-0.223483	9.640861	0.006247
H	1.957455	-0.014232	5.187716	H	-1.218436	9.721127	0.461635
C	2.994531	3.723454	0.002521	H	0.450571	10.312933	0.547775
H	3.845409	4.380621	-0.034696	H	-0.307027	10.014216	-1.023817
C	2.913674	2.335737	-0.000914	C	-5.246295	0.036271	0.043063
C	5.196083	-1.291789	-0.042068	C	-5.982100	0.703779	-0.966397
H	5.749333	-2.226999	-0.051671	C	-5.977456	-0.625315	1.054520
C	-3.022345	0.024311	1.246853	C	-7.382428	0.705218	-0.957276
H	-3.549482	0.053772	2.193620	H	-5.459729	1.255652	-1.744608
C	3.785670	-1.261742	-0.026133	C	-7.382683	-0.622470	1.057207
C	-0.177564	0.004985	4.747331	H	-5.453044	-1.179813	1.829602
H	-0.500050	0.009541	5.783960	C	-8.122852	0.041723	0.053348
C	1.528341	0.002059	-3.065457	H	-7.905387	1.240640	-1.744921
H	2.573109	-0.006636	-2.779177	H	-7.898197	-1.154643	1.848982
C	-3.037180	0.029367	-1.184883	C	-9.666892	0.068086	0.022260
H	-3.575899	0.004710	-2.125275	C	-10.157044	1.545479	0.093171
C	-0.237179	0.017660	-4.720624	H	-9.781453	2.142396	-0.746817
H	-0.572631	0.020934	-5.753145	H	-11.253768	1.579544	0.062663
C	-1.122654	0.012267	3.710131	H	-9.825772	2.025035	1.023162
H	-2.182427	0.023086	3.939875	C	-10.165441	-0.576214	-1.305964
C	1.136279	0.007179	-4.409772	H	-9.841706	-1.622219	-1.381709
H	1.892315	0.002624	-5.187761	H	-11.262167	-0.554011	-1.345780
C	-1.168979	0.023640	-3.671422	H	-9.789127	-0.041475	-2.186534
H	-2.231685	0.031273	-3.887495	C	-10.293987	-0.709974	1.205648
C	5.887523	-0.064096	-0.045150	H	-10.011360	-1.770774	1.193645
C	5.227089	1.180479	-0.032663	H	-10.004542	-0.283873	2.175143
H	5.803527	2.101620	-0.035118	H	-11.387612	-0.660237	1.138056
C	1.079438	-5.549151	-0.017074				

4.7							
Atom	X	Y	Z	Atom	X	Y	Z
Ru	-0.690871	-0.669621	0.334580	C	0.318184	4.040305	0.455850
Br	0.729345	5.967456	0.505609	C	4.651063	-1.786034	1.520378
N	3.436085	-0.987620	1.212419	H	4.389891	-2.814837	1.253602
N	-2.537275	0.191431	-0.077619	H	4.820137	-1.748009	2.602890
N	1.342219	-0.660159	0.771859	C	-1.004337	3.638911	0.182268
N	-0.348898	-1.117956	-1.676507	H	-1.773402	4.385335	0.003810
C	-1.513029	-3.275743	1.433933	C	8.094709	-0.263161	0.778091
N	-1.120988	-2.655689	0.280578	H	8.905682	0.183241	1.347274

N	-3.751750	-0.324746	-0.328676	C	5.878364	-1.296210	0.773249
N	-4.578736	0.768216	-0.526485	C	6.953359	-0.704267	1.467473
N	-1.205295	-1.039863	2.325431	H	6.905756	-0.595257	2.549941
C	1.947992	0.608106	0.872164	C	7.122155	-0.989403	-1.311130
C	-1.220509	-0.137986	3.346452	H	7.163912	-1.117558	-2.387204
H	-0.935226	0.874087	3.086037	C	5.979379	-1.435773	-0.625115
C	3.292292	0.378033	1.155221	H	5.165839	-1.897412	-1.183191
H	4.121740	1.050401	1.292781	C	9.483060	0.101725	-1.347462
C	-0.269467	1.295570	0.386103	C	9.662413	1.627214	-1.087444
C	-1.719816	-5.354226	0.205077	H	9.754984	1.851421	-0.017917
H	-1.955590	-6.413335	0.175344	H	10.571860	1.989368	-1.584053
N	2.244121	-1.636676	0.977966	H	8.809518	2.195927	-1.480098
C	-1.557573	-2.358955	2.590893	C	10.718985	-0.664523	-0.788816
C	-1.015159	-3.320693	-0.908850	H	10.623864	-1.744222	-0.961337
C	-1.287739	2.257319	0.149504	H	11.633381	-0.318057	-1.287671
C	-0.576540	-2.447456	-2.015854	H	10.846209	-0.505111	0.288727
C	-1.579172	-0.486564	4.654492	C	9.421951	-0.126018	-2.878320
H	-1.573842	0.271203	5.430855	H	9.327476	-1.190411	-3.130133
C	-3.884122	1.951910	-0.399382	H	8.586691	0.416556	-3.340458
H	-4.361811	2.909655	-0.518284	H	10.347317	0.240113	-3.339421
C	-2.569111	1.601077	-0.111641	C	-5.984978	0.589065	-0.824031
C	1.357954	3.120177	0.695445	C	-6.896896	0.469846	0.250358
H	2.363325	3.476691	0.901605	C	-6.392839	0.542503	-2.175928
C	-1.821900	-4.647520	1.419547	C	-8.259091	0.310563	-0.064120
H	-2.134924	-5.160703	2.322090	C	-7.767627	0.382532	-2.438617
C	1.050779	1.743594	0.657895	C	-8.715102	0.271054	-1.399832
C	-1.939403	-1.819519	4.932674	H	-8.977639	0.213933	0.746840
H	-2.222208	-2.120239	5.936779	H	-8.103022	0.341704	-3.472279
C	0.063321	-0.253815	-2.645852	C	-5.392659	0.647231	-3.311969
H	0.228067	0.768321	-2.327013	H	-4.896124	1.626840	-3.328228
C	-1.314884	-4.693165	-0.971273	H	-4.607364	-0.114474	-3.223753
H	-1.239593	-5.241379	-1.903931	H	-5.889145	0.511714	-4.277634
C	0.033375	-1.994916	-4.327590	C	-6.429801	0.499222	1.693400
H	0.179442	-2.332994	-5.348881	H	-5.703311	-0.299018	1.892536
C	-1.926044	-2.756662	3.888424	H	-5.943867	1.451791	1.944450
H	-2.198732	-3.788781	4.079965	H	-7.274573	0.366837	2.376204
C	8.207672	-0.392757	-0.627497	C	-10.193060	0.124086	-1.706345
C	0.264188	-0.651168	-3.973544	H	-10.714348	1.084935	-1.591936
H	0.592762	0.078058	-4.706535	H	-10.359825	-0.220046	-2.732763
C	-0.389056	-2.893609	-3.336213	H	-10.674356	-0.588751	-1.026183
H	-0.571784	-3.933119	-3.585857				

4.8							
Atom	X	Y	Z	Atom	X	Y	Z
Ru	-0.090069	-0.772498	0.345591	H	-6.402674	3.754875	-2.350155
Br	-4.766262	-5.691803	0.495100	C	-5.288767	3.373351	-0.554695
N	-3.431699	1.640507	1.302671	H	-4.343208	3.288118	-1.088641
N	1.031503	-2.463369	-0.103618	C	-9.028893	4.078801	-1.377173
N	-1.821727	0.274952	0.822394	C	-10.053489	2.933978	-1.120165
N	-0.180542	-0.180860	-1.656632	H	-10.281572	2.820526	-0.053528

C	1.995584	1.012634	1.423704
N	1.310231	0.700125	0.285298
N	2.334657	-2.654677	-0.367229
N	2.466897	-4.016312	-0.584404
N	0.584432	-0.745712	2.324426
C	-2.999788	-0.492270	0.925502
C	0.149750	-1.537208	3.344533
H	-0.624165	-2.251388	3.090531
C	-4.022674	0.401447	1.233681
H	-5.079427	0.258458	1.381670
C	-1.473238	-2.228671	0.394831
C	3.243242	2.721084	0.200348
N	-2.078680	1.575171	1.050993
C	1.578062	0.193485	2.581028
C	1.542958	1.348370	-0.893179
C	-1.110645	-3.577090	0.131840
C	0.696010	0.844976	-1.994906
C	0.663052	-1.442536	4.644001
H	0.280012	-2.097072	5.419818
C	1.257078	-4.664251	-0.456447
H	1.162414	-5.728490	-0.590754
C	0.321873	-3.682229	-0.146675
C	-3.810828	-2.939534	0.720390
H	-4.851739	-2.722178	0.943110
C	2.967221	2.023844	1.404578
H	3.494121	2.296640	2.311842
C	-2.830217	-1.925718	0.687436
C	1.668426	-0.493906	4.913954
H	2.085270	-0.395074	5.911541
C	-0.994856	-0.694017	-2.620970
H	-1.657935	-1.489933	-2.303702
C	2.508827	2.363319	-0.959263
H	2.719654	2.860554	-1.899248
C	-0.099500	0.807785	-4.294784
H	-0.066915	1.188418	-5.311041
C	2.123894	0.325597	3.869978
H	2.896545	1.063626	4.055303
C	-7.715781	3.770609	-0.622231
C	-0.984256	-0.229854	-3.942066
H	-1.653953	-0.674387	-4.670747
C	0.742976	1.343628	-3.308775
H	1.432634	2.142764	-3.557596
C	-3.407850	-4.263025	0.453875
C	-4.046621	2.951431	1.630435
H	-3.268301	3.690229	1.414541
H	-4.249053	2.976791	2.707585
C	-2.074019	-4.607510	0.158586
H	-1.811364	-5.642746	-0.040816
C	-7.730650	3.615776	0.785083
H	-8.666156	3.710497	1.329830
H	-10.995589	3.147978	-1.641289
H	-9.670233	1.973347	-1.488088
C	-9.616056	5.423611	-0.854005
H	-8.917026	6.251720	-1.028040
H	-10.554628	5.653287	-1.374941
H	-9.831476	5.384835	0.220574
C	-8.815586	4.204470	-2.906474
H	-8.129135	5.023405	-3.158354
H	-8.424794	3.275981	-3.343365
H	-9.775210	4.418808	-3.392608
C	3.756839	-4.594506	-0.898895
C	4.564188	-5.071777	0.159672
C	4.160056	-4.660417	-2.251376
C	5.807494	-5.640633	-0.172668
C	5.413254	-5.239260	-2.532491
C	6.246996	-5.739379	-1.510779
H	6.445933	-6.011599	0.626181
H	5.743711	-5.298536	-3.566849
C	3.287826	-4.115728	-3.366627
H	2.312775	-4.619750	-3.404445
H	3.094310	-3.043809	-3.230823
H	3.771704	-4.252399	-4.338512
C	4.119169	-4.966712	1.606320
H	3.885669	-3.929066	1.877190
H	3.217836	-5.564049	1.799259
H	4.904483	-5.324449	2.279210
C	7.581003	-6.381897	-1.838937
H	7.505917	-7.477976	-1.807643
H	7.926945	-6.104310	-2.840437
H	8.354544	-6.089325	-1.118814
C	4.271051	3.792702	0.155319
C	4.119612	4.919354	-0.689325
C	5.435445	3.725384	0.951900
C	5.090460	5.928232	-0.727943
H	3.222068	5.027804	-1.294171
C	6.407403	4.739153	0.906856
H	5.608877	2.860217	1.588081
C	6.261887	5.867024	0.068218
H	4.926157	6.780621	-1.381711
H	7.289338	4.636216	1.529310
C	7.307773	7.001511	-0.004541
C	8.511285	6.755129	0.938729
H	9.220837	7.587053	0.851957
H	8.201458	6.695681	1.990276
H	9.051325	5.834100	0.682978
C	6.636335	8.347114	0.402892
H	7.367390	9.164051	0.346604
H	5.798564	8.603360	-0.256935
H	6.254683	8.300532	1.430936
C	7.844169	7.114443	-1.462897

C	-5.318814	3.219166	0.845466	H	8.331462	6.182126	-1.776045
C	-6.557226	3.343790	1.507295	H	7.041574	7.332850	-2.177738
H	-6.606799	3.237944	2.589961	H	8.581265	7.925008	-1.530645
C	-6.466680	3.640654	-1.273562				

4.9

Atom	X	Y	Z	Atom	X	Y	Z
C	-1.074338	0.206877	-4.413718	N	-2.820448	2.333007	0.111389
C	-1.459519	0.148773	-3.068520	C	3.843362	-0.000615	-0.000030
C	0.799294	0.107205	-2.354674	C	5.340329	-0.000727	-0.000017
C	1.235224	0.165298	-3.690332	C	6.046601	-1.166461	0.418852
C	0.297216	0.214971	-4.732917	C	6.046781	1.164910	-0.418855
H	-1.834423	0.244612	-5.186774	C	5.388133	-2.386226	0.818117
H	-2.503417	0.141465	-2.779185	C	7.500380	-1.155079	0.421842
H	2.296770	0.171639	-3.912292	C	7.500559	1.153325	-0.421782
H	0.626613	0.259180	-5.766293	C	5.388502	2.384769	-0.818144
C	1.714236	0.053355	-1.195026	C	6.110611	-3.497323	1.213736
C	3.118850	0.052422	-1.215386	H	4.303946	-2.438982	0.794574
H	3.662720	0.084329	-2.153110	C	8.216286	-2.329536	0.844660
C	1.714220	-0.054185	1.194956	C	8.186119	-0.000925	0.000044
C	3.118833	-0.053521	1.215322	C	8.216647	2.327684	-0.844564
H	3.662693	-0.085514	2.153049	H	4.304321	2.437675	-0.794653
C	0.799267	-0.107812	2.354605	C	6.111152	3.495767	-1.213726
C	1.235188	-0.166109	3.690257	C	7.545061	-3.471033	1.235812
C	0.297171	-0.215562	4.732845	H	5.591982	-4.406810	1.506635
H	2.296733	-0.172785	3.912210	H	9.303498	-2.301109	0.845467
C	-1.459554	-0.148751	3.068462	H	9.274436	-0.001000	0.000069
C	-1.074382	-0.207046	4.413654	C	7.545599	3.469277	-1.235739
H	0.626561	-0.259927	5.766218	H	9.303855	2.299106	-0.845324
H	-2.503451	-0.141108	2.779135	H	5.592662	4.405327	-1.506647
H	-1.834474	-0.244601	5.186713	H	8.093257	-4.353935	1.552395
N	-0.558372	-0.098422	2.048236	H	8.093932	4.352104	-1.552294
N	1.049719	-0.000350	-0.000036	C	-1.497640	-5.767766	-0.285602
N	-0.558346	0.098236	-2.048296	C	-2.462396	-6.714712	0.134538
Ru	-0.981982	0.000011	-0.000030	C	-0.257154	-6.240495	-0.776749
C	-0.827283	-3.254627	-0.170013	C	-2.197581	-8.092111	0.059755
C	-1.776222	-4.320671	-0.215689	H	-3.414157	-6.377248	0.539088
H	0.250209	-3.313029	-0.161948	C	0.011979	-7.617888	-0.843457
C	-3.027167	-3.685680	-0.176280	H	0.491752	-5.534120	-1.128415
H	-4.020887	-4.103096	-0.214045	C	-0.957823	-8.550887	-0.427585
C	-3.692073	-1.202101	-0.056785	H	-2.949893	-8.804854	0.387486
C	-5.097378	-1.238189	-0.058130	H	0.968567	-7.963552	-1.226979
C	-5.770111	0.001153	0.000097	H	-0.751744	-9.616444	-0.482367
H	-5.660965	-2.164727	-0.102243	C	-1.494884	5.768037	0.285558
C	-3.691495	1.203417	0.056848	C	-0.254179	6.240189	0.776706
C	-5.096782	1.240173	0.058280	C	-2.459192	6.715431	-0.134602
H	-5.659927	2.166978	0.102430	C	0.015600	7.617456	0.843403
C	-3.025399	3.686680	0.176276	H	0.494391	5.533466	1.128388
C	-1.774149	4.321074	0.215655	C	-2.193730	8.092706	-0.059832
H	-4.018917	4.104573	0.214091	H	-3.411107	6.378407	-0.539158

C	-0.825721	3.254580	0.169852	C	-0.953763	8.550906	0.427514
H	0.251799	3.312461	0.161689	H	0.972346	7.962676	1.226930
N	-1.439643	2.052599	0.105397	H	-2.945705	8.805798	-0.387577
N	-1.440627	-2.052355	-0.105455	H	-0.747186	9.616367	0.482288
C	-2.969807	0.000486	0.000012	Br	-7.734727	0.001618	0.000164
N	-2.821567	-2.332106	-0.111380				

4.10

Atom	X	Y	Z	Atom	X	Y	Z
C	-0.148051	-1.006187	-4.415468	C	-1.165664	6.114977	-0.418821
C	-0.107093	-1.391147	-3.069637	C	2.384607	5.456034	0.818944
C	-0.077052	0.867820	-2.355693	C	1.154264	7.568814	0.421259
C	-0.118129	1.303505	-3.692088	C	-1.154543	7.568759	-0.421333
C	-0.153406	0.365347	-4.735036	C	-2.384783	5.455920	-0.819022
H	-0.174741	-1.766448	-5.188826	C	3.496123	6.178199	1.213851
H	-0.102202	-2.434972	-2.779971	H	2.436178	4.371736	0.796819
H	-0.122337	2.365040	-3.914177	C	2.329189	8.284365	0.843411
H	-0.184382	0.694574	-5.768959	C	-0.000156	8.254492	-0.000036
C	-0.038685	1.782767	-1.195692	C	-2.329502	8.284253	-0.843483
C	-0.038075	3.187408	-1.215946	H	-2.436301	4.371620	-0.796900
H	-0.058858	3.731413	-2.153930	C	-3.496335	6.178031	-1.213926
C	0.038646	1.782772	1.195618	C	3.470481	7.612735	1.234558
C	0.037995	3.187413	1.215867	H	4.405388	5.659407	1.507112
H	0.058767	3.731422	2.153849	H	2.301322	9.371608	0.843674
C	0.077037	0.867830	2.355622	H	-0.000182	9.342823	-0.000035
C	0.118099	1.303520	3.692017	C	-3.470762	7.612568	-1.234629
C	0.153407	0.365365	4.734966	H	-2.301688	9.371498	-0.843748
H	0.122272	2.365055	3.914104	H	-4.405576	5.659195	-1.507186
C	0.107153	-1.391134	3.069572	H	4.353853	8.160683	1.550311
C	0.148100	-1.006170	4.415402	H	-4.354162	8.160475	-1.550378
H	0.184373	0.694595	5.768889	C	5.770383	-1.423834	-0.208387
H	0.102298	-2.434961	2.779909	C	6.721545	-2.385692	0.196086
H	0.174823	-1.766429	5.188761	C	6.250725	-0.170107	-0.666946
N	0.070970	-0.489781	2.048837	C	8.101236	-2.124326	0.146158
N	-0.000010	1.118109	-0.000035	H	6.389679	-3.349725	0.575449
N	-0.070945	-0.489791	-2.048904	C	7.618833	0.109446	-0.715200
Ru	0.000013	-0.913008	-0.000037	H	5.549402	0.587571	-1.008954
C	3.257010	-0.758324	-0.124342	C	8.555437	-0.867928	-0.309821
C	4.325043	-1.706519	-0.159720	H	8.800299	-2.889237	0.467978
H	3.314275	0.319183	-0.113305	H	7.990266	1.065679	-1.070040
C	3.688842	-2.957557	-0.132173	C	-5.770324	-1.424019	0.208561
H	4.105393	-3.951652	-0.167765	C	-6.250687	-0.170378	0.667321
C	1.203697	-3.622616	-0.042208	C	-6.721461	-2.385831	-0.196082
C	1.240045	-5.028148	-0.043258	C	-7.618804	0.109138	0.715618
C	0.000083	-5.700668	-0.000053	H	-5.549372	0.587254	1.009455
H	2.167236	-5.591362	-0.076113	C	-8.101160	-2.124507	-0.146100
C	-1.203597	-3.622654	0.042153	H	-6.389563	-3.349777	-0.575639
C	-1.239901	-5.028189	0.043170	C	-8.555389	-0.868191	0.310083
H	-2.167073	-5.591435	0.075999	H	-7.990255	1.065305	1.070616
C	-3.688757	-2.957674	0.132212	H	-8.800204	-2.889380	-0.468056

C	-4.324985	-1.706654	0.159827	Br	0.000117	-7.666034	-0.000089
H	-4.105280	-3.951781	0.167829	O	9.889765	-0.491965	-0.398089
C	-3.256987	-0.758419	0.124487	O	-9.889723	-0.492270	0.398422
H	-3.314288	0.319090	0.113492	C	10.923259	-1.448564	-0.013666
N	-2.053805	-1.372274	0.077395	H	10.831387	-1.725670	1.045305
N	2.053835	-1.372212	-0.077459	H	10.881362	-2.349069	-0.641262
C	0.000038	-2.901135	-0.000026	H	11.868707	-0.929196	-0.177539
N	2.333461	-2.752125	-0.082404	C	-10.923203	-1.448821	0.013844
N	-2.333387	-2.752194	0.082357	H	-10.831323	-1.725751	-1.045173
C	-0.000052	3.911682	-0.000040	H	-10.881297	-2.349430	0.641291
C	-0.000086	5.408839	-0.000039	H	-11.868660	-0.929495	0.177799
C	1.165456	6.115032	0.418743				

4.11

Atom	X	Y	Z	Atom	X	Y	Z
C	-1.076055	0.146128	4.359401	Br	-6.692331	3.525366	-0.226356
C	-1.327619	0.418698	3.009017	C	0.569671	4.598176	0.375218
C	0.719430	-0.580149	2.356420	C	-3.383496	-3.051619	-0.455466
C	1.015704	-0.876240	3.698643	C	-3.762098	-4.472259	-0.634908
C	0.116395	-0.514069	4.713150	C	-4.844473	-5.086200	0.101392
H	-1.799988	0.445585	5.109783	C	-3.043529	-5.235974	-1.558584
H	-2.232068	0.923968	2.692731	C	-5.591804	-4.405994	1.117254
H	1.939966	-1.385815	3.947944	C	-5.177368	-6.464162	-0.176003
H	0.339023	-0.740356	5.751218	C	-3.362425	-6.599344	-1.809313
C	1.607767	-0.922906	1.224747	H	-2.241909	-4.769427	-2.126616
C	2.846895	-1.578084	1.283402	C	-6.627500	-5.037533	1.794650
H	3.245565	-1.913568	2.234000	H	-5.328347	-3.387229	1.382872
C	1.760047	-0.768283	-1.154680	C	-6.255680	-7.084133	0.531297
C	3.004056	-1.416407	-1.139106	C	-4.418982	-7.198604	-1.139836
H	3.551193	-1.576258	-2.061183	H	-2.785465	-7.158119	-2.540996
C	1.027233	-0.260821	-2.334759	C	-6.973930	-6.387776	1.492501
C	1.499253	-0.371802	-3.654750	H	-7.176434	-4.504467	2.566890
C	0.738860	0.138171	-4.718319	H	-6.500190	-8.119688	0.305482
H	2.452167	-0.851934	-3.848786	H	-4.682680	-8.234869	-1.338342
C	-0.922694	0.843639	-3.105617	H	-7.790504	-6.867575	2.025207
C	-0.494403	0.756822	-4.435974	C	1.445110	5.769065	0.614412
H	1.097660	0.055740	-5.739536	C	2.670128	5.980902	-0.122810
H	-1.863939	1.311269	-2.843603	C	1.071137	6.688996	1.597711
H	-1.115661	1.165295	-5.225906	C	3.099043	5.132691	-1.194823
N	-0.192916	0.352407	-2.065348	C	3.492954	7.119922	0.211066
N	1.094679	-0.534885	0.017549	C	1.873876	7.823027	1.903176
N	-0.462673	0.070804	2.015951	H	0.160502	6.519626	2.167275
Ru	-0.704303	0.409879	-0.036458	C	4.287104	5.374333	-1.873598
C	0.925135	3.217780	0.286906	H	2.470424	4.302639	-1.502038
H	1.905719	2.771717	0.349142	C	4.715541	7.337109	-0.499829
C	-0.828707	4.613781	0.274308	C	3.069957	8.027428	1.231522
H	-1.509158	5.450879	0.274026	H	1.550532	8.514164	2.676539
C	-2.556344	2.724652	0.000095	C	5.112950	6.481390	-1.517068
C	-3.785846	3.405229	-0.036769	H	4.588703	4.723605	-2.690754
C	-4.949942	2.618529	-0.170842	H	5.328114	8.195629	-0.233644

H	-3.860853	4.485686	0.032139	H	3.698916	8.882012	1.469982
C	-3.657909	0.594434	-0.223938	H	6.041526	6.657405	-2.053398
C	-4.920666	1.210768	-0.266913	H	7.686903	-2.793351	2.082633
H	-5.844271	0.650264	-0.369650	H	5.526343	-1.648452	2.016258
C	-4.203574	-1.913702	-0.428711	H	4.621380	-3.592847	-1.741168
H	-5.274466	-1.829933	-0.524137	H	6.798413	-4.706159	-1.686979
C	-2.054904	-2.544410	-0.335945	C	8.819787	-4.537816	0.274494
H	-1.130511	-3.100536	-0.295894	C	9.078432	-5.473183	-0.932459
N	-2.048789	-1.196449	-0.240486	H	8.340480	-6.284184	-0.988181
N	-0.169464	2.437737	0.145435	H	9.067729	-4.926897	-1.884689
C	-2.467260	1.326645	-0.092268	H	10.067711	-5.935536	-0.831040
N	-1.267110	3.322434	0.136432	C	8.909191	-5.385931	1.578058
N	-3.402239	-0.808329	-0.302787	H	9.893883	-5.865805	1.646101
C	3.573093	-1.836530	0.091492	H	8.775792	-4.772236	2.477092
C	4.888450	-2.524025	0.130293	H	8.144070	-6.172715	1.589171
C	5.783481	-2.333614	1.211481	C	9.930903	-3.445081	0.293204
C	5.293192	-3.390347	-0.909730	H	9.897110	-2.833844	-0.617800
C	7.025385	-2.979754	1.241079	H	9.830557	-2.773574	1.154618
C	6.538354	-4.040147	-0.871656	H	10.920250	-3.916845	0.351273
C	7.438076	-3.851714	0.201842				

4.12							
Atom	X	Y	Z	Atom	X	Y	Z
C	1.070539	-0.514123	4.368359	C	-1.717730	5.744466	0.781147
C	1.175701	-0.879804	3.020605	C	-6.799373	2.403009	-0.718559
C	-0.360696	0.804213	2.375120	H	-4.791029	1.733349	-0.440700
C	-0.499336	1.208387	3.714776	C	-7.255345	4.774197	-0.394502
C	0.218282	0.548924	4.724397	C	-5.406107	6.293433	0.246987
H	1.644352	-1.052378	5.115265	C	-3.596184	7.856986	0.893817
H	1.819733	-1.690899	2.703014	H	-0.975610	4.954082	0.722111
H	-1.161580	2.029805	3.965522	C	-1.314974	7.027693	1.103694
H	0.115725	0.855479	5.760639	C	-7.713658	3.508849	-0.703619
C	-1.075734	1.439993	1.248691	H	-7.173830	1.407148	-0.941868
C	-1.984252	2.509760	1.309254	H	-7.940997	5.617996	-0.367078
H	-2.243801	2.967837	2.257336	H	-6.113437	7.119949	0.278397
C	-1.331916	1.311330	-1.126095	C	-2.265221	8.100943	1.169031
C	-2.244504	2.379135	-1.106206	H	-4.323854	8.664535	0.928642
H	-2.692122	2.747483	-2.022801	H	-0.266664	7.233943	1.304657
C	-0.863737	0.552279	-2.304619	H	-8.763554	3.340145	-0.926280
C	-1.282598	0.818160	-3.620538	H	-1.928103	9.101044	1.426765
C	-0.788932	0.046478	-4.683591	Br	4.893149	-5.840423	-0.171661
H	-1.986653	1.620706	-3.811391	C	-2.225420	-4.067369	0.487934
C	0.512691	-1.214447	-3.078249	C	4.315574	1.492682	-0.571227
C	0.124444	-0.988669	-4.404730	C	5.195091	2.660643	-0.808054
H	-1.107513	0.246526	-5.701852	C	6.458844	2.834329	-0.127136
H	1.213079	-1.999291	-2.819920	C	4.780035	3.621120	-1.734598
H	0.531449	-1.610945	-5.194617	C	6.936482	1.942975	0.887870
N	0.041654	-0.470892	-2.038370	C	7.275236	3.977947	-0.462470
N	-0.773652	0.869519	0.042266	C	5.578657	4.757303	-2.041705
N	0.483745	-0.247575	2.032293	H	3.839274	3.481228	-2.262090

Ru	0.535484	-0.683804	-0.015244	C	8.161737	2.148703	1.509868
C	-2.031179	-2.657352	0.375091	H	6.319120	1.105871	1.197519
H	-2.769738	-1.872681	0.430536	C	8.536761	4.157486	0.188491
C	-0.938512	-4.614442	0.387561	C	6.810369	4.925469	-1.426628
H	-0.626682	-5.647079	0.402001	H	5.225260	5.477714	-2.774226
C	1.373402	-3.526846	0.063970	C	8.979351	3.260597	1.149893
C	2.252678	-4.623352	0.037077	H	8.500597	1.463298	2.282644
C	3.625376	-4.339931	-0.128832	H	9.144447	5.018573	-0.080557
H	1.914423	-5.649776	0.136888	H	7.437320	5.780490	-1.668840
C	3.195222	-1.978977	-0.228982	H	9.938638	3.406077	1.639108
C	4.129590	-3.028661	-0.264514	C	-3.482683	-4.809602	0.739175
H	5.194790	-2.862161	-0.389428	C	-4.685692	-4.562281	-0.022861
C	4.644850	0.129796	-0.518662	C	-3.500804	-5.769527	1.754231
H	5.600966	-0.356487	-0.629293	C	-4.742137	-3.652663	-1.128446
C	2.897250	1.529073	-0.416095	C	-5.885907	-5.288818	0.319532
H	2.252152	2.393936	-0.383865	C	-4.680711	-6.499645	2.069256
N	2.384442	0.286722	-0.277531	H	-2.601204	-5.942649	2.339980
N	-0.723853	-2.353405	0.218083	C	-5.922289	-3.447105	-1.832540
C	1.818586	-2.201912	-0.067302	H	-3.838900	-3.138026	-1.441495
N	-0.044005	-3.588365	0.224835	C	-7.088510	-5.047602	-0.417320
N	3.488414	-0.586186	-0.345068	C	-5.855326	-6.253730	1.374048
C	-2.584373	2.995147	0.122341	H	-4.656556	-7.235545	2.868079
C	-3.556818	4.132569	0.165507	C	-7.113722	-4.141885	-1.468157
C	-4.931149	3.897233	-0.131672	H	-5.939490	-2.762770	-2.677370
C	-3.100225	5.439910	0.504240	H	-7.986423	-5.597505	-0.144315
C	-5.457348	2.590522	-0.441639	H	-6.766315	-6.794593	1.619606
C	-5.867624	5.008625	-0.094508	H	-8.030981	-3.970629	-2.025177
C	-4.053524	6.536661	0.550057				

7.3 Isodensity orbital plots.

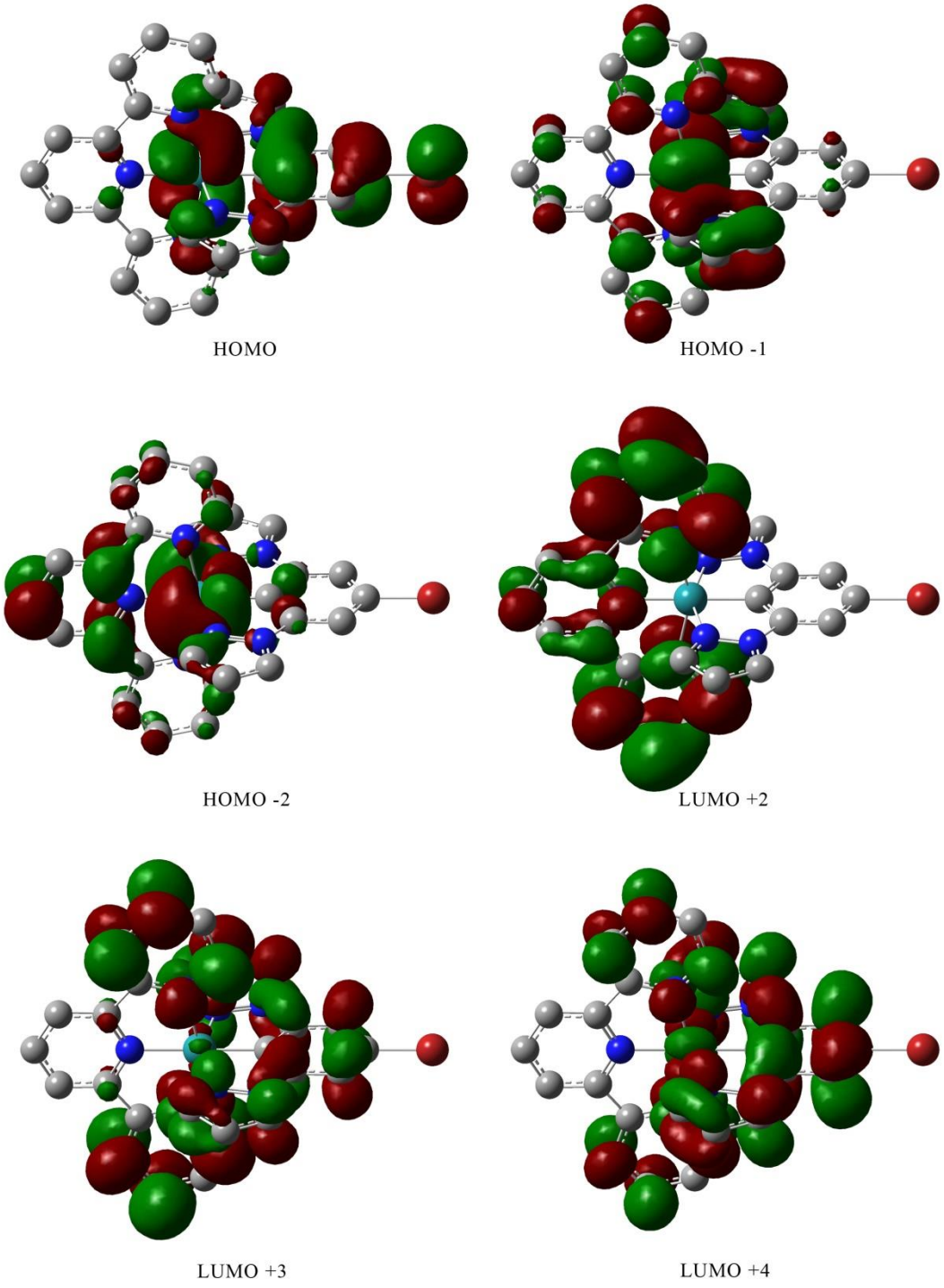

Figure 7.3.1: Isodensity plots (isovalue 0.02) of selected frontier orbitals that are involved in the 2nd lowest energy MLCT for **2.2** from DFT calculation *in vacuo*.

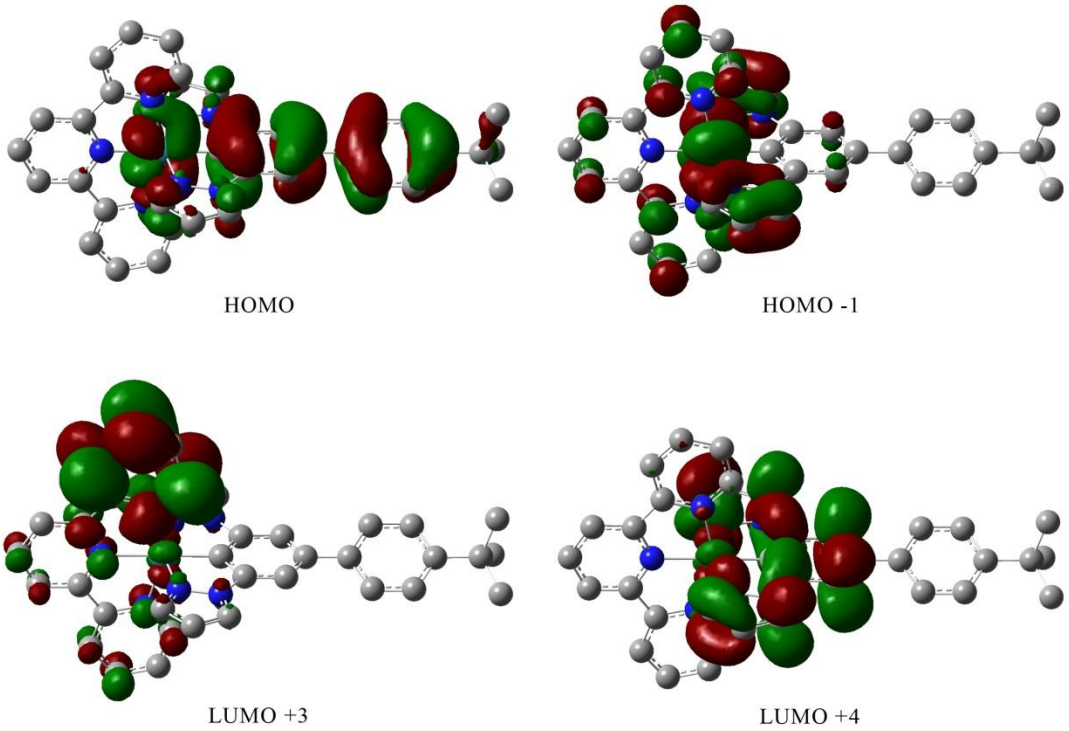

Figure 7.3.2: Isodensity plots (isovalue 0.02) of selected frontier orbitals that are involved in the 2nd lowest energy MLCT for **2.3** from DFT calculation *in vacuo*.

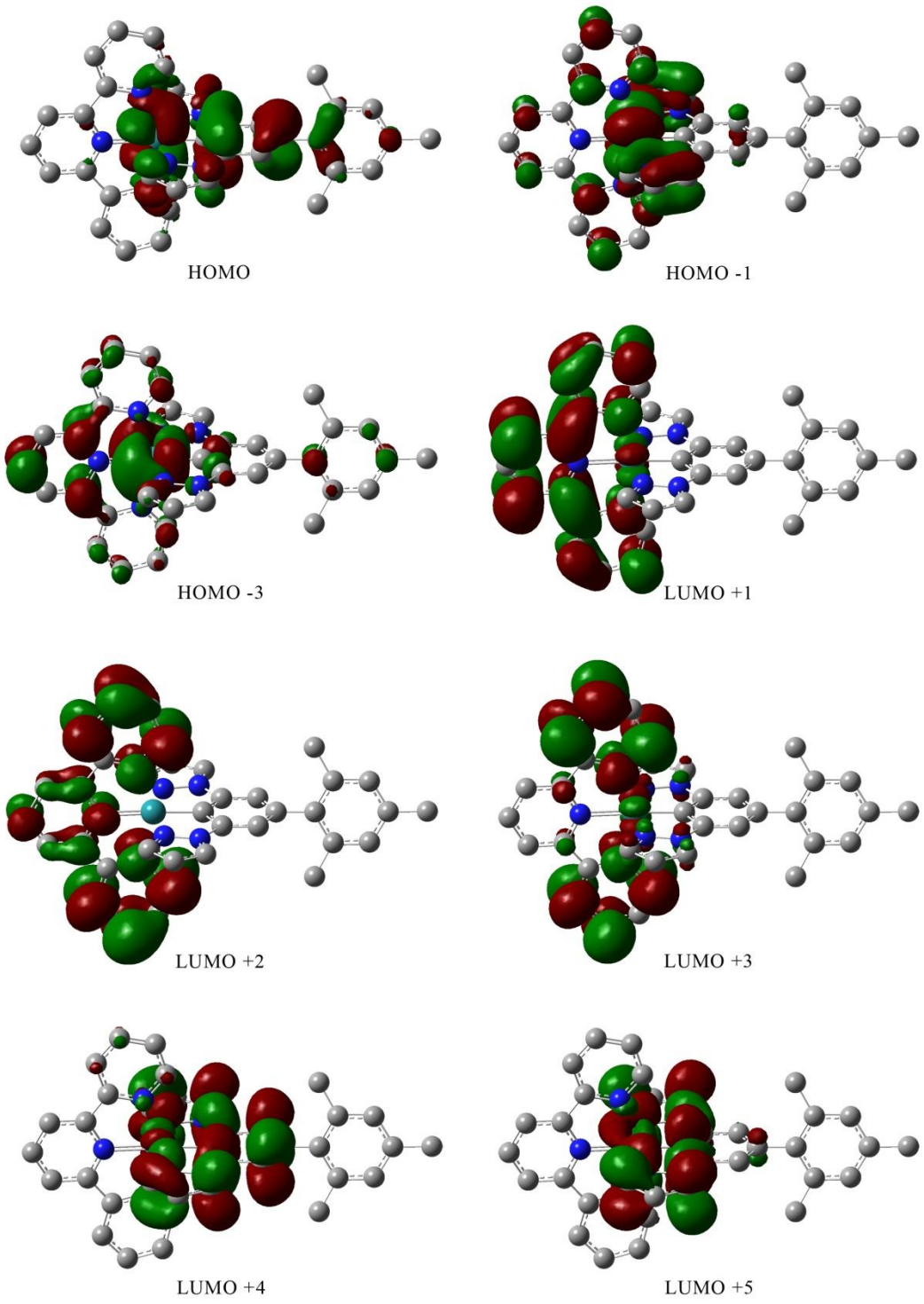

Figure 7.3.3: Isodensity plots (isovalue 0.02) of selected frontier orbitals that are involved in the 2nd lowest energy MLCT for **2.4** from DFT calculation *in vacuo*.

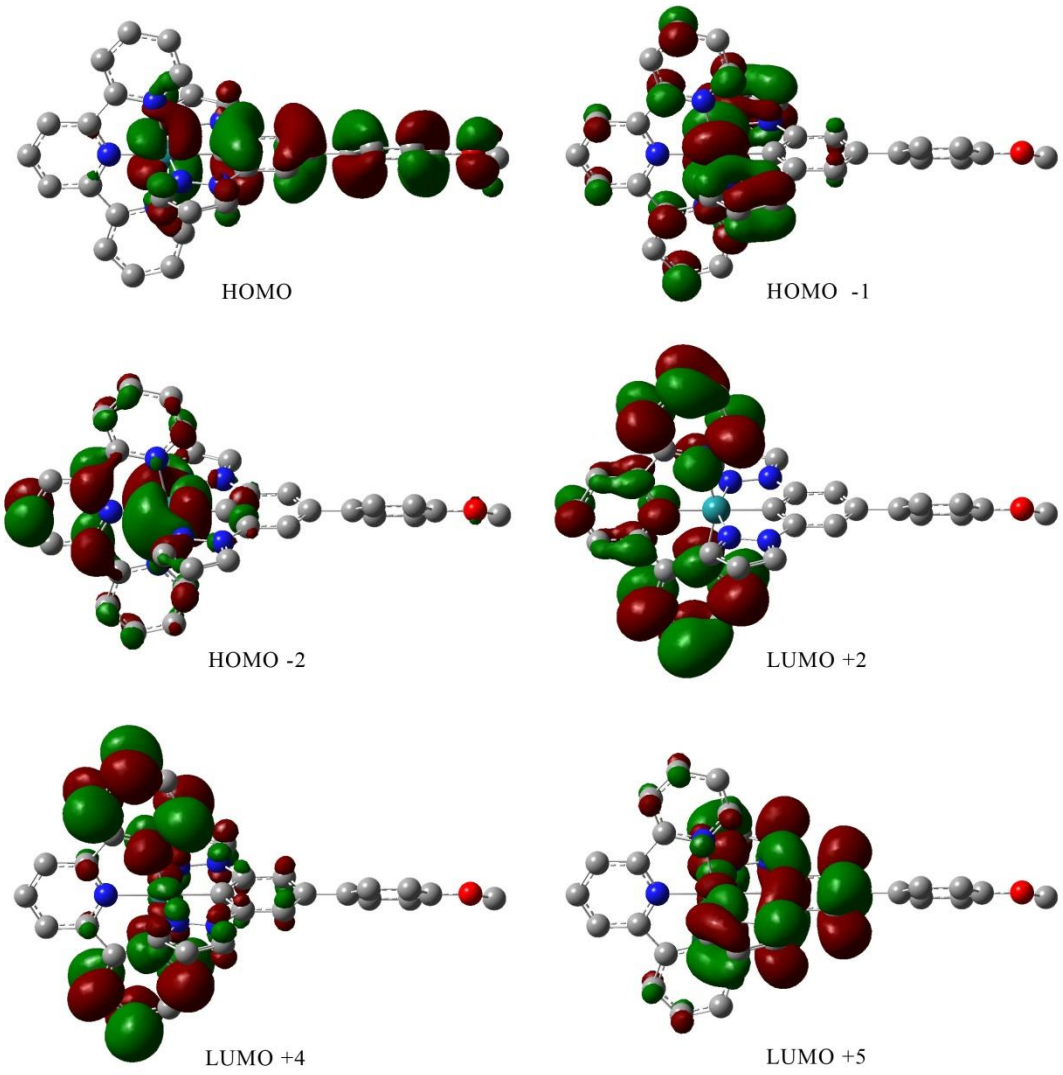

Figure 7.3.4: Isodensity plots (isovalue 0.02) of selected frontier orbitals that are involved in the 2nd lowest energy MLCT for **2.5** from DFT calculation *in vacuo*.

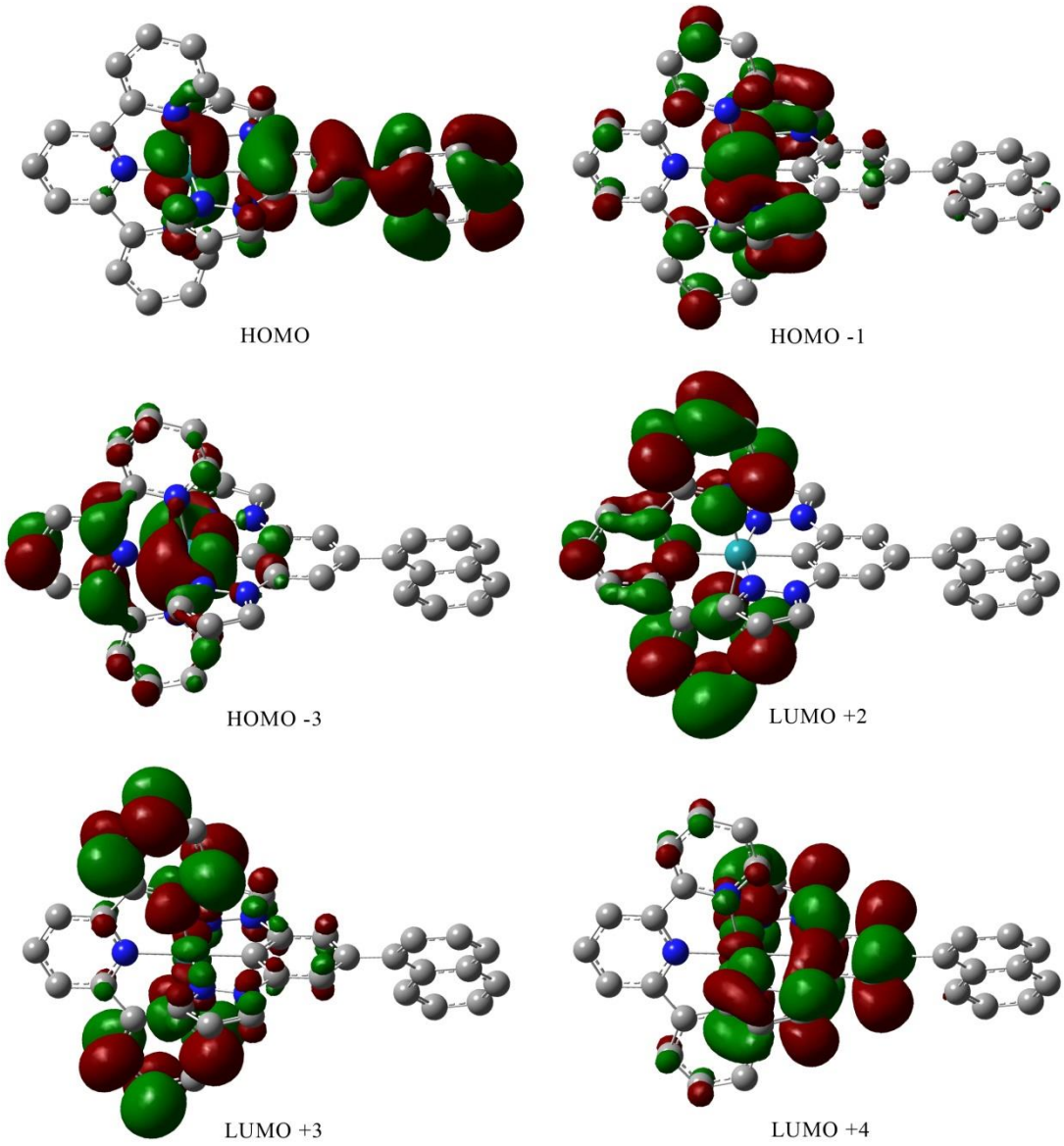

Figure 7.3.5: Isodensity plots (isovalue 0.02) of selected frontier orbitals that are involved in the 2nd lowest energy MLCT for **2.6** from DFT calculation *in vacuo*.

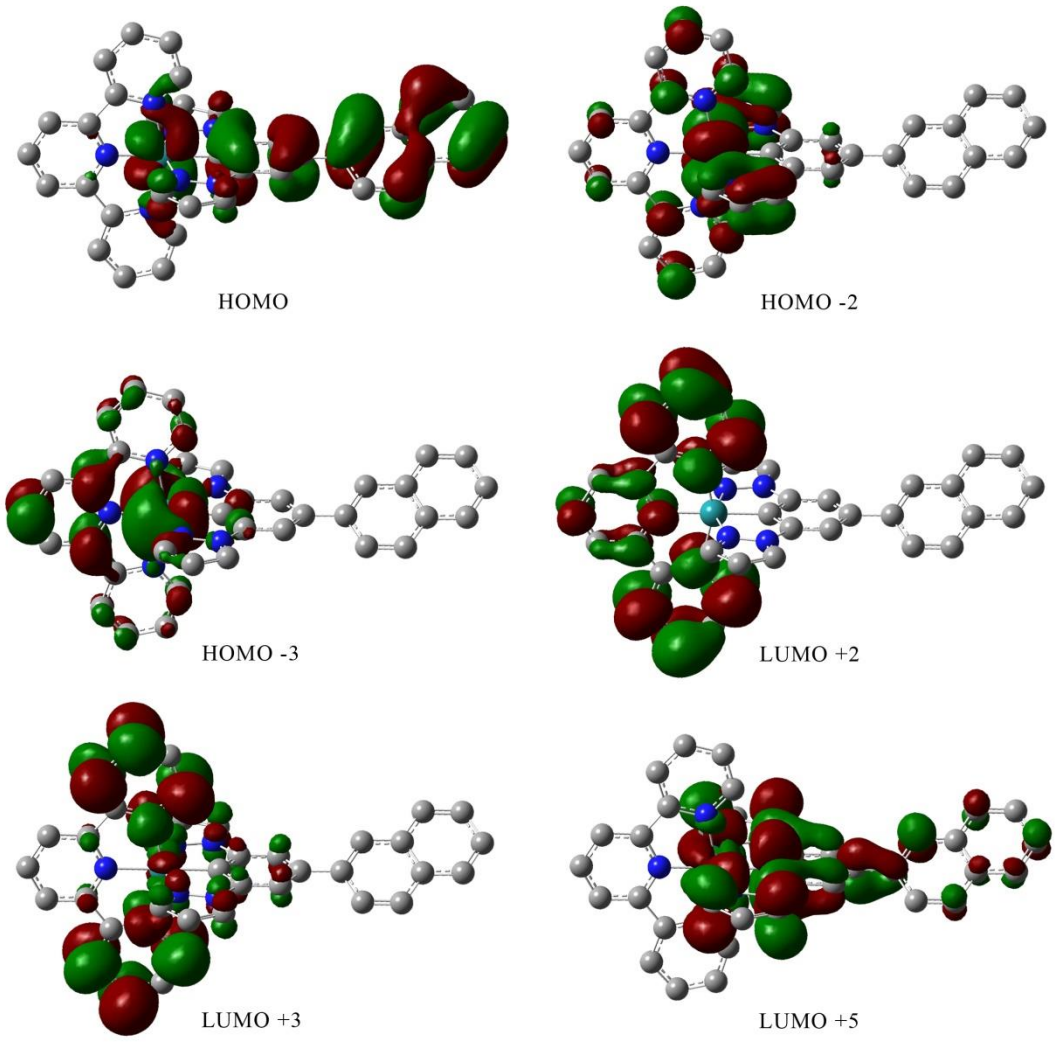

Figure 7.3.6: Isodensity plots (isovalue 0.02) of selected frontier orbitals that are involved in the 2nd lowest energy MLCT for **2.7** from DFT calculation *in vacuo*.

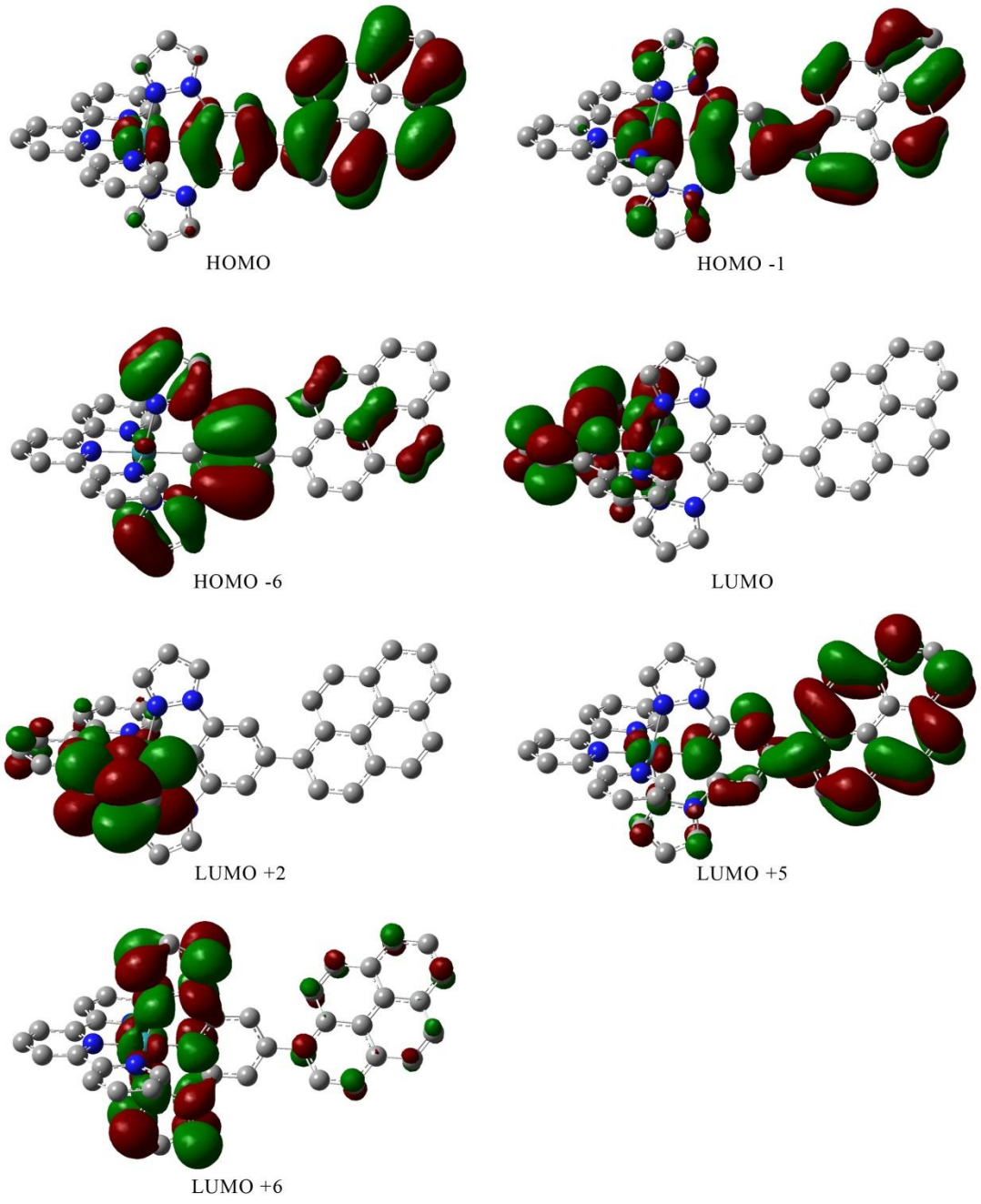

Figure 7.3.7: Isodensity plots (isovalue 0.02) of selected frontier orbitals that are involved in the 2nd lowest energy MLCT for **2.8** from DFT calculation *in vacuo*.

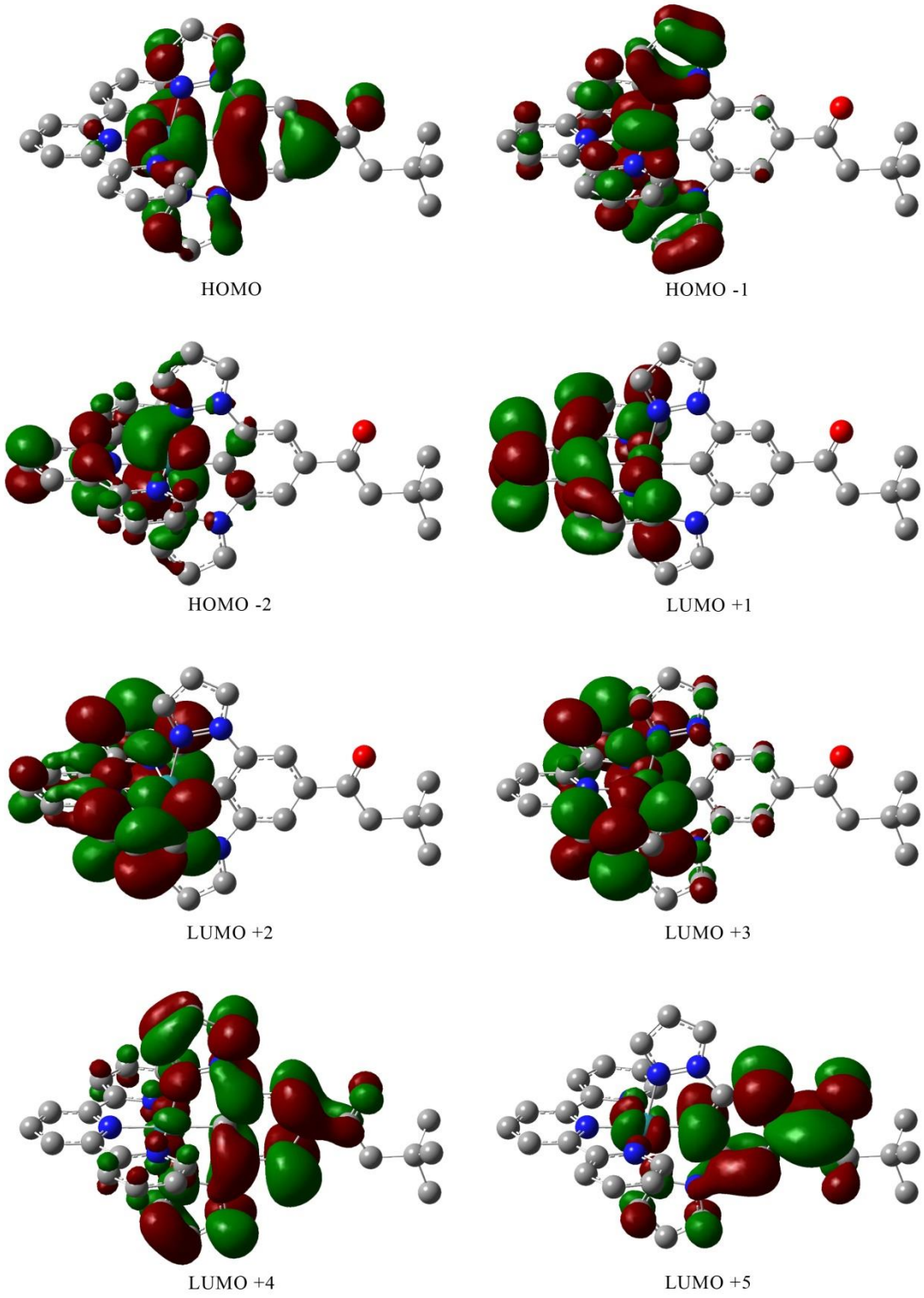

Figure 7.3.8: Isodensity plots (isovalue 0.02) of selected frontier orbitals that are involved in the 2nd lowest energy MLCT for **2.9** from DFT calculation *in vacuo*.

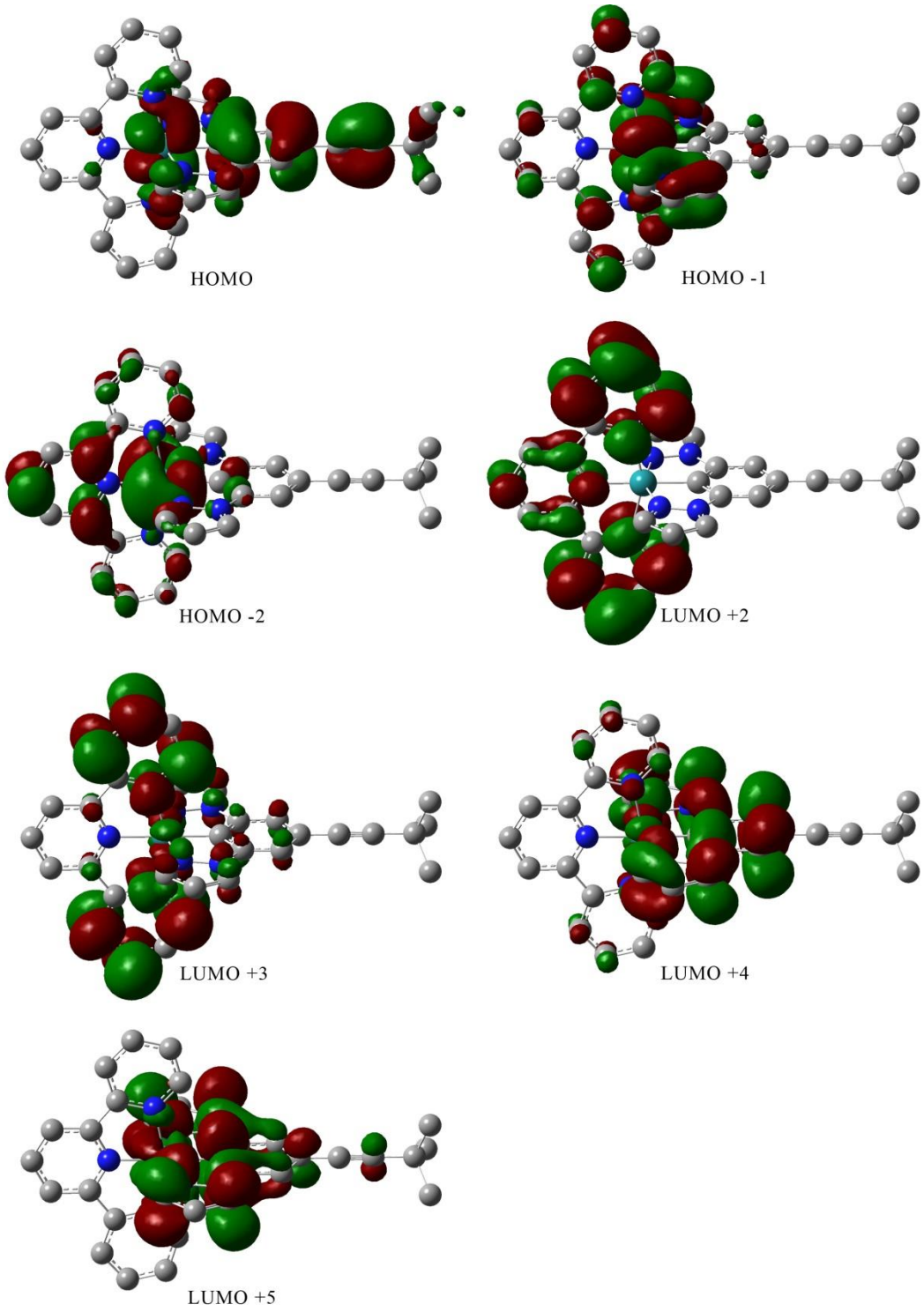

Figure 7.3.9: Isodensity plots (isovalue 0.02) of selected frontier orbitals that are involved in the 2nd lowest energy MLCT for **2.9a** from DFT calculation *in vacuo*.

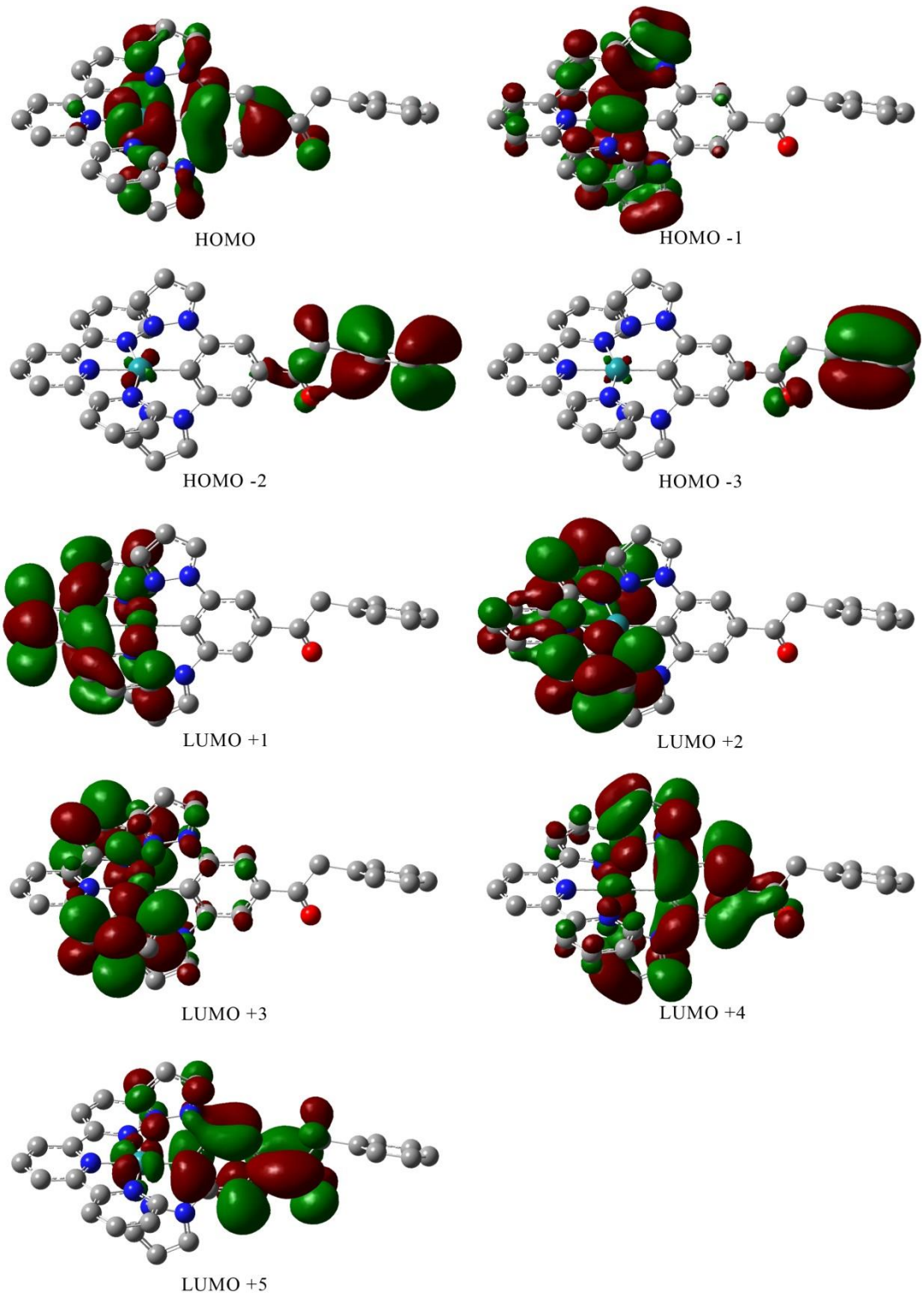

Figure 7.3.10: Isodensity plots (isovalue 0.02) of selected frontier orbitals that are involved in the 2nd lowest energy MLCT for **2.10** from DFT calculation *in vacuo*.

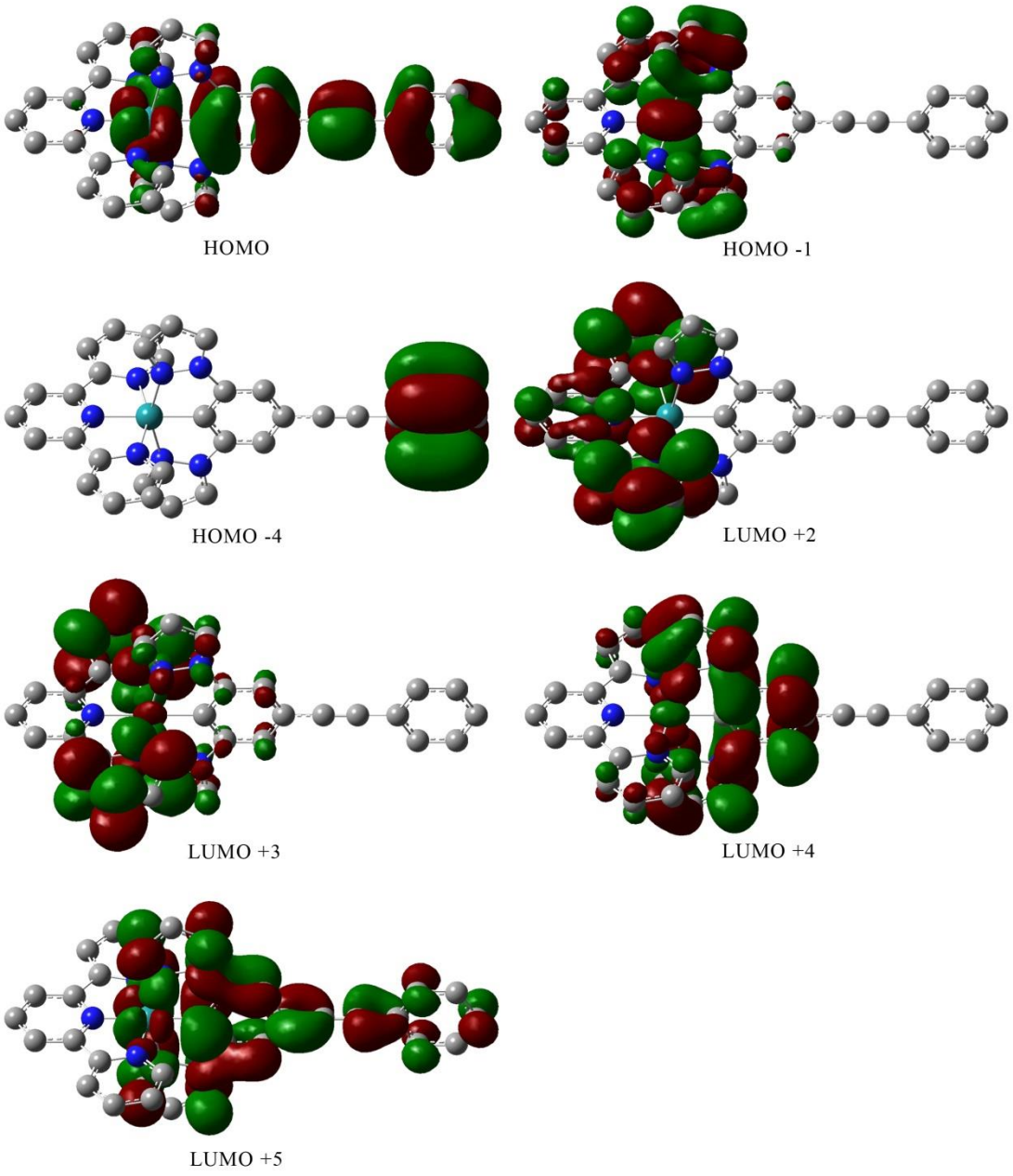

Figure 7.3.11: Isodensity plots (isovalue 0.02) of selected frontier orbitals that are involved in the 2nd lowest energy MLCT for **2.10a** from DFT calculation *in vacuo*.

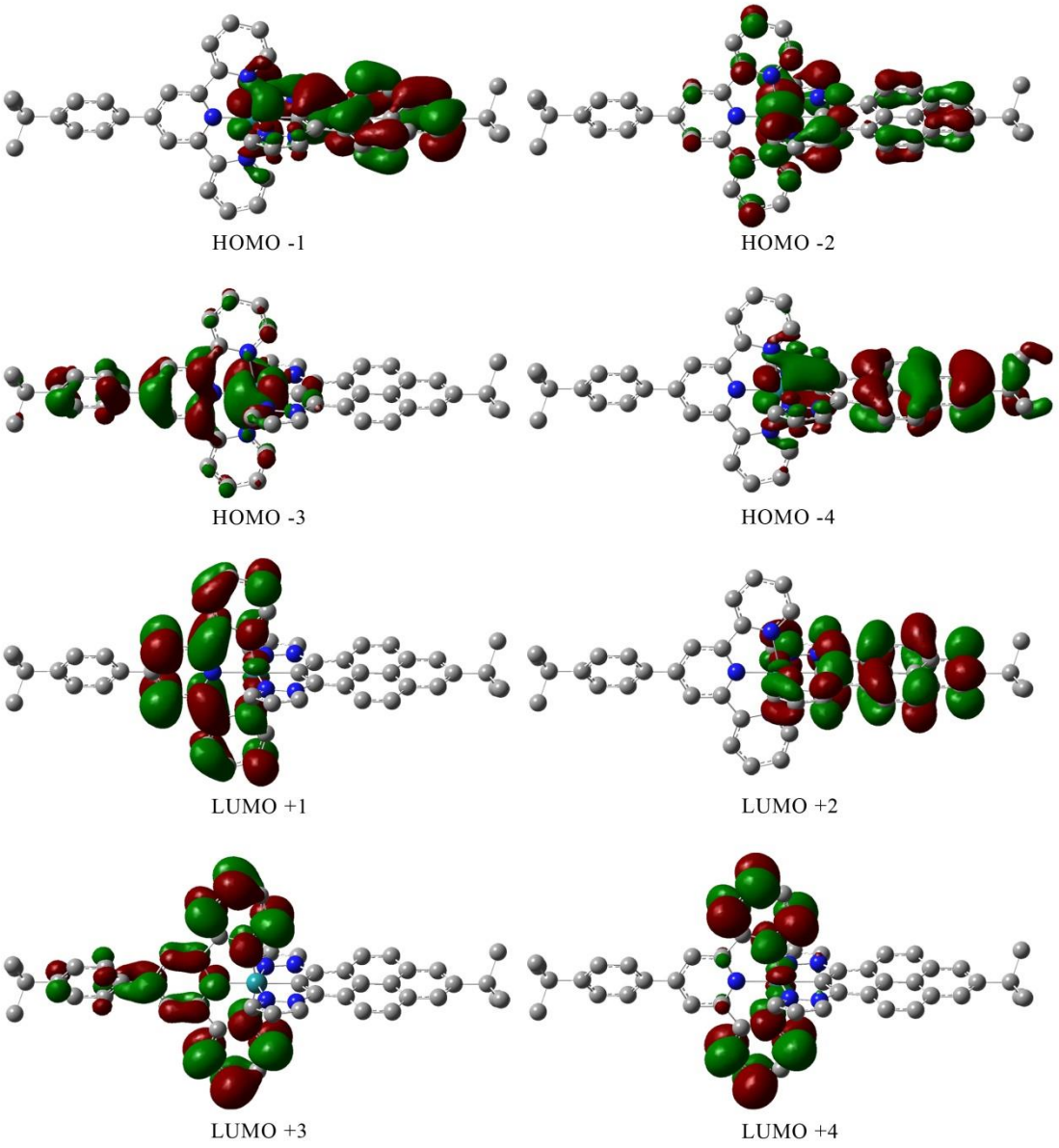

Figure 7.3.12: Isodensity plots (isovalue 0.02) of selected frontier orbitals that are involved in the 2nd lowest energy MLCT for **2.11** from DFT calculation *in vacuo*.

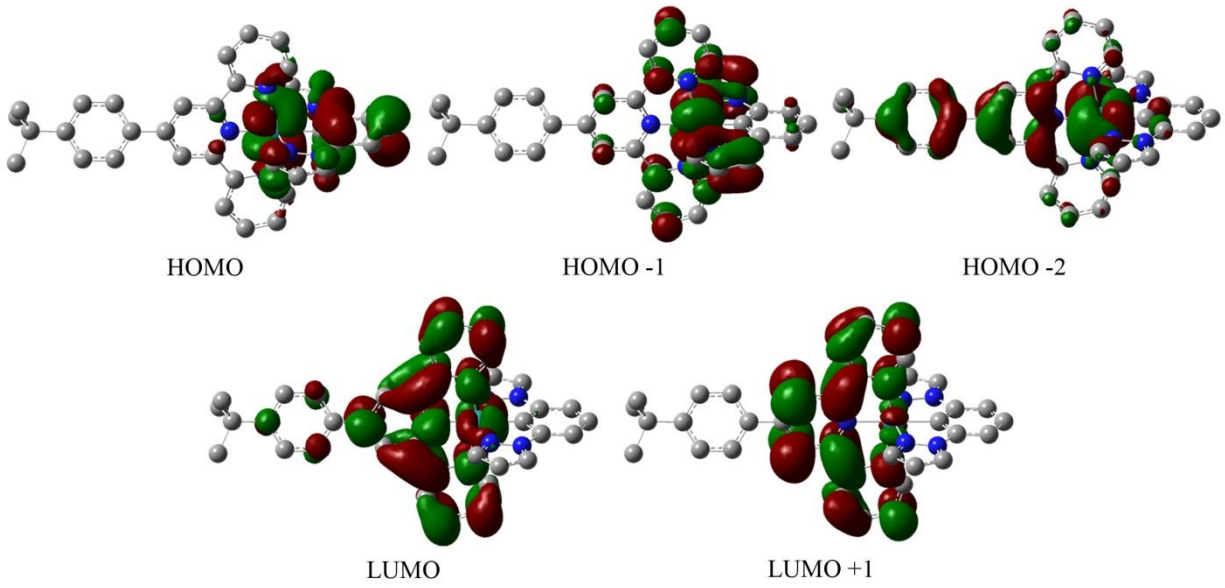

Figure 7.3.13: Isodensity plots (isovalue 0.02) of selected frontier orbitals that are involved in the 2nd lowest energy MLCT for **3.1** from DFT calculation *in vacuo*.

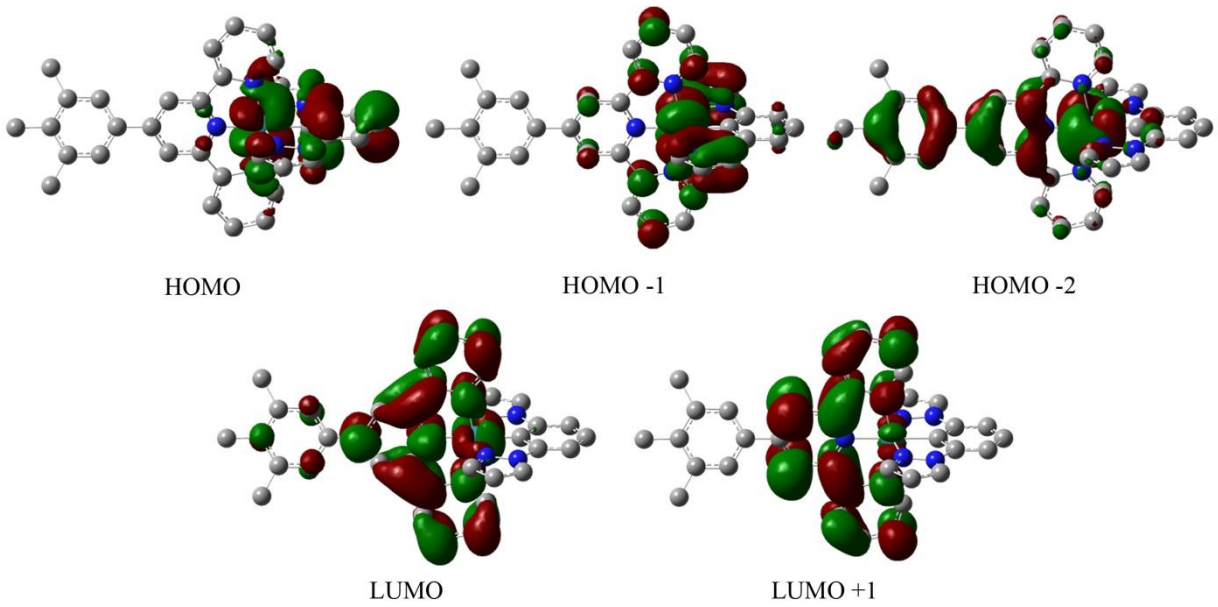

Figure 7.3.14: Isodensity plots (isovalue 0.02) of selected frontier orbitals that are involved in the 2nd lowest energy MLCT for **3.2** from DFT calculation *in vacuo*.

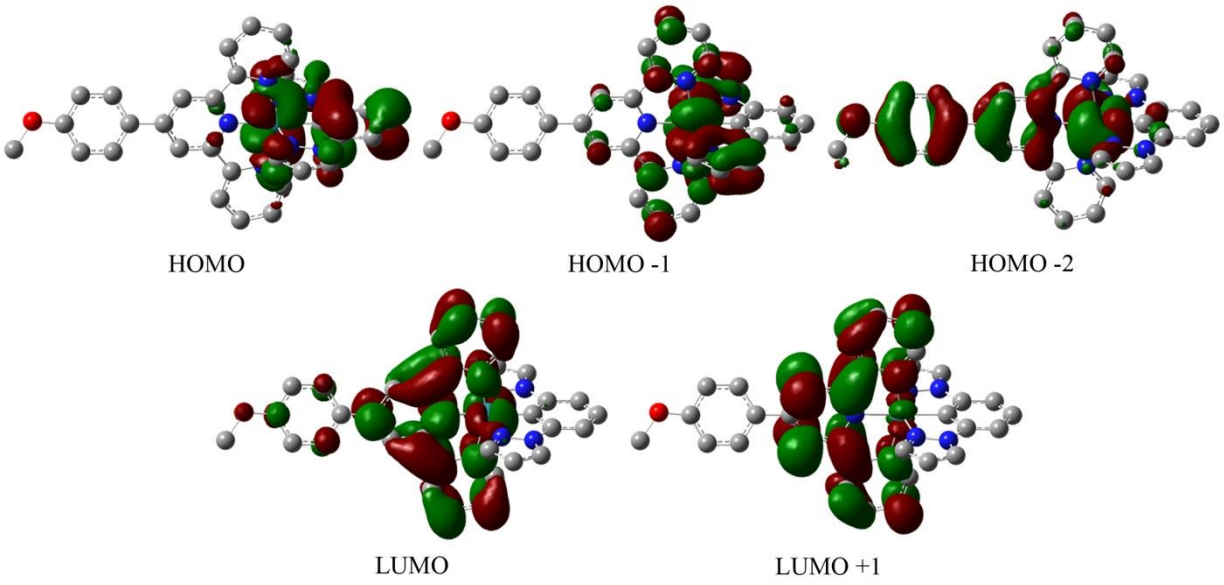

Figure 7.3.15: Isodensity plots (isovalue 0.02) of selected frontier orbitals that are involved in the 2nd lowest energy MLCT for **3.3** from DFT calculation *in vacuo*.

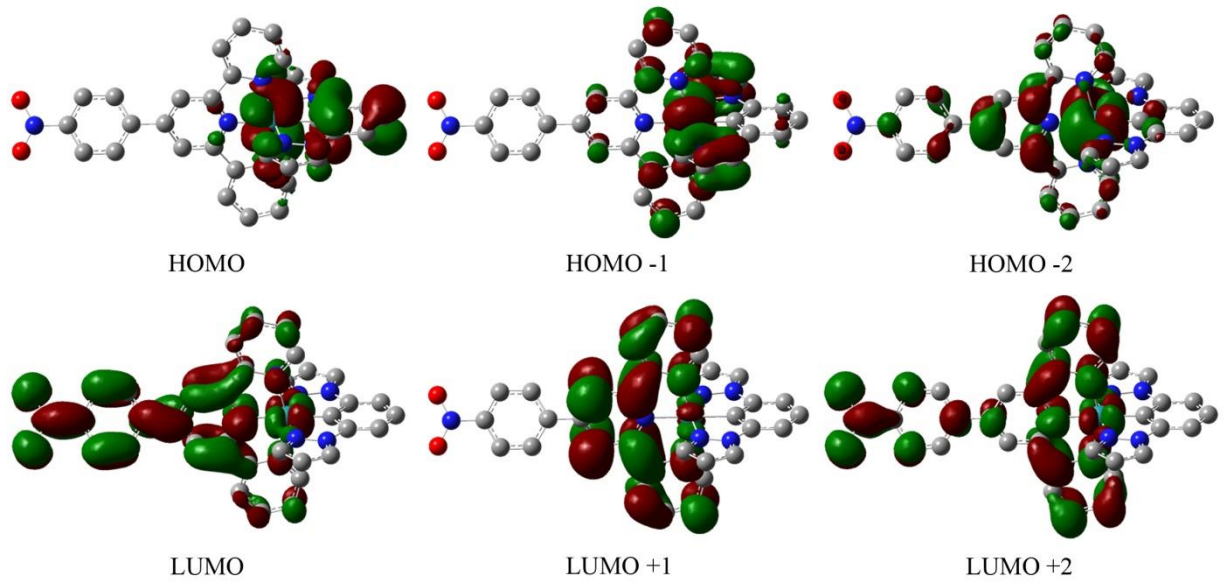

Figure 7.3.16: Isodensity plots (isovalue 0.02) of selected frontier orbitals that are involved in the 2nd lowest energy MLCT for **3.4** from DFT calculation *in vacuo*.

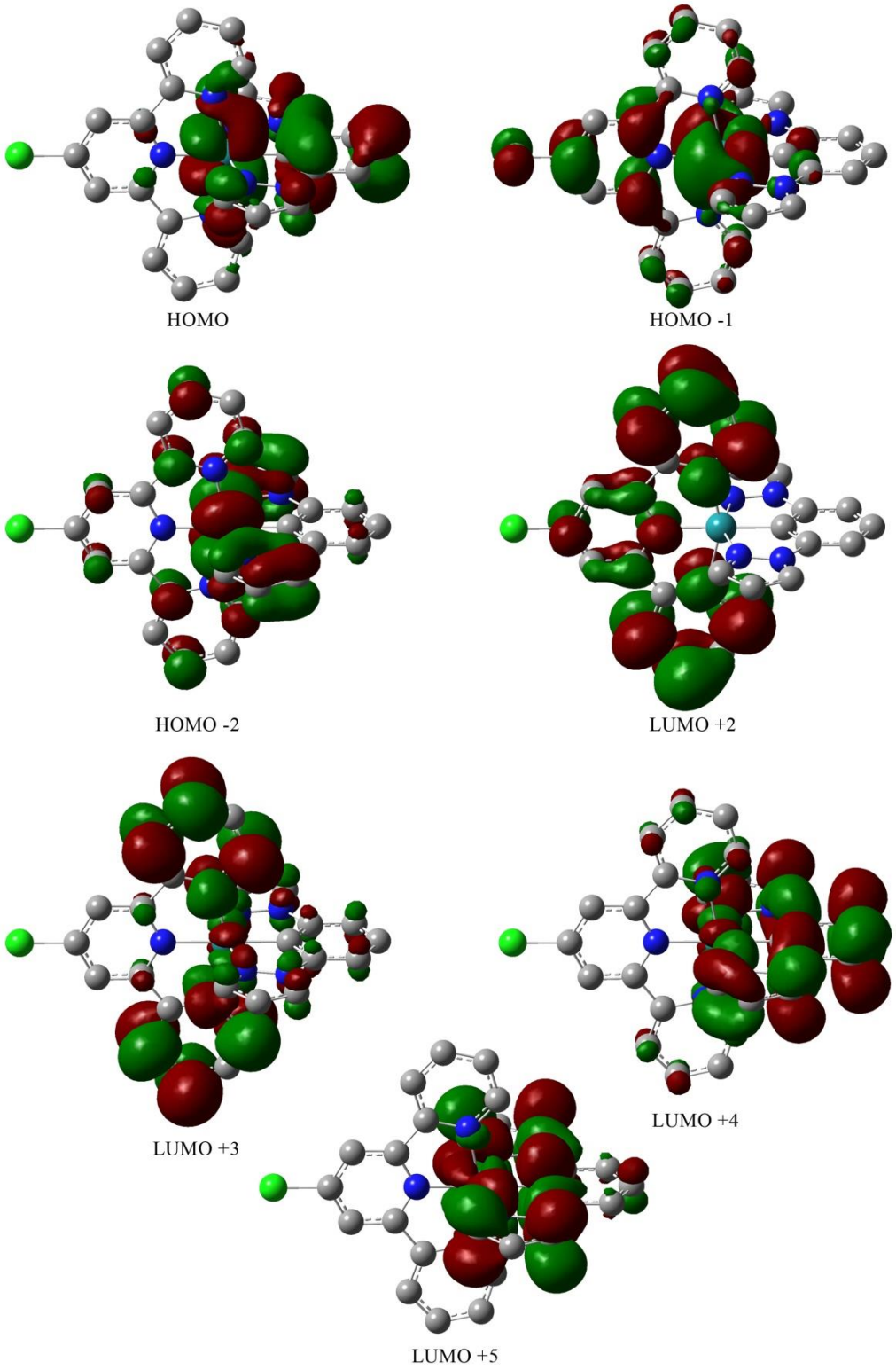

Figure 7.3.17: Isodensity plots (isovalue 0.02) of selected frontier orbitals that are involved in the 2nd lowest energy MLCT for **3.5** from DFT calculation *in vacuo*.

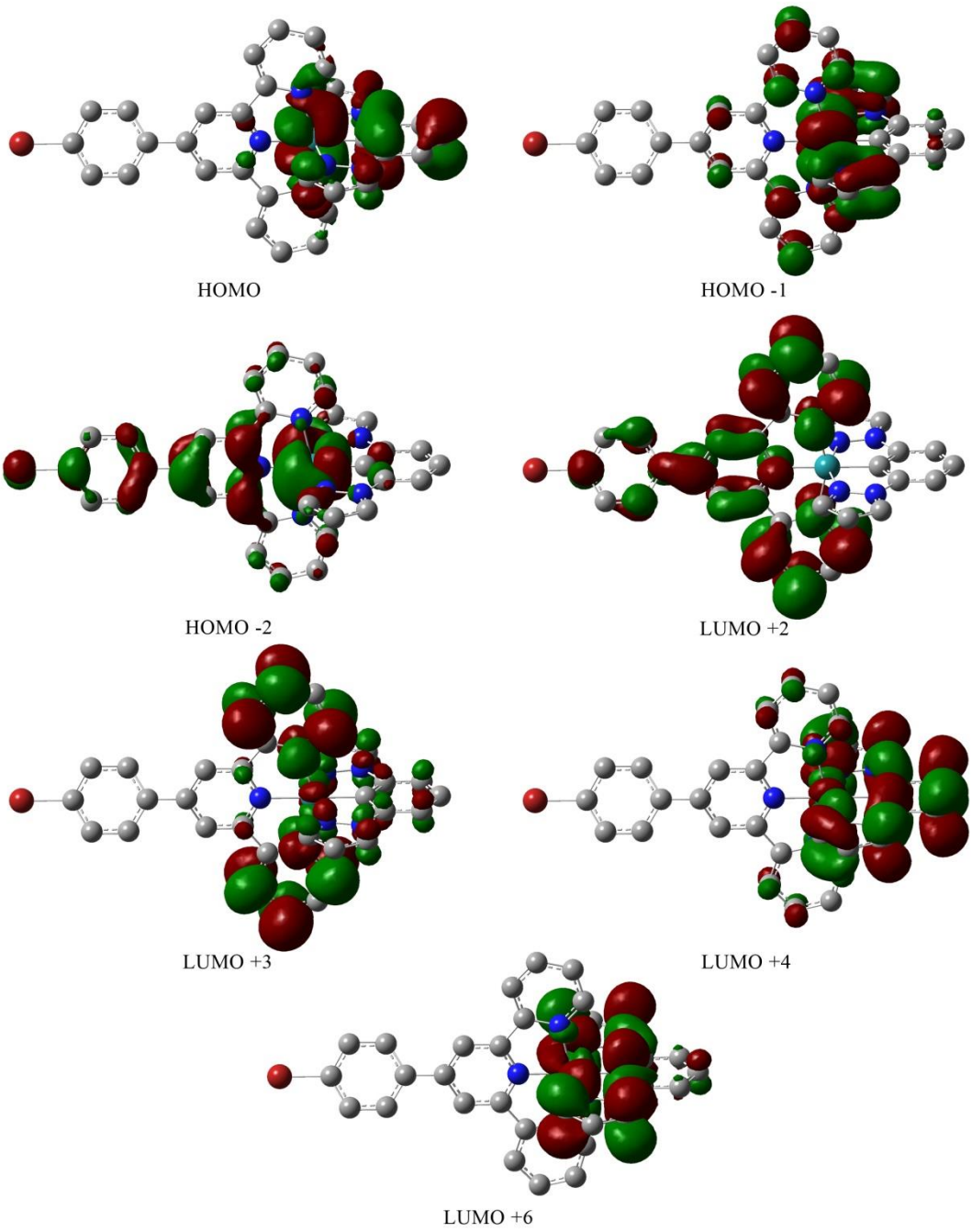

Figure 7.3.18: Isodensity plots (isovalue 0.02) of selected frontier orbitals that are involved in the 2nd lowest energy MLCT for **3.6** from DFT calculation *in vacuo*.

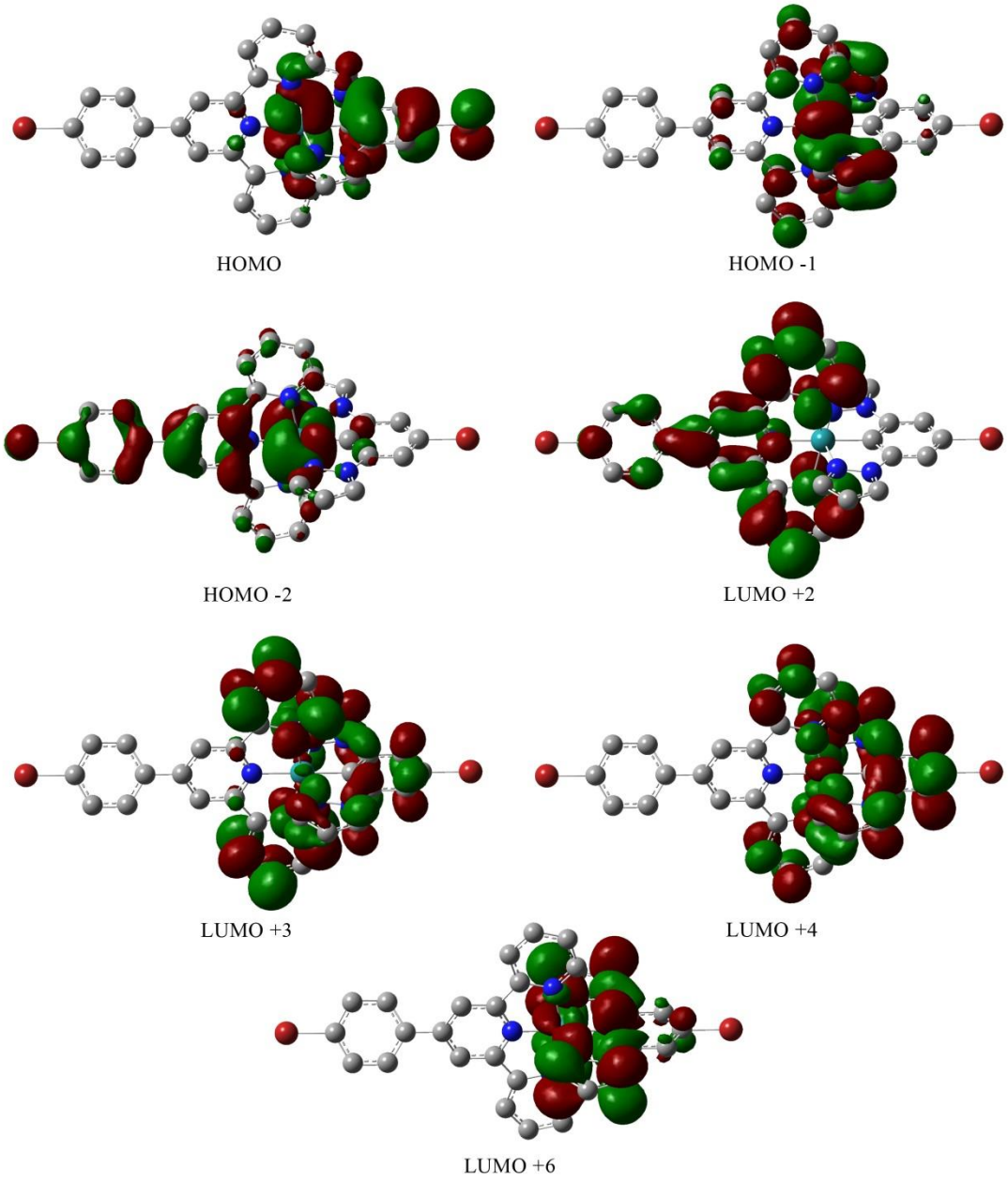

Figure 7.3.19: Isodensity plots (isovalue 0.02) of selected frontier orbitals that are involved in the 2nd lowest energy MLCT for **3.7** from DFT calculation *in vacuo*.

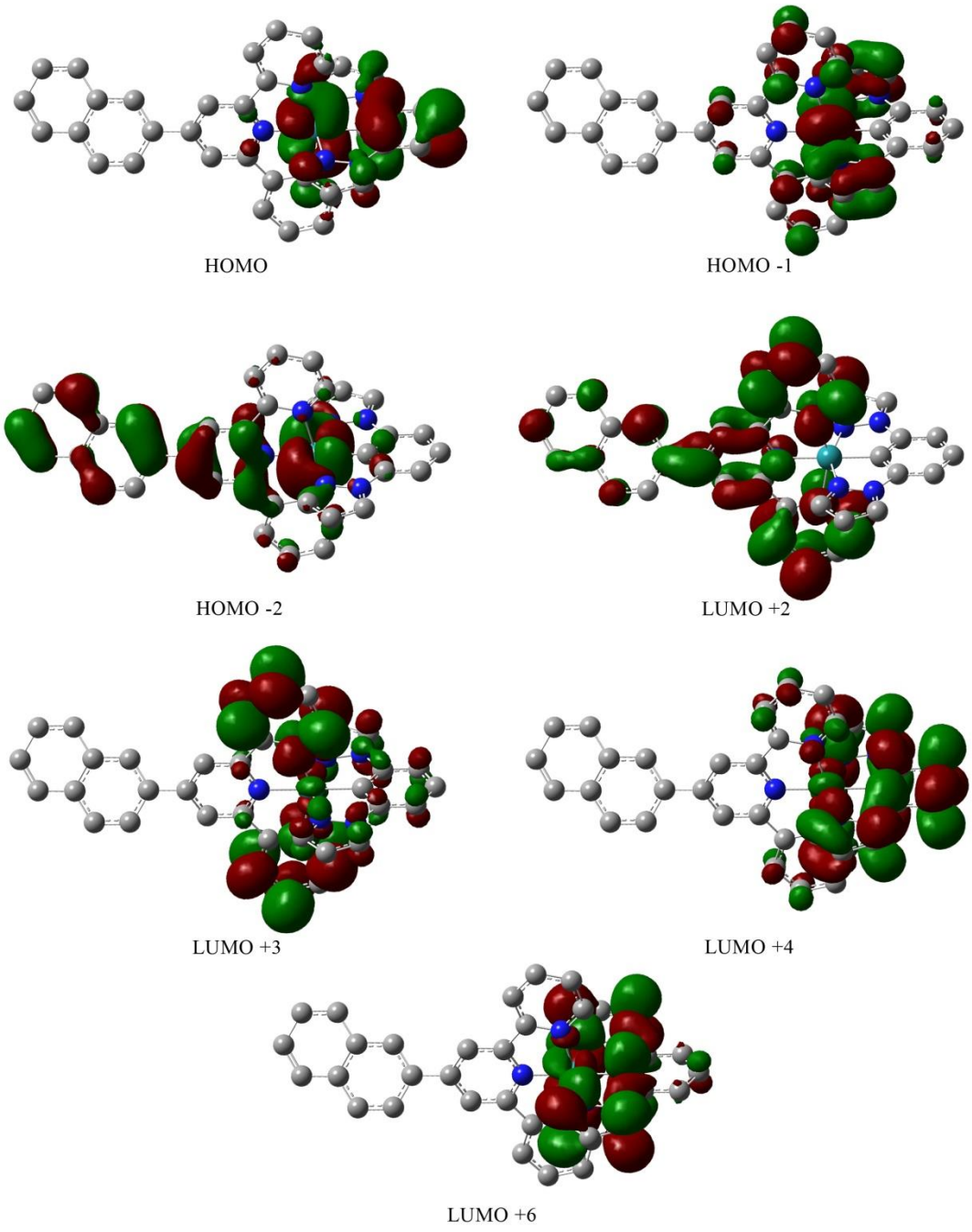

Figure 7.3.20: Isodensity plots (isovalue 0.02) of selected frontier orbitals that are involved in the 2nd lowest energy MLCT for **3.8** from DFT calculation *in vacuo*.

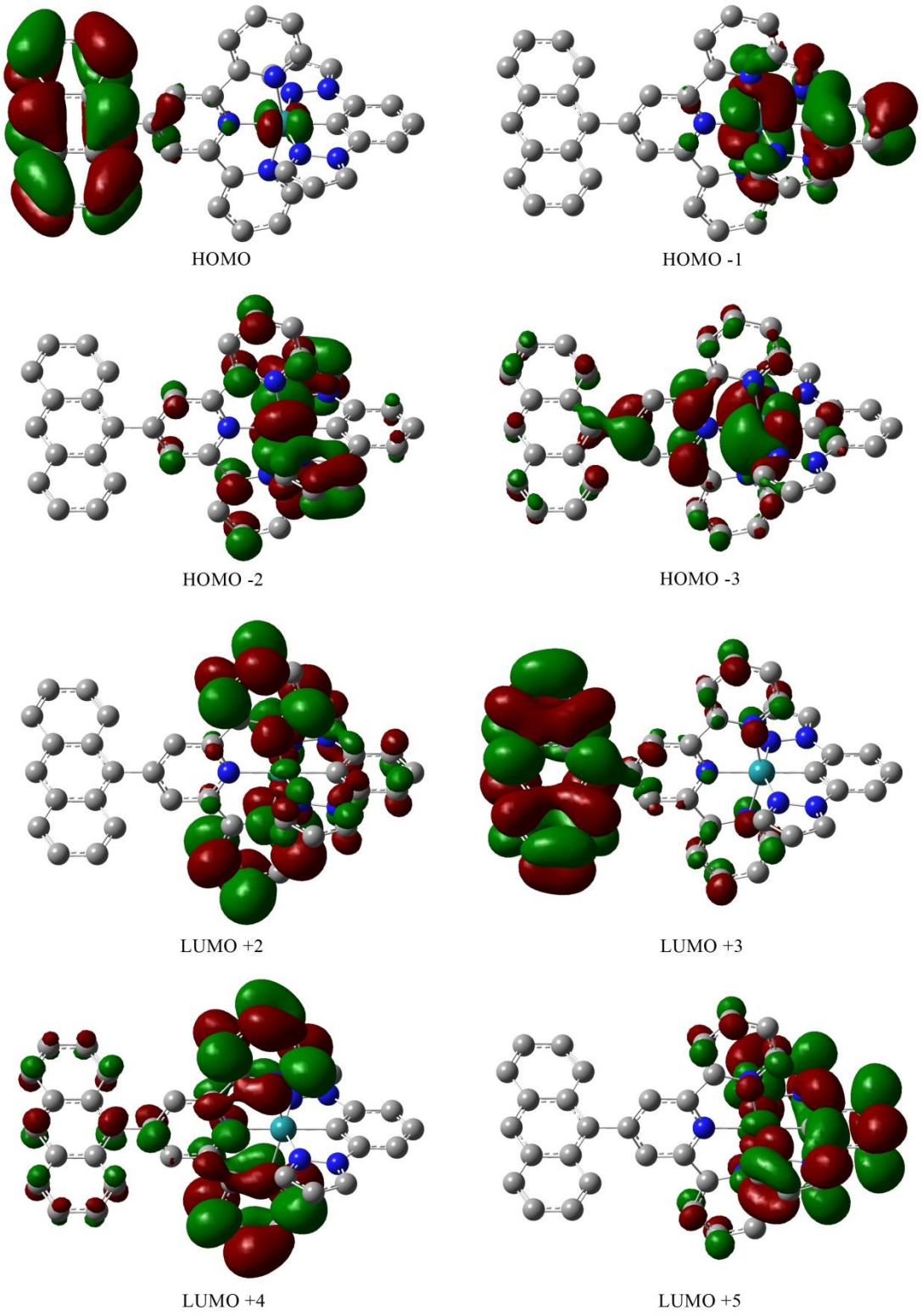

Figure 7.3.21: Isodensity plots (isovalue 0.02) of selected frontier orbitals that are involved in the 2nd lowest energy MLCT for **3.9** from DFT calculation *in vacuo*.

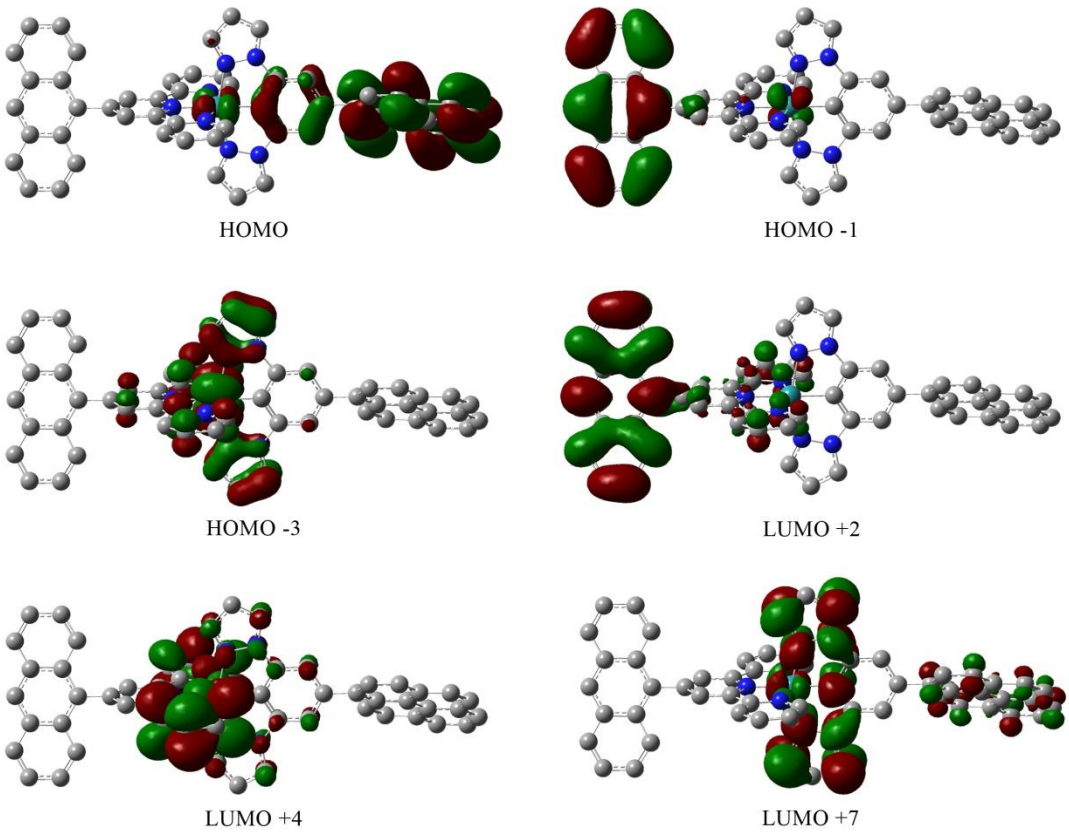

Figure 7.3.22: Isodensity plots (isovalue 0.02) of selected frontier orbitals that are involved in the 2nd lowest energy MLCT for **3.10** from DFT calculation *in vacuo*.

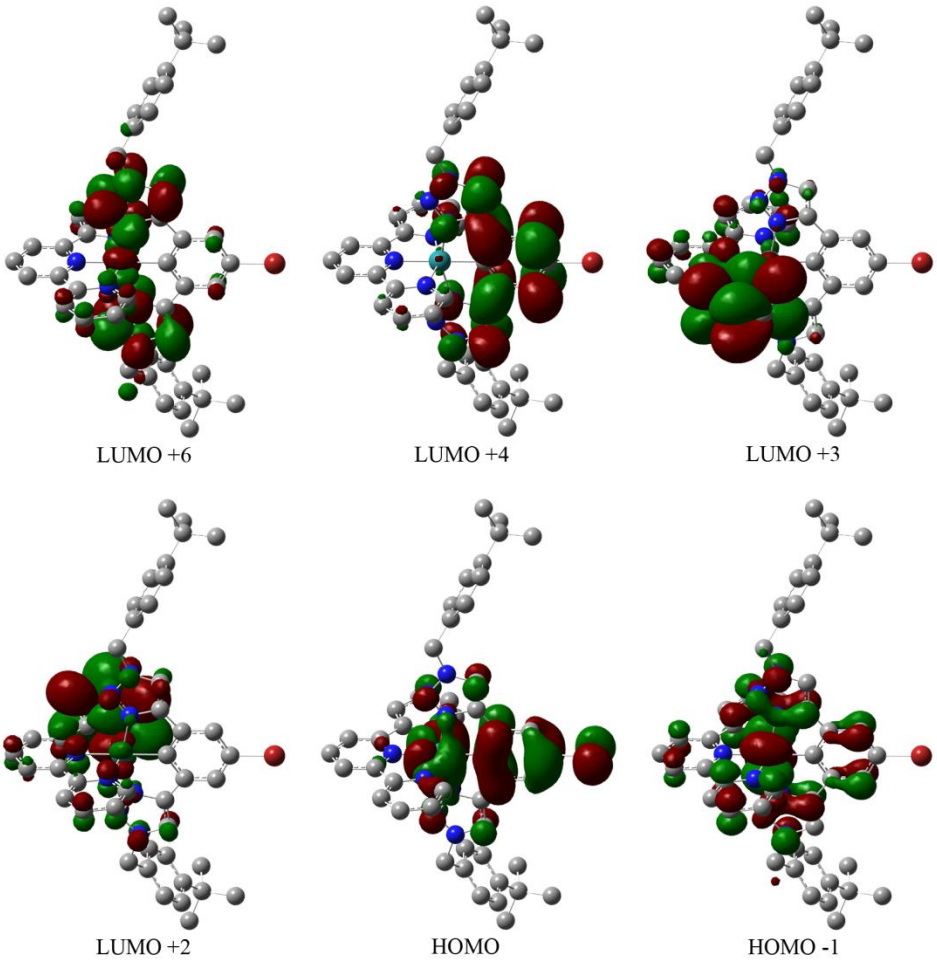

Figure 7.3.23: Isodensity plots (isovalue 0.02) of selected orbitals that are involved in the 2nd lowest energy MLCT for **4.1** from DFT calculation *in vacuo*.

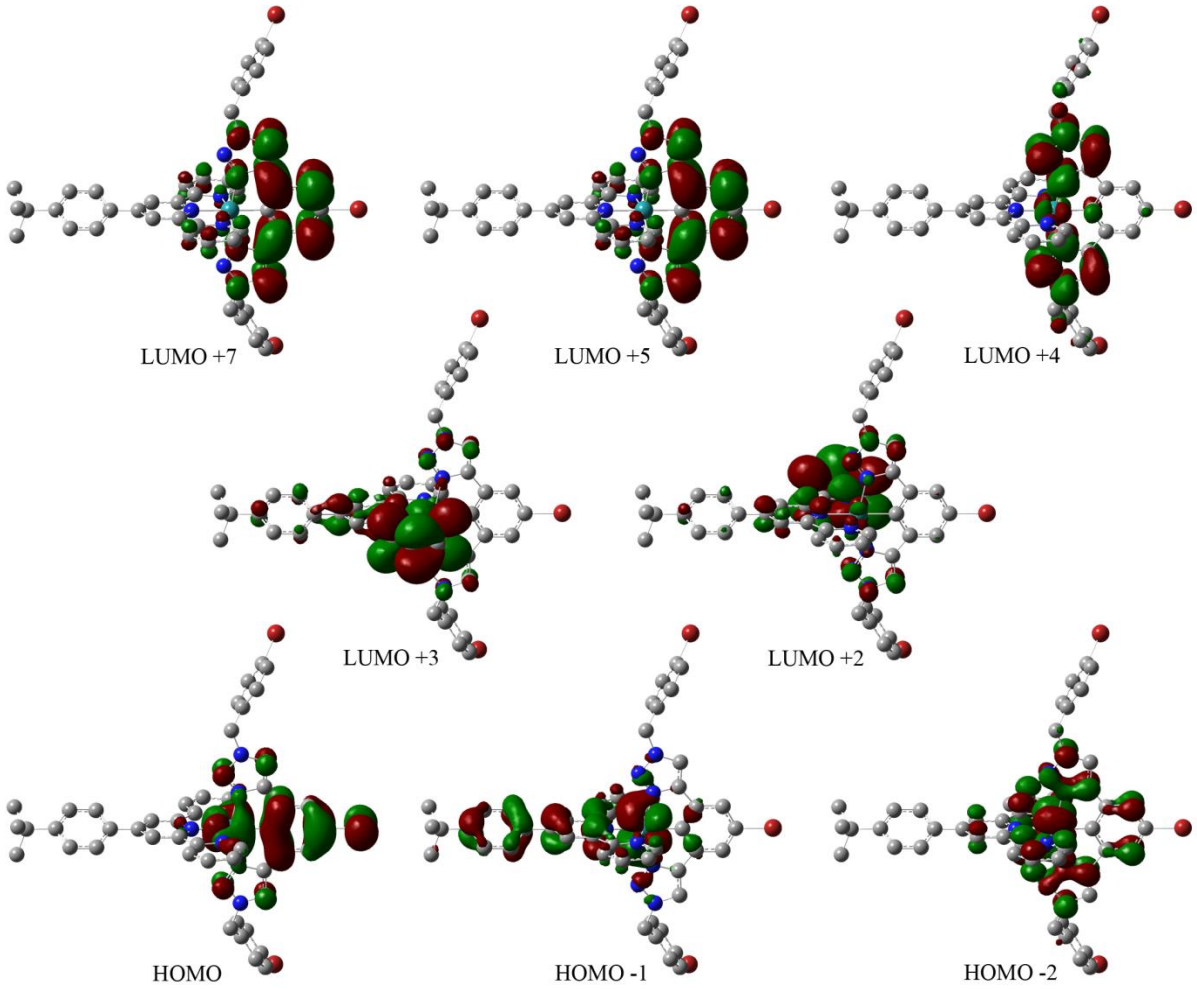

Figure 7.3.24: Isodensity plots (isovalue 0.02) of selected orbitals that are involved in the 2nd lowest energy MLCT for **4.2** from DFT calculation *in vacuo*.

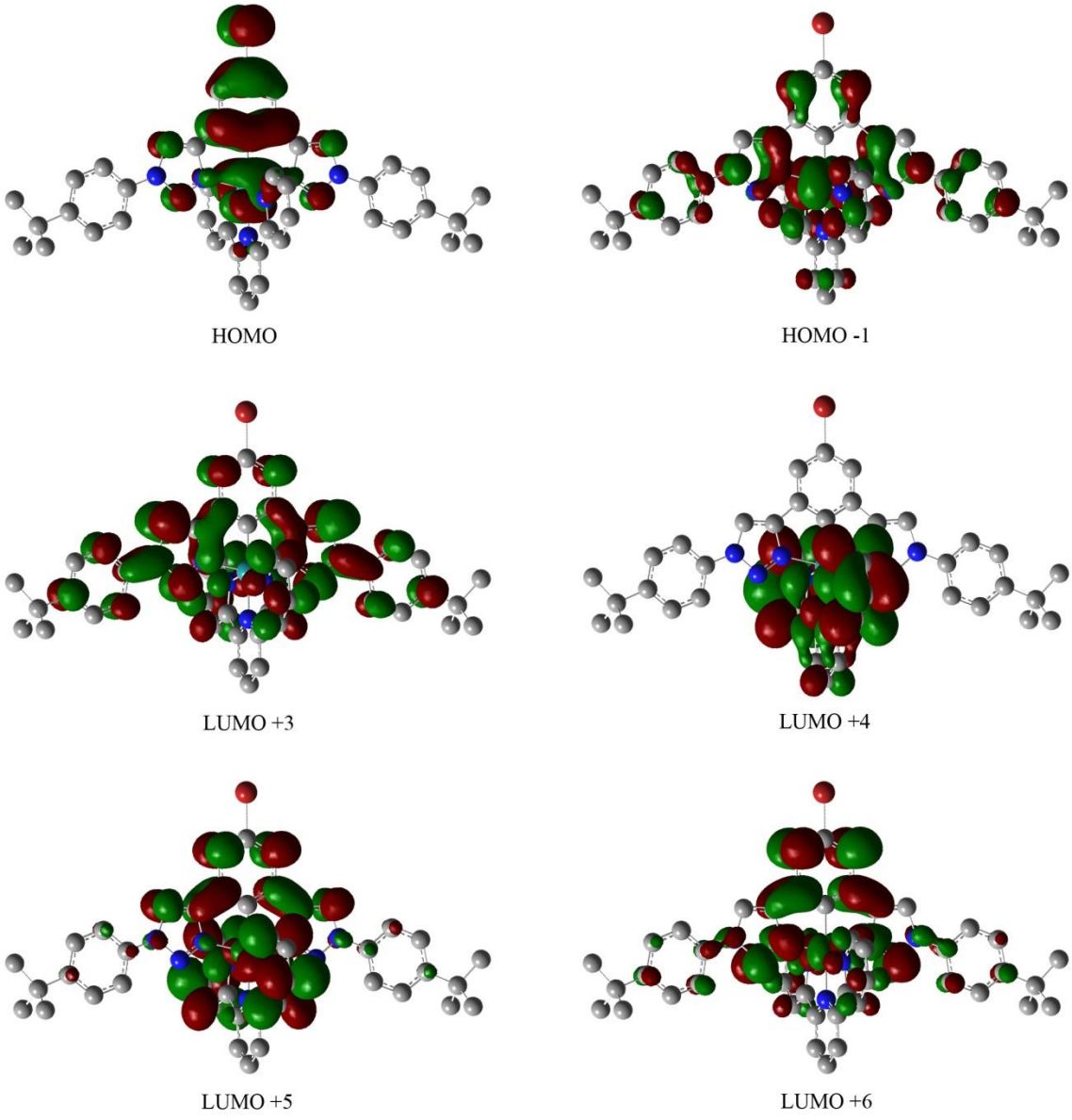

Figure 7.3.25: Isodensity plots (isovalue 0.02) of selected orbitals that are involved in the 2nd lowest energy MLCT for **4.3** from DFT calculation *in vacuo*.

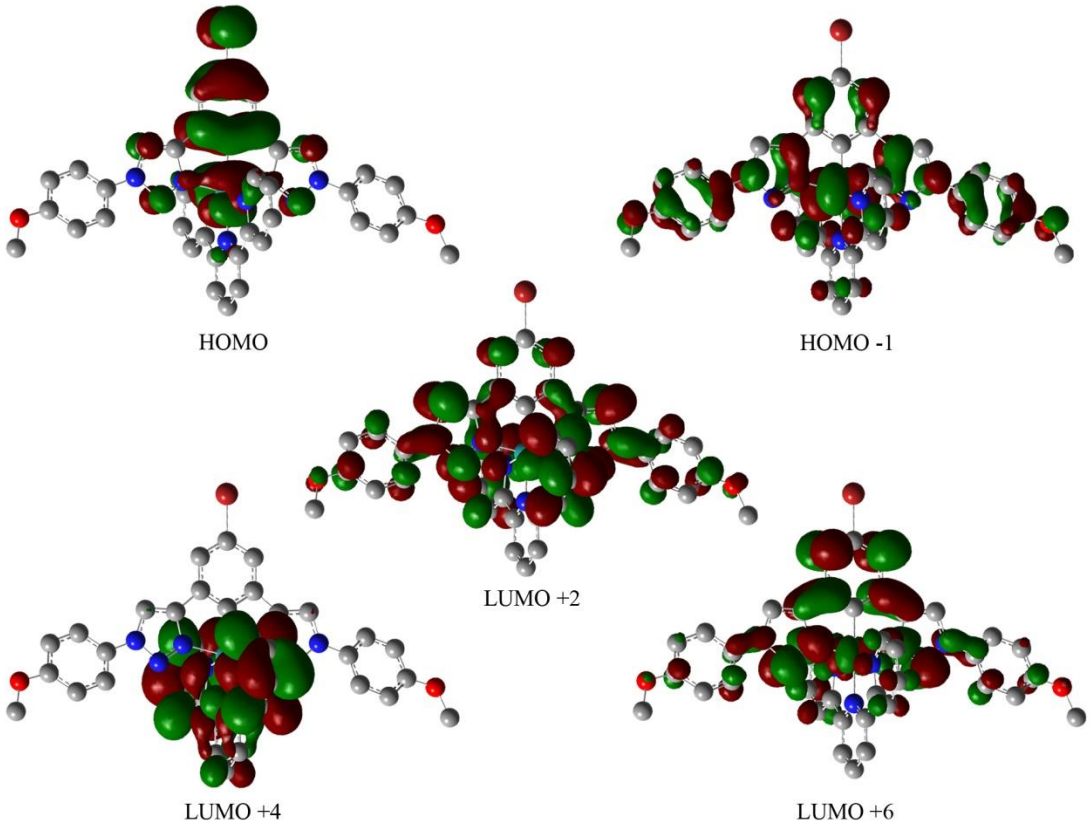

Figure 7.3.26: Isodensity plots (isovalue 0.02) of selected orbitals that are involved in the 2nd lowest energy MLCT for **4.4** from DFT calculation *in vacuo*.

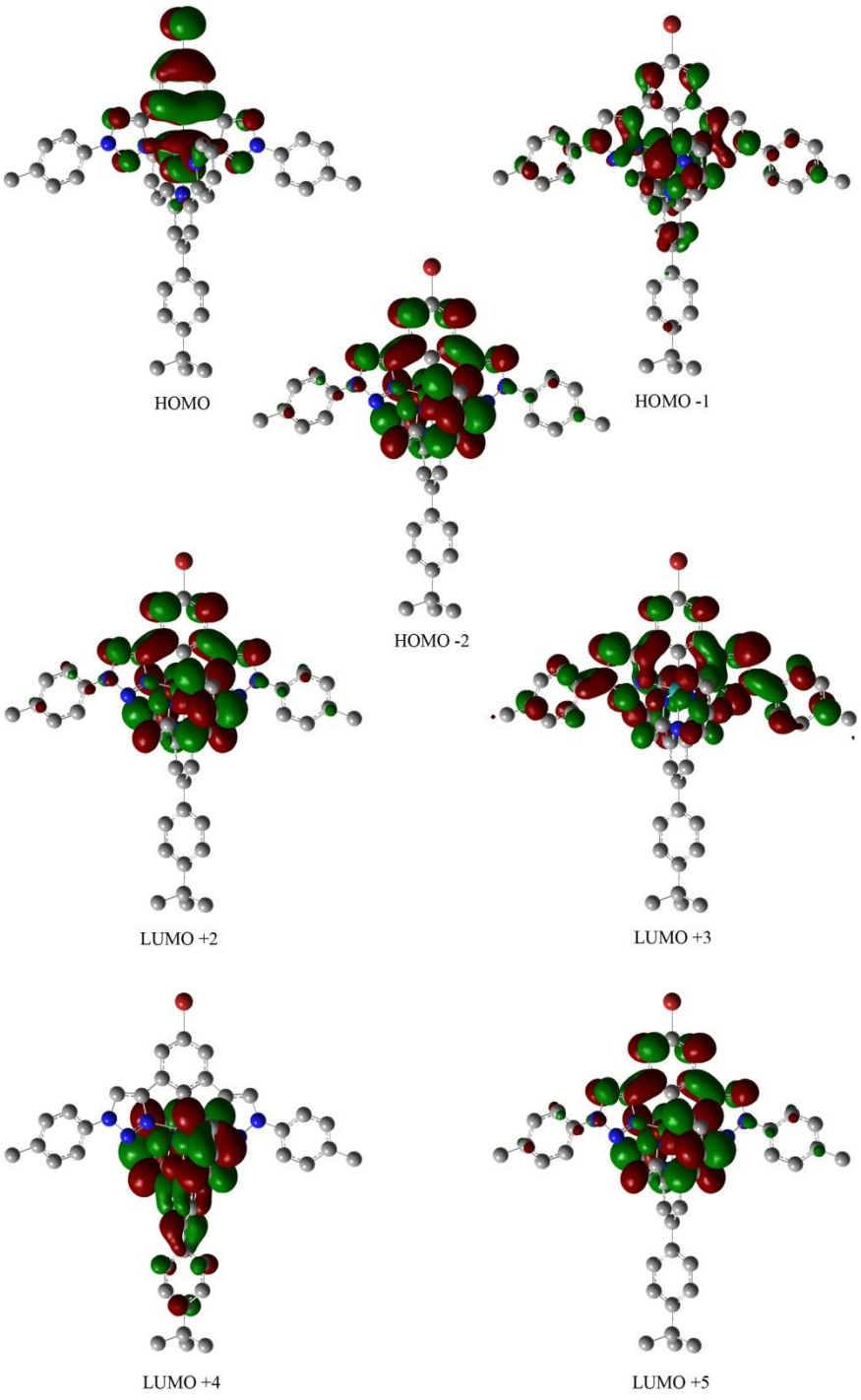

Figure 7.3.27: Isodensity plots (isovalue 0.02) of selected orbitals that are involved in the 2nd lowest energy MLCT for **4.5** from DFT calculation *in vacuo*.

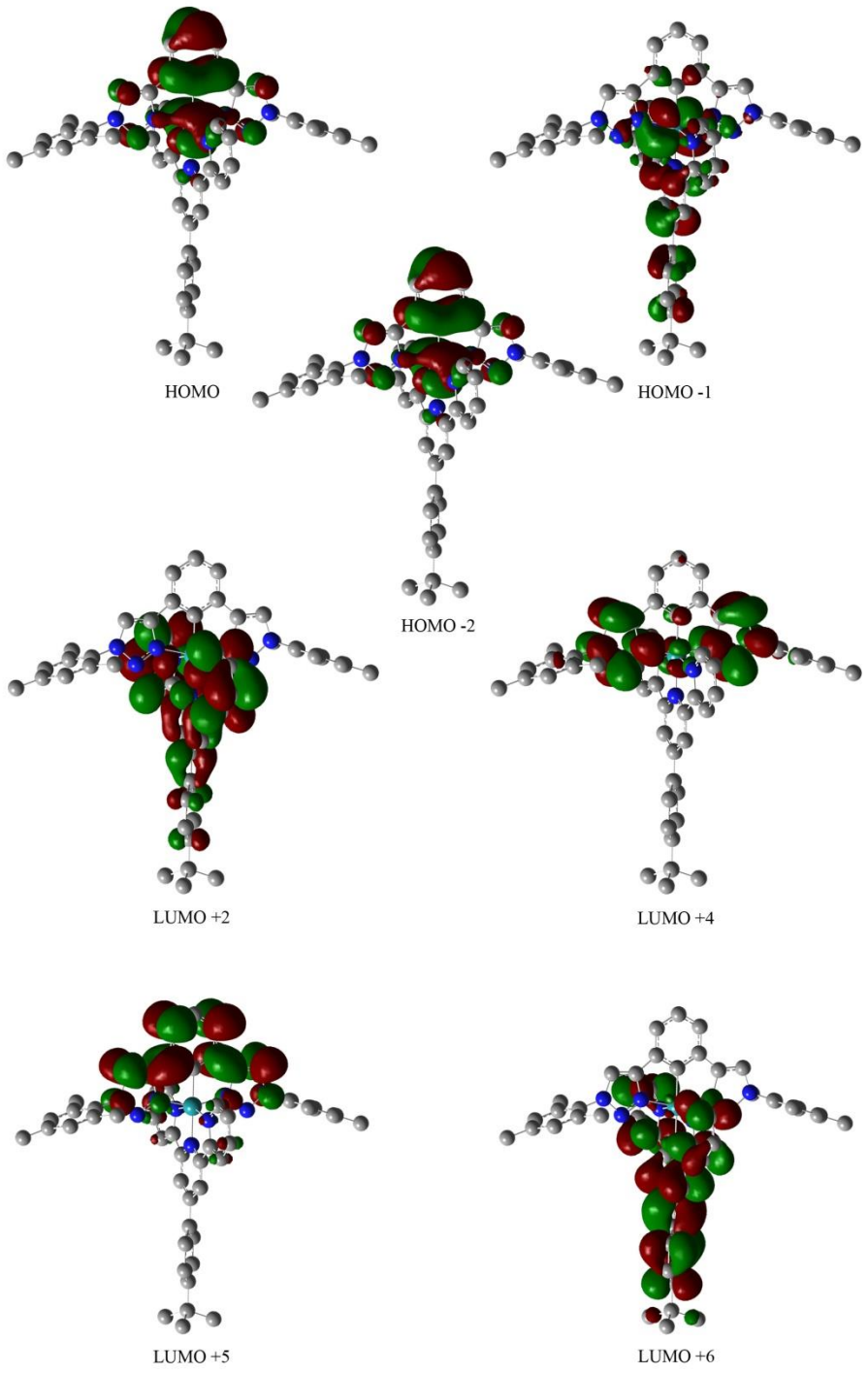

Figure 7.3.28: Isodensity plots (isovalue 0.02) of selected orbitals that are involved in the 2nd lowest energy MLCT for **4.6** from DFT calculation *in vacuo*.

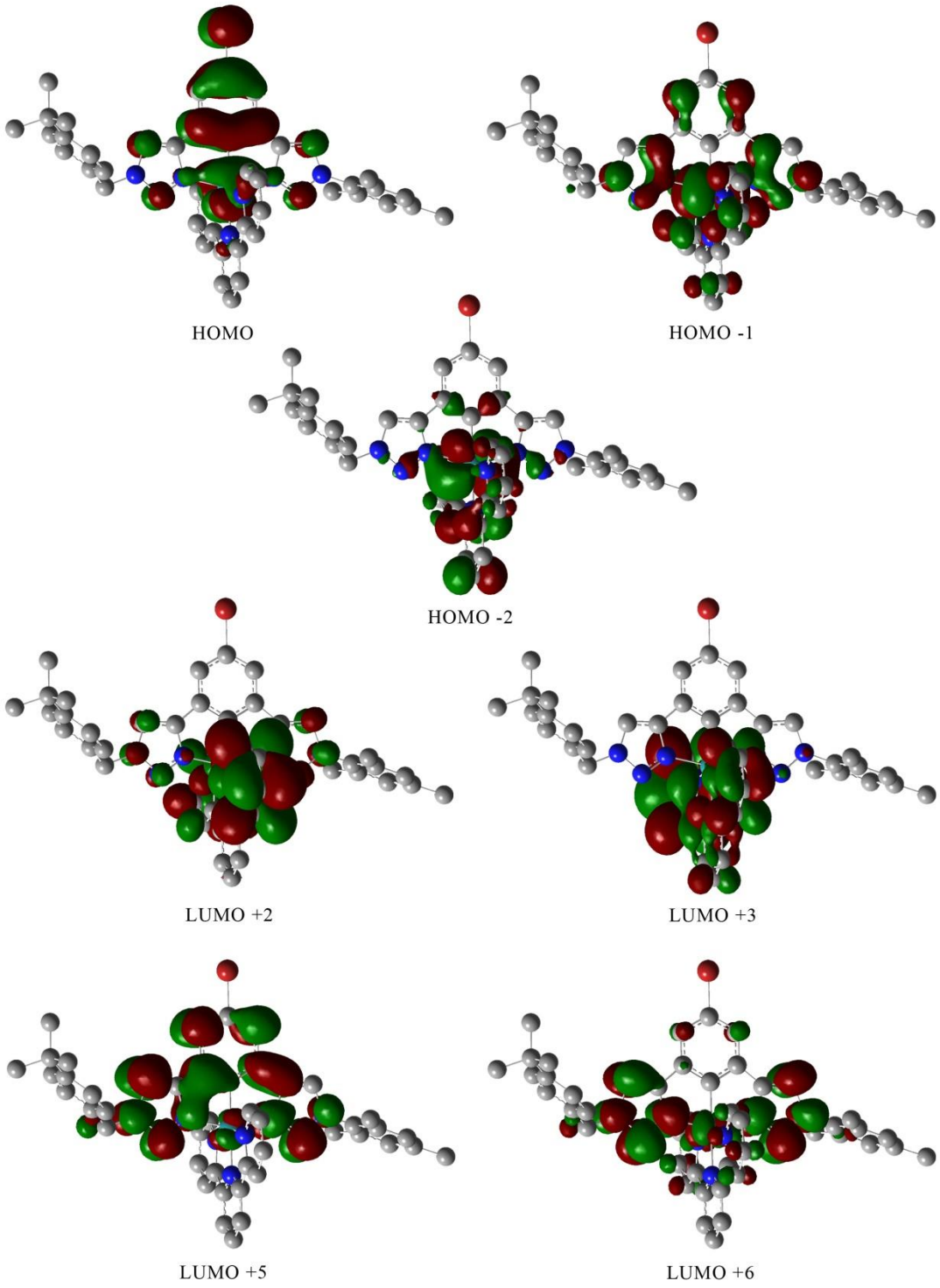

Figure 7.3.29: Isodensity plots (isovalue 0.02) of selected orbitals that are involved in the 2nd lowest energy MLCT for **4.7** from DFT calculation *in vacuo*.

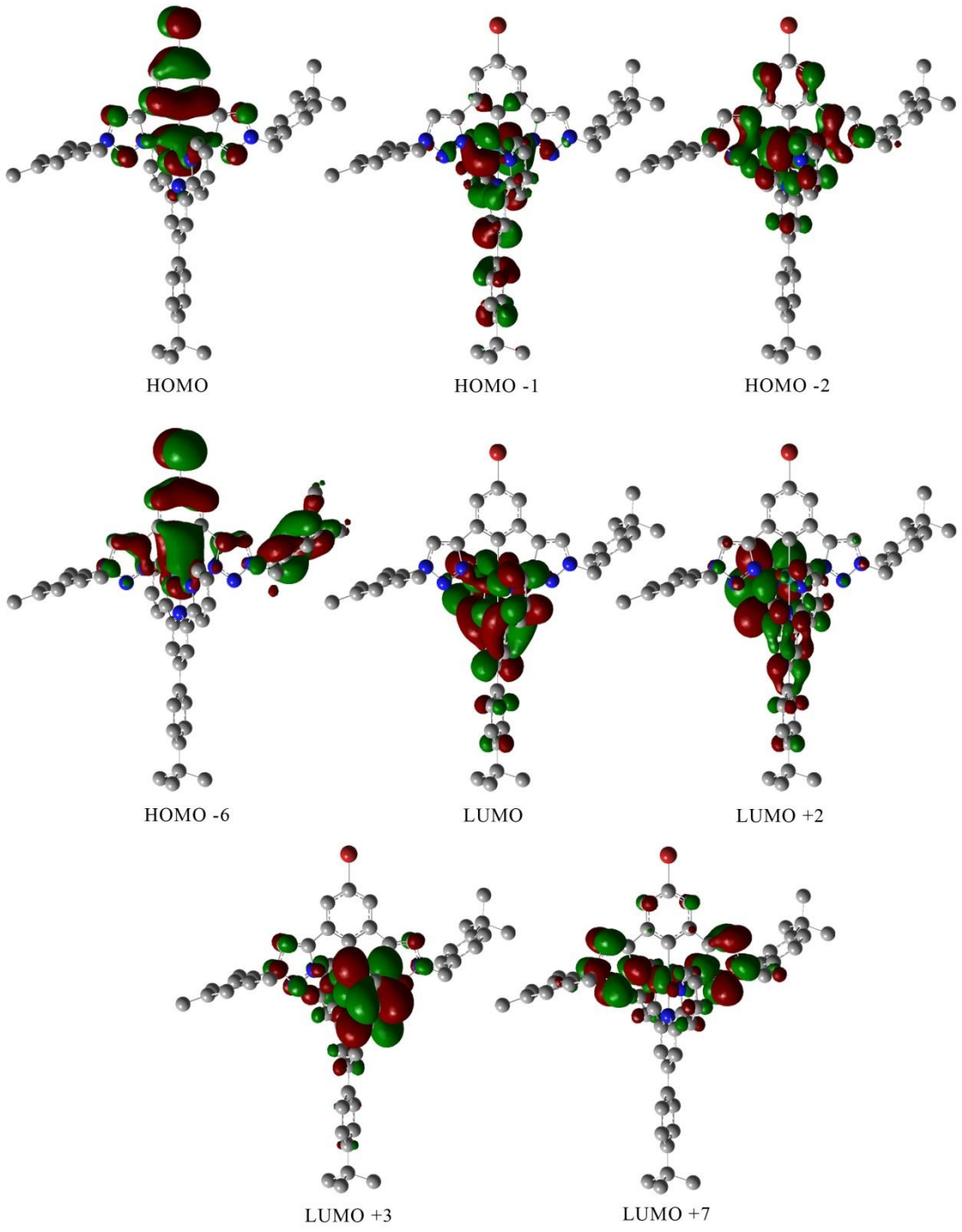

Figure 7.3.30: Isodensity plots (isovalue 0.02) of selected orbitals that are involved in the 2nd lowest energy MLCT for **4.8** from DFT calculation *in vacuo*.

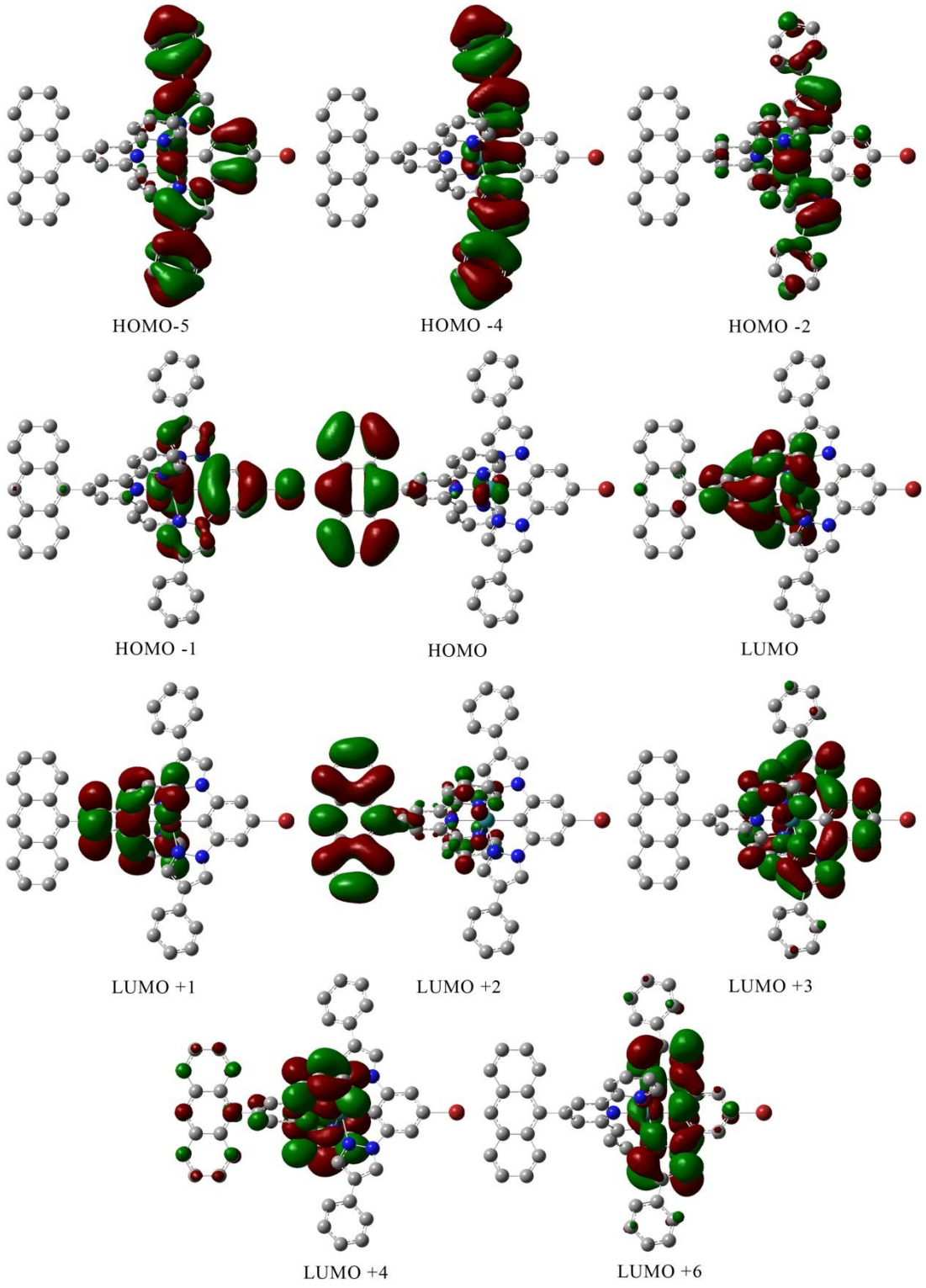

Figure 7.3.31: Isodensity plots (isovalue 0.02) of selected orbitals that are involved in the 2nd lowest energy MLCT for **4.9** from DFT calculation *in vacuo*.

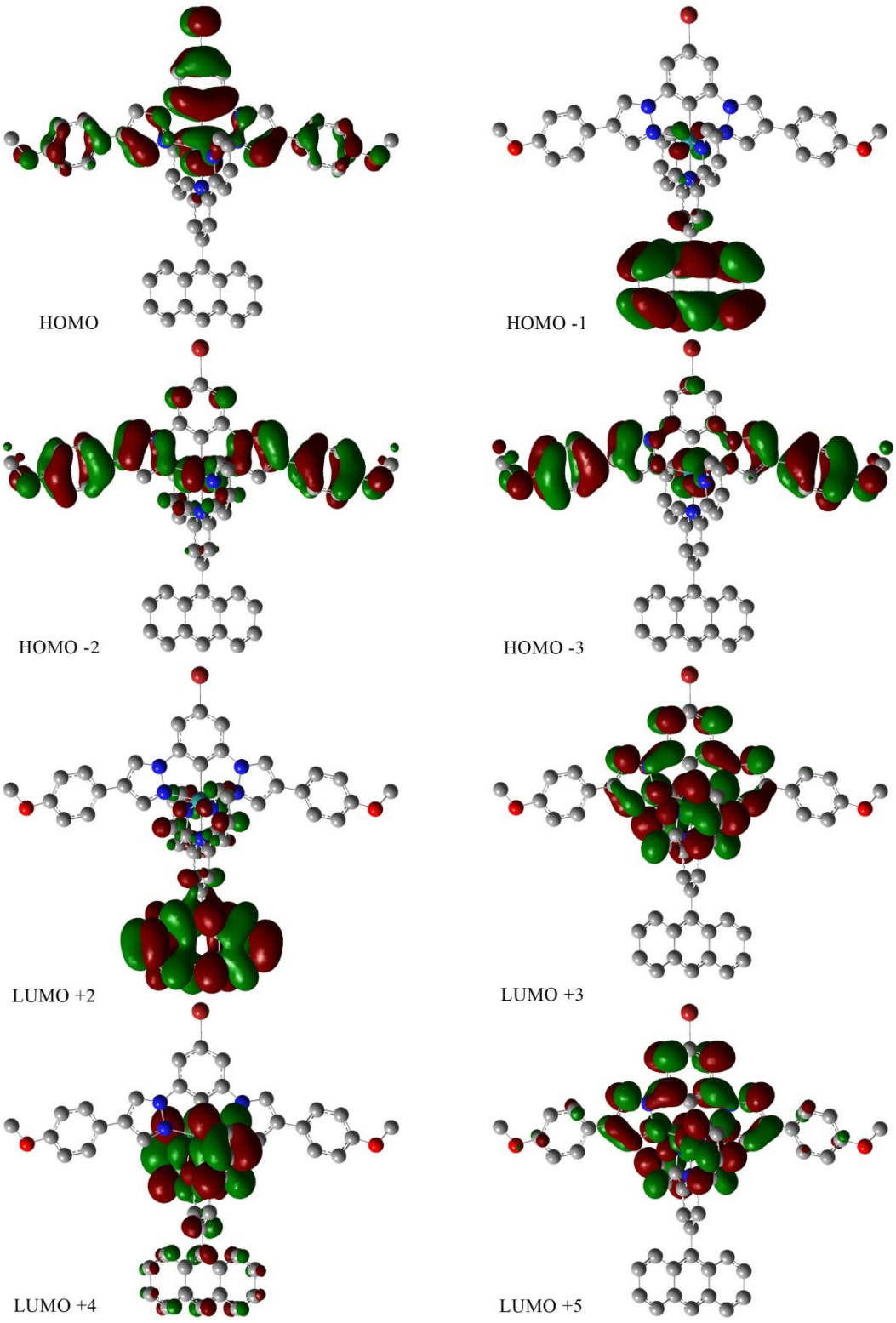

Figure 7.3.32: Isodensity plots (isovalue 0.02) of selected orbitals that are involved in the 2nd lowest energy MLCT for **4.10** from DFT calculation *in vacuo*.

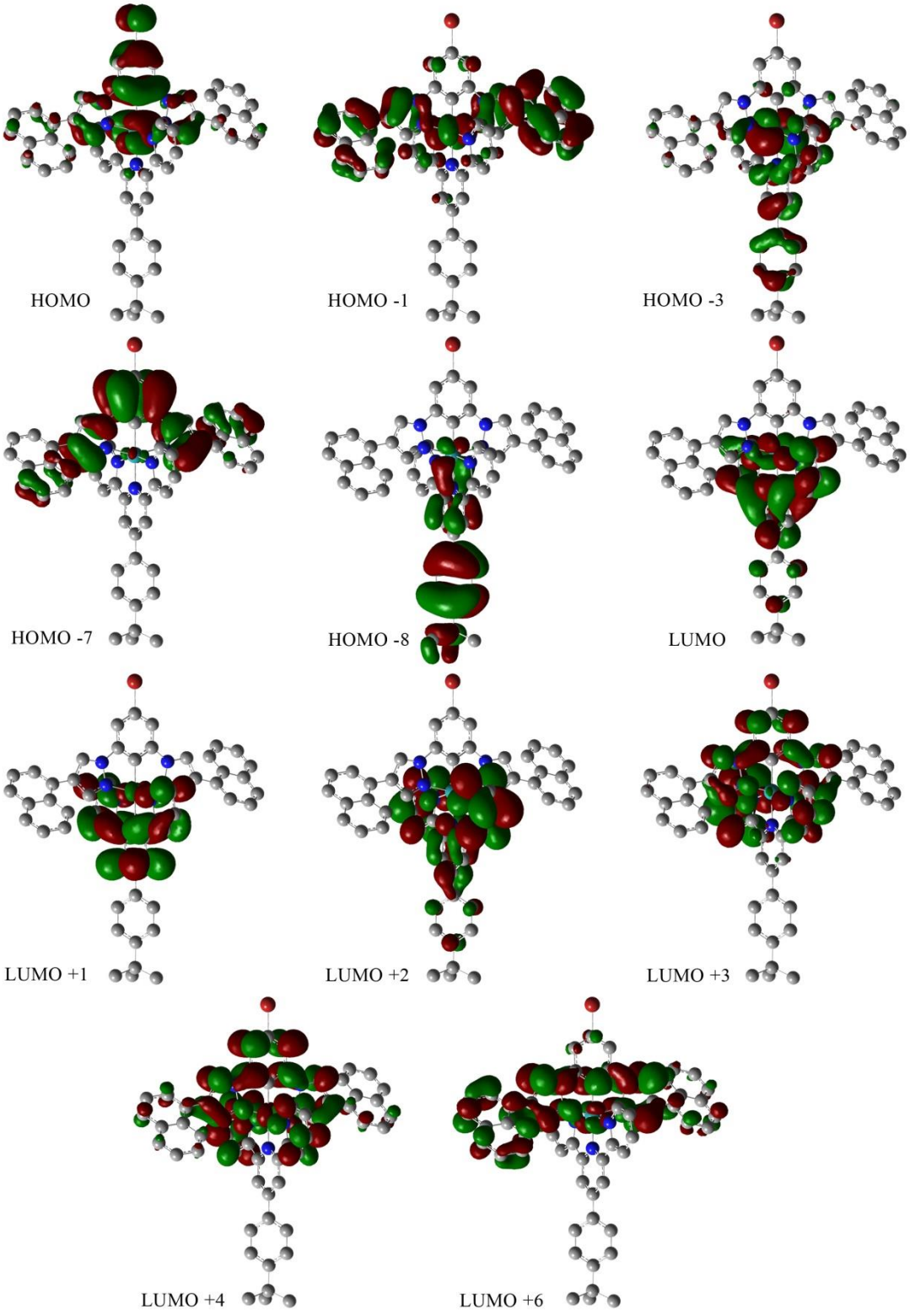

Figure 7.3.33: Isodensity plots (isovalue 0.02) of selected orbitals that are involved in the 2nd lowest energy MLCT for **4.11** from DFT calculation *in vacuo*.

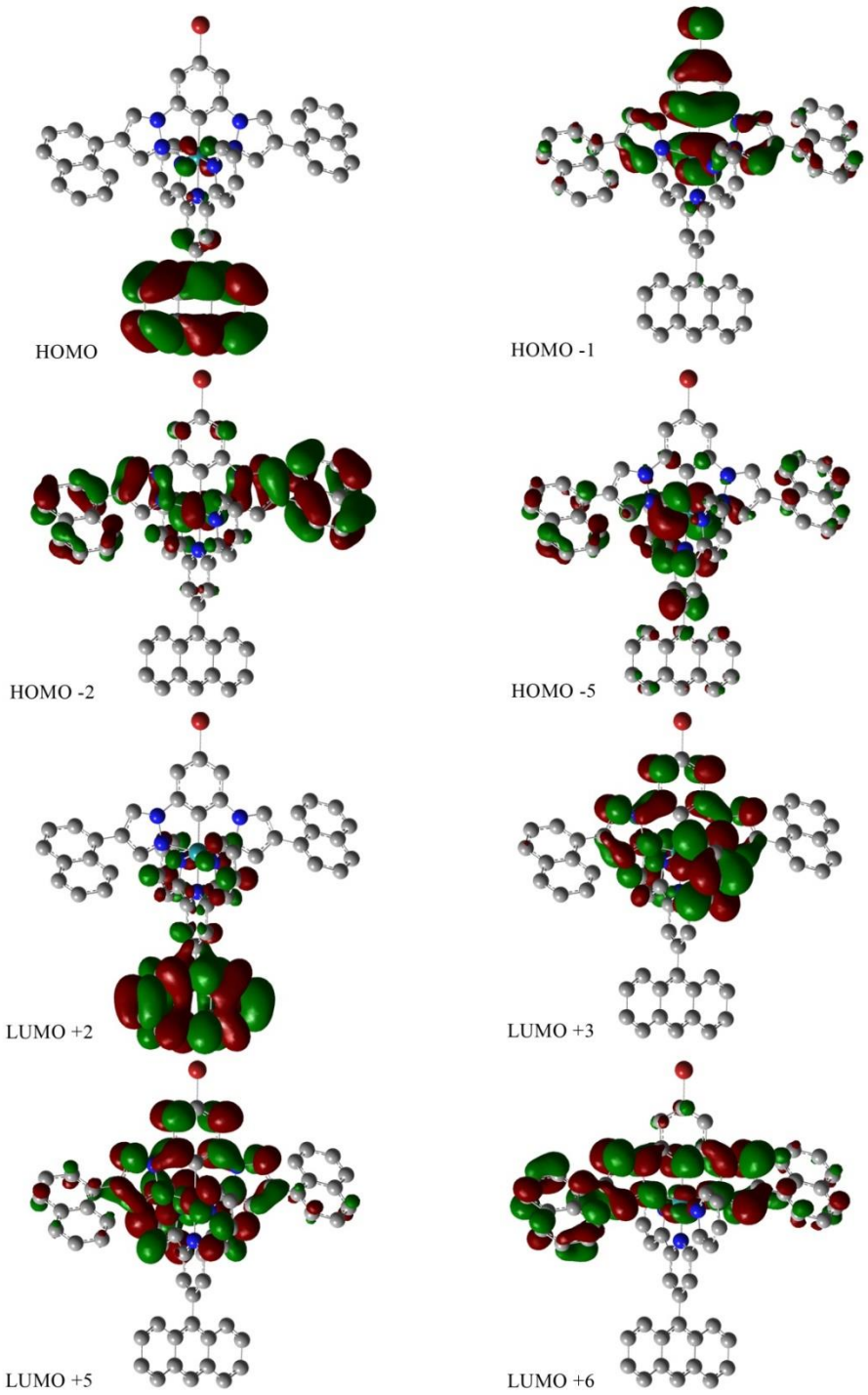

Figure 7.3.34: Isodensity plots (isovalue 0.02) of selected orbitals that are involved in the 2nd lowest energy MLCT for **4.12** from DFT calculation *in vacuo*.

7.4 Orbital energies.

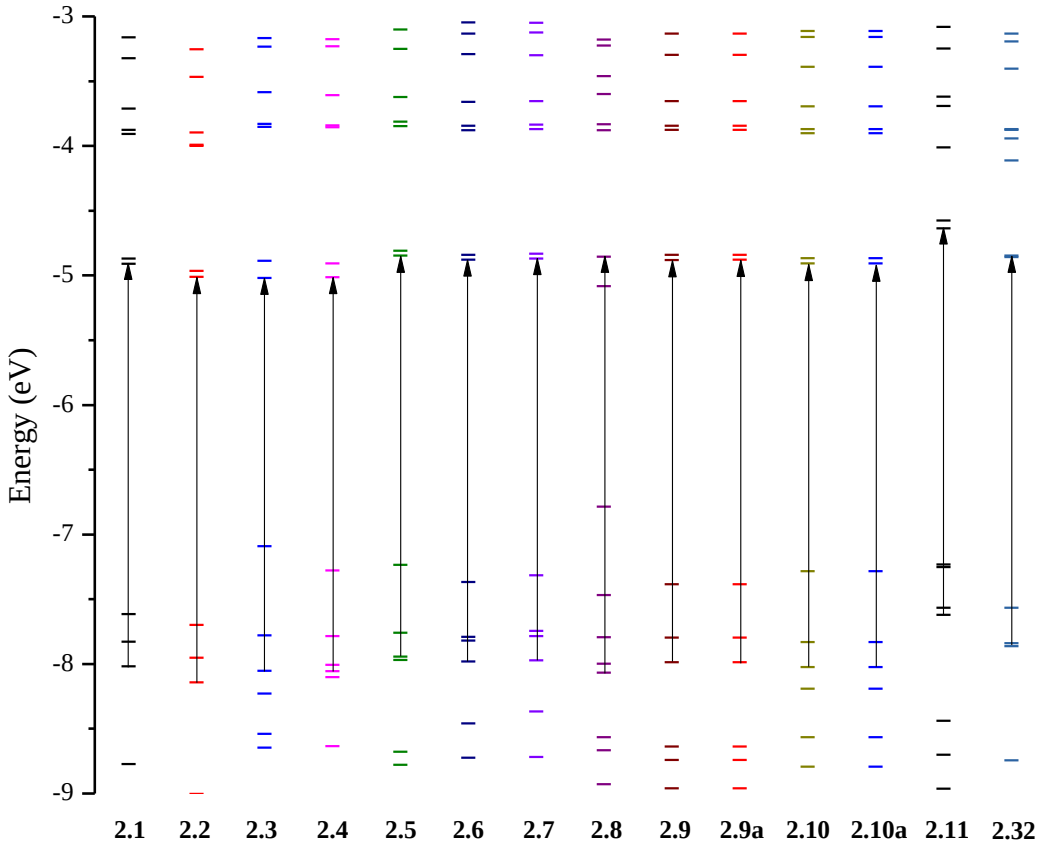

Figure 7.4.1: Orbital energies for complexes **2.1**-**2.11** and reference complex **2.32** from DFT calculations *in vacuo*. The arrows indicate the dominate transition involved in the lowest energy MLCT for each complex.

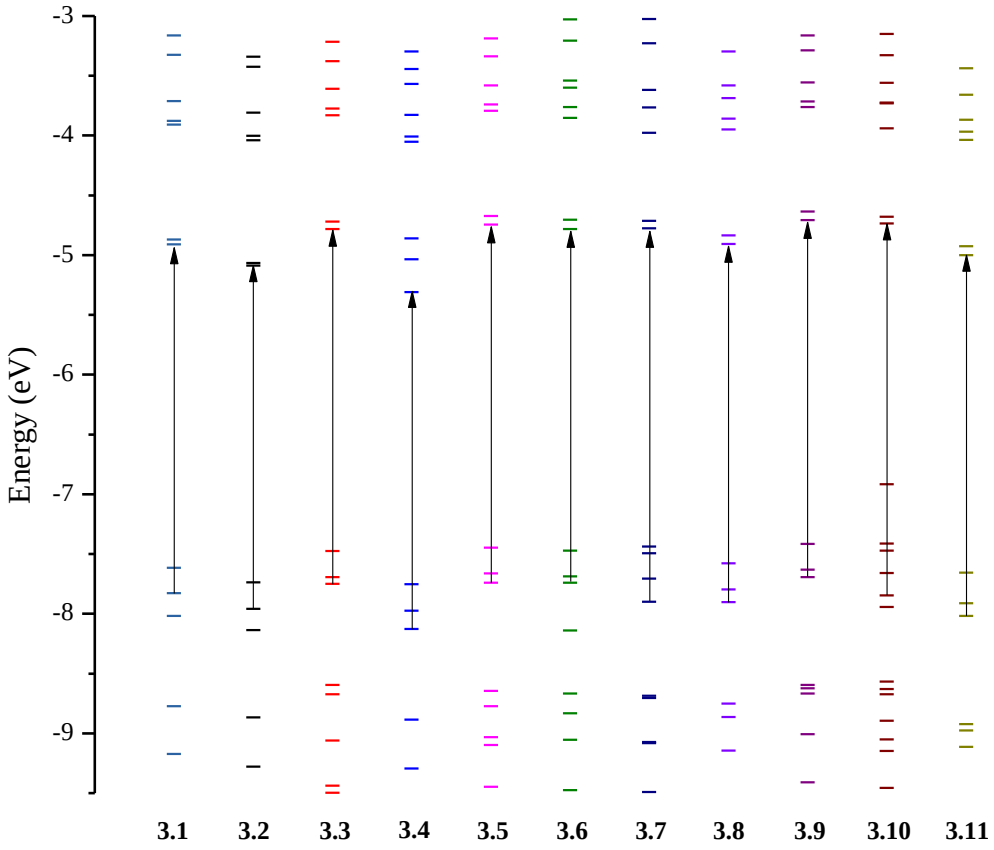

Figure 7.4.2: Orbital energies of complexes **3.1-3.10** and **2.1** from calculated DFT *in vacuo*. The arrow indicates the dominate transition involved in the lowest energy MLCT for each complex.

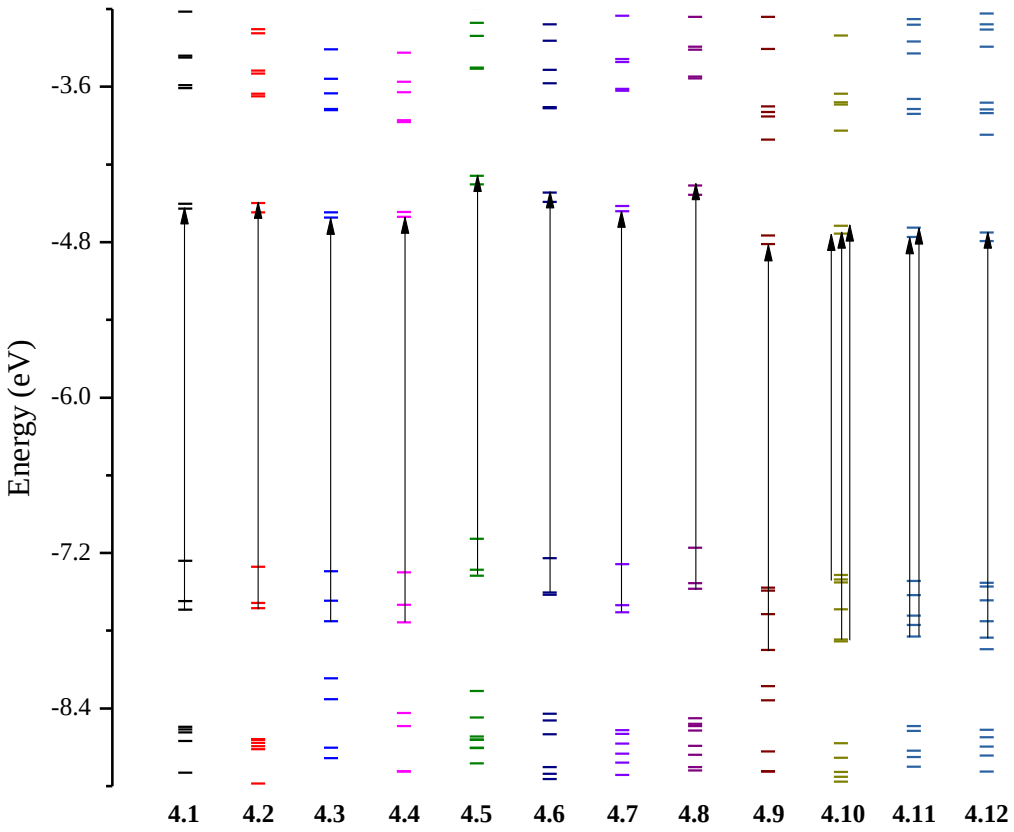

Figure 7.4.3: Orbital energies for complexes **4.1**-**4.12**, showing dominant transitions involved in the lowest energy MLCT for each complex.

7.5 List of complexes.

A list of complexes is provided to help follow discussion of complexes in each chapter more easily.

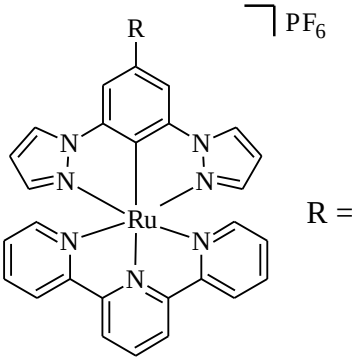

R =	H	**2.1**
	Br	**2.2**
	tertbutylphenyl	**2.3**
	mesityl	**2.4**
	methoxy	**2.5**
	1-naphthyl	**2.6**
	2-naphthyl	**2.7**
	1-pyrenyl	**2.8**
	3,3-dimethylbutanoyl	**2.9**
	phenylacetyl	**2.10**

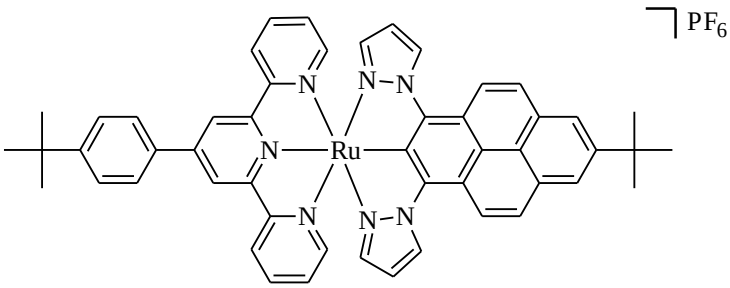

2.11

Figure 7.5.1: Complexes described in this chapter two.

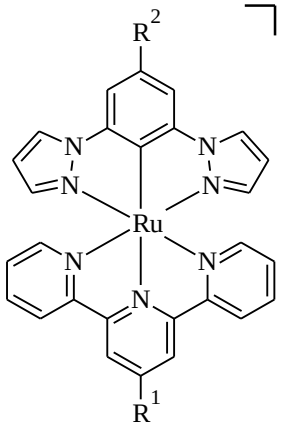

R^1 = H	R^2 = H	**2.1**
R^1 = Ph(4-^{t}Bu)	R^2 = H	**3.1**
R^1 = Ph(3,4,5-triMe)	R^2 = H	**3.2**
R^1 = Ph(4-OMe)	R^2 = H	**3.3**
R^1 = Ph(4-NO_2)	R^2 = H	**3.4**
R^1 = Cl	R^2 = H	**3.5**
R^1 = Ph(4-Br)	R^2 = H	**3.6**
R^1 = Ph(4-Br)	R^2 = Br	**3.7**
R^1 = 2-naphthyl	R^2 = H	**3.8**
R^1 = 9-anthracenyl	R^2 = H	**3.9**
R^1 = 9-anthracenyl	R^2 = 1-pyrenyl	**3.10**

Figure 7.5.2: Complexes described in this chapter three.

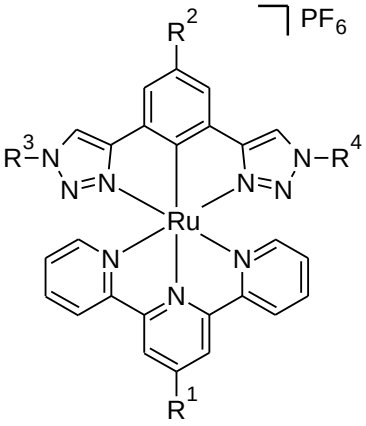

R^1 = H	R^2 = Br	R^3/R^4 = 4-Tertbutylbenzyl	**4.1**
R^1 = 4-Tertbutylphenyl	R^2 = Br	R^3/R^4 = 4-Bromobenzyl	**4.2**
R^1 = H	R^2 = Br	R^3/R^4 = 4-Tertbutylphenyl	**4.3**
R^1 = H	R^2 = Br	R^3/R^4 = 4-Methoxyphenyl	**4.4**
R^1 = 4-Tertbutylphenyl	R^2 = Br	R^3/R^4 = 4-Tolyl	**4.5**
R^1 = 4-Tertbutylphenyl	R^2 = H	R^3/R^4 = 4-Mesityl	**4.6**
R^1 = H	R^2 = Br	R^3 = mesityl, R^4 = 4-Tertbutylbenzyl	**4.7**

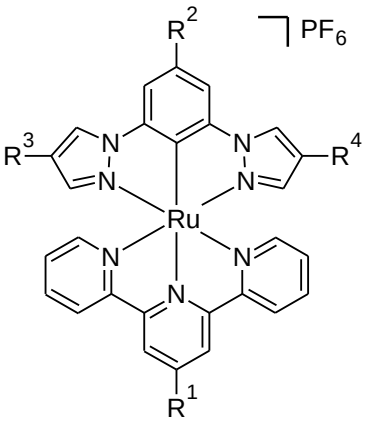

R^1 = 4-Tertbutylphenyl	R^2 = Br	R^3 = mesityl, R^4 = 4-Tertbutylbenzyl	**4.8**
R^1 = 9-Anthracenyl	R^2 = Br	R^3/R^4 = Phenyl	**4.9**
R^1 = 9-Anthracenyl	R^2 = Br	R^3/R^4 = 4-Methoxyphenyl	**4.10**
R^1 = 4-Tertbutylphenyl	R^2 = Br	R^3/R^4 =1-Naphthyl	**4.11**
R^1 = 9-Anthracenyl	R^2 = Br	R^3/R^4 =1-Naphthyl	**4.12**

Figure 7.5.3: Complexes described in this chapter four.

REFERENCES

[1] A. Juris, V. Balzani, F. Barigelletti, S. Campagna, P. Belser, A. Von Zelewsky, *Coord. Chem. Rev.* **1988**, *84*, 85–277.
[2] J. P. Sauvage, J. P. Collin, J. C. Chambron, S. Guillerez, C. Coudret, V. Balzani, F. Barigelletti, L. De Cola, L. Flamigni, *Chem. Rev.* **1994**, *94*, 993-1019.
[3] E. Baranoff, J. P. Collin, L. Flamigni, J. P. Sauvage, *Chem. Soc. Rev.* **2004**, *33*, 147–155.
[4] J. A. Treadway, B. Loeb, R. Lopez, P. A. Anderson, F. R. Keene, T. Meyer, *J. Inorg. Chem.* **1996**, *35*, 2242–2246.
[5] L. De Cola, P. Belser, *Coord. Chem. Rev.* **1998**, *177*, 301–346.
[6] B. O'Regan, M. Grätzel, *Nature* **1991**, *353*, 737–740.
[7] R. C. Lasey, S. S. Banerji, M. Y. Ogawa, *Inorg. Chim. Acta* **2000**, *300*, 822–828.
[8] H. J. Bolink, L. Cappelli, E. Coronado, P. Gavina, *Inorg. Chem.* **2005**, *44*, 5966–5968.
[9] H. J. Bolink, L. Cappelli, E. Coronado, M. Grätzel, M. K. Nazeeruddin, *J. Am. Chem. Soc.* **2006**, *128*, 46–47.
[10] S. Fantacci, E. Ronca, F. De Angelis, *J. Phys. Chem. Lett.* **2013**, *5*, 375-380.
[11] N. J. Turro, *Modern Molecular Photochemistry*, The Benjamin/Cummings Publishing Co., Inc., California, **1978**.
[12] A. Gilbert, J. Baggot, *Essentials of Molecular Photochemistry*, Blackwell Scientific Publications, Oxford, **1991**.
[13] P. Borrell, *Photochemistry: A Primer*, Edward Arnold Ltd., London, **1973**.
[14] F. H. Burstall, *J. Chem. Soc.* **1936**, 173-175.
[15] A. C. Benniston, A. Harriman, F. M. Romero, R. Ziessel, *Dalton Trans.* **2004**, 1233-1238.
[16] A. Orpen, *Acta Crystallogr. Sect. B* **2002**, *58*, 398-406.
[17] F. Allen, *Acta Crystallogr. Sect. B* **2002**, *58*, 380-388.
[18] M. Maestri, N. Armaroli, V. Balzani, E. C. Constable, A. M. W. C. Thompson, *Inorg. Chem.* **1995**, *34*, 2759–2767.
[19] Y. Q. Fang, N. J. Taylor, G. S. Hanan, F. Loiseau, R. Passalacqua, S. Campagna, H. Nierengarten, A. Van Dorsselaer, *J. Am. Chem. Soc.* **2002**, *124*, 7912–7913.
[20] M. Abrahamsson, M. Jäger, R. J. Kumar, T. Österman, P. Persson, H. C. Becker, O. Johansson, L. Hammarström, *J. Am. Chem. Soc.* **2008**, *130*, 15533.
[21] H. Wolpher, O. Johansson, M. Abrahamsson, M. Kritikos, L. Sun, B. Åkermark, *Inorg. Chem. Commun.* **2004**, *7*, 337.
[22] M. Abrahamsson, H. Wolpher, O. Johansson, J. Larsson, M. Kritikos, L. Eriksson, P. O. Norrby, J. Bergquist, L. Sun, B. Åkermark, L. Hammarström, *Inorg. Chem.* **2005**, *44*, 3215.
[23] G. A. Parada, L. A. Fredin, M.-P. Santoni, M. Jäger, R. Lomoth, L. Hammarström, O. Johansson, P. Persson, S. Ott, *Inorg. Chem.* **2013**, *52*, 5128-5137.
[24] M. Cocchi, D. Virgili, V. Fattori, D. L. Rochester, J. A. G. Williams, *Adv. Funct. Mater.* **2007**, *17*, 285–289.
[25] A. J. Wilkinson, H. Puschmann, J. A. K. Howard, C. E. Foster, J. A. G. Williams, *Inorg. Chem.* **2006**, *45*, 8685–8699.
[26] J. P. Collin, P. Gavina, V. Heitz, J.-P. Sauvage, *Eur. J. Inorg. Chem.* **1998**, 1–14.
[27] J.-Y. Shao, J. Yao, Y.-W. Zhong, *Organometallics* **2012**, *31*, 4302-4308.
[28] B. Schulze, D. Escudero, C. Friebe, R. Siebert, H. Görls, S. Sinn, M. Thomas, S. Mai, J. Popp, B. Dietzek, L. González, U. S. Schubert, *Chem. Eur. J.* **2012**, *18*, 4010-4025.

[29] W.-W. Yang, L. Wang, Y.-W. Zhong, J. Yao, *Organometallics* **2011**, *30*, 2236-2240.
[30] J. Djukic, J. Sortais, L. Barloy, M. Pfeffer, *Eur. J. Inorg. Chem.* **2009**, *2009*, 817-853.
[31] M. Albrecht, *Chem. Rev.* **2009**, *110*, 576-623.
[32] Y.-R. Luo, *Comprehensive Handbook of Chemical Bond Energies*, CRC Press, **2007**.
[33] C. Bonnefous, A. Chouai, R. P. Thummel, *Inorg. Chem.* **2001**, *40*, 5851-5859.
[34] G. Schwarzenbach, *Helv. Chim. Acta.* **1952**, *35*, 2344-2359.
[35] I. Omae, *J. Organomet. Chem.* **2011**, *696*, 1128-1145.
[36] F. Barigelletti, B. Ventura, J. P. Collin, R. Kayhanian, P. Gavina, J.-P. Sauvage, *Eur. J. Inorg. Chem.* **2000**, 113–119.
[37] S. H. Wadman, M. Lutz, D. M. Tooke, A. L. Spek, F. Hartl, R. W. A. Havenith, G. P. M. van Klink, G. van Koten, *Inorg. Chem.* **2009**, *48*, 1887-1900.
[38] S. H. Wadman, J. M. Kroom, K. Bakker, M. Lutz, A. L. Spek, G. P. M. van Klink, G. van Koten, *Chem. Commun.* **2007**, 1907.
[39] B. D. Koivisto, K. C. D. Robson, C. P. Berlinguette, *Inorg. Chem.* **2009**, *48*, 9644-9652.
[40] P. G. Bomben, K. C. D. Robson, P. A. Sedach, C. P. Berlinguette, *Inorg. Chem.* **2009**, *48*, 9631-9643.
[41] C.-J. Yao, L.-Z. Sui, H.-Y. Xie, W.-J. Xiao, Y.-W. Zhong, J. Yao, *Inorg. Chem.* **2010**, *49*, 8347-8350.
[42] L. Wang, W.-W. Yang, Y.-W. Zhong, J. Yao, *Dalton Trans.* **2013**, *42*, 5611-5614.
[43] S. Develay, O. Blackburn, A. L. Thompson, J. A. G. Williams, *Inorg. Chem.* **2008**, *47*, 11129-11142.
[44] R. J. Watts, J. S. Harrington, J. Van Houten, *J. Am. Chem. Soc.* **1977**, *99*, 2179-2187.
[45] C. M. Flynn, J. N. Demas, *J. Am. Chem. Soc.* **1974**, *96*, 1959-1960.
[46] N. P. Ayala, C. M. Flynn, L. Sacksteder, J. N. Demas, B. A. DeGraff, *J. Am. Chem. Soc.* **1990**, *112*, 3837-3844.
[47] M. Indelli, C. Chiorboli, F. Scandola, *Photochemistry and Photophysics of Coordination Compounds: Rhodium, Vol. 280*, Springer Berlin Heidelberg, **2007**.
[48] M. Y. Kim, W. K. Seok, Y. Dong, H. Yun, *Inorg. Chim. Acta* **2001**, *319*, 194-198.
[49] Z. Wang, E. Turner, V. Mahoney, S. Madakuni, T. Groy, J. Li, *Inorg. Chem.* **2010**, *49*, 11276-11286.
[50] S. J. Farley, D. L. Rochester, A. L. Thompson, J. A. K. Howard, J. A. G. Williams, *Inorg. Chem.* **2005**, *44*, 9690-9703.
[51] J. Brooks, Y. Babayan, S. Lamansky, P. I. Djurovich, I. Tsyba, R. Bau, M. E. Thompson, *Inorg. Chem.* **2002**, *41*, 3055-3066.
[52] S. Kumar, http://nsdl.niscair.res.in/jspui/handle/123456789/793, **2006**.
[53] J. C. Fetzer, *Polycyclic Aromat. Compd.* **2007**, *27*, 143-162.
[54] B. H. Bransden, C. J. Joachain, *Quantum mechanics (2nd ed.)*, **2000**.
[55] D. A. Skoog, D. M. West, F. J. Holler, *Analytical Chemistry: An Introduction*, 7th ed., Saunders Golden Sunburst Series, **1999**.
[56] D. A. Skoog, D. M. West, F. J. Holler, S. R. Crouch, 8th ed., Brooks Cole, **2003**.
[57] A. Jabłoński, *Nature* **1933**, *131*, 839-840.
[58] J. A. Halstead, *J. Chem. Educ.* **2012**, *90*, 70-75.
[59] M. Kasha, *Farad. Discuss.* **1950**, p 14-19.
[60] A. Gilbert, J. Baggott, *Essentials of Molecular Photochemistry*, **1991**.
[61] W. B. Connick, H. B. Gray, *J. Am. Chem. Soc.* **1997**, *119*, 11620-11627.

[62] J. V. Caspar, E. M. Kober, B. P. Sullivan, T. J. Meyer, *J. Am. Chem. Soc.* **1982**, *104*, 630-632.
[63] J. V. Caspar, T. J. Meyer, *J. Phys. Chem.* **1983**, *87*, 952-957.
[64] K. R. Barqawi, Z. Murtaza, T. J. Meyer, *J. Phys. Chem.* **1991**, *95*, 47-50.
[65] M. J. Frisch, G. W. Trucks, H. B. Schlegel, G. E. Scuseria, M. A. Robb, J. R. Cheeseman, G. Scalmani, V. Barone, B. Mennucci, G. A. Petersson, H. Nakatsuji, M. Caricato, X. Li, H. P. Hratchian, A. F. Izmaylov, J. Bloino, G. Zheng, J. L. Sonnenberg, M. Hada, M. Ehara, K. Toyota, R. Fukuda, J. Hasegawa, M. Ishida, T. Nakajima, Y. Honda, O. Kitao, H. Nakai, T. Vreven, J. A. Montgomery, Jr. , J. E. Peralta, F. Ogliaro, M. Bearpark, J. J. Heyd, E. Brothers, K. N. Kudin, V. N. Staroverov, T. Keith, R. Kobayashi, J. Normand, K. Raghavachari, A. Rendell, J. C. Burant, S. S. Iyengar, J. Tomasi, M. Cossi, N. Rega, J. M. Millam, M. Klene, J. E. Knox, J. B. Cross, V. Bakken, C. Adamo, J. Jaramillo, R. Gomperts, R. E. Stratmann, O. Yazyev, A. J. Austin, R. Cammi, C. Pomelli, J. W. Ochterski, R. L. Martin, K. Morokuma, V. G. Zakrzewski, G. A. Voth, P. Salvador, J. J. Dannenberg, S. Dapprich, A. D. Daniels, O. Farkas, J. B. Foresman, J. V. Ortiz, J. Cioslowski, D. J. Fox, Gaussian, Inc., Wallingford CT, **2010**.
[66] http://www.britannica.com/EBchecked/topic/705881/Moores-law.
[67] E. Schrödinger, *Phys. Rev.* **1926**, *28*, 1049-1070.
[68] F. Jensen, *Introduction to Computational Chemistry*, Second ed., John Wiley & Sons, Ltd, West Sussex, **2007**.
[69] A. D. Becke, *J. Chem. Phys.* **1993**, *98*, 1372-1377.
[70] S. B. Braun-Sand, O. Wiest, *J. Phys. Chem.* **2003**, *107*, 285-291.
[71] S. H. Wadman, R. W. A. Havenith, F. Hartl, M. Lutz, A. L. Spek, G. P. M. van Klink, G. van Koten, *Inorg. Chem.* **2009**, *48*, 5685-5696.
[72] https://bse.pnl.gov/bse/portal.
[73] A. Hantzsch, *Ber. Dtsch. Chem. Ges.* **1881**, *14*, 1637-1638.
[74] F. H. Case, T. J. Kasper, *J. Am. Chem. Soc.* **1956**, *78*, 5842-5844.
[75] F. Kröhnke, W. Zecher, J. Curtze, D. Drechsler, K. Pfleghar, K. E. Schnalke, W. Weis, *Angew. Chem. Int. Ed. Engl.* **1962**, *1*, 626-632.
[76] F. Krohnke, *Synthesis* **1976**, *1*.
[77] P. E. Fanta, *Synthesis* **1974**, *1974*, 9-21.
[78] D. Ma, Q. Cai, *Synlett* **2004**, 128-130.
[79] W. L. F. Armarego, C. Chai, *Purification of Laboratory Chemicals (Seventh Edition)*, Butterworth-Heinemann, Boston, **2013**.
[80] K. Sonogashira, *J. Organomet. Chem.* **2002**, *653*, 46-49.
[81] T. Ljungdahl, T. Bennur, A. Dallas, H. Emtenäs, J. Mårtensson, *Organometallics* **2008**, *27*, 2490-2498.
[82] R. Chinchilla, C. Najera, *Chem. Soc. Rev.* **2011**, *40*, 5084-5121.
[83] N. Miyaura, A. Suzuki, *Chem. Rev.* **1995**, *95*, 2457-2483.
[84] http://www.nobelprize.org/nobel_prizes/chemistry/laureates/2010/.
[85] A. Suzuki, *Angew. Chem. Int. Ed.* **2011**, *50*, 6722-6737.
[86] H. C. Kolb, M. G. Finn, K. B. Sharpless, *Angew. Chem. Int. Ed.* **2001**, *40*, 2004-2021.
[87] F. Himo, T. Lovell, R. Hilgraf, V. V. Rostovtsev, L. Noodleman, K. B. Sharpless, V. V. Fokin, *J. Am. Chem. Soc.* **2005**, *127*, 210-216.
[88] A. Bernanose, M. Comte, P. Vouaux, *J. Chim. Phys.* **1953**, *50*, 64.
[89] C. W. Tang, S. A. VanSlyke, *Appl. Phys. Lett.* **1987**, *51*, 913-915.

[90] G. Gu, Z. Shen, P. E. Burrows, S. R. Forrest, *Adv. Mater.* **1997**, *9*, 725-728.
[91] M. Grell, D. D. C. Bradley, *Adv. Mater.* **1999**, *11*, 895-905.
[92] S. Lamansky, P. Djurovich, D. Murphy, F. Abdel-Razzaq, H. Lee, C. Adachi, P. E. Burrows, S. R. Forrest, M. E. Thompson, *J. Am. Chem. Soc.* **2001**, *123*, 4304-4312.
[93] J. Slinker, D. Bernards, P. L. Houston, H. D. Abruna, S. Bernhard, G. G. Malliaras, *Chem. Commun.* **2003**, 2392-2399.
[94] T. R. Hebner, C. C. Wu, D. Marcy, M. H. Lu, J. C. Sturm, *Appl. Phys. Lett.* **1998**, *72*, 519-521.
[95] M. A. Baldo, D. F. O'Brien, Y. You, A. Shoustikov, S. Sibley, M. E. Thompson, S. R. Forrest, *Nature* **1998**, *395*, 151-154.
[96] M. A. Baldo, S. Lamansky, P. E. Burrows, M. E. Thompson, S. R. Forrest, *Appl. Phys. Lett.* **1999**, *75*, 4-6.
[97] S. J. Yeh, M. F. Wu, C. T. Chen, Y. H. Song, Y. Chi, M. H. Ho, S. F. Hsu, C. H. Chen, *Adv. Mater.* **2005**, *17*, 285-289.
[98] E. Holder, B. M. W. Langeveld, U. S. Schubert, *Adv. Mater.* **2005**, *17*, 1109-1121.
[99] M. E. Thompson, P. E. Burrows, S. R. Forrest, *Curr. Opin. Solid State Mater. Sci.* **1999**, *4*, 369-372.
[100] V. Cleave, G. Yahioglu, P. L. Barny, R. H. Friend, N. Tessler, *Adv. Mater.* **1999**, *11*, 285-288.
[101] M. A. Baldo, M. E. Thompson, S. R. Forrest, *Nature* **2000**, *403*, 750-753.
[102] C. Lee, K. B. Lee, J. Kim, *Appl. Phys. Lett.* **2000**, *77*, 2280-2282.
[103] K. M. Vaeth, C. W. Tang, *J. Appl. Phys.* **2002**, *92*, 3447-3453.
[104] V. V. Grushin, N. Herron, D. D. LeCloux, W. J. Marshall, V. A. Petrov, Y. Wang, *Chem. Commun.* **2001**, 1494-1495.
[105] Y. Wang, N. Herron, V. V. Grushin, D. LeCloux, V. Petrov, *Appl. Phys. Lett.* **2001**, *79*, 449-451.
[106] X. Gong, J. C. Ostrowski, D. Moses, G. C. Bazan, A. J. Heeger, *Adv. Funct. Mater.* **2003**, *13*, 439-444.
[107] A. J. Wilkinson, A. E. Goeta, C. E. Foster, J. A. G. Williams, *Inorg. Chem.* **2004**, *43*, 6513-6515.
[108] K. W. Lee, J. D. Slinker, A. A. Gorodetsky, S. Flores-Torres, H. D. Abruna, P. L. Houston, G. G. Malliaras, *Phys. Chem. Chem. Phys.* **2003**, *5*, 2706-2709.
[109] F. G. Gao, A. J. Bard, *J. Am. Chem. Soc.* **2000**, *122*, 7426-7427.
[110] M. Gratzel, *Nature* **2001**, *414*, 338-344.
[111] L. Spiccia, G. B. Deacon, C. M. Kepert, *Coord. Chem. Rev.* **2004**, *248*, 1329-1341.
[112] A. S. Polo, M. K. Itokazu, N. Y. Murakami Iha, *Coord. Chem. Rev.* **2004**, *248*, 1343-1361.
[113] K. Kalyanasundaram, M. Grätzel, *Coord. Chem. Rev.* **1998**, *177*, 347-414.
[114] P. Péchy, T. Renouard, S. M. Zakeeruddin, R. Humphry-Baker, P. Comte, P. Liska, L. Cevey, E. Costa, V. Shklover, L. Spiccia, G. B. Deacon, C. A. Bignozzi, M. Grätzel, *J. Am. Chem. Soc.* **2001**, *123*, 1613-1624.
[115] M. K. Nazeeruddin, A. Kay, I. Rodicio, R. Humphry-Baker, E. Mueller, P. Liska, N. Vlachopoulos, M. Graetzel, *J. Am. Chem. Soc.* **1993**, *115*, 6382-6390.
[116] M. K. Nazeeruddin, S. M. Zakeeruddin, J. J. Lagref, P. Liska, P. Comte, C. Barolo, G. Viscardi, K. Schenk, M. Graetzel, *Coord. Chem. Rev.* **2004**, *248*, 1317-1328.
[117] L. Hammarström, O. Johansson, *Coord. Chem. Rev.* **2010**, *254*, 2546 – 2559.

[118] D. I. Davies, *Aromatic heterocyclic chemistry*, Oxford University Press, Oxford; New York, **1991**.
[119] D. L. Jameson, J. K. Blaho, K. T. Kruger, K. A. Goldsby, *Inorg. Chem.* **1989**, *28*, 4312-4314.
[120] H. Fu, Y.-M. Cheng, P.-T. Chou, Y. Chi, *Mater. Today* **2011**, *14*, 472-479.
[121] L. Yang, F. Okuda, K. Kobayashi, K. Nozaki, Y. Tanabe, Y. Ishii, M.-a. Haga, *Inorg. Chem.* **2008**, *47*, 7154-7165.
[122] M. Loï, M. W. Hosseini, A. Jouaiti, A. De Cian, J. Fischer, *Eur. J. Inorg. Chem.* **1999**, *1999*, 1981-1985.
[123] A. Jouaiti, M. Loi, M. W. Hosseini, C. A. De, *Chem. Commun.* **2000**, 2085-2086.
[124] P. E. Fanta, *Chem. Rev.* **1964**, *64*, 613-632.
[125] J.-Y. Hu, X. Feng, N. Seto, J. H. Do, X. Zeng, Z. Tao, T. Yamato, *J. Mol. Struct.* **2013**, *1035*, 19-26.
[126] K. Suzuki, A. Seno, H. Tanabe, K. Ueno, *Synth. Met.* **2004**, *143*, 89-96.
[127] H.-J. You, Q. Du, Z.-Y. Zhang, C.-J. Li, J. Guan, B.-M. Wei, *Polycyclic Aromat. Compd.* **2012**, *32*, 589-599.
[128] T. Leermann, F. R. Leroux, F. Colobert, *Org. Lett.* **2011**, *13*, 4479-4481.
[129] H.-S. Kim, Y.-H. Kim, S.-K. Ahn, S.-K. Kwon, *Macromolecules* **2003**, *36*, 2327-2332.
[130] C. Wang, S. Rakshit, F. Glorius, *J. Am. Chem. Soc.* **2010**, *132*, 14006-14008.
[131] P. A. Bonvallet, C. J. Breitkreuz, Y. S. Kim, E. M. Todd, K. Traynor, C. G. Fry, M. D. Ediger, R. J. McMahon, *J. Org. Chem.* **2007**, *72*, 10051-10057.
[132] G. Venkataramana, S. Sankararaman, *Eur. J. Org. Chem.* **2005**, 4162-4166.
[133] B. P. Sullivan, J. M. Calvert, T. J. Meyer, *Inorg. Chem.* **1980**, *19*, 1404-1407.
[134] B. J. O'Keef, P. J. Steel, *Organometallics* **2003**, *22*, 1281-1292.
[135] T. Nagashima, T. Nakabayashi, T. Suzuki, K. Kanaizuka, H. Ozawa, Y.-W. Zhong, S. Masaoka, K. Sakai, M. Haga, *Organometallics* **2014**, *33*, 4893-4904.
[136] K. C. D. Robson, B. D. Koivisto, A. Yella, B. Sporinova, M. K. Nazeeruddin, T. Baumgartner, M. Grätzel, C. P. Berlinguette, *Inorg. Chem.* **2011**, *50*, 5494-5508.
[137] R. M. Silverstein, G. C. Bassler, T. C. Morrill, *Spectrometric Identification of Organic Compounds*, Wiley, **1991**.
[138] M. G. Loudon, *Organic Chemistry*, Fourth ed., Oxford University Press, **2002**.
[139] R. G. Pearson, *J. Am. Chem. Soc.* **1963**, *85*, 3533-3539.
[140] R. G. Pearson, J. Songstad, *J. Am. Chem. Soc.* **1967**, *89*, 1827-1836.
[141] Y. Chen, D. M. Ho, C. Lee, *J. Am. Chem. Soc.* **2005**, *127*, 12184-12185.
[142] C. Richardson, P. J. Steel, *Dalton Trans.* **2003**, 992-1000.
[143] P. J. Steel, E. C. Constable, *J. Chem. Soc., Dalton Trans.* **1990**, 1389-1396.
[144] G. Orellana, C. Alvarez Ibarra, J. Santoro, *Inorg. Chem.* **1988**, *27*, 1025-1030.
[145] A. J. Downard, G. E. Honey, P. J. Steel, *Inorg. Chem.* **1991**, *30*, 3733-3737.
[146] A. Almenningen, O. Bastiansen, S. Gundersen, S. Samdal, *Acta. Chem. Scand.* **1989**, *43*, 932-937.
[147] R. P. Thummel, Y. Jahng, *Inorg. Chem.* **1986**, *25*, 2527-2534.
[148] M. Gagliardo, D. J. M. Snelders, P. A. Chase, R. J. M. Klein Gebbink, G. P. M. van Klink, G. van Koten, *Angew. Chem. Int. Ed.* **2007**, *46*, 8558-8573.
[149] B. J. Coe, S. J. Glenwright, *Coord. Chem. Rev.* **2000**, *203*, 5-80.
[150] J. V. Quagliano, L. E. O. Schubert, *Chem. Rev.* **1952**, *50*, 201-260.
[151] B. Braïda, P. C. Hiberty, A. Savin, *J. Phys. Chem. A* **1998**, *102*, 7872-7877.

[152] T. H. Dunning, Jr., *J. Chem. Phys.* **1970**, *53*, 2823–2833.
[153] T. H. Dunning, Jr., P. Hay, *J. Mod. Theor. Chem.* **1977**, *3*, 1–27.
[154] D. Andrae, U. Haussermann, M. Dolg, H. Stoll, H. Preuss, *Theor. Chim. Acta* **1990**, *77*, 123–141.
[155] P. J. Hay, W. R. Wadt, *J. Chem. Phys.* **1985**, *82*, 270.
[156] M Cossi, V. Barone, B. Menucci, J. Tomasi, *Chem. Phys. Lett.* **1998**, *286*, 253–260.
[157] B. Menucci, J. Tomasi, *J. Chem. Phys.* **1997**, *106*, 5151–5158.
[158] S. Campagna, F. Puntoriero, F. Nastasi, G. Bergamini, V. Balzani, *Photochemistry and Photophysics of Coordination Compounds: Ruthenium, Vol. 280*, Springer Berlin Heidelberg, **2007**.
[159] J. V. Caspar, T. J. Meyer, *J. Am. Chem. Soc.* **1983**, *105*, 5583-5590.
[160] A. S. Coolidge, H. M. James, R. D. Present, *J. Chem. Phys.* **1936**, *4*, 193-211.
[161] F. Barigelletti, P. Belser, A. Von Zelewsky, A. Juris, V. Balzani, *J. Phys. Chem.* **1985**, *89*, 3680-3684.
[162] U. Resch-Genger, K. Rurack, *Pure Appl. Chem.* **2013**, *85*, 2005.
[163] K. Rurack, M. Spieles, *Anal. Chem.* **2011**, *83*, 1232-1242.
[164] J. N. Demas, D. G. Taylor, *Inorg. Chem.* **1979**, *18*, 3177-3179.
[165] G. A. Crosby, J. N. Demas, *J. Am. Chem. Soc.* **1970**, *92*, 7262-7270.
[166] R. P. Thummel, V. Hegde, Y. Jahng, *Inorg. Chem.* **1989**.
[167] H. J. Bolink, L. Cappelli, E. Coronado, P. Gaviña, *Inorg. Chem.* **2005**, *44*, 5966-5968.
[168] D. Maity, S. Das, S. Mardanya, S. Baitalik, *Inorg. Chem.* **2013**, *52*, 6820-6838.
[169] E. C. Constable, M. D. Ward, *J. Chem. Soc., Dalton Trans.* **1990**, 1405-1409.
[170] D. L. Jameson, L. E. Guise, *Tet. Lett.* **1991**, *32*, 1999-2002.
[171] P. Misra, C.-Y. Liao, H.-H. Wei, S. Mohanta, *Polyhedron* **2008**, *27*, 1185-1192.
[172] A. Gulyani, R. Srinivasa Gopalan, G. U. Kulkarni, S. Bhattacharya, *J. Mol. Struct.* **2002**, *616*, 103-112.
[173] W. Goodall, K. Wild, K. J. Arm, J. A. G. Williams, *J. Chem. Soc., Perkin Trans. 2* **2002**, 1669-1681.
[174] J. Chambers, B. Eaves, D. Parker, R. Claxton, P. S. Ray, S. J. Slattery, *Inorg. Chim. Acta* **2006**, *359*, 2400-2406.
[175] S. Yin, J. Zhang, H. Feng, Z. Zhao, L. Xu, H. Qiu, B. Tang, *Dyes and Pigments* **2012**, *95*, 174-179.
[176] Y. Tan, J. Gao, J. Yu, Z. Wang, Y. Cui, Y. Yang, G. Qian, *Dalton Trans.* **2013**, *42*, 11465-11470.
[177] J. D. Worley, *J. Chem. Educ.* **1993**, *70*, A89.
[178] W.-W. Yang, J. Yao, Y.-W. Zhong, *Organometallics* **2012**, *31*, 1035-1041.
[179] L. Wang, W.-W. Yang, R.-H. Zheng, Q. Shi, Y.-W. Zhong, J. Yao, *Inorg. Chem.* **2011**, *50*, 7074-7079.
[180] O. A. Borg, S. S. M. C. Godinho, M. J. Lundqvist, S. Lunell, P. Persson, *J. Phys. Chem. A* **2008**, *112*, 4470-4476.
[181] Y. Jahng, Y. H. Hong, A. F. M. M. Rahman, *J. Coord. Chem.* **2010**, *63*, 1774-1784.
[182] R. P. Thummel, Y. Jahng, *Inorg. Chem.* **1986**, *25*, 2527-2534.
[183] A. N. Singh, R. P. Thummel, *Inorg. Chem.* **2009**, *48*, 6459-6470.
[184] D. M. Klassen, C. W. Hudson, E. L. Shaddix, *Inorg. Chem.* **1975**, *14*, 2733-2736.
[185] M. L. Stone, G. A. Crosby, *Chem. Phys. Lett.* **1981**, *79*, 169-173.

[186] M. Beinhoff, W. Weigel, M. Jurczok, W. Rettig, C. Modrakowski, I. Brüdgam, H. Hartl, A. D. Schlüter, *Eur. J. Org. Chem.* **2001**, *2001*, 3819-3829.
[187] V. N. Kozhevnikov, O. V. Shabunina, D. S. Kopchuk, M. M. Ustinova, B. Koenig, D. N. Kozhevnikov, *Tetrahedron* **2008**, *64*, 8963-8973.
[188] S. J. Stoessel, J. K. Stille, *Macromolecules* **1992**, *25*, 1832-1837.
[189] F. Wu, E. Riesgo, A. Pavalova, R. A. Kipp, R. H. Schmehl, R. P. Thummel, *Inorg. Chem.* **1999**, *38*, 5620-5628.
[190] A. Juris, S. Campagna, V. Balzani, G. Gremaud, A. Von Zelewsky, *Inorg. Chem.* **1988**, *27*, 3652-3655.
[191] Z. Ye, B. Song, Y. Yin, R. Zhang, J. Yuan, *Dalton Trans.* **2013**, *42*, 14380-14383.
[192] R. Chinchilla, C. Nájera, *Chem. Rev.* **2007**, *107*, 874-922.
[193] J. D. Crowley, P. H. Bandeen, L. R. Hanton, *Polyhedron* **2010**, *29*, 70-83.
[194] S. Malashikhin, N. S. Finney, *J. Am. Chem. Soc.* **2008**, *130*, 12846-12847.
[195] V. Lozan, P. Y. Solntsev, G. Leibeling, K. V. Domasevitch, B. Kersting, *Eur. J. Inorg. Chem.* **2007**, *2007*, 3217-3226.
[196] M. Beley, J. P. Collin, R. Louis, B. Metz, J. P. Sauvage, *J. Am. Chem. Soc.* **1991**, *113*, 8521-8522.
[197] M. Jäger, R. J. Kumar, H. Görls, J. Bergquist, O. Johansson, *Inorg. Chem.* **2009**, *48*, 3228-3238.
[198] J. G. Rodríguez, T. Laparra, *Tetrahedron* **2009**, *65*, 2551-2555.
[199] T. Figueira-Duarte, S. Simon, M. Wagner, S. Druzhinin, K. Zachariasse, K. Müllen, *Angew. Chem. Int. Ed.* **2008**, *47*, 10175-10178.
[200] C. Cativiela, M. D. Diaz de Villegas, K. P. Gainza, *Synth. Commun.* **1987**, *17*, 165-172.
[201] A. Rilak, I. Bratsos, E. Zangrando, J. Kljun, I. Turel, Z. D. Bugarcic, E. Alessio, *Inorg. Chem.* **2014**, *53*, 6113-6126.
[202] M. M. R. Choudhuri, W. Kaim, B. Sarkar, R. J. Crutchley, *Inorg. Chem.* **2013**, *52*, 11060-11066.
[203] S. Li, C. N. Moorefield, C. D. Shreiner, P.-S. Wang, R. Sarkar, G. R. Newkome, *New J. Chem.* **2011**, *35*, 2130-2135.
[204] R. Lopez, S. A. Moya, C. Zuniga, M. Yanez, J. C. Bayon, P. Aguirre, *Appl. Organomet. Chem.* **2006**, *20*, 315-321.
[205] M.-P. Santoni, G. S. Hanan, B. Hasenknopf, A. Proust, F. Nastasi, S. Serroni, S. Campagna, *Chem. Commun.* **2011**, *47*, 3586-3588.
[206] D. Maity, C. Bhaumik, D. Mondal, S. Baitalik, *Inorg. Chem.* **2013**, *52*, 13941-13955.
[207] S. Braese, C. Gil, K. Knepper, V. Zimmermann, *Angew. Chem., Int. Ed.* **2005**, *44*, 5188.
[208] S. Cacchi, C. L. Cotet, G. Fabrizi, G. Forte, A. Goggiamani, L. Martín, S. Martínez, E. Molins, M. Moreno-Mañas, F. Petrucci, A. Roig, A. Vallribera, *Tetrahedron* **2007**, *63*, 2519-2523.
[209] B. Basu, B. Mandal, S. Das, P. Das, A. K. Nanda, *Beilstein J. Org. Chem.* **2008**, *4*, 53.